DRAFT SF 298

1. Report Date (dd-mm-yy) 10 Oct 94	2. Report Type conference proceedings	3. Dates covered (from... to) 29 June - 2 July 1994

4. Title & subtitle 4th International Symposium on Stratified Flows	5a. Contract or Grant # N00014--94-J-9018
	5b. Program Element #
6. Author(s) Emil Hopfinger, Bruno Voisin, Genevieve Chavand, editors	5c. Project # 5202
	5d. Task # EUR
	5e. Work Unit #
7. Performing Organization Name & Address Laboratoire des Ecoulements Geophysiques et Industriels, Institut de Mecanique de Grenoble, B.P. 53 X - 38041 Grenoble Cedex 9 France	8. Performing Organization Report #
9. Sponsoring/Monitoring Agency Name & Address Office of Naval Research Europe PSC 802 BOX 39 FPO AE 09499-0700	10. Monitor Acronym ONREUR
	11. Monitor Report #

12. Distribution/Availability Statement A

13. Supplementary Notes 4 volumes

14. Abstract

15. Subjec .ms

stratified flows

Security Classification of			19. Limitation of Abstract	20. # of Pages	21. Responsible Person (Name and Telephone #)
16. Report Unclassified	17. Abstract Unclassified	18. This Page Unclassified	Unlimited		Mike Shear, 011-44-0171-514-4921

Thursday – June 30 – Morning

8:45 – 9:30 **General Session**

Recent developments in second-moment closure for buoyancy-affected flows
T. J. Craft, N. Z. Ince, B. E. Launder

Time	**Session A3 ERCOFTAC TURBULENCE**	Time	**Session B3 INTRUSIONS, EXCHANGE FLOW**
9:30	Some similarity states of homogeneous stably-stratified turbulence – 42 *J. R. Chasnov*	9:30	Nonlinear effects in the unsteady, critical withdrawal of a stratified fluid – 23 *S. R. Clarke, J. Imberger*
9:45	A study of decaying stratified turbulence by a two-point closure EDQNM model and by direct numerical simulations – 241 *L. van Haren, C. Staquet, C. Cambon*	9:45	Density intrusions with large relative thickness – 57 *S. J. Wright, D. Paez-Rivadeneira*
10:00	Some current problems in stratified turbulent flows – 118 *C. W. van Atta*	10:00	Experimental and numerical investigation of laminar multilayer injection and withdrawal in a stratified environment – 177 *M. Priven, G. A. Bemporad, J. Atkinson* *H. Rubin*
10:15	Diffusion in the presence of stable stratification – 263 *J. R. Herring, Y. Kimura*	10:15	Axisymmetric intrusion in a stratified fluid – 256 *N. E. Kotsovinos*
10:30	On gradient-transport turbulence models for stably stratified shear flow – 12 *C. Kranenburg*	10:30	The influence of bottom topography on internal seiches in continuously stratified media – 107 *M. Münnich*
10:45 – 11:15	**COFFEE BREAK**		
11:15	Experiments on turbulence in stratified and rotating flows – 162 *P. F. Linden, B. M. Boubnov, S. B. Dalziel*	11:15	Stability and mixing of a two-layer exchange flow – 111 *G. Pawlak, L. Armi*
11:30	Measurements of a turbulent patch in a rotating, linearly stratified fluid – 179 *A. M. Folkard, P. A. Davies, H. J. S. Fernando*	11:30	Constricted flows from the Pacific to the Indian Ocean – 137 *D. Nof*
11:45	Direct numerical simulation of a vigorously heated low-Reynolds-number convective boundary layer – 198 *G. N. Coleman, J. H. Ferziger*	11:45	Exchange flow through a channel with an underwater sill – 157 *Z. Zhu, G. A. Lawrence*
12:00	Decay of turbulence in fluid with density fluctuations under the stable stratification – 47 *V. M. Emilianov, V. A. Frost*	12:00	Laboratory experiments on two-layer exchange through long straits – 60 *V. S. Maderich, A. I. Kulik, V. V. Oleksiuk*
12:15	Statistical approach of the wave-vortex interactions in stably stratified homogeneous turbulence – 246 *F. S. Godeferd, C. Cambon*	12:15	Hydraulic control analysis of an integrated gravity current model – 134 *G. Alendal*
12:30	Inverse cascade in stably-stratified rotating turbulence – 252 *O. Métais, P. Bartello, E. Garnier, J. J. Riley, M. Lesieur*	12:30	One kind of instability for a fluid with heavy particles – 194 *G. I. Burde*

12:45 – 2:00 **LUNCH**

Thursday – June 30 – Afternoon

2:00 – 3:30 **General Session**

Stably stratified flows in meteorology
J. C. R. Hunt, G. Shutts, S. Derbyshire

Direct and large eddy simulations of stratified homogeneous shear flows
U. Schumann

3:30 – 4:00 **Poster Presentation GP2**

1. Stratified flows in urban scale atmosphere – 123
S. Anquetin, C. Guilbaud, J.-P. Chollet
2. Transition to stable state and mixing of initially unstable continuously stratified fluid – 216
Ya. D. Afanasyev
3. Laboratory measurements of vortex evolution in a stratified shear flow – 186
D. P. Delisi
4. The motion of coherent structures – 238
Y. G. Morel, X. J. Carton
5. Multifractal analysis of coherent structures in tropical stratified troposphere – 255
Y. Chigirinskaya, D. Schertzer, S. Lovejoy, A. Lazarev, A. Ordanovich
6. Stability criterion of a stratified two-layer shear flow with hyperbolic-tangent velocity profile – 168
S. Nishida, S. Yoshida
7. Stability of vortices with nonstationary elliptical streamlines in stratified fluid – 227
E. Gledzer, V. Ponomarev
8. Numerical study of thermally stratified flow and its interaction with a conducting wall – 203
C. Péniguel
9. Microstructure simulation of suspended sediments – 224
P. D. Scarlatos, M. H. Kamel
10. Turbulent entrainment of solid particle suspensions in a two-layer fluid – 6
X. E. W. Wang

4:00. 4:30 **COFFEE BREAK AND POSTER VIEWING**

Session A4 ERCOFTAC
INSTABILITY AND TURBULENCE

4:30 Layer formation in stratified circular Couette flow – 226
B. M. Boubnov, E. B. Gledzer, E. J. Hopfinger

4:45 Stratified Taylor Couette flow: numerical simulation – 45
P. Orlandi

5:00 Streamwise vortices near a density interface – 71
N. Baba

5:15 Characteristics of turbulence by a breaking gravity wave below its critical level – 127
A. Dörnbrack, T. Gerz

5:30 Simulated and experimental two-layer flows past isolated two-dimensional obstacles – 259
P. F. Cummins, D. R. Topham, H. D. Pite

5:45 Mixing efficiency of decaying grid turbulence in a stratified fluid – 119
C. R. Rehmann, J. R. Koseff

6:00 Mathematical modeling of wind-induced turbulent flows in a stratified water body – 55
O. F. Vasiliev, V. I. Kvon, D. V. Kvon

6:15 The horizontal and vertical structure of the vorticity field in freely-decaying, stratified grid-turbulence – 197
A. M. Fincham, T. Maxworthy, G. R. Spedding

Session B4
JETS, PLUMES AND WAKES

4:30 Stability of a laterally confined round plume – 155
W.-T. Lee, J. H.-W. Lee

4:45 Buoyant surface discharges into unsteady ambient flows – 147
J. D. Nash, G. H. Jirka

5:00 Investigation of a bubble plume in a cross flow – 163
A. Müller, C. Hugi

5:15 Destratification of reservoir with bubble plume – 159
T. Asaeda, H. Ikeda, J. Imberger, V. T. Ca

5:30 Plume interaction above an outfall diffuser – 61
M. J. Davidson, I. R. Wood

5:45 Particle clouds in density stratified environments – 250
D. Luketina, D. Wilkinson

6:00 Internal waves, vortices and turbulence in a wake past a bluff body in a continuously stratified liquid – 29
Yu. D. Chashechkin

6:15 The structure and long-time evolution of bluff body wakes in a stable stratification – 196
G. R. Spedding, F. K. Browand, A. M. Fincham

7:15 – 8:15 **PRESENTATION OF COMPUTER CODES AND ROUNDTABLE ERCOFTAC DISCUSSIONS IN LEGI**

Recent Developments in Second-Moment Closure for Buoyancy-Affected Flows

by

T J Craft, N Z Ince and B E Launder
UMIST, Manchester, England

Abstract

The paper summarizes a new type of second-moment closure, more elaborate in form than earlier versions but designed to satisfy the two-component limit to which turbulence reduces at a wall or at a sharp density interface. Because they are intrinsically *realizable*, closures of this type are believed to offer the prospects of a wider range of applicability than earlier schemes. They may also be expected to display better numerical stability. Several illustrative applications are provided including the downward directed warm jet, the stratified mixing layer and buoyancy affected grid-turbulence decay. Extension of the scheme to near wall flows appears possible without introducing empirical 'wall-reflection' terms, at least in flows parallel to walls.

1 Introduction

Second-moment closure is widely regarded as being the most productive level at which to treat problems of turbulent flow if one seeks a model of wide applicability (with acceptable computational costs). The principal reason is that the generation terms in the second-moment equations appear in a form that requires no modelling. Nowhere is the truth of this assertion more evident than in buoyancy-modified turbulence where, with a few simple approximations applied to the unknown processes, predictions of complex phenomena can be achieved with surprising accuracy, Launder (1989).

However this "basic" modelling of second-moment closure (hereinafter referred to as *the* basic model) is known to have limitations, perhaps especially in free shear flows where flow conditions depart far from local equilibrium. In recent years there has, however, been a great deal of effort directed at improving second-moment closures focusing in particular on devising *realizable* models, Schumann (1977), Lumley (1978), that is to say, models which, by their construction, are unable to generate physically impossible - as opposed to merely incorrect - results. Prime among the various impossible results that are eliminated in a realizable model are negative values of any normal stress.

While the principles of realizability and the associated *two-component limit*, Lumley (1978), were known in the late 1970's, it was a decade before general modelling proposals were put forward and, only now, is a reasonably full picture beginning to emerge of the capabilities of these new approaches.

The focus of the present contribution is to review one of these new-generation approaches to closure and to give examples of some of the buoyant flow predictions that have been computed with it. In addition, we illustrate how important the treatment of triple moments are in certain stably stratified turbulent flows.

2 Modelling Proposals

2.1 The Exact Equations

The exact second-moment equations for the turbulent stresses and scalar fluxes may be written

$$\frac{D\overline{u_iu_j}}{Dt} = P_{ij} + G_{ij} + d_{ij} + \phi_{ij} - \varepsilon_{ij} \tag{1}$$

$$\frac{D\overline{u_i\theta}}{Dt} = P_{i\theta} + G_{i\theta} + d_{i\theta} + \phi_{i\theta} - \varepsilon_{i\theta} \tag{2}$$

The symbols P_{ij}, G_{ij}, $P_{i\theta}$ and $G_{i\theta}$ denote the generation terms due to shear, scalar gradient and buoyancy which are given in detail in Tables 1 and 2. Since each comprises second-moment and mean-field quantities, they may all be regarded as known or determinable quantities. The buoyant contribution to the turbulent scalar flux contains $\overline{\theta^2}$, the mean square scalar variance, and this, in turn, is determined from a closed form of its own transport equation

$$\frac{D\overline{\theta^2}}{Dt} = P_{\theta\theta} + d_\theta - 2\,\varepsilon_\theta \tag{3}$$

Again $P_{\theta\theta} = -2\overline{\theta u_j}\,\partial\Theta/\partial x_j$ can be regarded as known.

The Reynolds stress and scalar flux equations each contain three processes for which models must be devised: the non-dispersive pressure interactions, ϕ_{ij} and $\phi_{i\theta}$; the diffusion terms, d_{ij} and $d_{i\theta}$; and the dissipative terms ε_{ij} and $\varepsilon_{i\theta}$. For the last group it is convenient, following Lumley (1978), to assume local isotropy ($\varepsilon_{i\theta} = 0$; $\varepsilon_{ij} = 2/3\,\delta_{ij}\varepsilon$ where ε is the viscous dissipation rate of turbulent kinetic energy, k) absorbing shortcomings of this assumption into the modelling of ϕ_{ij} and $\phi_{i\theta}$. The diffusion terms can, as discussed later, be of vital importance when stable stratification leads to a general decay of turbulence. In many engineering and environmental flows, however, their influence is fairly weak and a gradient diffusion approximation is then both mathematically convenient and physically adequate. The authors' group commonly adopts the Daly-Harlow (1970) proposal:

$$\begin{aligned} d_{ij} &= \frac{\partial}{\partial x_k}\left[c_s\frac{k}{\varepsilon}\overline{u_ku_l}\,\frac{\partial\overline{u_iu_j}}{\partial x_l}\right] \\ d_{i\theta} &= \frac{\partial}{\partial x_k}\left[c_\theta\frac{k}{\varepsilon}\overline{u_ku_l}\,\frac{\partial\overline{u_i\theta}}{\partial x_l}\right] \\ d_\theta &= \frac{\partial}{\partial x_k}\left[c_\theta\frac{k}{\varepsilon}\overline{u_ku_l}\,\frac{\partial\overline{\theta^2}}{\partial x_l}\right] \end{aligned} \tag{4}$$

while still simpler schemes, employing an *isotropic* diffusion coefficient are used by many groups. Others adopt the so-called *algebraic second-moment*, ASM closures among whom Rodi (1982) has made extensive explorations of buoyancy driven flows. These economical approaches all work adequately when diffusion is of little importance in the overall second-moment budget.

Generation Terms (exact):

$$P_{ij} \equiv -\left\{\overline{u_j u_k}\frac{\partial U_i}{\partial x_k} + \overline{u_i u_k}\frac{\partial U_j}{\partial x_k}\right\} \qquad G_{ij} \equiv -\left\{\beta_i \overline{u_j \theta} + \beta_j \overline{u_i \theta}\right\}$$

Pressure-Strain Model:

$$\phi_{ij} = \phi_{ij1} + \phi_{ij2} + \phi_{ij3}$$

where

$$\begin{aligned}
\phi_{ij1} &= -c_1\epsilon\left(a_{ij} + c_1'\left(a_{ik}a_{jk} - {}^1\!/\!_3 A_2\delta_{ij}\right)\right) \\
\phi_{ij2} &= -0.6\left(P_{ij} - {}^1\!/\!_3\delta_{ij}P_{kk}\right) + 0.3\epsilon a_{ij}\left(P_{kk}/\epsilon\right) \\
&\quad - 0.2\left[\frac{\overline{u_k u_j}\,\overline{u_l u_i}}{k}\left(\frac{\partial U_k}{\partial x_l} + \frac{\partial U_l}{\partial x_k}\right) - \frac{\overline{u_l u_k}}{k}\left(\overline{u_i u_k}\frac{\partial U_j}{\partial x_l} + \overline{u_j u_k}\frac{\partial U_i}{\partial x_l}\right)\right] \\
&\quad - c_2\left[A_2\left(P_{ij} - D_{ij}\right) + 3a_{mi}a_{nj}\left(P_{mn} - D_{mn}\right)\right] \\
&\quad + c_2'\left\{\left(\frac{7}{15} - \frac{A_2}{4}\right)\left(P_{ij} - {}^1\!/\!_3\delta_{ij}P_{kk}\right)\right. \\
&\quad + 0.1\epsilon\left[a_{ij} - {}^1\!/\!_2\left(a_{ik}a_{kj} - {}^1\!/\!_3\delta_{ij}A_2\right)\right]\left(P_{kk}/\epsilon\right) - 0.05a_{ij}a_{lk}P_{kl} \\
&\quad + 0.1\left[\left(\frac{\overline{u_i u_m}}{k}P_{mj} + \frac{\overline{u_j u_m}}{k}P_{mi}\right) - {}^2\!/\!_3\delta_{ij}\frac{\overline{u_l u_m}}{k}P_{ml}\right] \\
&\quad + 0.1\left[\frac{\overline{u_l u_i}\,\overline{u_k u_j}}{k^2} - {}^1\!/\!_3\delta_{ij}\frac{\overline{u_l u_m}\,\overline{u_k u_m}}{k^2}\right]\left[6D_{lk} + 13k\left(\frac{\partial U_l}{\partial x_k} + \frac{\partial U_k}{\partial x_l}\right)\right] \\
&\quad \left. + 0.2\frac{\overline{u_l u_i}\,\overline{u_k u_j}}{k^2}\left(D_{lk} - P_{lk}\right)\right\} \\
\phi_{ij3} &= -\left(\frac{4}{10} + \frac{3A_2}{80}\right)\left(G_{ij} - {}^1\!/\!_3\delta_{ij}G_{kk}\right) + \frac{1}{4}a_{ij}G_{kk} \\
&\quad + \frac{3}{20}\left(\beta_i\frac{\overline{u_m u_j}}{k} + \beta_j\frac{\overline{u_m u_i}}{k}\right)\overline{u_m\theta} - \frac{1}{10}\delta_{ij}\beta_k\frac{\overline{u_m u_k}}{k}\overline{u_m\theta} \\
&\quad - \frac{1}{4}\beta_k\left(\frac{\overline{u_k u_i}}{k}\overline{u_j\theta} + \frac{\overline{u_k u_j}}{k}\overline{u_i\theta}\right) + \frac{1}{20}\delta_{ij}\beta_k\frac{\overline{u_m u_n}\,\overline{u_m u_k}}{k^2}\overline{u_n\theta} \\
&\quad - \frac{1}{8}\left[\frac{\overline{u_m u_j}}{k}\overline{u_i\theta} + \frac{\overline{u_m u_i}}{k}\overline{u_j\theta}\right]\frac{\overline{u_m u_k}}{k}\beta_k + \frac{1}{8}\left[\frac{\overline{u_k u_i}\,\overline{u_m u_j}}{k^2} + \frac{\overline{u_k u_j}\,\overline{u_m u_i}}{k^2}\right]\beta_k\overline{u_m\theta} \\
&\quad - \frac{3}{40}\left(\beta_i\frac{\overline{u_m u_j}}{k} + \beta_j\frac{\overline{u_m u_i}}{k}\right)\frac{\overline{u_m u_n}}{k}\overline{u_n\theta} + \frac{1}{4}\beta_k\frac{\overline{u_m u_k}\,\overline{u_i u_j}}{k^2}\overline{u_m\theta}
\end{aligned}$$

Table 1 : Exact generation terms and pressure-strain model in $\overline{u_i u_j}$ equations

2.2 Modelling Non-Dispersive Pressure Interactions.

The pressure terms are traditionally decomposed into turbulence-turbulence interactions (ϕ_{ij1}, $\phi_{i\theta 1}$), mean strain contributions (ϕ_{ij2}, $\phi_{i\theta 2}$) and buoyant effects (ϕ_{ij3}, $\phi_{i\theta 3}$). The basic model, alluded to in the Introduction, adopts Rotta's (1951) linear return-to-isotropy model for ϕ_{ij1}:

$$\phi_{ij1} = -c_1 \varepsilon a_{ij}$$

where a_{ij} is the stress anisotropy tensor $(\overline{u_i u_j} - 1/3\, \delta_{ij} \overline{u_k u_k})/k$. Recent closures, however, mainly adopt non-linear representations in which the coefficients are functions of one or both of the independent stress invariants, Lumley (1978). The form adopted in the present computations, Cresswell et al (1989), Craft and Launder (1989) is given in Table 1. Its form was arrived at by reference to *non*-buoyant flows and in particular satisfies the two-component limit wherein $\phi_{\alpha\alpha 1}$ and $\phi_{\alpha\theta 1}$ vanish if $\overline{u_\alpha^2} = 0$. This is achieved by way of the "flatness parameter" $A = 1 - 9/8\,(A_2 - A_3)$ where $A_2 = a_{ij}\, a_{ji}$; $A_3 = a_{ij}\, a_{jk}\, a_{ki}$ are the second and third invariants of the anisotropy stress tensor. The quantity A has the important property that it always vanishes in two-component turbulence (Lumley, 1978). The specific forms adopted for c_1 and c_1' are:

$$c_1 = (3.75 A_2^{1/2} + 1)A \quad ; \quad c_1' = 0.7$$

The formulation for $\phi_{i\theta 1}$, given in Table 2, is analogous in form. Note the inclusion of the scalar:dynamic time-scale ratio, $R = c_\theta k/1/2\overline{\theta^2}\varepsilon$ and the final term in $\phi_{i\theta 1}$ that involves the mean scalar gradient, $\partial\Theta/\partial x_j$, a practice first introduced by Jones & Musonge (1983) to handle flows where the normalized generation rates of k and $\overline{\theta^2}$ were greatly different. Although largely empirical, ϕ_{ij1} and $\phi_{i\theta 1}$ have both been fixed by reference to *non*-buoyant flows.

Mean strain influences on ϕ_{ij} and $\phi_{i\theta}$ are arrived at by first making the usual assumption (Rotta, 1951) that

$$\begin{aligned} \phi_{ij2} &= \left(a_{\ell\ j}^{m\ i} + a_{\ell\ i}^{m\ j}\right) \frac{\partial U_\ell}{\partial x_m} \\ \phi_{i\theta 2} &= b_{\ell\ i}^{m} \frac{\partial U_\ell}{\partial x_m} \end{aligned} \tag{5}$$

The tensor $a_{\ell j}^{mi}$ is then expressed in ascending powers of the stress-anisotropy tensor. The first approach of this type was made by Launder et al (1972) who retained only terms linear in a_{ij}. More recent attempts have retained non-linear formulations and the additional free coefficients that result are determined, mainly, by requiring that the pressure-strain process should fall to zero if u_2 (say) should vanish, i.e.:

$$a_{\ell\ 2}^{m\ 2} = 0 \quad if \quad a_{22} = -2/3$$

For the corresponding term in the heat-flux equation, the recommended route (Craft & Launder, 1989) is to require:

$$2\frac{\partial U_m}{\partial x_\ell}\, b_{m\ 2}^{\ell} = \overline{u_\ell \theta}\frac{\partial U_2}{\partial x_\ell}$$

in the two-component limit. This leads, with other constraints associated with homogeneous turbulence, to the representation shown in Table 2.

Generation Terms (exact):

$$P_{i\theta} \equiv -\left(\overline{u_i u_j}\frac{\partial \Theta}{\partial x_j} + \overline{u_j\theta}\frac{\partial U_i}{\partial x_j}\right) \qquad G_{i\theta} \equiv -\beta_i\overline{\theta^2}$$

Pressure-Scalar Gradient Model:

$$\phi_{i\theta} = \phi_{i\theta 1} + \phi_{i\theta 2} + \phi_{i\theta 3}$$

where

$$\begin{aligned}
\phi_{i\theta 1} \;=\;& -1.7\left[1 + 1.2\,(A_2 A)^{1/2}\right] R^{1/2}\frac{\epsilon}{k}\left[\overline{u_i\theta}\,(1 + 0.6A_2) - 0.8a_{ik}\overline{u_k\theta}\right. \\
& \left. + 1.1a_{ik}a_{kj}\overline{u_j\theta}\right] - 0.2A^{1/2}Rka_{ij}\frac{\partial \Theta}{\partial x_j} \\
\phi_{i\theta 2} \;=\;& 0.8\overline{u_k\theta}\frac{\partial U_i}{\partial x_k} - 0.2\overline{u_k\theta}\frac{\partial U_k}{\partial x_i} + {}^1\!/_6\frac{\epsilon}{k}\overline{u_i\theta}(P_{kk}/\epsilon) \\
& - 0.4\overline{u_k\theta}a_{il}\left(\frac{\partial U_k}{\partial x_l} + \frac{\partial U_l}{\partial x_k}\right) \\
& + 0.1\overline{u_k\theta}a_{ik}a_{ml}\left(\frac{\partial U_m}{\partial x_l} + \frac{\partial U_l}{\partial x_m}\right) \\
& - 0.1\overline{u_k\theta}\left(a_{im}P_{mk} + 2a_{mk}P_{im}\right)/k \\
& + 0.15a_{ml}\left(\frac{\partial U_k}{\partial x_l} + \frac{\partial U_l}{\partial x_k}\right)\left(a_{mk}\overline{u_i\theta} - a_{mi}\overline{u_k\theta}\right) \\
& - 0.05a_{ml}\left[7a_{mk}\left(\overline{u_i\theta}\frac{\partial U_k}{\partial x_l} + \overline{u_k\theta}\frac{\partial U_i}{\partial x_l}\right) - \overline{u_k\theta}\left(a_{ml}\frac{\partial U_i}{\partial x_k} + a_{mk}\frac{\partial U_i}{\partial x_l}\right)\right] \\
\phi_{i\theta 3} \;=\;& {}^1\!/_3\beta_i\overline{\theta^2} - \beta_k\overline{\theta^2}a_{ik}
\end{aligned}$$

Table 2 : Exact generation terms and pressure-scalar flux model in $\overline{u\beta}$ equations

In fact, the model for ϕ_{ij2} is intimidatingly bulky and, in all the free-flow examples quoted, it has been simplified by setting c_2' to zero (with $c_2 = 0.6$). However, very recently (Launder & Li, 1994) it has been discovered that retention of c_2' (set equal to 0.6 with c_2 reduced to 0.55) enables both free flows and flows near walls to be predicted satisfactorily without the need for the "wall reflection" terms that are habitually employed in computing near-wall flows. It is unlikely that this change would have had any significant effect in the prediction of the free flow examples quoted hereunder which employed the original values for the two empirical coefficients.

The buoyant terms in the pressure containing correlations are obtained in precisely the same way as the mean-strain effects. The resultant formulations, obtained by Craft (1991) as a fragment of his PhD study and first employed by Cresswell et al (1989), appear in Tables 1 and 2. Note that the buoyant contribution to ϕ_{ij} is very long but, as with the much shorter term in $\phi_{i\theta}$, it contains *no* empirically tunable coefficients. These models of the 'rapid' parts of the non-dispersive pressure fluctuations are far more complex than the usually adopted basic-model formulations:

$$\phi_{ij2} + \phi_{ij3} = -0.6\left[P_{ij} + G_{ij} - \frac{1}{3}\delta_{ij}\left(P_{kk} + G_{kk}\right)\right]$$

$$\phi_{i\theta 2} + \phi_{i\theta 3} = -0.5\left[-\overline{u_i u_j}\frac{\partial \Theta}{\partial x_j} + G_{i\theta}\right]$$

The comparisons will attempt to show that the greater complexity brings a considerably greater width of applicability.

2.3 Determining the Dissipation Rates

The kinetic energy dissipation rate, ε, remains as an unknown and is found from an equation identical in overall form to that of the Basic Model:

$$\frac{D\varepsilon}{Dt} = \frac{\partial}{\partial x_k}\left[\left(c_\varepsilon \frac{k}{\varepsilon}\overline{u_k u_\ell} + \nu\delta_{k\ell}\right)\frac{\partial \varepsilon}{\partial x_\ell}\right] + \frac{c_{\varepsilon 1}}{2}\left(P_{kk} + G_{kk}\right)\frac{\varepsilon}{k} - c_{\varepsilon 2}\frac{\varepsilon^2}{k} \qquad (6)$$

The difference from earlier forms, however, is that the coefficient $c_{\varepsilon 2}$ is taken as a function of the stress invariants and $c_{\varepsilon 1}$ takes a lower value than formerly:

$$c_{\varepsilon 1} = 1.0 \qquad c_{\varepsilon 2} = \frac{1.92}{1 + 0.7 A_2^{1/2} A_{25}}$$

$$\text{where } A_{25} = max\,(A,\ 0.25)$$

The above change to $c_{\varepsilon 2}$ goes a significant way to reducing the plane/round jet anomaly and, moreover, to making predictions of weak turbulent shear flows far more sensitive to initial conditions than hitherto - in line with experiment. The enforced reduction of $c_{\varepsilon 1}$ to unity to accommodate that made to $c_{\varepsilon 2}$ brings the substantial side benefit of enabling the effect of buoyant damping on the dissipation rate to be approximately accommodated. Examples will be provided later.

The scalar dissipation rate may also be obtained via a transport equation (see, for example, Craft & Launder, 1989) and, in the long term, that is what we would expect to see employed. However, given the exploratory form of such model equations, in computing buoyant flows, our present experience is that one can do better by obtaining ε_θ via ε by means of the algebraic connection

$$\varepsilon_\theta = \frac{R}{2} \frac{\overline{\theta^2}\varepsilon}{k}$$

where the time-scale ratio R is related to the heat-flux correlation coefficient by

$$R = \frac{3}{2}(1 + A_{2\theta}) \quad ; \quad A_{2\theta} = \overline{u_i\theta}\,\overline{u_i\theta} \,/\, (k\,\overline{\theta^2}) \tag{7}$$

3 Some Applications of the Model to Buoyant Flows

The model presented in §2 was first applied by Craft (1991) to consider homogeneous, horizontal, stably stratified flow that had been created by passing a uniform flow past a screen of differentially heated horizontal rods, Webster (1964), Young (1975). The computations shown in Fig 1 have assumed local equilibrium (i.e. $1/2\,(P_{kk} + G_{kk}) = \varepsilon$) which is what has traditionally been adopted for this test case (though it may have been some way from the truth). Evidently, as the gradient Richardson number, R_i, increases, the shear-stress correlation coefficient decays, the turbulent Prandtl number increases and the horizontal heat-flux correlation decreases moderately. The non-linear model reproduces these measured responses at least as accurately as the Basic Model[1] even though the two empirical coefficients in the buoyant terms of the latter model were optimized by reference to these data. The non-linear scheme, in contrast, has no adjustable coefficients in the buoyant pressure-strain model.

We turn now to *inhomogeneous* cases of self-preserving free shear flows: the plane and axisymmetric vertical, buoyantly-driven plumes. Their spreading behaviour, obtained by Cresswell et al (1989), is summarized in Table 3; for comparison the behaviour of the plane and axisymmetric jets in stagnant surroundings is also given. Comparisons are drawn both with experiments and with predictions obtained with the Basic Model. What is evident is that a far better overall agreement is achieved with the new invariant-dependent closure than with the Basic Model. Even where discrepancies remain with experimental data, as in the case of axisymmetric flows, these are both smaller in magnitude than with the Basic Model and show a consistent behaviour across both the plumes and the jets.

Table 3 Rate of growth of half-width for some self-preserving free shear flows

Flow	Basic Model	Recommended experimental values	New Model
Plane plume	0.078	0.120	0.118
Round plume	0.088	0.112	0.122
Plane jet	0.100	0.110	0.110
Round jet	0.105	0.093	0.101

---

[1] An extensive review of the capabilities of the Basic Model in buoyant flow has been given by Launder (1989).

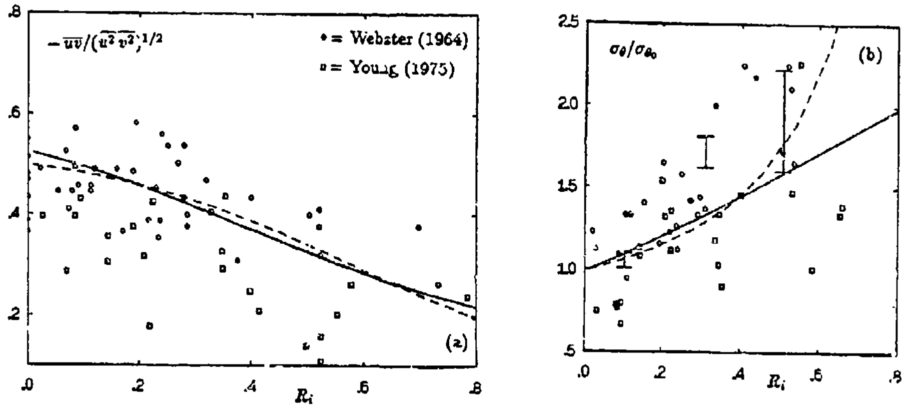

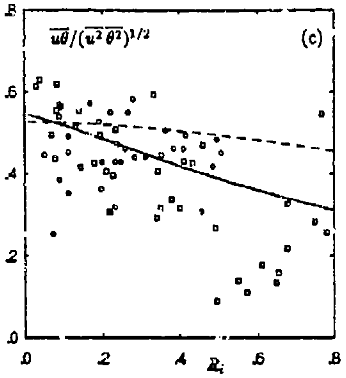

Fig 1

Second-moment sensitivity to buoyant stratification in nominally horizontal, equilibrium, homogeneous shear flow:
Symbols: experiments, o Webster (1964); □ Young (1975);
Lines: predictions, Craft (1991):
—— Non-linear model
- - - - Basic Model
a) Shear stress correlation coefficient
b) Normalized turbulent Prandtl number
c) Correlation coefficient of horizontal heat flux

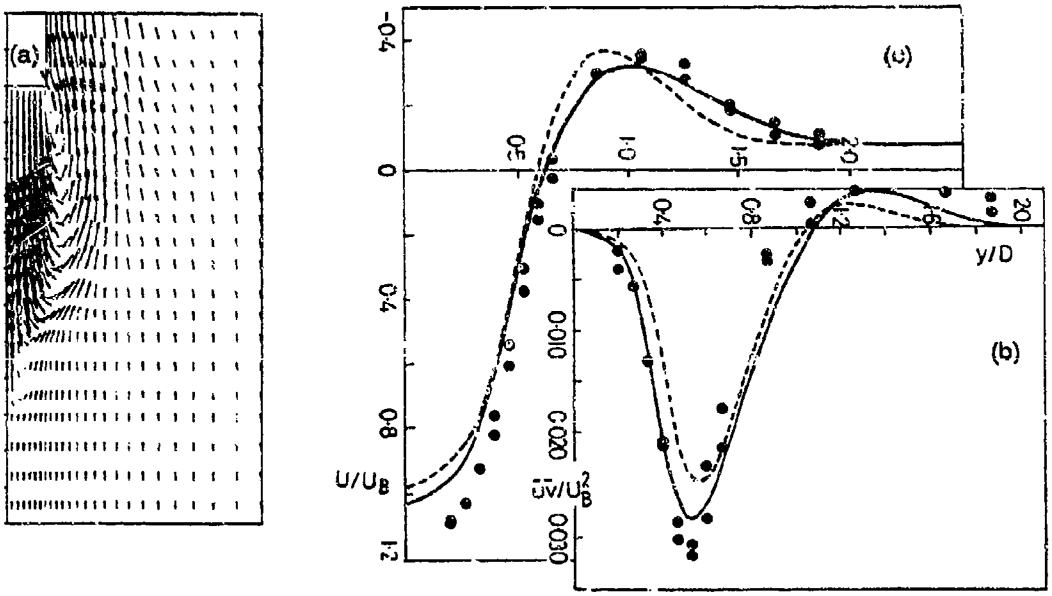

Fig 2 Axisymmetric downward directed buoyant jet, Cresswell et al (1989)
a) Computed velocity vector plot
b) Turbulent shear stress at x/D = 1.0
c) Mean velocity profile at x/D = 1
Symbols, experiment; lines predictions:
——— non-linear model; - - - - Basic Model

The same workers extended their study to the case of a hot jet discharged vertically downwards into a cold water environment moving upwards at less than 2% of the jet velocity. The penetration length, of course, is crucially dependent on mixing. Figure 2a is a vector velocity plot in the vicinity of discharge showing the reversal in the jet direction while Fig 2b and 2c present respectively the shear stress and resultant mean velocity profiles. Evidently, the new model does significantly better in capturing the effects of buoyancy and shear in this quite complex recirculating flow. Cresswell et al (1989) were, moreover, agreeably surprised to report that, because the new model respected realizability, it led to a faster rate of numerical convergence and to a reduction of some 30% in computing time per run relative to the Basic Model, despite the algebraic complexity of the model itself.

A more recent application of the model, which focuses especially on the buoyant terms has been reported by Van Haren (1992). The model is believed to be the same as that presented in §2 save that $c_{\varepsilon 1}$ and $c_{\varepsilon 2}$ took the constant values 1.44 and 1.76 and a transport equation was solved for ε_θ. Van Haren considered the decay, in the absence of mean strain, of stably stratified turbulence and, in particular, the oscillatory pattern that is known to be established during the decay due to reversals in sign of the vertical heat flux. Van Haren generated 2-point EDQNM results of such a flow and then tested how well various single-point closures did in reproducing the behaviour. Figure 3 compares the time history of the normalized vertical heat flux $\overline{w\theta}/(\overline{w^2}\,\overline{\theta^2})^{1/2}$ versus normalized time where N is the Brünt-Väisälä frequency. Quite clearly, the "extended" *k*-ε model and a simple second-moment closure[2] shown in the left-hand figure exhibit a significantly too long period and a too rapid decay of the heat flux compared with the EDQNM data. In contrast the new formulation shown in Fig 3b is rather successful at mimicking the EDQNM results.

It is perhaps worth remarking that the present authors, in a short unpublished internal study (Craft & Launder, 1990) had earlier looked at the same problem (in this case, the focus was measurements by Itsweire et al, 1986) and reproduced the oscillatory behaviour of the scalar flux but not the correct oscillatory period nor the amplitude decay rate. Van Haren's results may indicate that we should simply have persevered longer or perhaps that the different treatment of the dissipation rates in the two studies may have been responsible for the difference. What should not be overlooked in considering the reason for differences, however, is that, unequivocally, second-moment closure *can* reproduce an oscillatory behaviour in the scalar flux which, probably, most workers would have said was a signal of the collapse of turbulence into wave-like oscillations - and thus outside the scope of conventional turbulence modelling.

A further application of the model to a free shear flow is the stably-stratified saline mixing layer of Uitenbogaard (1988). This is a test case that clearly brings out the superiority of second-moment over eddy viscosity modelling. Fig 4 compares the authors' predictions with the present closure with those of the standard *k*-ε model. Evidently, because eddy viscosity schemes are insufficiently sensitive to buoyant damping, mixing proceeds at far too great a rate so that, by the final station, a nearly uniform salinity level is predicted. The second-moment predictions are far better: both those with the proposed closure and those generated by the Basic Model that are omitted for clarity. However, it appears that, even at second-moment level, rather too rapid mixing is taking place, as evidenced by the

---

[2] No details were provided of this scheme but it was presumably the 'basic' or the (in this case) very similar 'quasi-isotropic' model frequently used by the group at the ECL.

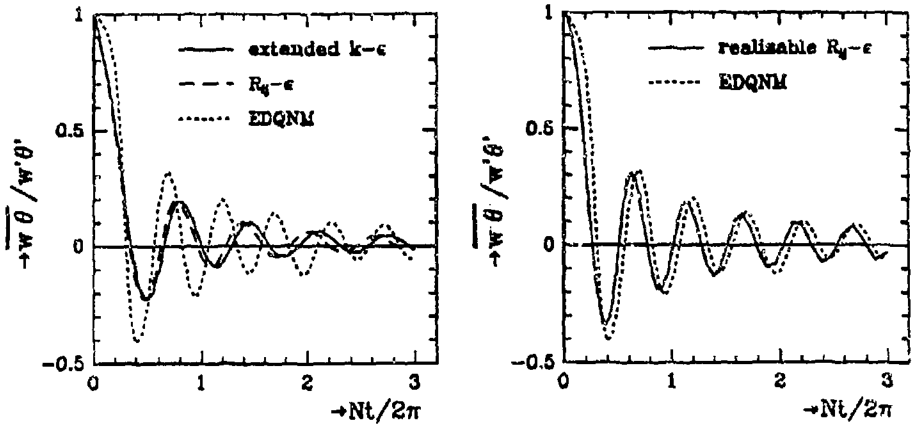

Fig 3 Development of oscillatory waves in stably-stratified grid turbulence, from Van Haren (1992). (Note: in right hand graph "realisable R_{ij} - ε" refers to non-linear model; in left hand graph "R_{ij} - ε" refers either to basic model or a similar linear model)

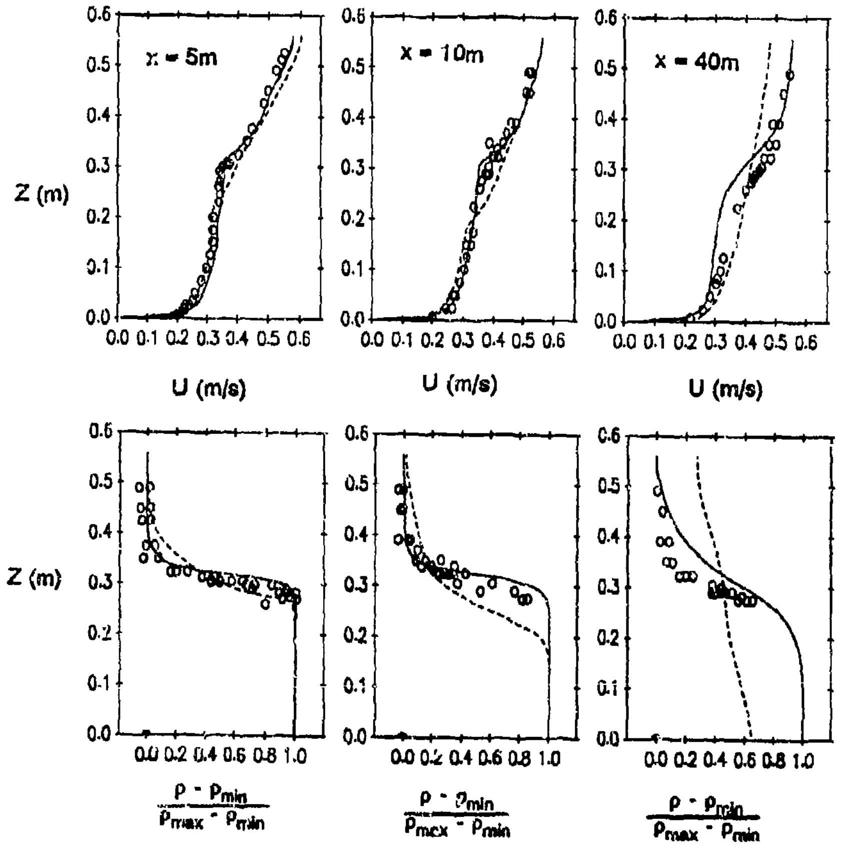

Fig 4 Development of horizontal stably-stratified saline-mixing layer: Experiments (Symbols), Uittenbogaard (1988): Computations (present study):

—— non-linear second-moment closure

- - - - k-ε EVM

a) Mean velocity profiles;

b) Mass fraction of salt water

predicted mean salinity profile being rather too broad at the downstream station[3]. It was suspected that the problem arose from modelling diffusive transport: in these strongly stratified flows one may expect buoyant influences on the transport processes to be significant (see, for example, the work of Zeman & Lumley, 1979, on the stably stratified atmospheric boundary layer). No such effects are incorporated in the GGDH. In fact, the diffusion of $\overline{\theta^2}$ turns out to be the most crucial process for $\overline{\theta^2}$ appears in the budget of the vertical salinity flux, $\overline{w\theta}$, which, in turn, enters the buoyant term in the $\overline{w^2}$ equation. Accordingly, for illustration, we have just aimed at improving the model of $\overline{u_i\theta^2}$. For this purpose we have essentially applied the same approximations to $\overline{u_i\theta^2}$ as are made in the Basic Model of the second moments. In addition, convective transport is discarded while the fourth-rank products are expressed in terms of the second by the Millionshtchikov (1941) hypothesis. The resultant model equation is

$$\overline{u_i\theta^2} = -c'_\theta\frac{k}{\varepsilon}\left[\left(\overline{u_i u_k} - \frac{3}{4}\frac{\overline{\theta^2}\beta_i}{\varepsilon_\theta}\overline{\theta u_k}\right)\frac{\partial\overline{\theta^2}}{\partial x_k} + 2\overline{\theta u_k}\frac{\partial\overline{u_i\theta}}{\partial x_k}\right] \tag{8}$$

where the coefficient c'_θ takes the value 0.11.

Key aspects of the computations with this more complete model for $\overline{u_i\theta^2}$ appear in Fig 5. A somewhat smaller and less dispersed level of $\overline{\theta^2}$ is predicted and this leads to a substantially modified profile of $\overline{w\theta}$ and to the somewhat steeper mean profile of salinity concentration which accords better with the measured data. This result suggests that a more general and comprehensive treatment of second-moment transport processes in highly stratified flow may be warranted, since the additional computational cost is not significant.

Attention is now turned to near-wall flows. Applications to date have been especially concerned with mimicking the varying effects of shear and viscosity as the wall is approached. It has been found, Launder & Li (1994), that when both c_2 and c'_2 in the model of ϕ_{ij2} are retained and appropriate low-Reynolds-number forms are introduced to the dissipation rate equations, it is possible to predict complex shear flows up to the wall itself without introducing wall-damping effects. Figure 6 shows, for example, predictions of flow in a square sectioned duct. The well-known bulging of the contours towards the corners is due to the secondary flow which in turn, arises from the source of streamwise vorticity associated with gradients of the Reynolds stresses lying in the cross-sectional plane of the duct. The level of agreement achieved with the closure is far better than that with the Basic Model, despite the fact that that scheme employs wall-proximity corrections to ϕ_{ij}

To date no applications of precisely the above model have been reported for force-field affected flows. However, in an intermediate exploration, Launder and Tselepidakis (1994) have applied an earlier version of the model to flow in a two-dimensional channel rotating in orthogonal mode. The modelling details are not reproduced here but, briefly, because c'_2 was taken as zero (with $c_2 = 0.6$), it was necessary to incorporate a wall-reflection correction, albeit one much weaker than for the Basic Model. The Coriolis force that acts on the Reynolds stress field in this case creates a flow similar to, if not identical with, that of a horizontal, gravitationally modified heated channel flow: on the suction side of the duct

---

[3] The fact that the predicted profiles lie above the measurements is believed to be due to weak three dimensionality in the experiment. Comparisons between measurement and predictions should thus ignore this displacement.

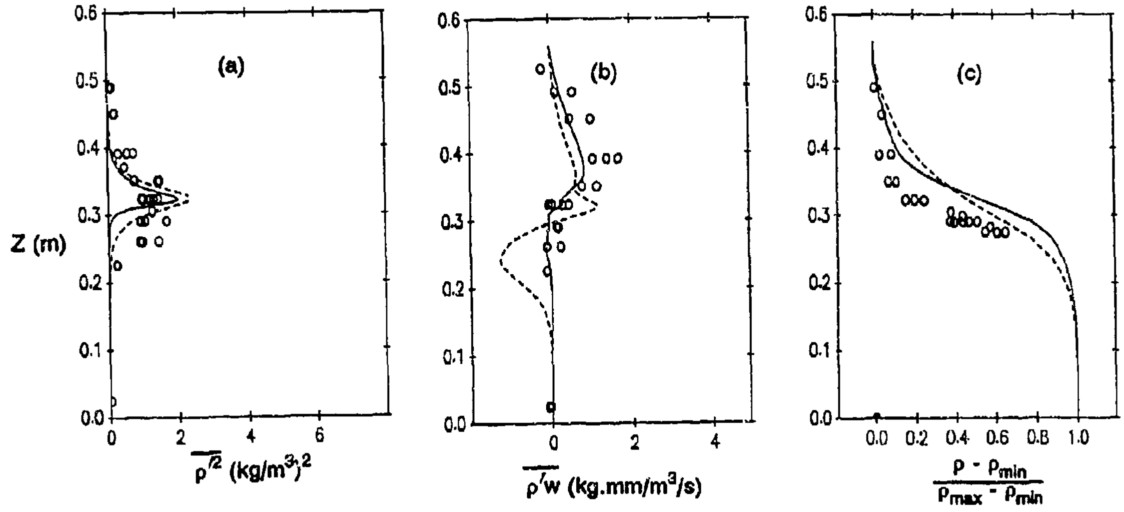

Fig 5 Effect of refining diffusion model in prediction of stably stratified mixing layer (present study):
Symbols - Uitenbogaard (1988), measurements;
---- GGDH diffusion of $\overline{\theta^2}$; ___ eq (8) for diffusion
a) $\overline{\theta^2}$ at 10 m downstream b) vertical heat flux $\overline{w\theta}$ at 10 m downstream
c) mean salinity profile at 40 m downstream

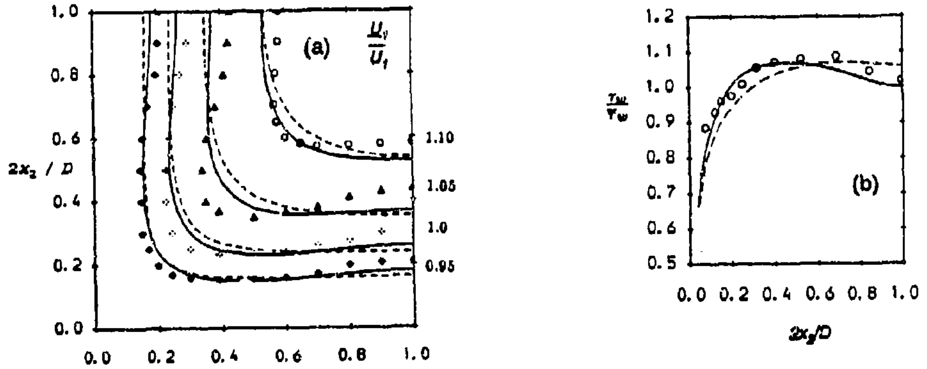

Fig 6

Prediction of turbulence-driven secondary flow in a square duct without 'wall reflection' agencies, from Launder & Li (1994):
Symbols: experiments, Gessner & Emery (1981);
Lines: second-moment predictions:
—— non-linear model (without 'wall reflection')
---- basic model, including wall correction
a) Axial velocity contours;
b) Perimetral wall stress

Fig 7

Prediction of flow in plane channel rotating in orthogonal mode. Symbols: DNS results, Kristoffersen and Andersson (1990);
Lines: second-moment closure predictions using low-Reynolds-number formulations:
---- Kristoffersen et al (1990)
(using Launder-Shima, 1989 model)
—— non-linear model, Launder & Tselepidakis

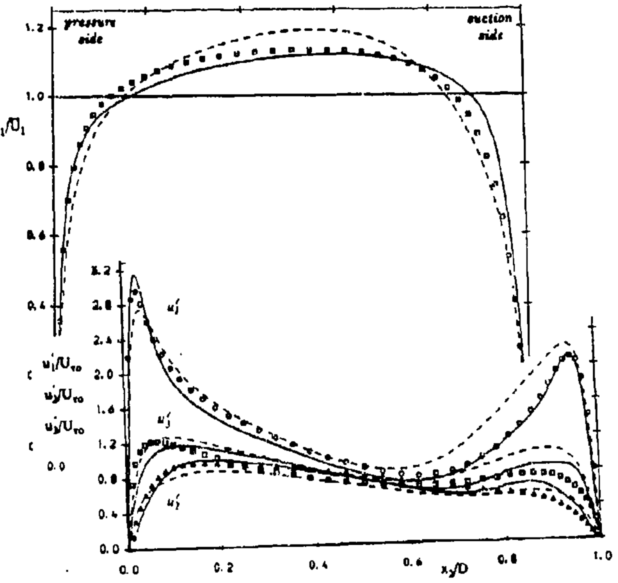

turbulent transport is damped by the rotation while on the pressure side it is augmented, at least for the moderate rotation rates considered here. Comparisons are drawn in Fig 7 between the second-moment computations and the direct numerical simulations of Kristoffersen and Andersson (1990). Also included are predictions obtained by Kristoffersen et al (1990) using the earlier model of Launder and Shima (1989), essentially a low-Reynolds-number version of the Basic Model. We see that both models capture quite well the strong asymmetry of the Reynolds stresses that arises from the rotation and the associated strongly asymmetric mean velocity field. Overall, however, the new scheme achieves decidedly the more complete agreement with the direct numerical simulation. In contrast, any eddy viscosity model would show *no* effect of rotation for this flow since the extra generation in the $\overline{u_2^2}$ component, normal to the wall, is exactly balanced by an equal and opposite source in the streamwise normal stress ($\overline{u_1^2}$) and consequently there is no net augmentation of the generation rate of turbulence energy.

Finally, it is of interest to note that a group from the LNH of the EDF Research Laboratories in Paris has begun to apply the new approach to tackle some of the physically very complex problems of sediment transport, which are, of course, intrinsically affected by buoyant modifications to turbulent mixing (Laurence et al, 1993). While the results are only preliminary in character they predict alterations in the viscous layer thickness due to the sediment loading which seem to be broadly in line with experiments.

4 Concluding Remarks

The paper has reported results obtained with a new form of second-moment closure designed to satisfy the two-component limit. Turbulence approaches this limit at a wall and in other circumstances where turbulent fluctuations in one direction are strongly damped. This strategy is naturally appealing for the prediction of buoyancy-affected flows because there a stabilizing gravitational field can, indeed, produce a quasi two-component fluctuating velocity field.

At present the model requires more extensive testing and, doubtless, refinement. There seems little doubt, however, that the main elements of the modelling set out in this paper, including proposals for modelling second-moment transport, give closure schemes that achieve a significantly wider range of applicability than those founded on the Basic Model.

Nomenclature

a_{ij}	dimensionless anisotropic stress, $(\overline{u_iu_j} - 1/3\,\delta_{ij}\,\overline{u_ku_k})/k$
$a_{\ell j}^{ml}$	fourth rank tensor in mean-strain part of pressure-strain model
A	Lumley's flatness parameter
A_2, A_3	invariants of Reynolds stress
$A_{2\theta}$	heat flux invariant
$b_{\ell i}^{m}$	third rank tensor in mean-strain part of pressure-scalar gradient model
c's	coefficients in turbulence models
d	diffusive transport (subscript denotes diffused quantity)
D	diameter or distance between parallel planes
g_i	gravitational acceleration
G_{ij}	buoyant generation rate of $\overline{u_iu_j}$

G_{ij}	buoyant generation rate of $\overline{u_iu_j}$
$G_{i\theta}$	buoyant generation rate of $\overline{u_i\theta}$
k	turbulent kinetic energy, $\overline{u_k^2}/2$
P_{ij}	shear-generation rate of $\overline{u_iu_j}$
$P_{i\theta}$	generation rate of $\overline{u_i\theta}$ by mean gradients of U_i and Θ
$P_{\theta\theta}$	generation rate of $\overline{\theta^2}$
R_i	gradient Richardson number
u_i, U_i	fluctuating and mean velocity in direction x_i
$\overline{u_iu_j}$	kinematic Reynolds stress
$\overline{u_i\theta}$	kinematic scalar flux
u, U_1	fluctuating and mean velocity in direction x_1
w	vertical velocity fluctuations
x_i	position coordinate
z	vertical coordinate
ϕ_{ij}	pressure-strain term of $\overline{u_iu_j}$
$\phi_{i\theta}$	pressure-scalar gradient term of $\overline{u_i\theta}$
ε_{ij}	dissipation rate of $\overline{u_iu_j}$
$\varepsilon_{i\theta}$	dissipation rate of $\overline{u_i\theta}$
ε_{θ}	dissipation rate 1/2 $\overline{\theta^2}$
$\overline{\theta^2}$	r.m.s. scalar fluctuations
Θ	mean scalar
β_i	buoyancy parameter in direction x_i

Acknowledgements

Special thanks are expressed to Dr D Laurence of EDF, Paris for providing hard-to-find French papers. Mr Michael Newman has prepared the manuscript in camera-ready format.

Authors' names are listed alphabetically.

References

Craft T J, 1991, 'Second-moment modelling of turbulent scalar transport', PhD Thesis, Faculty of Technology, University of Manchester, Manchester

Craft T J and Launder B E, 1989, 'A new model for the pressure scalar gradient correlation and its application to homogeneous and inhomogeneous free shear flows', Paper 17-1, 7th Symposium Turbulent Shear Flows, Stanford, 1989

Craft T J and Launder B E, 1990, 'The decay of stably stratified grid turbulence', Paper 1.5, 4th Colloquium on CFD, UMIST, Manchester

Cresswell R, Haroutunian V, Ince N Z, Launder B E and Szczepura R T, 1989, 'Measurement and modelling of buoyancy-modified elliptic turbulent flows', 7th Symp Turbulent Shear Flows, Stanford, 1989

Daly B J and Harlow F H, 1970, Phys Fluids 13, 2634

Gessner F B and Emery A, 1981, J Fluids Engineering 103, 445-455

Itsweire E C, Holland K N and Van Atta C W, 1986, J Fluid Mech 162, 299

Jones W P and Musonge P, 1983, 'Modelling of scalar transport in homogeneous turbulent flows', pp 17.18 - 17.24 Proc 4th Symposium on Turbulent Shear Flows, Karlsruhe

Kristoffersen R and Andersson H, 1990, 'Direct Simulations of low-Reynolds-number turbulent flow in a rotating channel', Proc 3rd European Turbulence Conference, Stockholm, Sweden

Kristoffersen R, Nilsen P J and Andersson H, 1990, 'Validation of Reynolds stress closures for rotating channel flows by means of direct numerical simulations' Proc Int Symp on Eng'g Turbulence Modelling and Measurements, Dubrovnik, Yugoslavia

Launder B E, 1989, 'The Prediction of force-field effects on turbulent shear flow via second-moment closure' in Advances in Turbulence - 2 (Ed H H Fernholz and H E Fiedler) pp 338-358, Springer Verlag, Berlin

Launder B E and Li S-P, 1994, Phys Fluids 6, 999

Launder B E, Morse A P, Rodi W and Spalding D B, 1972, *Free Turbulent Shear Flows - Vol 1*, 361 - 426, NASA - SP 321

Launder B E and Shima N, 1989, AIAA J 27, 1319

Launder B E and Tselepidakis D P, 1994, Int J Heat Fluid Flow 15, 2

Laurence D, Maupu V, Galland J-C and Teisson C, 1993, 'A sediment laden open channel flow simulation with recent Reynolds-stress/flux transport models' in 2nd Int Symp on Eng'g Turbulence Modelling and Measurements (Ed W Rodi & F Martelli) Elsevier, Amsterdam

Lumley J L, 1978, Advances in Applied Mechanics 18, 123

Millionshtchikov M D, 1941, C R Acad Sci SSSR 32, 619

Rodi W (Ed), 1982, *Turbulent Buoyant Jets and Plumes*, Pergamon Press, Oxford

Rotta J C, 1951, Z Phys 129, 547

Schumann U, 1977, Phys Fluids 20, 721

Uittenbogaard R E, 1988, 'Measurement of turbulent fluxes in a steady, stratified mixing layer', Proc 3rd Int Symp on Refined Flow Modelling and Turbulence Measurement' Tokyo

Van Haren L, 1992, 'Comparison between 1- and 2- point closure models for freely decaying stratified flow', PEPIT Conference on Stratified Turbulence, Paris, France (see also 'Etude-théorique et modélisation de la turbulence en présence d'ondes interne' Thèse de Docteur-ingénieur, Ecole Centrale de Lyon, 1992)

Young S T B, 1975, 'Turbulence measurements in a stably stratified shear flow', Rep QMC-EP6018, Queen Mary College, London

Zeman O and Lumley J L, 1979, 'Buoyancy effects in entraining turbulent boundary layers' in *Turbulent Shear Flows - 1*, 295-306, Springer Verlag, Heidelberg

Submitted to the Fourth International Symposium on Stratified Flows

Some similarity states of homogeneous stably-stratified turbulence

By J. R. Chasnov

The Hong Kong University of Science and Technology, Clear Water Bay, Kowloon, Hong Kong

The decay of statistically homogeneous velocity and density fluctuations in a stably-stratified fluid is considered. Over decay times long compared to the turbulence timescale but short compared to the period of internal gravity waves, three distinct high Reynolds number similarity states may develop. These similarity states are a consequence of the invariance of the low wavenumber coefficients of the three-dimensional kinetic or potential energy spectrum; and their preferential development depends on the relative magnitudes of the initial kinetic and potential energy per unit mass of the fluid. When the turbulence has decayed over a time comparable to the period of the gravity waves, the three similarity states mentioned above are disrupted. Evidence will be presented of a new similarity state which then develops asymptotically.

1. Introduction

The statistics of homogeneous turbulence in fluids of infinite extent typically depend on time throughout their entire evolution. In homogeneous turbulence at high Reynolds numbers, similarity states of the flow field may replace the statistically stationary states that typically occur in bounded flows. In these similarity states the turbulence spectrum decays without change of shape so that in an appropriately scaled coordinate system the spectrum is independent of time. Some of the homogeneous flow fields for which similarity states have been observed by large-eddy simulation include decaying isotropic turbulence, passive scalars transported by isotropic turbulence with or without a uniform mean gradient, and buoyancy-generated turbulence. The existence of a similarity state for decaying homogeneous isotropic turbulence was postulated early on (Kolmogorov, 1941) as was that for a transported homogeneous isotropic passive scalar field (Corrsin, 1951). More recent work (Batchelor, Canuto & Chasnov, 1992; Chasnov, 1994) indicates that hitherto unsuspected similarity states of homogeneous turbulence may exist for non-isotropic flows which contain more complicating physics, such as flows with buoyancy forces and uniform passive scalar gradients.

It is a natural extension of our earlier work in buoyancy-generated turbulence and turbulence with uniform passive scalar gradients to consider whether high Reynolds number similarity states exist for homogeneous turbulence in a stably-stratified fluid with both buoyancy effects and active scalar (density) gradients. In this paper, we first show how some of the flows previously considered can occur in a stably-stratified fluid at large Froude numbers. We will also present some analytical arguments and numerical results which provide evidence for a new similarity state which develops at small Froude numbers.

2. The governing equations

Choosing our co-ordinate system such that the z-axis is pointed vertically upwards, we assume a stable density distribution $\rho = \rho_0 - \beta z + \rho'$, where ρ_0 is a constant, uniform reference density, $\beta > 0$ is a constant, uniform density gradient along z, and ρ' is the density deviation from the horizontal average. The kinematic viscosity ν and molecular diffusivity D of the fluid are assumed constant and uniform. After application of the well-known Boussinesq approximation, the governing equations for the fluid velocity $\mathbf{u}$ with zero mean and the density fluctuation ρ' are

$$\nabla \cdot \mathbf{u} = 0, \tag{2.1}$$

$$\frac{\partial \mathbf{u}}{\partial t} + \mathbf{u} \cdot \nabla \mathbf{u} = \frac{\rho' \mathbf{g}}{\rho_0} - \frac{\nabla (p + \rho_0 g z)}{\rho_0} + \nu \nabla^2 \mathbf{u}, \tag{2.2}$$

$$\frac{\partial \rho'}{\partial t} + \mathbf{u} \cdot \nabla \rho' = \beta u_3 + D \nabla^2 \rho', \tag{2.3}$$

where $\mathbf{g} = -\mathbf{j} g$ with $g > 0$, $\mathbf{j}$ is the vertical (upwards) unit vector, and p is the fluid pressure.

Our earlier work considered various limiting forms of (2.1)-(2.3) for which one of g or β was taken equal to zero. By a suitable non-dimensionalization of Eqs. (2.1) - (2.3), we will show that under certain conditions the terms containing g and β may also be negligible in a stably-stratified fluid. It is convenient to define a normalized density fluctuation θ such that it has units of velocity, $\theta = \sqrt{g/\rho_0 \beta}\,\rho'$. Use of θ instead of ρ' in (2.2) - (2.3) modifies the terms proportional to g and β into terms proportional to N, where $N = \sqrt{g\beta/\rho_0}$ is the Brunt-Väisälä frequency associated with the internal waves of the stably stratified flow. The mean-square statistics $\frac{1}{2}\langle \mathbf{u}^2 \rangle$ and $\frac{1}{2}\langle \theta^2 \rangle$ are the kinetic and potential energy of the fluid per unit mass, respectively. The equations of motion conserve the total energy per unit mass in the absence of viscous and diffusive dissipation.

Now, defining dimensionless variables as

$$T = t\frac{u_0}{l_0}, \quad X = \frac{x}{l_0}, \quad \mathbf{U} = \frac{\mathbf{u}}{u_0}, \quad P = \frac{(p + \rho_0 g z)}{\rho_0 {u_0}^2}, \quad \Theta = \frac{\theta}{\theta_0}, \tag{2.4}$$

where l_0, u_0 and θ_0 are as yet unspecified length, velocity, and normalized density scales, the equations of motion (2.1)-(2.3) become

$$\nabla \cdot \mathbf{U} = 0, \tag{2.5}$$

$$\frac{\partial \mathbf{U}}{\partial T} + \mathbf{U} \cdot \nabla \mathbf{U} = -\mathbf{j}\frac{1}{F_0}\frac{\theta_0}{u_0}\Theta - \nabla P + \frac{1}{R_0}\nabla^2 \mathbf{U}, \tag{2.6}$$

$$\frac{\partial \Theta}{\partial T} + \mathbf{U} \cdot \nabla \Theta = \frac{1}{F_0}\frac{u_0}{\theta_0}U_3 + \frac{1}{\sigma R_0}\nabla^2 \Theta, \tag{2.7}$$

where

$$F_0 = \frac{u_0}{N l_0}, \quad R_0 = \frac{u_0 l_0}{\nu}, \quad \sigma = \frac{\nu}{D}. \tag{2.8}$$

The dimensionless groups F_0 and R_0 can be regarded as initial Froude and Reynolds numbers of the flow, respectively, although their precise definition is yet dependent on our specification of l_0, u_0, and θ_0; σ is the Schmidt (or Prandtl) number of the fluid.

3. Three large Froude number flows

We show here that particular initial fluctuating velocity and density fields in a stably-stratified fluid can result in the establishment of distinctly different flows when the initial Froude number of the turbulence is large. The important point here is that with well-chosen initial flow fields either or both of the source/sink terms, (those terms proportional to the inverse Froude number in (2.6) and (2.7)), may be negligible over long times.

Flow 1: Isotropic turbulence transporting an isotropic passive scalar

We consider an initial generation of isotropic velocity and density fields of comparable integral scales and kinetic and potential energies. We identify the unspecified length scale l_0 with the initial integral scale of the flow, and u_0 and θ_0 with the initial root-mean-square values of the velocity and normalized density fluctuations, respectively. If $F_0 \gg 1$, both of the terms multiplied by $1/F_0$ in (2.6) and (2.7) are small initially. Over times in which these terms remain small, the velocity fluctuations decouple from the density field and the turbulence decays isotropically while transporting an isotropic passive scalar field.

Flow 2: Isotropic turbulence in a passive scalar gradient

Here, we envision the generation of an initial isotropic velocity field with given kinetic energy and integral length scale, and no initial density fluctuations. We identify l_0 and u_0 as in flow 1. However, the initial conditions introduce no intrinsic density scale. So that Θ attains a value close to unity, we set the dimensionless group multiplying U_3 in (2.7) equal to one, yielding $\theta_0 = Nl_0$. The dimensionless group multiplying Θ in (2.6) then becomes $1/F_0^2$, so that if $F_0 \gg 1$, this term is small initially. As long as it remains small, the generated density fluctuations are passive and the resulting equations govern the evolution of decaying isotropic turbulence in the presence of a mean passive scalar gradient.

Flow 3: Buoyancy-generated turbulence

The fluid is assumed to be initially at rest with some given random density distribution. We identify l_0 and θ_0 with the initial integral scale and root-mean-square value of the θ-field, respectively. So that U attains a value of order unity, we set the dimensionless group multiplying Θ in equation (2.6) equal to one, yielding $u_0 = \sqrt{Nl_0\theta_0}$. The dimensionless group multiplying U_3 in (2.7) is now equal to $1/F_0^2$, so that if $F_0 \gg 1$ this term is small at the initial instant. Over times for which this term remains small, the resulting equations govern the evolution of buoyancy-generated turbulence.

How long do the above flows evolve before the effects of the neglected terms become important? Consider the evolution equations (2.6) and (2.7) after the flow fields have evolved over a time t. The relevant length, velocity, and normalized density scale of the flow are now those which characterize the fields at time t. The source/sink terms are of the same order when the velocity and normalized density scales are of comparable magnitude. This condition is satisfied by flow 1 from the initial instant. However, the density scale θ' and velocity scale u' at time t in flows 2 and 3, respectively, increase from initial values of zero and can be estimated as $\theta' \propto Nu't$ in flow 2, and $u' \propto N\theta't$ in flow 3. Hence, the density and velocity scales become comparable when $t > 1/N$. Also, the Froude number of the flow at time t can be shown to be proportional to $1/Nt$, so that it also becomes small when $t > 1/N$.

We have thus arrived at the intuitive result that physical effects associated with internal gravity waves affect the flow dynamics only after an evolution time comparable to the period of the gravity waves. For flows of initially large Froude number, the velocity and density fields evolve over many turbulence time scales before internal waves become dynamically important. Hence, similarity states associated with each of the above flow regimes may be established before a significant decrease in the flow Froude number. In the next Section, we briefly review the salient features of these similarity states.

4. Asymptotic similarity states at large Froude numbers

The similarity states which develop in the above flows depend on the form of the kinetic and potential energy spectra at low wavenumbers. Defining the kinetic energy spectrum $E_k(k,t)$ and the potential energy spectrum $E_p(k,t)$ to be the spherically-integrated three dimensional Fourier transform of $\frac{1}{2}\langle u_i(\mathbf{x},t)u_i(\mathbf{x}+\mathbf{r},t)\rangle$ and $\frac{1}{2}\langle\theta(\mathbf{x},t)\theta(\mathbf{x}+\mathbf{r},t)\rangle$, respectively, we write an asymptotic expansion of the spectra near $k=0$ as

$$E_k(k,t) = 2\pi k^2(B_0 + B_2k^2 + \ldots), \qquad E_p(k,t) = 2\pi k^2(C_0 + C_2k^2 + \ldots), \tag{4.1}$$

where $B_0, B_2, \ldots$, and $C_0, C_2, \ldots$ are the lowest-order coefficients of the expansion. For brevity, we consider here only flow fields for which B_0 and C_0 are non-zero unless the entire spectrum is zero. The invariance of one or both of these low wavenumber coefficients lead directly to the establishment of different similarity states.

Flow 1: Isotropic turbulence transporting an isotropic passive scalar

The low wavenumber coefficients B_0 and C_0 are separately invariant (Saffman, 1967a; Corrsin, 1951), and when they are non-zero the high-Reynolds number asymptotic results for the kinetic energy, scalar-variance and integral scale may be determined by dimensional analysis to be (Saffman, 1967b; Larcheveque, *et al.*, 1980)

$$\langle \mathbf{u}^2\rangle \propto B_0^{\frac{2}{5}}t^{-\frac{6}{5}}, \qquad \langle\theta^2\rangle \propto C_0B_0^{-\frac{3}{5}}t^{-\frac{6}{5}}, \qquad l \propto B_0^{\frac{1}{5}}t^{\frac{2}{5}}. \tag{4.2}$$

The nature of this similarity state is such that the kinetic and potential energy spectra decay without change of shape so that stationary spectra may be defined by the appropriate scaling of the wavenumber and spectral amplitudes.

Flow 2: Isotropic turbulence in a passive scalar gradient

The passive density (scalar) fluctuations for this flow are generated by velocity fluctuations along the direction of the mean gradient; consequently, the low wavenumber coefficient of the potential energy spectrum is no longer invariant in time. Rather, C_0 depends directly on the invariant B_0, N and t by

$$C_0(t) = \frac{1}{3}N^2B_0t^2. \tag{4.3}$$

Use of (4.3) in (4.2) yields the asymptotic growth of the scalar variance (Chasnov, 1994)

$$\langle\theta^2\rangle \propto N^2B_0^{\frac{2}{5}}t^{\frac{4}{5}}. \tag{4.4}$$

Flow 3: Buoyancy-generated turbulence

Here, the velocity fluctuations are generated by density fluctuations and B_0 is no longer invariant; however C_0 is invariant. The coefficient B_0 is related to C_0, N and t by

$$B_0(t) = \frac{2}{3} N^2 C_0 t^2; \tag{4.5}$$

and substituting (4.5) into (4.2) [illegible] (Batchelor, *et al.*, 1992)

$$\langle \mathbf{u}^2 \rangle \propto (N^2 C_0)^{\frac{2}{5}} t^{-\frac{2}{5}}, \qquad \langle \theta^2 \rangle \propto C_0 (N^2 C_0)^{-\frac{3}{5}} t^{-\frac{12}{5}}, \qquad l \propto (N^2 C_0)^{\frac{1}{5}} t^{\frac{4}{5}}. \tag{4.6}$$

An interesting and unusual feature of the similarity state for buoyancy-generated turbulence is an increase in the flow Reynolds number asymptotically.

5. The flow at small Froude numbers

After the stratified flow evolves over a time $t \sim 1/N$, the Froude number is of order unity so that the above large Froude number similarity states are no longer valid. As the flow evolves further so that $Nt \gg 1$, the Froude number may be expected to become small, and it is of some interest to consider whether a different similarity state of the flow field is established asymptotically provided the Reynolds number of the flow remains large. To construct a similarity state, an invariant of the kinetic and potential energy spectra near $k = 0$ must be determined. Such an invariant does indeed exist and is associated with the low wavenumber coefficient of the total energy spectrum $E(k)$, defined by $E(k) = E_k(k) + E_p(k)$. An expansion of the total energy spectrum near $k = 0$ yields

$$E(k, t) = 2\pi k^2 (A_0 + A_2 k^2 + \ldots), \tag{5.1}$$

where $A_0 = B_0 + C_0$ and $A_2 = B_2 + C_2$ are the sum of the low-wavenumber kinetic and potential energy spectral coefficients. The coefficient A_0 can be shown to be an exact invariant of the flow. Here, we consider its value to be non-zero at the initial instant.

We thus have a new invariant A_0 upon which to base an asymptotic similarity state. However, a straightforward dimensional analysis is now complicated by the addition of another relevant dimensionless group, namely Nt, which is directly proportional to the number of wave periods over which the flow has evolved. For asymptotically large Froude number flows, Nt is vanishingly small and does not enter into the scalings; however, this may not be the case at small Froude numbers when Nt is large.

Despite the above difficulty, we nevertheless attempt a dimensional analysis of this problem by considering the evolution of the total energy of the flow, $e = (\langle \mathbf{u}^2 \rangle + \langle \theta^2 \rangle)/2$, for which there exists an associated invariant A_0. Dimensional analysis then yields

$$e = c_e A_0^{\frac{2}{5}} t^{-\frac{6}{5}} (Nt)^x, \tag{5.2}$$

where we write the proportionality constant c_e explicitely, and x is an unknown exponent.

In addition to the total energy decay, it is of interest to consider the evolution of the integral scales of the flow field associated with the total energy. The integral scales may evolve differently depending on whether they are measured parallel or perpendicular to the vertical axis. Defining the horizontal integral scale of the total energy to be l_h, and that of the vertical integral scale to be l_v, dimensional analysis yields

$$l_h = c_{l_h} A_0^{\frac{1}{5}} t^{\frac{2}{5}} (Nt)^y, \qquad l_v = c_{l_v} A_0^{\frac{1}{5}} t^{\frac{2}{5}} (Nt)^z, \tag{5.3}$$

where c_{l_h} and c_{l_v} are proportionality constants, and y and z are two additional exponents.

A heuristic argument can be given to determine the unknown exponent x. At small Froude numbers, two disparate timescales of the flow exist: a fast time-scale of the wave field and a slow time scale of the turbulence. If we assume that the correlation time of the nonlinear transfer is directly proportional to the fast time scale $1/N$, then dimensionally

$$\frac{d\langle \mathbf{u}^2 \rangle}{dt} = \frac{1}{N} A_0^{-\frac{2}{3}} \langle \mathbf{u}^2 \rangle^{\frac{8}{3}}, \tag{5.4}$$

which may be integrated directly to yield the value $x = 3/5$ in (5.2).

We do not yet have have any *a priori* argument to determine the remaining unknown exponents y and z. Rather, in the next Section we present the results of large-eddy simulations in which all three exponents may be computed.

6. Large-eddy simulations at small Froude numbers

To obtain a high Reynolds number flow at small Froude numbers, we perform large-eddy simulations of Eqs. (2.1) - (2.3) using a pseudo-spectral code for homogeneous turbulence (Rogallo, 1981). For the subgrid scale model, we employ a spectral eddy-viscosity and eddy-diffusivity similar to that of Chollet and Lesieur (1981). We take the initial kinetic energy spectrum of the form given by Chasnov (1994) with the low wavenumber portion of the spectrum proportional to k^2. The initial potential energy spectrum is taken to be zero. In the large Froude number regime, this corresponds to flow 2 above: isotropic turbulence in a passive scalar gradient. Preliminary calculations showed that the horizontal integral scales grew more rapidly than the vertical scales, in agreement with previous direct numerical simulation results (Riley, *et al.*, 1981), and that it was optimal to use a computational box which was eight times longer in the horizontal directions than in the vertical. Accordingly, we took a computational box length of 4π in the two horizontal directions and $\pi/2$ in the vertical direction, with a corresponding grid resolution of $512 \times 512 \times 64$ so that the grid remained cubic at the smallest resolved scales. With a periodic box, the horizontal wavenumbers then took the values $k_x, k_y = 1/2, 1, \ldots, 128$ and the vertical wavenumbers $k_z = 4, 8, \ldots, 128$. The peak of the initial isotropic kinetic energy spectrum k_p was placed at a wavenumber of 64. Two computations were performed with initial Froude number $F_0 = u_0/Nl_0$ given by $F_0 = 16.5$ and 93.2. In the definition of F_0, u_0 is taken as the initial root-mean square velocity fluctuation, and $l_0 = \sqrt{\pi}/k_p$. The computations were performed holding u_0 and l_0 fixed and varying N by a factor of approximately 5.65. The results of the computation are used here to test the postulated scalings given in §5 and to compute values of the unknown exponents x, y, and z.

In Figure 1a, we plot the power-law exponent of t (*i.e.*, the logarithmic derivative with respect to t) of the total energy as a function of t/τ_0 for both initial Froude number flows,

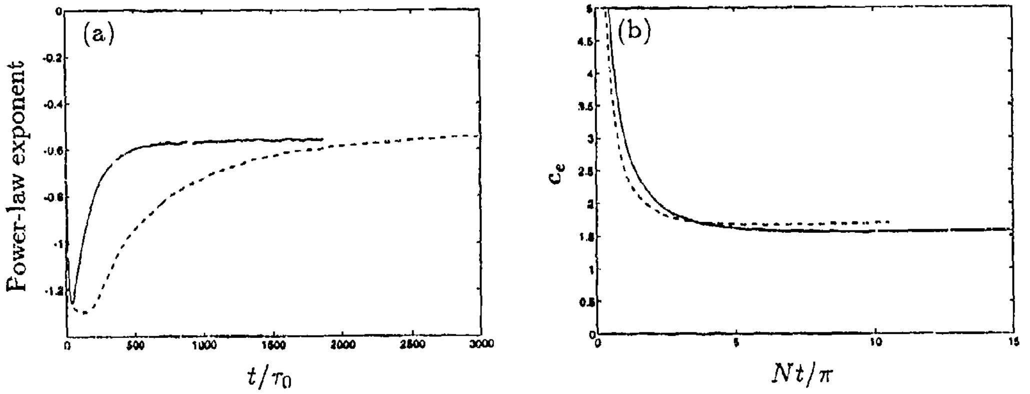

FIGURE 1. The energy statistics: ——, $F_0 = 16.5$; - - - -, $F_0 = 93.2$; (a) time-evolution of the power-law exponent of e; (b) verification of the scaling relation given by (5.3) with $x = 3/5$.

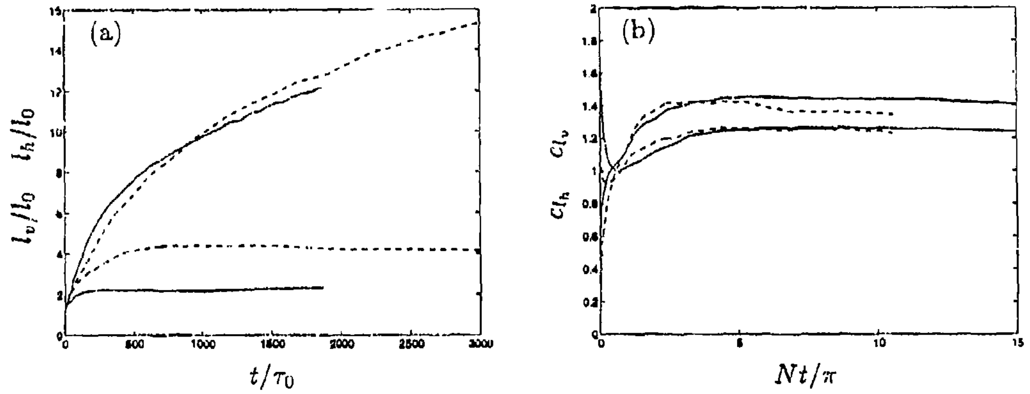

FIGURE 2. The integral length scales: ——, $F_0 = 16.5$; - - - -, $F_0 = 93.2$; (a) time-evolution of the horizontal and vertical integral length scales of the total energy; (b) verification of the scaling relations given by (5.4) with $y = 0$ and $z = -2/5$.

where $\tau_0 = l_0/u_0$. The asymptotic value of the time exponent is approximately $-3/5$, indicating a value of x in (5.2) equal to $3/5$, in agreement with our heuristic argument. In figure 1b, we plot the proportionality constant c_e in (5.2), *i.e.*, we plot the evolution of $e/(A_0^{2/5}t^{-3/5}N^{3/5})$, for both initial Froude number flows. The approximate convergence of the two curves at large values of Nt confirms the overall scaling given by (5.2), with $c_e \approx 1.6$.

The horizontal and vertical integral scales of the total energy are plotted versus t/τ_0 in Figure 2a for both initial Froude number flows. Evidently, a large-times the horizontal integral scale is independent of the initial Froude number and the vertical integral scale is independent of time. This implies that $y = 0$ and $z = -2/5$ in (5.3). In Figure 2b, we plot the evolution of c_{l_h} and c_{l_v} for both flows. Again the overall scaling given by (5.3) is confirmed, with $c_{l_h} \approx 1.2$ and $c_{l_v} \approx 1.4$.

We have thus presented findings of a new similarity state which develops at large Reynolds numbers and small Froude numbers when the initial flow field consists of an isotropic velocity distribution and no density fluctuations. It is also possible that the similarity state which develops at small Froude numbers depends on the way in which the initial flow fields are initialized. Metais and Herring (1989) demonstrated by direct numerical simulations that the nature of the flow at small Froude numbers does depend on the relative state of the turbulence and wave field before entering the low Froude number regime. Some preliminary computations which we have performed verify that this is indeed the case; we intend to report on these findings at a later date.

Acknowledgments

Extensive discussions with R. Rogallo are gratefully acknowledged, as are the helpful comments of G. Batchelor, J. Riley, and K. Squires. The simulations were performed on the NAS Intel hypercube using software developed by R. Rogallo and A. Wray.

REFERENCES

BATCHELOR, G. K., CANUTO, V. M. & CHASNOV, J. R. 1992 Homogeneous buoyancy-generated turbulence. *J. Fluid Mech.* **235**, 349-378.

CHASNOV, J. R. 1994 Similarity states of passive scalar transport in isotropic turbulence. *Phys. Fluids.* **6**, 1036.

CHOLLET, J. P. & LESIEUR, M. 1981 Parameterization of small scales of three dimensional isotropic turbulence utilizing spectral closures. *J. Atmos. Sci.* **38**, 2747-2757.

CORRSIN, S. 1951 The decay of isotropic temperature fluctuations in an isotropic turbulence. *J. of the Aeronautical Sciences.* **18**, 417-423.

KOLMOGOROV, A. N. 1941 On degeneration of isotropic turbulence in an incompressible viscous liquid. *Dokl. Akad. Nauk. SSSR.* **31**, 538-541.

LARCHEVEQUE, M., CHOLLET, J. P., HERRING, J. R., LESIEUR, M., NEWMAN, G. R., & SCHERTZER, D. 1980 Two-point closure applied to a passive scalar in decaying isotropic turbulence. *Turbulent Shear Flows II,* Springer Verlag.

MÉTAIS, O. & HERRING, J. R. 1989 Numerical simulations of freely evolving turbulence in stably stratified fluids. *J. Fluid Mech.* **202**, 117-148.

RILEY, J. J., METCALFE, R. W. & WEISSMANN, M. A. 1981 Direct numerical simulation of homogeneous turbulence in density-stratified fluids. *Nonlinear Properties of Internal Waves* (ed. B. J. West), *AIP Conf. Proc.,* **76**, 79-112.

ROGALLO, R. S. 1981 Numerical experiments in homogeneous turbulence. *NASA TM 81315.*

SAFFMAN, P. G. 1967a The large-scale structure of homogeneous turbulence. *J. Fluid Mech.* **27**, 581-593.

SAFFMAN, P. G. 1967b Note on decay of homogeneous turbulence. *Phys. Fluids.* **10**, 1349.

A study of decaying stratified turbulence by a two-point closure EDQNM model and by direct numerical simulations

L. van HAREN[1], C. STAQUET[2] and C. CAMBON[3]

[1] EDF, Laboratoire National d'Hydraulique, 6 quai Watier 69400 CHATOU

[2] Laboratoire de Physique, Ecole Normale Supérieure de Lyon
46 allée d'Italie 69364 LYON Cédex 07, FRANCE

[3] Laboratoire de Mécanique des Fluides et d'Acoustique URA CNRS n° 263
Ecole Centrale de Lyon BP 163, 69131 ECULLY Cédex, FRANCE

15 avril 1994

Abstract

The evolution of the anisotropic structure of homogeneous turbulence in a stably-stratified fluid is investigated. Our study is based upon a comparison between Direct Numerical Simulations (DNS), a statistical closure model (anisotropic EDQNM) and its linear or "Rapid Distortion Theory" (RDT) approximation. A very good agreement is found between DNS and EDQNM. Particular emphasis is given to the reversible conversion of turbulent kinetic energy into potential energy and to the angular dependency of energy in spectral space. The rise of an irreversible trend controlled by nonlinear interactions as opposed to a reversible trend controlled by linear motions is shown.

1 Introduction

The theoretical and numerical works presented here are motivated to a great extent by recent experimental studies on decaying stratified grid turbulence performed either in a windtunnel, by Lienhard & van Atta (1990) and Yoon & Warhaft (1990), or in a water tank, by Barrett & van Atta (1991). The measurements made in these experiments have a high level of spectral resolution and accuracy compared to the salt water experiments reported up to now (e.g. Itsweire et al., 1986), which enable the authors to present a more detailed picture of the decay process.

When the Froude number (ratio of inertial to buoyancy forces) is much larger than one initially, the turbulence decays as a result of the usual cascade process. During this decay, buoyancy forces gain importance with respect to inertial effects. When the Froude number becomes smaller than about two, the large scales of the motion are influenced by the stratification and vertical transport is weakened, while the small scales continue their normal mixing. LV show that the small scales are in universal equilibrium, in other words they are not affected by the stratification. This picture is especially clear with regard to the co-spectrum of the heat flux. For small wavenumbers a counter-gradient flux is observed, while for larger wavenumbers the mixing along the gradient continues. This usually leads to a net flux along the temperature gradient. It should be noticed that YW observe a net counter-gradient heat flux for their most stable run.

In the present study, we present results concerning the influence of the initial Froude and Reynolds numbers on the flow development and the occurence of the counter-gradient heat flux. A form of anisotropy in the small scales is also put to the fore. To get these results, we solved numerically a hierarchy of mathematical models, namely (i) the fully three-dimensional Boussinesq equations (performing Direct Numerical Simulations), (ii) an Eddy Damped Quasi- Normal Markovian (EDQNM) closure model and (iii) its Rapid Distortion Theory (RDT) approximation.

The EDQNM model is a turbulence closure model in spectral space for axisymmetric stratified flow (Cambon, 1989). The non-linear transfer terms of energy between the various wavenumbers are explicitly calculated and the full 3-D (axisymmetric) energy spectrum is available. The model is thus very suitable to study the anisotropy of the flow. However, the validation of the EDQNM model by the DNS is a prerequisite before reaching higher values of the Reynolds number with the EDQNM model.

The RDT approximation consists of neglecting the non-linear energy transfer terms in the EDQNM equations and highlights the importance of the linear terms in the decay process. Moreover, analytical solutions of the RDT approximations can be easily obtained.

2 Equations, models and relevant variables

The Boussinesq assumptions for turbulence in a stably-stratified fluid give the following system of equations for the fluctuating velocity field $u_i(\mathbf{x},t)$ and a modified temperature $T(\mathbf{x},t)$:

$$\begin{aligned}(\frac{\partial}{\partial t}+u_j\frac{\partial}{\partial x_j}-\nu\nabla^2)u_i+\frac{\partial p}{\partial x_i} &= T\delta_{i3}\\ (\frac{\partial}{\partial t}+u_j\frac{\partial}{\partial x_j}-\nu\nabla^2)T &= -N^2u_3\end{aligned} \qquad (1)$$

$$\frac{\partial u_i}{\partial x_i}=0, \qquad (2)$$

where ν is the kinematic viscosity (the Prandtl number is chosen equal to unity) and N is the Brünt-Väisälä frequency. The definition of N,

$$N=(\beta\gamma g)^{1/2} \qquad (3)$$

involves the thermal expansion coefficient β, the vertical mean temperature gradient γ and the gravitational acceleration g. Equation 1 displays N as the unique stratification parameter if T is scaled as an acceleration (using the coefficient βg), so that $(T/N)^2/2$ can be interpreted as a potential energy.

In order to include in the models the detailed dispersion law of the linear wave regime and to reduce the number of variables, u_i and T are 3D Fourier transformed (superscript $\hat{}$). Then the 4-component set $(\hat u_i,\hat T)$ is reduced to a 3-component set by introducing a new vector:

$$\hat v_i(\mathbf{k},t)=\hat u_i(\mathbf{k},t)+I\frac{k_i}{k}\frac{\hat T}{N}(\mathbf{k},t),\qquad I^2=-1 \qquad (4)$$

The reduction of the number of components reflects the solenoidal property of the velocity field, in accordance with equation 2, $k_i\hat u_i=0$. The equation governing $\hat v_i$ is directly derived from equations 1, 2 and reads:

$$\left(\frac{\partial}{\partial t}+\nu k^2\right)\hat v_i(\mathbf{k},t)+N\,L_{ij}(\mathbf{k})\hat v_j(\mathbf{k},t)=\int_{\mathbf{p}+\mathbf{q}=\mathbf{k}}M_{ijl}(\mathbf{k},\mathbf{p},\mathbf{q})\,\hat v_j(\mathbf{p},t)\hat v_l(\mathbf{q},t)\,d^3p \qquad (5)$$

Here $\hat v$, and its statistical correlations of any order and related equations, can be studied in other orthonormal frames of reference quoted below; all tensorial properties are preserved by such projections, including the definitions of invariants (energy) and realizability constraints.

According to the Craya-Herring decomposition, a first orthonormal frame $(\mathbf{e}^1,\mathbf{e}^2,\mathbf{e}^3)$ is defined such that $\mathbf{e}^3$ is aligned with $\mathbf{k}$ ($e_i^3=k_i/k$) and $\mathbf{e}^1$ lies in a horizontal plane. We thus have:

$$\hat v_i(\mathbf{k},t)=\hat\varphi^j(\mathbf{k},t)\,e_i^j(\mathbf{k}) \qquad (6)$$

Then $(\mathbf{e}^1,\mathbf{e}^2)$ generates $\hat u_i$, located in the plane normal to $\mathbf{k}$; $\hat\varphi^1\mathbf{e}_i^1$ (vortex mode) and $\hat\varphi^2\mathbf{e}_i^2$ (wave mode) contains respectively all of the vertical vorticity and all of the vertical velocity of the flow, whereas $\hat\varphi^3=I\,T/N$ solely contributes to the potential energy.

The local frame $(\mathbf{e}^1,\mathbf{e}^2,\mathbf{e}^3)$ is particularly convenient for studying the statistical quantities $\hat V_{ij}(\mathbf{k},t)$ and $\hat V_{ijl}(\mathbf{k},\mathbf{p},t)$ obtained from the two covariance matrices $<\hat v_i^*(\mathbf{k})\hat v_j(\mathbf{k})>$ and $<\hat v_i^*(\mathbf{k})\hat v_j(\mathbf{p})\hat v_l(\mathbf{q})>$.

For axisymmetric turbulence (simplest symmetry consistent with equations 1, 2) $\hat V_{ij}/2$ has only four non-zero components in $(\mathbf{e}^1,\mathbf{e}^2,\mathbf{e}^3)$:

$$\frac{1}{2}\hat V_{ij}=\begin{pmatrix}\phi_1 & 0 & 0\\ 0 & \phi_2 & \psi\\ 0 & \psi & \phi_3\end{pmatrix} \qquad (7)$$

which depend on $k = |\mathbf{k}|$ and $\cos(-\mathbf{g}, \mathbf{k}) = \cos\theta$. Thus ϕ_i, $i = 1, 2, 3$ represents the different modes of the spectral density of energy and ψ generates the vertical buoyancy flux, according to:

$$\begin{aligned}
\Phi_i = \frac{1}{2} < (\varphi^i)^2 > &= \int \phi_i \, d^3\mathbf{k} \\
\frac{1}{2} < u_3 T > &= -\int \psi \sin\theta \, d^3\mathbf{k}
\end{aligned} \tag{8}$$

Additional constraints are $\phi_1 = \phi_2$ and $\psi = 0$ for $\cos\theta = \pm 1$ (polar isotropy) and $\phi_i \geq 0$, $i = 1, 2, 3$; $\phi_2\phi_3 - |\psi|^2 \geq 0$ (realizability). These four components are governed by the following system of equations:

$$\begin{aligned}
\left(\frac{\partial}{\partial t} + 2\nu k^2\right) \phi_1(\mathbf{k}, t) &= T_1 \\
\left(\frac{\partial}{\partial t} + 2\nu k^2\right) \phi_2(\mathbf{k}, t) &= T_2 - (N \sin\theta)\psi \\
\left(\frac{\partial}{\partial t} + 2\nu k^2\right) \phi_3(\mathbf{k}, t) &= T_3 + (N \sin\theta)\psi \\
\left(\frac{\partial}{\partial t} + 2\nu k^2\right) \psi(\mathbf{k}, t) &= T_\psi + 2N \sin\theta(\phi_2 - \phi_3)
\end{aligned} \tag{9}$$

where T_i, $i = 1, 2, 3$ and T_ψ are energy transfer terms which involve triple correlations. These terms are zero in the linear viscous regime, which is given by the linear part of equation 5. This regime will be referred to as the Rapid Distortion Theory (RDT) limit.

In the extended EDQNM model (Cambon, 1989), the system of equations 9 is numerically solved with an implicit treatment of the linear terms (exact in the RDT limit) and an explicit form of T_i and T_ψ.

The closure of these terms derives from the application of EDQNM to equation 5. The procedure is the same as for rotating flows (Cambon and Jacquin, 1989) and is not given here for the sake of brevity. Only the crucial parameters, which are characteristic times connected with triple correlations, are quoted:

$$\theta_{kpq}^{\alpha\beta\gamma} = \theta_{kpq}[1 + IN\theta_{kpq}(\alpha \sin(-\mathbf{g}, \mathbf{k}) + \beta \sin(-\mathbf{g}, \mathbf{p}) + \gamma \sin(-\mathbf{g}, \mathbf{q}))]^{-1} \tag{10}$$

with $\alpha, \beta, \gamma = 0, \pm 1$ and θ_{kpq} includes both viscous and eddy damping terms, according to standard procedures, with one unique constant.

The sophisticated model 10 may cause realizability problems for particular initial data, because of the sudden application of the stratification (the discontinuity in N leads to a discontinuity in $\theta_{kpq}^{\alpha\beta\gamma}$). So the simplest and less expensive model, which corresponds to $N = 0$ in equation 10, will be used here for the detailed study of the system of equations 9, in which the stratification affects explicitly the linear terms. Note that although stratification effects are not explicitly taken into account in equation 10, they do enter implicitly in the transfer terms, since they involve double correlations by means of the closure assumption.

2.1 Direct numerical simulations: numerical method

In order to ensure energy conservation, equations 1 are rewritten using the vector identity $(\mathbf{u} \cdot \nabla)\mathbf{u} = \omega \times \mathbf{u} + \nabla|\mathbf{u}^2|/2$. Here $\omega = \nabla \times \mathbf{u}$ is the vorticity. The numerical domain is a cubic box of side 2π. The boundary conditions are periodic in all three directions. The spatial derivatives and nonlinear terms are treated numerically using a pseudo-spectral method in Fourier space. Time marching is done using a third order Adams-Bashforth scheme. The viscous term is integrated exactly using the new variable $\mathbf{v}(\mathbf{k}) = \mathbf{u}(\mathbf{k}) \exp(\nu k^2 t)$ (e.g. Vincent and Meneguzzi, 1991).

3 Results

3.1 Initial conditions and physical parameters

Six direct numerical simulations of a homogeneous stably-stratified fluid for a resolution equal to 64^3 are presented (see Table 1 for a description of these calculations). The initial condition consists of a homogeneous and isotropic flow field, initialized with the energy-density spectrum

Run	N	$1/\nu$	t_0	Φ_1/Φ_2	Φ_3	Fr	Re
1	$\pi/6$	200	1.5	1.007	0.0	5.8	49
2	$\pi/6$	100	1.5	0.9967	0.0	4.02	27.5
3	$\pi/3$	200	1.5	1.007	0.0	2.9	49
4	$\pi/3$	100	1.5	0.9967	0.0	2.01	27.5
5	π	200	1.5	1.007	0.0	0.97	49
6	π	100	1.5	0.9967	0.0	0.67	27.5

Table 1: Description of the initial conditions (at $t = t_0$) of the 64^3 simulations presented in this paper; t_0 is the time at which the Brünt-Väisälä frequency N is set to a non-zero value; dt=0.0125. We use the following definitions: $Fr = (u^2)^{1/2}/l_{11}^3 N$, $l_{11}^3 = \int_{-\infty}^{\infty} < u_1(x, y, z + dz) u_1(x, y, z) > dz / < u_1^2 >$, $Re = (u^2)^{1/2} l/\nu$, with $l = (3\pi/4) \int_0^{\infty} E(k)/k dk / \int_0^{\infty} E(k) dk$.

$$E(k) = 16\ (2/\pi)^{1/2}\ u_0{}^2\ k^4\ k_i^{-5} \exp[-2(k/k_i)^2]. \tag{11}$$

$E(k_i)$ is the maximum of the energy spectrum and u_0 = rms(u) = rms(v) = rms(w); here $k_i = 4.760$ (Orszag and Patterson, 1972; Metais and Herring, 1989; Gerz and Schuman, 1990). The Brünt-Väisälä frequency is set to a nonzero value as soon as the triple correlations have built and isotropy is equal to 1 (we use Φ_1/Φ_2 as an indicator of isotropy, following Vincent and Meneguzzi). Let $t = t_0$ be the time at which stratification is added. Three different values of the Brünt-Väisälä frequency have been chosen, $N = \pi/6$, $N = \pi/3$ and $N = \pi$. The corresponding values at $t = t_0$ of a dynamical Froude number based upon rms(u) and a vertical integral lengthscale of u are indicated in Table 1. Each of these three stratified calculations has been carried out with two different values of the viscosity, $\nu = 0.01$ and $\nu = 0.005$.

3.2 Discussion of results

In figure 1 the evolution of the total energy (kinetic+potential) is shown as a function of time for the stratified case with a Brünt-Väsäilä frequency of $N = \pi$, for both the DNS and the EDQNM model. The energy is made dimensionless by its initial value and the time axis is scaled with the Brünt-Väsäilä period $2\pi/N$. The results are compared with an isotropic run ($N = 0$), for which the total energy only contains kinetic energy.

Figure 1 shows that for the isotropic case DSN and EDQNM are in good agreement, with a slope of decrease of energy of -1.1 at the end of the run. However, the EDQNM model does not show any difference between the isotropic and stratified case, whereas for the DNS the energy dissipation is clearly reduced near the end of the run. (The other stratified runs we have performed display a similar behavior.) This latter effect is due to a reduction of energy transfer by the stratification. As discussed in the presentation of the models, the EDQNM model that we use here takes into account only implicitely the effect of stratification in the transfer terms. An EDQNM version with these effects explicitely incorporated in the EDQNM closure (see equation 10) already exists (and works successfully for rotationnal flows). We are currently working on the specific problem of realizability for the case of stratified flows.

In figure 2, we consider the contributions of the kinetic energy to the total energy in both Craya modes Φ_1 and Φ_2; the potential energy, denominated as Φ_3, is also plotted. Only the runs described in Table 1 with viscosity $\nu = 1/200$ are shown. Figure 2 shows that the EDQNM model compares very well with the DNS, both qualitatively and quantitatively. The Φ_1 mode remains unaffected by the stratification, while Φ_2 and the potential energy show an oscillatory behavior, in a mutual exchange of energy. Note that from equations 9, it appears that only these two modes contain a linear contribution due to the stratification. Furthermore, the oscillations appear to be smaller for the lowest values of N (and of the viscosity ν, but this result is not shown). In other words, both a higher initial Froude number and a higher initial Reynolds number reduce the oscillations. We will come back to this point further on in this paper, where we will find that the non-dimensionalized heatflux is a good indicator of this trend.

Let us now consider the RDT approximation, which highlights the importance of the linear terms. (figure 2c). A very good qualitative agreement with EDQNM and DNS is found, which confirms that the oscillations in Φ_2 and Φ_3 are produced by the linear terms in the equations of motion. The decay of energy is only due to the direct action of viscosity on all scales of motion.

The RDT approximation is a very convenient reference case, when considering the dimensionless heatflux $< wT > /(< w^2 >< T^2 >)^{1/2}$. This quantity is a measure of the correlation of the velocity and temperature field. On integrating the RDT approximation of equations 9, it is found that the dimensionless heatflux is independent of the initial spectrum prescribed as well as on the viscosity. When the time-axis is made nondimensional by $Nt/2\pi$, it becomes also independent of N and reduces to a unique form, which can be considered as a low Reynolds and/or Froude number limit.

In figure 3, the dimensionless heatflux is shown for all values of N and ν, versus the normalized time $Nt/2\pi$; the RDT case has also been included. The data collapse very well with this scaling. (Such a scaling has already been used successfully by Lienhard & van Atta, 1990, and yield an analogous collapse of data caracterizing the stratified turbulence). In the present case, both a strong stratification (high value of N) and a high viscosity tend to increase the dimensionless heatflux. The DNS results for $\nu = 1/100$ are in somewhat less agreement than for $\nu = 1/200$. One reason might be that EDQNM model becomes less apt to properly model flow dynamics when the Reynolds number is low.

The fact that the RDT solution is independent of the viscosity does not necessarily mean that the maxima and minima of correlation reached are $+1$ or -1. The correlation is scrambled by the dispersion relation for the linear terms which makes every wavenumber mode to oscillate with a different frequency $N \sin\theta$, depending on its angle θ with the vertical direction.

In order to give an explanation for the dependency of the correlation on the Reynolds and Froude numbers, we need to realize that in terms of spectra of energy, linear terms are only dominant where the non-linear terms are weak. Hence, the oscillations will be present for small wavenumbers and are thus a phenomenon of the large flow structures.

For the RDT, linear terms will be present at all scales and impose an upper limit to the correlation between velocity and temperature field that can be obtained. Now since the RDT limit can be regarded as a low Reynolds number reference, increasing the Reynolds number will inevitably destroy a part of the correlation. For high Reynolds numbers, the linear terms will eventually disappear and the correlation will reach the positive value of about 0.7, found for the case of a passive scalar. It is worth noticing that in most grid turbulence experiments, the Reynolds number is higher than the values considered in this study, and this may very possibly be responsible for the non observation of any counter gradient heatflux.

The influence of the initial Froude number is less clear. On the one hand it is evident that a stronger stratification promotes the presence of the linear terms and thus a stronger correlation. But on the other hand, we represent the time scale in a non-dimensional form, using the Brünt-Väisälä period. For instance, when the heatflux reaches its most negative value at $Nt/2\pi \sim 0.4$, time has advanced 6 times further for the case $N = \pi/6$ than for the case $N = \pi$. So, although the stratification is much weaker in the former case, viscosity has had much more time to reduce the non-linear terms. We can only conclude that apparently, the balance is such that a stronger stratification produces a stronger correlation.

As a final result, we will make a remark on the development and the definition of flow anisotropy. We will use results from the EDQNM model. In figure 2, the classical type of anisotropy is expressed by means of the spherically integrated spectra of ϕ_1 and ϕ_2. This confirms the statements made above that a reversible kind of anisotropy is produced by the linear terms in the equation of motion and that this anisotropy is limited to low wavenumbers (figure 4a).

We found that on the other hand an irreversible kind of anisotropy develops, which has the character of a directional (angular) dependency of the spectra. This is illustrated in figure 4b, where the energy spectrum is given for three different spectral angles θ, between the wavenumber vector and the vertical direction. ($\cos\theta = 1$ corresponds to the vertical direction).

We have found that generally this irreversible kind of anisotropy is stronger for higher Reynolds numbers. Also the effect is important in the region of the spectrum where the non-linear terms are dominant, as is confirmed by figure 4b.

4 Conclusions

We have investigated the influence of the initial Froude and Reynolds number on the evolution of freely decaying stably stratified turbulence. We have compared results obtained by means of Direct Numerical Simulations (DNS) on a 64^3 grid with those of a statistical EDQNM model extended to anisotropic flows. The results of the comparison are as follows.

The EDQNM model compares very well with the DNS results, both qualitatively and quantitatively, especially for the high Reynolds number case. However, for the DNS a reduction of the energy transfer terms has been found, which is not reproduced by the EDQNM model. A more elaborated model is actually being developed; such a model has already proved to successfully reproduce the reduction of the energy transfer in the case of rotational flows.

It is shown, on using Rapid Distortion Theory (RDT), that the linear terms in the equation of motion are responsible for the oscillatory behavior observed and that they are located at the low wavenumber end of the energy spectrum. The RDT serves as a reference low Reynolds limit case in which linear terms dominate. These terms create a strong oscillatory behavior of the dimensionless heatflux with periodically counter gradient heat fluxes. As the Reynolds number is increased, the linear terms become relatively less important and the correlation between the temperature and velocity fields decreases.

A high Froude number has in principle the same effect, since it makes the linear terms less important compared to the non-linear ones. However for a given dimensionless time $Nt/2\pi$, the corresponding low value of the Brünt-Väisälä frequency N, makes that time evolves longer than for a high value of N and thus non-linear terms have more time to decrease. We found for the Froude and Reynolds considered here that a high Froude number reduces the correlation of the velocity and temperature fields.

We furthermore found for the EDQNM calculations that it is necessary to distinguish between two different kinds of anisotropy. The directional anisotropy is caused by the linear terms and has a reversible character. The second kind of anisotropy describes the directional dependence of the energy density and is not reversible. The tendency is such as to create a surplus of energy in the vertical direction (the pole of the spectrum). This trend corresponds in physical space to a larger variability in the vertical direction than in horizontal planes, in accordance with pancake turbulent structures observed in the atmosphere for instance (e.g. Dalaudier et Sidi, 1994).

Acknowledgements

This work has been supported by EDF (Direction des Etudes et Recherches, Laboratoire National d'Hydraulique) under contract no. 2J67.3. and by the European Economic Community under contract no. SCI*0285.

References

BARRETT T.K. & C.W. VAN ATTA 1991 Experiments on the inhibition of mixing in stably stratified decaying turbulence using laser Doppler anemometry and laser-induced fluorescence. *Phys. Fluid A*, **3** (5), 1321-1332.

CAMBON C. 1989 Spectral approach to turbulence in a stratified fluid. In Advances in Turbulence 2 (ed. H.-H. Fernholz & H.E. Fiedler). Springer-Verlag.

CAMBON C. & L. JACQUIN 1989 Spectral approach to non-isotropic turbulence subjected to rotation *J. Fluid Mech.* **202**, 295-317.

DALAUDIER F., C. SIDI, M. CROCHET & J. VERNIN 1992 Direct evidence of "sheets" in the atmospheric temperature field. *J. Atmos. Sci.*, **51**, 2, 237-248.

GERZ T. & U. SCHUMANN 1990 Direct simulation of homogeneous turbulence and gravity waves in sheared and unsheared stratified flows In Turbulence Shear Flows 7 (ed. W.C. Reynolds). Springer-Verlag.

ITSWEIRE E. C., K.N. HELLAND & C.W. VAN ATTA 1986 The evolution of grid-generated turbulence in a stably-stratified fluid. *J. Fluid Mech.* **162**, 299-338.

LIENHARD V J.H. & C.W. VAN ATTA 1990 The decay of turbulence in thermally stratified flow *J. Fluid Mech.* **210**, 57-112.

MÉTAIS O. & J. HERRING 1989 Numerical simulations of freely evolving turbulence in stably stratified flows *J. Fluid Mech.* **202**, 117-148.

ORSZAG S.A. & C.S. PATTERSON 1972 Numerical simulation of turbulence. In *Statistical Models and Turbulence* (ed. M. Rosenblatt and C. van Atta). Lecture Notes in Physics, **12**,127-147. Springer.

VINCENT, A. & MENEGUZZI, M. 1991 The spectral structure and statistical properties of homogeneous turbulence. *J. Fluid Mech.*, **225**, 1-20.

YOON K.& Z. WARHAFT 1990 The evolution of grid-generated turbulence under conditions of stable thermal stratification. *J. Fluid Mech.* **215**, 601-638.

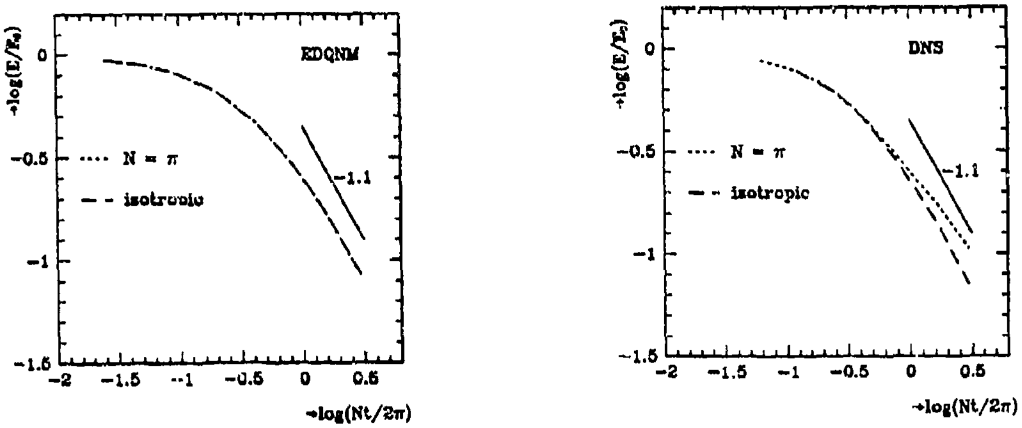

Figure 1: Evolution of the total mean energy (kinetic + potential) E/E_0, as a function of $Nt/2\pi$ for both DNS and EDQNM ($\nu = 1/200$; E_0 is the initial energy of the stratified run). For the isotropic case the potential energy is zero and the time-axis has been multiplied by $N/2\pi$ with $N = \pi$.

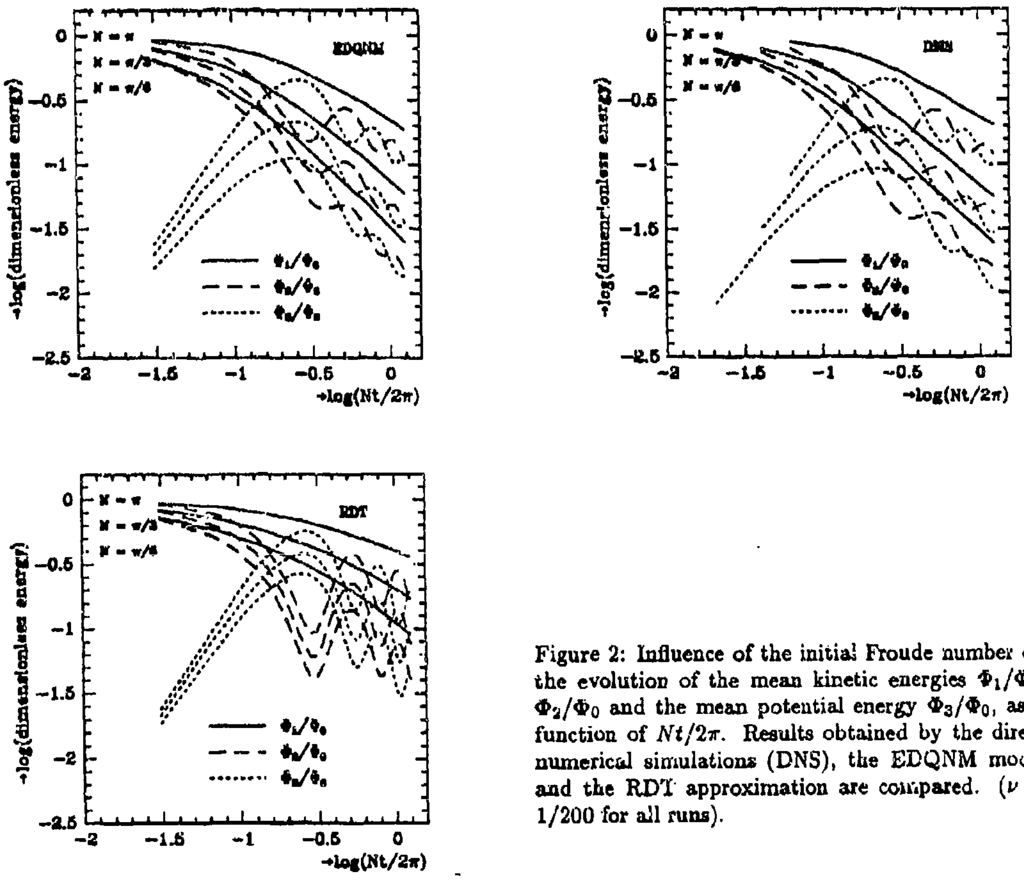

Figure 2: Influence of the initial Froude number on the evolution of the mean kinetic energies Φ_1/Φ_0, Φ_2/Φ_0 and the mean potential energy Φ_3/Φ_0, as a function of $Nt/2\pi$. Results obtained by the direct numerical simulations (DNS), the EDQNM model and the RDT approximation are compared. ($\nu = 1/200$ for all runs).

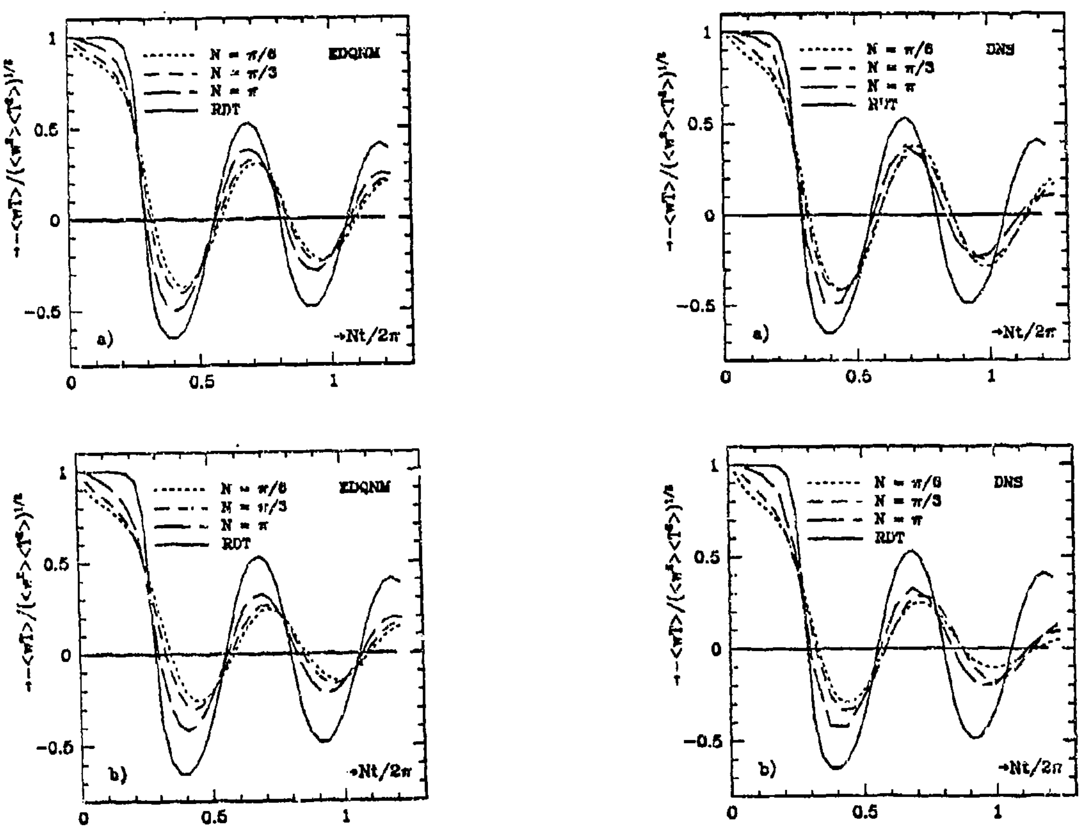

Figure 3: Influence of the initial Froude number on the evolution of the dimensionless heat-flux $< wT > /(< w^2 >< T^2 >)^{1/2}$ as a function of $Nt/2\pi$; a) $\nu = 1/100$; b)$\nu = 1/200$.

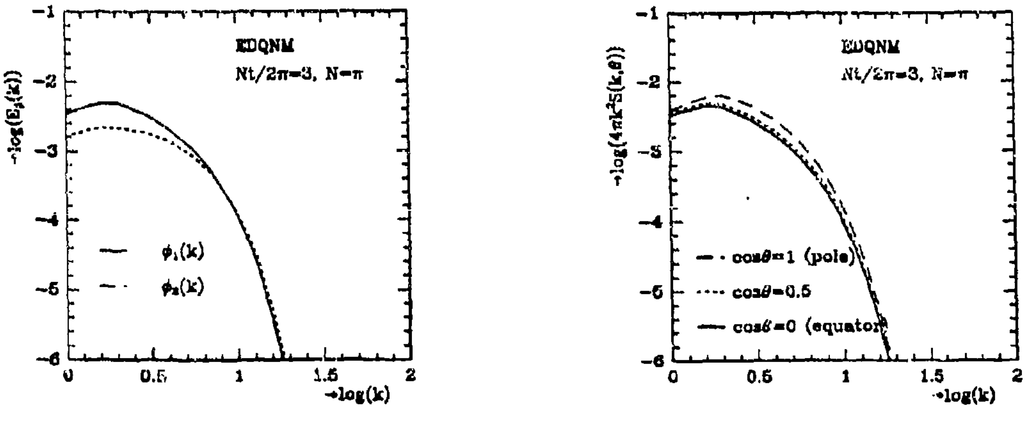

Figure 4: Spectral density of the total energy (kinetic + potential) $S(k,\theta)$ as a function of the wavenumber k and the spectral angle $\theta(\vec{k},\vec{e}_z)$ between the wavenumber vector $\vec{k}$ and the vertical direction $\vec{e}_z$ for EDQNM at $Nt/2\pi = 1.0$. The convention is such that $\theta = 0$ corresponds with the pole of a sphere of radius k and $\theta = \pi/2$ with the equator. All curves are multiplied by $4\pi k^2$, the area of the sphere of radius k, so that under isotropic conditions they reduce each to the usual spectrum of energy $E(k) = 4\pi k^2 S(k)$.

Some current problems in stratified turbulent flows

C W Van Atta

Applied Mechanics and Engineering Sciences and Scripps Institution of Oceanography,
University of California, San Diego, La Jolla CA 92093

INTRODUCTION

An essential ingredient of turbulent flow is fluctuating vorticity, and the main effect of stable stratification on fluctuating vorticity is the *baroclinic* generation of new vorticity, acccording to Bjerknes' famous theorem.

There is presently uncertainty over which, if any, well established properties of turbulence in homogeneous fluids can be exported for use in stably stratified fluids, and, when these laws fail to describe the behavior in the stably stratified case, what must replace them.

This talk will attempt to illustrate the flavor of some current research problems by considering several questions presently under study which address aspects of the evolution of baroclinically generated vorticity in turbulent flows. Both qualitative and quantitative differences with homogeneous fluid flow behavior will be discussed.

BAROCLINIC VORTICITY GENERATION IN THE STABLY STRATIFIED MIXING LAYER

To clearly illustrate the process of baroclinic vorticity generation we first look at the initial, laminar, development region of a stably stratified turbulent shear layer undergoing Kelvin-Helmholtz instability. This instability plays a prominent role in both atmospheric and oceanic shear layers, and may often be observed in cloud patterns. As an idealization of real geophysical flows, consider a laminar shear layer flow in which lighter fluid flows horizontally over a heavier fluid, with gravity acting in the vertical direction. When the interface between the two fluids of different density moving at different speeds rolls up due to Kelvin-Helmholtz instability, a cross section through the K-H roller looks like the spiral pattern of a jelly roll. The jelly is one fluid, the dough is the other. In some places along the interface between the two fluids one has light fluid over heavy (statically stable) but at others one finds heavy fluid over light (unstable). For a homogeneous fluid, in the next step of the instablility process three-dimensional vortices form, smaller in cross section than the K-H billows, which have their axes wrapped around the K-H billows. These 3-D vortices are efficient at transporting momentum and scalar properties, and so the rate of stirring and mixing of the fluid increases. But for the density stratified case Schowalter et al (1994 a,b) found that the initial formation of the "streamwise" vortices produces baroclinically generated vorticity of opposite sign at the stable interfaces and baroclinically generated vorticity of the same sign as the initial vortices at the statically unstable portions of the interface. The net result is that the vortices formed at the stable portions of the interface are much weaker than in the homogeneous case, and the 3-D stirring and subsequent molecular mixing is dominated by the vortices formed by the *convective* instability on the statically unstable parts of the interface.

A conceptual model of Broadwell and Breidenthal (1982) examines the rate at which a turbulent shear layer actually molecularly mixes the different species in the two streams, which depends on the rates of entrainment, macroscopic deformation, and molecular diffusion. Entrainment is the slowest step unless $D \ll \nu$, where D is the molecular diffusivity and ν is the kinematic viscosity. In gases, $D/\nu \sim 1$ and entrainment is the bottleneck. In liquids, however, ν may exceed D by a factor of hundreds or more, so that entrainment and diffusion may both provide important constraints on the mixing rate. Many analytical, experimental, and numerical studies have been made for the homogeneous fluid case. By comparison, only a few results are available (e.g. Koop and Browand, 1979) for the stably stratified turbulent mixing layer, and the time would seem to be ripe for more experiments, numerical simulations, and analytical models.

EFFECTS OF MEAN STRAIN ON TURBULENCE DYNAMICS IN A STRATIFIED FLUID

In flows over vertical topography in the ocean and atmosphere the bunching together (or divergence) of the mean streamlines in a vertical plane is accompanied by a similar bunching (or divergence) of the isopycnals (surfaces of constant mean density). As the isopycnals bunch together the mean density gradient increases, and where they diverge the mean density gradient decreases. There are thus two, sometimes competing, effects, mean strain and spatially variable buoyancy effects. The turbulence levels and vertical turbulent transports can be highly variable in such flows. The question arises whether one can explain this behavior as an effect of the mean strain of the flow and the spatial changes in the Vaisala frequency $N=(-g/\rho\ d\rho/dz)^{1/2}$ on the turbulence.

For homogeneous fluids the effect of mean strain on turbulence was examined in the early 1900's in connection with wind tunnel contractions, which were employed to reduce the relative turbulence level u'/U in the stream, where u' is the rms streamwise fluctuation in velocity and U is the mean velocity. The longitudinal fluctuations decrease passing through the contraction, while the rms lateral fluctuation w' increases through the contraction due to the stretching of streamwise vortices (Prandtl, 1933).

The simplest stably stratified flow for consideration of strain and variable buoyancy effects is flow of a turbulent stratified fluid with zero mean shear through a vertical contraction. The vertical contraction confines the flow to a shorter vertical extent, thus increasing the stratification strength and tending to damp vertical w' fluctuations, but at the same time it stretches longitudinal vortices as in the homogeneous case.

Experiments by Thoroddsen and Van Atta (1994) show that the addition of stable stratification changes the evolution of u' very little. However, w' decays more rapidly before the contraction because of the non zero value of N, and flattens out in the contraction. Then, as the flow leaves the contraction a surprising behavior of w' is observed. w' first decreases to a very low level, and then *increases* to a relative maximum value and then oscillates for the rest of its observed evolution!

The physics behind this behavior becomes apparent when examining the evolution of the rms density fluctuation ρ'. ρ' increases before, inside, and after the contraction, reaching a maximum value at the same location where w' reached a minimum, and then decreases. As ρ' is proportional to the rms fluctuating potential energy of the turbulence, and w' is proportional to the fluctuating kinetic energy of the turbulence the observed behavior reflects exchange of energy between the potential and kinetic energies. Gerz and Yamazaki (1993) found a similar growth of the vertical kinetic energy in numerical simulations which had an initial density fluctuation field and zero initial velocity fluctuation field, and suggested the term *zombie turbulence* to describe the phenomenon.

HOMOGENEOUS TURBULENT SHEAR FLOWS

In homogeneous turbulent shear flows, the mean velocity U in the x direction is a linear function of the lateral coordinate z, i.e. U(z)=az. All statistical quantities are independent of z. Experiments show that for a nonstratified, homogeneous fluid the turbulence production exceeds the dissipation and the velocity fluctuations grow spatially with x without bound, roughly exponentially with x. Similar behavior is found in direct numerical simulations in which the turbulence develops in time rather than spatially. If the flow is stably stratified Rohr et al (1988) found that the growth rate of the turbulence is a decreasing function of the Richardson number for $R<R_{cr}$, and becomes negative for $R>R_{cr}$, with R_{cr} equal to roughly 0.3. For $R=R_{cr}$ the turbulence kinetic energy production, kinetic energy dissipation, and buoyancy sink term which produces potential energy are in balance, and the rms energies in the velocity and density fluctuations is constant. There is, however, a continual spectral redistribution from small to large scales taking place, so that equilibrium is not reached in wave number space. Direct Numerical Simulations (DNS) of Holt et al (1992) suggest that the critical Richardson number might be a function of Reynolds number, but this has not so far been seen experimentally. DNS results also suggest that there are coherent structures in homogeneous shear flows in the form of horseshoe-like vortices oriented nearly along the principal extensional strain direction and that the effect of stable stratification in reducing the vertical transport is associated with a weakening of these vortical structures. The observation of such structures, should they exist, is a challenging problem. Piccirillo and Van Atta (1994a) have extended the large Schmidt number results of Rohr et al (1988) to Prandtl number of order one using temperature stratification in air. These data were obtained in a novel stratified shear flow channel described by Piccirillo and Van Atta (1994b). The lower value of a Pr number will allow a more definitive comparison of a direct numerical simulation, which are so far limited to small Pr, with experiments. Some aspects of these data and simulations will be compared in the present talk.

DOES LOCAL ISOTROPY EXIST IN TURBULENT SHEAR FLOWS IN A STABLY STRATIFIED FLUID?

In Large Eddy Simulations the form of the small scale motion must be assumed before doing a flow calculation. The simplest possible form is a small scale turbulent field obeying the constraints of local isotropy. According to Kolmogorov's original ideas, in a homogeneous fluid one should expect to see local isotropy in the small scales in a turbulent shear flow, provided that the scale separation between large and small scales is sufficiently large. "Local Isotropy" means isotropic behavior over a certain restricted or "local" wave number range. The relations for locally isotropic behavior of spectra, gradient moments, etc. are derived purely from kinematical and continuity arguments, not from dynamics. A large Reynolds number is not necessary for local isotropy, but the extent of the region of local isotropy is expected to increase with Reynolds number. The smallest scales in a low Reynolds number turbulent flow often exhibit local isotropy. However, it seems reasonable that if the ratio of mean strain to fluctuating strain is large enough one would expect anisotropic behavior. For energy spectra of the velocity and scalar fluctuations, Kolmogorov's idea appears to be borne out. Experiments and DNS at low R_λ show isotropic behavior at the smallest scales only, while experiments in the laboratory, atmosphere, and ocean show that the extent of isotropy increases as R_λ increases. For a review and recent laboratory experiments at high R_λ see Praskovsky et al (1993). For moments of velocity and scalar gradients the available data show a marked degree of anisotropic behavior. This is at first puzzling, as taking gradients is expected to emphasize the contributions of the fine structure. However, as is well known for nondifferentiated velocity and temperature fluctuations, such moments do include contributions from all scales, can be very sensitive to sharp gradients found near the edges of large scale coherent structures, and are generally not suitable for examining particular wave number ranges for locally isotropic behavior. The degree of local isotropy may be unambiguously examined by comparing the relative behavior of spectra of the gradients directly with the appropriate relations for local isotropy, as discussed in Van Atta (1991). This has yet to be done for turbulent shear flows, as most studies to date have measured only moments and not the spectra of gradients. An exception is the work of Dahm et al (1991), in which it was found that the spectra of the small scale scalar gradient field (all three components were measured) obeyed isotropic relations within the uncertainty of the somewhat limited statistical sample.

But what is the expected behavior in a stably stratified flow? If a range of scales exists that are not affected by stratification then there might be local isotropy in that range. The common wisdom tells us that in a steady state stratification most strongly affects scales larger than the Ozmidov scale $L_O = (\varepsilon/N^3)^{1/2}$, where ε is the dissipation rate of turbulent kinetic energy, and that in decaying shear free turbulence stratification should affect the largest scales first. However, Thoroddsen and Van Atta (1993) found experimentally that for decaying stratified grid turbulence moments and spectra of velocity derivatives, which emphasize the smaller scales and initially obey isotropic relations early in the decay, very strongly departed from isotropic behavior right after the beginning of the decay. A similar behavior is found for temperature gradients. Since one would have expected the largest scales to be affected first, it is surprising that the gradients are affected even before there are large effects on large scale properties like turbulence intensities and buoyancy flux. Perhaps the range of scales in these experiments is too small to expect substantial local isotropy under stratified conditions. It would be very useful to have further experiments or numerical simulations covering several more decades in R_λ. Such a range would be very difficult for experimentalists to achieve and is presently not yet possible even for direct numerical simulations.

REFERENCES

Broadwell JE and Breidenthal RE, A simple model of mixing and chemical reaction in a turbulent shear layer, *J Fluid Mech* **125**, 397-410 (1982).

Dahm WJA, Southerland KB, and Buch KA, Direct, high resolution, four-dimensional measurements of the fine scale structure of Sc>>1 molecular mixing in turbulent flows, *Phys. Fluids A*, 3(5), 1115-1127 (1991).

Gerz DT and Yamazaki H, Direct numerical simulation of buoyancy -driven turbulence in stably stratified fluid, *J Fluid Mech* , **206**, 563-594 (1993).

Holt SE, Koseff JR, and Ferziger JH, A numerical study of the evolution and structure of homogeneous stably stratified sheared turbulence, *J Fluid Mech* , **237**, 499-539 (1992).

Koop CG and Browand FK, Instability and turbulence in a stratified fluid with shear, *J Fluid Mech* , **93**,135-159 (1979).

Piccirillo P and Van Atta CW, The evolution of a uniformly sheared thermally stratified turbulent flow, *J Fluid Mech* . (in preparation, 1994a).

Piccirillo P and Van Atta CW, An experimental facility for producing thermally stratified turbulent flows with arbitrary velocity and density profiles, *Experiments in Fluids*. (in preparation, 1994b).

Prandtl L, Attaining a steady air stream in wind tunnels, NACA TM, 726 (1933).

Praskovsky AA, Karyakin M Yu, and Kuznetsov VR, Experimental verification of local isotropy assumption in high Reynolds number flows, in *Proceedings of the Third European Turbulence Conference*, Stockholm, 1990 (1991).

Rohr JJ, Itsweire EC, Helland KN, and Van Atta CW, Growth and decay of turbulence in a stably stratified shear flow, *J Fluid Mech* , **195**, 77-111 (1988).

Schowalter DG, Van Atta CW, and Lasheras JC, A study of streamwise vortex structure in a stratified shear layer, submitted to *J Fluid Mech* (1994a).

Schowalter DG, Van Atta CW, and Lasheras JC, Baroclinic generation of streamwise vorticity in a stratified shear layer, *Meccanica* (in press, 1994b).

Thoroddsen ST and Van Atta CW, The influence of stable stratification on small-scale anisotropy and dissipation in turbulence, *J. Geophys. Res.- Oceans*, 97, C3, 3647-3658 (1992).

Thoroddsen ST and Van Atta CW, The effect of mean strain on turbulence dynamics in a stably stratified fluid, *J Fluid Mech* (in press, 1994).

Van Atta CW, Local isotropy of the smallest scales of turbulent scalar and velocity fields, Proc. Roy. Soc. London Ser. A, 434,139-147 (1991).

Diffusion in the Presence of Stable Stratification

J.R. Herring and Y. Kimura
N.C.A.R., Boulder CO 80307
U.S.A.

Abstract

We examine results of direct numerical simulations (DNS) of homogeneous turbulence in the presence of stable stratification with the goal of contributing to understanding the effect of stratification on eddy-diffusion, and the distribution of pairs of particles released in stable stratified flow. Both rotating and non-rotating studies will be included in our purview. On a simple level, stratified turbulence may be considered as a mixture of turbulence (with vortex stretching) and waves, with the waves at larger scales, and turbulence at smaller scales (smaller than the Ozmidov scales (Ozmidov (1963)). We first discuss whether such characterization is reasonable. This assessment is made by comparing DNS results for diffusion of a scalar with simple closure estimates, which are extensions of the method introduced by Larcheveque and Lesieur (1981) to the case of stratified flows. As may be expected, the stable stratification reduces the pair separation in the direction of stratification, and leaves the separation in the transverse directions unaltered. The pair-dispersion is well predicted by a theory which includes the anisotropic nature of the flow and incorporates the Brunt-Väisälä frequency as a damping rate for dispersal. We also discuss the reduction of eddy-diffusion due to stratification, and compare the numerical findings with the theoretical estimates of Csanady (1964) and Pearson *et al.* (1983).

1. Introduction

The inhibition of eddy transport by stable stratification is a topic of interest both in atmospheric and oceanic dynamics. The source of this inhibition is clear if we recall that stability implies that the total energy is partitioned between waves and turbulence, and only the latter is efficient in eddy transport. In this paper we examine this issue using direct numerical simulation (DNS), and simple scaling laws and underlying concepts drawn from the statistical theory of turbulence. Such statistical ideas are cleanest at asymptotically large Reynolds numbers, a domain remote from DNS. However, the basic assumptions of the statistical theory apply equally to low Reynolds number, rapidly decaying flows, and in this paper we check to see to what degree DNS and statistical theory agree in the low Reynolds number limit ($R_\lambda \sim 20$). Our method is to use the statistical theory to extract the functional dependence of dispersive effects on turbulence spectra and control parameters, and compare these to the DNS. More importantly, the DNS should provide clean and independent data quantifying the effects of stratification. Sec. 2 records the equations of motion of the DNS, and describes simple statistical predictions for eddy diffusion and particle dispersion in the presence of stable stratification. Sec. 3 describes the numerical techniques of the DNS, and discusses its relation to statistical theory.

2. Eddy Conductivity and Particle Dispersion for Stratified Flows

(a) Eddy Diffusion with Stratification.

We sketch some theoretical notions about the effects of stratification on eddy diffusion. We do this within the limits of incompressible Navier–Stokes which we write in standard non- dimensional form:

$$(\partial_t - \sigma\nabla^2)\mathbf{u} = -\mathbf{u}\nabla\cdot\mathbf{u} - \nabla p + \hat{\mathbf{g}}\theta - 2\mathbf{\Omega}\times\mathbf{u} \tag{1}$$

$$(\partial_t - \nabla^2)\theta = -N^2 w - \mathbf{u}\cdot\nabla\theta \tag{2}$$

$$\nabla\cdot\mathbf{u} = 0 \tag{3}$$

Our notation is that $(\mathbf{u},\theta)$ are the velocity– temperature fluctuations. The (x,y,z) components of $\mathbf{u}$ are (u,v,w). N is the Brunt–Väisälä frequency, $\sqrt{g\alpha(\partial\overline{T}/\partial z)/T_0}$, and $\mathbf{g} = (0,0,-1)$. In the present preliminary version of this paper, shall not discuss the effects of rotation.

Consider first unstratified turbulence. We may estimate eddy conductivity by the formula of Kraichnan (1976), (see also Lesieur (1990) for more discussions):

$$\kappa_{eddy} = (2/3)\int_0^\infty dkE(k)/\eta(k), \tag{4}$$

where $E(k) \equiv (1/2)\langle\mid \mathbf{u}(\mathrm{k}) \mid^2\rangle$ is the kinetic energy spectrum, $\eta(k)$ the eddy circulation time at scale $2\pi/k$. In Herring *et al.* (1982) p.419 *et seq.* it is argued that an approximate formula, derived from the Test Field Model (TFM), is

$$\eta(k) \sim \sqrt{\int_0^k dpp^2E(p)} \tag{5}$$

Consider next how effects of stratification may be included by modification of (4). Folklore has it that stratification means waves (oscillations at large scales), and " turbulence " (overturning events) at small scales. The dividing scale between these is the Ozmidov scale at which the eddy turnover rate is equal to the gravity wave frequency. Denoting this scale by k_O, we estimate its value from:

$$\eta(k) \equiv N \tag{6}$$

At large Reynolds numbers, for which $E(k) \sim \epsilon^{2/3}k^{-5/3}$, $k_O = \sqrt{N^3/\epsilon}$. A naive suggestion is that wave–motion contributes little to particle dispersion, so that (4) should be replaced by:

$$\kappa_{eddy} = (2/3)\int_{k_O}^\infty dkE(k)/\eta(k) \tag{7}$$

Of course, we must take account of the change of $E(k,t)$ induced by stratification. A closure estimate of $E(k)$ is obtained by equating the energy flux to small scales (ϵ) to the integral of the energy transfer, $T(k)$,

$$(\partial_t + 2\nu k^2)E(k) = T(k) \tag{8}$$

and evaluating the latter as entirely local in wave number space. There results:

$$\epsilon = \{k^3E(k)/(\eta(k) + N)\}E(k)[k] \tag{9}$$

Here, $\{\cdot\}$ is the square of the turbulence force, $(\eta(k))^2$ (estimated here as $\sim k^3E(k)$)) times the length of time this force acts ($\sim 1/(N + \sqrt{k^3E(k)})$). The factor $[k]$ estimates $\int_k^\infty \{\text{etc.}\}dk'$, an integral over all scales that comprise the net flux, ϵ. Note that (9) suggests that the energy spectrum changes from its wave dominated form ($\sqrt{\epsilon}Nk^{-2}$) to the turbulence dominated form ($\epsilon^{2/3}k^{-5/3}$) at k_O. Then using (9), (7) becomes:

$$\kappa_{eddy} \sim \epsilon/N^2 \tag{10}$$

We remark that (10) also results from Taylor's classical formula that evaluates κ_{eddy} in terms of an integral of the Lagrangian autocorrelation, $U(\mathbf{x},t \mid s)$, along particle trajectories:

$$\kappa_{eddy} \sim \int_0^t U(\mathbf{x},t \mid s)ds \tag{11}$$

$$U(\mathbf{x},t \mid s) \equiv \langle \mathbf{u}(\mathbf{x},t) \cdot \mathbf{u}(\mathbf{x},t \mid s)\rangle, \tag{12}$$

provided we take for the Lagrangian decorrelation of $U(k,t \mid s)$

$$U(k,t \mid s) \sim U(k,t \mid t)\exp\{-(\eta(k) + i\sin(\vartheta)N)(t-s)\} \tag{13}$$

Here, ϑ is the angle $\mathbf{k}$ makes with the vertical. Of course, the exponential characterization in (13) is a matter of convenience rather than of accuracy.

(b) Pair Dispersion.

Let $\mathcal{P}(\rho,t)$ be the probability density that two particles of fluid initially at $(\mathbf{r}_1(0), \mathbf{r}_2(0))$ have a displacement ρ at time t:

$$\mathcal{P}(\rho,t) = \langle \delta(\rho - (\mathbf{r_1(t)} - \mathbf{r_2(t)}))\rangle \tag{14}$$

where $\langle\cdot\rangle$ denotes an ensemble average, and

$$d\mathbf{r}_{(1,2)}(t)/dt \equiv \mathbf{u}(\mathbf{r}_{(1,2)},t). \tag{15}$$

Here $\mathbf{u}$ is the velocity field, and $d/dt\{\cdot\}$ is the rate of change of $\{\cdot\}$ following particle trajectories: $\equiv (\partial_t + \mathbf{u}\cdot\nabla)\{\cdot\}$. Here $\delta(\cdot)$ is the initial unaveraged distribution of particle pairs (Dirac's delta function). The equation of motion for $\mathcal{P}$ is:

$$\partial_t\mathcal{P}(\rho,t) = \langle(\mathbf{u}_1(t) - \mathbf{u}_2(t))\cdot\nabla_\rho\delta\rangle, \tag{16}$$

$$\partial_t \delta = (\mathbf{u}_1(t) - \mathbf{u}_2(t)) \cdot \nabla_\rho \delta, \ \Rightarrow$$

$$\delta = \delta(t=0) + \int_0^t ds \Delta \mathbf{u}(s) \cdot \nabla_\rho \delta(s), \ \Rightarrow \tag{17}$$

$$\partial_t \mathcal{P}(\rho, t) = \langle \Delta(\mathbf{u}(t)) \cdot \nabla_\rho \int ds \Delta(\mathbf{u}(s)) \cdot \nabla_\rho \delta(s) \rangle, \tag{18}$$

where $\Delta \mathbf{u}(t) \equiv \mathbf{u}_1(t) - \mathbf{u}_2(t)$. At this point, we invoke a quasinormal factorization of the ensemble mean, and interpret the time integrals as along Lagrangian trajectories. Thus,

$$\partial_t \mathcal{P}(\rho, t) \simeq \langle \Delta(\mathbf{u}(0, t)) \cdot \nabla_\rho \int ds \Delta(\mathbf{u}(\rho, s)) \cdot \nabla_\rho \rangle \mathcal{P}(\rho, s) \tag{19}$$

The evolution of moments such as

$$\langle \rho_n \rho_m \rangle \equiv \int d\rho \rho_n \rho_m \mathcal{P}(\rho, t) \tag{20}$$

follows from (19) after partial integrations:

$$\partial_t \langle \rho_n \rho_m \rangle = \int_0^t ds (2U_{nm}(0, t \mid s) - U_{mn}(\rho, t \mid s) - U_{mn}(\rho, t \mid s)) \tag{21}$$

In the long time limit, the terms depending on ρ may be dropped, and the first term is just the eddy conductivity, (4), as is well known. A crude estimate of dispersion is obtained by first writing the Lagrangian decorrelation $U(\rho, t \mid s)$ in its wave–number representation

$$U(\rho, t \mid s) = \int d\mathbf{k} \exp(-\iota \mathbf{k} \cdot \rho) U(\mathbf{k}, t \mid s) \tag{22}$$

and then approximating $U(\mathbf{k}, t \mid s)$ by (13), with $\eta(k)$ given by (5). In (22) we assume the total decorrelation is that produced by the internal (random) strain $(\sqrt{\int_0^k p^2 E(p)})$, and stratification. We estimate the net effect of these by their product. Here, ϑ is the angle $\mathbf{k}$ makes with the vertical.

The derivations of this section are quite heuristic in nature, and are presented to introduce various statistical quantities, and their possible utility in relating DNS results to theoretical concepts.

3. DNS Results and Discussion of Theoretical Issues

The DNS consists of an initial Gaussian isotropic velocity field, which is allowed to decay. After one eddy circulation time (when the skewness factor builds up to its nominal value of ~ .5), stratification is introduced, and temperature fluctuations are induced *via* (3). The basic code and numerical procedure is described in Kimura (1992); our treatment of the stratification is similar to Métais and Herring (1989). In order to obtain particle trajectory information (as well as Lagrangian covariances, as in (11)), trajectories were computed by solving $d\mathbf{X}(t)/dt = \mathbf{u}(\mathbf{X}, t)$, with cubic-spline interpolation used to get the necessary fine-scale information for $\mathbf{X}(t)$. The method is thus quite similar to that of Yeung and Pope (1989) and Yeung (1993). Computations were carried out on NCAR's IBM SP1, at resolution of 64^3. We plan to refine these calculations at higher resolution ($128^3 \rightarrow 256^3$), possibly on the Cray 3. At that stage, we shall also implement large-scale random stirring, in order to investigate stationary turbulence.

Fig. 1 shows histograms for the vertical dispersion of particle pairs for cases $N^2 = 0$, (a), and $N^2 = 50$ (b), at $t = 3.0$. Initially, the inter particle-pair distance was .5 mesh lengths. These distributions are un-normalized. Notice that stratification severely inhibits diffusion in the vertical, a result similar to that found by Riley and Metcalfe (1990) in their study of a turbulent patch introduced into stably stratified fluid. As time proceeds, ($t > 3.0$) the unstratified histogram continues to broaden, while the stratified histogram widens extremely slowly, if at all.

Fig. 2 illustrates the effects of stratification on enstrophy. The $N^2 = 0$ (case (c)) shows the familiar pattern of elongated vortex tubes, while for $N^2 = 10$ (case (a)) we see flattened vortex patches. Further analysis of this case (not shown) shows that the enstrophy here is comprised mainly of vertical vorticity. Fig. 2 (b) shows the temperature fluctuation field for $N^2 = 10$; a pattern similar to (a) for the enstrophy. It would be of interest here to also examine the associated heat flux distribution, $w\theta$.

Fig. 3 shows the mean vertical dispersion of particle pairs for ($N^2 = 0, 1, 2, 5, 10, 20, \& \ 50$). At late times, there are step-like increases in $\langle\rho^2\rangle$, which may be explained by the relationship between $\langle\rho^2\rangle$ and the Lagrangian autocorrelation function (see (21)).

Normalized autocorrelation functions are shown in Fig. 4, for several values of N^2. Notice that $R(N, \tau)$ has an oscillatory behavior, much like that proposed by Csanady (1964), and as crudely parameterized here by (13). It would be of interest to explore the functional form that should replace (13), and this can be done with the numerical data presented here, especially if extended to the stationary case. An interesting question here is the extent to which Csanady's model,

$$R(\tau) = \exp(-p\tau)\sin(\alpha\tau + \delta) \tag{23}$$

is accurate.

Figure Captions

Fig. 1 Distribution function, $\mathcal{P}(\rho, t)$ for $N^2 = 0$ (a), and $N^2 = 50$ (b).

Fig. 2 (a,b): Iso-surfaces enveloping regions where enstrophy (squared vorticity) or squared temperature fluctuations (b) exceed 4 times their averaged value for $N^2 = 10$. (c): Iso-surfaces enveloping regions where enstrophy exceeds 4 times its averaged value for $N^2 = 0$.

Fig. 3 Mean vertical dispersion of particle pairs, $\langle\rho^2\rangle(t)$ for $N^2 = 0, 1, 2, 5, 10, 20, 50$.

Fig. 4 Lagrangian velocity auto-correlation function $\langle w(t_0)w(t_0 + \tau)\rangle / \langle w^2(t_0)\rangle$ for $N^2 = 0, 2, 10, 50$. Here, t_0 is one eddy circulation time (about twice the time needed for enstrophy to achieve its maximum for the unstratified case).

References

Csanady, G.T. 1964: *J. Atmos. Sci.*, **21**, 439.

Larcheveque, M., and M.Lesieur, 1981: *J. de Mécanique*, **20**, 113.

Lesieur, M. 1990: *Turbulence in Fluids*, 2nd Edition.*Kulwar Academic Publishers*, Dordrecht. 412pp.

Herring, J. R., D. Schertzer, M. Lesieur, G. R. Newman, J. P. Chollet, and M. Larcheveque 1982, *J. Fluid Mech.*, **124**, 411.

Kraichnan, R. H.: 1976, *J. Atmos. Sci.*, **33**, 1521.

Kimura, Y. 1992: Proceedings of NATO Advanced Research Workshop on " Topological Fluid Dynamics ", 1-5 Nov. 1991,(H.K. Moffatt, R.M.Zaslavsky, M. Tabor, & P. Comte, Eds.), Kluwer Acad. Press, Dordrecht, Netherlands.,401.

Métais, O. and J. R. Herring, 1989: *J. Fluid Mech.*, **202**, 117.

Pearson, H.J., J.S. Puttock, and J.C.R.Hunt: 1982 *J. Fluid Mech.*,**129**, 219.

Ozmidov, R.V.,1965: *Izv. Acad. Sci. USSR Atmos. Oceanic Phys.*, **1**, 493.

Riley, J.J., & Metcalfe, R.W., 1990: *Stratified Flows*, E.J. List & G.H. Jirka Ed., Am. Soc. Civil Eng., N. Y., N.Y. 10017- 2398, 541.

Yeung. P.K., 1993: 9th *Symposium on Turbulent Shear Flows*, Kyoto, Japan, August 16-18, 1993, 17-2-1–17-6.

Yeung. P.K., and Pope, S. B. 1989: *J. Fluid Mech.*, **207**, 531.

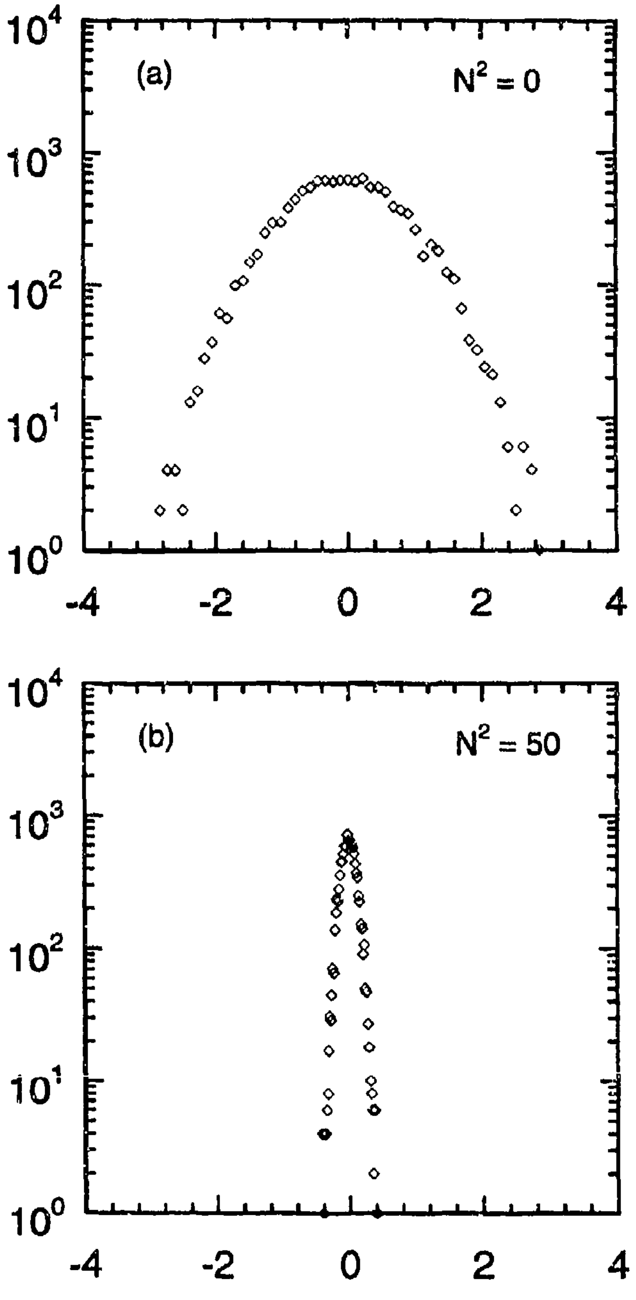

Fig. 1

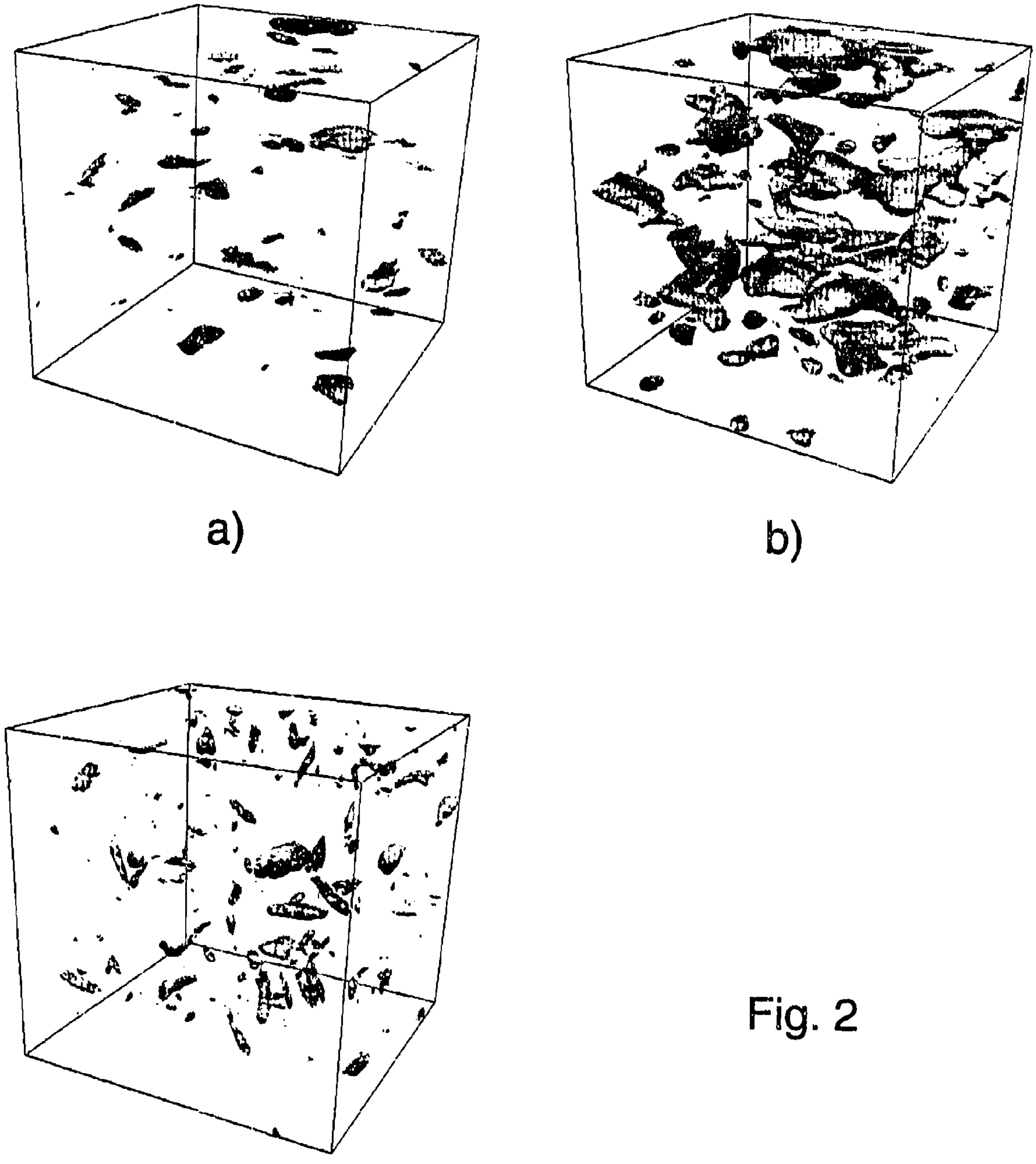

a)

b)

c)

Fig. 2

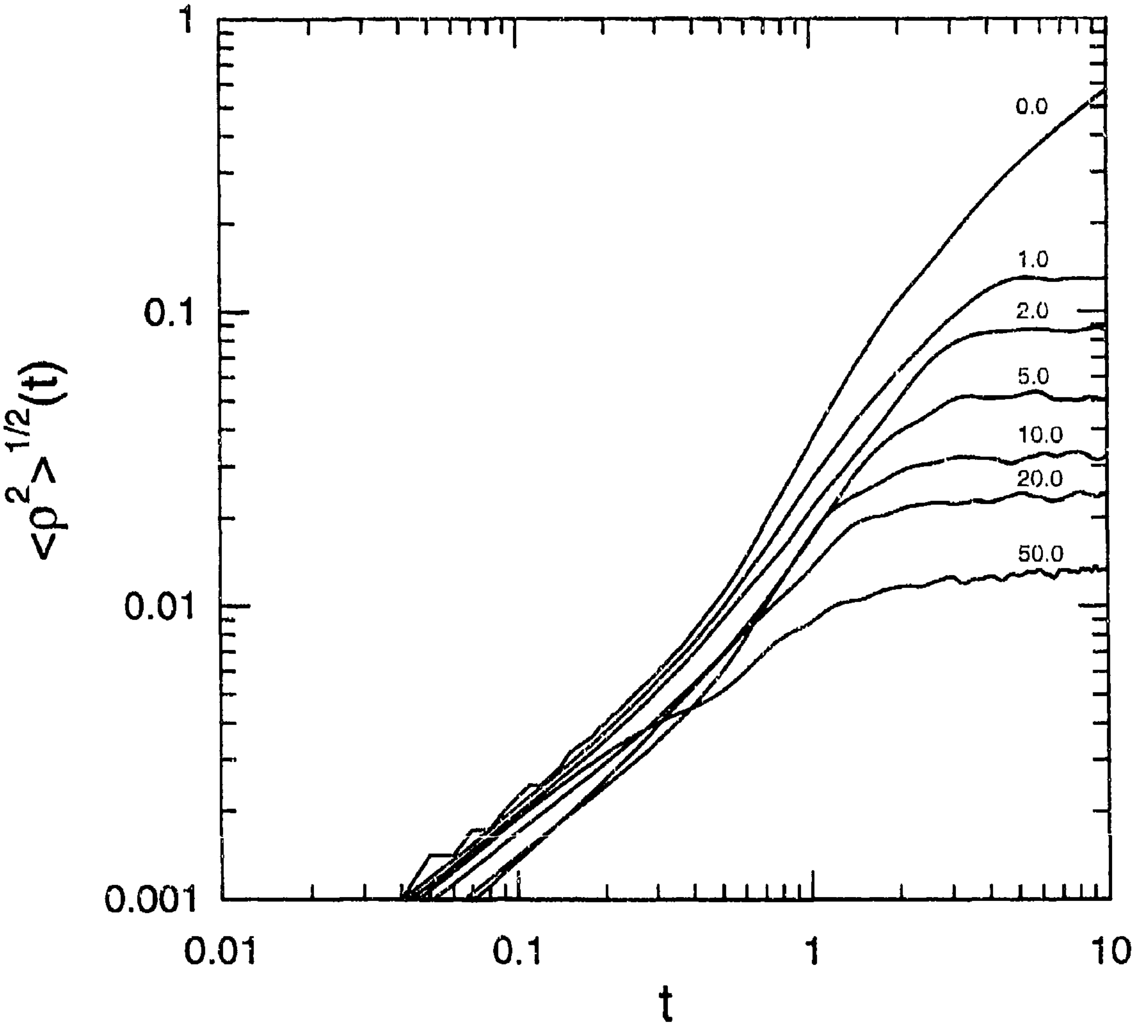

Fig. 3

ON GRADIENT-TRANSPORT TURBULENCE MODELS
FOR STABLY STRATIFIED SHEAR FLOW

C. Kranenburg

Dept. of Civil Engineering, Delft University of Technology, P.O. Box 5048, 2600 GA Delft, The Netherlands

The gradient transport model for stably stratified horizontal shear flow in which eddy diffusivity and viscosity are assumed to depend on the gradient Richardson number, *Ri*, is augmented with terms representing the finite adjustment time of the exchange coefficients. Barenblatt et al. (1993) showed that using such a model, initial value problems for the formation of a step-wise structure of the buoyancy distribution are well posed. The model proposed is analyzed taking into account the interaction between buoyancy and velocity fields. A condition for the formation of steps is derived from a linear stability analysis. Numerical computations show that a realistic step-wise finestructure develops, provided linear instability is allowed on a finite interval of *Ri* only.

1. Introduction

In simple gradient-type turbulence models of horizontal shear flows the vertical transports of momentum and scalar quantities like mass or heat are assumed to be proportional to (minus) the vertical gradients of mean velocity and scalar, respectively. Under stably stratified conditions the proportionality coefficients, that is, eddy viscosity and diffusivity, decrease with increasing gradient Richardson number *Ri*, because the stratification reduces the exchange. As a result the vertical distributions of mean velocity and buoyancy associated with the scalar quantity are coupled, *Ri* depending on both velocity and buoyancy gradients.

Gradient-type turbulence models have been invoked to explain the development of step-wise structure (a system of layers and interfaces) in buoyancy distributions observed in the deep ocean, lakes and estuaries. Phillips (1972) considered the buoyancy equation only, and suggested that an effective diffusivity related to the eddy diffusivity could become negative for large *Ri* thus leading to instability and possibly a step-wise structure. Posmentier (1977) solved the buoyancy equation numerically and obtained a step-wise buoyancy profile for a linearly unstable case. However, substantial filtering was needed to suppress instabilities, which arouses some doubt as to what turbulence model was actually considered. Kranenburg (1982) showed that including the interaction between buoyancy and velocity fields results in more stable behaviour, and argued that solutions should be stable because ensemble-averaged model equations may no longer exhibit the small-scale instabilities of diffusion-type models with negative diffusivity.

Barenblatt et al. (1993, hereafter BBDPU) stated that such models are inadequate because initial-value problems are ill-posed and solutions are non-unique. These authors took into account the finite adjustment time of the turbulence by introducing a time delay in the eddy diffusivity together with a Taylor expansion for small time delays, and showed that in this way a well-posed problem results. BBDPU presented accurate numerical solutions of their model equation, and thus were able to show that in the linearly unstable case a step-wise structure evolves from an initially smooth buoyancy distribution. BBDPU did not consider the interaction with the velocity field.

On the experimental side, Long (1972) reported the spontaneous development, at a particular value of an overall Richardson number, of three layers in the stratified shear-flow apparatus also used by Moore & Long (1971). Ruddick et al. (1989) observed the formation of multiple layers and interfaces in a laboratory tank in which a linearly stratified liquid was present initially. The liquid was stirred so as to avoid generating a mean flow. Layers developed provided stirring was weak, although a minimum level of stirring was needed presumably to overcome molecular effects.

In the work reported here the suggestion of BBDPU is explored in conjunction with the interaction between mean buoyancy and velocity fields. The finite adjustment time of eddy diffusivity and eddy viscosity is taken into account, in Section 2, in a somewhat different way by augmenting the usual relationships between exchange coefficients and Ri with terms consisting of the time derivatives of these coefficients multiplied by a time constant. In Section 3 the linear stability of the turbulence model thus modified is addressed, and numerical solutions are presented in Section 4. In Section 5 the implications for the development of finestructure are briefly discussed.

2. Mathematical model

Consider a stably stratified shear flow that is horizontally homogeneous so far as mean quantities are concerned. Assuming the vertical turbulent transports may be modelled as gradient transports and adopting the Boussinesq approximation, the conservation equations for mean horizontal momentum and buoyancy are

$$\frac{\partial U}{\partial t} = \frac{\partial}{\partial z}\left(K_m \frac{\partial U}{\partial z}\right) \tag{2.1}$$

$$\frac{\partial B}{\partial t} = \frac{\partial}{\partial z}\left(K_b \frac{\partial B}{\partial z}\right) \tag{2.2}$$

where U is the mean horizontal velocity, $B = -g\delta\rho/\rho_0$ the mean buoyancy, g the acceleration of gravity, ρ_0 a reference density, $\delta\rho$ the deviation from ρ_0, z the vertical coordinate (positive upwards), t time, and K_m and K_b are the eddy viscosity and eddy diffusivity.

The method of averaging, which defines U and B, for example, is not trivial here. If the mean quantities were ensemble averages, step-wise solutions would be unrealistic. The initial conditions affect step-wise solutions for all times because of the intrinsic instability of these solutions. As a consequence, steps would develop at different levels in each realization so that, upon averaging, smooth distributions of U and B would result. For step-wise solutions to be physically acceptable, mean quantities therefore must be assumed to represent horizontal averages obtained from a single realization.

As also noted by BBDPU, second-order closure turbulence models are usually based on the balance equation of turbulent kinetic energy. An additional equation is needed to estimate the length scale of the energy containing eddies, and the exchange coefficients. A formal expression for such equations can be written as (e.g., Launder & Spalding, 1972)

$$\frac{\partial \Psi}{\partial t} = S_\Psi \tag{2.3}$$

where Ψ is a turbulence parameter, e.g., turbulent kinetic energy, or dissipation rate, and S_Ψ a source term representing production, destruction and redistribution of Ψ. Because S_Ψ does not contain any time derivatives, equations like (2.3) can in principle be combined to yield evolution equations for the exchange coefficients of the form

$$\frac{\partial K}{\partial t} = S_K \tag{2.4}$$

where $K = K_m$ or K_b and S_K again a source term. In local-equilibrium models the time derivative of K is neglected, which gives $S_K = 0$. In a model of Prandtl-Kolmogorov type $S_K \propto - K + u_* l F(Ri)$, where u_* is the friction velocity, l a length scale of the large eddies under neutral conditions, F a positive damping function representing the influence of stratification ($F(0) = 1$ and $dF/dRi < 0$ for finite Ri), and $Ri = (\partial B/\partial z)(\partial U/\partial z)^{-2}$ the gradient Richardson number ($Ri \geq 0$). Expressions that do take the finite adjustment time of the exchange coefficients in this model into account therefore are

$$\tau \frac{\partial K_m}{\partial t} = -K_m + u_* l F_m(Ri) \tag{2.5}$$

$$\tau \frac{\partial K_b}{\partial t} = -K_b + u_* l F_b(Ri) \tag{2.6}$$

where τ is a time scale of the large eddies. Equations 2.5 and 2.6 ensure that the exchange coefficients never become negative. The length scale l is not well known for stratified flows so that using (2.5) and (2.6), quantitatively correct results are not easily obtained.

Equation 2.6 is the counterpart of the expression proposed by BBDPU (equation 2.5 is new). A first-order regular asymptotic expansion for $\tau \partial K_b/\partial t \rightarrow 0$ gives, when applied to (2.6),

$$K_b \approx u_* l \left[F_b(Ri) - \tau F_b'(Ri) \frac{\partial Ri}{\partial t} \right] \tag{2.7}$$

where the prime refers to differentiation with respect to Ri. Equation 2.7 is equivalent to equation (15) of BBDPU. However, the time-derivative term in (2.6) does not always remain small for large wave numbers. BBDPU show that it is the behaviour at large wave numbers that determines the ill-posedness or well-posedness of initial-value problems. Some difference between the models therefore exists.

An alternative formulation of the eddy diffusivity would be to replace (2.6) with an expression also resulting from algebraic stress/flux turbulence models,

$$K_b = K_m \sigma_t^{-1}(Ri) \tag{2.8}$$

where σ_t is the turbulent Prandtl number, which in free turbulence increases with Ri (e.g., Mizushina et al., 1978).

Introducing dimensionless variables according to $U = U_1 U^*$, $B = B_1 B^*$, $t = Tt^*$, $\tau = T\tau^*$, $K = u_* l K^*$ and $z = hz^*$, where the asterisk (superscript) denotes a dimensionless variable, and T and h are constants, equations 2.5 and 2.6 become (the asterisks are dropped)

$$\tau \frac{\partial K_{m,b}}{\partial t} + K_{m,b} = F_{m,b}(Ri) \tag{2.9}$$

Equations 2.1 and 2.2, and the expression for Ri, remain unchanged by putting $T = h^2/(u_* l)$ and $U_1^2 = B_1 h$. If it is assumed that $\tau \sim 1/N_1$, where N_1 is an overall buoyancy frequency given by $N_1^2 = B_1/h$, the dimensionless time constant τ^* will be of the order of $(l/h)/Ri_*^{1/2}$. Here $Ri_* = B_1 h/u_*^2$ is an overall Richardson number.

3. Linear stability analysis

The undisturbed velocity and buoyancy distributions are assumed to be time-independent and linear functions of z. Perturbations are introduced according to

$$U(z,t) = U_0 + \gamma_m[z + u(z,t)] \tag{3.1}$$

$$B(z,t) = B_0 + \gamma_b[z + b(z,t)] \tag{3.2}$$

$$K_m = F_{m0} + k_m \tag{3.3}$$

$$K_b = F_{b0} + k_b \tag{3.4}$$

where U_0, B_0, γ_m, γ_b, $F_{m0} = F_m(Ri_0)$ and $F_{b0} = F_b(Ri_0)$ are constants. Here $Ri_0 = \gamma_b/\gamma_m^2$.

Substituting from (3.1) - (3.4) and linearizing, equations 2.1, 2.2 and 2.9 give as perturbation equations

$$\frac{\partial u}{\partial t} = F_{m0}\frac{\partial^2 u}{\partial z^2} + \frac{\partial k_m}{\partial z} \tag{3.5}$$

$$\frac{\partial b}{\partial t} = F_{b0}\frac{\partial^2 b}{\partial z^2} + \frac{\partial k_b}{\partial z} \tag{3.6}$$

$$\tau\frac{\partial k_m}{\partial t} + k_m = Ri_0 F'_{m0}\left(\frac{\partial b}{\partial z} - 2\frac{\partial u}{\partial z}\right) \tag{3.7}$$

$$\tau\frac{\partial k_b}{\partial t} + k_b = Ri_0 F'_{b0}\left(\frac{\partial b}{\partial z} - 2\frac{\partial u}{\partial z}\right) \tag{3.8}$$

A harmonic solution to (3.5) - (3.8) is sought by putting

$$u = u_h \exp(\lambda t + i\kappa z) \tag{3.9}$$

$$b = b_h \exp(\lambda t + i\kappa z) \tag{3.10}$$

where κ is a real wave number, λ a possibly complex frequency, and u_h and b_h are constants. The solutions are linearly stable for $\mathrm{Re}\lambda \leq 0$, whereas $\mathrm{Re}\lambda > 0$ implies instability of the solution.

The case where λ is complex with $\mathrm{Re}\lambda > 0$ is not acceptable from a physical point of view. Numerical calculations using the full set of equations in this case produced wave-like solutions in which interfaces continued to travel up and down between upper and lower boundaries of the computational domain. Such results are at variance with the experimental evidence addressed in the Introduction. Therefore, only linearly unstable solutions having $\mathrm{Im}\lambda = 0$ can be physically realistic.

Substituting from (3.9) and (3.10), equations 3.5 - 3.8 yield a homogeneous, linear set of equations. Equating the coefficient determinant to zero gives as a dispersion relation (the subscript *0* is dropped)

$$\tau\lambda^3 + [1 + \kappa^2\tau(F_b + F_m)]\lambda^2 + \kappa^2(p + \kappa^2\tau F_b F_m)\lambda + \kappa^4 q = 0 \tag{3.11}$$

where

$$p = F_b + F_m + Ri(F'_b - 2F'_m) \tag{3.12}$$

$$q = F_b F_m + Ri(F'_b F_m - 2F_b F'_m) \tag{3.13}$$

For $\tau = 0$ equation 3.11 reduces to an expression derived by Kranenburg (1980). The stability of a solution given by (3.9) and (3.10) depends on the signs of the coefficients p and q. Equation 3.12 can be written as

$$p = \left(1 + \frac{dRf}{dRi}\right)F_m - (2 - \sigma_t^{-1})RiF_m' \tag{3.14}$$

where Rf is the flux Richardson number given by $Rf = Ri\, K_b/K_m$, which in the undisturbed situation is equal to $Ri\, F_b/F_m$. For stable stratification it may be safely assumed that $\sigma_t^{-1} < 2$. Equation 3.14 then shows that a sufficient condition for p to be positive is $dRf/dRi > -1$, which condition seems to be in agreement with observations (e.g., Mizushina et al., 1978). Therefore, p is assumed to be positive herein. Equation 3.11 then will yield unstable solutions, only if $q < 0$, which condition can be written as

$$\frac{d}{dRi}\left(\frac{Rf}{F_m}\right) < 0 \tag{3.15}$$

If $q < 0$ instability occurs for all wave numbers κ, and λ is real. Condition 3.15 is more restrictive than the condition $dRf/dRi < 0$ obtained for zero mean-velocity gradient, see the discussion by Ruddick et al. (1989), for example.

Equation 3.11 shows that for a purely diffusive model ($\tau = 0$) the growth rate λ is proportional to κ^2, that is, $\lambda \to \infty$ for $\kappa \to \infty$ if $q < 0$. If $\tau > 0$ the growth rate remains finite for $\kappa \to \infty$,

$$\lambda\tau \to -\frac{q}{F_b F_m} \tag{3.16}$$

BBDPU show that it is this difference in behaviour for $\kappa \to \infty$ that results in well-posed initial-value problems for $\tau > 0$. In this sense the present model shows the same behaviour as that of BBDPU. Equation 3.16 also shows that for large wave number the left-hand side terms in (2.5) and (2.6) do not necessarily remain small.

As an example consider the often used damping functions

$$F_m = \frac{\sigma_{t0}}{(1 + \alpha Ri)^m} \tag{3.17}$$

$$F_b = \frac{1}{(1 + \beta Ri)^n} \tag{3.18}$$

where m, n, α and β are positive constants and $\sigma_{t0} = \sigma_t(0)$. The instability condition (3.15) then becomes

$$n \geq 2m + 1 \tag{3.19}$$

In the case of the equal sign an additional condition is $2\beta m > \alpha(2m + 1)$. If (3.19) is satisfied, instability will ensue beyond a certain value of Ri. It is shown in Section 4 that such an unbounded instability interval has far-reaching consequences as to the character of the solutions obtained.

Condition (3.19) is quite restrictive. The well-known Munk-Anderson and Rossby-Montgomery relations, for example, do not satisfy it. Excluding a run with low Reynolds number, the laboratory data of Mizushina et al. (1978) can be represented fairly well with $m \approx 0.5$ to 0.7 and $n \approx 2.5$ to 3.0, which values do satisfy (3.19). However, instability, if it occurs, tends to be only marginal.

The above analysis was repeated using (2.8) rather than (2.6) to model the eddy diffusivity. In this case λ was found to be always complex when $\mathrm{Re}\lambda > 0$. As stated before this alternative for step formation therefore is not physically realistic.

4. Numerical computations

Equations 2.1, 2.2, 2.5 and 2.6 together with the damping functions given by (3.17) and (3.18) were solved numerically for unsteady, stratified Couette flow. The initial conditions considered are

$$U(z,0) = \mu_m z - (\mu_m - 1)z^3 \tag{4.1}$$

$$B(z,0) = Ri_U[\mu_b z - (\mu_b - 1)z^3] \tag{4.2}$$

where Ri_U is an overall Richardson number, μ_m and μ_b are constants ($0 \leq \mu_{m,b} \leq 3/2$), and the computational domain is given by $0 \leq z \leq 1$. Alternatively, the plane $z = 0$ is a plane of antisymmetry in a flow domain given by $-1 \leq z \leq 1$. The boundary conditions are $U(0,t) = B(0,t) = 0$, $U(1,t) = 1$ and $B(1,t) = Ri_U$. The equations were solved using an explicit scheme that is of second-order accuracy with respect to space and of first order with respect to time. No additional filtering was applied. The number of grid points, N, was chosen so as to obtain convergence of the solutions. For the results presented herein N was equal to 200, which is also the value used by BBDPU. The time step was $1/(2N^2) = 1.25 \times 10^{-5}$. To obtain sufficient accuracy, the time step should be much less than the time constant τ.

The results of the computations showed that solutions were stable when the instability condition (3.19) was not satisfied, and that solutions were initially unstable when it was satisfied in a substantial subdomain of the flow field. It was found, in the latter case, that in a qualitative sense the solutions behaved in the same way for a wide range of the various coefficients involved, even in the case where the shear rate was kept constant (this case is obtained by putting $\mu_m = 1$ and $m = 0$, which gives $\partial U(z,t)/\partial z = 1$). In some part of the vertical a number of small steps in the buoyancy distribution developed sooner or later. The associated interfaces were stationary, but in the layers the buoyancy either increased or decreased. As a result layers always merged after some time to form larger steps, while the merging process continued. The steps in the buoyancy distributions were very distinct, whereas those in the velocity distributions were more gradual. The gradient Richardson numbers in the layers tended to zero, but those in the interfaces were large (usually > 1). As already noted by BBDPU the formation and merging of steps proceeded more slowly when τ was increased. In all cases having $n > 2m + 1$ a steady state was eventually reached, in which only two layers and one interface remained.

For the results shown in figure 1, the coefficients in the damping functions given by (3.17) and (3.18) were estimated from the measurements of Mizushina et al. (1978). Thus the values $m = 0.5$, $\alpha = 10$ (in agreement with the corresponding Munk-Anderson relation) and $n = \beta = 3$ were selected. The values of m and n were deliberately chosen so as to satisfy the instability condition (3.19). The neutral turbulent Prandtl number was equated to 0.7. The resulting maximal value of Rf is about 0.13 at $Ri \approx 0.28$. The critical value of Ri beyond which solutions become linearly unstable is about 0.53.

Figure 1 shows typical computational results. The four-layer structure at $t = 2$ has developed from the merging of smaller steps. The process of merging is seen to go on: first the upmost interface disappears, next the lowest one, and in the long run the central interface is the only one that survives. The way the interfaces vanish is in agreement with the observations of Ruddick et al. (1989). A direct comparison with Moore & Long's (1971) or Narimousa & Fernando's (1987) experiments is hampered by the large influence of sidewall friction in these experiments. Including sidewall friction in the present computational model

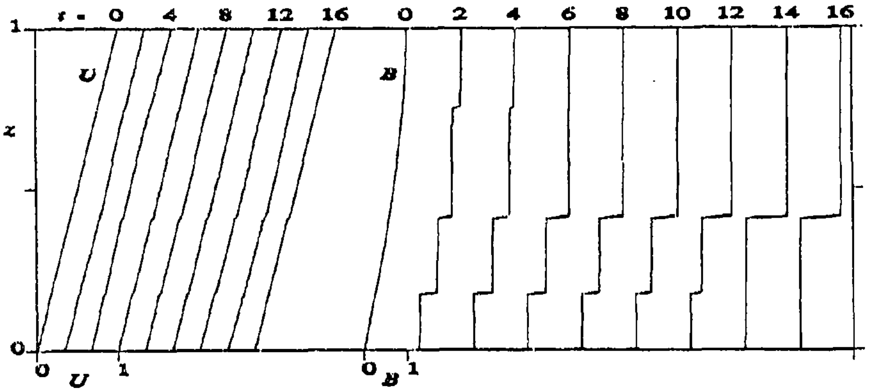

FIGURE 1. Velocity and buoyancy distributions computed using (3.17) and (3.18) for $m = 0.5$, $\alpha = 10$, $n = \beta = 3$, $Ri_0 = 1$, $\tau = 5.0 \times 10^{-3}$, $\mu_m = 1$ and $\mu_b = 1.5$. Note the offsets. The solution at $t = 16$ almost coincides with the final steady-state solution.

showed that a two-layer flow and a diffused interface at mid-depth developed in the stable case where no steps are formed. Such flow structure was also observed by Moore & Long and Narimousa & Fernando. These experiments therefore do not provide evidence for the instability mechanism considered. A layered structure as shown in figure 1 was also obtained, when sidewall friction was included in the linearly unstable case. Therefore, the three-layer structure reported by Long (1972) seems to be in accord with the present results (the antisymmetric case with $-1 \leq z \leq 1$).

The results discussed so far would lead to the paradoxical conclusion that eventually any buoyancy distribution would develop, in the linearly unstable case, into a layered structure with only one or two interfaces. Obviously, this result is at complete variance with empirical evidence. The explanation for the continual merging of layers is that, if $n > 2m + 1$, instability will occur for Ri up to infinity. The interfaces then never stabilize. Merging was found to cease at a certain stage, when instability was allowed in a finite interval of Ri values only. Small changes in the damping functions are sufficient to achieve this. An example is F_m given by (3.17) in which $m = 1$ and $\alpha = 5$, and

$$F_b = \left[Ri - 0.4 + \frac{2(1 - Ri)}{1 + 4(1 - Ri)^2}\right]\left[1.24Ri(1 + 5Ri)^2\right]^{-1} \tag{4.3}$$

These functions still agree fairly well with Mizushina et al.'s (1978) experimental results (the factor 1.24 ensures that $F_b \rightarrow 1$ for $Ri \rightarrow 0$). With these functions the maximal flux Richardson number is about 0.20 at $Ri \approx 0.57$. The instability condition (3.15) is satisfied for $0.757 < Ri < 1.243$. As an alternative to obtain instability on a finite Ri - interval, molecular effects could be invoked (Hearn, 1988).

A result of computations using the modified damping functions is shown in figure 2. This figure shows a stable layer for z larger than about 0.54. However, numerous small steps are formed below this level. As opposed to what is shown in figure 1, the merging of steps comes to a halt and a steady-state finestructure develops. Similar results were obtained for other values of the various parameters involved.

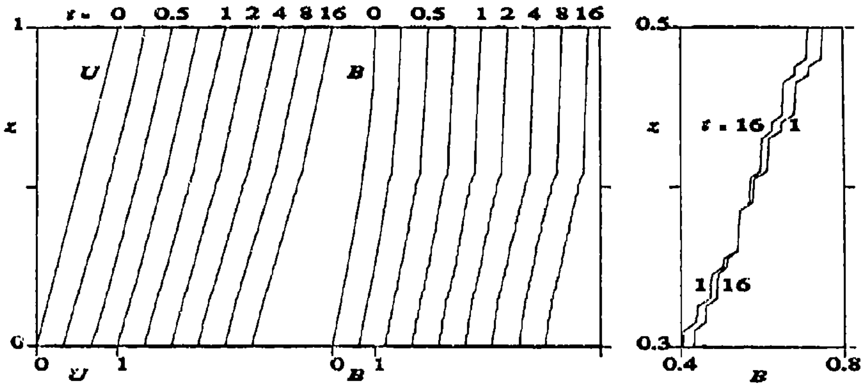

FIGURE 2. Velocity and buoyancy distributions computed using (3.17) and (4.3) for $m = 1$, $\alpha = 5$, $Ri_U = 1$, $\tau = 5.0 \times 10^{-3}$, $\mu_m = 1$ and $\mu_b = 1.5$. The plot on the right shows enlarged parts of two buoyancy distributions.

5. Discussion

The gradient-transport model in conjunction with the finite adjustment time of exchange coefficients as proposed by BBDPU is able to mimic the formation, in shear flow, of small-scale constant-density layers, which from a physical point of view would be a consequence of the overturning of internal waves. However, the agreement may be of a qualitative nature only, because no physical wave-breaking mechanism is explicitly included. In addition some rather restrictive conditions must be satisfied to obtain the desired model behaviour. These conditions seem to make the model a bit artificial. However, it is not inconsistent with empirical evidence. The buoyancy distributions shown in figure 2, correspond to those of a mixed upper layer overlying a thermocline and a stratified lower layer in which finestructure develops. It remains to be seen whether such results are satisfactory in a quantitative sense.

REFERENCES

BARENBLATT, G.I., BERTSCH, M., DAL PASSO, R., PROSTOKISHIN, V.M. & UGHI, M. (1993) *J. Fluid Mech.* 253, 341 - 358.

HEARN, C.J. (1988) *Appl. Math. Modelling* 12, 450 - 456.

KRANENBURG, C. (1980) *J. Phys. Oceanogr.* 10, 1131 - 1133.

KRANENBURG, C. (1982) *Geophys. Astrophys. Fluid Dynamics* 19, 93 - 104.

LAUNDER, B.E. & SPALDING, D.B. (1972) *Mathematical Models of Turbulence*, Academic Press.

LONG, R.R. (1972) In *Proc. Int. IAHR Symp. Stratified Flows*, 315 - 332, ASCE.

MIZUSHINA, T., OGINO, F., UEDA, H. & KOMORI, S. (1978) In *Proc. 6th Int. Conf. Heat Transfer* 1, 91 - 98, Hemisphere.

MOORE, M.J. & LONG, R.R. (1971) *J. Fluid Mech.* 49, 635 - 655.

NARIMOUSA, S. & FERNANDO, H.J.S. (1987) *J. Fluid Mech.* 174, 1 - 22.

PHILLIPS, O.M. (1972) *Deep-Sea Res.* 19, 79 - 81.

POSMENTIER, E.S. (1977) *J. Phys. Oceanogr.* 7, 292 - 300.

RUDDICK, B.R., MCDOUGALL, T.J. & TURNER, J.S. (1989) *Deep-Sea Res.* 36, 597 - 609.

Experiments on turbulence in stratified and rotating flows

by

P.F. Linden, B.M. Boubnov* and S.B. Dalziel
Department of Applied Mathematics and Theoretical Physics,
Silver Street, Cambridge CB3 9EW
* Institute of Atmospheric Physics, Moscow

Abstract

We present results of a novel set of experiments which investigate the structure of turbulent stratified and rotating flows. The turbulence is generated by an array of sources and sinks located around the boundary of a tank. The tank contains a linear stratification and the sources and sinks are directed horizontally and are located in the same horizontal plane. Their action is to extract fluid and to re-inject it with horizontal momentum but with a minimum of mixing. In some of the experiments the tank is rotated at a constant angular velocity about a vertical axis. Small, neutrally buoyant particles which follow the flow are placed in the fluid and recorded on video. The video images are automatically digitised and the particles located on each video frame and from this information various characteristics of the flow field are determined. Up to 4095 particles may be tracked at any one time giving high spatial resolution. In non-rotating flows the form of the motion is determined by two parameters: $F = V/Nd$, where V is the orifice velocity of the jets of diameter d and N is the buoyancy frequency of the stratification, and the Reynolds number $Re = Vd/\nu$, where ν is the kinematic viscosity of the fluid. At high values of F vertical motions occur and turbulent mixing takes place. A mixed layer is produced at the level of the sources and sinks, and its depth increases with time by entrainment of fluid above and below. Under these flow conditions the scale of the motions observed are determined by the forcing scale. At low values of the forcing parameter F, the motion behaves in a qualitatively different way with transfer of energy to the largest scale available within the experimental tank. This transfer of energy occurs because the vertical motions are inhibited and the flow is approximately two-dimensional. As a result the 'inverse energy cascade' causes the energy to accumulate at large scale. The dynamics of this large scale circulation particularly the way in which turbulent eddies are excluded from its centre, and decay of the circulation when the forcing is removed are investigated. In the rotating case the effect of rotation is to introduce a further lengthscale, the Rossby deformation scale $R = Nh/f$, where h is the depth of the fluid and f is the Coriolis parameter. At low values of the forcing parameter the flow is again approximately horizontal with no appreciable vertical motion. Unlike the non-rotating case, however, energy does not accumulate at the largest scale as a result of baroclinic instability at the Rossby deformation scale. As a consequence eddies are continually regenerated at small scales and they interact with each other in a variety of ways. Merging, splitting by shear flow and interactions of vortex pairs have been observed in this flow. One result of these interactions is the eventual predominance of anticyclones. This bias appears to result from the observation that cyclones merge more readily than anticyclones, and may explain why many sub-mesoscale oceanic vortices are anticyclonic.

MEASUREMENTS OF A TURBULENT PATCH IN A ROTATING, LINEARLY STRATIFIED FLUID

Andrew M Folkard[1], Peter A Davies[1] and Harindra JS Fernando[2]

[1] Dept. of Civil Engineering, The University, Dundee, DD1 4HN, U.K.
[2]Environmental Fluid Dynamics Laboratory, Dept. of Mechanical & Aerospace Engineering, Arizona State University, Tempe, AZ 85287-6106, USA

ABSTRACT

A series of experiments is described in which an oscillating grid, positioned at one end and mid-depth of a rotating channel, filled initially with a linearly-stratified fluid, produces a turbulent, mixed patch about itself. As the patch develops, it spreads down the channel. Measurements are made of vertical density profiles at the grid both during production of turbulence and after the grid is turned off, during its decay. Patch size and structure, Thorpe scales, mixedness parameters and available potential energy are deduced from these measurements, and the effects of varying the rotation rate, Ω, ambient buoyancy frequency, N_0, and grid action K (Long, 1978), are investigated. During the growth phase, several previous results are confirmed and extended (Davies *et al.*, 1991 - DFBS herein; De Silva and Fernando, 1992 - DF herein). During the decay phase, Thorpe scales are found to persist to N_0t~10 after turbulent production ceases, except in the case of no rotation, where they decay immediately the grid is turned off. The potential energy of the flow, conversely, decays rapidly in all cases, suggesting that mixing rather than overturning is an important mechanism in the early stages of decay in rotating turbulence. This behaviour is also suggestive of the fossil turbulence model of turbulent decay (e.g. Gibson, 1980).

INTRODUCTION

This paper presents a study of some aspects of the growth and decay of turbulence in a rotating, linearly-stratified fluid. In one sense it is a continuation of work previously carried out previously on the same apparatus (DFBS). These authors measured the vertical extent of mixed patches formed by the vertical oscillation of a horizontal grid in an initially-undisturbed stratified fluid in solid-body rotation. Here, details of the internal structure of these patches themselves are deduced, by using density probes with faster response times than those used previously. In all cases, the measurements of the patch structures were made within the source region above and below the oscillating grid. The results are also compared with those of DF. These authors measured many of the same parameters in a non-rotating experiment in which the fluid was contained within a tank with vertical walls very close to the grid on all four sides.

MEASUREMENTS

The measurements made here were concerned with length scales and other parameters relevant to the growth of the mixed patch produced by the oscillating grid. The length scales measured were the vertical extent of both the mixed and turbulent patches (the distinction is explained below) and the r.m.s and maximum Thorpe scales, L_T and $L_{T_{max}}$ (Thorpe, 1977). The mixedness parameter, defined by DF as $\gamma = 1 - (N/N_0)^2$, where N_0 is the ambient buoyancy frequency and N is that of the mixed patch was used to measure the homogeneity of the patch in relation to the ambient density gradient. Finally, the available potential energy function (APEF) was also measured. This is defined (Dillon, 1984) as

$$APEF = \frac{g}{n\rho_0}\sum_{i=1}^{n}\left[\rho(z_i) - \rho_T(z_i)\right] z_i \qquad (1)$$

where z is measured vertically upwards from the centre of the grid oscillation range, g is the acceleration due to gravity, n is the number of data points, ρ_0 is the mean density, $\rho(z)$ is the actual density at z and ρ_T is the density at z in the Thorpe-ordered profile (Thorpe, 1977).

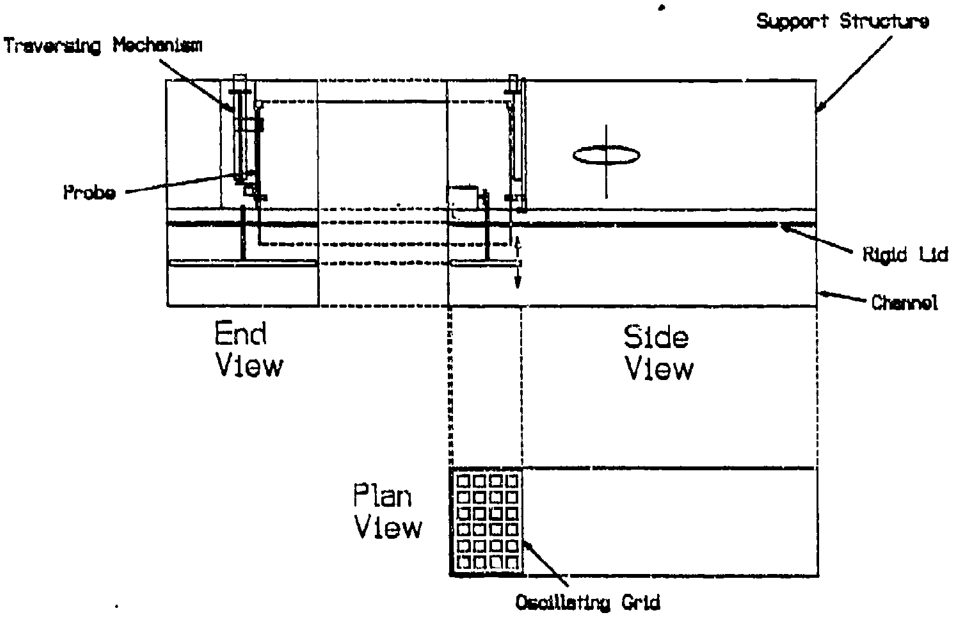

Figure 1 Schematic diagram of the rotating tank arrangement used in the turbulent patch experiments

APPARATUS AND PROCEDURE

A rectilinear, perspex channel (2.1 m long x 0.46 m wide x 0.31 m deep) was fitted with a rigid lid to form an enclosed space ~0.24 m deep into which the stratified fluid was placed (Fig 1). At one end of the channel a grid suspended at an intermediate depth could be oscillated vertically with an amplitude of ~1.5 cm, at a variable rate (5 - 35 rad/s). The grid consisted of a 6x4 array of square elements made up of perspex limbs separated by a mesh width of 6 cm in either direction and extended across the whole width of the tank with a spacing between it and the sidewalls of approximately 3 mm.

Density profiles through the turbulent patch at the grid were measured by traversing the patch vertically with a micro-conductivity probe (Head, 1983). The probe was mounted on the tank in the position shown in Figure 1 and traversed the entire depth of the fluid in a little under 2 seconds, at a speed of ~15 cm/s.

The tank was filled and its initial buoyancy frequency measured. The rotation rate of the channel was then gradually increased from rest to within ±1% of the operator-specified value. Once the required rotation rate had been reached, the system was left to rotate until the fluid had reached a state of solid-body rotation.

The rotation rate (Ω), initial buoyancy frequency (N_0) and grid oscillation rate (described herein in terms of the grid action, K) were varied between runs. A standard combination of values was adopted, namely Ω=0.16 rad s^{-1}, N_0=1.0 rad s^{-1} and K = 6.0 cm^2s^{-1}. Only one parameter at a time was varied from these standard values. Experiments using this set of parameters are referred to as "standard runs". Other than this set, the following values were used: Ω = 0.0, 0.08, 0.32 rad s^{-1}; N_0 = 0.5, 1.25 rad s^{-1}; K = 3.0, 9.0 cm^2s^{-1}. Those experiments in which Ω was varied from its "standard value" are referred to as "Ω-varying runs". N_0-varying runs and K-varying runs are defined in a similar fashion.

The grid was oscillated in all cases for a non-dimensional time N_0t=200. This was chosen to be long enough for a reasonable number of data points to be recorded, but short enough to ensure that the intrusive flow, generated at the grid and forced by the Coriolis force to flow as boundary current, did not have time to circulate the entire channel and return to the mixed patch.

Profiles were measured at intervals of N_0t=20, to allow the disturbances caused by the traverse of the probe to die away. In order to obtain data of a higher temporal resolution than this, three identical experiments were carried out for each run: in the first of these, the first traverse during the growth (decay) phase was recorded at the moment the grid was turned on (off); in the second a five second delay was incorporated, and in the third a ten second delay. A total of 8 standard runs were carried out: two each with 0, 5, 10 and 15 second delays.

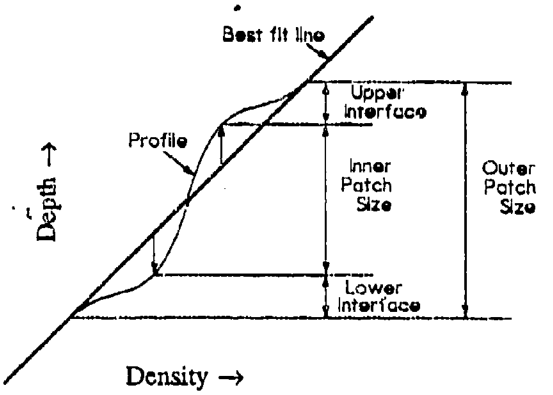

Figure 2 Definitions of the mixed-patch and interface sizes used herein, as deduced from the Thorpe ordered profile

RESULTS

Three different definitions of the patch size were used: the *turbulent* patch size, L_{PT}, is calculated, following DF, as the region in which all Thorpe displacements greater than 5% of the maximum Thorpe displacement are found. This definition was found to cause some problems, especially during the decay phase, when it was somewhat misleading. Therefore, a *mixed* patch was measured from the Thorpe ordered profile using the method illustrated in Figure 2. A straight line was fitted to the profile. Since the mixed patch is always approximately symmetrical, this should pass through the ambient density gradient. The maximum positive and negative deviations of the Thorpe ordered profile from this straight line are found, and the distance between the depths of these two points is defined as the "inner mixed patch size", L_{PI}. The Thorpe ordered profile is then tracked from the most negative (positive) deviation from the straight line towards the nearest end of the profile until the first point above (below) the straight line is found. The distance between the depths of these two points is defined as the "outer mixed patch size", L_{PO} (this is the patch size used by DFBS). (L_{PO} - L_{PI}) is defined as the total interface size, I_T. Mixedness' of these two patches were calculated, and are denoted as γ_I ("inner mixedness") and γ_O ("outer mixedness") respectively.

Growth Phase Measurements

Figure 3 illustrates the relationship between the three patch sizes defined above. The data shown are from the standard runs. The growth can be seen to occur in two phases: in the first ($N_0t \leq 15$), growth is rapid since the effects of buoyancy are not significant. Once buoyancy does take effect, the growth becomes much slower. Note that for $N_0t \leq 5$, $L_{PT} > L_{PO}$, but that after this period, $L_{PO} > L_{PT} > L_{PI}$ in general. L_{PO} grows at a significantly more rapid rate than the other two scales. All the patch size data for varying Ω, N_0 and K are collapsed by scaling with $(K/N_0)^{1/2}$, as in DF and DFBS.

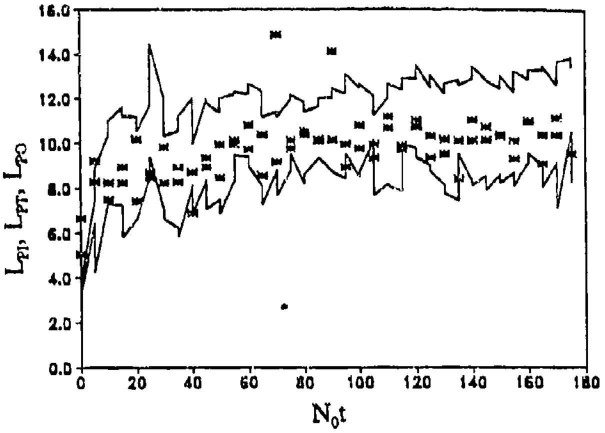

Figure 3 Relationship between the outer and inner mixed patch sizes (upper and lower solid lines respectively) and the turbulent patch size (asterisks) during the phase of turbulent production. Data are from the "standard runs"

Following DF, the ratio L_T/L_P was plotted against mixedness. Most of the data presented by DF are for $\gamma > 0.9$, i.e. during what they call the "fully mixed" stage. Here, the data here are for $\gamma < 0.9$ (Figure 4), where γ is the mixedness of the turbulent patch, as in DF. No discernable variation due to either rotation, buoyancy frequency or grid oscillation rate is apparent. Most of the data are close to the L_T/L_{PT}=0.1 line, in good agreement with the (few) plots of DF in this range. Above $\gamma \sim 0.55$, however, there is evidence of slightly higher values, approaching DF's value of 0.27 for $\gamma \geq 0.9$. The relationship between L_T and $L_{T\max}$ for the growth phase is clearly unaffected by rotation: from these data, $\sum L_T/\sum L_{T\max}$ = 0.35 - a value very close to DF's value of 0.365.

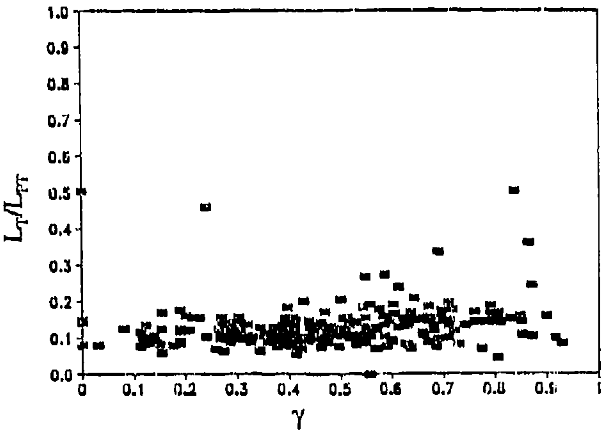

Figure 4 Graphs showing the (lack of) variation of L_T/L_{PT} with the mixedness, γ. Data from all runs are included

Mixedness is plotted, once again following DF, against Kt/L_{PT}^2, for all the K-varying runs in Figure 5, using the mixedness and patch size of the turbulent patch. Note that, as observed by DF, the values of γ for the lowest K-value runs are consistently higher than those for higher K-value runs.

Decay Phase Measurements

An illustration of the relationship between the three patch sizes during the decay phase is shown in Figure 6. Both L_{PO} and L_{PI} show small fluctuations only, the former decreasing significantly and the latter remaining almost constant. L_{PT}, on the other hand, fluctuates markedly and becomes smaller than L_{PI} on a timescale of O(1 s).

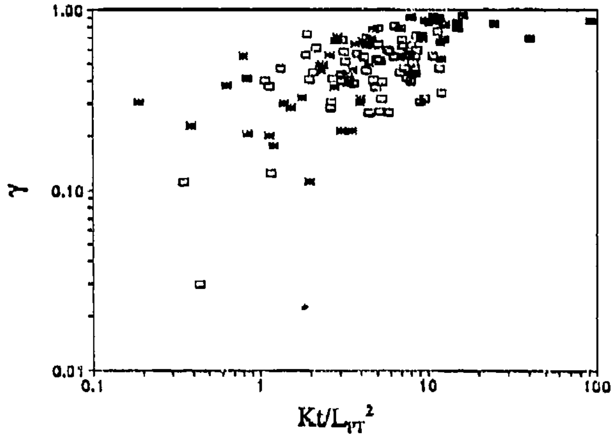

Figure 5 γ vs. Kt/L_{PT}^2 for the K-varying runs. Solid boxes - $K = 3$ cm^{2}s^{-1}; clear boxes - $K = 6$ cm^{2}s^{-1}; asterisks - $K = 9$ cm^{2}s^{-1}.

Figure 6 also illustrates the growth of the interfacial region during the decay phase. The effects of varying Ω, N_0 and K on the total interface size, I_T, were measured. The data from the K and N_0-varying runs were collapsed in general by scaling the interface size by $(K/N_0)^{1/2}$ and the time by $1/N_0$. Results from the Ω-varying cases show that an increased rotation rate causes a monotonic increase in the rate of growth of $I_T/(K/N_0)^{1/2}$ during the decay phase.

The mixedness parameter, γ, was measured for the inner and outer mixed patches in every run. Almost all runs had indistinguishable γ_O's, which decayed very gradually from ~0.3 at $N_0t = 0$ to ~0.2 by the end of the measurement period; the only exception was in the case of no rotation, which decays faster than the rotational cases, especially after N_0t~50.

In the case of γ_I, most of the runs show a very gradual decrease from ~0.9 to ~0.85 during the measurement period. The data for the Ω = 0 runs, however, decrease notably more rapidly after N_0t~20.

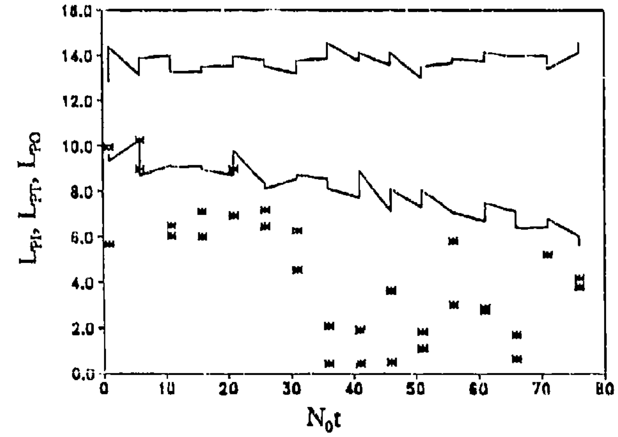

Figure 6 Relationship between the outer and inner patch sizes (upper and lower solid lines respectively) and the turbulent patch size (asterisks) during the turbulent decay phase

The immediate sharp drop of APEF once grid oscillation ceases is clearly illustrated in Figure 7. The data are from the standard runs and have been normalized by the mean value at $N_0t = 0$. After N_0t~20, the data are found only in the region between 0 and 0.05 - these can be taken to represent values due to noise in the probe, which becomes prominent because of the very small density gradient in the mixed patch. Data from other runs show a very similar trend. It is noted that the data at N_0t=5 and 10 increase with increasing rotation rate, suggesting that

APEF decays more slowly in faster rotating media. No dependence of APEF on N_0 and K is observed.

A linear plot of $L_T/L_T(N_0t = 0)$ against N_0t for data from the standard runs is shown in Figure 8, for comparison with the corresponding plot of APEF decay in Figure 7. Unlike the APEF, the Thorpe scale appears to be sustained at ≥80% of its initial value up to $N_0t \sim 10$. It then decays rapidly until $N_0t \sim 25$, after which time, it displays consistently low values. Data from other runs show this same persistence, except for the case of no rotation. The data for $L_{T\max}$ show very much the same trends as the L_T data, suggesting that the spectrum of Thorpe scales remains relatively constant throughout the decay phase.

DISCUSSION

Growth phase observations

The initial period of fast growth undergone by the patch appears to extend to $N_0t \sim 15$, both in these experiments and those of DFBS. This is significantly longer than the $N_0t \sim 4$ reported by DF. This is assumed to be due to the presence of an outflowing intrusion, not present in DF's fully constrained configuration, which retards the growth of the patch to the Ozmidov scale, where it is arrested by buoyancy forces. This would not, however, affect the onset of mixing. Note that the patch size measured by DFBS is equivalent to L_{PO} here, but that those measured by DF are L_{PT} and those measured by visual methods, such as shadowgraphs are likely to be L_{PI} since this is defined by boundaries at the points of maximum $\partial^2\rho/\partial z^2$ and it is variations in this parameter that cause the light and dark regions to appear in shadowgraphs. The definitions given here provide an objective and consistent framework within which these measurements can be compared.

The growth of the patch size is shown to be unaffected by rotation and to be well scaled for buoyancy frequency

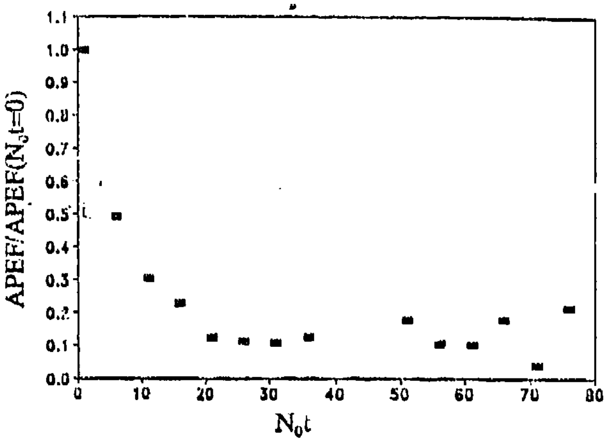

Figure 7 Linear plot of the decay of the available potential energy function (APEF) during the turbulent decay phase. The data are normalized mean values for each time at which profiles were recorded during the standard runs

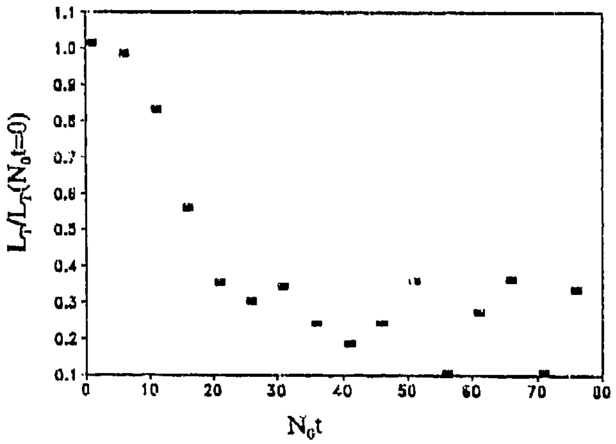

Figure 8 Linear plot of the decay of L_T. The data are derived as in Figure 7. Note the presence of values ≥0.8 up to $N_0t \sim 10$ - a feature absent from Figure 7

and grid oscillation frequency variation by $(K/N_0)^{1/2}$, in good agreement with DFBS. The agreement between the ratio $L_T/L_{T\max}$ found here and that reported by DF is evidence of the lack of effect of varying Ω, N_0 or K on the behaviour of the turbulent overturns in the ranges of those parameters used here. Comparison of the constancy of the ratio L_T/L_{PT} for $\gamma < 0.55$ found here with the results of DF suggests that L_T/L_{PT} only depends on γ in the range $0.55 < \gamma < 0.9$.

The plot of γ against Kt/L_P^2 (Figure 5) shows that values of γ are consistently higher for the $K = 3$ cm^{2}s^{-1} case than for the other cases. This is consistent with the results of DF, who varied K by varying the solidity of their grid. In this case, however, the same grid is used in all cases and it is the oscillation frequency that is used to vary K. This suggests that an increase in mixedness is due to a decrease in K rather than any individual factor that affects it. If K can be taken to represent the input of energy by the grid, then this is consistent with the reasoning that at low K there is less energy to fuel entrainment mechanisms at the interface, leading to a lack of unmixed inflow into the patch, so that the mixed patch becomes well-mixed more rapidly. As the patch becomes more fully-mixed, more energy becomes available to fuel entrainment. Thus entrainment and mixing would be expected to occur more episodically at low values of K and more continuously at high values. Clearly, more data for a range of K-values are needed to test this supposition.

Decay phase observations

Once the grid has been turned off, comparisons with the work of Dillon (1984), Crawford (1986) and many others shows that the velocity scales decay within the range $0 < N_0t < 3$. Ro will decrease rapidly, therefore, and the presence of rotation can be expected to become significant during the decay phase. These results show this to be the case, in that the patch in the non-rotating case behaves differently from those in the rotating cases: in the former case, immediately following the cessation of turbulent production, erosion of the patch takes place across the boundary between the interfacial region and the inner mixed patch, causing a growth in interface size. Once this sharp boundary has been eroded somewhat (at $N_0t \sim 25$), restratification takes place, spreading from the inner patch to the interfacial region at $N_0t \sim 50$. The behaviour of the patch in the rotating cases appears to be identical with that seen in the first stage of the non-rotational case, namely the erosion of the inner mixed patch, only at a slower rate, implying that rotation retards the restratification process.

The preservative effect of rotation is also apparent in the data concerning the effect of rotation on the APEF and Thorpe scale decay. In the former, the evidence suggests a decrease in the decay rate of APEF with increasing Ω. Note that this decay occurs over several buoyancy periods, and is certainly an order of magnitude slower than that observed by Dillon, Crawford and many others for turbulent kinetic energy decay. That the two forms of energy decay at very different rates is not surprising, given that different mechanisms are responsible: the decay kinetic energy is due to viscous dissipation, whereas that of the APEF is caused by saline diffusion and buoyancy-induced motions. Comparison of the results obtained here for APEF and L_T decay show that, initially, overturnings persist whilst potential energy decreases. Referring to Equation (1), the persistence of L_T corresponds to z_t remaining relatively constant. Since $g/n\rho_0$ is constant, the initial decrease of APEF can only be brought about by a decrease in $\rho(z_i) - \rho_T(z_i)$, i.e. by mixing, rather than buoyancy-induced motions.

The persistence of Thorpe scales in rotating runs, when compared with their immediate decay in the non-rotating case is also evidence that rotation tends to preserve the characteristics of the density profile once turbulent production has ceased. This persistence after turbulent production has ceased for timescales an order of magnitude longer than the often reported decay e-folding times for turbulent kinetic energy is suggestive of the definition of fossil turbulence (e.g. Gibson, 1980). That background rotation appears to have the effect of enhancing the preservation of vertical density fluctuations suggests that rotation exacerbates fossilization.

CONCLUSIONS

(i) Objective definitions have been given for mixed patch and interface sizes derived from Thorpe-ordered vertical density profiles. These have been found to be useful in determining the development of the patch structure, during both growth and decay phases.

(ii) During the growth phase, L_T/L_{PT} is found to be a function of the mixedness, γ, only in the range $0.55 < \gamma < 0.9$. Also during this phase, low values of the grid action, K, are deduced to cause consistently higher values of γ

(iii) During the decay phase, rotation is found to retard the restratification of the mixed patch. Diffusive mixing, rather than buoyancy-induced motions, are observed to dominate the early stages of the decay of the internal structure of the patch. A persistence of Thorpe scales is observed at time scales an order of magnitude greater than that reported elsewhere for the decay of turbulent kinetic energy. This is consistent with the concept of fossil turbulence.

REFERENCES

Crawford, W.R., 1986, A comparison of length scales and decay times of turbulence in stably stratified flows, J. Phys. Oceanogr., 116, 1847-1854

Davies, P.A., Fernando, H.J.S., Besley, P., and Simpson, R.J., 1991, Generation and spreading of a turbulent mixed layer in a rotating stratified fluid, J. Geophys. Res., 96, C7, 12567-12585

De Silva, I.P.D., and Fernando, H.J.S., 1992, Some aspects of mixing in a stratified turbulent patch, J. Fluid Mech., 240, 601-625

Dillon, T.M., 1984, The energetics of overturning structures: implications for the theory of fossil turbulence, J. Phys. Oceanogr., 14, 541-549

Gibson, C.H., 1980, Fossil temperature, salinity, and vorticity turbulence in the ocean, in J.C.J. Nihoul (ed.) Marine Turbulence, Elsevier, Amsterdam, 221-257

Head, M.J., 1983, The use of miniature four-electrode conductivity probes for high resolution measurement of turbulent density or temperature variations in salt-stratified water flows, Ph.D. thesis, University of California, San Diego

Long, R.R., 1978, A theory of mixing in stably stratified fluids, J. Fluid Mech., 84, 113-124

Thorpe, S.A., 1977, Turbulence and mixing in a Scottish loch, Phil. Trans. R. Soc. London Ser. A, 286, 125-181

Direct numerical simulation of a vigorously heated low-Reynolds-number convective boundary layer

G. N. Coleman[a] and J. H. Ferziger[b]

[a]Mechanical, Aerospace and Nuclear Engineering Department, University of California at Los Angeles, Los Angeles, California 90024-1597, U.S.A.

[b]Department of Mechanical Engineering, Stanford University, Stanford, California, 94305-3030, U.S.A.

Abstract

Computations of the buoyantly unstable Ekman layer are performed at low Reynolds number. The results are obtained by directly solving the three-dimensional time-dependent Navier-Stokes equations with the Boussinesq buoyancy approximation, resolving all relevant scales of motion (no turbulence closure is needed). The flow is capped by a stable temperature inversion and heated from below at a rate that produces an inversion-height to Obukhov-length ratio $-z_i/L_* = 32$. Temperature and velocity variance profiles are found to agree well with those from an earlier vigorously heated under-resolved computation at higher Reynolds number, and with Deardorff & Willis' [1] experimental data. Significant helicity is found in the layer, and helical convection patterns of the scale of the inversion height are observed.

1. INTRODUCTION

Due to the very large Reynolds numbers found in the atmosphere [2], most numerical studies of the planetary boundary layer (PBL) utilize large eddy simulation (LES) (see [3]-[9], for example). The price one pays for the ability to consider realistic Reynolds numbers is the uncertainty introduced by the LES's sub-grid scale (SGS) parameterization. In this (and previous [10]-[12]) work, the alternative strategy of direct numerical simulation (DNS) is used: turbulent fields are obtained by numerically solving the three-dimensional time-dependent Navier-Stokes equations, resolving all of the relevant scales of motion, so that no SGS parameterization is needed. While only very low Reynolds number turbulence may be computed, the results are free from modeling errors, and can provide a complement to information found in the LES studies. The DNS data can also be used as a reference for Reynolds-averaged turbulence closures, to test the accuracy (and importance) of SGS models, and in some instances ([10]-[12]) be directly applied to high-Reynolds-number PBL flows.

The focus here is on an idealization of the convective planetary boundary layer (CBL), the buoyantly unstable turbulent Ekman layer. (Neutrally and stably stratified results are presented in [10] and [11]; a similar CBL study was recently made by Bohnert [13].) The convective case has the numerical advantage that the largest scales are the most energetic, which diminishes the significance of SGS errors. This was recently demonstrated to the present authors, when in the course of a CBL study concerned with roll cells in the mildly heated regime [12] (with $-z_i/L_* \approx 2$), it was found that results from a vigorously heated reference run ('Case CA,' with $-z_i/L_* \approx 26$) agreed reasonably well with atmospheric and LES data, despite that fact that the small-scale flow was not fully resolved. The objective of the present work is to further investigate the importance and nature of small-scales motions in a vigorously heated CBL, using well-resolved DNS fields. The latter are obtained by increasing the number of collocation points, compared to the earlier Case CA values, and decreasing the Reynolds number, allowing the full range of scales of both velocity and vorticity to be captured (the small-scale dynamics [14] of the stable inversion above the CBL cannot be represented; cf. [9] and [12]). The fact that both velocity and vorticity (and therefore helicity) are accurately resolved is noteworthy, since it has been observed that helical motions can be especially significant in convective flows [15], as we shall illustrate below.

2. APPROACH

Numerical solutions of the pressure-driven turbulent boundary layer over a heated smooth flat surface are generated using the Boussinesq buoyancy approximation. The viscous flow is exposed to a vertical gravity field and steady system rotation about an axis normal to the surface. At the surface, isothermal no-slip boundary conditions are assumed; an isothermal geostrophic balance is prescribed in the freestream. The nondimensional parameters for this flow include a Reynolds number $Re \equiv GD/\nu = G/(\nu f/2)^{1/2}$ (where G is the geostrophic wind speed, f the Coriolis parameter, D the laminar Ekman layer depth, $D = (2\nu/f)^{1/2}$, and ν the kinematic viscosity); the Prandtl number, $Pr = \nu/\kappa$ (κ is the kinematic thermal diffusivity); the 'shape factors' of the initial temperature profile (which define the inversion height and surface heat flux – see [12]); and (since the flow is not statistically stationary) the nondimensional time, tf.

The governing equations [12] are solved using the spectral method of Spalart *et al.* [16]. Spatial variations are represented by Fourier series in planes parallel to the surface, and in the vertical direction by expansions in Jacobi polynomials in the mapped coordinate $\zeta = \exp(-z/Z)$, where Z is the mapping length scale; the time-advance scheme is a mixed implicit-explicit second order algorithm. See [16] or [12] for details.

TABLE 1: Run parameters.

Case	Re	Pr	N_x	N_z	L_x/z_i	Z/z_i	N_{z_i}	Δx^+	$(\Delta z/\eta)_{z_i}$
CA	400	0.7	96	45	6.2	0.77	28	13.0	6.7
CC	200	0.7	192	90	5.5	0.68	60	1.9	1.7

Two cases, denoted CA and CB (C for 'convective') have been previously discussed in [12] (respectively, the vigorously and mildly heated flows mentioned above). Here we introduce another convection-dominated simulation, denoted Case CC. Its parameters differ from CA's in the numerical resolution, Reynolds number and initial history. Whereas the earlier runs were begun by instantaneously superimposing an unstable surface heat flux and stable capping inversion upon a fully developed (statistically stationary) unstratified turbulent field and advancing in time, the present simulation is the result of imposing the same unstable temperature field (and small velocity perturbations) upon the laminar Ekman layer solution at the same Reynolds number ($Re = 400$) using twice the number of collocation points in each coordinate direction. After a time of $t = 0.11/f$, during which the fine-grid flow reached a quasi-equilibrium state [12], the viscosity was increased by a factor of 4 so that the laminar depth D was doubled, and both the Reynolds number and the acceleration of gravity (since the Froude number gD/G^2 was kept equal to one) were halved. The resulting $Re = 200$ histories of the 'surface Richardson number' $(g/T_\infty)\Gamma_0/(G/D)^2$ (i.e. surface heat flux) and volume-integrated turbulent kinetic energy $E = \frac{1}{2}\int_0^\infty \langle u_i' u_i' \rangle \mathrm{d}z$ are shown in Figure 1. (In the above, $\Gamma_0 = (\mathrm{d}T/\mathrm{d}z)_{z=0}$ is the surface lapse rate, T_∞ the freestream reference temperature at $z \to \infty$, and the angle brackets denote an average over horizontal planes.) Towards the end of the run the turbulence is deemed to be in quasi-equilibrium with the slowing changing mean field. The symbols in Figure 1 indicate the beginning and end of the $0.04/f$ time period from which 24 fields were averaged to obtain Case CC mean quantities (denoted by overbars); the resulting mean temperature and velocity profiles are shown in Figure 2.

3. RESULTS

A summary of the Case CA and CC run parameters is given in Table 1. Included are the number of streamwise and spanwise (with respect to the geostrophic wind) and vertical collocation points, $N_x = N_y$ and N_z, the horizontal domain size, $L_x = L_y$, and the vertical-mapping length scale, Z. Note that the lateral grid spacing decreases from $\Delta x^+ = \Delta y^+ = u_* \Delta x/\nu = 13$ to 2 in the fine-resolution run (u_* is the surface friction velocity), while the new vertical resolution (which places the first 10 grid points below $z^+ = 0.3$) increases the number of collocation points between the surface and the inversion, N_{z_i}, from 28 to 60, and decreases the ratio of

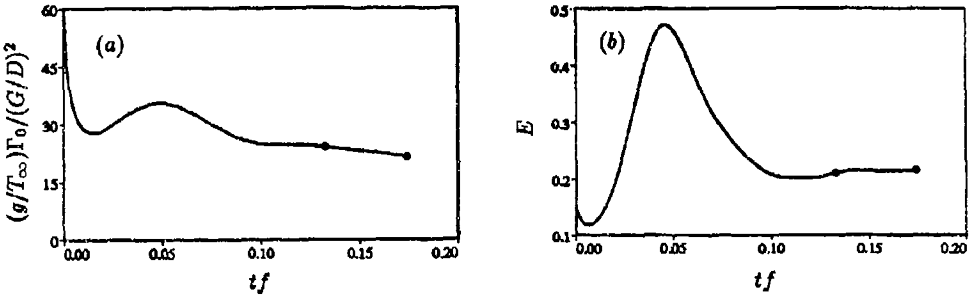

FIGURE 1. History of (a) surface heat flux and (b) volume-integrated turbulent kinetic energy for Case CC: •, beginning and end of averaging period.

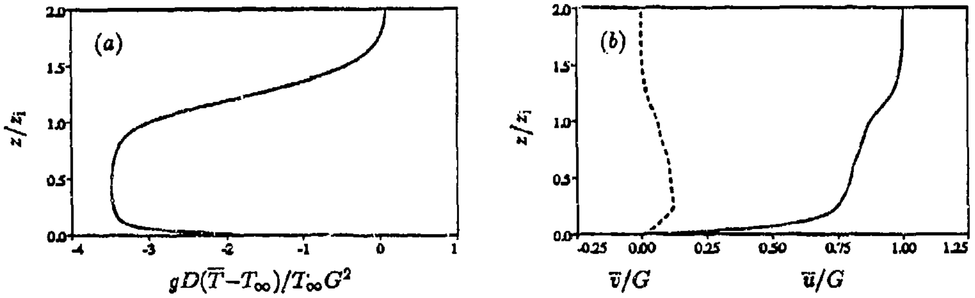

FIGURE 2. Time-averaged profiles of (a) mean temperature and (b) mean velocity for Case CC.

the vertical grid spacing to the Kolmogorov length scale at the inversion from $(\Delta z/\eta)_{z_i} = 7$ to 2 ($\eta = (\nu^3/\epsilon)^{1/4}$, and ϵ is the dissipation rate of $\frac{1}{2}\overline{u_i'u_i'}$). Given that the lateral domain size remains greater than 5 times the inversion height, this improvement suggests that both the largest and smallest spatial scales are accurately captured. More compelling evidence of the numerical fidelity of the new results is provided in Figure 3, where one-dimensional energy and enstrophy spectra at various elevations from runs CA and CC are presented. The $Re = 200$ spectra show the effect of low Reynolds number in the small separation between the energy and enstrophy peaks. They also show that the full range of horizontal velocity and vorticity variations is captured in the high-resolution case. Since even at the inversion the vertical grid spacing is of the order of the Kolmogorov length scale, vertical gradients are expected to be accurately represented, especially near the surface. (At the inversion, however, any small-scale dynamics that are not precluded by the low Reynolds number cannot be fully supported.)

Despite having significant energy in the highest resolved wavenumbers (Figure 3(a),(d)), second-order statistics from Case CA[1] are not vastly different from the fully resolved (or experimental) data. As illustrated in Figure 4, both cases produce realistic heat flux profiles (note the smaller

---

[1] All Case CA data are from the 'State CA1' field at $tf = 0.18$ [12].

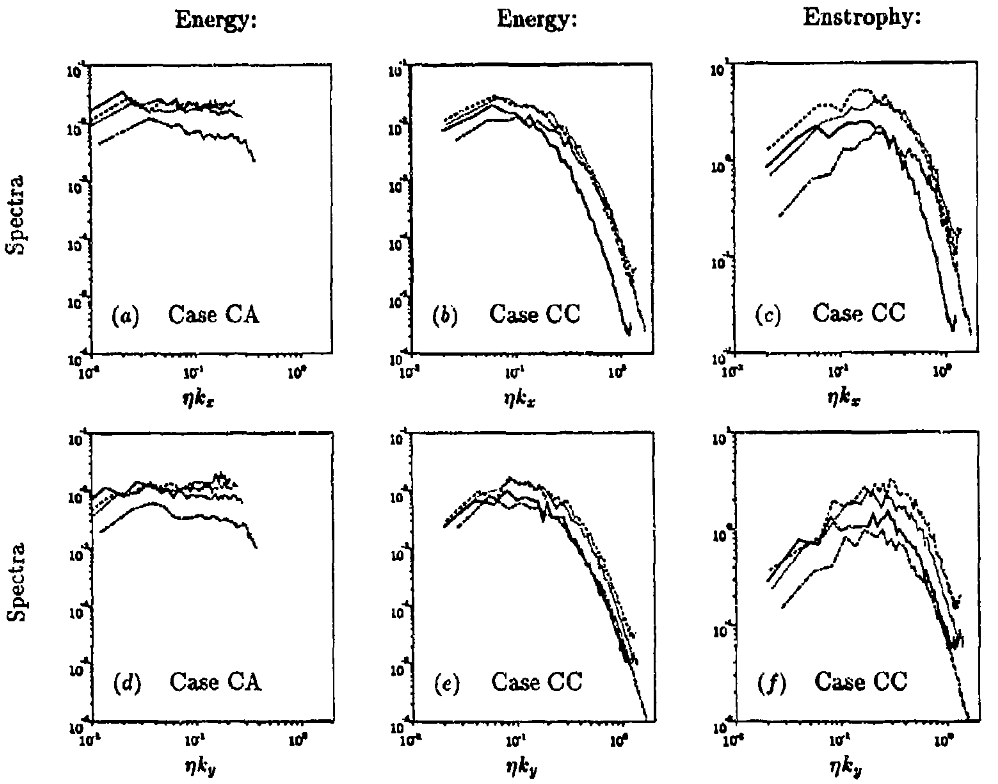

FIGURE 3. One-dimensional streamwise (k_x) and spanwise (k_y) turbulent kinetic energy and enstrophy spectra: (a) & (d), Case CA energy at $tf = 0.18$; (b) & (e), Case CC energy at $tf = 0.17$; (c) & (f), Case CC enstrophy at $tf = 0.17$; ——— , $z/z_i = 0.05$; ---- , $z/z_i = 0.2$; ········ , $z/z_i = 0.5$; —–— , $z/z_i = 0.9$. Energy spectra normalized by w_*^2/k_x or w_*^2/k_y; enstrophy spectra by $(w_*/z_i)^2/k_x$ or $(w_*/z_i)^2/k_z$.

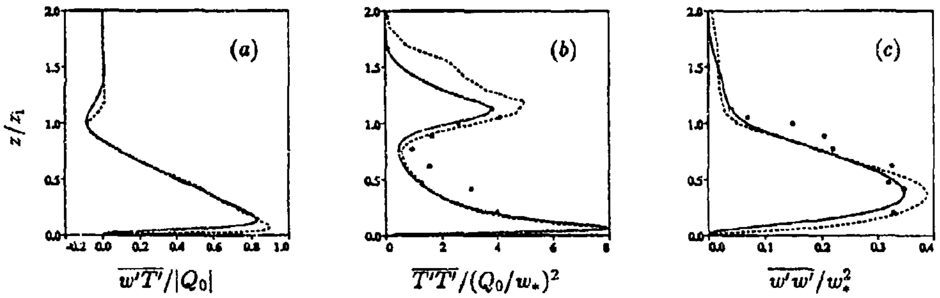

FIGURE 4. Profiles of (a) turbulent heat flux, (b) temperature and (c) vertical velocity fluctuation variance: ---- , Case CA; ——— , Case CC; •, Deardorff & Willis' (1985) laboratory data.

TABLE 2: Global results.

Case	u_*/G	u_*/w_*	β(deg)	δ/D	$-L_*/\delta$	$-z_i/L_*$	$w_*/z_i f$
A90	0.0652	-	28.5	13.0	∞	–	–
CA	0.1195	0.249	11.2	23.9	0.0067	26.45	22.50
CC	0.1362	0.235	7.1	13.6	0.0056	31.69	24.18

near-surface maximum and larger interfacial thickness in Case CC, consistent with lower *Re*). The temperature and velocity fluctuation profiles from both runs are also reasonable, agreeing fairly well with Deardorff & Willis' [1] convection tank results.

Global mean quantities are tabulated in Table 2. The inversion height, z_i, the surface friction velocity, u_*, the angle between the surface shear stress and geostrophic wind, β, the turbulent Ekman depth, $\delta = u_*/f$, the convection velocity $w_* = (gQ_0 z_i/T_\infty)^{1/3}$ (where Q_0 is the surface heat flux), and the Obukhov length, $L_* = -u_*^3 T_\infty/g\mathcal{K}Q_0$) ($\mathcal{K}$ is the von Kármán constant) are given. Values from a DNS study of the unstratified $Re = 400$ Ekman layer (Case A90 of [10]) are included for comparison.

The convection-dominated nature of the two heated cases is indicated by the relatively large (compared to the unstratified values) u_*, w_* and $-z_i/L_*$ (and small β); Case CC is slightly more vigorous. For both runs the large rotation-to-convection timescale ratio, $w_*/z_i f$, implies that the large convective eddies are relatively unaffected by system rotation.

Another type of 'rotational effect' – that involving rotation of the convection patterns themselves – appears to be more significant: the alignment between vorticity and velocity tends to be greater than that found in non-convective flows [17]. This is illustrated by the probability density function (PDF) of the relative helicity density $h = \boldsymbol{u}\cdot\boldsymbol{\omega}/|\boldsymbol{u}||\boldsymbol{\omega}|$ ([15],[17],[18]) at $z/z_i = 0.2$ and 0.5 shown in Figure 5, for the Case CC flow at $tf = 0.17$. The vorticity-velocity alignment is less pronounced at other elevations; as $z \rightarrow z_i$ it becomes more random, and near the surface $\boldsymbol{u}$ and $\boldsymbol{\omega}$ are most often at right angles (cf. [17]). The PDF of relative fluctuation helicity density $h' = \boldsymbol{u}'\cdot\boldsymbol{\omega}'/|\boldsymbol{u}'||\boldsymbol{\omega}'|$ (not shown) indicates a slight preference at $z = 0.2z_i$ for $\boldsymbol{u}'$ and $\boldsymbol{\omega}'$ to align, but not to the extent that the total fields do. At $z = 0.5z_i$, however, the PDF's of h and h' are fairly similar, which suggests (since the mean vertical velocity and vorticity are both zero) that most of the helical motions in the core of the mixed layer are associated with convective motions. The contours of vertical velocity w and vertical helicity $w\omega_z$ presented in Figure 6 reveal that the helical motions are almost exclusively located in the convective updrafts. This is also apparent in the $z = 0.2z_i$ joint vertical velocity-vorticity PDF, Figure 7, in that large ω_z (of both signs) is correlated with large positive w. As the iso-surface plot of vertical helicity in Figure 8 illustrates, the helical convection patterns extend through the depth of the mixed layer.

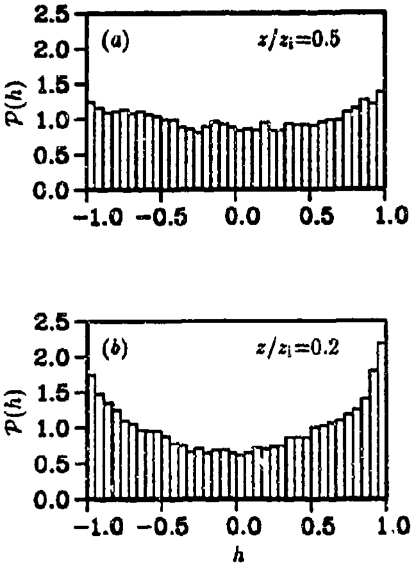

FIGURE 5. Helicity density PDF, $\mathcal{P}(h)$, at (*a*) $z/z_i = 0.5$ and (*b*) $z/z_i = 0.2$ for Case CC at $tf = 0.17$, normalized such that $\mathcal{P}(h) = 1$ represents value associated with random alignment between $\boldsymbol{u}$ and $\boldsymbol{\omega}$ [17].

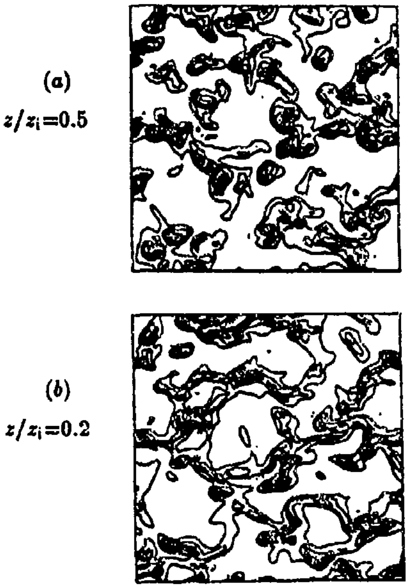

FIGURE 6. Vertical helicity extrema superimposted upon vertical velocity contours at (*a*) $z/z_i = 0.5$ and (*b*) $z/z_i = 0.2$ for Case CC at tf=0.17: ——, $w/G \geqslant 0$ (contour interval 0.3); solid regions, $w\omega_z > 0.05(w\omega_z)_{\max}$; shaded regions, $w\omega_z < 0.05(w\omega_z)_{\min}$; $(w\omega_z)_{\max}$ and $(w\omega_z)_{\min}$ are maximum and minimum vertical helicity over entire domain. Freestream flow from left to right; planes represent full flow domain

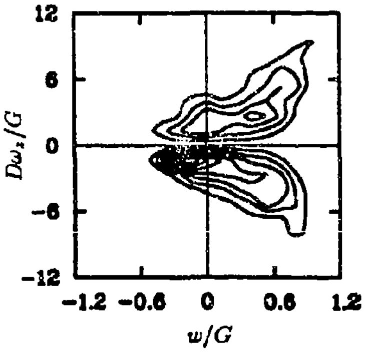

FIGURE 7. Contours of joint PDF of vertical velocity and vertical vorticity, $\mathcal{P}(w, \omega_z)$, at $z/z_i = 0.2$ for Case CC at $tf = 0.17$, weighted by $(\omega_z/(G/D))^2$ (contour interval 0.05).

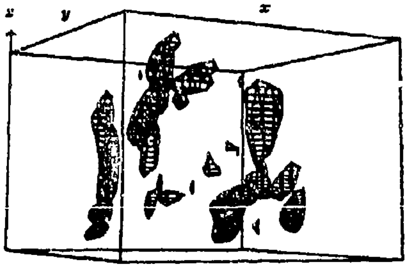

FIGURE 8. Iso-surfaces of vertical helicity for Case CC at $tf = 0.17$: surfaces denote 10% of maximum (over entire domain) positive value; (surfaces of 10% of negative are qualitatively similar). Subdomain shown extends from surface to inversion, over $L_x/4$ and $L_y/4$ in lateral directions.

In future work we plan to investigate the dynamics of the ‘tornado-like’ convection patterns, to compare them to coherent structures found in LES studies (such as Schmidt & Schumann’s ‘spokes’ [5]), and to determine if they are at all related to ‘dust devils,’ ‘water spouts’ and ‘steam devils’ found in the atmosphere – or perhaps even share some features with large-scale rotating ‘supercell’ convective storms [15]. In particular, we would like to ascertain the source of their vertical vorticity and understand the role of mean shear in their formation and evolution, and thereby shed light on the creation mechanisms of related atmospheric phenomena.

ACKNOWLEDGEMENTS

Computations were performed at NASA Ames Research Center. The authors are grateful to Prof. D. K. Lilly and Dr. P. R. Spalart for their contributions to this work.

REFERENCES

[1] J.W. Deardorff & G.E. Willis, ‘Further results from a laboratory model of the convective boundary layer.’ Boundary-layer Met. **32**, 1985.

[2] J.C. Wyngaard, ‘Atmospheric turbulence.’ Ann. Rev. Fluid Mech.**24**, 1992.

[3] J.W. Deardorff, ‘Numerical investigation of neutral and unstable planetary boundary layers.’ J. Atmos. Sci. **29**, 1972.

[4] C.-H. Moeng, ‘A large-eddy-simulation model for the study of planetary boundary-layer turbulence.’ J. Atmos. Sci. **41**, 1984.

[5] H. Schmidt & U. Schumann, ‘Coherent structure of the convective boundary layer derived from large-eddy simulations.’ J. Fluid Mech. **200**, 1989.

[6] R.I. Sykes, W.S. Lewellen & D.S. Henn, ‘Numerical simulation of the boundary-layer eddy structure during the cold-air outbreak of GALE IOP 2.’ Mon. Wea. Rev. **118**, 1990.

[7] P.J. Mason & S.H. Derbyshire, ‘Large eddy simulation of the stably-stratified atmospheric boundary layer.’ Boundary-layer Met. **53**, 1990.

[8] F.T.M. Nieuwstadt, P.J. Mason, C.-H. Moeng & U. Schumann, ‘Large-eddy simulation of the convective boundary layer: a comparison of four computer codes.’ Proc. 8th Symp. on Turbulent Shear Flows, Munich, Germany, September 9–11, 1991.

[9] A. Chlond, ‘Three-dimensional simulation of cloud street development during a cold air outbreak.’ Boundary-layer Met. **58**, 1992.

[10] G.N. Coleman, J.H. Ferziger & P.R. Spalart, ‘A numerical study of the turbulent Ekman layer.’ J. Fluid Mech. **213**, 1990

[11] G.N. Coleman, J.H. Ferziger & P.R. Spalart, ‘Direct simulation of the stably stratified turbulent Ekman layer.’ J. Fluid Mech. **244**, 1992. Corrigendum: J. Fluid Mech. **252**.

[12] G.N. Coleman, J.H. Ferziger & P.R. Spalart, ‘A numerical study of the convective boundary layer.’ To appear in Bound-Layer Met., 1994.

[13] M. Bohnert, ‘A numerical investigation of cloud-topped planetary boundary layers.’ Ph.D. dissertation, Department of Mechanical Engineering, Stanford University, 1993.

[14] S.J. Caughey, ‘Observed characteristics of the atmospheric boundary layer. Equations and concepts.’ In Atmospheric Turbulence and Air Pollution Modelling (ed. F.T.M. Nieuwstadt and H. Van Dop), D. Reidel. 1982.

[15] D.K. Lilly, ‘The structure, energetics and propagation of rotating convective storms. Part II: Helicity and storm stabilization.’ J. Atmos. Sci. **43**, 1986

[16] P.R. Spalart, R.D. Moser & M.M. Rogers, ‘Spectral methods for the Navier-Stokes equations with one infinite and two periodic directions.’ J. Comp. Phys. **96**, 1991.

[17] M.M. Rodgers & P. Moin, ‘Helicity fluctuations in incompressible turbulent flows.’ Phys. Fluids **30**, 1987.

[18] R.B. Pelz, V. Yakhot, S.A. Orszag, L. Shtilman & E. Levich, ‘Velocity-vorticity patterns in turbulent flow.’ Phys. Rev. Let. **54**, 1985.

DECAY OF TURBULENCE IN FLUID WITH DENSITY FLUCTUATIONS UNDER THE STABLE STRATIFICATION

V.M Emelianov, V.A. Frost
Institute for Problem in Mechanics, Russian Academy of Science,
101, prospect Vernadskogo, Moscow, 117526, Russia

Introduction. Turbulent mixing significantly affects various processes in atmosphere and ocean, chemical reactors. power plants etc.. In most of these cases the effect of buoyancy forces is of profound importance. The modelling of these processes is very difficult problem because of effect of buoyancy forces on the turbulent micromixing is not well understood. On the other hand there are no data on intensity of turbulent micromixing when buoyancy forces are significant. At the same time it is the process of turbulent micromixing that defines the density distribution and hence buoyancy forces. Owing to turbulent micromixing occur density fluctuations decrease and hence buoyancy forces decrease also. Therefore significant interaction of mixing up to the molecular level with buoyancy forces exists. Because the closed mathematical models for developed turbulence are absent and semi-empirical models are not well developed the main features of the interaction process between turbulent mixing and buoyancy forces must be studied experimentally.

One of the most attractive type of laboratory experiment on turbulence is to study decaying turbulence downstream of a turbulizing grid. A number of experiments on decaying stratified turbulence have been conducted up to date. The experiments were carried out in salt-stratified water closed loop channels and tow-tanks with stationary salt-stratified fluid and also in wind-tunnels having thermal stratification. Each of the experiments has shortcomings and advantages and there is no ideal type of experiment on decay of turbulence in stratified fluid. For instance the results obtained on the same experimental set up (Stillinger's closed loop channel [1]) but by different scientists are directly opposite. The results of [1] show that the decay rate of turbulence in stratified water is less than decay rate in non-stratified case. Alternatively the experiments carried out by Itsweiere et al [2] reveal the opposite results. As a rule these studies are carried out for a linear stratification and for a single value of average flow velocity. In addition these experiments do not provide a direct determination of micromixing intensity and the effect of buoyancy forces on the decay of turbulence is described on the base of several qualitative considerations. From this point of view a density discontinuity between two layers of mixed fluid of different density and having stable density distribution is very interesting object for studies. This object is a direct analog of atmospheric and oceanic phenomena and is convenient for developing mathematical models. In addition the increasing of thickness of interface layer after ceasing all turbulent fluctuations allows us to obtain integral quantitative features of turbulent micromixing process.

Experimental setup and instruments. The experiments were carried out in the steel water channel of 50x50 cm cross-section and 3 m length. The channel has two carriages one of which is provided with a turbulizing grid and the other with measuring instruments. The carriages are towed along the channel. The side walls of the channel are provided with optical glasses. The turbulizing grid is made of Plexiglass bars (1x1 cm) and has a mesh size M = 5,0 cm. The channel was filled with two layer fluid: top layer is fresh water and bottom layer is salt water. A shadow setup and laser scanning refractometer are used for measuring of vertical distribution of density. The intensity of micromixing is evaluated by measuring difference between initial (before mixing) and final (after all motions ceased) vertical density distributions of initial S_0 and final S_f values of thickness of the intermediate layer ΔS. A hot-film technique with standard DANTEC quartz-coated wedge-shaped sensors are used for measuring of the velocity fluctuations. Density difference between two layers $\Delta\rho$, grid velocity U and mesh size M were changed in experiments to obtain dependencies of integral micromixing intensity ΔS and integral effect of buoyancy forces on these parameters. A Richardson number may be built as a form of $Ri = \frac{g \cdot \Delta\rho \cdot M^2}{\rho S U^2}$ and then may be rewritten in the form $Ri = \frac{Mi}{Fr}$, where $Mi = \frac{\Delta\rho}{\rho} \cdot \frac{M}{S}$ and $Fr = \frac{U^2}{g \cdot M}$. This is an integral form of the criteria. In the local form $Mi = \frac{\partial\rho}{\partial z} \cdot \frac{l_t}{\rho}$ and $Fr = \frac{q^2}{l_t \cdot g}$, where l_t is turbulent length scale and $q^2 = \langle u'^2 \rangle + \langle v'^2 \rangle + \langle w'^2 \rangle$. Both criteria have a clear physical sense. The Mi number is a ratio of turbulent length scale to the stratification length scale. The Fr number is the ratio of kinetic energy which is fed to the fluid to the potential energy that liquid particles are received displacing at a distance l_t.

Experimental results. Measurements of the streamwise component ofa the turbulent kinetic energy $\frac{\langle u'^2 \rangle}{U^2}$ are presented in Fig. 1 for non- stratified and stratified cases as a function of the non-dimensional distance from the grid x/M. In the uniform case the results obtained follow a power law with -0.8 power exponent. In the stratified case the accelerated decay starts at some point, then levels out, and finally steepens again to the parallel line to the non- stratified curve.The difference between areas under these curves characterizes an integral effect of buoyancy forces on decaying turbulence. In addition the magnitude of micromixing intensity defined as a ratio $\frac{\Delta S^2}{M^2}$ as a function of Fr number $\frac{U^2}{M \cdot g}$ for different values of Mi number are presented in Fig. 2. The figure shows that for small values of Fr number the curves for different Mi number are in coincidence with each other. As Fr increases the common curve splits into three different curves for different values of Mi number at some point. The higher Mi number the higher integral micromixing intensity. In addition we have found the two principally different mixing regimes in our experiments. The first regime is 'usual' one when the thickness of the intermediate layer increases and the maximum of gradient decreases after passing the grid. This regime occurred if the mesh size M of the grid was sufficiently greater than initial effective thickness of the intermediate layer $\frac{S_0}{M} < 1$. It was a surprise for us when we found that with increasing of this ratio (by increasing time delay before towing the grid) sharpening of the interface and increasing of the maximum gradient occur. This phenomenon can be explained by more easy mixing in the top and bottom layers owing to that only a small gradient is presented in the layers after a time delay. In the same time the two-layer system is still sufficiently strong. In other words it seems that in this case the bottom and top layers are mixed separately (each as a whole) and only a small mass exchange occurs between the layers. As the result the intermediate layer is sharpened and maximal gradient increases.

Approbation of the method proposed As the test samples we choose the results of experimental researches of turbulent decay [3] and the process of changing the turbulence in flow with homogeneous gradient of the mean velocity (i.e. uniform shear flow) [4]. For the description of non-isotropic case [3] all fluctuation component equations are necessary. As in [5] the second moment equations in homogeneous conditions with zero third moments become:

$$\frac{\partial S_\gamma}{\partial t} = -2 \cdot \alpha \cdot S_\gamma + \varepsilon \qquad (1)$$

where S_γ is the turbulent fluctuation intensity, α is the turbulent friction intensity, and ε is the intensity of pulsating forces caused by pressure and friction. The dimension arguments ($[\alpha] = T^{-1}$, $[\varepsilon] = L \cdot T^{-3}$)) lead to the next relations [5]:

$$\alpha = \alpha_0 \cdot E^{1/2}/L; \varepsilon = \varepsilon_0 \cdot E^{3/2}/L, \qquad (2)$$

where $E = (S_1 + S_2 + S_3)$ is the turbulent kinetic energy, L is the integral turbulent scale, α_0 and ε_0 are the dimensionless constants.The integrating of the set (1) was fulfilled with the second order Runge method with the time step about 0.0002 sec. or the equivalent step for axial direction. The best coincidence of calculated and experimental data were obtained for values $\alpha_0 = 0.75$ and $\varepsilon_0 = 0.30$, some different from the values obtained in [5] by the comparison of our equations with equations of some two parametric turbulence models [6] where $\alpha_0 = 0.45$ and $\varepsilon_0 = 0.20$. The results of energy decay calculations depicted on Fig. 3.

In [3] turbulent scales themselves have not been measured but they can be assessed from the measurements of turbulent energy dissipation if a relationship for determining of the scale takes the form:

$$\varepsilon_E \sim \frac{E_{3/2}}{L} \qquad (3)$$

The experimental data for the scale have been approximated with linear dependance obtained by least-squares method.

For stationary turbulent uniform shear flow only one component of velocity differs from zero and changes along the transverse coordinate. The shear is called uniform if velocity is a linear function of the coordinate. In the process of flow rebuilding the integral scale is changed strongly and, as it will be shown below, our model results in appearance of the third moments, i.e. the turbulence became non-uniform regardless of initial uniformity and uniformity of the shear.

Preliminary analysis has been performed for plane layer and in the absence of gradient of average pressure and third moments. The last assumption is the same as the assumption of uniformity of turbulence. In this case the equations for turbulent intensities are:

$$U_1 \cdot \frac{\partial S_i}{\partial X_1} = -(1 + \delta_{ij}) \cdot S_{i\gamma} \cdot \partial U_i/\partial X_\gamma - 2 \cdot \alpha \cdot S_i + \varepsilon \qquad (4)$$

For the example in consideration the magnitude of $\langle u' \cdot w' \rangle = S_{13}$ is the only different from zero from the others second moments. The equation for S_{13} is:

$$U(Z) \cdot \frac{\partial S_{13}}{\partial X} = -S_{13} \cdot \partial U_1/\partial Z - 2 \cdot \alpha \cdot S_{13} \tag{5}$$

The calculations are performed by using the set of equations (4)and (5).The calculations were performed for a given value of shear by Runge-Kutta method with time defined by a relationship $t = X/U(0)$ and with a step $dt = 0.001$.

Equilibrium parameters. Some possible regimes were tested to assess dependencies typical for quasi state or stationary regimes. If proposed that the turbulent characteristics reach their stationary values rather rapidly, so that values of the parameters are defined by the local values of shear and are independent of history, the results obtained can be called equilibrium. The calculation of equilibrium values was performed using a set of algebraic equations deduced with setting to zero of the right hand parts of our set of equations wherein spatial derivatives of second moments are also omitted. The set of equations takes the form:

$$\langle w'^2_{00} \rangle = \frac{\varepsilon_0}{2 \cdot \alpha_0} \cdot E_{00} \tag{6}$$

$$\langle v'^2_{00} \rangle = \langle u'^2_{00} \rangle = \frac{\varepsilon_0}{2 \cdot \alpha_0} \cdot (E_{00} + (\frac{\partial U/\partial Z \cdot L)^2}{(2 \cdot \alpha_0)^2}) \tag{7}$$

$$\langle u' w'_{00} \rangle = \frac{\varepsilon_0}{2 \cdot \alpha_0} \cdot \frac{\partial U}{\partial Z} \cdot L \cdot E^{1/2} \tag{8}$$

$$\langle E_{00} \rangle = \frac{\varepsilon_0}{(2 \cdot \alpha_0)^2 \cdot (2 \cdot \alpha_0 - 3 \cdot \varepsilon_0)} \cdot (\frac{\partial U}{\partial Z} \cdot L)^2 \tag{9}$$

For the comparisons, data obtained in the case of uniform shear have been chosen [4]. These data was recommended by STANFORD PROGRAM 90/91 . The measurements have been carried out in wind tunnel downstream of turbulizing grid. Intensity of turbulent velocity component and turbulent scales were measured for different shears and meshes of the turbulizing grid.

Preliminary calculations show that as opposed to the uniform case if changing of integral scale does not take into account the results obtained are not in agreement with experimental data. Much better agreement of calculation with experiment has been found when an experimental dependence is used for integral scale. The best coincidence is observed when $\alpha_0 = 1.1$ and $\varepsilon_0 = 1.1$ that somewhat differ from the constants used for the uniform case.

Fig.4 shows turbulent energy and intensity of longitudinal component of velocity as functions of time for typical value of shear. When the shear is minimal (caseL[4]) the agreement is somewhat worse. Equilibrium values of parameters E, $\langle$ and $u'^2 \rangle$ are shown on the same figures by dashed lines.

Besides the conditions of our own experiments in water channel were modeled. In this case a set of equations for turbulent intensity of velocity and concentration takes the form:

$$\frac{\partial C_R}{\partial t} = -\frac{\partial S_{34}}{\partial Z}$$

$$\frac{\partial S_4}{\partial t} = -2 \cdot \beta \cdot S_4 - S_{34} \cdot \frac{\partial C_R}{\partial Z} - \frac{\partial a_{344}}{\partial Z}$$

$$\frac{\partial S_1}{\partial t} = -2 \cdot \alpha \cdot S_1 + \epsilon - \frac{\partial a_{113}}{\partial Z}$$

$$\frac{\partial S_3}{\partial t} = -2 \cdot \alpha \cdot S_3 + \epsilon - 2 \cdot S_{34} \cdot Fr - 3 \cdot \frac{\partial a_{333}}{\partial Z}$$

$$\frac{\partial S_{34}}{\partial t} = -(\alpha + \beta) \cdot S_{34} - 2 \cdot S_4 \cdot Fr - S_3 \cdot \frac{\partial C_R}{\partial Z} - 2 \cdot \frac{\partial a_{334}}{\partial Z},$$

where C_R is averaged concentration, $S_4 = \langle c'^2 \rangle$ is intensity of concentration fluctuations, $S_{34} = \langle w'c' \rangle$ is turbulent vertical mass flux, β is concentration dissipation. The terms $a_{344} = \langle w'c'^2 \rangle$, $a_{113} = \langle u'^2 w' \rangle$, $a_{333} = \langle w'^3 \rangle$, and $a_{334} = \langle w'^2 c' \rangle$ are the third moments which are determined by equilibrium consideration. Factor Fr represents effect of bulk and pressure forces and is determined by following relationship:

$$Fr = \frac{-g - 2 \cdot \partial S_1 / \partial Z}{(a_\rho + b_\rho \cdot C_R) \cdot b_\rho}, \tag{10}$$

where g is acceleration of gravity, a_ρ and b_ρ are the coefficients in relationship between concentration and density which can be accepted in this case as the simplest linear relationship between inverse ρ and c and has a form:

$$\frac{1}{\rho} = a_\rho + b_\rho \cdot c$$

Zero boundary conditions (at the top and at the bottom) were accepted for vertical and longitudinal components of velocity fluctuations and zero derivatives for other variables. The results of calculations performed for decaying turbulence in the experimental water channel using this set of equations are shown on Fig. 5. Two cases are presented on the figure: one is the non- stratified case and the other is the case with stratification when salt concentration of bottom layer was c = 0.4%. The figure shows that as well as for the mentioned above calculations of decaying homogeneous turbulence in experiments of Lienhard [3] we have acceptable agreement between the calculations and our experimental data. As expected, in the stratification case the curve begins deflect from non-stratification one at some point and the calculating curve satisfactory describes the experimental data too.

REFERENCES

1. Stillinger, D.C., Helland, K.N., Van Atta, C.W., 1983, Experiments on the transition of homogeneous turbulence to internal waves in a stratified fluid, J. Fluid Mech.,131,91-122

2. Itswier, E.C., Helland, K.N., Van Atta, C.W., 1986, The evolution of grid-generated turbulence in stably stratified fluid, J. Fluid Mech.,162, 299-338

3. Lienhard, J.H., Van Atta C.W., 1990, The decay of turbulence in thermally stratified flow., J.Fluid Mech.,210,57-112

4. Tavoularis S.,Karnik U. Further experiments on the evolution of turbulent stresses and scales in uniformity sheared turbulence. J.Fluid.Mech., 1989, v.204, pp 457-478

5. Frost V.A.: Mixing processes description in turbulent flows with density variations. Preprint IPM RAS, No.483, 1990, pp.28.

6. Luschik V.G., Pavel'ev A.A., Yakubenko A.E.: Equations for transfer of turbulence characteristics: the models and the results. Itogi Nauki i Tekhn., MGG, 1988, vol.22, pp.3-61.

Figures

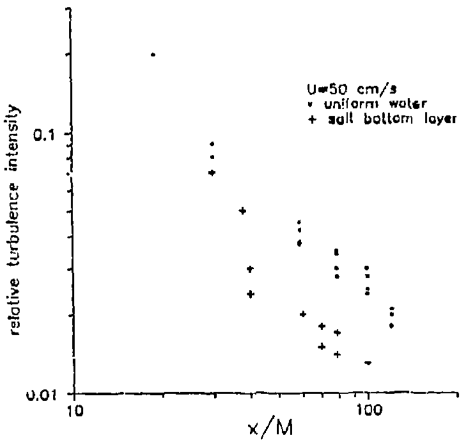

Fig.1.

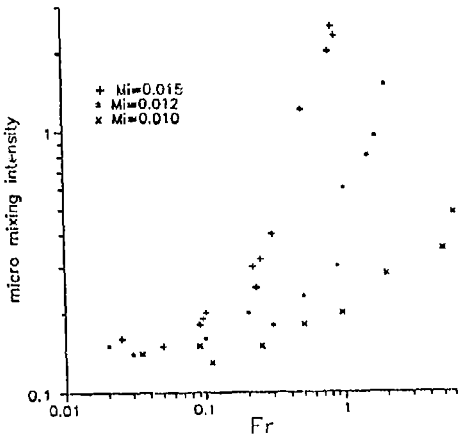

Fig.2.

Fig.1. Relative intensity of longitudinal component of turbulent fluctuations vs. down strean distance for non-stratified and stratified case.

Fig.2. Micro mixing intensity vs. Froud numbers for different values of mixing number Mi.

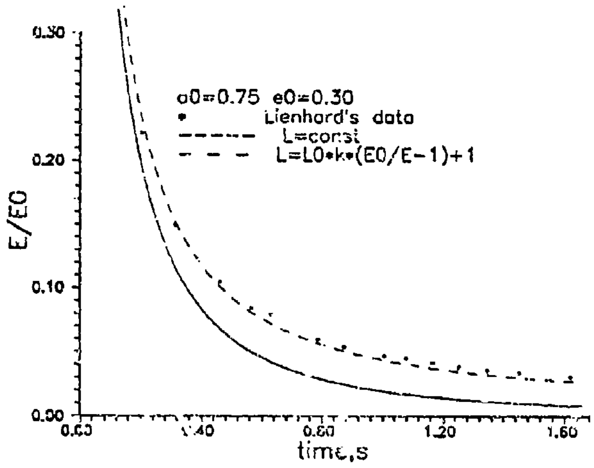

Fig.3.

Fig.3. Comparison of the calculations with Lienhard's data [3] on turbulence decay downstream of the grid.

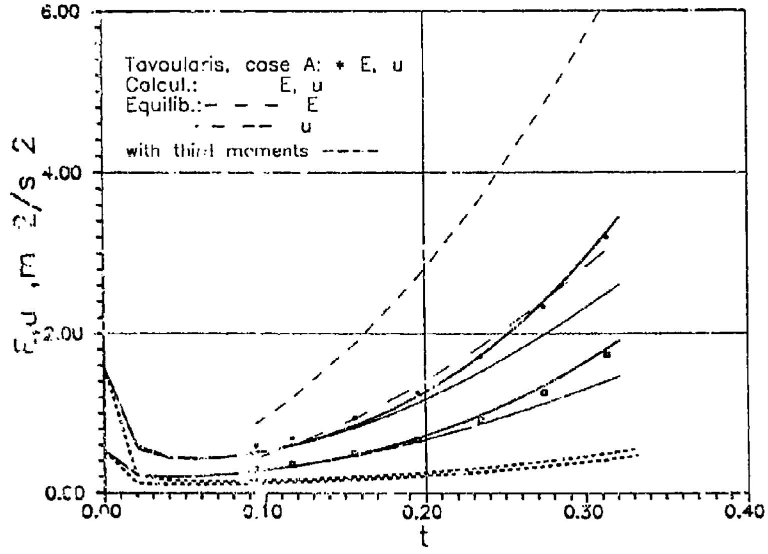

Fig.4.

Fig.4. Comparison of the calculations with Tavoularis's data [4] on developing turbu- shear flow downstream of the grid.

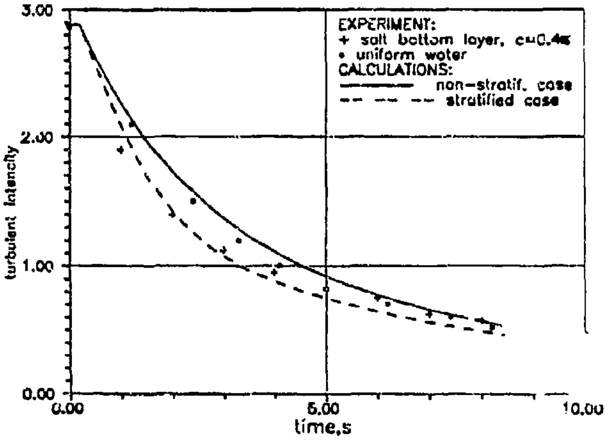

Fig.5.

Fig.5. Comparison of the calculations of turbulence decay within experimental water channel for non-strarified and stratified cases.

Statistical approach of wave-vortex interactions in stably stratified homogeneous turbulence

F. S. Godeferd and C. Cambon
Lab. de Méc. des Fluides et d'Accoustique - URA CNRS 263
Ecole Centrale de Lyon

1 Introduction

The gravity waves generating effect of the acceleration of gravity upon a density stratified fluid can be found in as various geophysical flows as the atmospheric layer, or in the ocean, where a stable stratification is found at a given depth, depending on the location and the season. The spectrum, *i.e.* the repartition of the energy of internal waves with their wavenumber, can be computed in different manners, and it is well known that a weakly non linear theory such as that by Garrett and Munk has led to both qualitative and quantitative agreement with measurements in the ocean [1]. However, a review by Müller *et al.* brought to light the main drawback of such weakly non linear techniques, which is to put aside every kind of vortical motion, since a "wave turbulence" cannot produce any vorticity [2]. Indeed, interactions of internal waves with turbulence, and specifically with vortical modes (within a given decomposition explained below) are shown to produce triadic energy exchanges when a resonance condition is fulfilled. Therefore, more sophisticated approaches of stably stratified turbulence (SST) are necessary to explain the apparition of anisotropic tendencies in such flows. Among them, the most important must be the severe restriction of motion in the direction of the mean density gradient, which suggests a horizontal layering of the flow with a strong vertical variability. The corresponding velocity field then becomes almost "two-component" but certainly not "two-dimensional". The importance of this distinction has appeared recently in order to avoid confusion with the bidimensionalization of flows created by solid body rotation (SBR) effects in some cases [3], or eventually by an external magnetic field. One can introduce this distinction in the behavior equations through a "componentality" and a "dimensionality" tensor. Hence, a quasi two-dimensional flow corresponds to a flow whose vertical variability is greatly reduced, or in other words, in which the length scale associated with vertical derivatives ($\partial/\partial x_{\|}$) is large. But the vertical component $u_{\|}$ of the velocity does not necessarily go to zero. In the SBR case, dominant structures are column like. On the contrary, in the case of SST, $u_{\|} \rightarrow 0$ but not $\partial/\partial x_{\|}$. Such vertically decorrelated structures are stretched in the two horizontal directions and are thin in the vertical one, suggesting pancakes slipping on one another, or sheet like structures brought to evidence by experiments in the atmospheric layers [5]. Our approach is to study these anisotropic tendencies in spectral space, where the identification of energy exchange mechanisms can be detailed. For this purpose, a statistical, two-point, EDQNM type model is used, rather than Direct Numerical Simulations, since it is based on a linear wave/vortex decomposition, and permit us to have a close view of the eight types of energy transfer arising from this splitting. Statistical approaches of the same kind have been used , in a somewhat simpler manner by Carnevale and Frederiksen [6], or by Holloway and Hendershot [7].

2 Overview of the statistical approach

2.1 Behavior equations

For stably stratified turbulence, we consider the Boussinesq equations where the density gradient γ has its only non zero component in the x_3 (vertical or gravity) direction, and leads to a constant Brunt-Väisälä frequency $N = (\beta|\gamma|g)^{1/2}$ in the whole flow, where g is the gravity, and β the thermometric expansivity. Moreover, the Prandtl number is assumed to be equal to one. The fluctuating velocity field $\boldsymbol{u}$, the pressure field p, and the perturbation temperature field τ around the barotropic equilibrium state, explicitly depend on the location in space $\boldsymbol{x}$ and on the time t at which they are evaluated. We assume that the turbulence is statistically homogeneous, which allows us to Fourier transform all the quantities, denoted by a $\hat{}$. The spectral equations for the fluctuating quantities are:

$$\begin{aligned}\left[\frac{\partial}{\partial t}+\nu k^2\right]\hat{u}_i(\boldsymbol{k},t)-P_{i3}(\boldsymbol{k},t)g\beta\hat{\tau}(\boldsymbol{k},t) &= -Ik_lP_{in}(\boldsymbol{k})\left\langle\widehat{u_lu_n}\right\rangle(\boldsymbol{k},t)\\ \left[\frac{\partial}{\partial t}+\nu k^2\right]\hat{\tau}(\boldsymbol{k},t)-\gamma\hat{u}_3(\boldsymbol{k},t) &= -Ik_l\left\langle\widehat{u_l\tau}\right\rangle(\boldsymbol{k},t)\end{aligned}\tag{1}$$

where $\gamma=|\gamma|$ and $I^2=-1$ and $P_{ij}(\boldsymbol{k})=\delta_{ij}-\frac{k_ik_j}{k^2}$ is the projector on the plane orthogonal to $\boldsymbol{k}$. The fluctuating pressure has been removed from consideration by projection of the equations on the plane orthogonal to $\boldsymbol{k}$, since the zero divergence property of the velocity field amounts to $\boldsymbol{k}\cdot\boldsymbol{u}(k,t)$. One of the original aspects of the present approach, introduced by Cambon [8], is to gather the fluctuating velocity and temperature fields under the same *vector*, using the (now free of velocity component) direction of $\boldsymbol{k}$ to hold the temperature component of the resulting vector, and a kinematic dimensioning, as follows:

$$\hat{v}_i(\boldsymbol{k},t)=\hat{u}_i(\boldsymbol{k},t)+I\frac{k_i}{k}\frac{\beta g}{N}\hat{\tau}(\boldsymbol{k},t)=\hat{u}_i(\boldsymbol{k},t)+\hat{\varphi}_i^3(\boldsymbol{k},t)\tag{2}$$

The component on the $\boldsymbol{k}$ direction is complex for the velocity-temperature $\hat{\boldsymbol{v}}$ to be real in physical space. Because of the orthonormal properties and the scaling coefficient $\beta g/N$, $\frac{1}{2}\hat{v}_i^*\hat{v}_i=\frac{1}{2}\hat{u}_i^*\hat{u}_i+\frac{1}{2}\left(\frac{\beta g}{N}\right)^2\hat{\tau}^*\hat{\tau}$ simply gives the spectral density of total energy (kinetic + potential). The resulting equation for $\hat{\boldsymbol{v}}$ has the following shape:

$$\left[\frac{\partial}{\partial t}+\nu k^2\right]\hat{v}_i(\boldsymbol{k},t)+L_{ij}(\boldsymbol{k})\hat{v}_j(\boldsymbol{k},t) = \int_{\boldsymbol{k}+\boldsymbol{p}+\boldsymbol{q}=0}M_{ipq}(\boldsymbol{k},\boldsymbol{p},\boldsymbol{q})\hat{v}_p(\boldsymbol{p},t)\hat{v}_q(\boldsymbol{q},t)\,d^3\boldsymbol{p}\tag{3}$$

in which we will not give detail for the linear and non linear operators **L** and **M** (see [9] for the complete set, or [10] for a comprehensive approach). The second order and third order spectral tensors can be computed using the relations: $\langle\hat{v}_i(\boldsymbol{p},t)\hat{v}_j(\boldsymbol{k},t)\rangle=\hat{V}_{ij}(\boldsymbol{k},t)\delta(\boldsymbol{k}+\boldsymbol{p})$ and $\langle\hat{v}_i(\boldsymbol{k},t)\hat{v}_j(\boldsymbol{p},t)\hat{v}_l(\boldsymbol{q},t)\rangle=\hat{V}_{ijl}(\boldsymbol{k},\boldsymbol{p},t)\delta(\boldsymbol{k}+\boldsymbol{p}+\boldsymbol{q})$; the resulting equations are easily derived from (3). The classical closure problem in the spectral formulation of homogeneous turbulence is present here for the $\hat{\boldsymbol{v}}$ variable as well: the equation for $\hat{V}_{ij}$ includes non linear terms containing the third order correlations $\hat{V}_{jpq}$, and the equation for the latter, in turn, include fourth order ones, ... The Eddy Damped Quasi Normal Markovian hypothesis [11] expresses the fourth order correlations in terms of the second order ones, as for a normal law with a gaussian distribution, but for a damping proportional to the third order correlations. Symbolically, one can sum up the whole process as :

$$<VVVV>=<VV><VV>-\eta<VVV>$$

where η is the damping. Following previous works [3, 4], the damping is chosen to follow the standard isotropic rule : $\eta(k,t)=\nu k^2+\eta'(k,t)=\nu k^2+A\left[\int_0^k p^2E(p,t)dp\right]$ where $A=0.366$ and E is the isotropically accumulated kinetic energy spectrum.

2.2 Decomposition on the eigen frame

The eigen modes of the linear operator L_{ij} correspond to the propagating mode of motion on the one hand, and to the stationary rotational mode on the other. For each propagating mode, associated to the internal waves in this linear decomposition, two directions of propagation are possible, labeled $\varepsilon=\pm1$, while the non propagating mode is labeled using $\varepsilon=0$. The velocity field is then decomposed in terms of its components on each of the three above modes, and this approach turns out to rejoin the decomposition of $\boldsymbol{u}$ in the Craya-Herring frame already used for axisymmetric turbulence [12, 13] :

$$\hat{u}_i=\hat{\varphi}^1e_i^1+\hat{\varphi}^2e_i^2\ ;\quad \boldsymbol{e}^1(\boldsymbol{k})=(\boldsymbol{k}\times\boldsymbol{n})/|\boldsymbol{k}\times\boldsymbol{n}|\ ;\quad \boldsymbol{e}^2(\boldsymbol{k})=(\boldsymbol{k}\times\boldsymbol{e}^1)/|\boldsymbol{k}\times\boldsymbol{e}^1|$$

in which it is necessary to use an auxiliary unit vector which bears the axis of symmetry. For stratified turbulence, the base vector is chosen to be $n_i=g_i/g$ as shown in figure 1. Such a decomposition can also be seen in physical space [14] as :

$$\boldsymbol{u}=\boldsymbol{\nabla}_h\times\Psi'\boldsymbol{n}+\boldsymbol{\nabla}_h\Phi+u_3\boldsymbol{n}\tag{4}$$

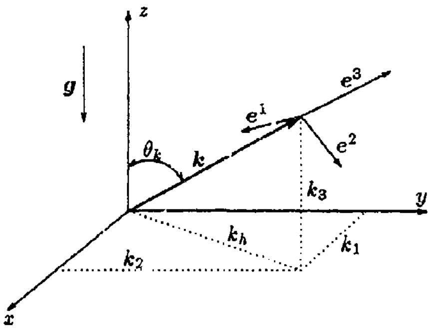

Figure 1: The Craya-Herring frame of reference for axisymmetric turbulence.

for the velocity field, for example, in which the first term in the right hand part contributes to the horizontal vorticity, with stream function Ψ', and the non divergent contribution comes out of the scalar potential Φ. Those two terms contain all the horizontal velocity. The third component u_3 comes entirely out of the temperature field, and plays the same role as the dilatational mode in the classical Helmholtz decomposition for compressible flows. u_3 is evidently not two dimensional since its associated potential Φ' depends on all three components of space. One can see a direct link of this linear decomposision with quasi-geostrophic turbulence. This latter theory, applied to both rotating *and* stably stratified flows, assumes a geostrophic balance of the pressure gradient in the (horizontal or) β-plane approximation, and a vertical velocity component coming from a decoupled variation of the motion in horizontal planes [15]. A potential vorticity equation for the geostrophic and Boussinesq approximations can be written as :

$$q = \nabla_h^2 \Psi' + \frac{f^2}{N^2}\frac{\partial \Psi'}{\partial x_3} \tag{5}$$

where the rotation is taken into account through the Coriolis parameter f. The first term in the right-hand side of (5) shows the contribution of the stream function Ψ' to the horizontal mode of motion, while the second one indicates that the vertical velocity plays a significant role in the flow. For low Rossby and Froude numbers, the statistical models have to rejoin the semi-geostrophic approximation. Indeed, it is clear that stably stratified turbulence is close to it at very low Froude number, since the vortex eigen mode component rejoins the horizontal geostrophic motion, which is not the case for SBR turbulence, even at low Rossby number, since it restricts its larger velocity component to the vertical direction, with no vertical variability. Thus, one may be able to use the statistical theory with a high stratification to predict features of geophysical flows that fall within the range of the quasi-geostrophic theory. In all the cases, the exact eigenmodes are obtained by single linear combinations of e^1, e^2, $e^3 = \boldsymbol{k}/k$, so that they form an orthonormal frame for the new vector $\hat{\boldsymbol{v}}$ [10].

2.3 Energy equations for axisymmetric stratified turbulence

The following equations are obtained for the spectral density of energy $\frac{1}{2} < \hat{\varphi}^{i*}\hat{\varphi}^{i} >$ of the components $\hat{\varphi}^{i}$ of the velocity-temperature field.

$$\begin{aligned}
\left[\frac{\partial}{\partial t} + 2\nu k^2\right]\Phi_1(\boldsymbol{k},t) &= T^1(\boldsymbol{k},t)\\
\left[\frac{\partial}{\partial t} + 2\nu k^2\right]\Phi_2(\boldsymbol{k},t) + N\sin\theta_k \Psi_R(\boldsymbol{k},t) &= T^2(\boldsymbol{k},t)\\
\left[\frac{\partial}{\partial t} + 2\nu k^2\right]\Phi_3(\boldsymbol{k},t) - N\sin\theta_k \Psi_R(\boldsymbol{k},t) &= T^3(\boldsymbol{k},t) \qquad (6)\\
\left[\frac{\partial}{\partial t} + 2\nu k^2\right]\Psi_R(\boldsymbol{k},t) - 2N\sin\theta_k[\Phi_2(\boldsymbol{k},t) - \Phi_3(\boldsymbol{k},t)] &= T^{\Psi_R}(\boldsymbol{k},t)
\end{aligned}$$

(7)

In these equations, the $\Phi_1 = \frac{1}{2} <\hat{\varphi}^1\hat{\varphi}^1>$ spectrum is the kinetic energy of the vortex mode, Φ_2 (same definition) is the kinetic energy of the wave mode, and Φ_3 is the potential energy of the wave mode. The real part of the Ψ spectrum corresponds to the heat flux. Each spectrum, as well as the corresponding non linear transfer term T^i depends on the wave vector $\boldsymbol{k}$, through its modulus k and its orientation to the vertical direction θ_k. The stratification appears explicitly in the linear operators of these equations through N, but also within the detailed form of the transfer terms T^1, T^2, T^3, T^{Ψ_R} which is not given here for the sake of of brevity. Each non linear transfer is the sum of the contributions in an eightfold decomposition according to the values ± 1 (wave) or 0 (vortex) of the 'polarity indices' ε, ε', ε''. These contributions are of the kind

$$T^{\varepsilon\varepsilon'\varepsilon''}(\boldsymbol{k},t) = \int_{\boldsymbol{k}+\boldsymbol{p}+\boldsymbol{q}=\boldsymbol{0}} \frac{S_{\varepsilon\varepsilon'\varepsilon''}(\boldsymbol{k},\boldsymbol{p},\boldsymbol{q},t)}{\theta^{-1}_{kpq} - IN(\varepsilon\sin\theta_k + \varepsilon'\sin\theta_p + \varepsilon''\sin\theta_q)} dpdq \tag{8}$$

where the numerator of the integrand involves double correlations and known geometric factors. It is no wonder that equation (8) contains an expression that resembles,in the limit of low Froude number, the resonance condition

$$\omega_k + \omega_p + \omega_q = 0 \tag{9}$$

on the pulsations $\omega_k = N\sin\theta_k$ of a triad $\boldsymbol{k}$, $\boldsymbol{p}$ and $\boldsymbol{q}$ of internal waves, such that

$$\boldsymbol{k} + \boldsymbol{p} + \boldsymbol{q} = \boldsymbol{0} \tag{10}$$

Since we deal with a linear decomposition of the velocity field, the linear eigenmodes that we consider indeed correspond to internal gravity waves for $|\varepsilon| = 1$ so that the three Fourier modes that are involved in the triple correlation tensor lead to the appearance of a phase that includes the sum of the three pulsations. The triadic condition (10) is given by the convolution product, which comes up to be an integration over triads of wave vectors only. Therefore, the bottom part of the expression under the integral in (8), which is the characteristic time introduced by the EDQNM model to damp the $S_{\varepsilon\varepsilon'\varepsilon''}$ interaction, does not explicitly depend on N for resonant triads only, and leads to a scrambling of the other triads. We notice that are permitted interactions between wave modes only, but also mixed interactions with vortex modes $\varepsilon = 0$, and finally pure vortex interactions, in which case, since all ε's are zero, the stratification no more explicitly appears. In the next section, within the light of this decomposition, we compute the detailed energy transfer spectra for the eight kinds of interaction. If we set $N = 0$, isotropic turbulence is obtained, for which we also retain the eightfold splitting, and compare them with their counterparts in a stratified case, in order to see the specific influence of the stable stratification on each term.

3 Numerical results

The axisymmetric equations for the EDQNM stably stratified model are solved using a discretized wave space, in which 37 spectral modes are retained, and 19 spectral angles. There are 21 azimuthal angles that permit the three dimensional triadic interactions. The computations correspond to freely decaying homogeneous turbulence which is subjected to the effect of gravity at time $T = 0$. We choose here to present the resulting energy spectra for one case of stratification, that corresponds to a Brunt-Väisälä frequency equal to π, at a time at which the non linear anisotropic trends have become significant. The actual EDQNM model which is used for the present computations includes the explicit effect of stratification at all the levels of the closure, *i.e.* in the non linear terms of both the equations for the second order *and* third order spectra. A simplified model, which achieves much lower irreversible anisotropic tendencies, can be used, in which the equation for the triple correlations retains stratification in the linear terms only (see vanHaren *et al.*, present meeting). Explicitly, the most complete EDQNM model shows that the vortex kinetic energy Φ_1 and the wave total energy $\Phi_2 + \Phi_3$ accumulate around the vertical direction in spectral space, the "polar zone" where $\cos\theta_k = 1$.

The computations have been initialized using an analytical isotropic spectrum $E(k)$ for the wave and vortex kinetic energy spectra : $\Phi_1 = \Phi_2 = E(k)/4\pi k^2$. Moreover, initial potential energy is supposed to be non zero at $T = 0$, so that $\Phi_3 = E(k)/4\pi k^2$ also. The purpose of this procedure is to see how the anisotropy evolves in the very first stage of the computation under the influence of the non linear transfer terms alone, in (6). These latter equations show that, if the Φ_2 and Φ_3 are different initially, the linear operators that include N makes them oscillate immediately, effect that is canceled if they are

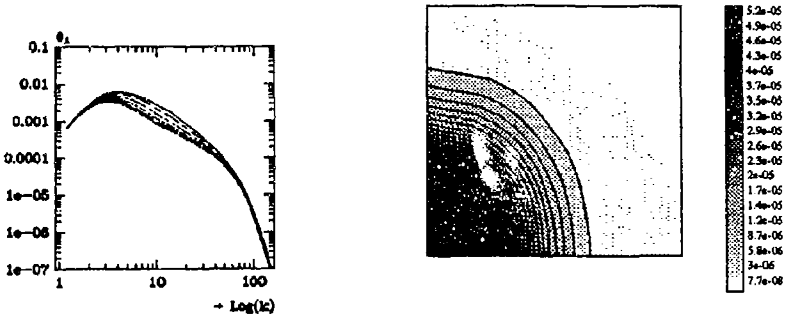

Figure 2: Two ways of representing the spectral distribution] of the vortex kinetic energy Φ_1: on a linear plot with curves depending on the orientation of the wave vector (left) ; on a (k_x,k_z) representation (right) ($N = \pi$ and non dimensional time $NT/2\pi = 3$).

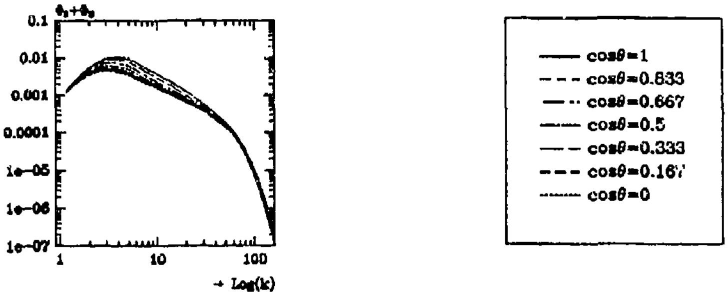

Figure 3: Same as left part of figure 2 for the spectral distribution of the total wave energy $\Phi_2 + \Phi_3$ (the caption holds for all the plots in this paper).

equal. However, Φ_2 and Φ_3 begin to oscillate somehow, after the non linear terms have built a difference between them. We do not bother with these temporal oscillations by looking at the spectra of the total energy of the waves, which is a non oscillating quantity as is Φ_1.

3.1 Anisotropic spectra

We show here the anisotropic Φ_1 and $\Phi_2 + \Phi_3$ spectra in two different ways : first, a linear plot, with the different curves corresponding to different directions of the wave vector. The polar zone corresponds to $\cos\theta_k = 1$ and the equatorial (horizontal) part to $\cos\theta_k = 0$. The second representation shows a vertical plane in spectral space, on which isolines of energy are represented on a (k_x,k_z) coordinate system. As seen on figure 2 and 3, the anisotropy is poorly reflected by such a representation, only through a somehow elliptic shape of the isoenergy areas. Whereas the advantage of the linear plot is to compare directly the levels of energy at different angles, which clearly shows that the inertial range contains more energy at the pole than at the equator.

3.2 Transfer spectra

On the contrary, the bidimensional representation gives a good view of the areas from which energy is removed, and those to which it is given, *i.e.* it is especially useful when looking at the transfer spectra. We show on figure 4 the non linear transfer terms occuring in the Φ_1 and in the $\Phi_2 + \Phi_3$ equations.

The detailed transfers for the eight types of interaction constituting the non linear transfer spectra give us some insight in the generating mechanisms of anisotropy. As figure 5 shows, the pure vortex

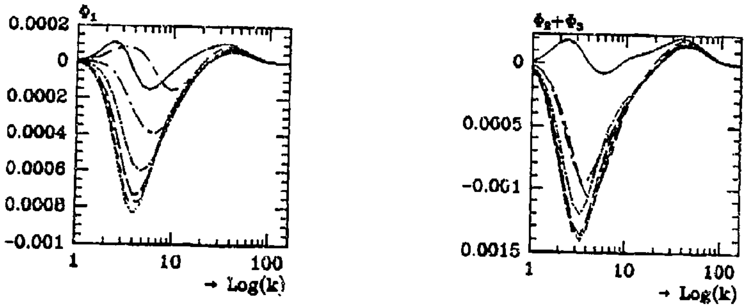

Figure 4: The non linear transfer T^1 spectrum for Φ_1 at time $NT/2\pi = 3$ for $N = \pi$ (left), and T^{2+3} for the total wave energy $\Phi_2 + \Phi_3$ (right).

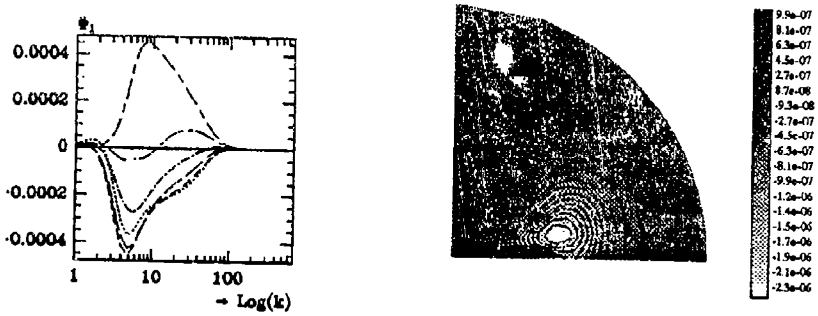

Figure 5: The pure vortex interactions (where $\varepsilon = 0$, $\varepsilon' = 0$ and $\varepsilon'' = 0$ in (8)) in the two representations (same conditions of the computation as previous figures). The isolines are dotted for the areas of negative transfer, and plain for the areas of positive transfer. It is clearly seen that the energy is transported towards the vertical direction of $\boldsymbol{k}$.

interaction consists only in the advection of vortex energy from the equatorial zone to the polar one. Since this term is not directly affected by the stratification, the shape of this part of the transfer is completely recovered in the case of isotropic turbulence, for which the EDQNM model still retains the eightfold splitting. The mixed interaction terms, between waves and vortex, are not presented here since their anisotropic features are not as clear as that of the pure vortex interaction. However, figure 6 shows the pure wave term, on which we see that it contributes to the scrambling in wave space, as is suggested by the characteristic time associated to it in (8). The latter equation shows that, when the resonance condition is not verified for a given triad, the N containing part of the nonlinear transfer acts as a scrambling mechanism in spectral space. It can also be seen that the pure vortex interaction leads to a zero energy transfer exactly at the pole. Therefore, the accumulation of energy due to the vortex interactions *around* the pole, cannot become a complete bidimensionalisation of the flow at larger times. The pure wave interaction, in turn, reajusts the scales at which the kinetic energy concentrates, at transports some of it to the vertical direction, but is definitely not sufficient to explain the collapse of stably stratified turbulence. Finally, if the vortex kinetic energy accumulates at the pole, the condition of axisymmetry states that $\Phi_1 = \Phi_2$ in this direction, which also leads to having an accumulation of wave kinetic energy, thus of the total wave energy.

The structure of the flow in physical space is may be caracterized in different ways. For example, figure 7 shows the temporal evolution of the length scales of the horizontal component of the velocity with respect to horizontal and vertical separations. Normally, in freely decaying turbulence, the length scales increase, as a consequence of the decrease of energy in the flow. It is the case for $l_{11,1}$ here. But

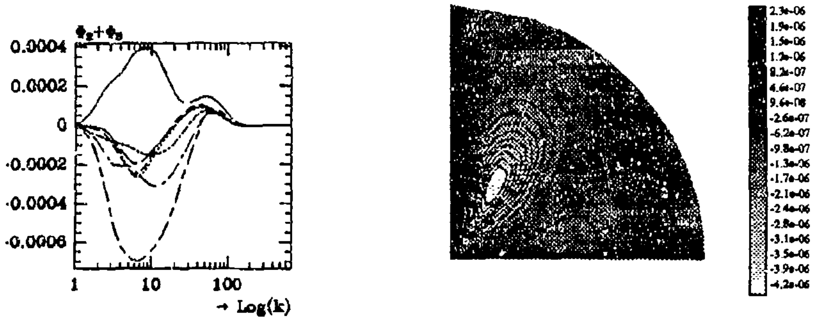

Figure 6: The pure wavy interactions (where $\varepsilon = 1$, $\varepsilon' = 1$ and $\varepsilon'' = 1$ contribute only to the T^{2+3} transfer. Patches in the spectral distribution seen on the left do not allow one to identified a specific mechanism at this point.

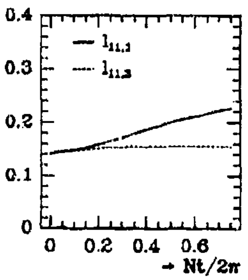

Figure 7: Length scales of the horizontal velocity component with respect to two directions of separation: $l_{11,1}$ for the horizontal separation and $l_{11,3}$ for the vertical separation.

$l_{11,3}$ starts from the same value, which corresponds to our initially isotropic conditinos, and stays roughly at this level. This behavior indicates that the transfers in the vertical direction are more or less inhibited by the presence of stratification. The resulting structures of the flow can then be viewed as elongated in the two horizontal directions, as could be a sphere, flatened on one of its axes. The image of "pancake" like structures may be a bit strong, for the layers in the flow are not *totally* decorrelated vertically, but remains anyway a good shortcut for expressing all the above mentioned ideas.

The main conclusion of this work is that the pure vortex interactions are the most important generator of non linear irreversible anisotropy for stably stratified turbulence. A simplified Reynolds stress tensor model that may reproduce these non linear tendencies has to account for this kind of interaction, in a first time.

References

[1] **C. Garrett & W. Munk** Internal waves in the ocean, *Ann. Rev. Fluid Mech.*, 11, p. 339, 1979

[2] **P. Müller** On the diffusion of momentum and mass by internal gravity waves *J. Fluid Mech.*, vol. 77, part 4, pp. 789–823, 1976

[3] **C. Cambon & L. Jacquin** Spectral approach to non-isotropic turbulence subjected to rotation, *J. Fluid Mech.* 202, 295 (1989)

[4] **J. C. André & M. Lesieur** Influence of helicity on high Reynolds number isotropic turbulence, *J. Fluid Mech.* **81**, pp. 187-207, 1977

[5] **F. Dalaudier, C. Sidi, M. Crochet & J. Vernin** Direct evidence of "sheets" in the atmospheric temperature field, *J. of the Atmospheric Sciences*, vol. 51, n° 2, 1994

[6] **G. F. Carnevale & J. S. Frederiksen** A Statistical Dynamical Theory of Strongly Nonlinear Internal Gravity Waves, Geophys. Astrophys. Fluid Dynamics, 1983, Vol. 23, pp. 175-207

[7] **G. Holloway & M. C. Hendershot** Statistical closure for nonlinear Rossby waves, J. Fluid Mech. (1977), vol. 82, part 4, pp. 747-765

[8] **C. Cambon** Spectral approach to axisymmetric turbulence in a stratified fluid, *Advances in Turbulence 2*, Springer-Verlag Berlin, 1989

[9] **L. vanHaren** Étude théorique et modélisation de la turbulence en présence d'ondes internes, *Thèse de Doctorat*, École Centrale de Lyon, January 1993

[10] **F. S. Godeferd & C. Cambon** Detailed investigation of energy transfers in homogeneous stratified turbulence, Phys. of Fluids **6**, June 1994

[11] **S. A. Orszag** Analytical theories of turbulence, *J. Fluid Mech.* 41, 363 (1970)

[12] **A. Craya** Contribution à l'analyse de la turbulence associée à des vitesses moyennes, *Publ. Sci. et Tech. du Ministère de l'Air*, n° 345, 1958

[13] **J. R. Herring** Approach of axisymmetric turbulence to isotropy, *The Physics of Fluids*, Vol. 17, N°5, pp. 859-872, May 1974

[14] **J.J. Riley, R.W. Metcalfe & M.A. Weissman** Direct numerical simulations of homogeneous turbulence in density-stratified fluids, *Proc. AIP conf. on Nonlinear properties of internal waves* (ed. B.J. West), pp. 79–112, 1981

[15] **J.G. Charney** Geostrophic turbulence, *J. of Atmosph. Sciences*, vol. 28, pp. 1087–1095, 1971

[16] **J. J. Riley, R. W. Metcalfe & M. A. Weisman** Direct numerical simulations of homogeneous turbulence in density-stratified fluids, in *Proceedings of AIP Conference on Nonlinear Properties of Internal Waves*, B. J. West Editor, American Institute of Physics, New York, pp. 79-112, 1981

INVERSE CASCADE IN STABLY-STRATIFIED ROTATING TURBULENCE

O. Métais[α,γ], *P. Bartello*[β], *E. Garnier*[α], *J.J. Riley*[γ]
and M. Lesieur[α]

[α] L.E.G.I./ Institut de Mécanique de Grenoble
B.P.53X, 38041 Grenoble Cédex, France

[β] Recherche en prévision numérique
Atmospheric Environment Service
Dorval (Québec) Canada H9P 1J3

[γ]Department of Mechanical Engineering, F.U. 10
University of Washington, Seattle, WA 98195, U.S.A.

INTRODUCTION

Rotation and stable density stratification modify the turbulence dynamics in many geophysical situations and on a large range of scales. Riley *et al.* (1981) and Lilly (1983) have suggested that, in the limit of small Froude numbers, stably-stratified turbulence could obey a two-dimensional turbulence dynamics. However, the numerical studies by Herring and Métais (1989) and Métais and Herring (1989) have shown that the horizontal motion dominates in a strongly stably-stratified environment, but the flow develops a strong vertical variability and reorganizes itself into decoupled horizontal layers. The shear of the horizontal velocity at the interface between the layers leads to energy dissipation, and prevents the turbulence from exhibiting the characteristics of two-dimensional turbulence.

Geophysical observations, laboratory experiments (Hopfinger *et al.*, 1982; Bidokhti and Tritton 1992) and numerical simulations (Lesieur *et al.* 1991; Métais *et al.* 1992, Bartello *et al.* 1994) have shown that a solid-body rotation stabilized the cyclonic eddies (with vorticity parallel and of the same sign as the solid-body rotation $2\vec{\Omega}$) . Conversely, anticyclones are three-dimensionalized for moderate rotation rate and stabilized at high rotation. Furthermore, as opposed to stratified turbulence, a solid-body rotation when applied to three-dimensional turbulence generates vertical coherence (see Bartello *et al.* 1994): for Rossby numbers close to unity, the three-dimensional flow reorganizes itself into two-dimensional cyclonic vortices. At a larger rotation rate, two-dimensional anticyclones also emerge from the initially-isotropic flow. Therefore, stable-stratification and rotation have antagonistic effects on turbulent flows: horizontal layering of the flow in one case and emergence of vertical quasi-two-dimensional rolls in the other one.

We numerically investigate the effects of solid-body rotation on stably-stratified turbulence: at first with energy injection at small scales and then in a freely-decaying situation. Various Rossby, R_o and Froude, F_r numbers are considered. The Brünt-Vaissälä frequency N is assumed to be constant. The three-dimensional Navier-Stokes equations within the Boussinesq approximation are simulated and homogeneous turbulence is investigated. In order to reduce the dissipative and diffusive ranges extension, the Laplacian operator in the viscous term is replaced with an iterated Laplacian (see Basdevant and Sadourny, 1983): in this study, we have employed Δ^2. The computational domain is a cubic periodic box, the resolution is 64^3 collocation points, and pseudo-spectral numerical methods are used.

FORCED-TURBULENCE SIMULATIONS

Turbulence and Waves

When solid-body rotation and stable density stratification are simultaneously present, one must find a simple way of discrimating between the turbulent part of the motion and the component associated with non linearly interacting [illegible] may use the fact that inertial gravity waves have no potential vorticity [illegible] turbulent component of the velocity field which is associated with the potential [illegible] This can be done in the limit of small Froude and Rossby numbers [illegible] Charney's (1971) geostrophic turbulence. Hydrostatic and geostrophic balances [illegible] imply that the (normalized) conserved potential vorticity can be [illegible] of a stream function ψ (Charney, 1971)

[illegible]

(N is the Brunt Vaissala frequency, f = 2Ω is the Coriolis parameter, H [illegible] horizontal and z the vertical direction). Therefore, from the potential [illegible] can derive ψ through (1). The geostrophic turbulent part of the horizontal velocity [illegible] (normalized) density fields can then be derived in the following way:

$$u_G = \frac{\partial\psi}{\partial y} \quad v_G = -\frac{\partial\psi}{\partial x} \quad \Theta_G = -\frac{\partial\psi}{\partial z}$$

E_G^x and E_G^y will designate the two components of the *geostrophic* kinetic energy and E_G the *geostrophic* available potential energy respectively associated to u_G, v_G and Θ_G.

As a first order approximation, one can consider that all the vertical velocity is associated with the wave motion: $w_w = w$ (where the w index stands for wave). The wave density field can be easily derived from:

$$\frac{\partial\Theta_w}{\partial t} = -i\omega\Theta_w = N^2 w \tag{3}$$

with $\omega^2 = \left(N^2 k_H^2 + f^2 k_z^2\right) / \left(k_H^2 + k_z^2\right)$. The facts that the wave field has no potential vorticity and also that the velocity field is non-divergent lead to:

$$\nabla_H^2 u_w = -\frac{\partial^2 w}{\partial z \partial x} - \frac{f}{N^2}\frac{\partial^2\Theta_w}{\partial z \partial y}\ , \ \nabla_H^2 v_w = -\frac{\partial^2 w}{\partial z \partial y} + \frac{f}{N^2}\frac{\partial^2\Theta_w}{\partial z \partial x} \tag{4}$$

These expressions were previously derived by Müller *et al.* (1986) and Lelong (1990).

Notice that for $f = 0$, one recovers the classical decomposition of the horizontal velocity field into rotational and divergent components. It is equivalent to Craya's (1958) decomposition, which has been used to discriminate between stratified turbulence and internal gravity waves (Riley *et al.*, 1981; Métais and Herring 1989). Subsequently, we call vortical mode the rotational component of the horizontal velocity field:

$$u_v = \frac{\partial\psi}{\partial y}; \quad v_v = -\frac{\partial\psi}{\partial x}\ , \text{ with } \omega_z = -\nabla_H^2\psi \quad , \tag{5}$$

where ω_z is the vertical vorticity component.

Numerical Simulations

For the present runs, the flow is forced at small scale: the forcing is random in space and Markovian in time, and acts on a wavenumber band ($k_B = 10 < k < 12 = k_T$). We define $k_f = [k_B + k_T]/2$ to be the centroid of the forcing wavenumber band. These conditions are analogous to those chosen by Herring and Métais (1989). The forcing is three-dimensional and acts equally on the three velocity components u, v, w (no density forcing). The intensity of buoyancy and rotation effects will be characterized by a Froude number F_r, and a Rossby number respectively defined as:

$$F_r = \frac{\sqrt{1/2\left\langle \omega_x^2 + \omega_y^2 \right\rangle}}{N}; \quad R_o = \frac{\sqrt{\langle \omega_z^2 \rangle}}{f} \tag{6}$$

where ω_x, ω_y and ω_z are the relative vorticity components, and the angular brackets stand for a spatial average. $\vec{\Omega}$ and the mean stratification are both oriented along the vertical direction. We here focus on the small Froude number régime when the Rossby number ranges from large (slow rotation) to small (rapid rotation) values. We concentrate on the energy transfer from the injection scales to the large scales.

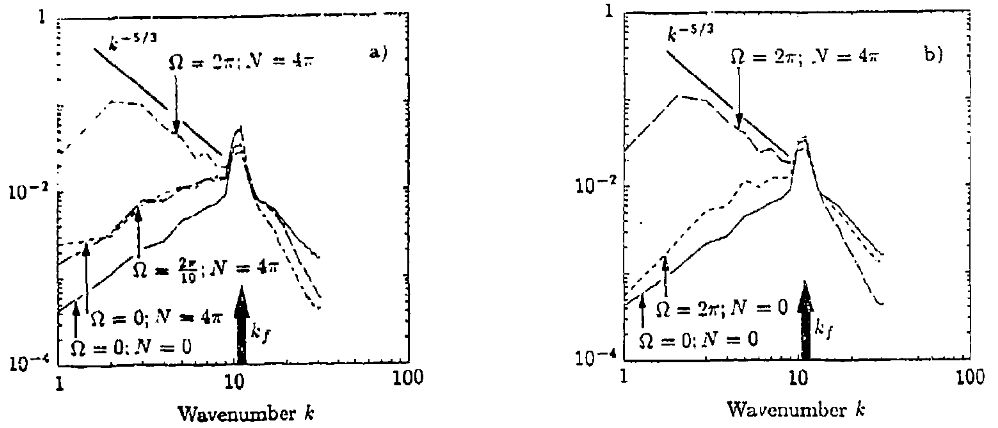

Fig.1. Three-dimensional wavenumber spectrum of the vertical kinetic energy for various values of Ω and N.

In Figure 1a, we display, for various cases, the three-dimensional wavenumber spectrum of the vertical kinetic energy when the system has reached an equilibrium. In the absence of rotation and stratification, for k smaller than the forcing wavenumber the energy is equipartitioned between the modes: this yields a k^2 spectrum. One may notice that, for $k > k_f$, the spectral shape closely corresponds to a $k^{-5/3}$ Kolmogorov energy cascade. In the non-rotating strongly-stratified case ($\Omega = 0; N = 4\pi; F_r \approx 0.2$), the vertical energy transfer towards the large scales is more efficient than in the non-stratified case and the spectrum is shallower than k^2. The buoyancy effects are still dominant when a weak rotation ($\Omega = 2\pi/10$; $N/f = 10$, $R_o \approx 1$) is imposed: the spectral behaviour remains almost unchanged. A complete change is observed for strong rotation ($\Omega = 2\pi$; $N/f = 1$, $R_o \approx 0.1$): the spectrum now follows a $k^{-5/3}$ law for $k < k_f$ and the spectral slope is increased for $k > k_f$.

As pointed out by Charney (1971), for geostrophic turbulence, both the total energy, and the potential enstrophy are conserved by the non-linear terms of the equations. One can write:

$$E_G = \int_0^\infty E(k)dk; D_p = \int_0^\infty k^2 E(k)dk \quad . \tag{7}$$

This double conservation property is analogous to two-dimensional turbulence, the difference being that $E(k)$ is here a three-dimensional spectrum. Furthermore, the energy possesses three components: two kinetic and one potential. Nevertheless, this constraint should prevent the energy injected at a wave-number k_f from cascading towards larger k and it should be uniformly transferred to lower wavenumbers along a $k^{-5/3}$ spectrum similar to the two-dimensional turbulence energy cascade proposed by Kraichnan (1967). The numerically observed $k^{-5/3}$ behaviour for small k could therefore be a manifestation of geostrophic turbulence dynamics. This will be confirmed by the subsequently presented results.

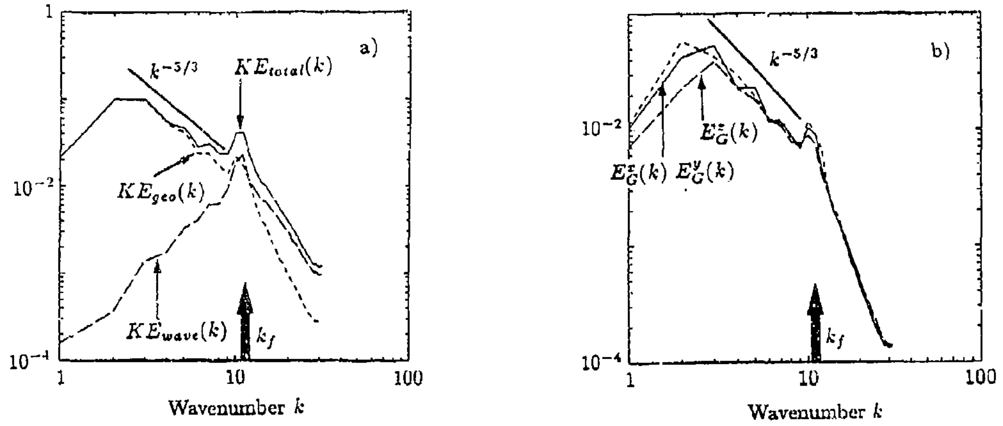

Fig.2. $\Omega = 2\pi$; $N = 4\pi$: a) three-dimensional wave-number spectrum of the total kinetic energy (KE_{total}) to the analogous spectra for the geostrophic kinetic energy ($KE_{geo} = E_G^x + E_G^y$) and the inertio-gravity wave kinetic energy (KE_{wave}) ; b) three-dimensional spectra of the geostrophy energy components E_G^x, E_G^y and E_G^z.

Figure 1b is the analogue of Figure 1a. Here, the vortical kinetic energy spectra of the isotropic (no rotation, no stratification) and the strongly-stratified, rapidly-rotating cases are compared to the one obtained when only fast rotation is applied without any stratification ($\Omega = 2\pi$; $N = 0$). We have checked that the large-scale flow exhibits quasi-two-dimensional vortices composed of both cyclones and anticyclones are present. However, although the flow contains these highly-anisotropic structures, the slope of the vortical kinetic energy spectrum for small k remains close to the isotropic k^2 spectrum (see Figure 1b).

A particular attention is now given to the strongly-stratified, rapidly-rotating regime. Due to the nature of the forcing, energy is injected in the inertio-gravity wave as well as in the geostrophic part of the motion. Figure 2a compares the three-dimensional wave-number spectrum of the total kinetic energy (KE_{total}) to the analogous spectra for the geostrophic kinetic energy ($KE_{geo} = E_G^x + E_G^y$) and the inertio gravity wave kinetic energy (KE_{wave}) constructed with the velocity field u_w, v_w and w_w defined by (6). Due to the combined effects of rotation and stratification, the two kinds of motions are segregated: the geostrophic energy dominates the $k^{-5/3}$ inverse cascade and reaches larger and larger scales. By contrast, the wave energy cascades towards the scales smaller than the injection scales and is therefore submitted to a strong dissipation. A similar picture can be drawn for the geostrophic and wave part of the available potential energy.

Charney (1971) concentrated on the potential enstrophy cascade and argued that the dynamics of quasi-geostrophic flow lead, at small scales, to an equipartition of energy among the x and y components of the kinetic energy and the available potential energy. Here, the geostrophy energy is equipartitioned among its three components E_G^x, E_G^y and E_G^z over almost the whole spectrum including in the large-scale inverse cascade (see Figure 2b).

DECAYING-TURBULENCE SIMULATIONS

Decay simulations were then integrated to explore the tendency of the flow to approach geostrophy. Fully-developed turbulent isotropic initial conditions were used with the buoyancy field set to zero. The initial Rossby and Froude numbers were unity with $N/f \approx 0.6$. The simulation was integrated for over 200 initial large-scale turnover times. Over this period R_o and F_r decreased by a factor of ten.

In this case, the normal modes of the equations linearized about a state of rest were used to separate geostrophic from ageostrophic motion. To express the energy decomposition, it is useful to introduce three sets of wavevectors: the barotropic set $B_k = \{ \mathbf{k} \mid k_x = k_y = 0\}$, the set with only vertical variability $V_k = \{\mathbf{k} | \; k_x = k_y = 0\}$ and the remaining baroclinic vectors $R_k = \{ \mathbf{k} \mid k_x^2 + k_y^2 \neq 0$ and $k_z \neq 0\}$. If the energy is

$$E = \frac{1}{2}\sum_{\mathbf{k}} U_{\mathbf{k}} = \frac{1}{2}\sum_{\mathbf{k}}\Big(GE_{\mathbf{k}} + AE_{\mathbf{k}}\Big) \,, \tag{8}$$

where $GE_{\mathbf{k}}$ and $AE_{\mathbf{k}}$ represent geostrophic and ageostrophic energy, respectively, then

$$GE_{\mathbf{k}} = \begin{cases} |A_{\mathbf{k}}^{(0)}|^2, & \text{if } \mathbf{k} \in R_k; \\ |\hat{u}_{\mathbf{k}}|^2 + |\hat{v}_{\mathbf{k}}|^2, & \text{if } \mathbf{k} \in B_k; \\ 0, & \text{if } \mathbf{k} \in V_k, \end{cases} \tag{9}$$

and

$$AE_{\mathbf{k}} = \begin{cases} |A_{\mathbf{k}}^{(+)}|^2 + |A_{\mathbf{k}}^{(-)}|^2, & \text{if } \mathbf{k} \in R_k; \\ |\hat{w}_{\mathbf{k}}|^2 + |\hat{b}_{\mathbf{k}}|^2/N^2, & \text{if } \mathbf{k} \in B_k; \\ U_{\mathbf{k}}, & \text{if } \mathbf{k} \in V_k, \end{cases} \tag{10}$$

where

$$A_{\mathbf{k}}^{(0)} = \frac{N^2\zeta_{\mathbf{k}} + ifk_z b_{\mathbf{k}}}{N\sigma_{\mathbf{k}} k} = \frac{PV_{\mathbf{k}}}{N\sigma_{\mathbf{k}} k} \,, \tag{11}$$

$$A_{\mathbf{k}}^{(\pm)} = \frac{\mp ifk_z^2\zeta_{\mathbf{k}} + \sigma_{\mathbf{k}} k^2\delta_{\mathbf{k}} \mp k_H^2 k_z b_{\mathbf{k}}}{2^{1/2}\sigma_{\mathbf{k}} k k_H k_z} \,, \tag{12}$$

$\zeta_{\mathbf{k}}$ is the vertical vorticity, $\delta_{\mathbf{k}}$ is the horizontal divergence and $\sigma_{\mathbf{k}} = (N^2 k_H^2 + f^2 k_z^2)^{1/2}/k$ is the linear wave frequency.

In Figure 3 we present both the geostrophic and ageostrophic contributions to the energy spectrum. After a few large-scale turnover times a monotonic approach to quasi-geostrophy was observed, with the geostrophic energy decreasing from its initial value by a factor of 1.9, while the ageostrophic energy decreased by a factor of 38.9. As in the forced case, an inverse energy cascade was manifested by a translation of the geostrophic-energy spectral maximum to smaller wavenumbers. The large scales became increasingly barotropic while the vertical vorticity kurtosis grew to 6.4 as quasi 2D coherent vortices began to emerge. These were not as apparent as in the simulations with initial $R_o = 1$ and $F_r = \infty$ of Bartello *et al.* (1994), implying considerable

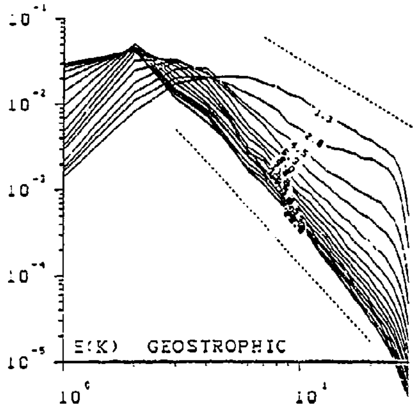

Figure 3a

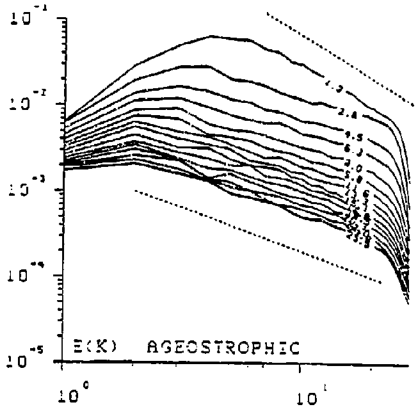

Figure 3b

Fig.3. a) Geostrophic energy specta (reference slopes correspond to $-5/3$ and -3) and b) ageostrophic energy spectra (reference slopes correspond to $-5/3$ and -1) as a function of time for the rotating-stratified simlation with unit initial Rossby and Froude numbers. Curves are labbeled with their corresponding times.

disruption of phase coherence by the stratification. By the end of the run the geostrophic energy spectrum was steeper than k^{-3} in the small scales, while the ageostrophic energy was much more shallow (k^{-1}).

CONCLUDING REMARKS

We have performed three-dimensional numerical simulations in a cubic domain of forced and freely-decaying, strongly-stratified, rotating turbulence. These have shown that, for small Rossby numbers, the largest scales are dominated by upscale-propagating geostrophic turbulence. In the forced case, even if substantial inertial-gravity wave energy is injected into the system, the flow exhibits a well defined three-dimensional $k^{-5/3}$ inverse cascade of geostrophic turbulence, while the wave energy propagates towards the smallest scales where it is dissipated. Furthermore, as suggested by Charney (1971), the energy in the inverse cascade is equally partitioned between its three components (kinetic and potential).

The observed atmospheric mesoscale spectra (see Gage and Nastrom 1986, for a review) exhibit several features in common with the present numerical results: $k^{-5/3}$ inverse cascades for both velocity and temperature spectra with equipartitioning between each of the two components of horizontal and potential energy. These striking similarities lead us to believe that the mesoscale spectra do correspond to geostrophic turbulence propagating towards the large scales. One can extract a turbulent Rossby number from the atmospheric spectra presented by Gage and Nastrom (1986), $R_o = \sqrt{kE(k)}/L_H f$, where $k, E(k)$ and L_H are respectively the wavenumber, energy spectrum and horizontal wavelength. For $L_H = 100km$, $kE(k) \approx 1ms^{-1}$ yields $R_o \approx 0.1$. The Rossby numbers in the inverse cascade of our rapidly-rotating simulations are of the same order.

As previously noticed by Métais and Herring (1989), the presence of stratification yields the formation of very strong vertical variability wh[illegible]s to destroy the vortices vertical coherence. In the present simulations, the two-dimensionalizing effect of rapid rotation does not seem to be sufficient to restore this coherence. In stably-stratified, rotating flows, quasi-two-dimensional organized vorticity structures are only observed in the presence of a well-defined horizontal density (temperature) front leading to baroclinic instability.

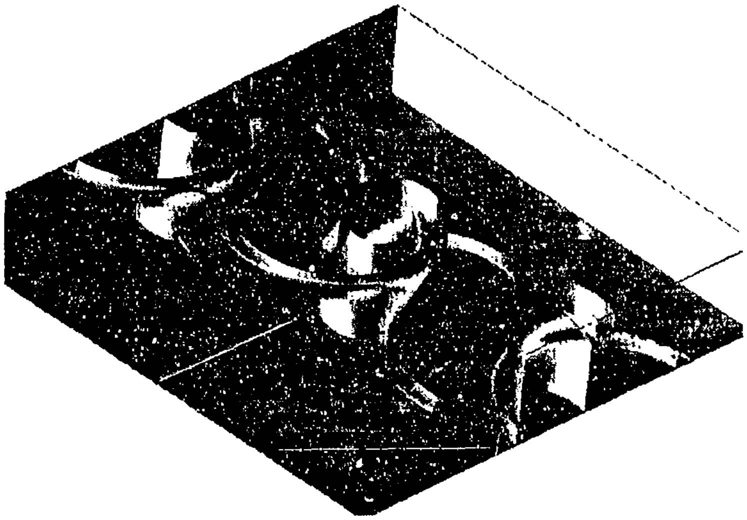

Fig.4. Cyclonic isovorticity surface resulting from a frontal instability: $R_o = 1$ and $F_r = 0.5$

This is illustrated on Figure 4 which shows the vorticity generation in baroclinic flows. On the basis of the three-dimensional Navier-Stokes equations (non-hydrostatic, Boussinesq flow), we have numerically investigated through direct numerical simulations the formation of baroclinic eddies. The basic initial state consists in an horizontal density front associated with an hyperbolic tangent profile. The corresponding mean velocity profile is a vertically sheared jet satisfying the thermal wind equation. Here, the Rossby number (R_o) and the Froude number (F_r) are respectively based upon the vertical and horizontal initial vorticity associated with the basic velocity profile. Here, $R_o = 1$ and $F_r = 0.5$, with $96 \times 96 \times 20$ grid points. A strong amplification of the cyclonic vorticity is observed yielding the formation of long-lived quasi-two-dimensional cyclones. By contrast, the anticyclonic vorticity is quickly dissipated.

Acknowledgments: Partial support for OM was provided by the U.S. Office of Naval Research (Contract No. N00014-86-K-0690), and for JJR by the U.S. Office of Naval Research (Contract No. N00014-90-J-1112). Computer resources were in part provided by the National Center for Atmospheric Research (N.C.A.R.) and by l'Institut du Développement et des Ressources en Informatique Scientifique (I.D.R.I.S.)

REFERENCES

Bartello, P., Métais, O. and Lesieur, M. (1994). Coherent structures in rotating three-dimensional turbulence. *J. Fluid Mech.*, in press.

Basdevant, C. and Sadourny, R. (1983) Modélisation des échelles virtuelles dans la simulation numérique des écoulements bidimensionnels, *J. Mec. Theor. et Appl., Numéro Spécial*, 243–269.

Bidokhti, A.A. and Tritton, D.J. (1992) The structure of a turbulent free shear layer in a rotating fluid, *J. Fluid Mech.*, **241**, 469–502.

Charney, J.G. (1971) Geostrophic turbulence, *J. Atmos. Sci.*, **28**, 1087–1095.

Gage, K.S. and Nastrom, G.D. (1986). Theoretical interpretation of atmospheric wavenumber spectra of wind and temperature observed by commercial aircraft during GASP. *J. Atmos. Sci.*, **43**, 729–740.

Herring, J.R. and Métais, O. (1989). Numerical experiments in forced stably stratified turbulence, *J. Fluid Mech.*, **202**, 97–115.

Hopfinger, E.J.,Browand, F.K., Gagne, Y. (1982) "Turbulence and Waves in a Rotating Tank", *J. Fluid Mech.*, **25**, 505–534

Kraichnan, R.H. (1967). Inertial ranges in two-dimensional turbulence. *Phys. Fluids*, **10**, 1417–1423.

Lelong, M.-P. (1990). Weakly non-linear internal wave-vortical mode interaction in stably stratified flows. *PhD Thesis*, University of Washington.

Lesieur, M., Yanase, S. , Métais, O. (1991) Stabilizing and Destabilizing Effects of a Solid-Body Rotation upon Quasi-Two-Dimensional Shear Layers, *Phys. Fluids A*, **3** (3), 403–407

Lilly, D.K. (1983). Stratified turbulence and the mesoscale variability of the atmosphere. *J. Atmos. Sci.*, **40**, 749–761.

Métais, O. and Herring, J.R. (1989). Numerical simulations of freely evolving turbulence in stably stratified fluids. *J. Fluid Mech.*, **202**, 117–148.

Métais, O., Yanase, S., Flores, C., Bartello, P., Lesieur, M. (1992) Reorganization of coherent vortices in shear layers under the action of solid-body rotation, Selected proceedings of the *Turbulent Shear Flows VIII*, Springer-Verlag, 415–430.

Müller, P, Holloway, G, Henyey, F. and Pomphrey, N. (1986). Nonlinear interactions among internal gravity waves. *Reviews of Geophysics*, **24**, N° 3, 493–536.

Riley, J.J., Metcalfe, R.W. and Weissman, M.A. (1981). Direct numerical simulations of homogeneous turbulence in density stratified fluids. *Proc AIP Conf. Nonlinear Properties of Internal Waves (ed B.J. West)*, 79–112.

Nonlinear effects in the unsteady, critical withdrawal of a stratified fluid.

By S. R. Clarke[1] and J. Imberger,

Department of Environmental Engineering and Centre for Water Research,
The University of Western Australia,
Nedlands, W.A. 6009, Australia.

The evolution of the withdrawal through a line sink of an initially quiescent, stratified fluid in a semi-infinite, horizontal duct is investigated in the inviscid, nondiffusive limit. A weakly nonlinear, long-wave formulation of the problem of critical withdrawal is presented, which is then used to study the critical withdrawal of a two-layer fluid from a sink at the base of the duct. Solutions for the evolution of the interfacial shear front are presented and related to the steady solutions for the critical withdrawal of a two-layer fluid.

1 Introduction.

When fluid is withdrawn from a vertically stratified water body it is found that at sufficiently low Froude numbers the withdrawn fluid comes from a narrow layer adjacent to the level of the sink. This process, known as selective withdrawal, has widespread application in the management of reservoirs. The density stratification of a reservoir typically consists of a well mixed layer near the surface, a rapid increase in the density over a few metres in the thermocline and then a more gradual increase in density in the hypolimnion. To model a complex stratification such as this would be very difficult, and also, of limited use. Therefore research in this field has concentrated on two alternative models of the fluid dynamics. In one case the reservoir is modelled as a two-layer fluid, and in the alternative case, as a linearly stratified fluid. For the two-layer model it is of interest to determine whether fluid is withdrawn from the upper layer. In particular the flow rate at which the upper layer is just drawn down into the sink is required, this is termed the point of critical withdrawal. For flow rates greater than this uniform withdrawal of the fluid will occur, while for smaller flow rates selective withdrawal of the lower layer fluid will occur. Here our interest is with this problem for the withdrawal from a semi-infinite horizontal duct through a line sink when viscosity and diffusivity are negligible. For a comprehensive review of the general topic of selective withdrawal the reader is referred to Imberger & Patterson (1990).

It is now well known that selective withdrawal is established by shear fronts, which are waves of zero frequency that propagate horizontally away from the sink with the long-wave speed and leave a permanently modified velocity and density structure in their wake. For a linearly stratified fluid Pao & Kao (1974) demonstrated that an infinite series of shear fronts would be generated when the sink was started. These shear fronts were shown to have permanent vertical form and horizontal form of a slowly dispersing step

---

[1] Present Address: Department of Mathematics, Monash University, Clayton, Vic. 3168, Australia.

function. Pao & Kao (1974) stated that the thickness of the withdrawal layer could be deduced by noting that the n^{th} mode could only propagate into the duct if its long-wave speed is greater than the average velocity in the duct. The withdrawal layer thickness will then be equal to the vertical wavelength of the last mode able to propagate into the duct. For a linearly stratified fluid with constant buoyancy frequency N, the densimetric Froude number is defined as

$$F = \frac{q}{Nh^2}, \tag{1}$$

where q and h are the flow rate per unit width into the sink and the height of the duct respectively. Therefore the average velocity in the duct is q/h. Defining the withdrawal layer thickness as $h\delta$, it was proposed by Pao & Kao (1974) that as the n^{th} mode has long-wave speed $Nh/n\pi$ and vertical wavelength h/n the withdrawal layer thickness will be

$$\delta \approx \pi F. \tag{2}$$

This gives a critical Froude number of $F_c = \pi^{-1}$, which is in agreement with the steady-state theory of Yih (1958), who showed that in these circumstances as $F \rightarrow \pi^{-1}$ uniform withdrawal will no longer occur. This was confirmed experimentally by Debler (1959) and using steady-state theories by Kao (1970) and Imberger (1972), who all showed that for $F < \pi^{-1}$ selective withdrawal will occur, where, adjacent to the sink is a region of potential flow, and immediately upstream of this a constant width withdrawal layer will form resulting from a balance between inertial and buoyancy forces. This layer will have thickness

$$\delta \approx (\pi F)^{\frac{1}{2}}. \tag{3}$$

Therefore, the argument of Pao & Kao (1974) incorrectly predicts δ. Imberger *et al.* (1976) modified this argument by proposing that the n^{th} mode could only propagate into the duct if its long-wave speed was greater that the average velocity in the withdrawal layer, $q/h\delta$. Using this argument gives the correct steady-state withdrawal thickness (3).

Kao (1976) proposed withdrawal criteria for nonlinear stratifications based on a similar approach to that used by Pao & Kao (1974). He made the long-wave approximation and showed that when the sink is started, shear fronts would be generated which will propagate into the fluid. It was proposed that the withdrawal layer thickness can be deduced from the wavelength of the last mode with long-wave speed greater than the average velocity in the duct. As shown above this approach fails for linear stratifications, thus we would not expect that it could be applied to nonlinear stratifications. However, it should be able to be used to determine the point of critical withdrawal for nonlinear stratifications. It is therefore of interest to apply the criteria of Kao (1976) to the withdrawal a two-layer fluid through a line sink. Again the fluid has total depth h, with lower layer depth h_1. The density of the upper and lower layers are ρ_0 and $\rho_0 + \Delta\rho$ respectively, thus the reduced gravity is $g' = \Delta\rho\ g/\rho_0$, where g is the magnitude of gravity. The flow rate per unit width into the sink is q, therefore we can define the densimetric Froude number based on the lower layer depth

$$F_1^2 = \frac{q^2}{g'h_1^3}. \tag{4}$$

The long-wave speed of the interfacial mode is $(g'hz_1(1 - z_1))^{\frac{1}{2}}$, where $z_1 = h_1/h$, while the average velocity in the duct due to the potential flow when the sink is turned on is q/h.

The point of critical withdrawal will occur when these two velocities are equal, therefore the critical Froude number at which fluid from the upper layer would be expected to be just drawn down into the sink is

$$F_{1c}^2 = \frac{1 - z_1}{z_1^2}. \tag{5}$$

Note that this value is independent of the height of the sink above the base of the duct.

The critical Froude number ranges from $F_{1c} = 0$ for $z_1 = 1$ to $F_{1c} = 1.41$ for $z_1 = \frac{1}{2}$ to $F_{1c} \to \infty$ for $z_1 \to 0$. These values can be compared against studies of the steady critical withdrawal of a two-layer fluid through a line sink at the base of the duct, for which limited results are available. Huber (1960) used approximate methods to show that when $z_1 = \frac{1}{2}$ the critical Froude number is $F_{1c} = 1.66$, which is in reasonable agreement with (5). When the upper layer is infinite, or equivalently $z_1 \to 0$ while h_1 remains finite, the average velocity q/h approaches zero. In this limit Hocking (1991a) used an integral equation approach which suggested that the critical Froude number was $F_{1c} = 0.42$. This was supported by experimental evidence from Hocking (1991b) of a value of $F_{1c} = 0.38$. The hypothesis here, is that in this limit (5) fails due to the neglect of nonlinear effects. This is apparent if it is noted that for a linearly stratified fluid with constant upstream energy Long (1953) showed that the full nonlinear steady problem reduces to a linear equation for the perturbation streamfunction. Therefore, the linear model of Pao & Kao (1974) is able to predict the point of critical withdrawal, since nonlinear effects are insignificant. However, for general stratifications nonlinear effects are important and cannot be ignored.

Our intention here is to use weakly nonlinear, long-wave theory to study the effect of nonlinearity on critical withdrawal. In §2 the appropriate equations are outlined, and in §3 these are used to study the specific problem of the critical withdrawal of a two-layer fluid from a line sink at the base of the duct.

2 Critical withdrawal in the long, weakly nonlinear limit.

It is apparent from the discussion of §1 that the problem of critical withdrawal is dependent on the behaviour of the first mode, as this is the fastest-propagating mode. If the first mode can propagate upstream then selective withdrawal will occur, if not, then uniform withdrawal will occur. The behaviour of this mode will be dependent on the forcing at the boundary and the potential flow in the interior of the duct. As no other modes propagate ahead of it, the first mode can be considered in isolation from the other modes and, also, the upstream flow is uniform over the height of the duct. To examine the effect of nonlinearity on critical withdrawal we will assume that the first mode is weakly nonlinear and of long wavelength, which allows the behaviour to be studied analytically. The limitations of this approach, are that firstly we are restricted to small amplitudes, and secondly, as the flow in the vicinity of the sink is radial, rather than horizontal, the solutions will not accurately describe the behaviour in this region. We will refer to the amplitude near the boundary, however it must be remembered that the solutions are invalid in this region.

To derive the governing equations for the first mode shear front we consider a two-dimensional, incompressible, stratified fluid contained in a duct of constant depth h, for which viscosity and diffusivity are negligible. A Cartesian co-ordinate system (hx, hz) is defined, where x is the horizontal direction and z is the vertical direction, with $z = 0$

being the base of the duct and $z = 1$ the undisturbed height of the fluid. The undisturbed density, $\rho(z)$, is used to define the buoyancy frequency

$$N^2 = -\frac{g\rho_z}{h\rho}. \tag{6}$$

This, in turn, is used to define the Boussinesq parameter

$$\beta = \frac{h\bar{N}^2}{g}, \tag{7}$$

where $\bar{N}$ is a characteristic value of N. As the fluid is weakly stratified $\beta \ll 1$. The time is defined as $\bar{N}^{-1}t$ and the undisturbed horizontal velocity of the fluid is $\bar{N}h\bar{u}$. It has been shown by many researchers that weakly nonlinear, long internal waves in this environment will satisfy the Korteweg-de Vries (KdV) equation. Following Grimshaw (1984), for waves with amplitude $O(\epsilon)$ and horizontal wavelength $O(\epsilon^{1/2})$, where ϵ is a small parameter, it can be shown that the density ρ and horizontal velocity u will satisfy

$$\rho(x,z,t) = \rho(z - A(x,t)\phi(z) + O(\epsilon^2)), \qquad u(x,z,t) = \bar{N}h(\bar{u} + UA\phi_z + O(\epsilon^2)), \tag{8}$$

where U is the long-wave speed in a quiescent fluid, A is the amplitude of the wave and ϕ is its permanent vertical stucture. In the limit $\beta \to 0$, U and ϕ satisfy the vertical eigenvalue problem

$$U^2\phi_{zz} + \frac{N^2}{\bar{N}^2}\phi = 0, \tag{9}$$

with
$$\phi = 0 \quad \text{on} \quad z = 0, 1.$$

The amplitude can then be shown to satisfy the KdV equation

$$A_t + cA_x + rAA_x + sA_{xxx} = 0, \tag{10}$$

where
$$c = U + \bar{u}, \qquad r = \frac{3U\int_0^1 \phi_z^3 dz}{2\int_0^1 \phi_z^2 dz}, \qquad s = \frac{U\int_0^1 \phi^2 dz}{2\int_0^1 \phi_z^2 dz}.$$

In critical withdrawal the velocity in the duct is

$$\bar{u} = -\frac{q}{\bar{N}h^2} = -F, \tag{11}$$

where F is the Froude number. In the long, weakly nonlinear limit of this problem the motion of fluid in the duct will be described by (8)–(10), where A and ϕ are respectively the amplitude and vertical structure of the first mode shear front. However, to fully describe the behaviour we must define initial and boundary conditions for the shear fronts. The initial condition throughout the duct and the boundary condition at the semi-infinite end of the duct are both that the amplitude is zero. The boundary condition at $x = 0$ is found by considering the velocity at this point. For a continuous stratification the eigenvalue problem (9) will have an infinite set of solutions, U_n and ϕ_n. The amplitude at the boundary, Λ, can be estimated by assuming that the velocity is the sum of these modes and the initial flow. At $x = 0$ the fluid must flow out of a line sink at height $z = z_0$, therefore the amplitudes satisfy

$$\bar{N}h\left(-F + \sum_{n=1}^{\infty} \Lambda_n U_n \phi_{nz}\right) = -\frac{q}{h}\delta(z - z_0), \tag{12}$$

where $\delta()$ is the Dirac delta function. Integrating this equation once and using the orthogonality condition for the modes gives the amplitude of the n^{th} mode;

$$\Lambda_n = \frac{F\int_0^1 N^2(z - H(z - z_0))\phi_n dz}{U_n \int_0^1 N^2 \phi_n^2 dz}, \tag{13}$$

where $H()$ is the Heaviside step function. Hence, the initial and boundary conditions for (10) are

$$\begin{aligned} &A(x,0) = 0 \qquad x > 0, \\ &A(0,t) = \Lambda_1 \quad \lim_{x\to\infty} A, A_x = 0, \qquad t \geq 0, \end{aligned} \tag{14}$$

3 Critical withdrawal of a two-layer fluid.

We now consider the application of the general formulation for critical withdrawal of §2 to the withdrawal of a two-layer fluid through a line sink at the base of the duct. In this case $z_0 = 0$ and the thermocline is at $z = z_1$, therefore, the buoyancy frequency is

$$N^2 = \bar{N}^2\delta(z - z_1). \tag{15}$$

This is simply the limit as $\epsilon \to 0$ of the continuous stratification

$$N^2 = \frac{\bar{N}^2}{2\epsilon}\operatorname{sech}^2\frac{z - z_0}{\epsilon}. \tag{16}$$

Since only the weakly nonlinear limit is being considered, the following results will only be valid for $|z_0 - z_1| \ll 1$. We will limit our discussion to $z_1 \leq \frac{1}{2}$, however, the upper limit of this is not strictly valid. For the stratification (15) it can be shown that the modal structure is

$$\phi = \begin{cases} z_1(1 - z)/(1 - z_1) & z > z_1, \\ z & z < z_1, \end{cases} \tag{17}$$

and the free long-wave speed is $(z_1(1 - z_1))^{1/2}$. Thus the long-wave speed is

$$c = (z_1(1 - z_1))^{\frac{1}{2}} - F. \tag{18}$$

The nonlinear and dispersive coefficients for the KdV equation are

$$r = \frac{3}{2}\left(\frac{z_1}{1-z_1}\right)^{\frac{1}{2}}(1-2z_1), \qquad s = \frac{1}{6}(z_1(1-z_1))^{\frac{3}{2}}, \tag{19}$$

and the amplitude of the shear front is

$$\Lambda_1 = -F_1(1-z_1)^{\frac{1}{2}}, \tag{20}$$

where F_1 is defined by (4). Note that this amplitude can also be derived by assuming that if the shear front can propagate away from the sink, it will adjust the uniform flow over the height of the duct to a uniform flow over the height of the lower layer, with a stagnant upper layer. For the two-layer fluid this is a more realistic formulation than the formulation for a continuous stratification of §2.

The solution of (10) and (14) is primarily dependent on the sign of $r\Lambda_1$. For $r\Lambda_1 < 0$, as is the case when $z_1 < \frac{1}{2}$, the nonlinear effect is negative and solutions have been presented by Marchant & Smyth (1991). If $c > -r\Lambda_1$ they showed that for large t linear dispersion will not be important, and therefore, the solution of (10) is well approximated by the solution to hydraulic approximation to (10) (*i.e.* the term A_{xxx} is neglected), which is

$$A = \begin{cases} 0 & x > ct, \\ \dfrac{x}{rt} - \dfrac{c}{r} & (c + r\Lambda_1)t < x < ct, \\ r\Lambda_1 & x < (c + r\Lambda_1)t. \end{cases} \tag{21}$$

When $c < 0$ Marchant & Smyth (1991) showed that as waves cannot propagate away from the boundary, the solution will rapidly become steady, and is given by

$$A = \frac{3c}{r}\operatorname{cosech}^2\left(-\frac{c}{4s}\right)^{\frac{1}{2}}(x + x_0), \tag{22}$$

where $$x_0 = \left(-\frac{4s}{c}\right)^{\frac{1}{2}} \ln\left[\left(\frac{3c}{r\Lambda_1}\right)^{\frac{1}{2}} + \left(\frac{3c}{r\Lambda_1} + 1\right)^{\frac{1}{2}}\right].$$

In the range $0 < c < -r\Lambda_1$ no solution was found, however an approximate solution can be constructed. Away from the boundary nonlinear dispersion will again dominate for large t, therefore the solution will be (21), however this will not satisfy the boundary condition at $x = 0$, where linear dispersion must be reintroduced. Since (21) is only valid for large t, we can assume that the solution in the boundary region will be steady. Hence, we can write

$$A = A'(x) + \begin{cases} 0 & x > ct, \\ \dfrac{x}{rt} - \dfrac{c}{r} & x < ct. \end{cases} \tag{23}$$

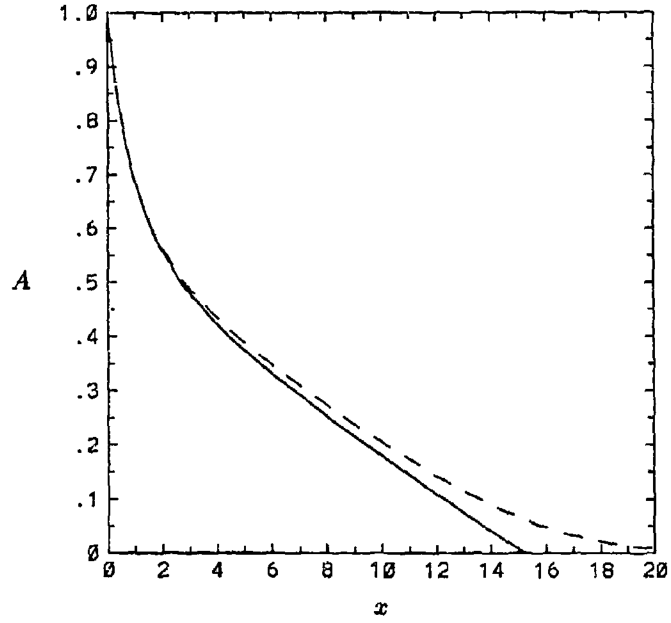

Figure 1: *Two solutions of (10) and (14) for* $c = 3$, $r = -6$, $s = 1$, $\Lambda_1 = 1$ *and* $t = 5$. *The solid line is the approximate solution given by (23) and (25), while the dashed line is the numerical solution of the full equations.*

Near the boundary this second part of A will be approximately equal to $-c/r$, in which case, to leading order, A' satisfies

$$rA'A'_x + sA'_{xxx} = 0, \tag{24}$$

with

$$A'(0) = \Lambda_1 + \frac{c}{r}, \qquad \lim_{x\to\infty} A', A'_x = 0.$$

This has the solution

$$A'(x) = \frac{\alpha}{(1 + (-r\alpha/12s)^{\frac{1}{2}}x)^2}, \tag{25}$$

where

$$\alpha = \Lambda_1 + \frac{c}{r}.$$

An example of this approximate solution to (10) is shown in figure 1, together with the equivalent numerical solution of (10). The numerical solution is obtained using the finite-difference method of Chu *et al.* (1983). The discrepency between the two solutions at large x in the region of the front is due to the fact that linear dispersion is ignored away from the boundary in the approximate solution. As time increases the front propagates further away from the boundary, and thus for very large t the solution A will consist of a constant level away from the boundary of height $-c/r$, with a dispersive solution near the boundary to match this to the boundary condition.

With the problem of two-layer withdrawal this intermediate solution can be thought of as a partial shear front, as it will modify the uniform upstream flow, but will not lead to selective withdrawal from the lower layer. The final solution, which has greater velocity in the lower layer than the upper layer, we will term partial withdrawal. Therefore, there are three withdrawal regimes: for $c < 0$ uniform withdrawal occurs, for $0 < c < -r\Lambda_1$ partial withdrawal will occur, and for $c > -r\Lambda_1$, when the full shear front can propagate upstream, selective withdrawal will occur. It can be shown that for the geometry being considered here, partial withdrawal will occur when the Froude number satisfies

$$\frac{2(1-z_1)^{\frac{1}{2}}}{3-4z_1} < F_1 < \frac{(1-z_1)^{\frac{1}{2}}}{z_1}. \tag{26}$$

It can be seen that the upper limit for F_1 is equal to (5), the value found using the criteria of Kao (1976). When $z_1 = \frac{1}{2}$ the upper and lower limit are equal and, therefore, the point of critical withdrawal is $F_1 \approx 1.41$, in agreement with Kao (1976). This is due to the fact that $r = 0$ and, hence, nonlinear effects are insignificant. When $z_1 \to 0$ the lower limit, which is the point of critical withdrawal, is $F_1 = \frac{2}{3}$, which is now in reasonable agreement with the results of Hocking (1991a,b).

References

Chu, C.K., Xiang, L.W. & Baransky, Y. 1983 Solitary waves induced by boundary motion. *Comm. Pure Appl. Maths.* **36**, 495–504.

Debler, W.R. 1959 Stratified flow into a line sink. *J. Eng. Mech. Div.* **85**, 51–65.

Grimshaw, G. 1984 Solitary waves in density stratified fluids. In *Nonlinear Deformation Waves.* U. Nigel and J. Engelbrecht, Eds., Springer Verlag.

Hocking, G.C. 1991a Critical withdrawal from a two-layer fluid through a line sink. *J. Engng. Maths.* **25**, 1–11.

Hocking, G.C. 1991b Withdrawal from a two-layer fluid through a line sink. *J.Hyd. Eng.* **117**, 800–805.

Huber, D.G. 1960 Irrotational motion of two fluid strata towards a line sink. *J. Eng. Mech. Div.* **86**, 71–86.

Imberger, J. & Patterson, J.C. 1990 Physical Limnology. *Adv. Appl. Mech.* **27**, 303–475.

Imberger, J. 1972 Two-dimensional sink flow of a stratified fluid contained in a duct. *J. Fluid Mech.* **53**, 329–349.

Imberger, J., Thompson, R. & Fandry, C. 1976 Selective withdrawal from a finite rectangular tank. *J. Fluid Mech.* **78**, 489–512.

Kao, T.W. 1970 Free streamline theory for inviscid stratified flow into a line sink. *Phys. Fluids* **13**, 558–564.

Marchant, T.R. & Smyth, N.F. 1991 Initial-boundary value problems for the Korteweg-de Vries equation. *IMA J. Appl. Maths.* **47**, 247–264.

Pao, H.-S. & Kao, T.W. 1974 Dynamics of the establishment of selective withdrawal of a stratified fluid in a line sink. Part 1: Theory. *J. Fluid Mech.* **65**, 657–688.

Yih, C.-S. 1958 On the flow of a stratified fluid. *Proc. 3rd U.S. Nat. Cong. Appl. Mech.* 857–861.

DENSITY INTRUSIONS WITH LARGE RELATIVE THICKNESS

Steven J. Wright and Diana Paez-Rivadeneira
Department of Civil and Environmental Engineering,
The University of Michigan
Ann Arbor, Michigan 48109-2125

Abstract

Previous analyses of density intrusions indicate that only relatively thin intrusions are allowed in order to satisfy a momentum balance at the current head. These constraints can be relaxed somewhat by various modifications to the basic theory, but are inconsistent with experimental observations indicating intrusions that occupy nearly the entire flow depth can be produced. An alternate theory of density current propagation does not possess these restrictions on intrusion layer thickness and provides a more satisfactory explanation of experimental observations. New experimental results are presented to corroborate this interpretation.

Introduction

The propagation of density intrusions has been previously analyzed with a variety of one-dimensional analyses which predict the propagation velocity as a function of the layer thickness and density difference. Most are based on the work of Benjamin (1968), who formulated a momentum balance in a frame of reference moving with the front. He showed that energy dissipation must generally be present at the density current head and assumed that it was confined to the continuous layer above the density current. Benjamin also showed that the requirement for no energy gain in the direction of the flow limited the intrusion thickness to no more than one-half the total flow depth. He also suggested a more restrictive criterion that the relative thickness could not exceed 0.347; this was later shown by Kranenburg (1978) as a necessary condition for maintenance of the discontinuity (shock) at the density current front. Wright (1986) observed density currents with thicknesses considerably in excess of either one of these limits. The analysis by Kranenburg (1978) also considered the possibility of energy loss within the density current head; this allows for a greater intrusion thickness while still retaining the requirement for maintenance of the shock. Wright, et al (1990) showed that a large variation in Kranenburg's energy loss coefficient is necessary to explain experimental observations. Subsequently, Kranenburg (1993) proposed a revision to his original model and suggested that a constant loss coefficient would be adequate to describe most observations. It can be shown that Kranenburg's revised model also requires a nonconstant loss coefficient both for the original experiments by Wright (1986) and in additional experiments conducted since that time. It is also found that the condition for maintenance of the shock does not hold for some of the recent experimental results. These results are, however, consistent with the minimum energy model proposed by Wright, et al (1990).

Experimental Results

Most previous studies have only reported visual layer thicknesses and observed front speeds. The present experimental results include measurement of the vertical density profile behind the current head in addition to observed frontal speeds. Figure 1 presents a general schematic of a density current. U_f is the front speed, h_1 is the intrusion thickness behind the current head and H is the total depth. Velocities relative to the current head are required since previous models analyze the flow in a frame of reference moving with the intrusion. C_1 is the approach velocity when the current head is brought to rest, while C_2 is the upper layer velocity in the same frame of reference. From Fig. 1, $C_1 = U_f - q/H$ and $C_2 = U_f - q_2/h_2$ with $q = q_1 + q_2$, q_1 the intrusion discharge, and q_2 the flow in the continuous layer above the intrusion (positive if in the same direction as the density current). Additional parameters used in the discussion below are the discharge ratio $q_r = q_2/q_1$ and the relative intrusion thickness $\eta = h_1/H$. The following definitions for the layer properties are made from the measured experimental data:

$$g' h_1 = \int_0^H g \frac{\Delta\rho}{\rho} dy \tag{1}$$

$$g' \frac{h_1^2}{2} = \int_0^H g \frac{\Delta\rho}{\rho} y \, d y \tag{2}$$

$$q_1 = U_f h_1 \tag{3}$$

$$q_2 = q - q_1 \tag{4}$$

Here $\Delta\rho$ is the density difference between the intruding and ambient fluids and y is distance from the boundary along which the intrusion propagates.

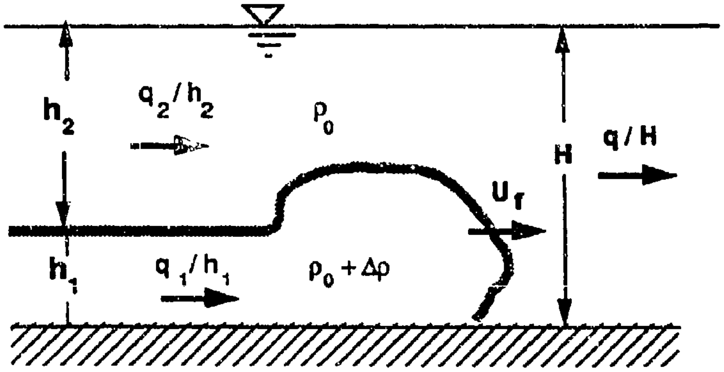

Figure 1. Schematic of Density Current.

Experimental results for density currents were presented by Wright (1986) for both counter-flows ($q_r < 0$) and co-flows ($q_r > 0$). This investigation focused on mixing in dense, horizontal discharges and the density currents resulted from initiation of the dense discharge along the horizontal channel bottom. The density excess was created by chilling salt water; racks of thermistor probes at selected locations along the channel provided continuous records of vertical density distribution with time.

The channel configuration involved an overflow weir at the downstream end to maintain a constant depth so there was a net throughflow in all experiments. However, the mixing in the source discharge produced an upstream flow in the ambient fluid to satisfy the entrainment demand. Later experiments included an ambient fluid flow created with a recirculating pump; the near source mixing still resulted in a net upstream flow in many of these experiments. The experimental design did not allow for large variations in q_r but many of these experiments involved quite large values of η, up to a maximum of 0.8.

Upon analysis of this original set of data, it became clear that more useful results could be obtained by minimizing the near-source mixing and varying q_r over a wider range. An additional series of experiments were performed with salt water intrusions in a 10 m long flume equipped with a pump to circulate the fluid in the upper layer. An overflow weir at one end of the flume was used to control the water level. By locating the salt water discharge at one or the other end of the flume, both co-flows or counter-flows could be established. The q_r ratio could be easily controlled with this experimental configuration. Zero recirculating pump discharge resulted in the commonly studied cases of starting flow ($q_r = 0$) and lock exchange flow ($q_r = -1$) with the discharge gate at the opposite or same end of the channel as the overflow weir. Density profiles were measured approximately 1 m behind the density current head at a location 4-5 meters downstream from the discharge gate; there the density current was well defined and the influence of the large starting vortex formed as the flow was initiated was no longer apparent. Results from these experiments were previously reported by Wright, et al (1990). In general, it was difficult to produce large values of η with this experimental configuration.

A final set of experiments similar to these is now underway in which the discharge gate has been modified in an attempt to produce larger values of η. Preliminary results have been obtained for starting and lock exchange flows with future experiments to be performed with the recirculating pump in order to vary q_r over a wider range. It has still been difficult to produce large density current thicknesses without also allowing near source mixing, so future experiments may also require this additional modification.

Background

Kranenburg's (1978) modification of Benjamin's (1968) analysis gives the density current speed as a function of the fractional layer thickness as

$$\frac{C_1}{\sqrt{g'H}} = \sqrt{\frac{\eta(1-\eta)(2-\eta)}{1+\eta + k(1-\eta)}} \qquad (5)$$

where k is a loss coefficient estimated by Kranenburg to have a magniutude of 0.6. Eq. (5) is derived from a momentum balance in the relative frame of reference moving with the current head and with the assumption that the nose of the density current at the channel bottom is a stagnation point. It also requires the assumption that energy dissipation at the density current head within the intruding layer is given by $k\rho C_1^2/2$. Kranenburg (1993) modified the dissipation term by adding an additional term which he deduced to take the form

$$\Delta E = \frac{\rho}{2}\left(k\,C_1^2 + (1+k)C_1\,\frac{q}{H}\right) \qquad (6)$$

so long as the boundary layer effects for flow over the boundary along which the intrusion propagates can be neglected. Regardless of which expression is used, the effect is to predict a slower, thicker density current for a given source condition. This is consistent with experimental observations in that Benjamin's analysis predicts larger than observed propagation velocities for miscible intrusions.

In order to completely analyze density current propagation, Kim and Wright (1987) attempted to define limits on physically admissible solutions; an example is the constraint by Benjamin (1968) that the requirement of no energy gain in the direction of flow limits solutions to $\eta \leq 0.5$. Kranenburg (1978) developed a criterion that requires the flow in the layer above the density current to be subcritical, or at most critical with respect to the density current itself:

$$\frac{C_2^2}{g'h_2} = \frac{(U_f - u_2)^2}{g'h_2} \leq 1 \tag{7}$$

Eq. (7) is necessary in order to maintain a sharp intrusion front. Benjamin's solution, Eq. (6) with $k = 0$, satisfies Eq. (7) so long as η is less than 0.347. Choosing a positive value for k in either Eq. (5) or (6) results in a larger admissible value of η. However, Wright (1986) showed that steady density currents with η far in excess of 0.347 could be produced (a maximum value of 0.8 was obtained in those experiments and this was apparently only limited by the experimental conditions selected). Kranenburg (1993) suggested a value for the loss coefficient k of 0.6 and presented a comparison with the data from Wright (1986) to partially justify this choice. However, the manner in which the comparison was made was misleading in that his resulting expression for C_1 was used to solve for the intrusion thickness η while substituting observed intrusion thicknesses for some terms in the solution. Leaving the intrusion thickness as a computed variable in all terms results in much less satisfactory agreement between observed and predicted layer thicknesses. Solving Kranenburg's expression for individual values of k for each experiment (using observed front velocities and layer thicknesses) resulted in one value in excess of 100 for an experiment that was considered to be verification of the analysis; several other experiments indicate k values an order of magnitude greater than 0.6. A presentation of the k values estimated from Eq. (5) for the data of Wright, et al (1990) is presented in Fig. 2 as a function of q_r while the k values considering the energy loss as given by Eq. (6) are presented in Fig. 3. This large and apparently systematic variation in the loss coefficient raises the possibility that either an alternate expression for the energy loss is required or that the density current propagation is controlled by some other principle.

These approaches fail to adequately describe the observed density current propagation for cases of relatively strong co-flow as experimental observations indicate that density currents propagate much more slowly than predicted by Benjamin's theory and a large loss coefficient is necessary to describe the experimental results. Also, large η experiments tend to require larger loss coefficients. This finding led Wright, et al (1987) to forsake the momentum balance at the density current head and to suggest that the density current propagation velocity is constrained to be no greater than the long wave speed of an interfacial disturbance. The notion behind this concept requires that energy dissipation at the current head adjusts to the level necessary to satisfy this condition, in which case the loss coefficient must vary consistently with q_r and η. However further investigation for the strong co-flow results indicated that the density currents were supercritical in an absolute frame of reference although not nearly as much as required by Eq. (5) or the equivalent modification utilizing Eq. (6). This observation led to an alternate derivation of a "critical" flow state by minimizing the total energy flux in the two layer flow subject to the requirement that the total depth remain constant across the intrusion front (Wright, et al, 1990). In terms of the density current propagation speed C_1, this analysis yields

$$\frac{C_1}{\sqrt{g'H}} = [1-(1+q_r)\eta]\sqrt{\frac{\eta(1-\eta)^3}{(1-\eta)^3-q_r^3\eta^3}} \tag{8}$$

Eq. (8) has been found to describe experimental results for intrusions in miscible fluids and has the advantage that no empirical coefficients are required to fit observations. In particular, the need for a highly variable loss coefficient as indicated in Figs. 2 and 3 is obviated. Wright (1986) suggested that Eq. (7) could be applied as a general constraint without regard to the application of the momentum balance. Eq. (7) (satisfying the equality) can be rewritten in terms of C_1 as

$$\frac{C_1}{\sqrt{g'H}} = \sqrt{(1-\eta)^3} \tag{9}$$

Wright, et al (1990) suggested that whichever of Eqs. (5), (8), or (9) predicts the most severe constraint on density current propagation (i.e. the slowest propagation speed) would prescribe the intrusion characteristics. However, the data from Wright (1986), particularly for co-flows and large η appear to contradict this assumption. There is, however, considerable scatter in the experimental results and this led to the current round of experimentation in an attempt to resolve this issue.

Experimental Results

Initial data were collected in a starting flow ($q_r = 0$) configuration with an attempt to collect data that be constrained by Eq. (9). Kranenburg (1993) suggested that density currents with a thickness greater than that prescribed by Eq. (9) would be unsteady and subsequently collapse to a smaller η in order to attain a steady frontal condition. However, this was not observed in the experiments and the

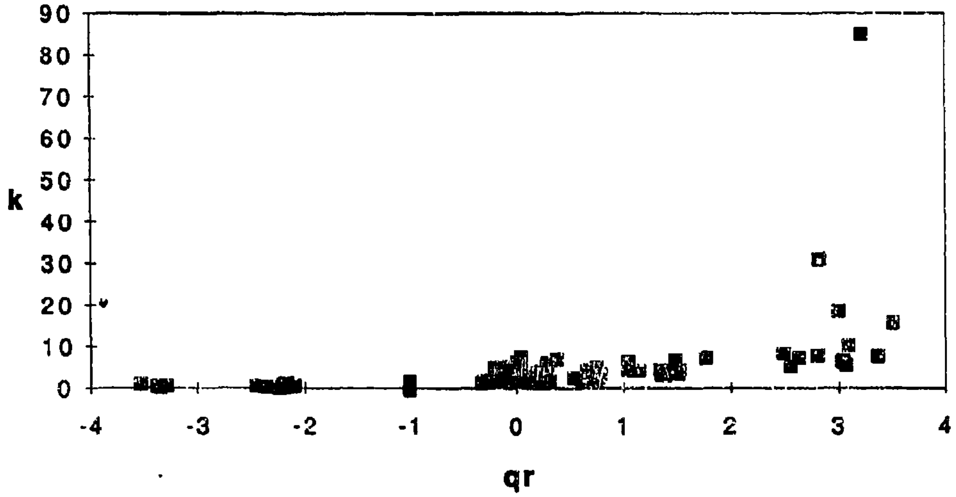

Figure 2. Loss coefficient vs. q_r for Kranenburg's (1978) model computed from data from Wright, et al (1990).

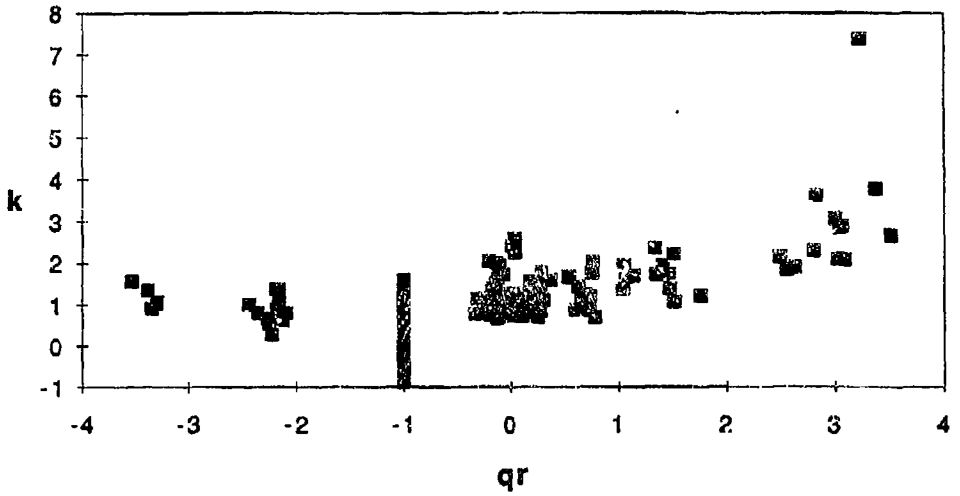

Figure 3. Loss coefficient vs. q_r for Kranenburg's (1993) model computed from data from Wright, et al (1990).

propagation conditions were more or less constant along the length of the channel. All density currents are subject to bottom and interfacial shear and thus slow down as they propagate along a horizontal channel. Although this effect is relatively small, it does complicate the interpretation of whether a density current would be steady in the absence of shear effects. However, the presentation of distance vs. time observations in Fig. 4 for typical intrusions that are supposedly constrained by Eq. (9) compared to those that are not indicates that the two situations are not discernibly different with regard to the unsteadiness of the flow.

Another way of examining the results is in terms of the non-dimensional propagation velocity $C_1/\sqrt{g'H}$. The predictions of Eqs. (5) (with $k = 0$), (8), and (9) are presented in Fig. 5 along with the data from Wright, et al (1990) and the current experimental results for both $q_r = 0$ and -1. Using the definitions of q_1 And q_2 in Eqs. (3) and (4) makes the starting flow q_r values slightly less than zero and not the same in all experiments while the lock exchange flow data are for q_r exactly equal to -1 with this definition. These results indicate that the density current propagation speed is not independent of the ambient velocity as required by Eq. (5). Although the expression of the energy loss by Eq. (6) makes C_1 dependent on the ambient velocity, the presentation in Fig. 3 indicates that a variable loss coefficient is required to describe the experimental results. The general trends predicted by Eq. (8) are quite well indicated by these data, especially considering the uncertainties introduced by the non-uniform velocity and density profiles. An additional finding from the present experiments is that Eq. (9) apparently does not provide a constraint on density current propagation as initially hypothesized. This conclusion is preliminary due to the limited range of experimental conditions investigated, but the experimental results do follow the predictions of Eq. (8) beyond the limits of η imposed by Eq. (9). A similar conclusion was obtained by Wright and Paez-Rivadeneira (1994) in a re-analysis of the data by Wright (1986). That interpretation, however, was hampered by the scatter in that data set. The current data are for a much more limited range of q_r and η values but are for more carefully controlled discharge conditions.

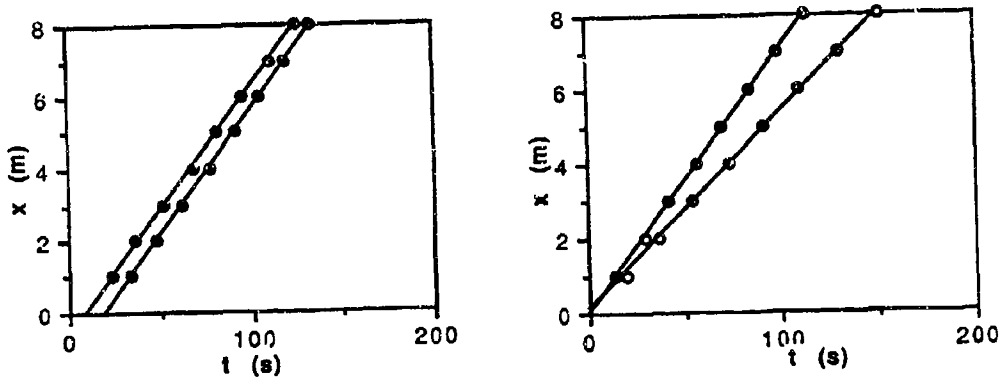

Figure 4. Typical density current propagation histories for starting flows: a.) η greater than Eq. (9) prediction; b.) η less than Eq. (9) prediction.

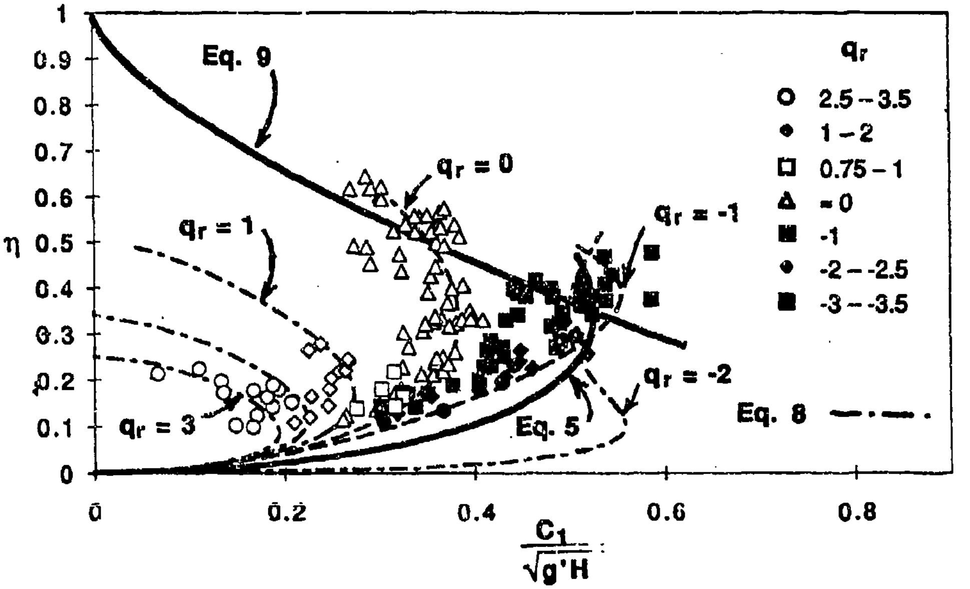

Figure 5. Experimental data for non-dimensional density current propagation speed compared to various analyses.

The data in Fig. 5 do indicate that Eq. (5) may be valid when it predicts a slower propagation speed than Eq. (9). This is reasonable since the faster propagation speeds predicted by Eq. (9) would require a negative loss coefficient or an energy gain at the intrusion front. Since this would not be physically possible, it appears that Eq. (5), possibly with a small loss coefficient should describe the density current propagation. Because of some uncertainties in the experiments of Wright, et al (1990), additional experiments will be performed for strong counter-flows to more clearly delineate this issue.

Conclusions

The experimental results presented in this paper serve to confirm that Benjamin's (1968) momentum balance is not generally a useful model for analyzing density current propagation. In particular, density currents with thickness in excess of the limits proposed by Benjamin can be created. Although Benjamin's analysis can be modified by consideration of energy dissipation at the density current head, this formulation requires a variable loss coefficient in order to reproduce experimental results. Also, the constraint on the maximum intrusion thickness suggested by Kranenburg (1978) appears not to govern density current propagation for moderate co-flows and counter-flows. On the other hand, a formulation based on minimum energy principles describes the present as well as previous experimental results. The only exception appears to be for strong counter-flows in which Benjamin's momentum balance prescribes a slow propagation velocity than the minimum energy formulation. Additional experimentation is underway to more thoroughly investigate this issue.

References

Benjamin, T.B., (1968), "Gravity Currents and Related Phenomena," *Journal of Fluid Mechanics*,, Vol. 31, 209-248.

Bühler, J., S.J. Wright and Y. Kim (1992), "Source Control of Intrusions Along Horizontal Boundary," *Journal of Hydraulic Engineering*, Vol. 118, 3, pp. 442-459.

Kim, Y. and Wright, S.J. (1988) "A Revised Theory of Density Current Propagation," *Proceedings, First National Fluid Dynamics Conference*, Cincinnati, Ohio, 1988, Vol. 3, pp. 2020-2027.

Kranenburg, C., (1978), Internal Fronts in Two Layer Flow, *Journal of the Hydraulics Division ASCE*, 104 (HY10), 1449-1453.

Kranenburg, C., (1993), Gravity-Current Fronts Advancing into Horizontal Ambient Flow, *Journal of Hydraulics Engineering* , Vol. 119 (3), pp. 369-379.

Wright, S.J., (1986), "Aspects of Far-field Control on Buoyant Jet Mixing," *Report 24-86, Institut für Hydromechanik und Wasserwirtschaft, ETH*, Zürich, Switzerland, March 1986.

Wright, S. J., Kim, Y., and Bühler, J., (1987), Controls of Density Current Propagation, Proceedings, 3rd IAHR Symposium on Stratified Flows, Los Angeles, California, 1987, pp. 675-684.

Wright, S. J., Kim, Y., and Bühler, J., (1990), Density Current Propagation in Flowing Receiving Fluid, *Proc. of the Int. Conf. on Physical Modeling of Transport and Dispersion*, Boston, pp. 12A19-12A24.

Wright, S. J., and Paez-Rivadeneira, D., (1993), Criticality of Density Intrusions, *Proc. of the National Hydraulic Engineering Conference*, San Francisco, pp. 845-850.

EXPERIMENTAL AND NUMERICAL INVESTIGATION OF LAMINAR MULTILAYER INJECTION AND WITHDRAWAL IN A STRATIFIED ENVIRONMENT

M. Priven, G.A. Bemporad‡ J. Atkinson†, and H. Rubin

CAMERI-Coastal and Marine Engineering Research Institute,
Technion City, Haifa 32000, Israel
† *Department of Civil Engineering, SUNY at Buffalo, Amherst, NY14260, USA*
‡ *ISMES Spa, V.le G. Cesare 29, 24100 Bergamo, Italy*

Abstract

The experimental and numerical analyses of flow development caused by the injection and withdrawal of multiple fluid layers in a stratified environment are presented. The injection of positively, neutral and negatively buoyant fluid layers was studied experimentally and an analytical approach was developed which considers temperature–stratified, salinity–stratified and doubly–stratified environments. A comparison of experimental and numerical data showed good agreement. The present experimental and numerical analyses demonstrate the feasibility of injecting and withdrawing several buoyant layers while preserving stable density stratification in a double–diffusion environment, such as would be found in a solar pond.

1. Introduction

Laminar or transitional (from laminar to turbulent) jets have not been investigated widely because flows inside and around a jet are usually turbulent. However, in a few particular cases laminar flow is needed in order to provide desirable flow conditions and maintain ambient fluid stratification (e.g., Kaghazchi, 1988). One particular application is the injection of a laminar jet or system of laminar jets as proposed for advanced solar pond (ASP) technology (e.g. Osdor, 1984; Rubin and Bemporad, 1989) in order to increase solar pond efficiency. Creation and maintenance of a so-called stratified flowing layer (SFL) in the bottom part of the solar pond gradient zone requires the simultaneous injection of several flowing layers of different temperature and salinity.

Only a few experimental studies are available on laminar jet injection and these are concerned with a salinity stratified environment (Manins, 1976; Maxworthy, 1972). Flow visualization from these studies shows that jets with moderate Reynolds numbers ($Re = Ud/\nu$) propagate without significant vertical spreading, which is obviously suppressed by the stratification. Therefore, ambient fluid entrainment into the jet body is low and molecular diffusion is the basic phenomenon which characterizes the transport of properties across the jet boundary. Tests were not conducted for temperature or double-diffusive (D–D) stratification. In particular, the SFL of an ASP has "diffusive" D–D stratification and phenomena associated with this condition should be considered. In addition, the injection and simultaneous withdrawal of a system of laminar layers has not been investigated sufficiently and it is not clear *a priori* how this type of system should operate.

In the present research an experimental study was conducted to evaluate the behavior of a laminar two-dimensional horizontal jet or system of several jets. It was desired to determine the influence of buoyancy force, double-diffusive effects and simultaneous operation of (horizontal) injection and withdrawal procedures on jet flow in single (temperature or salinity) and D–D stratified environments. A numerical model based on a Lagrangian approach was also developed and tested in order to simulate the propagation of the jet front. Some results from this study, particularly related to single jets, are described by Priven (1993) and Priven et al. (1994a, 1994b). Results relevant to the present paper may be summarized as follows:
a) a stable flowing laminar neutrally buoyant (with respect to ambient stratification at the injection/withdrawal level) layer can be created and maintained without significant mixing between the layer and ambient fluid;
b) any difference between injected and ambient fluid properties (at the injection level) leads to vertical movement of the jet, causing flow to the withdrawal port to be limited to a relatively restricted region above and below its location; as a result, the thickness of the jet increases due to mixing with surrounding fluid and ambient stratification may be affected;
c) horizontal injection of a neutrally buoyant D–D jet into a D–D stratified environment will exhibit vertical motion unless the jet properties are the same as the corresponding properties of the surrounding fluid; the jet deviation (from horizontal) in this case has a double–diffusive nature and depends on the magnitude of the salinity or temperature deficit; and
d) the Lagrangian approach provides a simple and effective means for calculating jet trajectory.

The present study extends the analyses of Priven et al. (1994a, 1994b) to examine multiple layer injection. The single-jet results indicated that the withdrawal procedure was a critical factor in determining resulting flow patterns. This was particularly true for D–D jets. In the present study multiple laminar jet injection into a salinity-stratified environment is examined. Flow observations are reported in Section 3 and the applicability of the numerical model to the multi-injection system is discussed in Section 4.

2. Experimental Set-up and Procedure

The laboratory set-up consisted of a flume whose length, width and depth were 320 *cm*, 60 *cm* and 100 *cm*, respectively. The entrance unit contained a series of outlet ports, or slots. Each slot was 56.0 *cm* wide and 2.0 *cm* high, and flows to each slot were monitored with a system of flowmeters. The main withdrawal port, 6.0 *cm* high and with the same width as the entrance slots, was positioned at the downstream end of the flume. The vertical dimensions of the outlets were calculated on the basis of Imberger's (1972) experimental study of two-dimensional sink flow. The system was operated in such a way that the the total outlet flow was always equal to the total inlet flow.

A linear ambient gradient was set up by slowly filling the tank in a series of thin layers in which different salinities (and temperatures, if a D–D gradient was desired) were determined by controlling the discharges from tanks with different concentrations (and temperatures). Density gradients were measured by slowly withdrawing fluid samples at a given height and measuring specific gravity with a hydrometer. The experimental uncertainty in the density measurements was 1.0 kgm^{-3}. The injection and filling discharges were measured by flowmeters with an estimated accuracy of 2%. Temperature profiles were measured by using 16 thermocouples fastened on a fiberglass bar and connected to a data logging unit. Calibration of temperature measurement showed that the expected accuracy is $\pm$ $0.3^{\circ}C$. Further details of the experimental set-up and procedures may be found in Priven (1993).

3. Experimental Observation

For purposes of illustration of the essential features of the observed flows, two representative tests are chosen, termed MJS2 and MJS3. Table 1 presents the main characteristics for each of these experiments. In this Table $\Delta\rho = \rho_{a,j} - \rho_j$ (kgm^{-3}) is the difference for each sublayer between the injected fluid density (ρ_j) and the density of the ambient fluid at the injection level ($\rho_{a,j}$), G_ρ (kgm^{-4}) is the density gradient, v_j ($cmsec^{-1}$) is the injection velocity for each sublayer, Fr and Re are the Froude and the Reynolds numbers for each sublayer, respectively.

Experiment MJS2 was characterized by injection of two neutrally buoyant fluid layers (1 and 3), with equal flowrates. The injection was performed from the upper and the lower slots; no fluid was discharged through the middle slot. Figure 1a illustrates the propagation of both jets with time. Initially the two fluid layers flowed with the same velocity, and propagated into the tank at the same distance. Later, the upper fluid layer accelerated and started to move more rapidly than

Run	Layer	$\Delta\rho$	G_ρ	v_j	Fr	Re
MJS2	1	0.0	71.4	0.4	--	100
	2	-		-	-	-
	3	0.0		0.4	-	100
MJS3	1	0.0	84.0	0.5	-	125
	2	-		-	-	-
	3	-0.1		0.6	0.4	150

Table 1: fluid layer and ambient fluid properties

the lower layer. This acceleration was accompanied with a corresponding decrease in thickness (about 2 cm, compared with about 4 cm for the lower "slug"), as determined from photographs of the flow. Therefore, although both fluid layers were injected into the same stratified environment with the same velocities, both with neutral buoyancy, the characteristics of the fluid propagation for the two jets were different. This behavior is assumed to be a direct result of the selective nature of the withdrawal procedure.

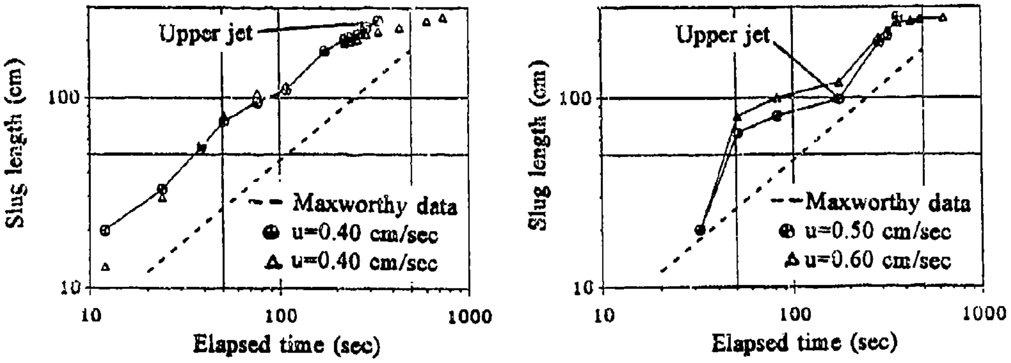

Fig. 1. Slug length versus elapsed time for MJS experiments. a) MJS2; b) MJS3

Similar results are shown in Figure 1b for experiment MJS3, where the velocity of the upper fluid layer was kept smaller than the velocity of the lower layer (0.5 cm/s and 0.6 cm/s, respectively). Fluid was discharged in the same manner as in the previous experiment. The upper layer had neutral buoyancy, while the lower layer density was somewhat smaller than the ambient density; this modification was introduced to force the jets to flow parallel and as close to each other as possible. Both figures show the development of slug length consistent with a result by Maxworthy (1972), which correlates laminar slug length with time as $l = t^{5/6}$. Our experiments show that this prediction is correct at least in the region where jet flow is not influenced by the end wall and withdrawal port. After that point the slug propagation is slower. Figure 2a shows flow visualization for experiment

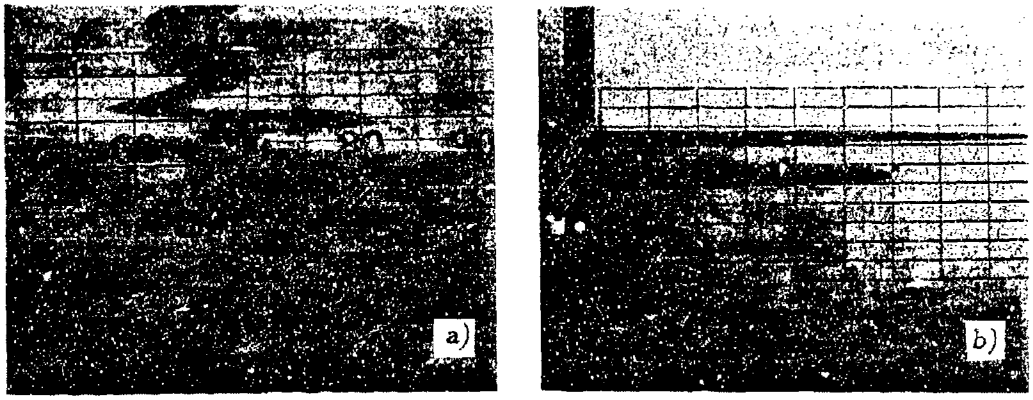

Fig. 2. Flow visualization for experiment MJS3. a) dye trace movement during injection (region close to the entrance unit); b) jets close to the withdrawal port.

MJS3 in the region close to the entrance port. Here, two sharp velocity profiles indicate that the layers were not mixed. From Figure 2b it is apparent that the jets flow without any mixing at the region close to the withdrawal port (at right edge of photo). As in the previous experimental run, after about 83.0 seconds the lower layer has moved about 100.0 *cm*, while the upper layer has moved about 80.0 *cm* (see Fig. 1b). It may be interesting to note that the thickness of the upper layer was about 2.0 *cm*, while the lower layer thickness changed from 2.0 *cm* at the injection to about 3.0 *cm* at the end of the injection process. Comparison with the experiments for single jet injection and withdrawal indicates that the upper layer essentially behaved as a neutrally buoyant fluid injection (Priven et al., 1994b). Instead, the lower layer behaved like a fluid layer of negative buoyancy which could not leave the tank and as a result its thickness increased. Therefore, even if the upper layer had a lower initial velocity, it accelerated and this may be explained by existing conditions at the withdrawal port.

4. Numerical Model

A mathematical model was developed earlier (Priven, (1993), Priven et al., (1994a)) to analyze the general behavior of a low *Re*, two-dimensional buoyant jet in a stratified water body. The model routes the injected fluid layer through the domain of interest by solving, in a local reference frame, the equations of conservation of mass flux, momentum flux, heat and salinity flux. The model assumes pressure variations from hydrostatic to be negligible, and includes entrainment, diffusion and dissipation terms. In this framework the equations expressing conservation of mass flux, momentum flux, heat and salinity fluxes are:

mass (continuity)

$$\frac{d}{d\zeta}(\varrho d|\mathbf{v}|) = 2\alpha\varrho_a|\mathbf{v}| \tag{1}$$

momentum

$$\begin{aligned} \frac{d}{d\zeta}\left[\varrho d|\mathbf{v}|v_x\right] &= -2\varrho C_D|\mathbf{v}|^2\frac{v_x}{|\mathbf{v}|} \\ \frac{d}{d\zeta}\left[\varrho d|\mathbf{v}|v_y\right] &= -2\varrho C_D|\mathbf{v}|^2\frac{v_y}{|\mathbf{v}|} + \varrho\ d\ g\ \frac{\varrho_a - \varrho}{\varrho_a} \end{aligned} \tag{2a - b}$$

heat and solute transport

$$\begin{aligned} \frac{d}{d\zeta}(\varrho d|\mathbf{v}|T) &= 2\alpha\varrho_a|\mathbf{v}|T_a - 2\varrho_a\frac{\kappa_T}{C_p}\frac{(T - T_a)}{d} \\ \frac{d}{d\zeta}(\varrho d|\mathbf{v}|C) &= 2\alpha\varrho_a|\mathbf{v}|C_a - 2\varrho_a\kappa_C\frac{(C - C_a)}{d} \end{aligned} \tag{3a - b}$$

were ζ is the axis of the local reference system, k_T and k_S are the thermal and solute diffusivities, ϱ is density, d is jet thickness, α is an entrainment coefficient. The set of equations (1–3) is completed by the following equation of state:

$$\varrho(T, C) = \varrho_o[1 - \beta_T(T - T_o) + \beta_C(C - C_o)] \tag{4}$$

where β_T and β_C are the thermal and solutal expansion coefficients, respectively, and subscript $_o$ refers to a reference state. Eqs. (1–3), together with eq. (4), represent a nonlinear system of six equations in the six unknowns ϱ, v_x, v_y, d, T and C. The fluid layer is discharged at vertical position Y_j, with jet width d_j, initial velocity $\mathbf{v}_j$, temperature T_j and solute concentration C_j. The fluid is injected into an ambient environment with linear temperature and solute concentration gradients G_T and G_C, respectively.

The numerical model was validated with results obtained from experiments on single laminar jet injections into temperature, salinity or D–D stratified environments. Comparison of numerical and experimental results demonstrated the capability of the numerical model to correctly simulate the jet trajectory (Priven, 1993). However this model does not simulate an ambient flow. Figure 3 shows the jet trajectory and density development for an initially nonbuoyant jet injected into D–D stratified environment. The injected fluid had lower temperature and salinity concentration than the ambient fluid, though the jet was initially at the same density as the ambient environment. Therefore, entrainment should not be important immediately after injection, however, some vertical deviation is expected due to diffusive effects. As seen in Figure 3a, the jet starts to deviate at a distance of about 1.0 m and at the same distance density decreased due to heat flux across the jet boundary. At a distance of 100.0 m the jet trajectory and density variations were stabilized. In the case of a system of layers turbulent mixing between the layers should not occur except perhaps in the region close to the injection slot, where momentum flux is important. Downstream, only D–D effects should influence the jet flow. Therefore, it is suggested that in the case of initially nonbuoyant jets the current model developed for single discharges may be used to simulate the system of multiple injection by simply running the model concurrently for each jet. Several simulations of this type have been run for three parallel neutrally buoyant jets, but further work is needed to investigate buoyancy effect.

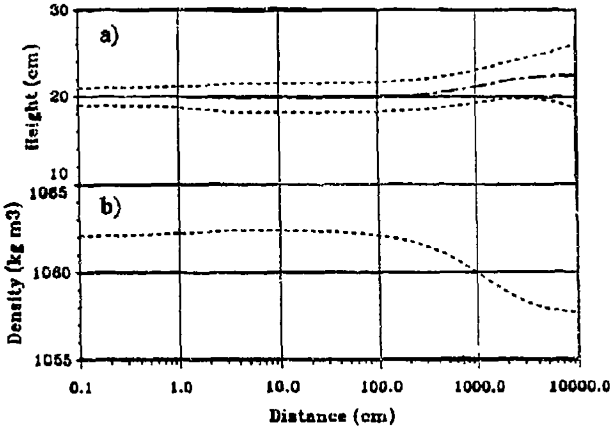

Fig. 3. Numerical simulation of initially nonbuoyant laminar D–D jet injected into D–D stratified environment. a) Jet trajectory; b) density variation

5. Conclusions

The experiments have shown that a system of multiple laminar flowing fluid layers can be created and maintained in a stratified environment without significant mixing between the layers. Some mixing may be expected near the entrance when the injected fluid is not at the same density as the ambient fluid, due to buoyancy. In the case of double-diffusive stratification some vertical movement and mixing is expected at some distance downstream of the entrance, due primarily to the relatively fast diffusion of heat. The initial propagation of the injected layers follows $t^{5/6}$, as first suggested by Maxworthy (1972). However, the propagation speed decreases as the flow approaches the far wall and here, the specific location of the withdrawal slot has an important effect on the downstream flow patterns.

It was found that the flow pattern of the multiple injection system was basically similar to that of single layer injection. Therefore, the numerical model developed for single jets, based on the Lagrangian approach for routing the leading front of the discharge, should be applicable for multiple injection, by solving the model concurrently for each individual discharge. This is useful for design and simulation of ASP operations. Optimal control of the multiselective injection procedure requires that the withdrawal port should be designed so that fluid may be withdrawn from any depth within the stratified flowing layer. This characteristic will probably have to be accomplished by providing each layer with a separate withdrawal port and a separate pumping system.

Acknowledgements

This study was funded by the Israel Ministry of Energy and Infrastructure, under contract no. 92-05-002/92-1-1 and by the Hydraulic and Structural Research Center of ENEL Spa. The material presented in this paper reports parts of M. Priven's D.Sc. thesis. M. Priven was supported by the Nate H. and Beatrice G. Sherman Fellowship. J. Atkinson was partially supported by the Lady Davis Fellowship Trust Fund.

References

1. Imberger, J., "Two-Dimensional Sink Flow of a Stratified Fluid Contained in a Duct," *J. Fluid Mech.*, Vol. 53, part 2, pp. 329-349, 1972
2. Kaghazchi, t., "Use of Laminar Jet in Determining the Overall Rate of Liquid-Liquid Reactions", Conference of the Division of Petroleum Chemistry, American Chemical Society, Vol. 33, no. 3, Washington, DC, 1988
3. Osdor. A., Method of Trapping and Utilizing Solar Hear, U.S. Patent No. 4462389, 1984
4. Manins, P.C., "Intrusion into a stratified fluid," *J. Fluid Mech.*, Vol. 74, N. 3, pp. 547-560, 1976
5. Maxworthy, T., "Experimental and Theoretical Studies of Horizontal Jets in a Stratified Fluid," *Int, Symposium on Stratified Flows*, Novosibirsk, 1972
6. Priven M., "Evaluation of the Basic Thermohydrodynamic Aspects of the Advanced Solar Pond," D.Sc. Thesis, Technion–Israel Institute of Technology, Haifa, 1993
7. Priven M., Atkinson J., Bemporad G.A. and Rubin H., "Theoretical Study of a Laminar Jet in a Double–Diffusive Environment," Submitted for publication to *J. of. Fluid Eng.*, 1994a
8. Priven M., Atkinson J., Bemporad G.A. and Rubin H., "Experimental Study of a Laminar Jet in a Stratified Environment," Submitted for publication to *J. of. Fluid Eng.*, 1994b
9. Rubin H. and Bemporad G.A., The Advanced Solar Pond (ASP): Basic Theoretical Aspects, *Solar Energy*, Vol. 43.,No. 1, pp. 35-44, 1989

AXISYMMETRIC INTRUSION IN A STRATIFIED FLUID

Nikolas E. Kotsovinos

Democritus University of Thrace,

67100 Xanthi,Greece

1. INTRODUCTION

A number of environmental flows can be approximated by the flow of a buoyant plume in stratified environment, e.g. the flow from a sewage outfall in a stratified sea, or the flow from a chimney in a stratified atmosphere. In those cases, the buoyant plume rises as high as its momentum and buoyancy will carry it and then it spreads horizontally at its neutral level.

Previous experimental studies of horizontal spreading due to continuous release of a constant flow rate refer i) to axisymmetric surface spreading of a buoyant fluid in homogeneous non-moving ambient fluid (e.g. Chen and List (1976), Lister and Kerr (1989)) ii) to the spreading of a heavy fluid on the bottom of a light fluid reservoir (e.g. Didden and Maxworthy 1982, Britter 1979, Huppert 1982) iii) to two-dimensional intrusion in a stratified fluid due to a finite volume release at neutral level (Cerasoli 1978, Maxworthy 1972). To our Knowledge, the only available experimental results which represent the axisymmetric intrusion in a stratified fluid due to continuous inflow are those of Zatsepin and Shapiro (1982), who, however, study only the viscous-buoyancy regime of the intrusion.

Theoretically,the axisymmetric lateral growth of the submerged spreading in a stratified environment has been studied by Chen (1980),Zatsepin and Shapiro (1982),Ivey and Blake (1985),Didden and Maxworthy (1982),and Lister and Kerr (1989).

All these investigators find that at large times there is a balance between the interfacial viscous forces and the buoyancy (or pressure) forces and that at this regime, the radius R(t) of the spreading layer increases with time t as $t^{1/2}$. For smaller times inertia forces are important and therefore there must be an asymptotic regime which is characterized by a balance of the inertia and buoyancy forces;experimental data do not exist for this regime but theoretical studies predict that in this regime $R(t) \sim t^{m}$,where $m=1/2$ according to Ivey and Blake (1985), $m=2/3$ according to Chen (1980),and $m=3/4$ according to Didden and Maxworthy (1982). One of the contributions of this paper is to clarify this conflict for the proper radial growth in the inertia-buoyancy regime .

2. ANALYSIS OF THE PROBLEM

2.1 Continuity equation

It is assumed that the buoyant plume impinges violently its neutral stability level, overshoots and then descends and spreads horizontally (see Figure 1). It is reasonable to distinguish two regions i) the impingement region within the control volume ABCD where the flow is in general very turbulent and is characterized by a lot of entrainment and ii) the main spreading region which is outside the control volume ABCD. On the average the entrainment in the region ABCD is proportional to the flowrate Q so that in general the radial (horizontal) volume flux is cQ where c is a constant larger than one which depends on the flow and stratification parameters.This constant clearly tends to one when the buoyant plume impinges with very small vertical momentum its neutral density level and increases with increasing the vertical impinging momentum. The flux of the entrained fluid in the spreading layer outside the region ABCD (see Fig. 1) is a small fraction of the flowrate cQ and therefore we may assume that to the first approximation the conservation of mass gives:

Volume of spreading fluid outside the control volume ABCD = cQt

If we assume that the typical vertical and horizontal extent of the intruding fluid are H and R respectively, then the continuity equation gives

$$HR^2 \sim Qt \qquad (2.1)$$

2.2 VERTICAL MOMENTUM EQUATION

By integrating the vertical component of the momentum equation over the spreading patch and by neglecting small terms (i.e. change of vertical inertia) we obtain the physically expected result that the total weight of the slug balances the total pressure force which acts on the slug surface S, i.e.

$$\int_V \rho_s(\vec{x})\, g n_3 dV = \int_S p(\vec{x}) \vec{n}(\vec{x})\, dS \qquad (2.2a)$$

where $\rho_s(\vec{x})$ is the density at any point $\vec{x}$ within the slug and $p(\vec{x})$ is the pressure at any point $\vec{x}$ at the interface of the slug due to the hydrostatic ambient pressure ; $n(x)$ is the unit vector perpendicular to the surface,and $n_3(x)$ is its vertical component. Since the hydrostatic ambient pressure depends on the ambient density profile (and the depth), it is clear that equation (2.2) imposes a relationship between the density of the slug and the ambient density.

Although the density within the slug is not known, we may assume that to the first approximation the density within the slug varies linearly with the depth. It is assumed also that the ambient density varies also linearly with the depth, so that it is easy to integrate equation (2.2) in a slug of constant depth H and radius R (see Figure 2) to find the following relationship between the ambient and slug densities:

$$\rho_{au} + \rho_{al} = \rho_u + \rho_l \qquad (2.3a)$$

where ρ_{au} and ρ_{al} are respectively the densities of the ambient fluid at the upper and lower interfacial layer of slug, and ρ_a and ρ_l are respectively the densities at the upper and lower interfacial layer within the slug. Similar equations to equation (2.3a) can be found for various combinations of ambient and slug density profiles.For example assuming that the density of the fluid in the slug is constant and equal to ρ_s and linear ambient stratification ,then it is easy to find that

$$\rho_s = \rho_u = \rho_l = (\rho_{al} + \rho_{au})/2 \qquad (2.3b)$$

It is interesting to notice that equation (2.3a) implies that

$$\rho_{al} - \rho_l = \rho_u - \rho_{au} \quad \text{i.e. since } \rho_{al} > \rho_l \text{ we must have } \rho_u > \rho_{au}$$

i.e. the upper region within the slug has a density smaller than the density of the ambient fluid. This is interesting because it indicates that the upper region of the slug is locally in unstable stratification i.e. the gradient Richardson number is negative,but the lower region is in stable stratification. Probably this explains why visual observations indicate that the lower region of the slug is smoother than the upper region.

Following Barenblatt (1978) and assuming linear densities profiles within the slug and in the ambient fluid , it is easy to calculate the pressure distribution inside and outside the slug and the excess horizontal pressure force F_p which drives the spreading :

$$F_p \sim \rho' g H^2 R \qquad (2.4)$$

where $$\rho' = \left(\rho_u - \rho_{au}\right) / 6 \qquad (2.5a)$$

The horizontal pressure force F_p which drives the intrusion is usually called "buoyancy " force ,and it is due to the "squeezing" vertical forces exerted on the upper and lower horizontal surfaces of the slug.

Assuming linear ambient density stratification but constant density ρ_s within the slug,then the driving buoyancy force is given again by equation 2.4 with

$$\rho' = (\rho_{al} - \rho_{au})/12 \qquad (2.5b)$$

2.3. HORIZONTAL MOMENTUM EQUATION-SCALING ANALYSIS

The methodology that we will follow to find the asymptotic growth rate of the radius R(t) with time is based on the balance of the forces, which drive and retard the flow. Similar methodology has been used previously by Chen and List (1976) and Didden and Maxworthy (1978) .

The forces which drive the flow are two: the initial radial momentum M_R flux out of the control volume ABCD (see Fig.1) and the pressure force F_p.The forces, which retard the flow are also two:the inertia of the slug fluid and the interfacial drag which is exerted by the ambient fluid on the intruding fluid.

. Subsequently we find the scaling of the above mentioned forces, where the continuity equation (2.1) has been considered and where the typical horizontal velocity U within the intrusion is given by R/t,where t is the time .We assume that t=0 when the vertical plume reaches its neutral density level.

F_I = rate of change of the inertia of the fluid within the slug $= O(\rho_s R^3 H t^{-2}) = O(\rho_s R Q t^{-1})$ (2.5)

F_p = pressure force = $O(\rho' g H^2 R) = O(\rho' g Q^2 R^{-3} t^2)$ (2.6)

F_{sh} = laminar interfacial shear force = $O(\mu R^3 H^{-1} t^{-1}) = O(\mu R^5 Q^{-1} t^{-2})$ (2.7)

We consider below the following four regimes of the radial growth R(t) under the balance of the corresponding driving and retarding forces:

I)First regime:

large radial momentum flux M_R and small times t ;in this regime the flow is similar to the radial momentum jet and on dimensional analysis we find:

$R_1(t) = C_1 M_R^{1/4} t^{1/2}$, (2.8) where C_1 is an experimental constant.

ii) Second regime:

balance of radial momentum flux M_R and the inertia force F_I

$R_2(t) = C_2(M_R/Q)t$, (2.9) where C_2 is an experimental constant.

iii) Third regime:

balance of the pressure (buoyancy) force F_p and the inertial force F_i : i.e. $F_p = F_I$, so that we obtain:

$$R_3(t) = C_3 (\rho' gQ/\rho_s)^{1/4} t^{3/4} \qquad (2.10)$$

where C_3 is an experimental constant.

iv) Fourth regime:

balance of the buoyancy driving force F_p and the retarding interfacial shear force F_{sh},

$$\text{i.e.} \quad R_4(t) = C_4(\rho' gQ^3 v/\rho_s)^{1/8} t^{1/2} \qquad (2.11)$$

where C_4 is an experimental constant.

Therefore, the radial submerged axisymmetric spreading is characterized by four regimes. Subsequently we describe experiments conducted to test the above asymptotic laws.

3. EXPERIMENTAL PROCEDURE

A well organized series of approximately 100 experiments were performed to make possible the appearance of all possible regimes in the radial growth history. For this purpose we varied considerably the initial parameters and the ambient stratification and we conducted the experiments in three different tanks of dimensions respectively a) 100cmX100cm by 30cm deep b) 120cmX120cm by 60cm deep and c) 270cm by 480cm by 200cm deep. Tap water and commercial salt was used to stratify the tank, in such away that the stratified fluid essentially consisted of three layers:a top layer and a bottom layer with constant densities ρ_1 and ρ_2 respectively and an intermediate pycnoline layer in which the density increased linearly with the depth from ρ_1 to ρ_2 . The intrusion was produced by discharging colored tap water of density $\rho_o = 1 gr/cm^3$ at constant volume flux (measured using a calibrated flowmeter) at the bottom of the tank through a pipe of diameter D, which varied between 0.2 cm to 1.25 cm. The constant input volume flux Q_o varied from 0.2 to 85 cm^3/sec (i.e. almost three orders of magnitude) and the initial Reynolds number from 63 to 6800. The initial densimetric Froude number varied from 1.5 to 200.

The spread of the buoyant plume at its neutral level was monitored using a video camera. The time from a large digital watch was also recorded. For small Reynolds numbers, the spreading interface was smooth, although not always axisymmetric. For larger Reynolds numbers (i.e.Re> the visual appearance of the intrusion was characterized by instability waves.We calculated the area A within the contour of the spreading patch at time t using a digitizer interfaced to a personal computer. The mean radius R(t) of the contour at time t was calculated from the relation

$$R(t) = \sqrt{A/\Pi} \qquad (3.1)$$

The Brunt-Vaissala frequency was calculated by the relation

$$N = \left(-g(\rho_l - \rho_u) / \rho_u H\right)^{1/2}$$

In these experiments varied N from 0.06 to 4 sec^{-1}.

4. EXPERIMENTAL RESULTS -DISCUSSION

For each experiment the radius R(t) of the spreading slug was determined using Equ. 3.1 and plotted as a function of time. Typical results are shown in Figures 2,3,4 showing the four regimes and the transition between these regimes. It can be seen in Figure 2 that there is a well-defined region in which the radius R(t) at small times growths like $t^{1/2}$ (regime of radial jet) and then the next regime of with slope t appears.

. In Fig. 3 it can be seen the transition of the inertia-buoyancy regime ($R_3 \sim t^{3/4}$) to viscous-buoyancy regime ($R_4 \sim t^{1/2}$). In some experiments the combination of the initial parameters was such that the regime $R_2(t) \sim t$ collapsed and the transition occurred from the radial jet regime ($R_1 \sim t^{1/2}$) to inertia - buoyancy regime ($R_3 \sim t^{3/4}$), as is indicated in Figure 4. It is also pointed out that for "small" Reynolds numbers at the jet exit (or for small input volume fluxes) the radial momentum is negligible and the regimes R_1, R_2 and R_3 could not be observed; in that case the only observed regime is the viscous-buoyancy regime $R_4 \sim t^{1/2}$, as indicated in Figure 6. All the experiments of Zatsepin and Shapiro (1982) clearly belong to this regime.

The driving horizontal radial momentum is larger than the driving buoyancy force when

$$M > \rho' g H^2 R \qquad \text{or for } t_1 < \left(\frac{M_R}{\rho' g H^{3/2} Q^{1/2}}\right)^2$$

It is therefore apparent that when the (driving) radial momentum is small the first two regimes R_1 and R_2 can not be observed. For $t > t_1$ the dominant driving force is the pressure force F_p ,and the balance of forces gives either the regime $R_3 \sim t^{3/4}$ or the regime $R_4 \sim t^{1/2}$.

The length R_c and time T_c scales which separate the inertia-buoyant regime R_3 from the viscous-buoyant regime R_4 are given respectively by

$$R_c = \left[\frac{Q^6}{(\rho' g Q v^3/\rho_s)}\right]^{1/8} \quad \text{and} \quad T_c = \left[\frac{Q^2}{(\rho' g Q v/\rho_s)}\right]^{1/2}$$

REFERENCES

Barenblatt,G.I.,1978,Bull.(Izv.),Acad. Sci. USSR,Atmosph. and Ocean Physics,vol.14, pp.195-205

Britter,R.E.,1979,Atmosph.Environ.,vol.13,pp.1241-1247

Chen,J.C.,and List,E.J.,1976,ICHMT Conference, Dubrovnik ,,pp.171-182

Chen,J.C.,1980,Report No KH-40,CALTECH, Pasadena, California

Didden,N. and Maxworthy T., 1982, J. Fluid Mech.,vol.121,pp 27-42

Huppert,H.E.,1982,J.Fluid Mech.,vol. 121, pp.43-58

Ivey,G.N.,and Blake,S.,1985, J.Fluid Mech.,vol.161,pp 115-137.

Maxworthy,T.,1972, International Symposium on Stratified Flows,Novosibirsk,pp.611-618

Lister,J.R., and Kerr,R.C.,1989,J.Fluid Mech., vol.203, pp.215-249

Zatsepin,A.G.,and Shapiro,G.I.,1982, Izvestiya,Atmosph.and Ocean Physics,vol.18,pp.77-80.

Zuguala-Angel,A.A.,Darden,R.B.,and Fischer,H.B.,1972,Report EPA-R2-72-037, U.S. Env.Prot. Agency,Washington DC,64pp.

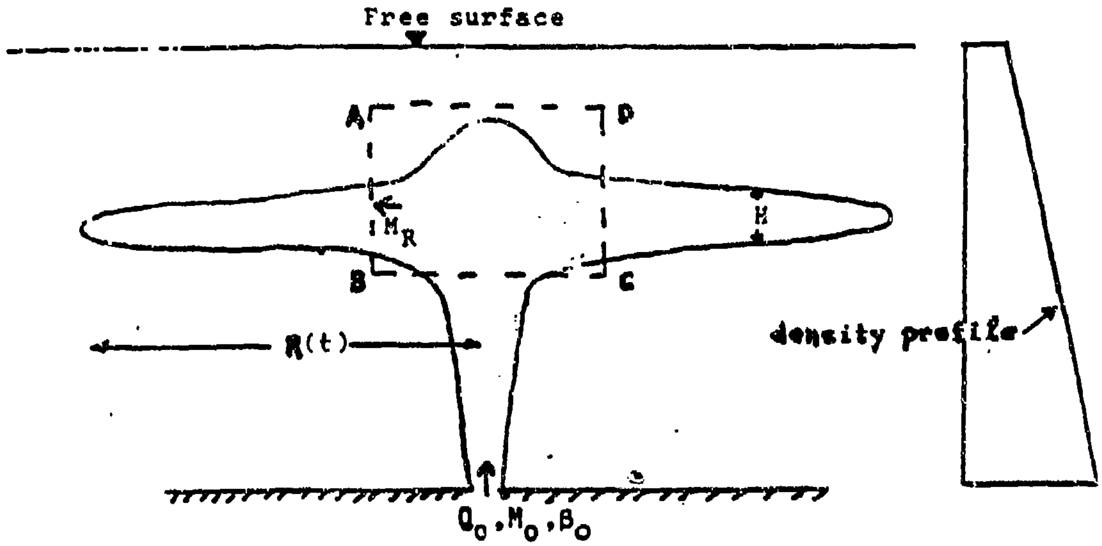

Fig. 1 Axisymmetric intrusion in stratified fluid

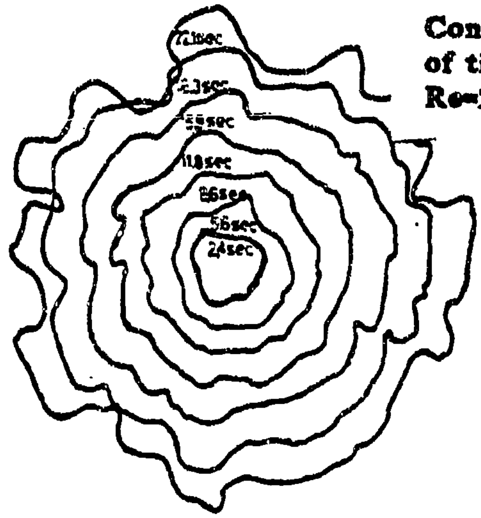

Contours of the intrusion as a function of time in sec. Q=26.8 cm ^{3}/sec,N=0.39 Re=2500

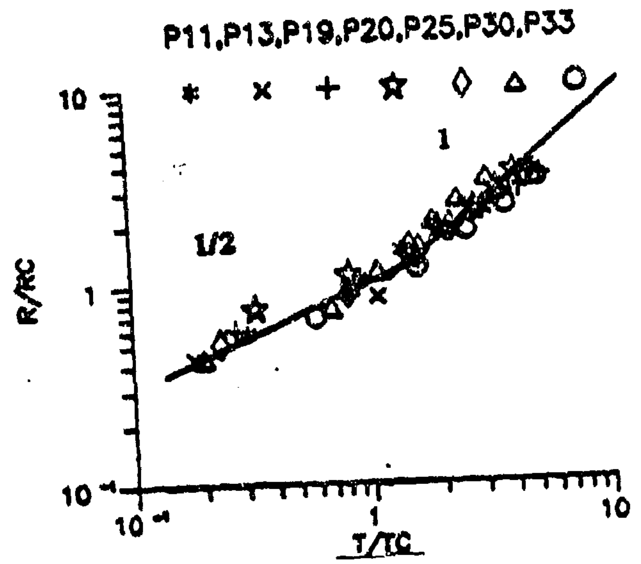

Fig. 2 Normalized growth history of the mean front radius R(t) from many experimental runs indicating transition from slope 1/2 (radial jet) to slope 1.

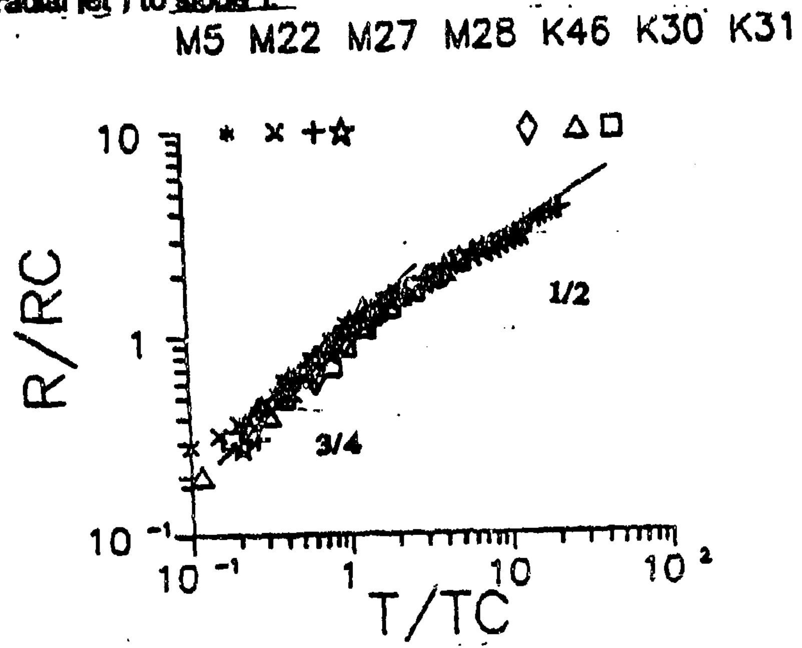

Fig. 3 Normalized growth history of the mean front radius R(t) from many experimental runs indicating transition from slope 3/4 (inertia - buoyancy regime) to slope 1/2 (viscous-buoyancy regime).

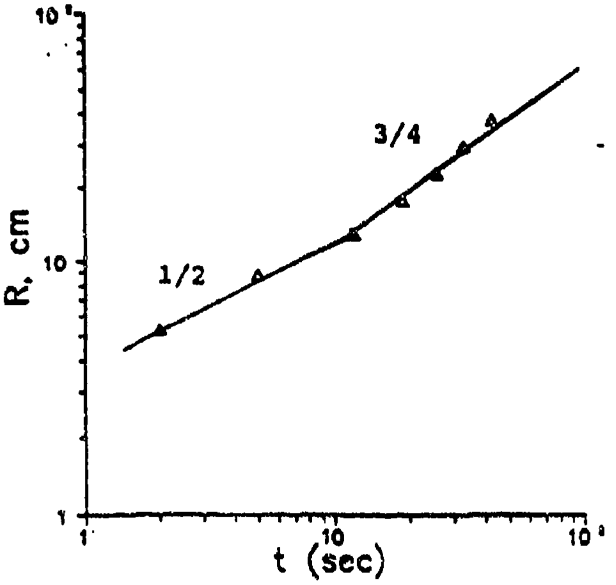

Fig.4 Typical growth history of radius R(t) indicating transition from the radial jet regime (slope 1/2) to inertia-buoyancy regime (slope 3/4).

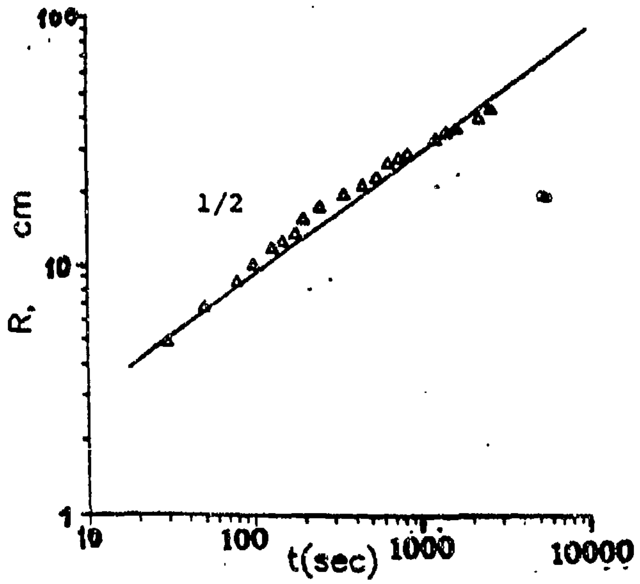

Fig.5 Viscous- buoyancy regime . Q_o= 0.37 cm ^{3}/sec, N=2.32, Re=211.

The influence of bottom topography on internal seiches in continuously stratified media

Matthias Münnich*
EAWAG/ETH Zürich

April 13, 1994

Abstract

Standing internal waves, so-called seiches, are ubiquitous in reservoirs and lakes. While the stratification in such basin is often continuous, the modeling of seiches has been confined mostly to two-layer models. Such models are unable to give reliable insights about the vertical structure of the seiches, which might be crucial for the understanding of vertical mixing in natural water basin. To obtain this knd of informations a 2-dim. computer model has been developed, which takes both the continuous stratification and the bottom topography into account. The results of this model are presented. The computed seiche modes reveal that

i. several large scale modes can exist with similar eigenfrequencies;

ii. the modes have a tendency to develop narrow jets;

iii. only the lowest modes are strongly influenced by the bottom topography.

1 Introduction

Standing internal waves, so-called internal seiches, are nearly omnipresent in reservoirs and lakes. Most of these are gravity waves, for which gravity, or more specifically buoyancy is acting as the restoring force. For a medium sized lake internal seiches have typically periods of hours and amplitudes of several meters.

Due to the large amplitudes, internal seiches are important for various processes in lakes. They cause a periodic vertical displacement of the suspended biomass and thus a periodic variation in the light intensity to which algal cells are exposed (Gaedke and Schimmele [2]). The bottom currents associated with internal seiches can enhance dissolution and remobilization of nutrients by transporting the products of bacterial decomposition away from the sediment-water interface into the bulk water. The shear field associated with bottom currents can lead to small-scale turbulence, which is able to resuspend material from the sediment (Gloor et al. [4]).

To study the influence of bottom topography on the vertical structure of internal seiches in lakes a two-dimensional numerical model has been developed. The vertical

---

*Present affiliation: Max-Planck-Institut für Meteorologie, Bundesstr. 55, 20146 Hamburg, Germany structure of seiches is well known for lakes with constant depth, i.e., lakes with a rectangular cross-section. In this case the vertical shape of the seiche is easily computed by separating the horizontal and vertical coordinates. If the depth varies, as is always the case in nature, such a separation of horizontal and vertical structure is no longer possible.

There are indications that the influence of bottom topography on the seiche modes is substantial. As internal seiches are a special form of internal gravity waves they are obliged to the same reflection laws as internal gravity waves. Now the reflection of internal gravity waves off a sloping boundary is quite peculiar. It is not the angle between the incident wave and the lake bottom which is conserved upon reflection, but the angle between the wave number vector and the vertical. Furthermore, neither the modulus of the wavenumber nor the amplitude of the wave is conserved. If the slope angle of the bottom is close to the angle between the wave number vector of the reflected wave and the horizontal, both the wave number and the amplitude of the wave undergo strong amplification. This increased amplitude of the reflected wave increases the probability of its breaking. Such breaking of internal waves is believed to play a key role in vertical mixing processes in the ocean (Garrett [3]).

In view of the reflection laws of internal gravity waves what is the shape of the their standing modes in a basin with sloping bottoms? Bringing some light to bear on this question has been a major motivation for the present study.

2 The model

In two dimensions (one vertical, one horizontal) the governing equation for a stream function ψ of free, infinitesimal internal gravity waves in a hydrostatic Boussinesq fluid is

$$\frac{\partial^4\psi}{\partial t^2 \partial z^2} + N^2 \frac{\partial^2\psi}{\partial x^2} = 0. \tag{1}$$

Here $N = N(z)$, t, x and z, denote Brunt-Väisälä frequency, time and the horizontal and vertical coordinates, respectively. Employing the rigid lid condition eliminates the surface waves. Then, assuming no outflow, the boundary conditions for ψ can be combined to

$$\psi = 0 \quad \text{at the boundary.} \tag{2}$$

For seiches the time dependence is sinusoidal $\psi = \phi(x, z)\sin(\omega t)$, which yields the following eigenvalue problem in ω for the spatial structure of the stream function:

$$\frac{\partial^2\phi}{\partial z^2} - \frac{\omega^2}{N^2}\frac{\partial^2\phi}{\partial x^2} = 0. \tag{3}$$

with $\phi = 0$ at the boundary. Note the hyperbolic form of (3). The dispersion relation following from (3) is

$$\omega^2 = N^2 \frac{k_x^2}{k_z^2}, \tag{4}$$

with $\boldsymbol{k} = (k_x, k_y)$ as the wave number vector. In a rectangular basin the waves number vectors, which fulfill the boundary condition (2) are $(k_x, k_z) = (lL\pi, mD\pi)$; $l, m = 1, 2, \ldots$. Inserting this in the dispersion relation yields for the frequencies of the seiche modes

$$\omega^2_{(l,m)} = N^2 \frac{D^2}{L^2}\left(\frac{l}{m}\right)^2 . \tag{5}$$

This shows that each eigenfrequency is infinitely degenerate, because $\omega^2_{(nl,nm)} = \omega^2_{(l,m)}$ for any $n = 1, 2, \ldots$. Furthermore, and even more remarkable, the spectrum is dense (in the mathematical sense) on the positive real axis, because each rational number can be written as l/m for suitable l and m. The frequencies connected with large scale motion, i.e. small l and m are surrounded by small scale motion, i.e. large l and m. This forms a major difficulty to find the desired frequencies of modes with large scale motions. The properties of the eigenvalue problem (3) prevents the usage of any of the usual numerical methods to solve such problems.

We discretized the domain using finite differences on a rectangular grid, which was adjusted to the stratification. The discretization itself filters all wavelengths shorter than twice the grid spacing. As the numerical to solve (3) we either used the QZ-algorithm (Moler and Stewart [5]) or the Schur-Raleigh-Ritz (SRR) variant of inverse vector iteration (Stewart [7]). For low resolution all eigenvectors were computed using the QZ-Algorithm. The eigenmodes were sorted by the overall shear of the connected flow field. This way only the modes with the largest scale motion were selected. For finer resolution and to test the independence of the eigenfrequencies and mode structures from the spatial grid used the SRR technique was used toe compute the eigenvectors in a narrow frequency interval. For more information see Münnich [6].

3 Model results

3.1 Parabolically shaped lake

As one type of lake with non-constant bottom topography we choose two differently scaled parts of a parabola to model a typical "bathtub-shaped" basin. Usually the thalweg of a lake is not symmetric, and it is interesting to investigate how this asymmetry influences the form of the seiches. The different scalings of the sections of a parabolas are used to obtain such a asymmetric basin and to allow a change the degree of the asymmetry. More specifically, the following one-parameter family depth function $D_a(x)$ is used

$$D_a(x) = \begin{cases} -1 + \left(\frac{x-a}{a}\right)^2 & \text{for } 0 \le x < a; \\ -1 + \left(\frac{x-a}{1-a}\right)^2 & \text{for } a \le x \le 1. \end{cases} \tag{6}$$

Here the free parameter a determines the asymmetry of the basin. Fig. 1 shows the largest scale mode for increasing asymmetry. The most striking result is the constancy of the location of the maximum of the stream function, i.e., the place of no motion. It looks as if the streamlines of the modes are pushed to this fixed location by the boundary, leading to an accumulation of these lines near the lake bottom. If this is true in reality there would be a "hot spot" of mixing in this region. Another feature is the depth of the node. It is not situated in the middle of the lake, as is the case for a rectangular basin, but is shifted towards the deeper region. To our knowledge this has not yet been observed in nature, but we must remember that a constant stratification throughout the whole water body is quite unrealistic. Usually there is one maximum of N in the upper region of the lake.

In Fig. 2 the some large-scale modes for $a = 0.3$ and shown. Each mode is numbered by its ranking in size of overall shear among all computed modes.

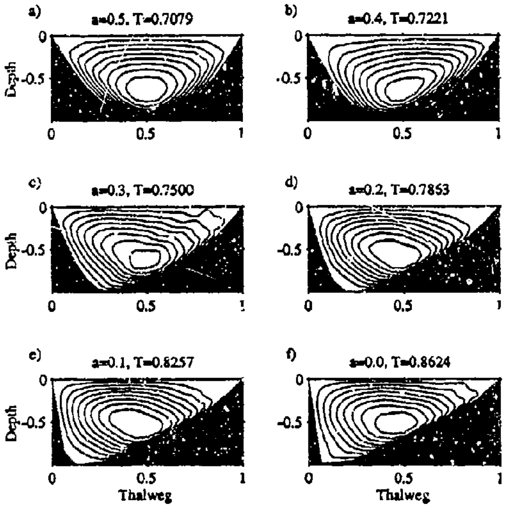

Figure 1: Streamlines of the first mode for a parabolic bottom with increasing asymmetry. The stratification has a constant buoyancy frequency N. The periods T are scaled by the V1H1 mode in a rectangular basin. The asymmetry parameter a is defined in (6). The grid resolution is $n_z = 20$ and $n_x = 15$. Due to the finite resolution, the parabola in f is cut off before it reaches its minimum.

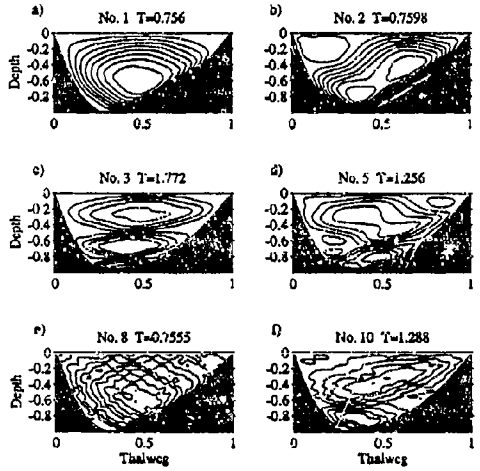

Figure 2: Some large-scale modes for a parabolically shaped lake with constant buoyancy frequency N. The modes are sorted as explained in Section 4.4. The order which the mode obtained is indicated in the title. The period T is scaled by the lowest mode ($l = m = 1$) of a unit rectangular basin with constant $N = 1$ stratification. The number of grid points vertically and horizontally is $n_z = n_x = 30$. The asymmetry parameter is $a = 0.3$.

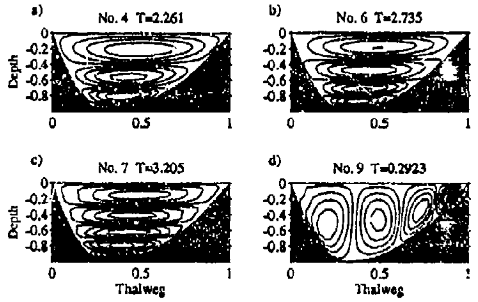

Figure 3: Higher modes for a parabolically shaped lake with constant buoyancy frequency N and asymmetry parameter $a = 0.4$. Resolution: $n_z = n_x = 30$.

Modes 1 (Fig. 2*a*) and 2 (Fig. 2*b*) have nearly identical periods. A region of strong currents near the bottom is associated with both modes, but mode 2 has nearly no motion in the upper left part of the lake. Both modes will become excited by winds with periods around $T = 0.755$. Mode 1 will have a stronger amplitude if the wind is blowing uniformly over the lake, whereas if there are some sheltering effects which lead to weaker winds above the left part of the lake, mode 2 might be dominant. In Fig. 2*e*, mode 8, with a similar period, is displayed. This mode appears to be similar to mode 1, but with small-scale noise superimposed on it.

Mode 3 (Fig. 2*c*) is easily identified as the analog of the third vertical first horizontal mode in the rectangular basin. Modes 5 (Fig. 2*d*) and 10 (Fig. 2*f*) seem to be two variants of the second vertical first horizontal mode. Both have appropriate periods and two (large-scale) extrema in their stream functions. Mode 10 shows some small scale noise, as does mode 8.

In Fig. 3 the rest of the first 10 modes are displayed. All these modes are rather unspectacular. There horizontal or vertical cell size (wave length) is small enough, that these mode are not very strongly influence by the basin topography. Only the flow cell adjust to the local depth. So only the low-order modes with space scales on the order of the size of the basin seem to be strongly influenced by the bottom topography.

3.2 Two basins separated by a sill

Another basin form often found in nature is a lake consisting of two (or even more) basins separated by sills. As the deviation of such a profile from the rectangular is more pronounced, we should also expect larger differences in the seiche modes.

Up until now we used a constant N stratification, whereas the buoyancy frequence profiles in natural reservoirs usually have a thermocline, i.e., a pronounced maximum N in the upper region. For this reason a stratification as shown in Fig. 4 is used in the following.

For the bottom topography we use a fourth-order polynomial. To be more specific, we use the one-parameter family of depth functions

$$D_a(x) = -1 + \left(\frac{(2x - 1 - a)(2x - 1 + a)}{(a + 1)(a - 1)} \right)^2 \tag{7}$$

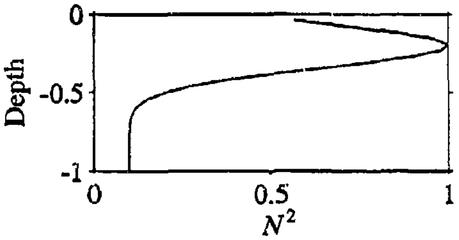

Figure 4: Stratification used in the following seiche calculations.

and choose $a = 0.6$, which gives a medium-sized sill. Fig. 5 shows the first few modes ordered by our sorting routine. Whereas the first three modes shown in Fig. 5 $a - c$ are higher modes, it is the 4th mode which we tend to interpret as the first basin mode. This mode has some interesting features. The streamlines accumulate at the boundaries, while the interior is relatively quiet. At the two ends of the lake the streamlines bend into the interior at a depth of about $z = -0.3$. To a lesser degree, a similar bending is also seen in the middle of the uppermost streamlines. The mode is quite noisy, and one might tend to believe that this is just due to computational flaws. Even though we do not think that the streamlines are reliable in all details, the overall pattern was found for different grid resolutions (see below) and for all topographies with small and medium-sized sills. We therefore believe that the general pattern is reliable.

Mode 6 again is a higher vertical mode. The last mode displayed in Fig. 5*f*, mode 10, has a similar period as mode 4. It can be interpreted as another first basin mode. In this mode we see again that the streamlines have moved together. Like mode 4 this mode is quite noisy but here the tendency of the streamlines to bend into the interior of the lake appears to be stronger.

In Fig. 6 a few other modes and their shear ranking are presented. As we have already seen in Fig. 3, for such higher modes the structure is not particularly dependent on the form of the topography. Again only the current cells adjust their size to the local width and height.

4 Conclusions

Motivated by the peculiarities of internal waves in continuously stratified waters and by the dominance of large scale standing internal waves, i.e., seiches, among the internal waves in lakes, we studied the influence of bottom topography on the vertical structure of internal seiches.

We established that the mode spectrum of a lake with continuous stratification is dense for a rectangular basin, which implies that such a lake can oscillate, at least in principle, at any frequency whatsoever. The reasons why lakes still show distinct resonant frequencies due to seiche motion are presumably two-fold. Firstly, most of these seiches are small-scale motions which are not directly excited by the basically homogeneous wind stress. Secondly, the shear stress associated with such modes is higher, and therefore these seiches

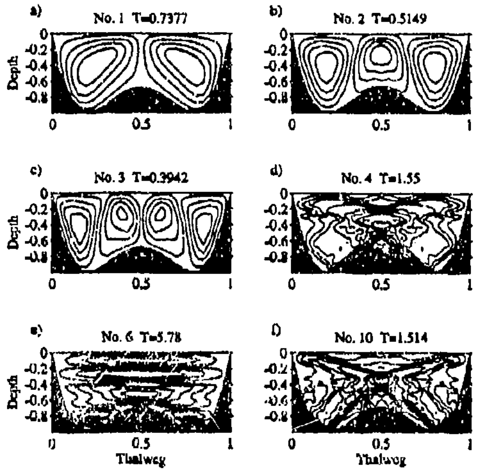

Figure 5: Modes for a medium-sized sill and the same peaked stratification as in Fig. 4. Higher modes are shown in Fig. 6. The numbers of grid points vertically and horizontally are $n_z = 20$ and $n_x = 25$, respectively. The periods given in the titles are scaled by the periods of the largest scale mode in a unit rectangular basin with constant $N = 1$ stratification.

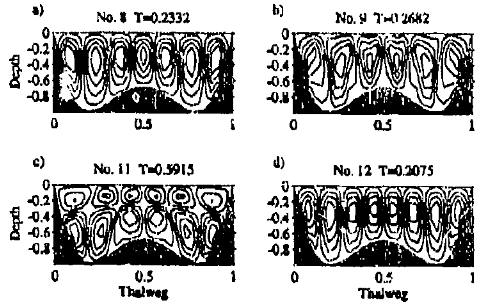

Figure 6: Higher modes for a shallow sill and the same peaked stratification as in Fig. 4. The parameters are: $\alpha = 0.6$, $n_z = 20$, $n_x = 25$.

are more strongly damped.

A linear, inviscid, two-dimensional numerical model was developed to compute the seiche structures and periods in lakes with any given morphometry and stratification. Using a stream function it was possible to use the exact boundary conditions for the seiche motion at the sloping bottom. The main numerical problem remaining was the density of the eigenvalues. As we were interested in pure modes, we did not build any friction or forcing into our model, and consequently the seiche spectrum remained dense.

Discretization was used to filter out most of the higher frequency seiches. Any finite difference model can only resolve structure on a scale similar to or larger than the grid size, so that modes with a finer structure are not represented.

The model was applied to two kinds of lake prototype: a "bathtub-shaped" lake constructed of parabolas, and a lake consisting of two basins separated by a sill.

In a bathtub-shaped lake with constant stratification (buoyancy frequency N = constant), the model predicted a region of strong currents in the hypolimnion near the gentle slopes at the lake bottom. Often two or even three kinds of large scale seiche modes were computed with similar periods but distinct mode structures. For higher modes with spatial scales smaller than the spatial scales of the variation of the thalweg, this variation was predicted to have only a moderate influence. These modes adjust smoothly to the changing depth.

For a lake with a sill, the largest-scale mode was predicted to result in strong currents above the sill. For some parameter values for the height and position of the sill, these currents spread out throughout the whole water column to form a closed, jet-like structure. Such a region of strong currents is consistent with the prediction made by Baines [1] of increased seiche wave amplitudes above convex bottoms. Again the small-scale modes adjusted smoothly to changing depth.

References

[1] P. G. Baines. The reflection of internal/inertial waves from bumpy surfaces. Part 2. Split reflexion and diffraction. *Journal of Fluid Mechanics*, 49(1):113–131, 1971.

[2] U. Gaedke and M. Schimmele. Internal seiches in Lake Constance: influence on plankton abundance at a fixed sampling site. *Journal of Plankton Research*, 13(4):743–754, 1991.

[3] C. Garrett. Marginal mixing theories. *Atmosphere-Ocean*, 29(2):313–339, 1991.

[4] M. Gloor, A. Wüest, and M. Münnich. Benthic boundary mixing and resuspension induced by internal seiches. *Hydrobiologia (in press)*.

[5] C. B. Moler and G. W. Stewart. An algorithm for generalized matrix eigenvalue problems. *SIAM Journal Numerical Analysis*, 10:241–56, 1973.

[6] M. Münnich. *On the influence of bottom topography on the vertical structure of internal seiches.* PhD thesis, Swiss Federal Institute of Technology Zürich, 1993.

[7] G. W. Stewart. Simultaneous iteration for computing invariant subspaces of non-hermitian matrices. *Numerische Mathemathik*, 25:123–136, 1975.

STABILITY AND MIXING OF A TWO-LAYER EXCHANGE FLOW

G. Pawlak and L. Armi

Scripps Institution of Oceanography
University of California at San Diego
La Jolla, California 92093-0203

ABSTRACT

The stability of a two layer exchange flow through a contraction is investigated experimentally and analytically. Experiments validated the predictions of hydraulic theory from cases with no net barotropic flowrates to wedge flows with high barotropic flowrates. Instabilities which depend on the shear layer Reynolds number and the local Richardson number exist at various scales. Linear stability analysis of a tanh velocity and density profile with varying thickness ratio and boundaries imposed at arbitrary distances shows the existence of several modes of instabilities including Holmboe and Taylor modes. The stability properties of exchange flows are described based on this model.

INTRODUCTION

Two layer exchange flow through a contraction of slowly varying geometry is described by the internal hydraulics model outlined by Armi and Farmer (1986). The exchange is controlled at locations where the flow is critical with respect to internal waves; at the narrowest section and at a second, 'virtual' control. For flows with no barotropic component these control locations coincide at the narrows. Addition of a moderate barotropic net flow creates a subcritical region between the two controls and changes the interface level at the narrows from half depth. Strong net barotropic flow arrests one layer and as the barotropic flowrate is increased, wedge or 'box' flows are established.

The assumptions used in the formulation of a hydraulics model for the exchange flow allow only long wave solutions. Attention to the stability of these flows has therefore been limited to infinitely long waves. Long (1956) obtained the criteria for stability of infinitely long waves in a bounded shear flow. Defining the stability Froude number by $F_\Delta^2 = \Delta U^2/g'h$, where g' is the reduced gravitational acceleration and h is the total depth, Long's criteria is $F_\Delta^2 \leq 1$, for stability.

Armi and Farmer considered long wave stability at the control locations. Flows with no barotropic component were found to be marginally stable whereas addition of net barotropic flow stabilized the flow at the controls with respect to long waves. Lawrence (1990) further studied the long wave stability of barotropic flows throughout the channel and found that a net barotropic flow caused shear to decrease upstream with respect to the net flow and to increase downstream. As a result these flows become unstable at a location downstream of the narrowest section, where the interface level is at half the total depth and beyond which $F_\Delta^2 > 1$.

Our laboratory experiments show that exchange flows are predicted well by hydraulic theory and that Lawrence's stability analysis for barotropic flows can give a general description of stability properties of a real flow over a range of Reynolds numbers. Flows are indeed found to be unstable to long waves following hydraulic analysis. However, we also find that exchange flows are unstable, in many cases, to smaller wavelength disturbances while long waves may be stable. Figure 1 shows low and high Reynolds number exchanges with no net barotropic flow illustrating the variation of stability.

The phenomena observed in the laboratory were also investigated analytically by considering the linear stability of a finite thickness shear layer bounded above and below by rigid boundaries.

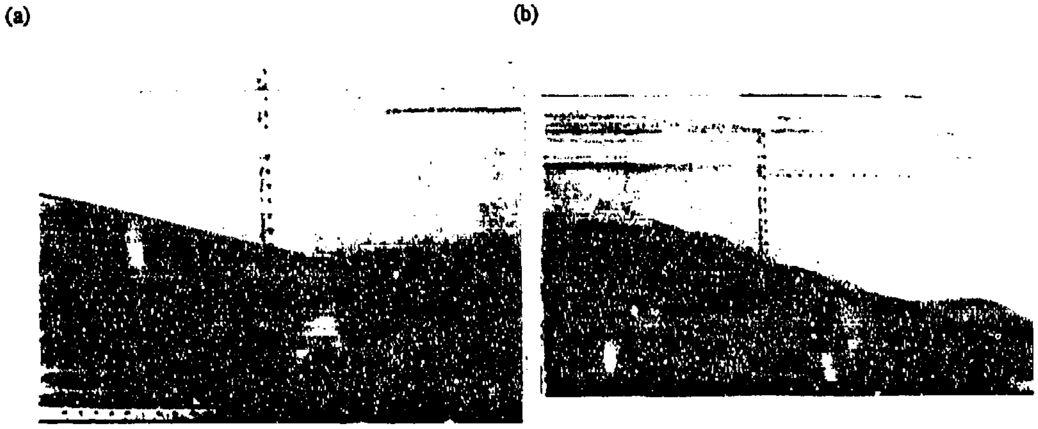

FIGURE 1. Exchange flows at (a) $g' = 0.39$, $Re_\delta \approx 500$ (b) $g' = 3.92$, $Re_\delta \approx 1000$

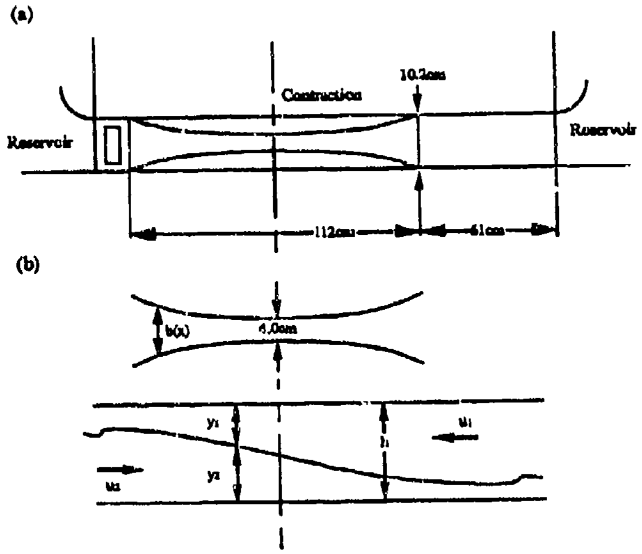

FIGURE 2. (a) Experimental setup (b) Exchange flow plan and side views

EXPERIMENTS

The experimental facility consisted of a plexiglas flat-bottomed, convergent-divergent channel connecting two reservoirs (figure 2). Each reservoir is 123cm x 246cm x 24cm. The contraction portion of the channel is 112cm long, 4 cm wide at the narrowest section and 10.2 cm wide at the ends. One end of the contraction has a 61cm long section attached, of constant, 10.2cm width. All experiments were conducted with the reservoirs and channels filled to 20cm. Density differences were obtained using salt and the fluid was dyed with food coloring to distinguish the layers.

Videotapes were used to obtain quantitative flow data. Potassium permanganate crystals dropped in the channel left sharp vertical streaks, the timing of which was used to measure flow velocities. With average interface heights and velocities, flowrates and Froude numbers were computed for selected locations. Errors in velocities of order 10% are due to measurement accuracy, boundary layers and the finite thickness shear layer.

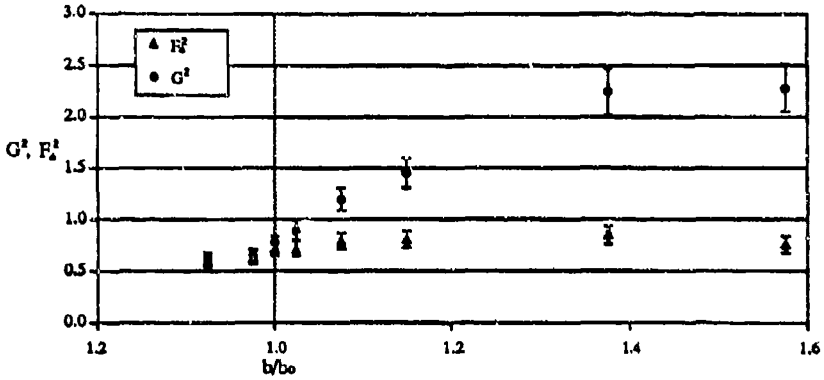

FIGURE 3. Stability Froude number, F_Δ^2 and composite Froude number, G^2 vs nondimensional width, b/b_o

Forcing instabilities along the interface was attempted by various techniques, the most successful employing a latex membrane attached to a sidewall and intermittently inflated with fluid. This reduced the width of channel and caused the interface height to change. The resulting disturbance would then be convected with the flow. This device was installed just downstream, with respect to the net barotropic flow, of the narrowest section.

Figure 3 shows composite Froude number, G^2, and the stability Froude number, $F_\Delta{}^2$, for a flow with nondimensional barotropic component, $U_0 = -0.21$ (see Armi and Farmer, 1986). This data demonstrates that the flow becomes supercritical downstream of the narrows. The data for $F_\Delta{}^2$ shows that shear increases downstream, destabilizing the flow. The effect of friction in the exchange is evident in lower values of G^2 and $F_\Delta{}^2$ than those predicted by inviscid hydraulic theory. For example, at $b/b_o = 1$, theory predicts $G^2 = 1$ and $F_\Delta{}^2 = 0.96$ for this flow. The influence of friction can be understood by first considering a single layer flow. The growth of boundary layers along the sidewalls will lead to an effectively narrower channel with the control existing downstream of the physical contraction. The related case of single layer flow over a sill was investigated by Pratt (1986). For the two layer exchange, the net result is the introduction of a subcritical region at the narrows for the case of no barotropic flow, or, in exchanges with net barotropic flow, an increase in the length of the subcritical region. This results in decreased flowrates and lower Froude numbers. Taking these effects into account, laboratory experiments validated the predictions of hydraulic theory for exchange flows with and without net barotropic flow.

Reynolds number effects were found to be significant in the stability of exchange flows. A finite velocity interface develops between the two layers as a result of viscous diffusion, the thickness of which is a function of the shear, ΔU, and the length of the channel, L; expressed in terms of channel Reynolds number, $\delta/L \sim \mathrm{Re}_L^{-1/2}$. The shear layer Reynolds number is given by: $\mathrm{Re}_\delta \sim \mathrm{Re}_L{}^{1/2}$. Below a critical Re_δ flows are stable to all wavenumber disturbances. At higher Re_δ, the interface eventually becomes unstable to disturbances which scale with the shear layer thickness. This is displayed in figure 1, for two exchange flows with no barotropic component. With small density differences ($\Delta\rho/\rho = 0.0004$) velocities were low and the flows were laminar and stable everywhere. With higher stratification ($\Delta\rho/\rho = 0.004$), the interface is unstable to high wavenumber instabilities and a turbulent mixing layer develops. For flows with a net barotropic component, Re_δ increases downstream due to changes in δ and ΔU. Moderate Reynolds number cases were chosen for more detailed study since, in these flows, the interface is distinct while there are significant regions of instability.

For the cases with no net barotropic flow, the depth at the narrows generally remained at half depth as predicted by hydraulic theory, with intermittent periods of instability occurring on either side. Finite amplitude waves would grow and break as they were swept outward from the center. As barotropic flow is introduced, the interface height at the narrows follows hydraulic theory and the upstream portion of the flow becomes noticeably more stable. Disturbances travel upstream (with respect to the net barotropic flow), but generally damp out.

Figure 4 shows images of a series of locations in the flow referred to in figure 3. The upstream portion is completely stable through the narrowest section. Just downstream of the narrows, disturbances begin to appear on the interface as the lower layer accelerates. Further downstream these have grown to finite amplitude

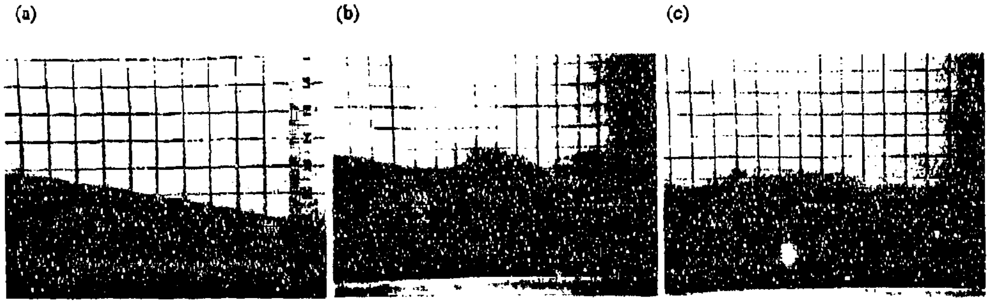

FIGURE 4. Exchange flow with net barotropic flow, U_0=-0.21, g'=0.97. (a)Upstream flow and narrowest section, -11cm to 1cm. (b)Downstream, 24cm to 39cm. (c) Downstream, 36cm to 50cm

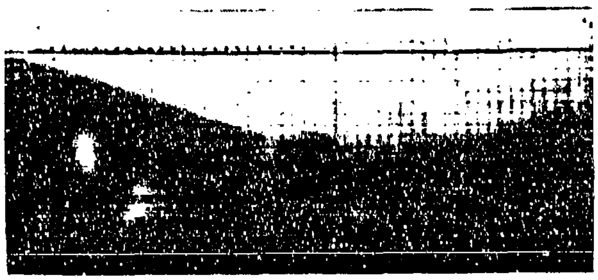

FIGURE 5. Wedge flow, g'=0.4

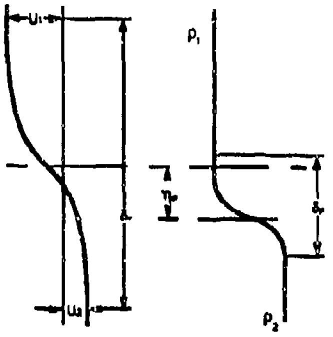

FIGURE 6. General velocity and density profile

overturning and breaking waves. Far downstream, the fluid is considerably mixed, with entraining vortices distinguishable along the interface.

As the net barotropic flow is increased beyond the rate at which one layer is arrested, a wedge flow is established. Inviscid hydraulic theory requires that the flow be internally critical at the narrowest section. Since one layer is arrested this requires: $F^2 = u^2/g'y = 1$ for the flowing layer at the narrowest section. From this we see that as long as the leading edge of the wedge remains upstream of the narrows, the flow will remain stable to long waves on the upstream side, since $F_\Delta^2 = (y/h)F^2 < 1.0$. As the flowing layer is accelerated downstream, shear increases and the flow becomes unstable to long waves downstream of the narrowest section. Figure 5 shows a wedge flow in which the lower layer is flowing. The net barotropic flow is from left to right. Here the lower layer plunges at the narrowest section and growing and breaking waves are seen to be convected downstream. The growth and subsequent pairing of these instabilities could be observed until the vortices were of the scale of the total depth of the flow.

ANALYSIS

We now consider a finite thickness shear layer and pursue a one dimensional inviscid analysis to obtain stability properties at a selected flow location. The exchange is represented by imposing rigid boundaries at arbitrary distances from the interface corresponding to the channel bottom and free surface.

Hazel (1972) performed a numerical study of hyperbolic tangent velocity and density profiles with variations in thickness ratios, R. He studied the effect of equidistant boundaries on flows with equal thickness scales (R=1) and found these destabilized long wavelengths at distances much larger than the layer thickness. Moving the boundaries nearer eventually stabilized the flow to all wavelengths. For unbounded flows, a sharper density interface (R>1) introduced an unstable region, corresponding to the Holmboe mode (c.f. Holmboe, 1962), for all α and J. Lawrence, Lasheras and Browand (1987) further investigated this problem analytically and experimentally, but for piecewise continuous, linear velocity and density profiles with varying scales and displaced centers. Again, variation of scales was found to produce a region of Holmboe instabilities. Displacing profiles resulted in a third more unstable mode, also existing at all α and J, which they called the 'hybrid' mode. More recently, Caulfield (1994) studied analytically a linear shear layer with an intermediate constant density layer separating the two homogeneous regions. Several unstable modes were found to exist including the Holmboe mode, a 'T' mode, after Taylor (1931) who studied the corresponding instability in equal scale stratified shear, and an additional mode called the 'R' mode, corresponding to a resonance of Rayleigh waves at low wavenumbers.

The studies discussed above form a basis for the consideration of finite thickness shear layers in exchange flows. An idealized general shear layer model is shown in figure 6. The stability of small disturbances in an inviscid, incompressible, stratified shear flow is governed by the Taylor-Goldstein equation, which, for Boussinesq flow, in dimensionless form is:

$$f'' + \left(\frac{J\beta'}{(u-c)^2} - \frac{u''}{u-c} - \alpha^2\right) f = 0$$

where f(y) is the nondimensional vertical disturbance velocity, c is the complex phase speed, u(y) is the basic velocity profile, J is the Richardson number at the origin, β' is the nondimensional density gradient and α is the nondimensional wave number. All velocities are nondimensionalized by half of the overall shear, ΔU = U_1 - U_2 and the length scale is one quarter of the shear layer thickness, δ. Using the Boussinesq approximation, we define β as:

$$\beta(y) = \frac{2\rho_o}{R\Delta\rho}\ln\left(\frac{\rho_1+\rho_2}{2\rho}\right)$$

with β scaled so that β' = 1 at y = η_ρ. We then use the profile:

$$\beta(y) = \frac{1}{R}\tanh R\left(y - \frac{4\eta_\rho}{\delta}\right)$$

and velocity profile:

$$u(y) = \tanh(y)$$

to obtain a general velocity profile of thickness δ with a density profile of thickness δ_ρ = δ/R, offset by η_ρ, given by:

$$\rho = \frac{\rho_1+\rho_2}{2}e^{-\frac{R\Delta\rho}{2\rho_o}\beta(y)}$$

The shear layer thickness is defined as the distance between the two points having 0.964 of the freestream velocity (tanh 2 = 0.964). As R → ∞, the density interface tends to a step. The Richardson number at the origin, J, is then given by: $J = Rg'\delta/2\Delta U^2$.

By using the appropriate boundary conditions and the background flow at a location of interest in an exchange flow, the problem is posed as an eigenvalue problem for the complex phase speed, c. The no-slip condition at the free surface and at the channel bottom require f=0 at these locations. For a slowly varying channel, the background flow can be obtained from hydraulic theory or from experimental data. Solving this problem, we can obtain stability data from the model.

For our experiments, shear layer thicknesses were measured from video recordings of dye traces. Density layer thicknesses were difficult to obtain precisely but from rough numerical analyses and consideration of the Schmidt number for salt, we estimate that the density interface is 10 times thinner than the velocity interface. Laboratory experiments show a very sharp interface between the layers at moderate Reynolds numbers (for example see figure 4a).

Eigenvalues for the Taylor-Goldstein equation above were obtained using a finite difference approximation, employing a two dimensional shooting method, with the no-slip condition on the boundary nearer to the interface as a target. Given flow conditions, including density difference, layer velocities and depths, and shear and density interface thicknesses, the complex phase speed is computed for a range of wave numbers at the resulting Richardson number, J.

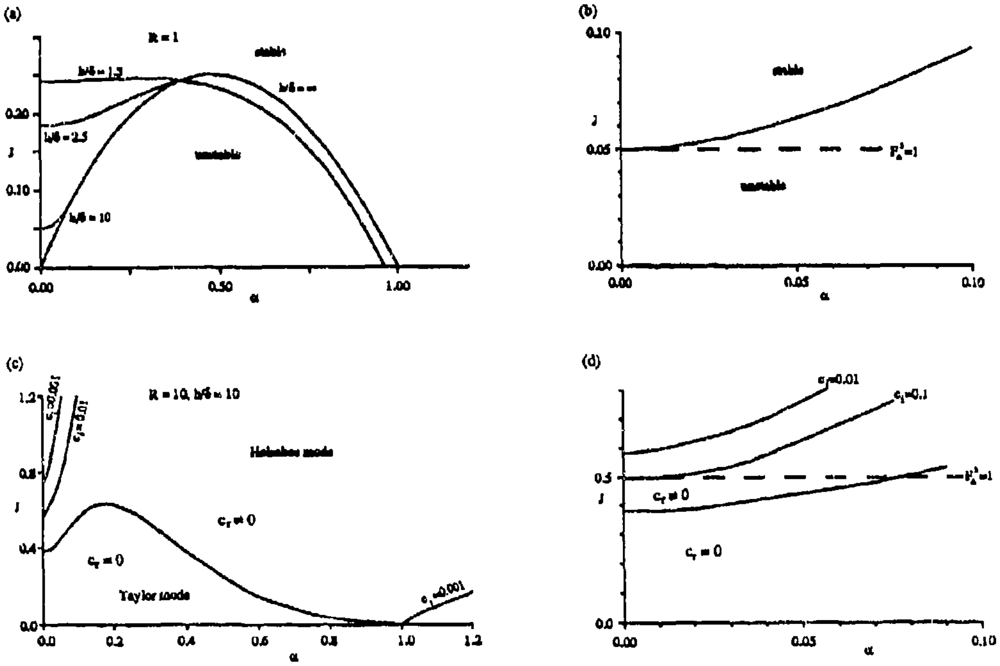

FIGURE 7. (a)Effect of rigid boundaries on tanh shear layer for R=1. (b)Long wave limit for R=1, h/δ=10. (c) Stability boundaries for R=10, h/δ=10 (d)Long wave limit for R=10, h/δ=10.

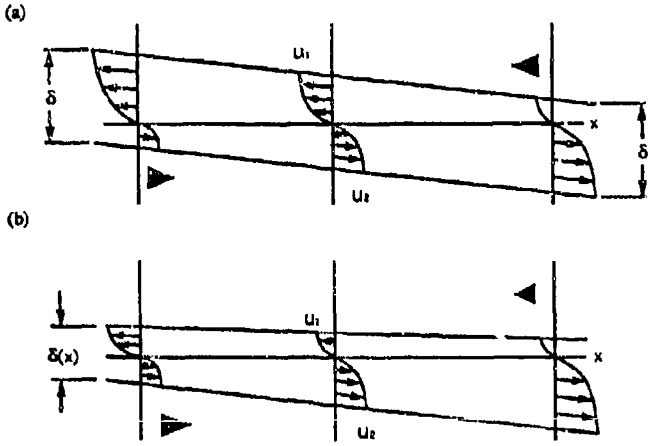

FIGURE 8. Shear layer for (a) zero net barotropic flow, (b) moderate net barotropic flow.

STABILITY PROPERTIES OF TANH PROFILES

Our problem is complicated by the various mechanisms for instability and their corresponding scales. The stability of disturbances which scale with the depth is dependent on the conflict between destabilizing pressure field variations and stabilizing stratification. The stability of disturbances which scale with δ is dependent on the balance between shear and stratification. In addition, Holmboe instabilities may exist, which result from an unstable phase coupling between disturbances on the velocity and density interfaces. For some ranges of wavenumbers all of these mechanisms have an effect on stability.

The J-α planes for some of the cases considered are sketched in figure 7. For the case of R=1, we obtain an unstable region corresponding to the Taylor mode, unstable only for a range of α and for $J<0.25$. This mode is characterized by zero phase velocity and most unstable wavenumbers of about 0.3-0.5. When $R>1$, this mode with $c_r=0$ includes a larger portion of the J-α plane and a Holmboe region appears, characterized by a nonzero propagating velocity and existing at all J.

The effect of imposing boundaries on the tanh profile is to destabilize the lower wavenumbers. Higher wavenumbers are generally unaffected by the presence of the boundaries, except at very low Reynolds numbers where the shear layer thickness may be of the order of the layer depth. The variations in relative layer depths also affect the lower wavenumber stability. Changing the ratio of layer depths results in the addition of a real component in the phase speed in the direction of the velocity of the thinner layer.

VARIATION OF STABILITY PARAMETERS IN AN EXCHANGE FLOW

In general, the inviscid stability of a shear flow depends on g', δ, ΔU, R, η_ρ, y_1, y_2 and L. For an exchange flow with a given density difference, these parameters are a function of channel geometry and net barotropic flowrate. The effect of viscosity will be to stabilize wavenumbers of scales less than $O(\delta)$.

With zero net barotropic flow, the shear, ΔU, was found to be constant throughout the channel (Lawrence, 1990). The density and velocity interface thicknesses are functions only of the length of the channel. This can be seen by considering boundary layers on either side of the interface growing in opposite directions as shown in figure 8a. At a given location the shear layer thickness is equal to the sum of the individual boundary layers. Layer depths are determined by channel width and energy difference between the two layers. The Richardson number, J, is then constant for an exchange with no barotropic flow and variations in stability are due only to changes in layer depths.

For exchanges with net barotropic flow, shear is increasing in the direction of the net flow. As a result the shear interface thickness is no longer constant. This is illustrated in figure 8b. Moderate barotropic flow will result in slight variation in δ, with J decreasing downstream as ΔU increases. The range of J for a given stratification is limited by the variations in ΔU, δ and the net barotropic flowrate. For the flow in figure 4, measured values of J range from 0.5 at 10cm upstream (figure 4a) to 0.37, 25cm downstream (figure 4b). Further downstream, mixing due to the instabilities causes J to increase once again.

For strong barotropic flowrates, in addition to a growing shear layer and increasing ΔU, changes in the depth of the non-flowing layer from zero to $O(\delta)$ to $O(h)$ lead to varying scales for the instabilities. At the leading edge of a wedge flow, stability is dominated initially by viscosity and by the presence of the near boundary.

We have not yet determined the variation of the density interface offset, η_ρ, for exchange flows. If we follow the model having two growing boundary layers on either side of the density interface, then η_ρ will be such that the interface is at the location of zero convective velocity. By looking at the interface in a local frame of reference, however, it seems there is nothing to suggest that momentum should diffuse more readily into one layer than the other. The cases referred to here then only consider $\eta_\rho=0$.

THE LONG WAVE LIMIT AND LONG'S CRITERIA

Long's criteria for long wave stability can be obtained from hydraulic analysis of two homogeneous layers of arbitrary relative depths with constant velocity profiles. The flow is found to be unstable to infinitely long waves, i.e. imaginary characteristics exist, for $F_\Delta^2 > 1$.

For an unbounded shear flow, the stability boundary in the J-α plane, shown in figure 7a, intersects with the origin. When equidistant rigid boundaries are imposed, this intersection point moves up the J axis reflecting the destabilizing of long waves at low Richardson number. As the boundaries are brought in closer, this effect increases until the depth of the flow is $O(\delta)$, where the intersection point again moves down the axis as all wavelengths become stable. The location of this intersection point can be interpreted in terms of Long's criteria if we relate J to F_Δ^2. We can rewrite J as:

$$J = \frac{R}{2}\frac{1}{F_\Delta^2}\frac{\delta}{h}$$

Examining the limit of $\alpha \to 0$ numerically (figure 7b), we find that the location of the intersection point for $R=1$ and $\delta/h \ll 1$, is predicted by Long's criteria:

$$J_0 = \frac{1}{2}\frac{\delta}{h}$$

For shear flows with R>1, in the limit of $\alpha \to 0$ (figure 7d), the intersection is not predicted exactly by Long's criteria, due to the presence of the Holmboe mode. For $J = J_0$ and $\delta/h \ll 1$ the flow remains unstable to infinitely long Holmboe waves.

Using inviscid hydraulic theory, Lawrence (1990) obtained the result that exchange flows with no net barotropic flow are marginally stable to long waves, satisfying Long's criteria identically throughout the channel. From this analysis we find then that these exchange flows will be unstable to long Holmboe waves at the narrows since R>1, even though $F_\Delta^2 = 1$. The stability of this mode is dependent on the relative depth of the layers, since it is a function of phase speed, which depends on layer depths. As relative layer depths vary, the flow becomes more unstable, until the depth of one layer is $O(\delta)$.

CONCLUDING REMARKS

The inviscid linear analysis of the bounded tanh velocity and density profile shows that various modes of instabilities may exist. For the case of $\eta_p=0$ these include the Taylor and Holmboe modes. The mode that results at a selected location in an exchange flow then depends on the local Richardson number. For R=10, analysis shows that the most unstable mode for J<0.6 will be the Taylor mode. The effect of boundaries is significant at low wavenumbers, but for $\delta/h \ll 1$ the effect on the fastest growing waves will be small.

The stability analysis agrees well with experimental observations. Using flow parameters measured 15cm downstream of the narrowest section for the flow in figure 4, the shear layer model with R=10 predicts a most unstable wavelength of approximately 6cm, roughly the distance from core to core of the instabilities seen in figure 4b.

For exchange flows with no net barotropic flow and $\delta/h \ll 1$, J will be small throughout the channel and the instabilities will be within the Taylor mode region. For flows with a net barotropic component, J varies through the channel. For $\delta/h \ll 1$, the unstable mode will most likely be the Taylor mode in the downstream region, where $F_\Delta^2=1$. For some exchanges, it is possible that instabilities in the upstream region, where $F_\Delta^2<1$, may lie within the Holmboe region. The nature of these waves will require further investigation.

ACKNOWLEDGEMENTS

This work was supported by the National Science Foundation. We wish to thank J. Lasheras for helpful discussion as well as for the use of his computer. David Farmer gave us useful insight while observing one of our experiments.

REFERENCES

ARMI, L. & FARMER, D.M. 1986 Maximal two-layer exchange through a contraction with barotropic net flow. *J Fluid Mech.*, 164, 27

CAULFIELD, C.P. 1994 Multiple linear instability of layered stratified shear flow. *J. Fluid Mech.*, 258, 255

HAZEL, P. 1972 Numerical studies of the stability of inviscid stratified shear flows. *J. Fluid Mech.*, 51, 39

HOLMBOE, J 1962 On the behavior of symmetric waves in stratified shear layers. *Geofys. Publ.*, 24, 67

LAWRENCE, G.A. 1990 On the hydraulics of Boussinesq and non-Boussinesq two-layer flows. *J. Fluid Mech.*, 215, 457

LAWRENCE, G.A., LASHERAS, J.C. & BROWAND, F.K. 1987 Shear instabilities in stratified flow. *Proc. 3rd Int. Symposium on Stratified Flows* , 15

LONG, R.R., 1956 Long waves in a two fluid system. *J. Meteorology*, 13, 7

PRATT, L.J. 1986 Hydraulic control of sill flow with bottom friction. *J. Phys. Oceanogr.*, 16, 1970

TAYLOR, G.I. 1931 Effect of variation in density on the stability of superposed streams of fluid. *Proc. Roy. Soc. Lond.*, A **132**, 499.

Constricted flows from the Pacific to the Indian Ocean

by

Doron Nof[1]

Abstract

The question of how light water flows from one ocean to another through connecting passages is addressed with the aid of a nonlinear analytical model. The focus is on the Indonesian passages, which are too broad to be influenced by the so-called "hydraulic control" and yet too narrow to allow free flow through them. The "choked" flows through the passages are driven by the sea-level difference between the two adjacent oceans which, in turn, is determined by the wind stress.

We consider two rectangular oceanic basins (each of which contains a light upper layer overlying a slightly heavier deep lower layer) separated by a thin meridional wall. The wall contains a gap which is initially blocked by a gate; westward winds are allowed to blow over the two oceans creating western boundary currents and a sea-level difference between the basins. The conceptual gate is then removed and the resulting nonlinear flow from the intense western boundary currents in the Pacific basin to the sluggish eastern Indian basin is computed. The final steady state is taken to be analogous to the actual oceanic situation.

The analytical calculations are based on a simple wind-driven general circulation model and a nonlinear integrated momentum constraint. The momentum integral allows both determination of the resulting currents and computation of the mass flux through the gap. Two classes of choked solutions are constructed. One mode corresponds to a situation where the flow through the gap originates from the right hand side (looking upstream toward the inner Pacific basin from the center of the gap) and the other mode to a situation where the flow originates from the left hand side.

A simple *gap formula* which enables one to compute the transports via the gaps is derived. Numerical simulations (using an isopycnic model for the first mode) illustrate that, after an initial period of oscillations, the theoretically predicted steady state is indeed reached. Similarly, qualitative "kitchen-type" laboratory experiments with a stratified fluid on a rotating table demonstrate the establishment of the predicted currents.

It is suggested that the actual Indonesian throughflow is composed of both classes of flows, i.e., the throughflow corresponds to an exchange via *two* adjacent gaps rather than one gap. The first gap (the southern passage) corresponds to South Pacific water entering the passages whereas the second gap (the northern passage) corresponds to North Pacific water entering the passages.

---

[1] Department of Oceanography 3048 and the Geophysical Fluid Dynamics Institute, The Florida State University, Tallahassee, Florida 32306-3048 U.S.A.

1. Introduction

The exchange of water between oceans is an interesting fluid dynamics problem. Of particular importance is the exchange between the warm Pacific Ocean and the relatively cold Indian Ocean (via the Indonesian passages) because of its potentially unique relationship to El Niño and the "Great Global Conveyor Belt" (see Fig. 1). In this article the question of how much water flows through the Indonesian passages and the origin of these waters will be addressed theoretically using nonlinear dynamics.

Our approach is to consider two idealized oceans separated by a meridional wall that contains a gap (Fig. 2). The eastern (inner) basin corresponds to the Pacific and the western (outer) basin corresponds to the Indian Ocean. The actual connecting flow between the two oceans begins in the northern hemisphere where the Pacific water enters; it then crosses the equator and exits in the southern hemisphere (Fig. 1). Since we are mainly interested in the composition and origin of the throughflow, we shall consider most of the area within the Indonesian Archipelago to be a part of the Indian Ocean. Consequently, the location of our gap corresponds to the eastern edge of the Archipelago which is located in the northern hemisphere, several degrees north of the equator.

Both of our conceptual oceans consist of a thin upper layer (and a passive infinitely deep lower layer) and are subject to westward winds which raise the sea level along the western boundaries and depress the sea level along the eastern boundaries. Initially, a conceptual gate is placed across the upper layer in the gap (Fig. 2) so that the pressure difference between the basins is not causing any flow. In this initial state both basins contain a closed wind-driven circulation consisting of a western boundary current and an interior Sverdrup flow.

The sea-level difference can be easily computed from the familiar vertically integrated x momentum equation,

$$-fV = -\frac{g'}{2}\frac{\partial}{\partial x}(h^2) + \frac{\tau_s^{(x)}}{\rho_w} \quad , \tag{1.1}$$

where, f is the Coriolis parameter, V the (northward) vertically integrated transport (i.e., in the y direction), g' the reduced gravity ($g\,\Delta\rho/\rho_w$), h the upper layer depth, $\tau_s^{(x)}$ the surface wind stress in the x direction (i.e., eastward), and ρw is the water density. Eq. (1.1) holds both in the sluggish ocean interior away from the boundaries and in the intense western boundary current where the flow is geostrophic in the cross-stream direction.

Integration of (1.1) from the western to the eastern boundary gives the desired (square of the) sea-level difference,

$$-h_{we}^2 + h_{ea}^2 = \frac{2}{g'}\int_0^L \frac{\tau_s^{(x)}}{\rho_w}\,dx \quad , \tag{1.2}$$

where, the subscripts "we" and "ea" denote association with the western and eastern boundaries, L is the basin's length, and it has been assumed that there is no net transport within the cross-section (i.e., the boundary current transport cancels the Sverdrup transport).

The associated western boundary current speed can be estimated from the curl of the wind stress. To do so, consider the linearized y momentum equation,

$$fU = -\frac{g'}{2}\frac{\partial}{\partial y}(h^2) - RV \quad , \tag{1.3}$$

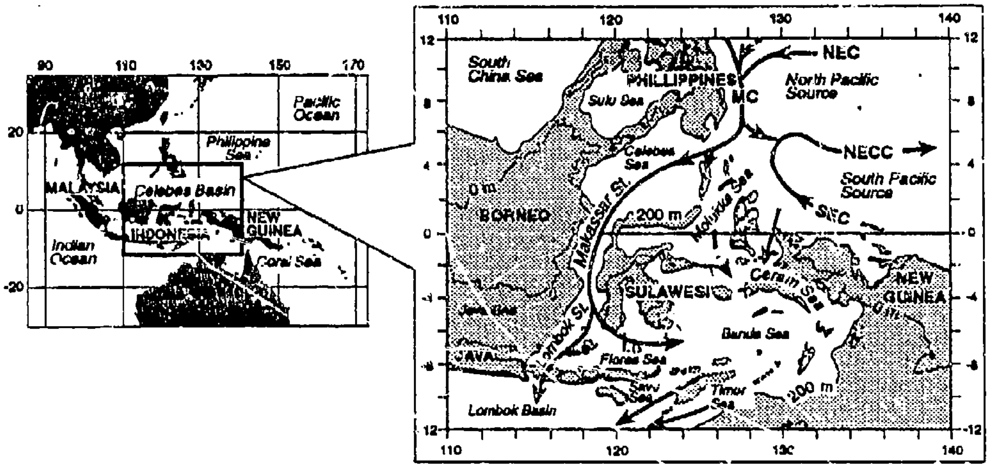

Fig. 1. The flow pattern in the Indonesian passages (adapted from Ffield and Gordon 1992). The North Equatorial current (NEC) and the resulting Mindanao Current (MC) approach the passages from the north, whereas the South Equatorial Current (SEC) approaches the passages from the south. The North Equatorial Counter Current (NECC) carries water to the east.

where R is the coefficient of interfacial friction (i.e., $R = \beta w$, where w is the width of the boundary current). Elimination of the pressure term between (1.1) and (1.3) gives,

$$\beta V = -\frac{1}{\rho_w}\frac{\partial \tau_s^{(x)}}{\partial y} + RV_x \quad ,$$

which, upon integrating across the basin and neglecting the transport along the eastern boundary, yields,

$$V_w = \frac{1}{\rho_w R}\int_0^L \frac{\partial \tau_s^{(x)}}{\partial y}\,dx \quad , \tag{1.3a}$$

where V_w is the vertically integrated meridional speed near the western wall. We shall see that, with this information, it is possible to determine the transport through the gap.

This article is organized as follows. The problem is formulated in Section 2, the constraints and solution are given in Section 3, and laboratory and numerical experiments are described in Section 4. The study is summarized in Section 5.

2. Formulation

Consider again the idealization shown in Fig. 2. As mentioned, the wind field is only important as far as setting up the pressure difference across the gap via the establishment of a western boundary current in the Pacific and a weak Sverdrup flow in the eastern Indian Ocean. The direct effect of the wind on the area in the immediate vicinity of the gap (i.e., the region within a few deformation radii away from the gap) is neglected due to its smallness compared to that associated with the entire Pacific and Indian Oceans. Namely, as far as the gap's nonlinear dynamics are concerned, we consider an inviscid model where both the Pacific and Indian basins extend to infinity.

With the above formulation, the complicated problem of exchange between two adjacent oceans with nonlinear circulation and wind stress above (Fig. 2) has been reduced to the inertial exchange of two oceans with no wind stress above. One of these oceans (the Indian) is stagnant and the other (the Pacific) contains a boundary current. All the variables prior to the removal of the gate are now known (in terms of the wind field) and the problem has been simplified to a highly nonlinear adjustment problem.

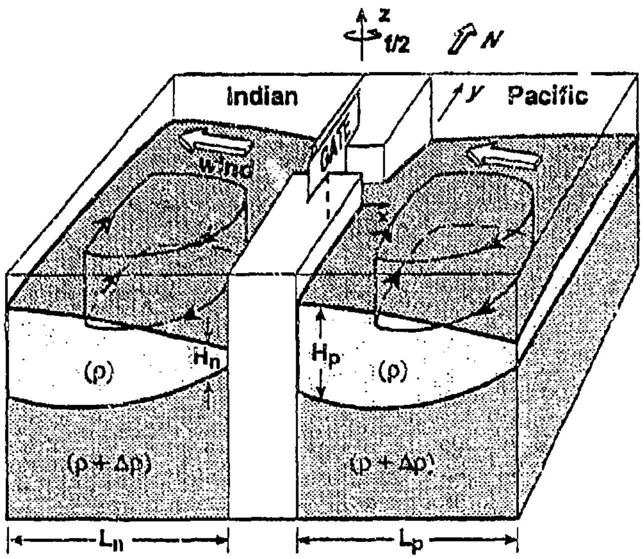

Fig. 2. A schematic three-dimensional view of the simplified conceptual model for the Indonesian throughflow. The two oceans are subject to westward winds which raise the sea level along the western boundary, create boundary currents, and depress the sea level along the eastern boundary. The Indonesian Seas are taken to be part of the (conceptual) Indian Ocean so that the gap corresponds to the easternmost passages (located in the northern hemisphere). The southern and northern panels of the boxes correspond to regions with a zero wind-stress curl rather than solid walls. An imaginary gate separates initially the two basins. The steady adjusted state reached after the removal of the gate is taken to be analogous to the average oceanic situation.

At $t = 0$ the gate is lifted and, subsequently, light fluid starts penetrating from the Pacific to the Indian Ocean. After some time of $O(f^{-1})$ a steady state will be reached and it is this state that we shall focus on. It is assumed here that information generated in the gap area can reach all the upstream and downstream regions via either Kelvin waves, Rossby waves, or eddies interacting with the walls [i.e., anticyclones and cyclones which translate due to the so-called image effect (Shi and Nof 1993, 1994) and can transmit information to the left or right (looking off-shore)].

We shall see that the exchange process has two modes (Fig. 3). The first corresponds to a situation where $H_p > H_n$ (i.e., the off-wall depth in the Pacific H_p is greater than the depth in the Indian H_n) and the western boundary current near wall depth in the Pacific is also greater than H_n. Under such conditions, the throughflow originates in the South Pacific and penetrates into the northern part of the Indian Ocean. The second mode, on the other hand, corresponds to a situation where H_p is *smaller* than H_n ($H_p < H_n$) but the western boundary current near wall depth in the Pacific is still larger than H_n. Under such conditions, the throughflow originates in the North Pacific and penetrates into the southern part of the Indian Ocean. It will be later argued that the actual throughflow corresponds to a combination of these two modes.

3. The integrated momentum constraints for a stratified rotating fluid

As mentioned, exact nonlinear solutions will be obtained using the integrated momentum. Consider a region S bounded by the dashed line for either mode one or mode two (Fig. 3). Multiplication of the y momentum equation by h and integration over S gives,

$$\iint_S \left(hu\frac{\partial v}{\partial x} + hv\frac{\partial v}{\partial y}\right)dxdy + \iint_S f_0 uh\, dxdy + \frac{g'}{2}\iint_S \frac{\partial}{\partial y}(h^2)\, dxdy = 0 \quad ,$$

which, by using the continuity equation and streamfunction ψ (defined by $\partial\psi/\partial y = -uh$; $\partial\psi/\partial x = vh$) can be reduced to,

$$\iint_S \left[\frac{\partial}{\partial x}(huv) + \frac{\partial}{\partial y}(hv^2)\right]dxdy - \iint_S f_0 \frac{\partial\psi}{\partial y}\, dxdy + \frac{g'}{2}\iint_S \frac{\partial(h^2)}{\partial y}\, dxdy = 0 \quad . \tag{3.2}$$

Application of Stokes' theorem to (3.2) gives,

$$\oint_\phi huv\, dy - \oint_\phi \left(hv^2 + \frac{g'h^2}{2} - f_0\,\psi\right)dx = 0 \quad , \tag{3.3}$$

where ϕ is the boundary of S.

By defining ψ such that along the free bounding streamline $\psi = g'H_n^2/2f_0$, and taking into account that away from the gap the flow is geostrophic, one ultimately finds,,

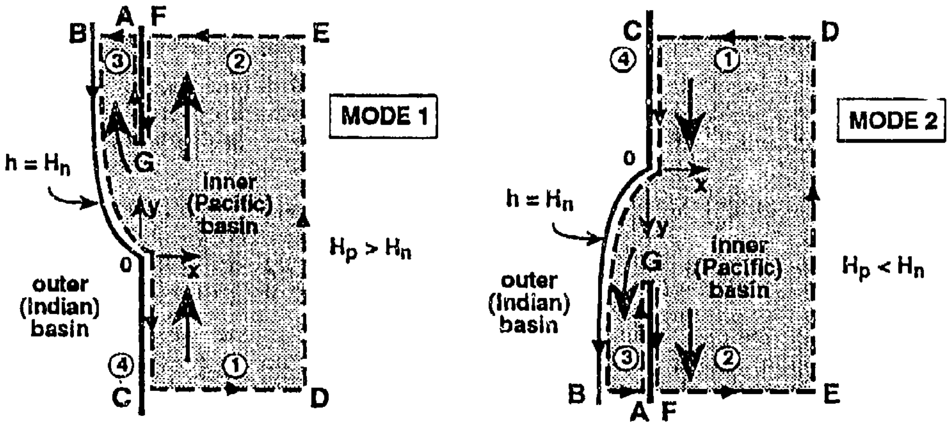

Fig. 3. A diagram of the integration area for modes 1 and 2. Mode 1 corresponds to water originating on the right hand side of the inner basin (looking toward the inner basin from the center of the gap) and mode 2 corresponds to water originating on the left. Mode 1 corresponds to a Pacific offshore depth (H_p) that is greater than the Indian offshore depth (H_n) and is relatively simple. Mode 2, on the other hand, corresponds to $H_p < H_n$ and is harder to understand because one gets the initial impression that water should flow from the outer to the inner basin rather than from the inner to the outer basin. This is not the case because of the (negative) western boundary current which raises the sea level along the wall. In the outer basin, the integration area is bounded by the wall, the free streamline ($h = H_n$, $\psi = 0$) and a section across region 3. In the inner basin, the integration area extends well beyond the expected decay region (i.e., DE is located several deformation radii away from the walls). It is bounded by sections across region 2 and 1, the walls and the line DE which is parallel to the walls.

$$\boxed{\int_0^{\infty} h_1 v_1^2\, dx + \int_{\infty}^{0} h_2 v_2^2\, dx + \int_0^{-\gamma_3} h_3 v_3^2\, dx = 0 \quad .} \qquad (3.4)$$

It is important to note that, even though the (uniform) Coriolis parameter f_0 does not explicitly appear in this integrated momentum constraint, there is an important fundamental difference between the rotating and the nonrotating constraint. The difference is that in the nonrotating case ($f_0 = 0$) the pressure term $g'h^2/2$ *does not drop* out of the equation (because f_0 is not present) so that instead of (3.5) one obtains the familiar relationship,

$$\int_0^{\infty} \left(h_1 v_1^2 + \frac{g'h_1^2}{2}\right) dx + \int_{\infty}^{0} \left(h_2 v_2^2 + \frac{g'h_2^2}{2}\right) dx + \int_0^{-\gamma_3} \left(h_3 v_3^2 + \frac{g'h_3^2}{2}\right) dx = 0 \ ; \quad f_0 = 0 .$$

Using the constraint mentioned above and other known constraints such a Bernoulli, potential vorticity and linear momentum, the transports are ultimately found to be,

$$\begin{aligned} T_1 &= \frac{g'(H_p^2 - H_n^2)}{2f_0} \\ T_2 &= \frac{g'H_p^2}{2f_0} \left\{ 1 - \left[1 - (1 - H_n/H_p) e^{\vartheta_{iw} + H_n/H_p - 1}\right]^2 \right\} \qquad (3.5) \\ T_3 &= \frac{g'H_p^2}{2f_0} \left\{ \left[1 - (1 - H_n/H_p) e^{\vartheta_{iw} + H_n/H_p - 1}\right]^2 - (H_n/H_p)^2 \right\} , \end{aligned}$$

4. Laboratory and numerical experiments

To examine the validity of the foregoing theory a set of qualitative "kitchen-type" laboratory experiments and a set of numerical experiments were performed for a special case of Mode 1 where there is no initial current in the inner basin and no light water in the outer basin (i.e., $H_n = 0$).

For this special case the analytically predicted transport which approaches the gap (from the right) is $g'H^2/2f_0$. The nonlinear transport through the gap is $0.3996\, g'H^2/2f_0$ implying that about 60% of the transport never enters the gap. The laboratory experiments show in a qualitative manner that indeed such a current system is clearly established (Fig. 4).

In addition, *quantitative* process-oriented numerical experiments using the Bleck and Boudra reduced gravity isopycnic model agree very well with the theoretical predictions (Fig. 5). For this numerical experiment we used a closed inner basin of 1200 × 3400 km and a closed outer basin of 3400 × 3400 km. The upper layer undisturbed depth in the inner basin was 150 m, the "reduced gravity" was 10^{-2} m sec^{-2}, and the Coriolis parameter was 2.5×10^{-5} sec^{-1}. These give a Rossby radius of about 50 km and we used a gap that is 250 km broad. The horizontal eddy viscosity was 2×10^2 m^2 sec^{-1}, the grid spacing was 6 km (in both the x and the y direction) and the time step was 360 sec. The boundaries were slippery and, as is frequently done, the vorticity was taken to be zero next to the walls. It is important to note that the adjustment process involves a considerable amount of energy loss. In the analytical model, the loss is removed by the radiation of waves but the loss cannot be removed in the numerical model. This causes the oscillations that are present in the runs.

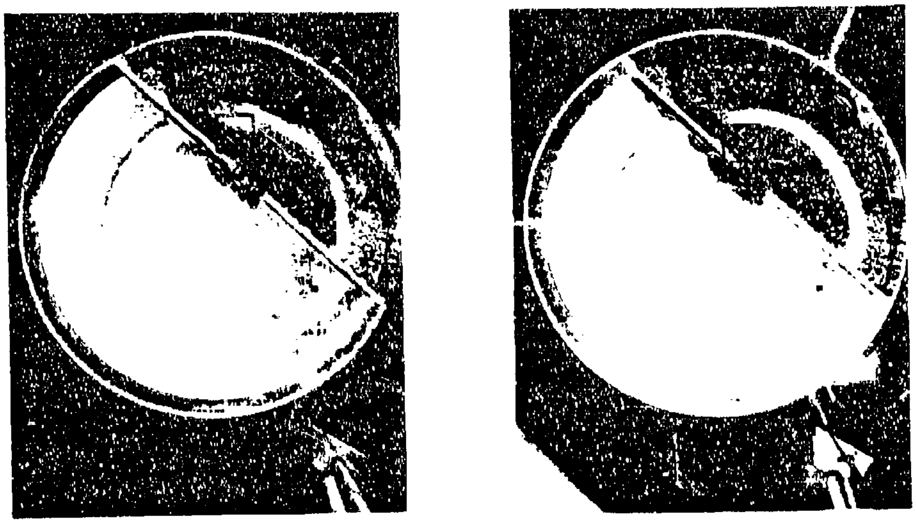

[a] t=0 [b] t= 2.4 sec

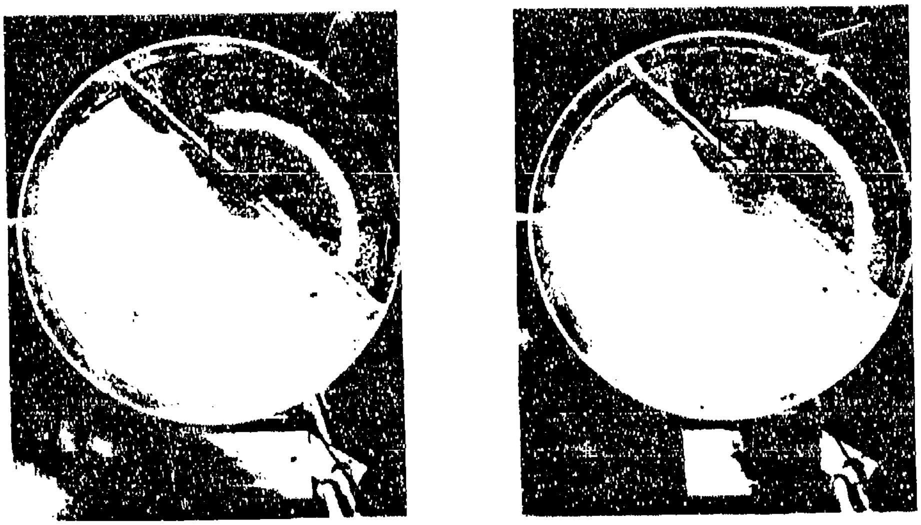

[c] t= 7.2 sec [d] t=9.0 sec

Fig. 4. Subsequent photographs of a typical experiment for the one gap problem. There is no initial current in the (dyed) inner basin and no upper layer in the outer basin. The dyed light fluid starts penetrating into the outer basin when the gate is lifted. The white ring is an (unavoidable) reflection of the fluorescent light shining from above. At $t = 0$ the white ring is still distorted due to gravity waves generated by the removal of the gate. Such waves disperse and change into Kelvin waves within a few seconds. It is clear that, as the theory predicts, a counter-clockwise flow pattern is established in the inner basin even though the basin was initially at rest. This can be easily seen by following the clusters of aluminum particles surrounded by the marked (small and large) circles, and the marked open square. Physical constants: $f = 1.26\ \mathrm{sec}^{-1}$; $\Delta\rho/\rho = 0.01$.

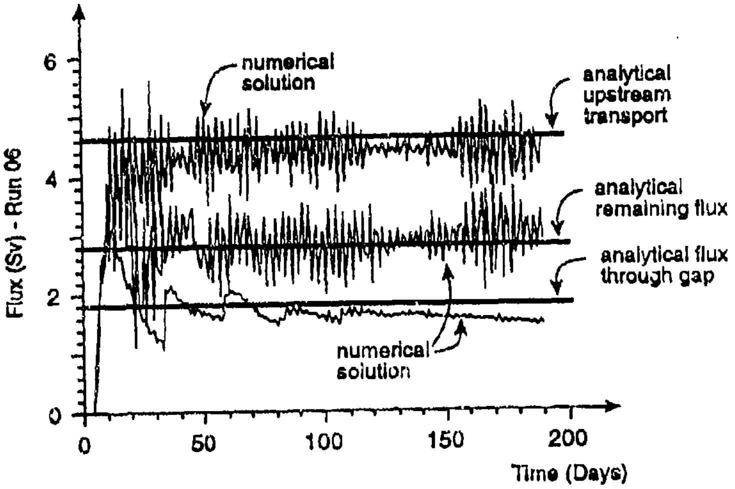

Fig. 5. A comparison between the analytical and numerical solution for the one gap problem with no initial boundary current. The numerically calculated transports in the various regions are shown as a function of time. The model used is the $1^1/2$ layer Bleck and Boudra isopycnic model (see text for details). The initial delay associated with the establishment of the currents reflects the time that it took for the information to reach the various regions in the model. Note that, given the simplicity of the analytical model and the lack of a mechanism to remove excess energy from the numerical model, the agreement is excellent. This indicates that neither friction nor the time dependent oscillations are essential for understanding the processes in question.

5. Summary

Our findings are:

1. An exact nonlinear analytical solution to the exchange process (Fig. 1) can be constructed. In terms of the undisturbed upper layer depths in the two adjacent oceans (set up by the wind field), the transports are given by (4.1). The transports can also be directly related to the wind stress and the curl of the wind stress via (1.2) and (1.3a). Detailed computations are given in Nof (1994a,b).

2. The above relationships are associated with two modes of exchange (Fig. 3). The first mode corresponds to water originating on the right hand side (looking toward the inner basin from the center of the gap) whereas the second corresponds to water originating on the left. Both laboratory (Fig. 4) and numerical experiments (Fig. 5) are in excellent agreement with the theoretical results.

3. It is suggested that the actual Indonesian throughflow is composed of flows through two (or more) gaps situated in the easternmost portion of the passages (Fig. 6). The southern gap corresponds to the so-called mode 1 and is associated with South Pacific water entering the passages. The northern gap, on the other hand, corresponds to mode 2 which is associated with North Pacific water entering the passages. Our nonlinear formulas suggest that 11 Sv (1 Sv = 10^6 m^3/sec) enter the passages from the North Pacific (mode 2) and 1 Sv from the South Pacific (mode 1) combining to a total of 12 Sv.

This new (inviscid) nonlinear theory differs markedly from the linear theory which suggests that most of the throughflow originates in the South Pacific rather than the North Pacific. Our inviscid nonlinear theory agrees with the observations (which also suggest a predominantly North Pacific origin) without invoking an additional physical process. Linear

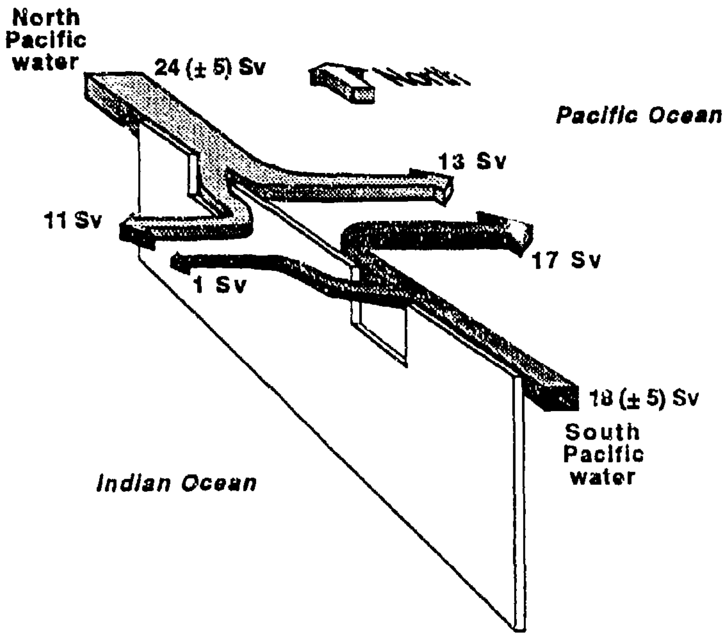

Fig. 6. A schematic three-dimensional view of the theoretically proposed circulation via two adjacent gaps in the easternmost part of the Indonesian Archipelago (compare to Fig. 1).

theory, on the other hand, must invoke intense mixing activity to explain the presence of North Pacific water within the throughflow. Readers who desire more detailed information are referred to Nof (1994a,b).

6. Acknowledgments

This study was supported by the National Science Foundation (NSF) under contracts OCE 9012114 and OCE 9102025, and the Office of Naval Research (ONR) under contract N00014-89-J-1606.

References

Ffield, A. and A. L. Gordon (1992): Vertical Mixing in the Indonesian Thermocline. *J. Phys. Oceanogr., 22*: 184-195.

Nof, D. (1994): Choked flows and interbasin exchange. *J. Marine Res.*, submitted.

Nof, D. (1994): Choked flows from the Pacific to the Indian Ocean. *J. Phys.Oceanogr.*, submitted.

Shi, C. and D. Nof (1993): The splitting of eddies along boundaries. *J.Mar.Res., 51*: 771-795.

Shi, C. and D. Nof (1994): The destruction of lenses and generation of wodons. *J. Phys. Oceanogr.*, in press.

Exchange Flow Through a Channel with an Underwater Sill

Zhiwei Zhu and Gregory A. Lawrence

Dept. of Civil Engineering, University of British Columbia,
Vancouver, BC, Canada, V6T 1Z4

ABSTRACT

We have performed theoretical and laboratory studies of the exchange of two fluids of slightly different density through a straight channel with an underwater sill. This exchange process is controlled at locations where the flow is internally critical, called controls. The position of these controls is shifted by frictional and non-hydrostatic forces. When internal hydraulic theory is extended to incorporate these effects the comparison with experimental results is much improved. Both Kelvin-Helmholtz and Holmboe instabilities are observed in the experiments. Measurements of the wave length and speed of the Holmboe instabilities agree with the theoretical predictions of Lawrence *et al.* (1991).

1. INTRODUCTION

This paper considers steady, two-layer exchange flow over a two-dimensional obstacle in a narrow channel (Fig. 1). The study was motivated in part by the exchange of Mediterranean and Atlantic water through the Strait of Gibraltar, and by the exchange flow through the Burlington ship canal connecting the heavily polluted Hamilton Harbor with Lake Ontario. Exchange flows were first studied by Stommel & Farmer (1953), and later by many researchers, including Armi and Farmer (1986), and Farmer and Armi (1986) assuming inviscid, hydrostatic flow.

Frictional effects may be important in exchange flows. Dalziel (1988) found that the inviscid predictions always over-estimate the flow rate. Bormans and Garrett (1989) included interfacial and bottom friction to study the role of friction in the exchange flow through the Strait of Gibraltar. Friction was found to shift the control at the sill eastwards. Cheung and Lawrence (1991) studied the exchange flow through a channel of constant depth, and obtained estimates of the interfacial frictional factor from their experimental measurements.

Non-hydrostatic pressures caused by streamline curvature above the obstacle can be of crucial importance in two-layer flows (Lawrence, 1993). Shen (1992) relaxed the hydrostatic equation in his study of two-layer flow over a very small sill. Forbes (1989) numerically solved the full non-linear equations for a semi-circular sill using conformal mapping. In the present study we place less stringent restrictions on the size and shape of the sill.

For two-layer exchange flows strong shear at the interface generates hydrodynamic instabilities, most notably Kelvin-Helmholtz and Holmboe instabilities. For small values of the bulk Richardson number, J, linear stability analysis predicts a Kelvin-Helmholtz instability with zero phase speed with respect to the mean flow. For sufficiently large values of J, however, there may be two unstable modes traveling in opposite directions. Holmboe (1962) studied the special case where both modes have equal growth rate and equal but opposite phase speeds. In previous experimental studies it has proven difficult to obtain clear realizations of Holmboe's instability, see Lawrence *et al.* (1991).

In the present paper we extend internal hydraulic theory to account for frictional and non-hydrostatic effects, and we present results of experiments that provide perhaps the best realizations of the Holmboe instability to date.

2. EXPERIMENTS

Experiments were conducted in a channel of dimensions 1200 × 300 × 100 (mm) (length × height × width) connecting two larger reservoirs containing water of slightly different density, see Fig. 1. A sill of the form $h(x) = h_m \cos^2(x/L)$ (for $|x / L| \leq \pi / 2$) was placed in the left side of the channel, where $h_m = 80$ mm, and L = 160 mm. The cosine squared function was chosen to have the relatively low values of obstacle slope and curvature. The driving buoyancy force was obtained by dissolving salt in the right reservoir. The position of the interface and its deformation by flow instabilities were visualized by dissolving a fluorescent dye into the lower layer and illuminating it with a thin sheet of laser light. Flow velocities were determined using recently developed image processing techniques, (Stevens & Coates, 1994), which allowed us to obtain an instantaneous record of the velocity field.

The experiments were started by removing the gate used to separate the two water bodies. After an initial start-up phase of about two-minutes a maximal-exchange (see Armi & Farmer, 1986) with one control at the sill and the other at the far (right) end of the channel was established. After about 4 - 8 minutes the exit control became submerged leaving a sub-maximal exchange with a single control near the crest of the sill. We are primarily concerned with the period of maximal-exchange during which the flow was quasi-steady.

One of the important features of the flow is the formation of Kelvin-Helmholtz and Holmboe instabilities at the interface between the two layers. The K-H waves grow to the left of the sill crest, where the shear is strong due to the high velocity of the lower layer; the Holmboe waves develop in the right part of the channel, where the shear is not as strong. Only positive Holmboe waves are observed initially. These positive waves are generated near the sill crest, move to the right and cusp into the upper layer. Eventually disturbances form at the right end of the channel and negative, left moving, waves are also observed. Fig. 1(c) is a sequence of photos showing the motion of both the positive and negative waves. For different shapes of the sill and different flow velocities, the nature of the instabilities change. The Holmboe instabilities are discussed further in Section 4.

3. EXTENDED INTERNAL HYDRAULIC THEORY

Internal hydraulic theory can be extended to include the frictional and non-hydrostatic effects for the two-layer exchange flow shown in Fig. 1(b). The following notation is adopted: u is the horizontal component of velocity, y is the layer thickness, q is the flow rate per unit channel width, p is the pressure, ρ is the density, g is the gravitational acceleration, and $z = Y_0$, $h + y_2$, h are respectively the positions for the free surface, the interface, and the bottom. The subscripts i=1,2 refer to the upper and lower layer, respectively.

We start by considering inviscid, incompressible, and irrotational flow with immiscible, layered (constant density within each layer), and Boussinesq ($\varepsilon = (\rho_2-\rho_1)/\rho_2 << 1$) approximations. Given the Boussinesq approximation, the "rigid lid" free surface assumption is valid. We also assume the sill is smooth, and the flow is shallow; i.e., $\sigma = (H/L)^2 << 1$, where H and L are the vertical and horizontal characteristic length, respectively. Note that the sill in our study can be of finite size, $h/H = 0(1)$. This is less restrictive than Shen's requirement that $h/H = 0(\sigma^2)$.

Assuming the horizontal velocity is constant across the layer depth, the vertical velocity can be obtained from the continuity equation. Both the pressure, and the internal energy (Bernoulli constant) have second order of accuracy $0(\sigma^2)$ after averaging across the layer depth. This averaged internal energy remains constant throughout the channel if frictional effects are ignored. A brief outline is given below, detailed derivations will be presented in a subsequent paper.

Assuming $$u_i(x) = \frac{q_i}{y_i(x)} \qquad (i=1,2) \tag{1}$$

We write the internal energy in the form:

$$EI = EI_H + \Delta EI_{cv} \tag{2}$$

where the hydrostatic component is given by:

$$EI_H = h + y_2 + \frac{1}{2g'}\left(\frac{q_2^2}{y_2^2} - \frac{q_1^2}{y_1^2}\right) \tag{3}$$

and the non-hydrostatic effects of flow curvature are given by:

$$\Delta EI_{cv} = \frac{q_2^2}{g'}\left(\frac{y_{2xx}}{3y_2} + \frac{h_{xx}}{2y_2} + \frac{h_x^2}{2y_2^2} - \frac{y_{2x}^2}{6y_2^2}\right) + \frac{q_1^2}{g'}\left(\frac{y_{2xx} + h_{xx}}{3y_1} + \frac{(y_{2x} + h_x)^2}{6y_1^2}\right) \tag{4}$$

where $g' = \varepsilon g$, is the reduced gravitational acceleration. EI should remains constant throughout the channel when frictional effects are not important. Thus, (2) can be solved for y_2 (the lower layer thickness) with the non-hydrostatic effects accounted for.

When frictional effects are also important, we follow classical hydraulic analysis (see Henderson, 1966), and introduce a frictional slope, S_f, where:

$$\frac{dEI}{dx} = S_f \tag{5}$$

Using (2), and letting $S_c = d(\Delta EI_{cv}) / dx$, (5) becomes:

$$\frac{d(y_2 + h)}{dx} = \frac{S_f - S_o - S_c}{1 - G^2} \tag{6}$$

where $F_i^2 = q_i^2 / g' y_i^3$, and $G^2 = F_1^2 + F_2^2$. The topographic slope $S_0 = F_2^2 \dfrac{dh}{dx}$ for the straight channel, the slope due to flow curvature $S_c = d(\Delta EI_{cv}) / dx$, and the friction slope

$$S_f = \frac{1}{g' y_2}\left\{ f_w \frac{q_2^2}{y_2^2} + f_i\left(\frac{q_1}{y_1} + \frac{q_2}{y_2}\right)^2 \right\} + \frac{1}{g' y_1} f_i \left(\frac{q_1}{y_1} + \frac{q_2}{y_2}\right)^2 \tag{7}$$

where f_i and f_w are the interfacial and bottom frictional factor. Solving (5) or (6) for exchange flow with both the frictional and non-hydrostatic effects included is much more complicated than solving for the frictionless and hydrostatic flow. The procedure used for solving the latter will be briefly reviewed first.

For the frictionless hydrostatic flow, the internal energy remains constant throughout the channel. As S_f and S_c both become zero, the flow should be critical at the point where $S_0 = 0$, i.e., at the sill crest. For maximal-exchange flow in a channel of constant width, the flow is also critical at the right end of the channel. Therefore, three equations, $G^2 = 1$ at the sill crest and the right exit, and the constant internal energy can be used to solve for three unknowns, q ($q_1 = q_2 = q$ for our experiments), y_2 at the sill crest and at the right exit of the channel.

For frictional hydrostatic flow, the internal energy is changed by friction and the control position is shifted from the sill crest. The bottom frictional factor can be obtained theoretically from the boundary layer theory. The interfacial frictional factor is determined indirectly by matching the theoretical and measured flow rates.

For the frictional non-hydrostatic flow, we may either use the iteration method starting from the frictional hydrostatic solution, or solve (5) as a boundary value problem. Fig. 2(a) shows the hydrostatic and non-hydrostatic frictional predictions of interfacial positions compared with the experimental measurements. Fig. 2(b) shows the change of the internal energy along the channel. The internal energy is changed significantly by friction. The inclusion of the non-hydrostatic effects is important in the sill region as it raises the internal energy. The extended theory provides excellent agreement with the experimental results, with the bottom and interfacial frictional factors estimated to be about 0.01.

4. INTERFACIAL INSTABILITIES

The stability of a two-dimensional, inviscid, stratified shear flow depends upon the vertical variation of density $\rho(z)$ and of the mean horizontal velocity $U(z)$. For the piecewise linear velocity and density profiles of Fig. 3, the stability diagrams can be obtained, see Lawrence *et al.* (1991). Four dimensionless variables are used: the Richardson number $J = g' h / \Delta U^2$; the wave number $\alpha = kh$, where $k = 2\pi/\lambda$, and λ is the wavelength; the relative displacement of the velocity and density profiles d/h; and the wave speed $c = (c^{\pm} - \bar{U}) / (\Delta U / 2)$, where $c^{\pm}$ are the wave speeds for the positive and negative waves. The Reynolds' and Keulegan numbers may also be important: $Re = \Delta U h / \nu$, and $K = \Delta U^3 / (g' \nu)$.

From the stability diagrams, we know that K-H waves only occur for the symmetric (zero displacement, $d/h = 0$) case with $J < 0.07$, while the Holmboe instabilities can occur for any larger J, and also for the asymmetric cases ($d/h \neq 0$). Fig. 1(c) shows the movements of the Holmboe waves observed in our experiments. In this flow $J = 0.3$, and the mean velocity is about 0.5 cm/sec. Thus both waves are traveling at about the same speed with respect to the mean flow, satisfying the requirements for Holmboe's (1962) instability.

The wave length and wave velocity, for both the positive and negative waves, can be obtained from measurements of variations in the interface elevation. Fig. 4 shows a typical wave characteristics plot, with the intensity representing the relative height of the interface. The positive and negative waves appear as oblique bands of dark and light. Wave speed and wave length can be easily obtained from the slope and spacing of the bands. These measurements can be used to compare with the theoretical predictions. A comparison for one experiment is listed in Table 1. The flow has: $\bar{U}$=0.6 cm/sec, ΔU=4.0 cm/sec, h=3.0 cm, g'=1.6 cm/sec^2, and $d/h = 0$. Thus J is about 0.3, with Reynolds number Re = 1200, and Keulegan number K = 3500. We can obtain the theoretical predictions for the flow, knowing that the wave which has the largest growth rate is the one most likely to be observed:

Table 1. Comparison of the Predicted and Measured Wave Characteristics

		Theory	Measurement
Wave Length	λ^+ (cm)	10.5	10
	λ^- (cm)	10.5	11
Wave Velocity	c^+ (cm/sec)	1.6	1.5 — 1.8
	c^- (cm/sec)	- 0.4	- 0.5 — - 0.6

Table 1 shows that the linear stability theory accurately predicts the wave length and speed. The theory can also explain further experimental observations. During the early stages of the experiment, the amount of the displacement of the interfaces is relatively large ($d/h > 0.1$) and the negative waves are suppressed. Later in the experiment the magnitude of the shift decreases, and we start to see both the positive and negative waves. The reasons for changes in the displacement of the velocity and density interfaces are not fully understood.

5. CONCLUSIONS

Exchange flows through a narrow channel with a sill are affected by both frictional and non-hydrostatic effects. Friction effects are important along the entire length of the channel, while the non-hydrostatic effects are important in the vicinity of the sill. An extended hydraulic theory including both the frictional and non-hydrostatic effects gives very good agreement with the experimental results. Both Kelvin-Helmholtz and Holmboe instabilities are observed on the interface. The wave lengths and phase velocities of the Holmboe instabilities compare well with the theoretical predictions of Lawrence *et al.* (1991).

ACKNOWLEDGMENTS

Funding from the Canadian Natural Sciences and Engineering Research Council (NSERC) in the form of the first author's graduate fellowship is gratefully acknowledged.

REFERENCES

Armi, L. and Farmer, D.M. 1986 Maximal two-layer exchange through a contraction with barotropic net flow, *J. Fluid Mech.*, Vol. **164**: 27.

Bormans, M. and Garrett C. 1989 The effects of Nonrectangular Cross Section, Friction, and Barotropic Fluctuations *J. Phys. Oceanography*. Vol.19, No.10

Cheung, E.A. and Lawrence, G.A. 1991 Two-layer exchange flow through a contraction with frictional effects, Proc. of the 1991 Conference of the CSCE, Vancouver.

Dalziel, S.B. 1988 Two-layer hydraulics: Maximal exchange flows. Ph.D. thesis, DAMTP, Univ. of Cambridge. Cambridge, England.

Farmer, D.M. and Armi, L. 1986. Maximal two-layer exchange over a sill and through the combination of a sill and contraction with barotropic flow. *J. Fluid Mech.* **164**: 53.

Forbes, L.K. 1989 Two-layer critical flow over a semi-circular obstruction. J. Eng. Math. **23**, 325

Henderson, F.M. 1966 *Open Channel Flow*, MacMillan

Holmboe, J. 1962 On the behavior of symmetric waves in stratified shear layers, *Geofysiske Publikasjoner*, **24**: 67

Lawrence, G.A. 1993 The hydraulics of steady two-layer flow over a fixed obstacle. J. Fluid Mech., **254**: 605.

Lawrence, G.A., Browand, F.K. & Redekopp, L.G. 1991 The Stability of a Sheared Density Interface, *Physics of Fluids A* 3(10), 2360-2370

Shen, S.S. 1992 Forced solitary waves and hydraulic falls in two-layer flows. *J. Fluid Mech.* **234**: 583

Stevens, C.L. and Coates, M.J. Application of a maximised cross correlation technique for resolving velocity fields in laboratory experiments. *J. Hyd. Res.*, in press, 1994.

Stommel, H. and Farmer, H.G. 1953 Control of salinity in and estuary by a transition. *J. Mar. Res.*. **12**: 13-20

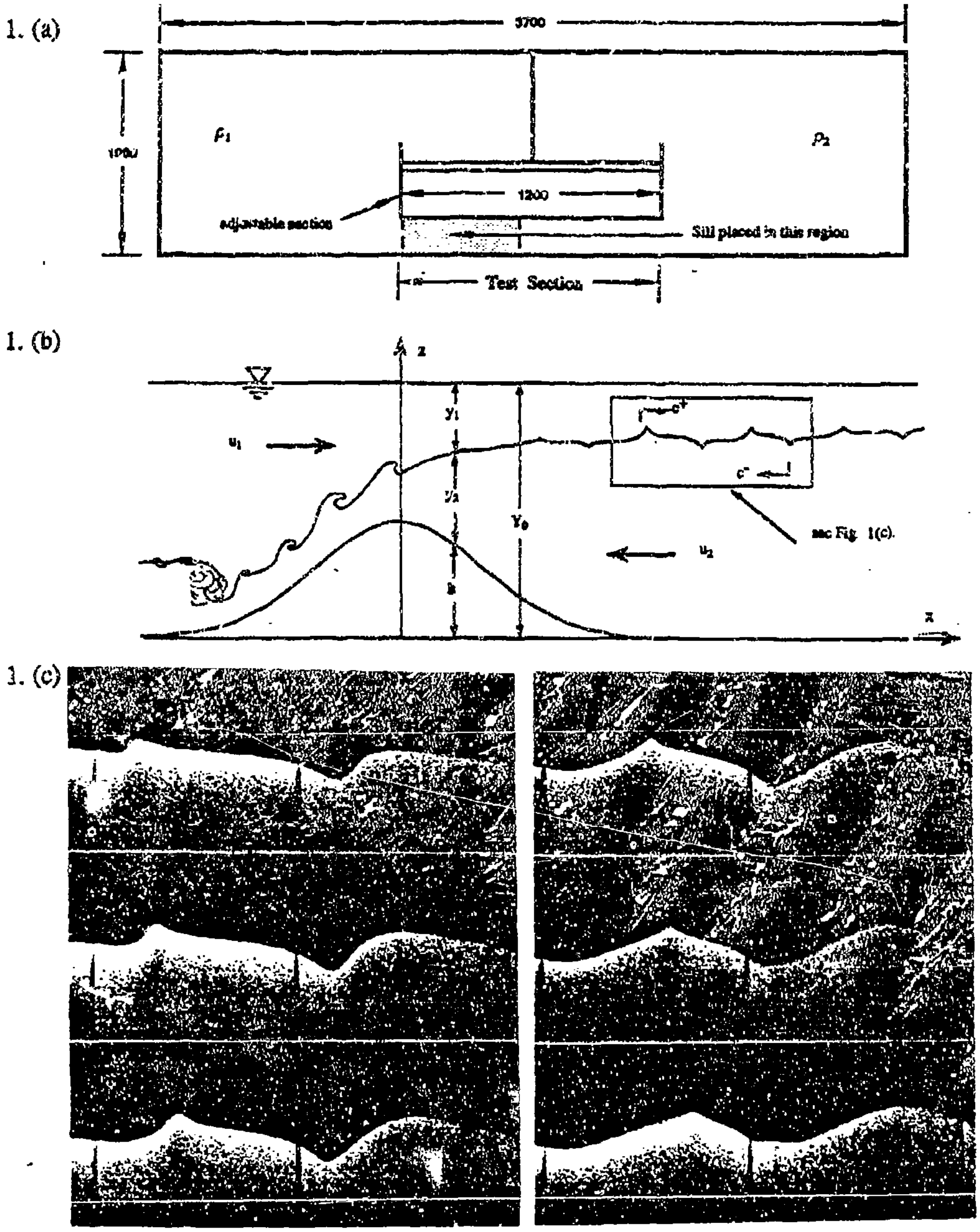

Fig. 1. (a) Plan view of the experimental setup. All dimensions are in millimeters. The sill is placed in the left part of the channel, shown as the dotted area. (b) Definition diagram of two-layer exchange flow over a sill, with both K-H and Holmboe waves. (c) Sequence of photographs showing Holmboe waves: The upper layer flow is from left to right, the lower layer from right to left. The flow has a mean velocity of about 0.5 cm/sec. Grids are 5 cm apart. Photos are taken at 0.5 second interval.

2. (a)

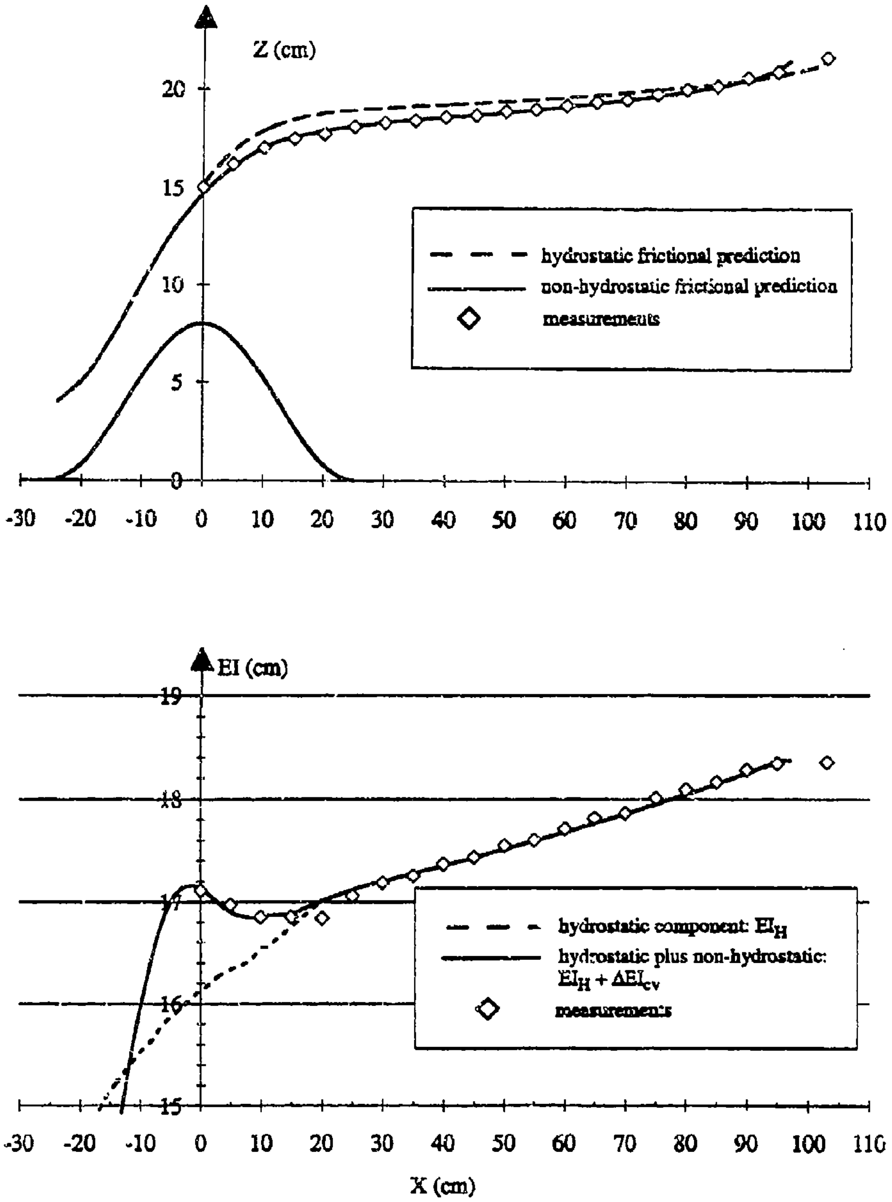

Fig. 2. (a) Comparison of the prediction and measurements of the interface position, with f_w=0.010, f_i = 0.011. (b) Comparison of the prediction and measurements of the internal energy.

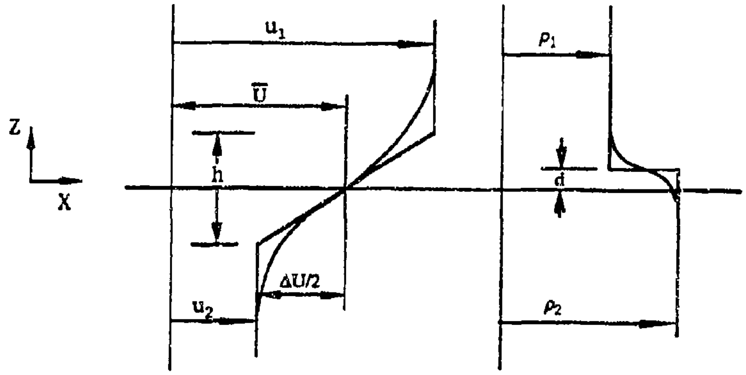

Fig. 3. Definition diagram for the piecewise linear velocity and density profiles.

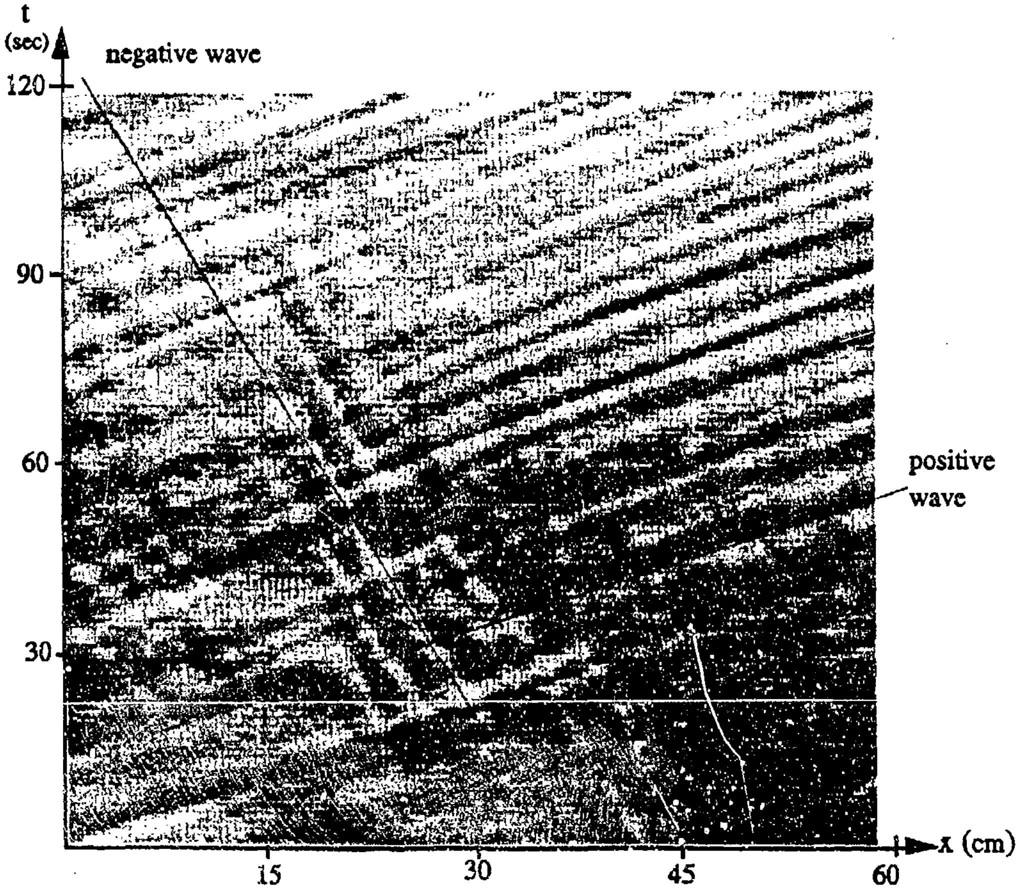

Fig. 4. Wave characteristics: the characteristics for the positive and negative waves appear as oblique bands of dark and light. The intensity represents the relative height of the interface (darker for the higher height).

Laboratory Experiments on Two-layer Exchange Through Long Straits

V.S.Maderich, A.I. Kulik, V.V. Oleksiuk

Institute of Hydromechanics of the Ukrainian Academy of Sciences
8/4, Zheliabov st., Kiev 252057, Ukraine

Abstract

An experimental study was carried out to investigate water exchange through the narrow strait with two-layer flow structure and net barotropic transport. The facility consisted the tank that was divided on the two basins connected by a shallow and narrow rectangular strait. One basin was heated at the bottom. Another basin was cooled at the top. The velocity and temperature measurements were made using the hydrogen-bubble technique and the temperature probes, respectively. The results of measurements were given for the short, intermediate, long strait in dependence on magnitude of the net barotropic transport. The experimental data were compared with the model calculations based on principle of the maximal exchange.

1 Introduction

The extremely important role of straits in forming hydrologic and ecological conditions in inland seas is well-known. The water exchange through strait depends on the adjacent seas water balance and hydrologic structure as well as the strait topography. Because of this the strait models remain to be the necessary part of the model of the inland seas climate evolution (see e.g., Nof, 1979; Maderich and Efroimson, 1986). Detailed hydrodynamic description of straits is difficult because many factors and processes should be consider – strait topography, momentum and mass transfer between layers influenced by turbulence and unsteady effects (tides and surges). So, development of simple one–dimensional or even simpler bulk (null–dimensional) models of sea straits is very important for hydrodynamic modeling and pre diction of environmental processes in seas.

There are many straits with two–layer structure of currents (e.g., the Bosphorus, Dardanelles, Gibraltar, Bab–el–Mandeb, Hormuz etc.). The internal hydraulics of a steady frictionless two–layer flow through channel was the most extensively studied at recent decade. The concept that was developed in such flows was maximal exchange (Armi and Farmer,1986; Farmer and Armi, 1986). The problem of the water exchange through long strait with friction (Assaf and Hecht, 1974; Anati et al., 1976; Oğuz et al., 1990) yet is less well understood.

In this paper, we present the results of an experimental study of water exchange through the narrow strait with two-layer flow structure and net barotropic transport. The simple model based on concept of maximal exchange is considered in Sect.2. The experimental arrangement is described in Sect.3. We used a channel with geometry similar to experiments of Anati et al., (1977) but with different measurement device. The results of experiments are given in Sect.4.

2 Model

Following Maderich and Efroimson (1986,1990) we consider a simple bulk model for a two-layer stationary water exchange through strait. The shallow and narrow strait connects two basins maintained at different density ρ_1 and ρ_2 respectively ($\rho_1 \leq \rho_2$) and net barotropic discharge Q_f from basin 1 to basin 2 ($Q_f \geq 0$). The rectangular strait is length L, constant depth D and width A. The mean along strait depths of upper layer and bottom layer are D_1, D_2, respectively

$$D = D_1 + D_2. \tag{1}$$

The volume discharges in the upper (Q_1) and bottom (Q_2) relates to the mean velocity in layers u_1, u_2 by $Q_1 = AD_1u_1$, $Q_2 = AD_2u_2$. The water balance of the system is

$$Q_1 + Q_2 = Q_f. \tag{2}$$

It is common practice in such cases to use models based on a so called "hydraulic control" principle, which requires that the internal composite Froude number G be equal to a critical value G_s. At small density difference ($(\rho_2 - \rho_1)/\rho_2 \ll 1$)

$$G^2 = F_1^2 + F_2^2 = G_s^2. \tag{3}$$

Here

$$F_1^2 = \frac{Q_1^2}{g'D_1^3A^2}, \quad F_2^2 = \frac{Q_2^2}{g'D_2^3A^2}, \tag{4}$$

$g' = g(\rho_2 - \rho_1)/\rho_2$, g is gravity acceleration. In the short straits $G_s \equiv 1$ whereas in the long straits with predominated friction effects parameter $G_s < 1$.

The system of equations (1)–(3) contains four variables besides G_s and g'. To close the system we used the condition of extreme water exchange in the strait, i.e., we supposed such layer thicknesses that the flow in the bottom layer is maximal

$$\frac{\partial Q_2}{\partial D_2} = 0. \tag{5}$$

The second extremum ($Q_2 = 0$) is achieved at the end of the range of possible values. Flows Q_1 and Q_2 are connected by (2), so Eq. (5) involves the extremum either for the upper flow. Taking a derivative of Eq. (3) with respect to D_2 and using (5), we have simple condition of maximal exchange

$$\frac{Q_1^2}{Q_2^2} = \frac{D_1^4}{D_2^4}. \tag{6}$$

From Eqs. (3) and (6) taking into account Eqs. (1) and (2) we obtain explicit formulae connecting thicknesses of layers and discharges with some morphometric and hydraulic parameters of the strait and with independent components of basins water balance

$$D_1 = \frac{1}{2}D(1 + rG_s^{-1}), \tag{7}$$

$$D_2 = \frac{1}{2}D(1 - rG_s^{-1}), \tag{8}$$

$$Q_1 = \frac{1}{4}G_s Q_m (1 + rG_s^{-1})^2, \tag{9}$$

$$Q_2 = -\frac{1}{4}G_s Q_m (1 - rG_s^{-1})^2, \tag{10}$$

where $Q_m = S(g'D)^{1/2}, S = AD$ is a cross section of the strait, $r = Q_f/Q_m$.

Following to approach of Maderich and Efroimson (1990) we accept a condition similar to (3) for a long strait either, but the averaged along the strait the Froude number G_s should now be less than 1. Generally G_s depends on the strait geometry and possibly on another external parameters. It is easy matter to derive explicit formula for G_s in particular case $Q_f = 0$. For a long sea strait the main balance in a bottom layer is a balance between baroclinic pressure gradient and bottom turbulent friction. In the laminar laboratory analog of this strait with $A \ll D$ the pressure gradients balance side wall friction in the layers except the ends of strait

$$\frac{\partial}{\partial x}g\zeta = \nu\frac{\partial^2 u_1}{\partial y^2}, \tag{11}$$

$$\frac{\partial}{\partial x}(g\zeta + g'\eta) = \nu\frac{\partial^2 u_2}{\partial y^2}. \tag{12}$$

The coordinates x and y are taken along and across the strait respectively. Here ζ is the surface elevation, η is the interface deviation, ν is the kinematic viscosity. Instantaneous local thicknesses of the layers H_1 and H_2 are defined by

$$H_1 = D_1 - \eta + \zeta, \quad H_2 = D_2 + \eta. \tag{13}$$

Integrating (11),(12) across the channel and excluding ζ we obtain

$$\frac{\partial H_2}{\partial x} = -\frac{12\nu}{A^3 g'}\frac{HQ_2 - H_2 Q_f}{(H - H_2)H_2}. \tag{14}$$

A using of the critical Froude condition at each ends of strait with $Q_f = 0$

$$\frac{Q_1^2}{A^2 b_s (D_1 - \eta)^3} + \frac{Q_2^2}{A^2 b_s (D_2 + \eta)^3} = 1. \tag{15}$$

is evident (Assaf and Hecht, 1974; Anati et al., 1977). Integrating (14) from 0 to L and eliminating Q_1, Q_2 in (15) we have:

$$G_s = \frac{\delta}{\gamma}(1 - \delta^2), \tag{16}$$

$$\delta^2(1 - \frac{1}{3}\delta^2)^2(1 + 3\delta^2) = \gamma^2(1 - \delta^2)^3. \tag{17}$$

Here $\delta = \eta(L) - \eta(0)$, $\gamma = 12\nu L/(A^2\sqrt{g'D})$ is friction parameter. For a short strait $\gamma \ll 1$, for an intermediate strait $\gamma \approx 1$ and for a long strait $\gamma \gg 1$. Some approaches when $Q_f \neq 0$ were considered Maderich and Efroimson (1990).

3 Experimental arrangement

The experiments were conducted in a rectangular Plexiglass tank, 200 cm long, 17 cm wide and 40 cm deep (Fig.1). The tank was divided on two basins. These basins were connected by shallow and narrow rectangular strait placed along front wall. The two-layer water exchange was maintained by heating of small basin (length 33 cm) by electric heater placed near the bottom and by the cooling of large basin by the tap water cooler. The cooling box was situated at the surface of the large basin.

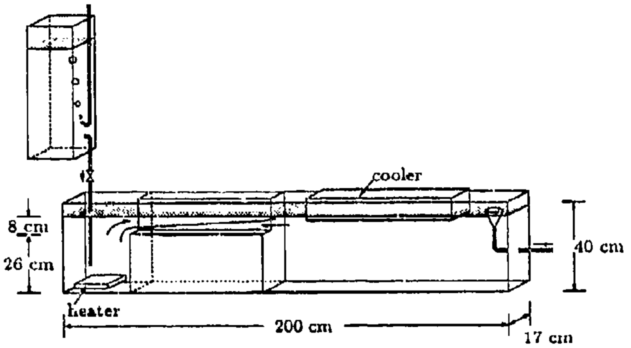

Fig.1. Schematic drawing of laboratory set-up

The three configuration of strait were used: short, intermediate and long. The depth of strait $D = 8$ cm was not changed. The short strait was modelled by plate with thickness $L = 2$ cm. The intermediate strait was length $L = 60.5$ cm and width $A = 2.0$ cm. The long strait was the same length but $A = 0.9$ cm. The strait and small basin were insulated. A barotropic flow was directed from heated basin to cooled one. The constant flow rate was provided by using of the constant pressure vessel. The outflow from large basin took place through the funnel at the surface. The rate of outlow from tank was calculated with help of measuring vessel.

The temperature distribution in the strait was observed by the vertical profiling in the ten sections with a thermistor probe attached to the traversing platform. The platform can be moved along strait. The velocity measurements in ten sections along strait were made using hydrogen–bubble technique (Matsui et al., 1979). The bubble generator was made by stretching a stainless wire (0.0027 cm in diameter) in a vertical section of the channel. A proper electrical pulse was applied between the wire as a cathod and plate on the bottom of channel as an anode. To diminish the buoyancy effects at low speeds we selected the electric parameters for generation of the small bubbles (pulse width 2 - 6 ms., voltage of 40 - 70 V). The pulse interval was 0.33 - 0.66 s. The wires also were attached to a small amplitude vibrator to enhance conditions of the bubbles tailing. As a result of these measures the velocity of the bubble rising was less 0.1 cm/s. The flash lamp with condenser was used as a light source.

4 Results

A series of experiments was run for the short ($\gamma \approx 0.1$), intermediate ($\gamma \approx 0.6$) and long ($\gamma \approx 3.0$) straits. The barotropic flux Q_f was varied systematically in the range: $0 \leq Q_f \leq 13.5$ cm^{3}sec^{-1} for short strait, $0 \leq Q_f \leq 6.4$ cm^{3}sec^{-1} for intermediate strait, and $0 \leq Q_f \leq 3.2$ cm^{3}sec^{-1} for long strait. In the experiments the buoyancy b_s typically lay between 1.20 and 1.28 cmsec^{-2}.

The longitudional distribution of the velocity and temperature in the long strait for $Q_f = 0$ are shown in Fig. 2. The temperature and current profiles consisted of two homogeneous layers with a thin thermocline and shear layer. The heights of the thermocline and zero speed changed almost linearly along strait. But the layer of maximal temperature gradient was shifted downward relatively to the position of the zero speed. This flow pattern was quite similar to Fig.10 Anati *et al.* (1977). The presence of the net barotropic flow did not change qualitatively the picture of currents for moderate Q_f as seen from Fig. 3. The interface between homogeneous layer was shifted downward but it shape and slope had not undergone the marked change. The diminishing of the velocity in bottom layer causes the transformation of temperature field at the cost of heat conductivity. The effect of "locking" strait for bottom undercurrent can be seen at $Q_f > 3.2$ cm^{3}sec^{-1}.

The comparison between the measured thickness of bottom layer and the local Froude number

$$G_L = \frac{Q_1^2}{A^2 b_s H_1^3} + \frac{Q_2^2}{A^2 b_s H_2^3}. \tag{18}$$

and computed ones from model is given in Fig.4. The figure shows a reasonable fit the model to the data. The model however overestimates the slope of interface. The most discrepancy between the predicted and experimental values G_L at the ends of the strait is due to the inertial effects that have been neglected by the viscous model and errors in the determination of zero speed points at the ends of the strait.

In Fig.5 the measured depth of the upper layer was plotted against the net barotropic flow. The straight line $G_s = 1$ corresponds to the model of maximal water exchange (see Eq. (7)). The dependence of $2D_1/D - 1$ on Q_f/Q_m for the intermediate and long straights also is the linear function, i.e. the G_s is an approximtely constant. The value $G_s = 0.42$ for long strait, that is in a good accordance with the model prediction $G_s = 0.41$ at $Q_f = 0$. What this means is parameter G_s in a first approximation depends only on the strait morphometry.

The relation between the discharge Q_1 and and averaged depth of the upper layer D_1 is given in Fig.6. Accordingly to Eqs. (7), (9) the function $(Q_1/Q_m)^{1/2}$ is depends linearly on D_1/D for constant G_s. The data is consistent with this relation but measured disharges were less than predicted with G_s calculated from Fig.5.

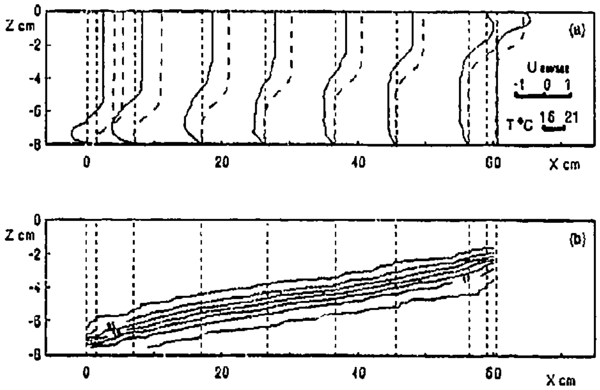

Fig.2 The temperature and velocity distributions in the long strait at $Q_f = 0$ and $b_s = 1.23$ cm/sec^2. (a) Velocity (solid) and temperature (dashed) profiles. (b) A longitudinal temperature section.

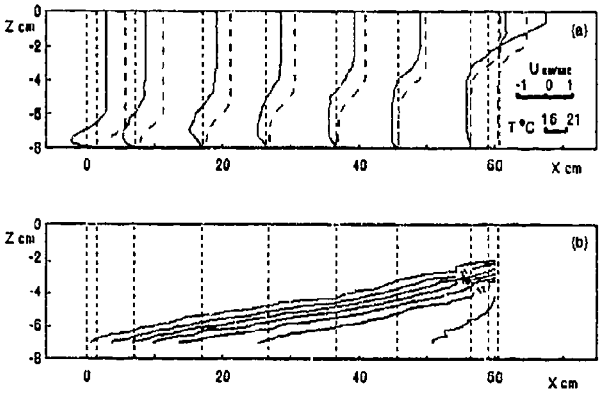

Fig.3 The temperature and velocity distributions in the long strait at $Q_f = 1.78$ cm^3/sec and $b_s = 1.23$ cm/sec^2. (a) Velocity (solid) and temperature (dashed) profiles. (b) A longitudinal temperature section.

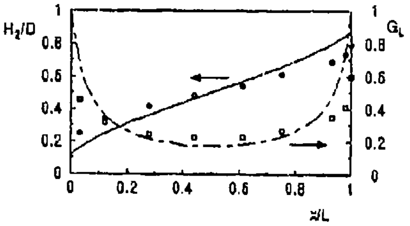

Fig.4 The measured thickness of bottom layer H_2/D (circles) and local Froude number G_L (squares) at $Q_f = 0$ and $b_s = 1.25$ cm/sec^2. Solid lines correspond to computed distributions H_2/D and G_L.

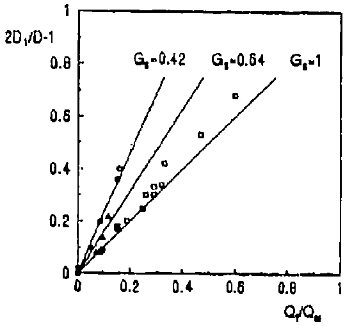

Fig.5 The measured depth of upper layer versus net barotropic flow in the short strait (squares), intermediate strait (triangles) and long strait (circles).

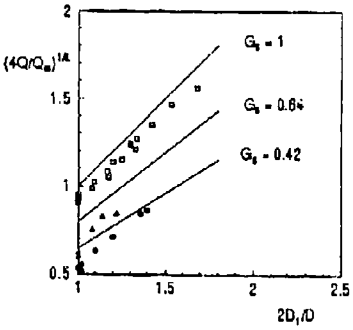

Fig.6 The discharge in the upper layer Q_1 versus averaged depth of upper layer D_1. The symbols as in Fig.5.

5 Conclusions

The present study has produced the following results:

(1) The simple one-parameter bulk model of water exchange in the long narrow laminar strait with net barotropic flow was proposed. This model was based on concept of the maximal exchange.

(2) The results of the laboratory experiments on the water exchange in the short, intermediate and long straits with net barotropic flow were consistent with model but the measured baroclinic flows were weaker than predicted by the model.

(3) The single parameter of model G_s in a first approximation was function of the strait morphometry only that gives possibility to use this model with empirical value of G_s for the parametrization of water exchange through straits in the models of general circulation.

Acknowledgments

This research was partially supported by IAEA under Research Contract N73341/RB.

References

Anati D. A., Assaf G., Thompson R. O. R. Y. Laboratory models of sea straits. *J. Fluid Mech., 81*, 341-352, 1977.

Armi L., Farmer D.M. Maximal two-layer exchange through a contraction with barotropic net flow. *J.Fluid Mech., 164*, 27-52, 1986.

Assaf G., Hecht A. Sea straits: a dynamical model. *Deep-Sea Res., 21*, 947-958, 1974.

Farmer D.M., Armi L. Maximal two-layer exchange over a sill and through the combination of a sill and contraction with barotropic flow. *J.Fluid Mech., 164*, 53-76, 1986.

Maderich V. S., Efroimson V.O. A simple model of a sea with the strait. *Oceanology, 26*, 403-408.

Maderich V. S., Efroimson V. O. On the theory of water exchange through straits. *Oceanology, 30*, 567-574, 1990.

Matsui T., Nagata H., Yasuda H. Some remarks on hydrogen bubble technique for low speed water flows. in *Flow visualisation*, ed. T. Asanuma, pp.209-214, Hemisphere Publ., 1979.

Nof D. On man-induced variations in the circulation of the Mediterranean sea. *Tellus, 31*, 558-564, 1979.

Oğuz T., Özsoy E., Latif M.A., Sur H.I. Ünluata Ü. Modeling of hydraulically controlled exchange flow in the Bosphorus strait. *J. Phys. Oceanogr. 20*, 945-965, 1990.

Hydraulic Control Analysis of an Integrated Gravity Current Model

GUTTORM ALENDAL

Nansen Environmental and Remote Sensing Center, Bergen, Norway

A steady state gravity current model which incorporates entrainment and friction is used to describe large scale gravity currents and channel flows. When the model includes pressure effects from varying current thickness, critical points occur when the current velocity is equal to the phase velocity of waves on the interface. Some solutions have the possibility to pass from super- to sub-critical flow, or vice versa. These solutions pass through a hydraulic control point and the objective is to analyse the behaviour of the solutions in the vicinity of such points.

Using a phase space in which the hydraulic control points occur as equilibrium points, performing standard Taylor expansion to the first order, the result is a system of autonomous differential equations with constant coefficients that can describe the behaviour of the solutions for different parameter regimes near a hydraulic control point. If an equilibrium point in phase space represents a saddle point it is distinguished between three different solution classes; solutions that approach the critical velocity but never reach it, solutions that reach the critical velocity and obtain infinitely large derivative, and the solutions (one from subcritical and one from supercritical) that reach the critical velocity exactly in the equilibrium point.

INTRODUCTION AND PROBLEM DEFINITION

Flows driven by gravity/buoyancy occur in many contexts both in the nature and in the laboratory, see Simpson (1987) for examples. One approach that is often used to model these events are integrated or bulk models, i.e., models which do not treat the interior fluctuations explicitly but model the variables averaged over a cross-section of the current (see for instance Smith, 1975; Killworth, 1977).

The steady state gravity current model is derived rigorously in Alendal *et al.* (1994) and since the main objective is to study the solutions in the neighbourhood of the hydraulic control point, the model will be stripped for the influence from salinity, temperature and density variations. Further, the current is assumed to flow in a channel with given width and inclination as function of the along stream direction, and rotational effects are neglected. The remaining model equations then read: (subscript x means $\partial/\partial x$)

$$(\rho\,A\,u)_x = \rho_e E\,w\,u, \tag{1}$$

$$\left(\rho\,A\,u^2\right)_x = A\,g(\rho-\rho_e)(\sin\theta - h_x) - C_D\,\rho\,w\,u^2. \tag{2}$$

These equations are the local steady state continuity and momentum equations averaged over a cross-section, with normal vector in the along stream direction x, and with area A. The quantities ρ, u, w, and h are, respectively, mean density and velocity over the cross-section, and the width and thickness of the flow. The density of the ambient fluid is denoted with ρ_e. The right-hand side of Eq. (1) represents entrainment of ambient water which is assumed to have no momentum. The entrainment parameter, E, is usually assumed to be dependent on the Richardson number, $Ri = g'h\cos\theta u^{-2}$, of the flow (Christodoulou, 1986). The first term on the r.h.s. of Eq. (2) is the gravity/buoyancy force while the last term represents the drag with the drag coefficient C_D which may also be dependent on the Richardson number (Alendal *et al.*, 1994). In this study both the entrainment parameter and the drag coefficient is, for the sake of simplicity, assumed constant.

The input of energy in the model is due to gravity/buoyancy while friction and entrainment of ambient water with no velocity represents sink of energy. The h_x term in the gravity/buoyancy term occurs as a result of incorporating the effect from variation in current thickness on the pressure.

The area of the cross-section is proportional to the width and the thickness of the current

$$A = \alpha w h \tag{3}$$

where α is a proportionality parameter. Assuming that the width of the current (channel) is given through constraints the system is closed and solvable.

Using Eq. (3) and substituting $v = u^2$ into the system gives

$$\frac{1}{2}hv_x + v\,h_x = \Gamma v - hvf(x) \tag{4}$$

$$\frac{1}{2}hv_x + hh_x = g'h\sin\theta - C_d v \tag{5}$$

where $g' = g(\rho - \rho_e)\rho^{-1}$ is the reduced gravity and

$$\Gamma = \frac{\rho_e}{\rho}\frac{E}{\alpha}, \qquad f(x) = \frac{w_x}{w}, \qquad C_d = (C_D + \Gamma)/\alpha. \tag{6}$$

If the inclination angle, θ, is dependent on x and the entrainment is neglected, $\Gamma = 0$, the model is similar, although differing in notation, to the one used by Pratt (1986) to study flows over an obstacle. Further, the model is also similar to the more general model of Wajsowicz (1993) with special choices for the friction and entrainment functions.

The system has critical points when $u^2 = g'h$, the phase-velocity of waves on the interface between the flow and ambient water. When the velocity of the flow is larger than the phase-velocity the flow is said to be super-critical, while for smaller velocities the current is sub-critical. Solutions passing from sub- to super-critical or vice versa are called hydraulically controlled and the points where these flows goes from one regime to the other are the hydraulic control points (Turner, 1973).

Nondimensionalising using

$$v = v_0\,\overline{v}, \quad h = h_0\,\overline{h}, \quad x = L\,\chi \tag{7}$$

with $h_0 = L$ and $v_0 = u_0^2 = gh_0$, where L is a characteristic length of the flow, gives the nondimensionalised system:

$$\frac{1}{2}\overline{h}\overline{v}_\chi + \overline{v}\,\overline{h}_\chi = \Gamma\overline{v} - \overline{h}\overline{v}f(\chi) \tag{8}$$

$$\frac{1}{2}\overline{h}\overline{v}_\chi + \overline{h}\,\overline{h}_\chi = \overline{h}\sin\theta - C_d\overline{v} \tag{9}$$

Subtracting Eq. (8) from Eq. (9) gives

$$\left(\overline{h} - \overline{v}\right)\overline{h}_\chi = \overline{h}\sin\theta - (C_d + \Gamma)\,\overline{v} + \overline{h}\overline{v}f(\chi). \tag{10}$$

If the r.h.s. of Eq. (10) do not approach zero as $\overline{v} \to \overline{h}$ the derivative of $\overline{h}$ will approach infinity (positive or negative), or in other words the hydraulic control point is given when

$$\overline{v} = \overline{h}, \quad \overline{h}\sin\theta - (C_d + \Gamma)\,\overline{v} + \overline{h}\overline{v}f(\chi) = 0 \tag{11}$$

simultaneously. Notice that if the inclination angle and the channel width is constant, $\theta = constant$ and $f(\chi) = 0$, a critical slope, $\sin\theta = C + \Gamma$, is defined for which the flow may freely go from sub- to super-critical flow, or vice versa. On the other hand if the slope is not critical there is no hydraulic control solutions for the steady state model. To analyse the solutions in the vicinity of hydraulic control points a phase space and a new independent variable is introduced which transform the singularity to an equilibrium point.

THE GENERAL ANALYSIS METHOD

Here follows a brief summary of the phase space analysis method. An exhaustive outline of the method may be found in Bilicki *et al.* (1987) where it has been used on two-phase flows. In Øien and Alendal (1993) the method was used on a model describing the heating and acceleration of the solar wind.

The method can be used on dynamical systems of the general form

$$\tilde{\mathcal{A}}(\sigma)\cdot\frac{d}{d\chi}\sigma = \mathbf{b}(\sigma,\chi), \tag{12}$$

where $\tilde{\mathcal{A}}$ is a $k \times k$ matrix and $\mathbf{b}$ and σ are k-dimensional vectors. Notice that the coefficient matrix $\tilde{\mathcal{A}}$ is not dependent on the independent variable χ. The system has unique solutions in regions where $\Delta \equiv det(\tilde{\mathcal{A}}) \neq 0$ and by use of Cramers rule (see for instance Anton (1984)):

$$\frac{d\sigma_i}{d\chi} = \frac{N_i(\sigma,\chi)}{\Delta(\sigma)}, \; i = 1, 2, \ldots, k, \tag{13}$$

where $N_i(\sigma,\chi)$ is the determinant of the matrix resulting from replacing column i in $\tilde{\mathcal{A}}$ with the vector $\mathbf{b}$. Introducing the new independent variable (η) such that

$$\frac{d\chi}{d\eta} = \Delta(\sigma), \tag{14}$$

it follows that

$$\frac{d\sigma_i}{d\eta} = \frac{d\sigma_i}{d\chi}\frac{d\chi}{d\eta} = \frac{N_i(\sigma,z)}{\Delta(\sigma)}\Delta(\sigma) = N_i(\sigma,z), \; i = 1, 2, \ldots, k, \tag{15}$$

giving an autonomous system with $k + 1$ differential equations:

$$\frac{dx}{d\eta} = \Delta(\sigma), \qquad \frac{d\sigma_i}{d\eta} = N_i(\sigma,\chi), \qquad i = 1, 2, \ldots, k. \tag{16}$$

Points in the $k+1$ dimensional phase space, denoted $\tau = (\sigma, \chi)$, where $\Delta \neq 0$ are called regular points and only one solution pass through these points. Points where $\Delta = 0$ are called critical points and defines a k-dimensional manifold in phase-space which separates the space into a sub- and a super-critical region. The normal vector to the manifold, called the critical manifold, is perpendicular to the χ-direction since Δ is not dependent on χ. A theorem in Bilicki *et al.* (1987) says that if $\Delta = 0$ and $N_j = 0$ for any j, then all the other N_i's are zero simultaneously. This gives the following classification of points in phase space:

1.Regular points when $\Delta \neq 0$,
2.Turning points when $\Delta = 0$ and $N_i \neq 0$ for all N_i,
3.Singular points when $\Delta = 0$ and $N_i = 0$ for all N_i.

The theorem states that each of the manifolds defined by $N_i = 0, i = 1, \ldots, k$, all intersects with each other simultaneously as they intersects with the critical manifold $\Delta = 0$. This means that the physically acceptable solutions that pass through the critical manifold passes in the manifold defined by the intersection between the critical manifold and the manifolds defined by the $N_i^{\prime}s$. Solutions going through a turning point in phase-space are not physically acceptable solutions since at least one of the dependent variables gain infinite derivative there.

To study the solutions in the vicinity of a singular point, $\tau = \tau^{**}$, Taylor series expansion in $\tau = \tau^{**} + \delta\tau$ is performed. Truncated after the linear term this gives a linear system with constant coefficients

$$\frac{d}{d\chi}\delta\tau = \delta\tau \cdot \nabla \mathbf{V}(\tau^{**}) = \delta\tau \cdot \tilde{\mathcal{J}}, \tag{17}$$

where $\mathbf{V}^T = [\Delta, N_1, \ldots, N_k]$ is the vector holding the dependent variables for the autonomous system given in Eq. (16), and

$$\tilde{\mathcal{J}} = \nabla \mathbf{V}(\tau^{**}) = \begin{pmatrix} 0 & \left.\frac{\partial \Delta}{\partial \sigma_1}\right|_{\tau^{**}} & \cdots & \left.\frac{\partial \Delta}{\partial \sigma_k}\right|_{\tau^{**}} \\ \left.\frac{\partial N_1}{\partial \chi}\right|_{\tau^{**}} & \left.\frac{\partial N_1}{\partial \sigma_1}\right|_{\tau^{**}} & \cdots & \left.\frac{\partial N_1}{\partial \sigma_k}\right|_{\tau^{**}} \\ \vdots & \vdots & & \vdots \\ \left.\frac{\partial N_k}{\partial \chi}\right|_{\tau^{**}} & \left.\frac{\partial N_k}{\partial \sigma_1}\right|_{\tau^{**}} & \cdots & \left.\frac{\partial N_k}{\partial \sigma_k}\right|_{\tau^{**}} \end{pmatrix} \tag{18}$$

is the Jacobian matrix evaluated at $\tau = \tau^{**}$.

Another theorem from Bilicki *et al.* (1987) assures that $\lambda = 0$ is an eigenvalue of the Jacobian matrix defined in Eq. (18) with multiplicity $(k-1)$. The remaining two nonzero eigenvalues with their eigenvectors control the behaviour of the solutions of the linearised system in the neighbourhood of the singular point. The eigenvalues of $\tilde{\mathcal{J}}$ are the roots of the characteristic polynomial on the form

$$\lambda^{(k-1)}\left(\lambda^2 - p\,\lambda + q\right) = 0. \tag{19}$$

and the classification of the equilibrium/singular points is now given (Jordan and Smith, 1987):

$$\begin{array}{lll} \text{Saddle point} & q < 0, & \\ \text{Node} & q > 0, & p^2 - 4q > 0, \\ \text{Spiral or Center} & q > 0, & p^2 - 4q < 0. \end{array} \tag{20}$$

If a singular point is a center or a focus there is no possibility to find any solutions passing through the point and further all solutions will eventually approach a turning point. These solutions are not physically acceptable unless the outlet of the channel is reached before the turning point is reached. For nodes all solutions passes through the singular point.

For saddle points the eigenvectors connected to the two non-zero eigenvalues span a two dimensional subspace in the $(k+1)$ dimensional phase space. Solutions passing through the singular point will, in the neighbourhood of the point, be directed along the eigenvectors. If these solutions where to be calculated numerically the algorithm is as follows; Since the singular point is a saddle point we know that the two nonzero eigenvalues are real, distinct and with different signs. The corresponding eigenvectors, $\mathbf{e}_i$, $i = 1, 2$, define four directions in the phase-space (remember that if $\mathbf{e}_i$ is an eigenvector then so is $-\mathbf{e}_i$). Taking one small step from the singularity in one of the four directions the ordinary differential equation system is again regular and ordinary numerical integration can be performed.

THE CHANNEL FLOW PROBLEM

Returning to the gravity current model, Eqs. (8) and (9), which written on the general vector-matrix notation in the previous section reads:

$$\tilde{A}\frac{d}{d\chi}\begin{bmatrix} v \\ h \end{bmatrix} = \begin{bmatrix} \frac{h}{2} & v \\ \frac{h}{2} & h \end{bmatrix}\frac{d}{d\chi}\begin{bmatrix} v \\ h \end{bmatrix} = \begin{bmatrix} \Gamma v - h v f(\chi) \\ h \sin\theta(\chi) - C v \end{bmatrix} \tag{21}$$

and according to the previous section

$$\Delta \equiv \tfrac{1}{2}h\,(h - v)$$

$$\begin{aligned} N_1 &\equiv \begin{vmatrix} \Gamma v - h v f(\chi) & v \\ h \sin\theta(\chi) - C_d v & h \end{vmatrix} = v\,\{C_d\,v + h\,(\Gamma - \sin\theta(\chi) - h\,f(\chi))\} \\ N_2 &\equiv \begin{vmatrix} \frac{h}{2} & \Gamma v - h v f(\chi) \\ \frac{h}{2} & h \sin\theta(\chi) - C_d v \end{vmatrix} = \frac{1}{2}h\,\{h \sin\theta(\chi) - v\,(C_d + \Gamma - hf(x))\} \end{aligned} \tag{22}$$

The critical points occur when

$$\bar{v} = \bar{h} \tag{23}$$

defining the critical plane, and the singular points when in addition

$$C_d + \Gamma - h_c f(\chi_c) - \sin\theta(\chi_c) = 0, \tag{24}$$

as already stated in Eq. (11). Acceptable solutions passing through the critical plane have to pass through points that satisfies Eqs. (23) and (24) simultaneously.

The eigenvalues of the Jacobi matrix, Eq. (18), are the roots of

$$\lambda\left[\lambda^2 - p\lambda + q\right] = 0 \tag{25}$$

where

$$p = \frac{1}{2}h_c\left[3C_d + \Gamma\right], \tag{26}$$

$$q = \frac{1}{2}h_c^3\left[C_d - \sin\theta(\chi_c)\right]f(\chi_c) - \frac{3}{4}h_c^3\left[h_c\left(\frac{d}{d\chi}f(\chi_c)\right) + \left(\frac{d}{d\chi}\sin\theta(\chi_c)\right)\right]. \tag{27}$$

Classification of the hydraulic control point is now given from Eq. (20).

SPECIAL CASES AND EXAMPLES

A Degenerated Case

A degenerated case arises when the c[illegible]h and the inclination are constant. Eq. (24) then contains only constants and if the [illegible]tion is not fulfilled there is no possibility for hydraulic controll solutions. If on the other hand the equations are fulfilled, defining a critical slope, solutions can pass the critical plane everywhere. Notice that in this case there is only one nonzero eigenvalue since $q = 0$. If either the entrainment parameter or the drag coefficient are not constant, but for instance are dependent on the Richardson number this is no longer true.

Constant Channel Width

If the inclination is dependent on χ and the channel width is constant, $f(\chi) = 0$, then Eq. (24) gives the position of the hydraulic control point.

Example. As an example the obstacle used by Pratt (1986)

$$\sin\theta(\chi) = b_m\chi. \tag{28}$$

may be illustrative. The singular point is located at

$$\chi_c = \frac{C_d + \Gamma}{b_m} \tag{29}$$

showing that not only the friction moves the the hydraulic point downstream from the top of the obstacle as stated by Pratt (1986), but also the entrainment is doing that. In the notation of Eq. (19)

$$p = \frac{1}{2}\left(3C_d + \Gamma\right) \qquad q = -\frac{3}{4}b_m \tag{30}$$

showing that the hydraulic control point always is a saddle point as long as $b_m > 0$.

Varying Channel Width

On the other hand, if the width of the channel is dependent on χ, then Eq. (24) defines a a curve laying in the critical plane which is a relation between the thickness of the current and the χ position for the hydraulic control points. In this case Eqs. (23) and (24) are two equations with three unknown leaving one undetermined. It is possible to use the freedom from the nondimensionalising to scale the current so that either the thickness of the current or χ_c is equal to 1 for the desired solution. It is then possible, at least for saddlepoints, to integrate backwards to the inlet of the channel and find the initial height and velocity needed in order to have the hydraulically controlled solution.

Example. Let the width of the channel be given by the function

$$w(\chi) = a\chi + b \tag{31}$$

with the inflow at $\chi = 0$ and let the inclination be constant. This gives

$$f(\chi) = \frac{a}{a\chi + b}, \Rightarrow \frac{d}{d\chi} f(\chi) = \frac{a^2}{(a\chi + b)^2} = f(\chi)^2. \tag{32}$$

Scaling the flow so that $h_c = 1$, the critical point x_c is now given as the solution of

$$f(\chi_c) = \frac{a}{a\chi_c + b} = C_d - \theta = -\epsilon \tag{33}$$

where $\epsilon = \sin\theta - (C_d + \Gamma)$. If $\epsilon > 0$ (< 0) there is net input (output) of energy in the neighbourhood of the point. This gives the position of the hydraulic control point at

$$x_c = -\frac{1 + \epsilon\frac{b}{a}}{\epsilon} \tag{34}$$

Since the inlet was assumed to be at $\chi = 0$ negative x_c cannot be accepted so in order to have a hydraulic control point $-ab^{-1} < \epsilon < 0$. From Eq. (26)

$$q = -\frac{1}{4}\epsilon\,(\epsilon - 2\Gamma) \tag{35}$$

and the hydraulic control point is always a saddle point as long as $\epsilon < 0$, for $\epsilon = 0$ it is a node.

$f(\chi)$ constant and constant inclination

For this case Eq. (24) becomes

$$h_c d + \sin\theta - C_d - \Gamma = 0 \tag{36}$$

and is only dependent on the thickness of the current. The location is undetermined and has to be found through shooting techniques. The width of the channel for this choice of f is given by

$$w(\chi) = w_0 \exp(d\chi). \tag{37}$$

CONCLUSION

An integrated gravity current model has been simplified, neglecting salinity, temperature and density variations together with rotational effects. This simplified model reduces to well known equations for flows in open channels, with possibility for obstacles and varying width of the channel.

Using a phase-space method, the hydraulic control points transform into equilibrium points. In the phase-space there are solutions passing the critical plane in turning points but these solutions have infinite derivative for at least one of the dependent variable with respect to the original independent variable making these solutions not physically acceptable.

It has also been shown that the hydraulic control point is not always a saddle point in the phase-space.

Acknowledgements. This work has been supported by the Norwegian Research Council.

REFERENCES

Alendal, G., H. Drange, and P. M. Haugan, Modelling of deep-sea gravity currents using an integrated plume model, *AGU, The Nansen Centennial Volume*, (in press), 1994.

Anton, H., *Elementary Linear Algebra*, John Wiley & Sons. , New York, 1984.

Bilicki, Z., J. Dafermos, J. Kestin, G. Majda, and D. L. Zeng, Trajectories and singular points in steady-state models of two-phase flows, *Int. J. Multiphase Flow*, *13*, 511–33, 1987.

Christodoulou, G. C., Interfacial mixing in stratified flows, *Journ. of Hydr. Res.*, *24*(2), 77–92, 1986.

Jordan, D. W., and P. Smith, *Nonlinear Ordinary Differential Equations*, Oxford Applied Mathematics and Computing Science Series, Claredon Press, Oxford, 1987.

Killworth, P. D., Mixing on the Weddell sea continental slope, *Deep-Sea Res.*, *24*, 427–448, 1977.

Pratt, L. J., Hydraulic control of sill flow with bottom friction, *J. Phys. Ocanogr.*, *16*, 1970–1980, 1986.

Simpson, J. E., *Gravity Currents in the Environment and the Laboratory*, Halsted Press, Chichester, 1987.

Smith, P. C., A streamtube model for bottom boundary currents in the ocean, *Deep-Sea Res.*, *22*, 853–873, 1975.

Turner, J. S., *Buoyancy effects in fluids*, Cambridge University Press, Cambridge, 1973.

Wajsowicz, R. C., Dissipative effects in inertial flows over a sill, *Dyn. Atmosph. Oceans*, *17*, 257–301, 1993.

Øien, A. H., and G. Alendal, A model of solar coronal heating by classical inverse bremsstrahlung and generation of the solar wind, *Astrophys. J.*, *412*, 827–840, 1993.

Guttorm Alendal, Nansen Environmental and Remote Sensing Center, Edvard Griegsvei 3a, N–5037 Solheimsviken/Bergen, Norway.

ONE KIND OF INSTABILITY FOR A FLUID WITH HEAVY PARTICLES

EXPANDED ABSTRACT

by **G. I. Burde**

Ben Gurion University, Jacob Blaustein Institute
for Desert Research, Sede Boker Campus, 84993, Israel

The subject of this paper is stability and wave motions, originating from an instability, in a two-component fluid consisting of a carrier fluid (gas) and solid particles dispersed throughout the gaseous component and settling downward. As the particles are treated as a passive scalar, affecting only the density of the mixture, the instability arising is of an Archimedian type [1] in the sense that the motion is caused by buoyancy forces due to spatial variations of the concentration of particles.

The ways in which suspended particles can influence the onset of Benard convection were studied beginning from Scanlon and Segel [2]. The effect of settling particles on the convective stability of a horizontal layer heated from below was considered by Dement'ev [3]. The stability problem of a two-component fluid layer, when spatial variations of a second component are added to the thermal gradient, has been examined in the series of papers initiated by Stern [4] ('thermohaline convection', see review of Turner [5]).

Our formulation of the problem differs from all the above mentioned. It is assumed that a thermal stratification is absent and the concentration of particles increases with height. In general, the fluid in such a state is unstably stratified in the sense that any perturbation grows with time, if dissipative effects are absent. It appears that coupling between the particles' distribution and gravitational settling can make such a state stable even though viscosity and diffusivity effects are negligible. This result is obtained from the linear theory in which the motion of the mixture is described by the system of the Boussinesq equations and of the equation of continuity for particles including the flux due to the gravitational settling of particles, as follows

$$\partial c/\partial t + \mathbf{u}\cdot\nabla c = -\nabla(-D\nabla c + w_s c\mathbf{g}/g)$$

where $w_s = g\tau$ is the terminal fall velocity of particles in gas (τ is the velocity relaxation time). Such an approach is a good approximation if $\omega\tau \ll 1$, where ω is a perturbation frequency. The more complicated formulation, incorporating the equations for two interpenetrating continua, produces results which are qualitatively similar to those obtained for the simpler one.

If the flow in a region bounded by the horizontal surfaces is considered, it is natural to take the basic state to be a solution of the governing equations which is independent of x, y and t and has $\mathbf{u} = 0$. but we will concentrate our attention on a somewhat different situation. The point is that a formulation of the problem mentioned above is not relevant to the case of dust (airborne particles) fallout in the atmosphere. If a dust cloud has been raised from the ground by an explosion or erupted from an elevated source , it will fall as a whole, preserving the initial particles' distribution within it. The same situation arises if the dust particles are involved into a high level atmospheric stream (for example, by strong vertical wind velocities ahead of a cold front over a desert region) and deposition from the stream occurs far from the source region. It is natural for such situations to take the basic state to be a solution of the initial equations for which the particles' concentration is independent of t in the coordinate system falling with the cloud at the terminal velocity w_s. The equilibrium solution in the presence of diffusion is $dc_0/dZ = G = const$, where Z is the vertical coordinate in the falling coordinate system. If diffusion is negligible, as it is in calm air when turbulence is absent, the equilibrium concentration profile may have an arbitrary form $c_0 = F(Z)$.

The stability of the basic state is studied in the usual way by superimposing small perturbations. As it follows from the aforesaid, the formulation of the problem which does not include dissipative effects is of the most interest, the more so, as for non-turbulent gas flows and particle sizes typical for atmospheric fallout the impact of the terms with viscosity and diffusivity in the stability is negligible. Then the linear problem for wave-like solutions of the form

$$c = A \exp[i(\mathbf{k}\cdot\mathbf{r} - \omega t)], \quad \mathbf{k} = (k, l, m) \tag{1}$$

is reduced to a dispersion relation with the roots expressed as

$$\omega = mw_s[1 \pm (1 - R/R_*)^{1/2}]$$

$$R = gGh^2/w_s^2, \qquad R_* = m^2h^2(k^2 + l^2 + m^2)/[4(k^2 + l^2)]$$

where h is a vertical scale and R is an adjustable dimensionless parameter.

One can see that for $R > 0$ ($G > 0$) both two real roots and two complex conjugate roots can occur. If no complex roots exist then stable dispersive wave propagation occurs. However, if complex conjugate roots exist: $\omega = \omega_r \pm i\omega_i$ then instability arises. As R is varied, the sign of the subradical expression can change and the system can switch, through a critical value of R, from stability to instability. Thus, the condition $\omega_i = 0$ determines a neutral stable curve . It should be emphasized that $\omega_i = 0$ not only on the curve but also in the whole region below the curve. This means that all this region corresponds to the neutral stability as the dispersive wave propagation with no growth and no decay takes place for any point below the curve. Note, that on the basis of the general considerations, presented by Gibbon and McGuinness [6], one can expect the existence of the soliton-like nonlinear regimes for this type of instability.

The effect of nonlinearity on the initial state, which is a harmonic solution of the form (1), is to cause a variation in the amplitude in both space and time. This is due to the production of higher harmonics, originating from the nonlinear terms, which react back on the original wave. In accordance with the framework of the multiple scales method one can define a set of "slow" space and time variables as

$$Z_n = \varepsilon^n Z, \qquad T_n = \varepsilon^n t$$

and to seek a solution of the initial equations in the form of a power series expansion in ε (the small parameter ε determines how far the system is from the neutral curve). The amplitude function A in (1) is a function of the slow variables Z_n and T_n and the subsequent calculations are aimed at finding the evolution equation for A. The $O(\varepsilon)$ problem is a restatement of the linear problem. Proceeding to the $O(\varepsilon^2)$ problem, one finds that the Z_1-scale must be excluded as producing secular terms. In the $O(\varepsilon^3)$ problem secular terms are removed if the amplitude function $A(Z_2, T_1)$ satisfies the equation which is a type of nonlinear Schrödinger equation with space and time interchanged:

$$i\partial A/\partial Z_2 + \partial^2 A/\partial T_1^2 + \beta A|A|^2 = 0$$

where the linear term has been absorbed in the first term. Thus, the nonlinear stage of the instability represents waves with an envelope in the form of solitary waves.

REFERENCES

1. W.S. Childress and E.A. Spiegel, *SIAM Rev.* 17, 136 (1975)
2. J.S. Scanlon and L.A. Segel, *Phys. Fluids* **16**, 1573 (1973)
3. O. N. Dement'ev, *J. Appl. Mech. and Tech. Phys.* **17**, 383 (1976)
4. M. E. Stern, *Tellus*, **12**, 172 (1960)
5. J.S. Turner, *Ann. Rev. Fluid Mech.* 6, 37 (1974)
6. J.D. Gibbon and M.J. McGuinness, *Proc. R. Soc. Lond.* **A 377**, 185 (1981)

Stably Stratified Flows in Meteorology

JCR Hunt, G Shutts and S Derbyshire
UK Meteorological Office, London Road, Bracknell, Berkshire RG12 2SZ, UK

In this paper we review three main ways that developments in the physical understanding and numerical modelling of stably stratified flows arising from recent research are being applied to the practice of meteorology.

(i) The cause of stable stratification

The fact that the mean state of the atmosphere is stably-stratified (in the sense that the dry entropy has a positive vertical gradient) is not immediately obvious since the absorption of solar radiation at the surface provides a strong destabilising influence. The resulting vertical stratification is a balance between the destabilising effect of radiative transfer and moist convective heat transfer. Here 'convective' is used in a generalised sense and is associated with the upward transfer of heat (or moist entropy) along all trajectories originating in the boundary layer, whether or not they form part of a deep cumulus circulation or frontal ascent in a developing depression. The horizontal scale of the vertical mass transfer accompanying this moist convection is highly asymmetrical since the buoyancy generating effect of latent heat release occurs primarily in ascending air. The greater proportion of the atmosphere is therefore free of cloud. In regions where active convection is taking place, there is a tendency for a suitably defined 'moist entropy' to be constant along angular momentum surfaces which are vertical in the Tropics but have frontal slopes in middle latitudes. The mean thermodynamics state of the atmosphere is strongly constrained by such processes and results in stable stratification almost everywhere.

(ii) Parameterization in weather forecasting models

Numerical weather and climate prediction (NWP) models reduce the relevant partial differential equations of physics and fluid mechanics to algebraic relations between physical variables and phenomena effectively averaged over finite volumes (with vertical dimensions ranging from 1 m near the ground to 1 km at 50 km altitude, and horizontal dimensions ranging from 15 km in mesoscale models to 300 km in global models) and time periods (from 10^2 secs to 10^4 secs depending on the atmospheric phenomenon involved). However, the basic relations for quantities such as mean velocity, temperature etc., require information about other quantities, especially fluxes of momentum, heat, radiation and water vapour, which cannot be derived formally (e.g., by a hierarchy of 'closed' equations). These averaged quantities cannot be modelled with complete generality (in terms of closed sets of equations) because the 'boxes' are sufficiently large that significantly different phenomena can occur. Nevertheless, in practical NWP models assumptions are made that, for different classes of atmospheric conditions (usually defined by average quantities and their gradients, e.g., the Richardson number), characteristic phenomena occur (or, in mathematical terms, eigensolutions of the governing equations slowly changing in time) which can be analysed in such a way (often with idealised models) that their net effects on fluxes and other terms in the equations can be represented at the mesh scale and time interval of the NWP models. This was essentially Luke Howard's revolutionary concept in 1802 when he recognised that atmospheric motions have definite patterns and that they are manifested in distinct cloud types [1].

Research is leading to new idealised models and thence representations (or parameterisations) of the characteristic patterns. One example is cumulus clouds in a moist atmosphere whose temperature and humidity profiles are such that they are stable to small perturbations but unstable to large perturbations; as a result of thermal convection, characteristic plumes develop and clouds form with a common structure. Their net effect is modelled by representing them as a single idealised entraining and detraining plume in the middle of the grid box, so as to estimate their effects on heat flux, water vapour, etc. [2]. Other examples of such models are scale dependent horizontal eddy viscosity and in modelling lee waves caused by the drag of orography (see below). Their improvements should come from representing different characteristic phenomena occurring in the same or nearby grid box (e.g., lee waves and convection over mountains, the interaction of cumulus and stratus cloud etc). The optimum selection of characteristic phenomena for improving the models is usually statistical, decided on the basis of which modelled phenomena improves the output best; the values of each change to the model is studied systematically by calculating how rapidly certain features of the numerical predictions depart from the measured changes of the atmosphere (e.g., [3]). The combination of physical modelling and a systematic statistical evaluation is providing the highly effective methodology for the steady improvement of models which all major NWP centres have achieved over the past few years (as reviewed in [4]).

(iii) Forecasting issues

The interpretation of NWP is an essential part of the practice of meteorology, and mainly the responsibility of forecasters. Their practice has changed substantially over the past fifteen years from mainly relying on data and dynamical concepts (particularly those of the Bergen school of fronts and air masses, and Sutcliffe's concepts of cyclonic generation or dissipation through horizontal convergence and divergence), to comparing, interpreting and correcting NWP forecasts, with the aid of new kinds data that were not available fifteen years ago, notably accurate satellite images and average values (over rather large depths) of temperature and concentrations of certain atmospheric constituents (water vapour, CO_2 etc). Recent research is clearly having an influence on current interpretation, particularly on phenomena occurring over length scales which the models do not resolve, for example, the air movement and precipitation bands within stably stratified flow along fronts and the effects of wave growth on the speed of cold fronts.

Forecasting offices are still experimenting with the use of potential vorticity computations over a wide field to infer the tendency of a low pressure region either to be 'cut off' and dissipated or to be amplified and develop into a local intense cyclone — still one of the major causes of errors in forecasts on short time scales of the order of 24 hours [5].

Another mesoscale phenomenon that is not accurately forecast is the 'break up' of layers of strato-cumulus cloud; probably because the key processes occur in the interface layers between a dry stable air and a moist turbulent layer within the cloud, [6]. There may be other velocity fluctuations such as lee waves from mountains to add to the turbulence within the cloud. Whether or not these are significant, in a westerly airstream (say over the Welsh mountains) the break up of the cloud determines the temperature and precipitation over much of the centre of England and the quality of the forecast. This is a not untypical example of an 'upscale' phenomenon in meteorology. While the phenomenon is not (or cannot, because of computer limitations) be simulated, its understanding by forecasters is improving as a result of detailed research of stratified flow, mixing and turbulence.

One of the reasons for the wider application of meteorology to environmental problems and to the environmentally sensitive operation of commerce and transport has been the improvements in understanding and modelling of atmospheric processes on the local scale. These phenomena are strongly influenced by local variations in surface elevation ('orography'), the covering of the ground surface (i.e., 'roughness') and surface temperature (e.g., land-sea contrast). For example, using the output of large- or meso-scale NWP and the results of theoretical, wind-tunnel and field research studies has led to improved forecasts and detailed local statistics for local winds (e.g., lee waves, slope winds), precipitation (including fog) and temperature. There is a steady move from providing this information from a combination of large scale NWP, or weather statistics, plus simple formulae (e.g., from the Forecasters' Reference Handbook [7]) to using large scale data plus small computer codes e.g., [8]).

Some of the practical applications of meteorological research at this length scale have been in air pollution dispersion and in wind energy. In both cases, concepts resulting from research on stably stratified flow over hills have been widely applied (notably, the structure of the flow being divided into a zone where streamlines pass over the hill and a lower zone where the streamlines pass round the hill, but see objections to this approach, [9]), leading in the first case to useful criteria as to when pollution from upwind sources would impact on a hill or pass over or round, and in the latter problem to models for estimating wind energy where there are large downslope winds on the lee side of hills, e.g., [10,11]. Recent research on these problems (especially the low Froud number 'cut off' hill effect and lee wave generation) will now help improve the representation of lee wave drag in large scale NWP [12]. Also, recent research on the structure of the stably stratified boundary layer (e.g., [12,13]), turbulence and diffusion (e.g., [14]) have led to more reliable and physically based methods for calculating the dispersion of air pollution, including methods for comparing different models [15]. However, there remain some significant uncertainties in these methods associated with the extreme sensitivity of stably stratified boundary layer flows to small slopes, and to changes in surface roughness and temperature (e.g., [16]).

References

[1] Howard, L, 1802. On the Modification of Clouds. Essay to the Askesian Society, London.

[2] Gregory, D and Miller, M J, 1989. A numerical study of the parameterisation of deep tropical connections, *Quart. J. R. Meteorol. Soc.*, 115, 1209–1241.

[3] Hollingsworth, A 1994. Validation and diagnosis of atmospheric models. *Dynamics of Atmospheres and Oceans*, 20, 227–246.

[4] Laursen, L and Geleyn, J-F, 1993. Developments of numerical weather models; small to medium range forecasting. Presented at the Euro. Conference on Applications of Meteorology.

[5] McIntyre, M E, 1988. Numerical weather predictions: a vision of the future. *Weather*, No. 8, 294–298.

[6] MacVean. M K and Mason, P J, 1990. Cloud-top entrainment instability through small-scale mixing and its parameterization in numerical models. *J. Atmos. Sci.*, 47, 1012–1030.

[7] *Forecasters' Reference Handbook*, UK Meteorological Office, 1993.

[8] Hunt, J C R, Tampieri, F, Weng, W-S, Carruthers, D J, 1991. Air flow and turbulence over complex terrain: a colloquium and a computational workshop. *J. Fluid Mech.*, 227, 667–688.

[9] Hunt, J C R, Puttock, J S and Snyder, W H, 1979. Turbulent diffusion from a point source in stratified and neutral flows around a three-dimensional hill. Part I. Diffusion equation analysis. *Atmos. Environ.*, 13, 1227–1239.

[10] Smith, R B, 1988. Linear theory of stratified flow past an isolated mountain in isostoric coordinates. *J. Atmos. Sci.*, 45, 3889–3896.

[11] Rasmussen, R M and Smolarkiewicz, P K, 1993. On the dynamics of Hawaiian cloud bands. Part III: Local aspects. *J. Atmos. Sci.*, 50, 1560–1572.

[12] Shutts, G J and Broad, A S, 1993. A case study of lee waves over the Lake District in Northern England. *Quart. J. R. Meteorol. Soc.*, 116, 127–158.

[13] Nieuwstadt, F T M, 1984. Some aspects of the turbulent stable boundary layer. *Boundary-layer Meteorol.*, 30, 31–55.

[14] Weil, J C, 1985. Updating applied diffusion models. *J. Clim. Appl. Met.*, 24, 1111–1130.

[15] Cuvelier, C, (Ed.) 1994. Proceedings of the workshop *Intercomparison of Advanced Practical Short-Range Atmospheric Dispersion Models*, August 30th – September 3rd 1993, Joint Research Centre, European Commission, Institute for Safety Technology.

[16] Derbyshire, S H, 1990. Nieuwstadt's stable boundary layer revisited. *Quart. J. R. Meteorol. Soc.*, 116, 127–158.

Direct and Large Eddy Simulations of Stratified Homogeneous Shear Flows

Ulrich Schumann
DLR, Institute of Atmospheric Physics, 82230 Oberpfaffenhofen, Germany

Abstract

An overview is given on direct numerical simulations and on large eddy simulations of homogeneous turbulence under the impact of shear and stable stratification. We describe the methods used and report on results of various studies. In particular, the vortex structure of turbulent motions is discussed. Moreover, the dynamics of statistical mean quantities is investigated. The mean variances are compared with experimental data. The turbulent diffusivity tensor for passive species in a stratified shear flow is computed. Moreover, a simple model is described which allows to estimate the vertical diffusivities for heat and momentum for such flows when the vertical velocity variance or the dissipation rate are known.

1. Introduction

Stratified shear flows are important in the stratosphere, in the free stable troposphere, in the stable atmospheric boundary layer (ABL) over cooled surfaces, and in the ocean. See Hopfinger (1987), Fernando (1991) and Etling (1993) for reviews. In this paper, we summarize briefly some recent results for ABLs and then concentrate on homogeneous stratified shear flows, with uniform shear and stratification (without mean rotation). In the homogeneous case, all turbulence statistics are independent of the spatial coordinates but vary with time. The paper summarizes the results of various recent numerical simulations, using either direct numerical simulation (DNS) resolving the whole spectrum of motions up to the dissipating scales, or using large-eddy simulation (LES), resolving only the main energy and flux carrying motion structures while the small-scale turbulent transports are approximated by a proper subgrid-scale (SGS) model. We will show that DNS and LES provide insight into the vortex structure of such flows, its basic dynamics, the vertical transport of heat and momentum, and the anisotropic diffusion of passive species.

Turbulence in stratified shear flows depends strongly on the Richardson number (Richardson, 1920). Let S denote the vertical velocity shear and s the vertical potential temperature gradient.

$$S = dU/dz, \quad s = d\Theta/dz > 0, \tag{1}$$

then the Brunt-Väisälä frequency N and the gradient Richardson number Ri are defined as

$$N = (\beta g s)^{1/2}, \quad Ri = N^2/S^2. \tag{2}$$

Here, β is the thermal volumetric expansion coefficient, and g is the acceleration of gravity. As summarized by Farrel & Ioannou (1993), for $Ri < 0.25$ somewhere in the flow, small perturbances in inviscid fluid may grow exponentially. In general one expects that existing turbulence decays with time when $Ri > 0.25$. In viscous flows this limit may be smaller. But even for $Ri = O(1)$, transient growth of perturbations can be substantial, and may cause overturning for $Ri < 0.4$. Turbulent motions get enhanced by shear at small Richardson numbers. Hence, turbulent mixing may occur under non-stationary conditions at all Richardson numbers.

The flow state depends also on the timescale of turbulence, e.g. $\tau = \ell/q$, where ℓ denotes the integral lengthscale and $q = (2E)^{1/2}$ the velocity scale as a function of the kinetic energy of turbulent motions E. (Alternative time scales may be defined in terms of the dissipation rate ε of kinetic energy.) Dimensionless numbers that relate the internal time scale to the outer time scales S^{-1} and N^{-1}, are the shear number Sh and the inverse Froude number Fi,

$$Sh = S\tau, \quad Fi = Fr^{-1} = N\tau, \quad Ri = Fi^2/Sh^2. \tag{3}$$

The shear number determines the importance of mean shear relative to turbulent shear. In strongly stratified flows, the inverse of the Froude number Fr becomes important. For Fi greater than a critical value of about 3 turbulent mixing dies out (collapse of turbulence), see Hopfinger (1987) and Etling (1993).

Turbulence in homogeneous shear flows has been measured by Rohr et al. (1988) in salt-stratified water. Reliable data for homogeneous air flows are available only for neutral stratification (Tavoularis and Karnik 1989). The early measurements by Webster (1964) were obtained from a wind-tunnel experiment at rather low Reynolds number with notable departure from a quasi-steady state.

Homogeneous stratified shear flows have been investigated by DNS in Gerz et al. (1989), Gerz and Schumann (1989, 1991) and Holt et al. (1992). They investigated the flow dynamics as a function of Richardson numbers in between zero and 1.32. On present computers, such simulations can be performed on grids with typically 128^3 grid points. For such grids, DNS is restricted to a Prandtl number of order unity and to a turbulent Reynolds number, based on root-mean square velocity fluctuations and Taylor's microscale, of less than about 50. For atmospheric flows, much larger Reynolds numbers are of interest. For this reason, the DNS method has been extended into a LES method by Kaltenbach et al. (1994). This extends formally the Reynolds number to infinity. However, the range of resolved scales is still limited by numerical resolution.

With respect to turbulence in the ABL, most previous studies concentrated on the convective and the neutral cases (Schumann, 1993). For comparison of various LES codes to these cases see Nieuwstadt et al. (1993) and Andrén et al. (1994). The stable ABL is much more demanding because of smaller turbulence scales and the tendency to turbulence collapse. Mason and Derbyshire (1990) showed that LES of the stable ABL is possible, giving results broadly similar to observations, and supporting the local scaling arguments of Nieuwstadt (1984). Coleman et al. (1992) found similar results in DNS of a stable ABL at moderate Reynolds number. Mason and Thomson (1992) raised the important issue of stochastic backscatter. They showed theoretically that the subgrid parametrization should be stochastic, and that this substantially improved LES performance in the neutral surface layer. Recently, Brown et al. (1994) extended that work applying LES with stochastic backscatter to the stable ABL. The forcing causes more turbulence and a deeper ABL and better agreement of the velocity profile gradients with observations. For strong stratification, when the turbulence scales with the local fluxes, the turbulence statistics of the ABL become directly comparable to results from homogeneous flows.

Since DNS and LES compute the details of the three-dimensional motions, at least in the energetic scales, they can be used to study the vortex structure and the related transports, as will be explained in chapter 3.1, based on the work of Rogers & Moin (1987), Gerz (1991), Gerz et al. (1994) and others. For related discussions of other stratified shear flows, see, e.g., Lesieur (1993) and Staquet (1993).

Turbulent transport in stably stratified shear flow is strongly anisotropic due to forcing of down-stream turbulent motions by shear and conversion of kinetic energy of vertical motions into potential energy by buoyancy forces (Richardson 1920). As a consequence, passive species within the flow are mixed by the turbulent motions much stronger in the horizontal directions than in the vertical. The relation between fluxes and gradients is described by the turbulent diffusivity tensor which is anisotropic and asymmetric in general. The diffusion tensor has been measured for neutral homogeneous shear flows in a wind tunnel by Tavoularis & Corrsin (1985) and computed using DNS by Rogers et al. (1989). For stratified turbulence, the diffusion tensor has been evaluated from DNS and LES (Kaltenbach et al., 1991, 1994), as will be summarized in this overview.

With respect to practical diffusion problems in stratified shear flows, the vertical diffusivity component is the most important one. For diffusion from a linear source, a Gaussian plume model (assuming a constant but anisotropic diffusivity tensor D_{ij}) results in second order moments of the concentration field

$$\sigma_{11} = 2t(D_{33}S^2t^2/3 + D_{13}St + D_{11}), \quad \sigma_{13} = \sigma_{31} = 2t(D_{13}t + 2D_{33}St), \quad \sigma_{33} = 2tD_{33}, \tag{4}$$

as functions of time t (Konopka, 1994). This shows clearly the importance of the vertical diffusivity D_{33} dominating horizontal dispersion when $D_{33}t^2S^2 > 3D_{11}$.

Simple relationships are required to estimate the magnitude of the mixing properties. Such relationships have been deduced, mainly for strongly stratified atmospheric and oceanic flows, on the basis of the energy budgets using simple closure assumptions for stationary flows, see, e.g., Itsweire et al. (1993). The present paper summarizes a simple model which takes into account the deviation from stationarity and applies to both stratified and unstratified shear flows.

2. The numerical method used for DNS and LES

The numerical method has been described in detail by Gerz et al. (1989) and Kaltenbach et al. (1994). It simulates the turbulent flow in a cubic domain, see Fig. 1, with side-lengths L. The mean velocity $(U, 0, 0)$ and the mean temperature Θ have uniform gradients in the vertical coordinate z while being constant in the two other directions. All mean gradients are kept fixed in time. The turbulent fluctuations relative to these mean values are $u_i = (u, v, w)$ for velocity, and θ for temperature.

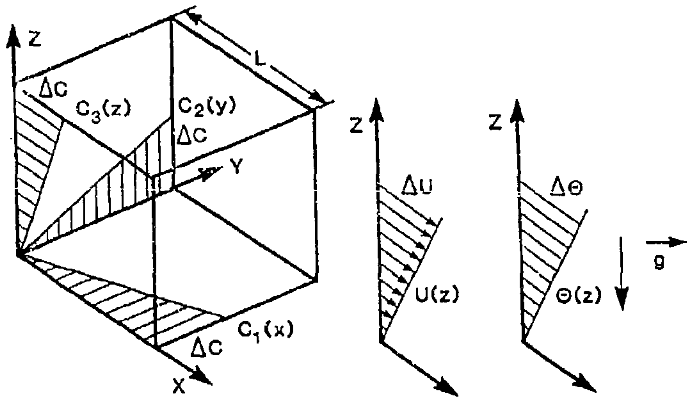

Fig. 1. Computational domain and mean profiles (Kaltenbach et al., 1994).

Shear imposes a problem with respect to the boundary conditions. The [illegible] choice of boundary conditions in DNS of homogeneous turbulence is periodic [illegible] space directions. However, in the presence of shear a field which is initially periodic in the vertical direction soon becomes non-periodic. Thus the common periodicity condition cannot be used in that direction. Rogers & Moin (1987) and Holt et al. (1992) applied a method using time-dependent coordinate transformation which corresponds to a Lagrangian reference frame, so that the flow may be assumed to be periodic in the direction of the transformed coordinate. This makes it possible to apply Fourier-spectral approximations of the fields with respect to this coordinate. The disadvantage of this approach is the need for remeshing at a frequency $(1/2)\, dU/dz$, which causes interpolation errors of the aliasing type. We use the alternative approach, where the equations are discretized in the Eulerian reference frame using the so-called "shear-periodic" boundary condition (Schumann 1985). This condition assumes periodicity in a direction which varies as a function of time. It corresponds to continuous remapping by applying horizontal periodicity and avoids interruptions at discrete times. This type of boundary condition is not applicable to Fourier spectral approximations in the vertical but can easily be implemented in a finite difference scheme. Both approaches produce very similar results (Holt et al., 1992).

The motion fields follow the continuity equation for an incompressible fluid with constant density ρ, the equations of motion including buoyancy due to density fluctuations and gravity g in the Boussinesq approximation, and the conservation laws for heat and mass as a function of spatial coordinates $x_i = (x,\ y,\ z)$ and time t. The density fluctuation is a linear function of temperature with a constant volumetrical expansion coefficient β.

In the study of Kaltenbach et al. (1994), the SGS turbulent transport is modelled using turbulent diffusivities, the so-called Smagorinsky model,

$$\nu_t = (c_{SGS}\Delta)^2 (2S_{ij}S_{ji})^{1/2}, \quad \gamma_t = \nu_t / Pr_{SGS}, \tag{4}$$

for velocity and temperature, respectively. Here, $S_{ij} = \partial u_i/\partial x_j + \partial u_j/\partial x_i$ is the resolved velocity deformation tensor, $c_{SGS} = 0.17$ is the Smagorinsky coefficient, and Pr_{SGS} is the turbulent Prandtl number of SGS motions. The velocity deformation tensor is evaluated excluding the mean shear dU/dz in order to avoid unrealistically strong damping for decaying turbulence. In fact, this model is justified theoretically only for locally isotropic turbulence where the local deformation induced by turbulence is large compared to the mean shear. In this sense, the mean shear should be negligible. The value of the Smagorinsky coefficient is based on the inertial subrange theory as described in Schmidt and Schumann (1989). The same theory gives $Pr_{SGS} \cong 0.42$, but larger values are expected for stable stratification (Schumann 1991, Canuto and Minotti 1993). Also, backscatter causes a larger value (about 0.6 to 0.7 for neutral stratification), see Mason & Thomson (1992).

It should be noted that simulations with 128^3 grid points do not yet resolve the inertial subrange. As a consequence of deviations from local isotropy, the SGS shear number $Sh_{SGS} = S\ell/u'$ is of order unity. In the inertial subrange, the shear number scales with $\Delta x^{4/3}$, Hence, a reduction of Sh_{SGS} by a factor of ten would be desirable, but this requires about 5.6 times more grid points or 1000 times more computer power.

Kaltenbach et al. (1994) compared DNS and LES results using this Smagorinsky model. They found that LES and DNS give the same results for weak stratification, when the constant molecular viscosity of the DNS is set equal to the initial mean turbulent viscosity of the LES. Hence, a LES is nothing else than a DNS with spatially and temporally variable viscosity. In the present cases, the spatial variability of the SGS viscosity is small, as also found by Métais and Lesieur (1992) for unsheared homogeneous turbulence. However, LES energy spectra decay more slowly than DNS spectra at high wavenumbers. Moreover, in LES the viscosity adjusts to the decaying turbulence at the large scales, see Fig. 2. Therefore, LES gives a better approximation than a DNS at a given resolution for studies of high Reynolds number flows and allows for a wider range of Richardson numbers.

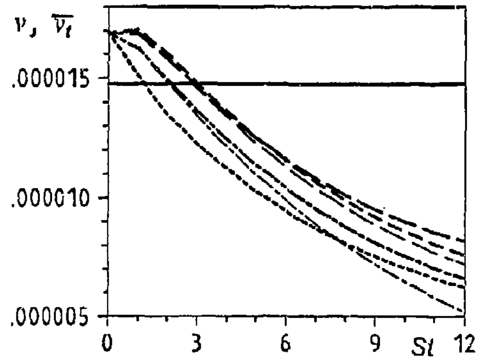

Fig. 2. Mean turbulent viscosity $\overline{\nu}_t$ of LES for various models and molecular viscosity ν of DNS versus shear time *St* (Gerz & Palma, 1994).

Gerz and Palma (1994) tested variants of two SGS models, one based on the first-order model using a budget for the SGS kinetic energy (as in Schumann, 1991) and the other based on Smagorinsky's closure. Tests with grid sizes of 64^3 showed that the details of the SGS closure are not critical and become even less important when resolution is increased. Production and dissipation of SGS energy are the two largest terms in the energy budget. The Smagorinsky model simply assumes that they are equal. For $Ri = 0.5$, the time tendency of the SGS energy is rather large, and this explains some differences in the effective viscosity, see Fig. 2. We have also tested the code with a new stochastic backscatter model (Schumann, 1994b). For isotropic turbulence, the effect of such forcing is very small. We are still working on testing the backscatter model for other cases.

3. Examples

3.1 Vortex Structure and Microfronts

Structures in turbulence are often viewed as regions of strong coherent vorticity (Lesieur, 1993) and zones of concentrated field gradients, sometimes called microfronts (Gerz et al., 1994). In shear flows without inflection points (in contrast to shear layers), horseshoe and hairpin structures of fluctuating vorticity have been found in unstratified boundary layers but also for homogeneous shear flows both in neutrally (Rogers and Moin, 1987) and weakly stably stratified situations (Gerz, 1991). Horseshoe-shaped vortex structures are present in flows with low to moderate Reynolds numbers, whereas hairpin-shaped vortices typically occur in high Reynolds number flows with large shear numbers.

As sketched in Fig. 3, horseshoe vortices form and decay transiently in four steps: 1. An initial disturbance due to vertical motions forms vertically distorted vortices. 2. The vertically deflected vortex curves get rotated by the mean rotating flow. 3. Stretching of the structure occurs strongest by the mean strain when they pass 45°. 4. Further rotation by the mean rotation reduces the inclination angle until the vortices get dissipated. Gerz (1991) found that the strongest vorticity is distributed around $\vartheta = 25°$ in a stratified shear flow with $Ri = 0.13$, but that most of the coherent horseshoe vortices are found at angles of approximately 36° as in unstratified shear flows (Rogers and Moin, 1987), see Fig. 4.

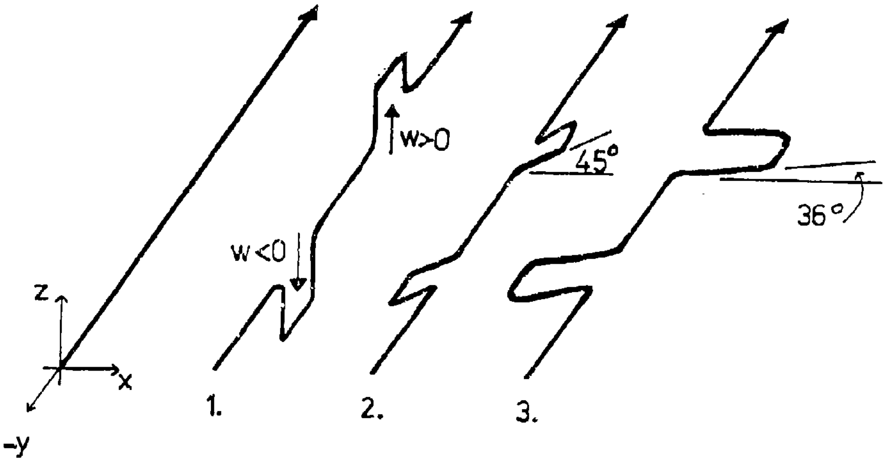

Fig. 3. Schematic illustration of the creation of horseshoe eddies (Gerz et al., 1994).

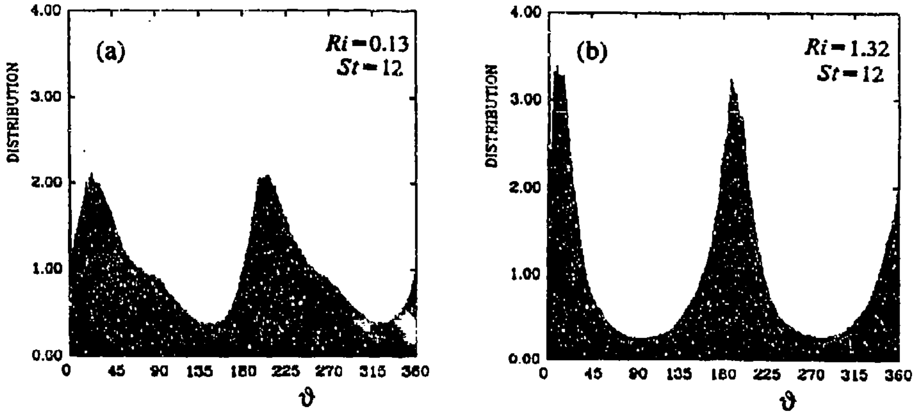

Fig. 4. Frequency of inclination angle of vortex vectors relative to downstream cooordinate. a) $Ri = 0.13$, b) $Ri = 1.32$ (Gerz, 1991).

In wall-bounded shear layers the mean velocity profile is curved. This causes a preference of horseshoe vortices with "head-up" orientation such that the curved part (the head) of the horseshoe forms in the outer region of the boundary layer whereas the legs of the horseshoe stay closer to the wall. In contrast, head-up and head-down horseshoes form at equal frequency in homogeneous turbulence with constant shear.

The flow in between the horseshoe legs is very efficient in transporting fluid and related momentum, heat, and other fluid properties. In between the legs, head-up horseshoe vortices pump fluid upwards, while head-down vortices pump fluid downwards. As shown by Gerz et al. (1994), see Fig. 5, this causes the formation of microfronts with strong gradients of the transported fields in the direction normal to the horseshoes. In a thermally stratified fluid, at moderate Richardson numbers, head-up vortices transport cold fluid upwards and hence, cause cold microfronts, whereas head-down vortices transport warm fluid downwards causing cold microfronts.

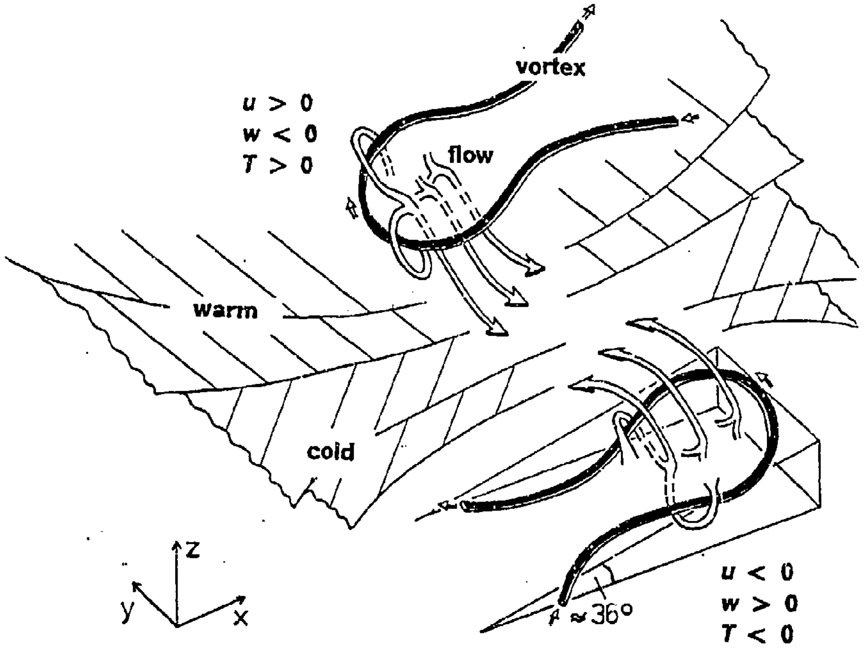

Fig. 5. Sketch of two horseshoe vortices forming a pair (Gerz et al., 1994).

The microfronts represent also regions of strong shear with spanwise vorticity. When the Reynolds number is high enough these vortex layers get dissipated slowly and may reach stronger vorticity than the horseshoe vortices. Such layers of maximum vorticity magnitude have been observed by Gerz et al. (1994). The layers are relatively thin vertically and have largest extent in the inclined downstream direction.

Collision of fluid lumps in between adjacent head-up and head-down horseshoe vortices cause smaller scale fragments which may cause counter-gradient momentum transfer, see Fig. 6. In moderately stably stratified flows, this collision of fluid lumps of different buoyancy also causes counter-gradient heat transfer at small scales (Gerz, 1993, Gerz and Schumann, 1994). This provides a mechanistic explanation of this phenomenon which supplements energetic considerations as in Schumann (1987).

At very strong stratification, horseshoe vortices do not form. Instead, Gerz (1991) found horizontally large but vertically thin sheets of maximum vorticity, see Fig. 7, which are inclined at rather small angles, see Fig. 4. Such sheets of vorticity are also found, with $\vartheta = 0°$, in simulations of strongly stratified unsheared turbulence (Métais and Herring, 1989). Staquet (1993) shows that the vortex part of such flows interacts strongly with wavy motion parts.

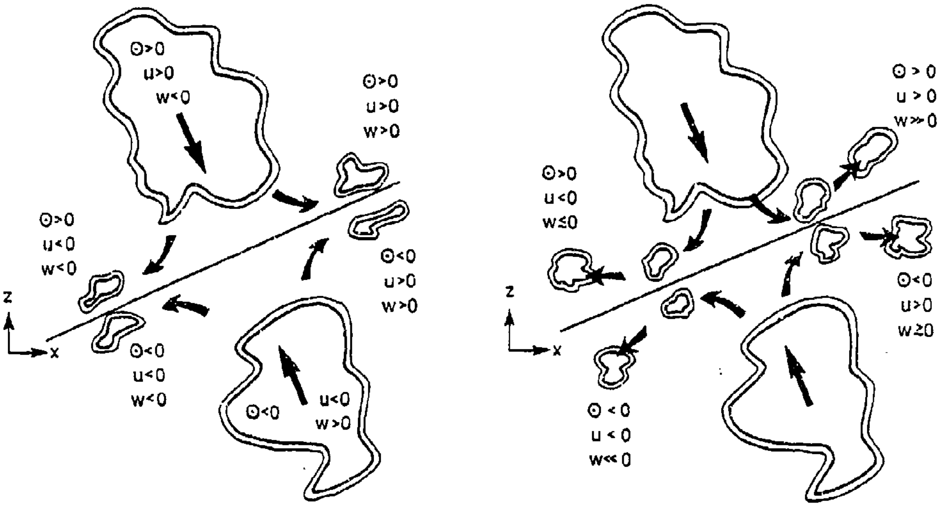

Fig. 6. Illustration of the collision of fluid lumps and the resultant transport of momentum and heat by smaller scale collision products in neutral (left) and stratified (right) shear flows (Gerz & Schumann, 1994).

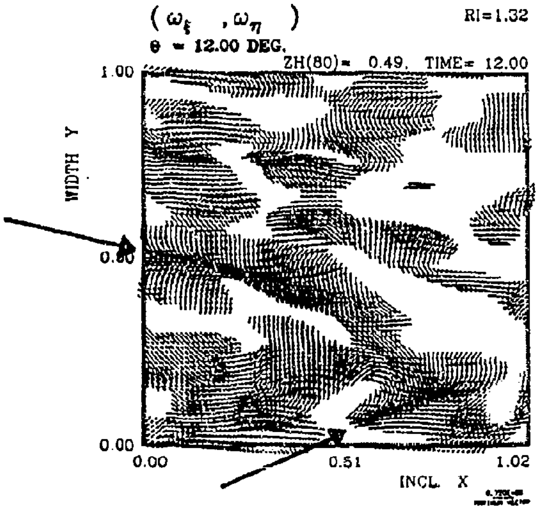

Fig. 7. Vortex structure at strong stratification as indicated by vorticity vectors in a plane inclined by $\vartheta = 12°$ relative to the horizontal. $Ri = 1.32$.

3.2 Dynamics and Diffusion in Homogeneous Stratified Shear Turbulence

LES of homogeneous turbulence for neutrally and stably stratified shear flow at gradient-Richardson numbers Ri in between zero and one have been performed by Kaltenbach et al. (1994). They investigated the dynamics and transport properties of such flows. For $Ri \leq 0.5$, the computed normalized variances and covariances are within the range of data of a large set of measurements in laboratory and atmospheric flows, see e.g. Fig. 12. Also the growth rate, the shear number, and the shape of spectra agree generally well with corresponding experimental observations. For neutral stratification, the turbulence grows about exponentially with time, see Fig. 8a, approaching a constant shear number of about $Sw'^2/\varepsilon \cong 2$, and a growth rate $G_0 = P/\varepsilon = 1.54 \pm 0.05$. The state of turbulence changes very slowly near a stationary Richardson number of about 0.13. For $Ri \geq 0.25$, both the kinetic and the potential energy decay with time. For $0.25 \leq Ri \leq 0.5$, the turbulent flow state becomes self-similar in the sense of approaching constant normalized flow statistics, as for example in Fig. 8b, after a shear time of about 6 when the initial value of the inverse Froude number is small. For Fi greater than a critical value of about 3 turbulent mixing dies out as observed in experiments, see e.g. Ivey and Imberger (1991). In this case the final statistics depend on the history of mixing in the past fully turbulent regime.

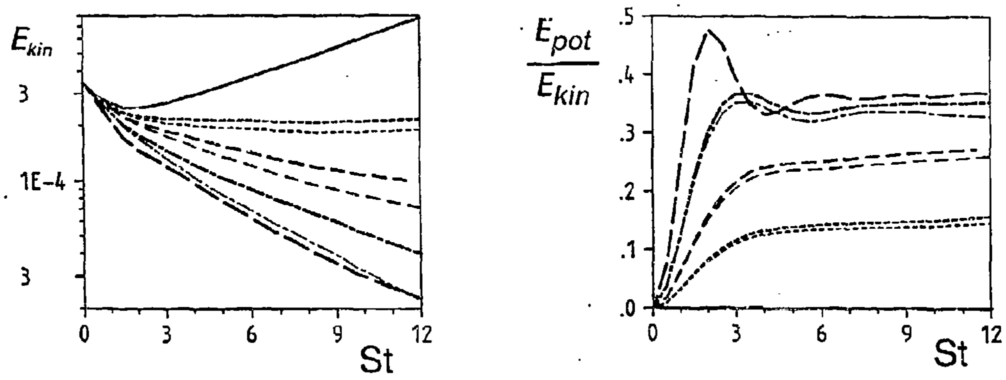

Fig. 8 a). Kinetic energy versus time in shear units for various Richardson numbers Ri = ______ 0, ------ 0.13, _ _ _ _ 0.25, _._._ 0.5, __ __ . __ 1.0. b) Ratio of potential to kinetic energy versus shear time, for the same Ri-values (Kaltenbach et al., 1994).

For analysis of the turbulent transport of passive species, the simulations treat three passive species with uniform gradients of mean concentrations C in either vertical, downstream or cross-stream direction, see Fig. 1. From the results, the full diffusivity tensor has been evaluated by relating the computed turbulent fluxes of concentration fluctuations c with the given mean gradients,

$$\overline{u_i c} = -D_{ij}\frac{\partial C}{\partial x_j}\,. \qquad (5)$$

Mean values of D_{ij}/D_{22} for different Ri, as obtained by the LES, are presented in Fig. 9. This figure also contains the results obtained by Rogers et al. (1989) from DNS for neutral shear flow and measurements of Tavoularis and Corrsin (1985). The dashed curves represent the results from a second-order closure (SOC) model. For neutral flow, D_{11} is about three times larger than D_{33}, and D_{33} is roughly half the value of D_{22}. This is a consequence of anisotropic velocity fluctuations and shear. Both off-diagonal components are negative and $D_{13} < D_{31} < 0$, as can be explained by SOC models. For increasing stratification, the vertical diffusivity D_{33} becomes much smaller than the horizontal ones because of buoyancy suppressing vertical motions. The differences between downstream and cross-stream diffusivities become smaller. The asymmetry of the tensor components depends strongly on Ri. D_{31} changes sign at $Ri \cong 0.2$ because buoyancy contributes more strongly than gradient fluxes to the production of vertical fluxes of a tracer with downstream mean gradient. The SOC model accounts for the given anisotropic Reynolds stresses and roughly describes the same trends but gives much less anisotropy at strong stratification, presumably because of neglect of anisotropic length and time-scales as defined by Tavoularis & Corrsin (1985).

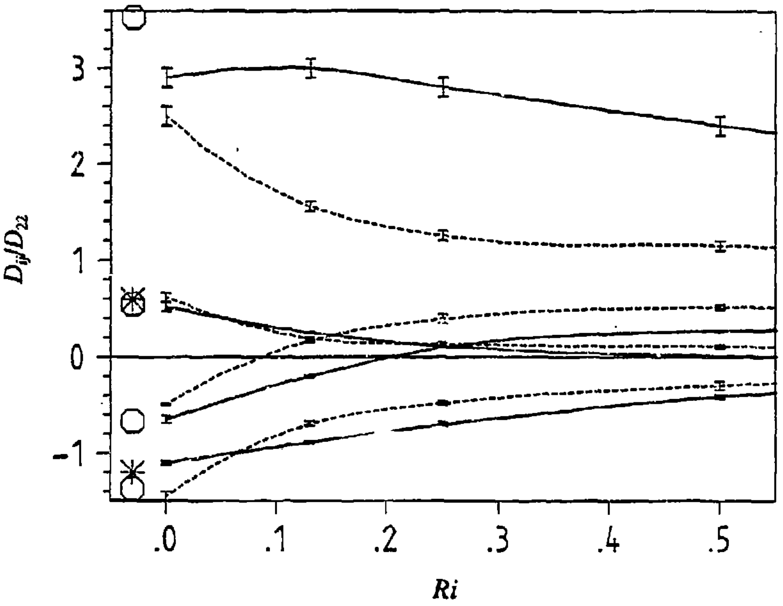

Fig. 9. Diffusivity tensor versus Ri. Full line with error bars from LES results. For $Ri = 0$, results from Rogers et al. (1990) are included. Stars represent data of Tavoularis & Corrsin (1985). stars. Dashed curves from SOC model. (Kaltenbach et al., 1994).

3.3 *A model for vertical diffusivites of heat and momentum*

In order to estimate vertical diffusivities as a function of Richardson number, for given dissipation rate ε or for given vertical velocity variance $w'^2 = w^2$, Schumann (1994a) and Schumann and Gerz (1994) deduced a simple model. As a consequence of the budget of kinetic energy the vertical diffusivities for momentum K_m and heat $K_h \equiv D_{33}$ are related to shear $S = dU/dz$, the Brunt-Väisälä frequency N and the dissipation rate ε by

$$K_m = c_m \frac{\varepsilon}{S^2}, \quad c_m = \frac{G}{1 - Ri_f G}, \tag{6}$$

$$K_h = c_h \frac{\varepsilon}{N^2}, \quad c_h = \frac{Ri_f G}{1 - Ri_f G}. \tag{7}$$

The coefficient c_h is often quoted as the "mixing efficiency" (see Itsweire, 1993). Here, $G = P/(\varepsilon + B)$ is a measure for the growth rate of kinetic energy due to shear production $P = -\overline{uw}S$, dissipation ε and buoyancy destruction $B = \beta g \overline{w\theta}$; $G > 1$ for flows in which shear production dominates as in neutral shear flows, $G = 1$ for stationary turbulence near a "stationary Richardson" number $Ri = Ri_s$, and $G < 1$ for decaying turbulence at strong stratification. The flux Richardson number $Ri_f = Ri/Pr_t = B/P$ enters as a function of Ri and the turbulent Prandtl number $Pr_t = K_m/K_h$. For closure, the model assumes a linear relationship between dissipation, shear and vertical velocity variance,

$$\varepsilon = A_S w'^2 S, \tag{8}$$

with A_S as an empirical model coefficient (equal to the inverse shear number). This model looks similar to classical dissipation closure models when written as $\varepsilon = A_S w'^3/\ell_w$, but fixes the mixing length as $\ell_w = w'/S$. This appears to be natural for strongly sheared flows. Hunt et al. (1988) suggested that such a model gives a good approximation also for stratified flows, and our results, see Fig. 10, support this relation for $0 \le Ri < 1$.

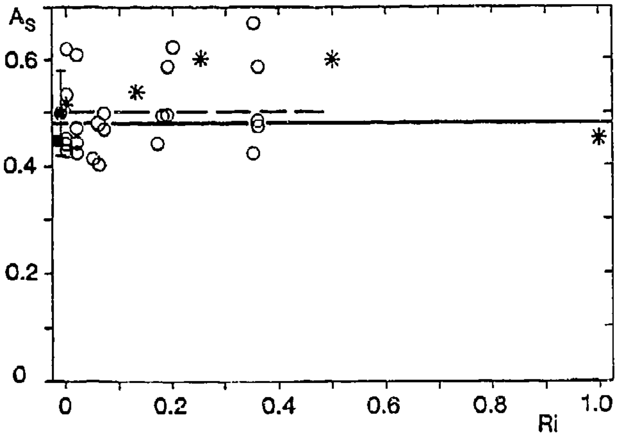

Fig. 10. Dissipation scaled by shear and vertical velocity variance, $A_S = \varepsilon/(w'^2 S)$, versus gradient Richardson number Ri. Data of Rohr (1985) in salt-water (circles) of Tavoularis and Karnik (1989) in a wind tunnel (full circle with error bar), and the LES results (stars). Square dot indicates boundary layer estimate of Hunt et al. (1988). (Schumann & Gerz, 1994).

The turbulent Prandtl number (see Fig. 11a) and the growth rate of kinetic energy (Fig. 11b) are specified by means of some interpolation functions of Richardson number,

$$Pr_t = Pr_{t0} \exp[-Ri/(Pr_{t0} Ri_{f\infty})] + Ri/Ri_{f\infty}, \tag{9}$$

$$G = G_0^{(1-Ri/Ri_s)}. \tag{10}$$

Model coefficients are determined from the LES results of Kaltenbach et al. (1994) and laboratory measurements of Tavoularis and Karnik (1989) for neutral stratification in a wind tunnel, and from Rohr et al. (1988) for stratified shear turbulence in a salt-water tank (data tabulated in Schumann, 1994a). The coefficient values are $A_S = 0.5$, $Pr_{t0} = 0.98$, $Ri_{f\infty} = 0.25$, $G_0 = 1.47$, $Ri_s = 0.13$, for air, and slightly different values for salt-water, see Schumann and Gerz (1994).

When comparing mixing properties in the atmosphere and in the ocean, one has to note the rather large molecular Schmidt number of salt diffusing in water (about 500) while the corresponding molecular Prandtl number of thermal diffusion in air is about 0.7. At high Reynolds numbers, one generally expects that the large scale turbulent motions become independent of the Prandtl number, at least for neutral stratification. However, for strong stratification, the vertical diffusivity is limited by small-scale mixing once the available kinetic energy is consumed to provide the potential energy required for vertical displacements. Such small-scale processes will depend on molecular diffusion.

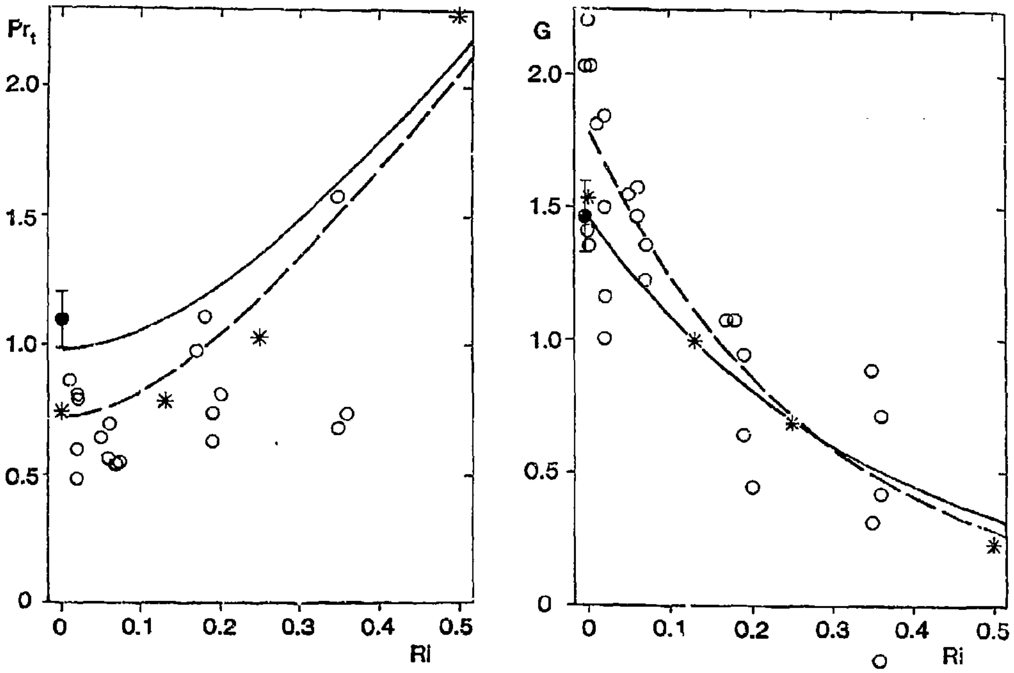

Fig. 11 a) (left). Turbulent Prandtl number $Pr_t = K_m/K_h$ versus Ri. Symbols as in Fig. 10. The full curve depicts the interpolation for air, the dashed curve for salt-water. b) (right) Growth factor $G = P/(B + \varepsilon)$ versus Ri. (Schumann & Gerz, 1994).

The results of the model compare well with data from laboratory experiments in air or salt-water, with measurements in the ABL, and in the stable troposphere, and with results from the numerical simulations, see, e.g., Fig. 12. It should be stressed that this model applies only for approximately homogeneous turbulent flows at high Reynolds numbers under conditions of equilibrium between kinetic and potential energy, i.e. in the absence of strong gravity wave oscillations. Further analysis (Schumann & Gerz, 1994) shows that the present model also describes the break-down of mixing for $Fi > 3$, as in Ivey & Imberger (1991).

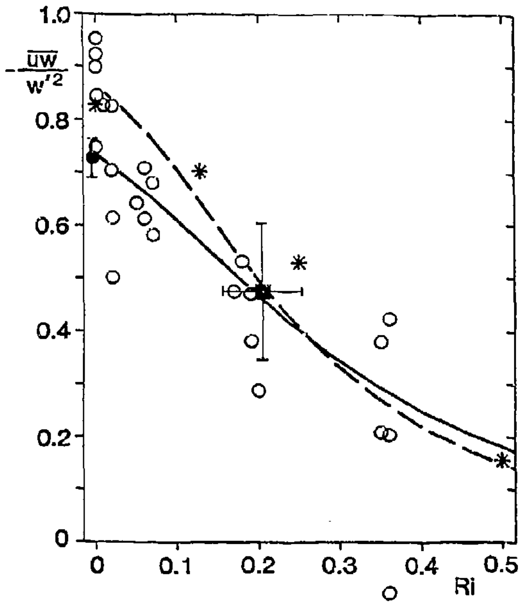

Fig. 12. Stress coefficient $\alpha_{uw} = -\overline{uw}/w'^2$ versus *Ri*. Symbols as in Fig. 10. Full square with error bars: Nieuwstadt (1984). (Schumann & Gerz, 1994).

4. Conclusions and Outlook

We have described various results obtained by DNS or LES of homogeneous turbulence in incompressible stably stratified shear flows. It has been shown that the simulations give insight into the vortex structure of such flows, allow to compute mean statistics of flows and their temporal dynamics, and give quantitative information on the diffusivity tensor and the vertical transport of heat and momentum.

We found that the LES and DNS give very similar results for weak stratification when the constant molecular viscosity of the DNS is set equal to the mean turbulent viscosity of the LES. At strong stratification, the LES resolves a wider range of energetic scales and gives thus a better approximation to high Reynolds number turbulence than a DNS with the same grid numbers. The more energetic motions in the medium wavenumber range cause the inverse Froude number to grow less quickly so that mixing persists longer. Hence, the LES results depend less on flow history than the DNS results. Finally, the LES adjusts its SGS diffusivities to the growing or decreasing level of grid-scale turbulence energy. This makes the LES method superior to the DNS for studies of high Reynolds number flows and for a wider range of Richardson and Froude numbers.

However, grids with about 128^3 grid points are much too coarse to resolve the inertial subrange of turbulence. Therefore, the results for small-scale properties depend on the details of the SGS model. For the future, within about a decade from now, one may expect that simulations will become possible with an order 1000 grid points in each coordinate direction. In view of the present developments of computers, such simulations require algorithms suitable for parallel computers. Such grids would make it possible to resolve scales truely within the inertial subrange for which the SGS models become much more reliable.

With respect to atmospheric turbulence in the free troposphere and above, it is probably very important to account for the large-scale anisotropy of such flows with much larger horizontal than vertical scales. An important topic here is the formation of turbulent spots due to locally overturning waves in an otherwise strongly stably stratified fluid. Such overturning waves often result from upward travelling gravity waves with certain horizontal phase speeds that interact with the mean flow at critical levels where the mean flow speed equals the phase speed of the waves. Simulation of such flows requires to prescribe a suitable gravity wave forcing at the bottom boundary and a non-reflective boundary condition at the top of the domain.

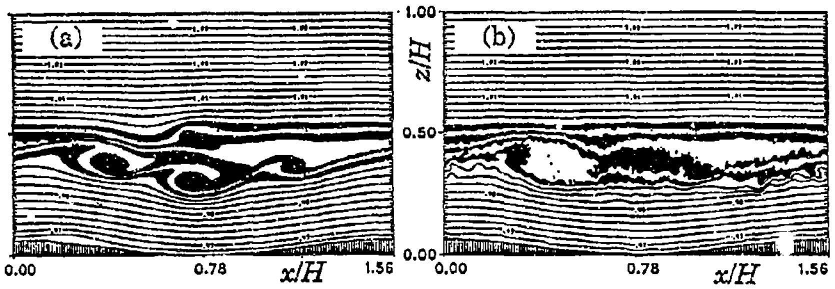

Fig. 13. DNS (left) and LES (right) of a breaking gravity wave at a critical layer (Dörnbrack & Schumann, 1994).

An example of such a flow is given in Fig. 13. It shows the flow field in a stably stratified fluid layer with uniform shear (zero mean flow) where gravity waves of zero phase speed are induced by a lower undulated surface. We clearly observe the turbulence layer caused by breaking gravity waves at and below the critical level (Dörnbrack and Schumann, 1994). However, details of this study are beyond the present overview.

Acknowledgements. I thank T. Gerz, A. Dörnbrack, H.-J. Kaltenbach, and J.M.L.M. Palma for the fruitful cooperation from which the results shown in this paper resulted.

References

Andrén, A., Brown, A., Graf, J., Mason, P., Moeng, C.-H., Nieuwstadt, F. T. M. & Schumann, U. 1994 Large-eddy simulation of a neutrally stratified boundary layer: A comparison of four computer codes. *Q. J. R. Met. Soc.*, in press.

Brown, A. R. & Derbyshire, S. H. & Mason, P. J. 1994 Large-eddy simulation of stable atmospheric boundary layers with a revised stochastic subgrid model. Submitted for publication.

Canuto, V.M. & Minotti, F. 1993 Stratified turbulence in the atmosphere and oceans: a new subgrid model. *J. Atmos. Sci.* **50**, 1925-1935.

Coleman, G. N., Ferziger, J. H. & Spalart, P. R. 1992 Direct simulation of the stably stratified turbulent Ekman layer. *J. Fluid Mech.* **244**, 677-712 (see Corrigendum).

Dörnbrack, A. & Schumann, U. 1994 Numerical simulation of breaking gravity waves below a critical level. Proc. First ERCOFTAC Workshop on Direct and Large-Eddy Simulation. March 28-30, 1994, Univ. of Surrey, Kluwer Acad. Publ., Dordrecht, in press.

Etling, D. 1993 Turbulence collapse in stably stratified flows: Application to the atmosphere. *Waves and Turbulence in Stably Stratified Flows.* (Mobbs, S.D. & King, J.C., eds.), Clarendon Press, Oxford, 1-21.

Farrell, B. F. & Ioannou, P. J. 1993 Transient development of perturbations in stratified shear flow. *J. Atmos. Sci.* **50**, 2201-2214.

Fernando, H. J. S. 1991 Turbulent mixing in stratified fluids. *Annu. Rev. Fluid Mech.* **23**, 455-493.

Gerz, T. 1991 Coherent structures in stratified turbulent shear flows deduced from direct simulations. In: *Turbulence and Coherent Structures* (O. Métais & M. Lesieur, eds.), Kluwer Academic Publishers, 449-468.

Gerz, T. 1993 Vortex structures and persistent counter-gradient fluxes. EUROMECH 305, Dynamics and Geometry of Vortical Structures, Cortona, June 28-July 2, 1993, Abstract, 13-14.

Gerz, T. & Palma, J.M.L.M. 1994 Sheared and stably stratified homogeneous turbulence: Comparison of DNS and LES. Proc. First ERCOFTAC Workshop on Direct and Large-Eddy Simulation. March 28-30, 1994, Univ. of Surrey, Kluwer Acad. Publ., Dordrecht, in press.

Gerz, T. & Schumann, U. 1989 Influence of initial conditions on the development of stratified homogeneous turbulent shear flow. *Finite Approximations in Fluid Mechanics II, Notes on Numerical Fluid Dynamics* (E.H. Hirschel, ed.), Vieweg, **25**, 142-156.

Gerz, T. & Schumann, U. 1991 Direct simulation of homogeneous turbulence and gravity waves in sheared and unsheared stratified flows. In: *Turbulent Shear Flow 7* (W.C. Reynolds, ed.), Springer-Verlag, 27-45.

Gerz, T., Schumann, U. & Elghobashi, S.E. 1989 Direct numerical simulation of stratified homogeneous turbulent shear flows. *J. Fluid Mech.* **200**, 563-594.

Gerz, T., Howell, J. & Mahrt, L. 1994 Vortex structures and microfronts. *Phys. Fluids* **6**, 1242-1251.

Gerz, T. & Schumann, U. 1994 A note on persistent counter-gradient fluxes in homogeneous turbulence. Prepared for submission. Institut für Physik der Atmosphäre, DLR.

Holt, S. E., Koseff, J. R. & Ferziger, J. H. 1992 A numerical study of the evolution and structure of homogeneous stably stratified sheared turbulence. *J. Fluid Mech.* **237**, 499-539.

Hopfinger, E. J. 1987 Turbulence in stratified fluids: A review. *J. Geophys. Res.* **92**, 5287-5303.

Hunt, J. C. R., Stretch, D. D. & Britter, R. E. 1988 Length scales in stably stratified turbulent flows and their use in turbulence models. *Stably Stratified Flows and Dense Gas Dispersion* (J.S. Puttock, ed.), Clarendon Press, Oxford, 285-321.

Itsweire, E. C., Koseff, J. R., Briggs, D. A. & Ferziger, J. H 1993 Turbulence in stratified shear flows: Implications for interpreting shear-induced mixing in the ocean. *J. Phys. Ocean.* **23**, 1508-1522.

Ivey, G. N. & Imberger, J. 1991 On the nature of turbulence in a stratified fluid. Part I: The energetics of mixing. *J. Phys. Ocean.* **21**, 650-658.

Kaltenbach, H.-J., Gerz, T. & Schumann, U. 1991 Transport of passive scalars in neutrally and stably stratified homogeneous turbulent shear flows. *Advances in Turbulence 3*, (A. Johansson & H. Alfredsson, eds.), Springer-Verlag, 327-334.

Kaltenbach, H.-J., Gerz, T. & Schumann, U. 1994 Large-eddy simulation of homogeneous turbulence and diffusion in stably stratified shear flow. *J. Fluid Mech.*, revised version submitted.

Konopka, P. 1994 Analytical Gaussian solutions for anisotropic diffusion in a linear shear flow. Prepared for submission. Institut für Physik der Atmosphäre, DLR.

Lesieur, M. 1993 Understanding coherent vortices through computational fluid dynamics. *Theoret. Comput. Fluid Dynamics* **5**, 177-193.

Mason, P. J. & Derbyshire, S. H. 1990 Large-eddy simulation of the stably-stratified atmospheric boundary layer. *Boundary-Layer Meteorol.* **53**, 117-162.

Mason, P. J. & Thomson, D. J. 1992 Stochastic backscatter in large-eddy simulations of boundary layers. *J. Fluid Mech.* **242**, 51-78.

Métais, O. & Herring, J. R. 1989 Numerical simulation of freely evolving turbulence in stably stratified turbulence. *J. Fluid Mech.* **202**, 117-148.

Métais, O. & Lesieur, M. 1992 Spectral large-eddy simulation of isotropic and stably stratified turbulence. *J. Fluid Mech.* **239**, 157-194.

Nieuwstadt, F. T. M. 1984 The turbulent structure of the stable, nocturnal boundary layer. *J. Atmos. Sci.* **41**, 2202-2216.

Nieuwstadt, F. T. M., Mason, P. J., Moeng, C. H. & Schumann, U. 1993 Large-eddy simulation of the convective boundary layer: A comparison of four computer codes. *Turbulent Shear Flows 8*, (F. Durst et al., eds.), Springer, Berlin, 343-367.

Richardson, L. F. 1920 The supply of energy from and to the atmospheric eddies. *Proc. Roy. Soc. London A* **97**, 354-373.

Rogers, M. M. & Moin, P. 1987 The structure of the vorticity field in homogeneous turbulent flows. *J. Fluid Mech.* **176**, 36-66.

Rogers, M. M. Mansour, N. N. & Reynolds, W. C. 1989 An algebraic model for the turbulent flux of a passive scalar. *J. Fluid Mech.* **203**, 77-101.

Rohr, J. J., Itsweire, E. C., Helland, K. N. & Van Atta, C. W. 1988 Growth and decay of turbulence in a stably stratified shear flow. *J. Fluid Mech.* **195**, 77-111.

Schmidt, H. & Schumann, U. 1989 Coherent structure of the convective boundary layer derived from large-eddy simulations. *J. Fluid Mech.* **200**, 511-562.

Schumann, U. 1985 Algorithms for direct numerical simulation of shear-periodic turbulence. *Lecture Notes in Physics*, Springer, **218**, 492-496.

Schumann, U. 1987 The countergradient heat flux in stratified turbulent flows. *Nucl. Engrg. Des.* **100**, 255-262.

Schumann, U. 1991 Subgrid length-scales for large-eddy simulation of stratified turbulence. *Theoret. Comput. Fluid Dynamics* **2**, 279-290.

Schumann, U. 1993 Large-eddy simulation of turbulent convection over flat and wavy terrain. *Large Eddy Simulation of Complex Engineering and Geophysical Flows.* (B. Galperin and S.A. Orszag, eds.), Cambridge Univ. Press, 399-421.

Schumann, U. 1994a Correlations in homogeneous stratified shear turbulence. *Acta Mech. (Suppl)* **4**, 105-111.

Schumann, U. 1994b Stochastic backscatter of turbulence energy and scalar variance from random subgrid-scale fluxes. Osborne Reynolds Centenary Symposium, 24 May 1994, UMIST, Manchester, to be published.

Schumann, U. & Gerz, T. 1994 Turbulent mixing in stably stratified shear flows. *J. Appl. Met.*, in press.

Staquet, C. 1993 Wave/vortex decompositions in stably stratified flows. *Theoret. Comput. Fluid Dynamics* **5**, 195-213.

Tavoularis, S. & Corrsin, S. 1985 Effects of shear on the turbulent diffusivity tensor. *Int. J. Heat Mass Transfer* **28**, 256-276.

Tavoularis, S. & Karnik, U. 1989 Further experiments on the evolution of turbulent stresses and scales in uniformly sheared turbulence. *J. Fluid Mech.* **204**, 457-478.

Webster, C. A. G. 1964 An experimental study of turbulence in a density-stratified shear flow. *J. Fluid Mech.* **19**, 221-245.

MICROSTRUCTURE SIMULATION OF SUSPENDED SEDIMENTS

Panagiotis D. Scarlatos
Department of Ocean Engineering
College of Engineering
Florida Atlantic University
Boca Raton, Florida 33431, U.S.A.

Mohamed H. Kamel
Eng. Mathematics & Physics Dept.
Faculty of Engineering
Cairo University
Giza, EGYPT

ABSTRACT

The vertical motion of fine particles suspended in aquatic systems is affected by gravitational settling, turbulent diffusion and the physicochemical characteristics of the particulate matter. These particle suspensions can lead to stratification which presents similarities to other density stratification phenomena. The leading difference between particulate and dissolved matter suspensions is that solid particles can aggregate and settle. Depending on the balance between density gradient and shear production, certain regions along the water column may become unstable leading to strong mixing and homogenization of those regions. This instability could create steeper density gradients between the homogenized region and its surroundings that would lead to the appearance of a step-wise density profile. Based on the nonlinear, one-dimensional advection-diffusion equation, the microstructure phenomenon is explained using the sufficient condition for interfacial instability in shear stratified flows ($R_{iu} < 0.25$). The analysis is verified by solving the governing equation numerically and observing a microstructure generation along the vertical density profile.

INTRODUCTION

Understanding of the suspended sediment concentration profile is very important for estimation of sediment discharge and contaminant transport in aquatic ecosystems. One of the earliest studies on the vertical distribution of suspended granular material was done by Rouse (1937). His analysis indicated that the concentration is always higher near the bed and it decreases toward the water surface. He also pointed that the concentration profile tends to be more uniform for smaller particle size (i.e., low settling velocity) or for higher turbulence level (i.e., high shear velocity). The original Rouse equation was later improved to account for the difference between the eddy viscosity and turbulent diffusion coefficients (Einstein and Chien, 1954). The density profile predicted by these theories was smooth and continuous. Also, these early models did not account for any particle aggregation effects; the fall velocity was a function of the particle diameter but not of the suspended sediment concentration. Recent experimental and field data are supporting the fact that the dynamics of cohesive sediment suspensions resemble the behavior of other density stratified systems, i.e., those caused by temperature or salinity. Field observations of tidal channels along the west coast of Korea showed interfacial waves and Kelvin-Helmholtz billows occurring on the suspended-sediment-related density gradient or lutocline (Adams, et al., 1990). Laboratory experiments conducted on soft, high concentrated bottoms revealed instability patterns resembling second-mode Holmboe waves (Winterwerp, et al., 1993). Computer simulation of lutocline instability and growth was accomplished by using a multi-layer vortex sheet model (Scarlatos and Mehta, 1993). In addition, density microstructure profiles have been frequently observed to occur in muddy estuarine systems in U.K. (Kirby, 1986; Leuttich, et al., 1993). A microstructure model for suspended sediment with negligible settling effects was developed by Scarlatos and Mehta (1990) based on the work on salinity microstructure by Posmentier (1977).

The phenomenon of microstructure has been extensively documented and studied for temperature- and salinity-induced density stratification in the oceans (Woods, 1968; Turner, 1973; LeBlond and Mysak, 1978; Dera, 1992). These quasi-homogeneous density steps can vary in thickness from few centimeters to tens of meters with lifetimes ranging from tens of minutes to hours (Tait and Howe, 1971; Monin and Ozmidov, 1986). There are various theories and models developed for explanation of the generation of microstructure profiles. Woods and Wiley (1973) suggested a model where a step-wise profile was generated by vertical patches of billows. McGorman and Mysak (1973) modelled oceanic microstructure by using a two-dimensional internal wave equation with a randomly varying Brunt-Väisälä frequency. Eriksen (1978) coupled an internal wave model with a "passive" fine structure model. McEwan (1983) explained local mixing in stratified system by comparing the potential energy gained through stratification to the kinetic energy lost in motions on the scales of the mixing processes. Koop and McGee (1986) experimentally showed the overturning of internal waves in continuously stratified shear flows. Gregg (1987) explained ocean microstructure using diapycnal fluxes of salt and heat. These are just few of the many studies on microstructure. However, there are still some remaining questions regarding the onset, growth and timing of microstructure generation.

This paper is focused on the microstructure developed in systems where stratification is caused by suspension of fine particulate subject to free settling, hindered settling and turbulent diffusion. The velocity profile is time-independent and is considered to remain unaffected by density changes. The phenomenon is mathematically described by a nonlinear, one-dimensional advection-diffusion equation. The eddy-diffusivity is taken as a function of the suspended sediment concentration and velocity gradients, while the settling velocity depends on the concentration.

GOVERNING EQUATIONS

Based on the coordinate system, density stratification, and flow conditions as presented in Figure 1, the vertical exchange of suspended sediment mass due to turbulent diffusion and gravitational settling can be described by the one-dimensional diffusion-advection equation as

$$\frac{\partial C}{\partial t}=-\frac{\partial F}{\partial C_z}\frac{\partial^2 C}{\partial z^2}-\frac{\partial (w_s C)}{\partial z} , \qquad (1)$$

where C is the concentration of the suspended sediments, w_s is the particle fall velocity, z is the vertical axis and t is the time. The variable C_z is the concentration gradient, i.e.,

$$C_z=\frac{\partial C}{\partial z} , \qquad (2)$$

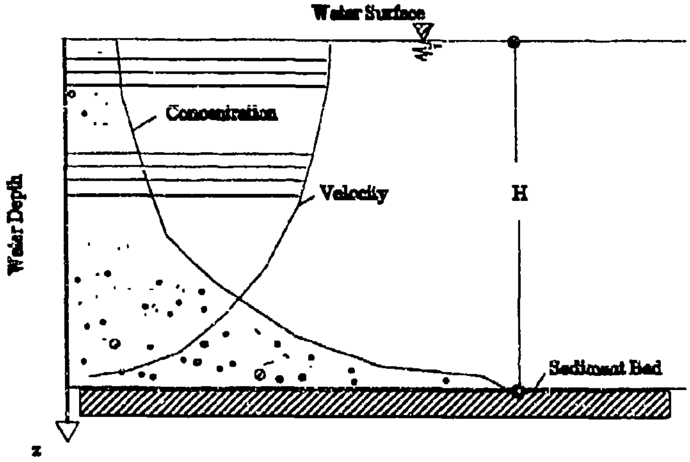

Figure 1. Vertical profile of suspended sediment concentration.

while the variable F denotes the diffusive flux,

$$F=-K\frac{\partial C}{\partial z}\ , \tag{3}$$

where K is the eddy diffusivity coefficient. In the r.h.s. of eq. 1, the first term represents the negative (upward) flux due to turbulent diffusion, while the second term represents the positive (downward) flux due to particle settling. Rearrangement of eq. 1 yields

$$\frac{\partial C}{\partial t}=\frac{\partial}{\partial z}\left(K\frac{\partial C}{\partial z}-w_s C\right)\ . \tag{4}$$

Furthermore, if K and w_s are depth invariant, by using the normalization variables,

$$Z=\frac{z}{H}\ ;\qquad T_s=\frac{w_s t}{H}\ ;\qquad T_d=\frac{Kt}{H}\ , \tag{5}$$

eq. 4 can be re-written in a non-dimensional form either as

$$\frac{\partial C}{\partial T_s}=\frac{\partial}{\partial Z}\left(\frac{1}{P_e}\frac{\partial C}{\partial Z}-C\right)\ , \tag{6a}$$

or as

$$\frac{\partial C}{\partial T_d}=\frac{\partial}{\partial Z}\left(\frac{\partial C}{\partial Z}-CP_e\right)\ , \tag{6b}$$

where P_e is the Peclet number, H is the water depth, Z is the length scale, and T_s, T_d are the advective and diffusive time scales respectively. Under steady-state conditions

$$P_e=\frac{1}{C}\frac{\partial C}{\partial Z}\ , \tag{7}$$

i.e., the Peclet number characterizes the stratification of the suspended particle system (Teeter, 1986). It is known however, that the eddy diffusivity coefficient, K, depends on the flow and stratification characteristics as given by the following relation:

$$K=A(1+sR_{iu})^{r}\ , \tag{8}$$

where A is a turbulent mixing coefficient, R_{iu} is the Richardson's number and s, r are experimental constants (Okubo, 1970). More specifically, the coefficient A is related to the velocity shear and turbulent fluctuations,

$$A=l_o^{2}\left|\frac{\partial u}{\partial z}\right|\ , \tag{9}$$

where u is the longitudinal flow velocity, l_o is the mixing length,

$$l_o=kz\left(1-\frac{z}{H}\right)\ , \tag{10}$$

and k is the Von Karman's constant. In addition, the Richardson's number reads

$$R_{iu}=g\frac{\rho_s-\rho}{\rho}\frac{\frac{\partial C}{\partial z}}{(\frac{\partial u}{\partial z})^2} , \qquad (11)$$

where g is the acceleration due to gravity, and ρ_s, ρ are the densities of sediment and water respectively (Scarlatos and Mehta, 1990). Using eq. 11, the eddy diffusivity coefficient (eq. 8) is rewritten as

$$K=A(1+B\frac{\partial C}{\partial z})^{r} , \qquad (12)$$

where the coefficient B is given by the following expression

$$B=sg\frac{\rho_s-\rho}{\rho}\frac{1}{(\frac{\partial u}{\partial z})^2} , \qquad (13)$$

For fine particle suspensions, the experimental constants s and r where found to vary between the limits: $3.33 < s < 10$ and $-2.0 < r < -0.5$ (Ross, 1988). These limits include the values reported for salinity or thermal stratification, i.e., $s = 4.17$, $r = -2$ (Delft Hydraulics Laboratory, 1974), and $s = 3.33$, $r = -1.5$ (Munk and Anderson, 1948).

Combination of eqs. 1-3 and 12, after some algebraic manipulations yields,

$$\frac{\partial C}{\partial t}=A[1+(1+r)B\frac{\partial C}{\partial z}](1+B\frac{\partial C}{\partial z})^{r-1}\frac{\partial^2 C}{\partial z^2}-\frac{\partial(w_s C)}{\partial z} . \qquad (14)$$

The critical state of the stratified system described by eq. 14, can be obtained from the following equation (Posmentier, 1977):

$$[1+(1+r)B\frac{\partial C}{\partial z}](1+B\frac{\partial C}{\partial z})^{r-1}=0 . \qquad (15)$$

Whenever C_z is such that the l.h.s. of eq. 15 is greater than zero, the interface tends to be diffusive leading to mixing between the layers of different density. Under these circumstances, if $s = 4$ and $r = -2$, then $R_{iu} < 0.25$ which is the sufficient criterion for instability in shear stratified flows (Turner, 1973). For $s = 3.33$ and $r = -1.3$, the instability relation becomes $R_{iu} < 1$, that is consistent with the sufficient stability criterion presented by Miles (1987). For $r = -1$, the system appears to be unconditionally stable (Scarlatos and Mehta, 1990).

The settling velocity, w_s, depends on the suspended sediment concentration, C. Initially, the settling velocity increases with increasing concentration until the concentration reaches a critical value, C_m, after which the settling rate is reduced due to hindered settling effects (Mehta, 1986). These relations are quantified as follows:

$$w_s=k_1C^{\alpha} , \qquad for \quad C\leq C_m , \qquad (16)$$

or

$$w_s=w_{s0}(1-k_2C)^{\beta} , \qquad for \quad C>C_m , \qquad (17)$$

where w_{s0} is a reference fall velocity, and k_1, k_2, α and β are experimental constants depending on the sediment characteristics. The values of these constants were reported in the literature as: $k_1 \approx 0.5$, $k_2 = 0.008$, $1 \leq \alpha \leq 2$, $\beta \approx 5$ and $w_{s0} \approx 2.6$ mm/s The value of the critical concentration, C_m, for the onset of hindered settling varies according to the sediment composition, between $3 \leq C_m \leq 15$ g/l (Mehta, 1986).

Depending on the settling mode of the falling particles (free or hindered), combination of eqs. 14, 16 and 17, leads to the following relations respectively

$$\frac{\partial C}{\partial t}=A[1+(1+r)B\frac{\partial C}{\partial z}](1+B\frac{\partial C}{\partial z})^{r-1}\frac{\partial^2 C}{\partial z^2}-(\alpha+1)k_1C^{\alpha}\frac{\partial C}{\partial z}\ , \qquad for \quad C\leq C_m \tag{18a}$$

and

$$\begin{gathered}\frac{\partial C}{\partial t}=A[1+(1+r)B\frac{\partial C}{\partial z}](1+B\frac{\partial C}{\partial z})^{r-1}\frac{\partial^2 C}{\partial z^2}+ \\ [w_{so}k_2\beta(1-k_2C)^{\beta-1}C-w_{so}(1-k_2C)^{\beta}]\frac{\partial C}{\partial z}\ , \qquad for \quad C>C_m\ .\end{gathered} \tag{18b}$$

For completeness of the mathematical problem, boundary conditions are properly assigned. Assuming, no particle re-entrainment from the bottom, both boundary conditions, i.e., at the water surface and the bottom are taken as of zero-flux,

$$K\frac{\partial C}{\partial z}-w_sC=0\ . \tag{19}$$

The system of eqs. 18a, 18b, and 19 constitutes the theoretical model used to simulate the microstructure profile of cohesive sediment suspensions. This model is a PDE, nonlinear parabolic system. The nonlinear terms involve power-raised combinations of the dependent variable, C, and its first and second spatial derivatives.

NUMERICAL APPLICATION

The governing system of equations (eqs. 18a, 18b and 19) cannot be solved analytically in its general form. An iterative, implicit finite difference scheme can be applied to solve the problem (Scarlatos and Mehta, 1990). However, in this study, eqs. 18a, 18b are discretized based on a linearized finite-difference scheme. Linearization is achieved by evaluating the concentration and its spatial derivatives of the nonlinear terms either from the initial conditions or from the previous time step:

$$\frac{\partial C}{\partial z}=\frac{\delta C}{\delta z}=\frac{C^j_{i+1}-C^j_{i-1}}{2\delta z}\ , \tag{20}$$

$$\frac{\partial^2 C}{\partial z^2}=\frac{\delta^2 C}{\delta z^2}=\frac{C^j_{i+1}-2C^j_i+C^j_{i-1}}{\delta z^2}\ , \tag{21}$$

$$\frac{\partial C}{\partial t}=\frac{\delta C}{\delta t}=\frac{C^{j+1}_i-C^j_i}{\delta t}\ , \tag{22}$$

where i, j are respectively the number of spatial steps, δz, and temporal steps, δt. The dependent variable, C, is known at time step $j\delta t$, and the solution marches to the new time step $(j+1)\delta t$. This explicit numerical scheme is subject to the CFL stability conditions

$$\delta t<\frac{2K}{w_s^2}\ , \qquad and \qquad \delta z<\frac{2K}{w_s}\ . \tag{23}$$

If the second stability criterion is violated oscillatory solutions may be expected (Fletcher, 1991).

The solution domain is unbounded along the longitudinal axis. For the upper and lower boundaries a no-flux condition (eq. 19) is used. A time-independent, parallel flow with the following hyperbolic-tangent velocity profile was applied:

$$u(z)=0.5(1+tanhz_*) \ , \qquad (24)$$

where z_* is a linear function of the depth z. Similarly, the initial concentration, C_o, is given by a hyperbolic-tangent relation,

$$C_o(z)=\epsilon(1+tanhz_+) \ , \qquad (25)$$

where z_+ is a linear function of the depth z and ϵ is a constant.

RESULTS AND DISCUSSION

The computer model was applied under different flow fields, initial concentrations, and experimental constants. The applications showed either development of a smooth concentration profile or generation of a step-wise density distribution. Microstructure was primarily observed above the lutocline. In general, the results were in good agreement with the theoretical discussion pertaining eq. 15. However, there were some cases where the numerical computations became unstable due to violation of the criteria for numerical stability (eq. 23).

The time-space variability of the eddy diffusivity and settling velocity in eq. 23 placed a lot of limitations to the selection of the time and space steps, δt, δx. Whenever, oscillatory motion was observed, the stability criteria were checked for compliance. However, due to the highly nonlinear character of the governing equation it is possible that the CFL stability criterion may not reflect accurately the conditions for numerical stability.

Two representative cases of smooth and microstructure profiles are presented in Figures 2 and 3 respectively. In Figure 2, the suspended sediment profile remains smooth in time; the value of r used for this particular run was -1. In Figure 3, a microstructure profile was established above the lutocline; the value for r was -2. Some possible microstructure effects can be observed also near the lower boundary.

A more robust, implicit numerical scheme is under development for comparison purposes. The simulation data are in qualitative agreement with limited field and experimental observations.

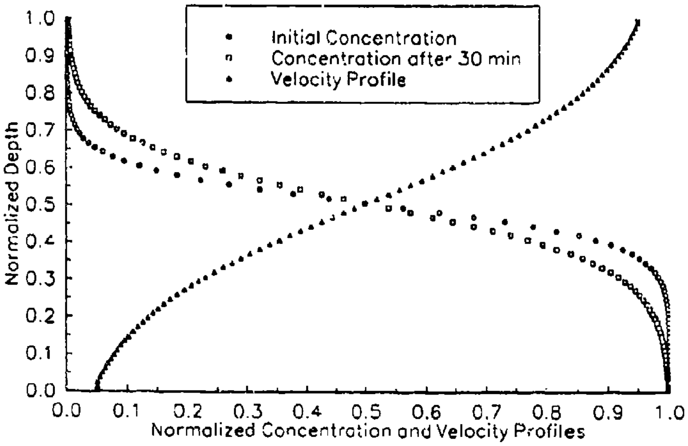

Figure 2. Development of a smooth suspended sediment concentration profile.

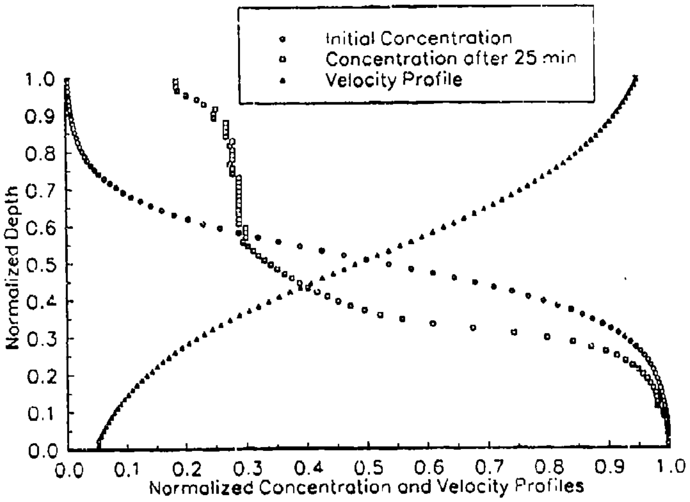

Figure 3. Generation of a microstructure suspended sediment concentration profile.

CONCLUDING REMARKS

The one-dimensional, nonlinear diffusion-advection model equation was able to produce vertical concentration profiles of suspended cohesive sediments with evident microstructural characteristics. This was attributed to the fact that under certain circumstances turbulent diffusive mixing is locally enhanced leading to step-like homogenized regions. The microstructure characteristics will vary for different velocity profiles, initial suspended sediment concentration profiles, and sediment characteristics.

ACKNOWLEDGEMENTS

Part of this research was conducted during the stay of the co-author at the Ocean Engineering Department, Florida Atlantic University, U.S.A. Support for his sabbatical was provided from the U.S. and Egyptian governments under the Peace Fellowship Post-Doctoral Program.

LITERATURE CITED

Adams, C.E., Wells, T.J. and Park, Y.-A., 1993. Wave Motions on a Lutocline Above a Stably Stratified Bottom Boundary Layer, in: Nearshore and Estuarine Cohesive Sediment Transport, A.J. Mehta, (Ed.), American Geophysical Union, Washington, D.C., 393-410.

Delft Hydraulics Laboratory, 1974. Momentum and Mass Transfer in Stratified Flows, Report No. R 880, Delft, The Netherlands.

Dera, J., 1992. Marine Physics, Elsevier Oceanography Series, 53, Elsevier, Amsterdam, The Netherlands.

Einstein, H.A. and Chien, N., 1954. Second Approximation to the Solution of the Suspended Load Theory, Research Report No. 3, University of California, Berkeley, California.

Eriksen, C.C., 1978. Measurements and Models of Fine Structure, Internal Gravity Waves, and Wave Breaking in the Deep Ocean, Journal of Geophysical Research, 83(6), 2989-3009.

Fletcher, C.A.J., 1991. Computational Techniques for Fluid Dynamics, 2nd Edition, Vol. I, Springer-Verlag, Berlin, Germany.

Gregg, M.C., 1987. Diapycnal Mixing in the Thermocline: A Review, Journal of Geophysical Journal, 92(5), 5249-5286.

Koop, C.G. and McGee, B., 1986. Measurements of Internal Gravity Waves in a Continuously Stratified Shear Flow, Journal of Fluid Mechanics, 172, 453-480.

LeBlond, P.H. and Mysak, L.A., 1978. Waves in the Ocean, Elsevier Oceanography Series, 20, Elsevier, Amsterdam, The Netherlands.

Luettich, R.A., Wells, J.T. and Kim, S.-Y., 1993. *In Situ* Variability of Large Aggregates: Preliminary Results on the Effects of Shear, in: Nearshore and Estuarine Cohesive Sediment Transport, A.J. Mehta, (Ed.), American Geophysical Union, Washington, D.C., 447-466.

McEwan, A.D., 1983. The Kinematics of Stratified Mixing Through Internal Wave Breaking, Journal of Fluid Mechanics, 128, 47-57.

McGorman, R.E. and Mysak, L.A., 1973. Internal Waves in a Randomly Stratified Fluid, Geophysical Fluid Dynamics, 4, 243-266.

Mehta, A.J., 1986. Characterization of Cohesive Sediment Properties and Transport Processes in Estuaries, in: Estuarine Cohesive Sediment Dynamics, A.J. Mehta, (Ed.), Springer-Verlag, Berlin, Germany, 290-325.

Miles, J., 1987. Richardson's Number Revisited, Proc. 3rd International Symposium on Stratified Flows, Vol. I, Pasadena, California, 1-7.

Monin, A.S. and Ozmidov, R.V., 1985. Turbulence in the Ocean, D. Reidel Publishing Co., Dordrecht, Holland.

Munk, W.H. and Anderson, E.R., 1948. Note on a Theory of the Thermocline, Journal Marine Research, Vol. 7, 276-295.

Okubo, A., 1970. Oceanic Mixing, Management Oceanic Services, Detroit, Michigan.

Posmentier, E.S., 1977. The Generation of Salinity Finestructure by Vertical Diffusion, Journal of Physical Oceanography, 7, 298-300.

Ross, M.A., 1988. Vertical Structure of Estuarine Fine Sediment Suspensions, Ph.D. Dissertation, University of Florida, Gainesville, Florida.

Rouse, H., 1937. Modern Conceptions of the Mechanics of Fluid Turbulence, Transactions ASCE, 102, 463-505.

Scarlatos, P.D. and Mehta, A.J., 1990. Some Observations on Erosion and Entrainment of Estuarine Fluid Muds, in: Residual Currents and Long-term Transport, R.T. Cheng, (Ed.), Springer-Verlag, Berlin, Germany, 321-333.

Scarlatos, P.D. and Mehta, A.J., 1993. Instability and Entrainment Mechanisms at the Stratified Mud-Water Interface, in: Nearshore and Estuarine Cohesive Sediment Transport, A.J. Mehta, (Ed.), American Geophysical Union, Washington, D.C., 205-223.

Tait, R.I. and Howe, M.R., 1971. Thermohaline Staircase, Nature, 231, 178-179.

Teeter, A.M., 1986. Vertical Transport in Fine-Grained Suspension and Newly-Deposited Sediment, in: Estuarine Cohesive Sediment Dynamics, A.J. Mehta, (Ed.), Springer-Verlag, Berlin, Germany, 170-191.

Turner, J.S., 1973. Buoyancy Effects in Fluids, Cambridge University Press, Cambridge, U.K.

Winderwerp, J.C., Cornelisse, J.M. and Kuijper, C., 1993. A Laboratory Study on the Behavior of Mud from the Western Scheldt Under Tidal Conditions, in: Nearshore and Estuarine Cohesive Sediment Transport, A.J. Mehta, (Ed.), American Geophysical Union, Washington, D.C., 295-313.

Woods, J.D., 1968. Wave-Induced Shear Instability in the Summer Thermocline, Journal of Fluid Mechanics, 32, 791-800.

Woods, J.D. and Wiley, R.L., 1972. Billow Turbulence and Ocean Microstructure, Deep-Sea Research, 19, 87-121.

TURBULENT ENTRAINMENT OF SOLID PARTICLE SUSPENSIONS IN A TWO-LAYER FLUID

Xuequan E and Wei WANG
Institute of Mechanics, Academia Sinica, Beijing 100080, PRC

ABSTRACT

The growth behaviour of zero-mean-shear turbulent mixed-layer containing suspended solid particles has been studied experimentally in a two-layer fluid system. The experimental results show that the relationship between the entrainment distance and time, and the variation of the dimensionless entrainment rate E with the local Richardson number Ri_l for the suspended particles differ from that of the pure two-layer fluid by the factors $\eta^{-1/5}$ and η^{-1} ($\eta = 1 + \sigma_0\rho_p/\Delta\rho_0$, where σ_0 is initial volume concentration of particles), respectively.

INTRODUCTION

Stratification of fluid exists extensively in geophysical and industrial fluids. The turbulent mixing in a stratified fluid is important in controlling water-quality and tackling pollution in the atmosphere and various bodies of water. If there are solid particles suspended in a turbulently mixed layer, kinetic energy will be consumed to keep the particles in suspension, thus changing the turbulent structure and affecting the behaviour of turbulent entrainment. Therefore, it is necessary to investigate the influence of suspended particle concentration on the turbulent entrainment.

E and Hopfinger[1] investigated turbulent entrainments on settled solid particles on the bottom in a uniform fluid, and obtained a relationship between the distance of turbulent entrainment and the r.m.s. turbulent velocity, and the local buoyancy flux. Barenblatt[2] studied the shear turbulence with the suspended particles saturated near the wall by means of dimensional analysis. In order to understand the entrainment of a turbulently mixed layer containing suspended particles, one has first to make clear the characteristics of turbulence. The features of the zero-mean-shear turbulence generated from the planer oscillating grid have been widely studied[3,4]. The grid stirring can simulate the natural processes in which turbulent energy is put in on a scale much smaller than the layer depth, such as the breaking of waves at the sea surface[5]. The oscillating grid was selected as the turbulent energy source. The investigation[3] show that the horizontal (u, v) and vertical (w) r.m.s. turbulent velocity components ($u \approx v \sim w$) and the integral lengthscale of turbulence l at a distance z away from the grid midplane, are given by

$$u = CM^{1/2}S^{3/2}fz^{-1} \tag{1}$$

$$l = \beta z \tag{2}$$

where C is the coefficient of proportionality, approximately 0.3, S(cm) is the stroke of grid oscillation, M(cm) is the mesh length, f(Hz) is the frequency of grid oscillation, and β is the constant related to stroke S, here $\beta = 0.1$[3]. Relation (1.1) is a good approximation to the r.m.s. turbulent velocity generated by the grid made from square bars with the mesh size M/d=5, oscillated at $f \leq 6Hz$ (where d is the bar size).

The aim of the present work is to study the growth law of a zero-mean-shear turbulent mixed-layer varying with the solid particle concentration (in terms of volume or mass) and external parameters of the turbulent source. The experiments have been conducted in a wide range: $S = 2 - 5cm, f = 2 - 5Hz$, initial particle volume concentration $\sigma_0 = 2.98\% - 7.24\%$.

EXPERIMENTAL PROCEDURE

The experiments were performed in an oscillating grid turbulence tank of 52cm×52cm×70cm as shown in the Fig.1. The tank was filled with two-layer fluid (the upper layer was clean water 9cm in depth). The plastic particles of diameter about $100\mu m$ and density $1.04g/cm^3$ were putted on the interface, and the increment of the water level after putting the particles was recorded so as to measure exactly the initial volume concentration of the particles.

Using the method of shadowgraph, we visualized the interface and the front of the turbulent entrainment. A digital clock with precision of 0.1s was installed at the front face. The position of the trubulent front and corresponding time were recorded by the photographs. On the shadowgraph (or film), the mean horizontal position of the turbulent front of the mixed layer (or the depth of the mixed layer) D would be found. The reading error was smaller than 2mm. The time digit on the film was the time when the front arrived at the corresponding position, thus, the entrainment rate of the mixed layer could be determined.

EXPERIMENTAL RESULTS AND DISCUSSIONS

A. Relations Between Entrainment Distance D and Time t

Under the given conditions (z_0 and $\Delta\rho_0/\rho_2$ were kept constant, $\Delta\rho_0 = \rho_2 - \rho_1$), the experiments were conducted for different frequencies f, strokes S and initial volume concentrations of particles σ_0($\sigma_0 = 0$, for the pure two-layer fluid). The results are shown in Fig.2, from which we know that D can be expressed as

$$D = at^k \ , \ k = 0.20 \begin{array}{l} +0.034 \\ -0.009 \end{array} , \tag{3}$$

where a is a constant related to the frequency f, the stroke S and the initial volume concentration σ_0 determined by experiment, (see Table 1). Fig.2 shows that the time-variation law of the entrainment of suspended particles in the mixed layer is the same as that of the pure two-layer fluid: $D \propto t^{1/5}$, but the D-t line for the suspended particles is below the line for the pure two-layer fluid under the same initial conditions (Fig.2(a)), showing that the growth of the mixed layer with suspended particles is slower than that without suspended particles when $\sigma_0 = 0, k = 0.20^{+0.034}_{-0.009}$, which is in good agreement with the results in [6].

Table 1 gives some of the values of the experimental results. They were obtained by using the least-square fitting to the measured datum points (D, t), with the linear correlativety above 0.99.

B. Relation Between the Entrainment Distance D and the Oscillation Frequency f

It is known from Figs. 2 that when S and σ_0 are given, the interception $\log a$ has different values for different frequencies f, and a depends only on f

$$a = a_1 f^{\alpha_1}, \ \alpha_1 = 0.80 \pm 0.05 \ , \tag{4}$$

where a_1 is the proportional constant related to S and σ_0. The variation of a with f is given in Fig.3. From (3) and (4) we obtain

$$D \propto f^{0.80}, \tag{5}$$

(5) also shows that the fluids with and without suspended particles have the same frquency relation. The corresponding values are given in Table 1.

C. Stroke Dependence

In order to determine the relation between D and S we have measured the turbulent entrainment distance for the various strokes S, at a fixed frequency ($f = 2Hz$) and the same values of σ_0 as those in the various frequency experiments. The measuremental results are given in Figs. 2(b). Evidently, when f is fixed, a in (3) is related to S and σ_0. Fig.4 gives the logarithmic relation between a and S in the case of given σ_0, consequently we have

$$a = a_2 S^{\alpha_2}, \ \alpha_2 = 1.20 \ {}^{+0.03}_{-0.04} \ . \tag{6}$$

Here a_2 is a constant related to f and σ_0, but it is only a function of σ_0 at fixed f. Corresponding values are given in Table 2. The mixed layer entrainment of both the pure two-layer fluid and the fluid with suspended particles, varies with S of 1.20 power

$$D \propto S^{1.20} \ . \tag{7}$$

D. Variation of Entrainment Distance with Initial Particle Concentration

After the relationship of D with f and S is obtained, it is not difficult to find the relation between the entrainment distance and the initial particle volume concentration. Fig.2(c) shows that at f and S, the interception *loga* has different values for different σ_0. This means that a is related to σ_0. a_1 and a_2 in Tables 1 and 2 also give some indications of such dependence. But, considering that the D-t relationship must degenerate into that for the pure two-layer fluid, it is reasonable to take $\eta = 1 + \sigma_0 \rho_p / \Delta\rho_0$ (here ρ_p is the density of plastic material of the particle) as a parameter to replace σ_0. The variations of a_1 and a_2 with η are given in Fig.5. Dividing a_1 and a_2 by $S^{1.20}$ and $f^{0.80}$ respecitively and making statistic average, we obtain the proportional constant a_3 related only to σ_0. Generally, a_3 is also related to $z_0, \Delta\rho_o/\rho_2$ and M, but these parameters were fixed in our experiments. Fig.6 shows the variation of a_3 with η, from which we get

$$a_3 = a_4 \eta^{\alpha_3}, \ \alpha_3 = -0.20 \pm 0.27 \ , \tag{8}$$

where a_4 is the proportional coefficient related to M, z_0 and $\Delta\rho_0/\rho_2$.

From (3), (4), (6) and (8) it is known that D is proportional to η^{α_3}:

$$D \propto \eta^{-0.20}, \tag{9}$$

Because $\sigma_{0max} = 1, \rho_p = 1.04 g/cm^3$ and $\rho_{2max} \approx 1.18 g/cm^3$, we have $\eta_{max} = 5.8$ which is impobable. Consequently, $1 \leq \eta < 5.8$. $\eta = 1$ for the prue two-layer fluid.

E. Growth Behaviour of the Turbulent Mixed Layer

The growth of the mixed layer is characterized by the entrainment distance D. As mentioned above, D is directly proportional to $t^{0.20}, f^{0.80}, S^{1.20}$ and $\eta^{-0.20}$. So D can be written as

$$D = a_5 \eta^{-0.20} S^{1.20} f^{0.80} t^{0.20}, \tag{10}$$

where a_5 is the proportional constant related to M, z_0 and $\Delta\rho_0/\rho_2$. (10) can be obtained from (3) by resolving a gradually. (10) gives the entrainment law of the mixed layer containing suspended particles. Actually, the proportional coefficient a_5 is equal to a_4, so $a_5 = 0.664$. When $\sigma_0 = 0$ and $\eta = 1$, (10) becomes

$$D = a_5 S^{1.20} f^{0.80} t^{0.20}. \tag{11}$$

(11) shows the entrainment behaviour of the pure two-layer, which is consistent with the results of Ref.[6].

F. Relation Between Entrainment Rate E and Richardson Number Ri_l

With the $D-t$ relation determined, it is not difficult to find the growth velocity of the mixed layer $u_e = dD/dt$. The dimensionless entrainment rate E and the local Richardson number Ri_l based on the horizontal r.m.s. turbulent velocity at $z = D$ are defined as [6]

$$E = u_e/u, \tag{12}$$

$$Ri_l = \left(g\frac{\Delta\rho}{\rho}l\right)/u^2, \tag{13}$$

where

$$\Delta\rho = (\rho_2 - \rho_1)\frac{z_0}{z_0 + D}, \quad \rho = \rho_1\frac{z_0}{z_0 + D} + \rho_2\frac{D}{z_0 + D}. \tag{14}$$

In Fig.7 the variation of entrainment rate E versus Richardson number Ri_l is plotted on a logaithmic scale. The fitting to the experimental data by the equation

$$E = KRi_l^{-1.50}, \tag{15}$$

is satisfactory. From Fig.7 we can see the dependence of K on σ_0 or η, which can be expressed as

$$K = K_0\eta^{-1}, \tag{16}$$

where K_0 is a constant at $\sigma_0 = 0, K_0 = 13.421$ (see Fig.8). The date are given in Table 3.

Eq. (15) shows that that the dimensionless entrainment rate E of the mixed layer with suspended particles does not change the power law of Ri_l, differing from the pure two-layer by only a factor η^{-1}. This means that when η (i.e. σ_0) increases, E decreases by the first power ($E\propto 1/\eta$). When $\sigma_0 = 0$, Eq. (15) becomes $E = K_0Ri_l^{-3/2}$, which is excellently consistent with the experimental results in Ref.[6].

CONCLUSIONS

In this paper, the entrainment of the turbulent mixed layer with suspended particles has been studied experimentally in the two-layer fluid system. The principal conclusions are drawn as follows.

1. The time dependence of turbulent entrainment for suspended particles is the same as that for a pure two-layer fluid: the entrainment distance (or depth) D varies with 1/5 power of time, i.e. $D = at^k, k = 1/5$.

2. The entrainment distance D depends on the exterior parameters of the oscillating grid gengerting a tubulent source, i.e. D is directly proportional to $f^{4/5}$ and $S^{6/5}$.

3. When $D \gg z_0$ (a long time procedure), the entrainment distance D can be estimated by

$$D = A\left(g\frac{\Delta\rho_0}{\rho_2}z\right)^{-3/10}\eta^{-1/5}M^{2/5}S^{6/5}f^{4/5}t^{1/5},$$

which differs from that for the pure two-layer fluid by a factor of $\eta^{-1/5}$.

4. The entrainment velocity u_e of a mixed layer decreases with an increase in η, i.e.

$u_e\propto\eta^{-1}$.

5. The dimensionless entrainment rate E for a fluid with suspended particles observes the same power law Ri_l as that without suspended particles, $E = KRi_l^{-3/2}$, where $K = K_0\eta^{-1}$, differing only by a factor η^{-1}. This shows that E for the former decreases as η increases. At $\eta = 1, E = K_0Ri_l^{-3/2}$, which describes the turbulent entrainment of a pure two-layer fluid.

REFERECES

[1] E Xuequan & Hopfinger, E.J., Stratification by solid particle suspensions, Proc. Int. Symp. Strtif. Flows, 3rd, 1987, Pasadena, Calif.

[2] Barablatt, G.I., Similarity self-similarity and intermediate asymptotics-Theory and application to geophysical hydrodynamics, Lenigrad Gidrometeoizdat 1982, 209-223 (in Russian).

[3] Hopfinger, E.J. & Toly, J.A, Spatially decaying turbulence and its relation to mixing across density interface, J.Fluid Mech., 78(1976), 155.

[4] Long, R.R., Theory of turbulence in a homogeneous fluid induced by an oscillating grid, Phys. FLuid, 21(1978), 1887.

[5] Turner, J.S., Buoyancy effects in fluids, Cambridge University Press 1973, P.288.

[6] E Xuequan & Hopfinger, E.J., On mixing across an interface in stably stratified fluid, J.Fluid Mech., 166(1986), 227.

[7] Carruthers, D.J. & Hunt, J.C.R., Velocity fluctuation near an interface between a turbulence region and a stably stratified layer, ibid., 165(1986), 475.

Table 1
Numerical Vaules for Relations (3), (4) and (8)
($z = 9\text{cm}, \Delta\rho_0/\rho_2 = 0.0584, S$=2cm)

σ_0	f (Hz)	a ($\text{cm}\cdot S^{-k}$)	a_1 ($\text{cm}\cdot S^{\alpha_1-k}$)	a_s ($\text{cm}\cdot S^{\alpha_1-k}$)	α_1 (0.80)	α_3 (-0.20)	k (0.20)
0.0000	2	2.73	1.57	1.56	0.846	-0.240	0.203
	3	4.14					0.214
	4	5.25					0.195
	5	5.86					0.196
0.0297	2	2.51	1.40		0.824		0.213
	3	3.46					0.234
	4	4.13					0.219
	5	5.51					0.209
0.0506	2	2.34	1.35		0.798		0.219
	3	3.31					0.230
	4	3.81					0.229
	5	5.06					0.218
0.0724	2	2.14	1.29		0.750		0.206
	3	2.93					0.240
	4	3.49					0.234
	5	4.31					0.229

Note: The values in parentheses are the theoretical values. $a_s = a_1/\eta^{\alpha_3}$

Table 2
Numerical Vaules for Relations (3), (4) and (8)
($z = 9\text{cm}, \Delta\rho_0/\rho_2 = 0.0584, f$=2Hz)

σ_0	S (cm)	a ($\text{cm}\cdot S^{-k}$)	a_2 ($\text{cm}^{1-\alpha}\cdot S^{-k}$)	a_f ($\text{cm}^{1-\alpha}\cdot S^{-k}$)	α_2 (1.20)	α_3 (-0.20)	k (0.20)
0.0000	3	4.27	1.13	1.13	1.23	-0.214	0.200
	4	6.46					0.191
	5	7.94					0.196
0.0297	3	3.85	1.04		1.20		0.215
	4	5.62					0.199
	5	7.08					0.193
0.0506	3	3.60	1.00		1.17		0.219
	4	5.15					0.201
	5	6.53					0.193
0.0724	3	3.41	0.95		1.16		0.227
	4	4.61					0.209
	5	6.18					0.205

$a_f = a_2/\eta^{\alpha_3}$

Table 3
Experimental Values for Relation $K = K_0\eta^{\alpha_4}$

z (cm)	S (cm)	f (Hz)	σ_0	η	K	K_0	α_4
9	2	2–5	0.0000	1.000	13.213	13.583	-0.984
			0.0297	1.498	9.638		(-1.000)
			0.0506	1.849	7.447		
			0.0724	2.214	6.026		
9	3–5	2	0.0000	1.000	12.972	13.490	-1.052
			0.0297	1.498	9.550		(-1.000)
			0.0506	1.849	7.015		
			0.0724	2.214	5.636		

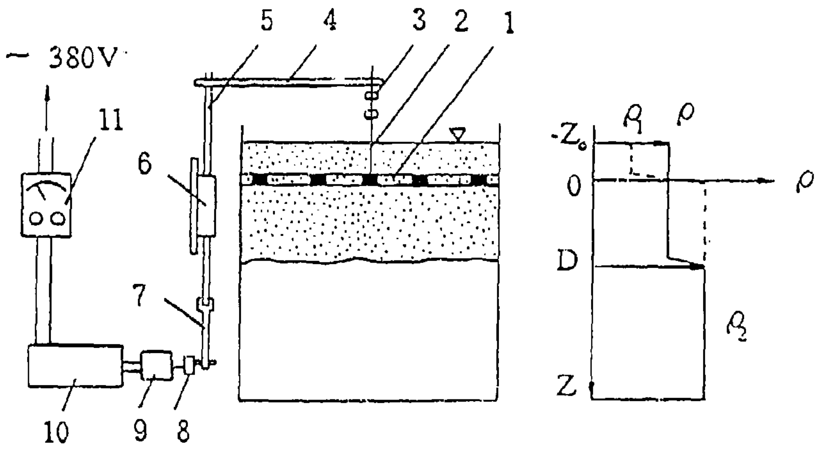

Fig.1 Schematic diagram of the experimental apparatus and arrangement.
1, grid; 2, connective rod; 3, localization sleeve; 4, cantilever beam; 5, sliding rod; 6, sliding sleeve; 7, crank; 8, cam; 9, reducing gear; 10, frequency-modulated electric machine; 11, frequency-modulated device.

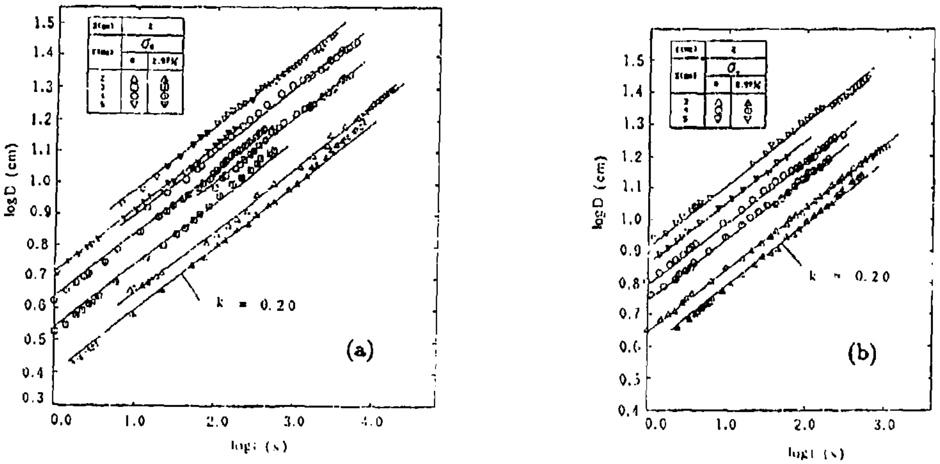

Fig. 2

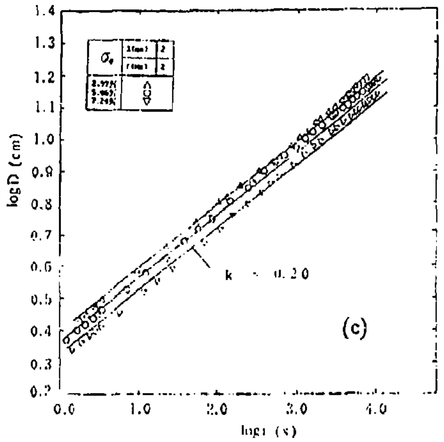

Fig.2 Variation of the turbulent entrainment D with time t.

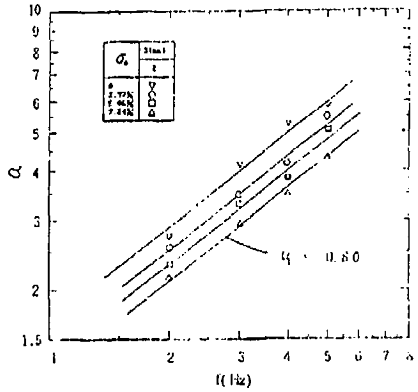

Fig.3 Variation of the proportional coefficient a with the oscillation frequency f.

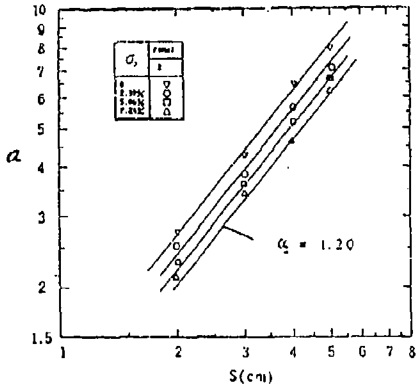

Fig.4 Variation of the proportional coefficient a with the stroke S.

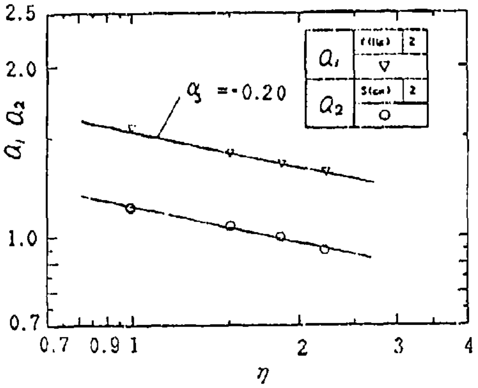

Fig.5 Dependence of a_1 and a_2 on η.

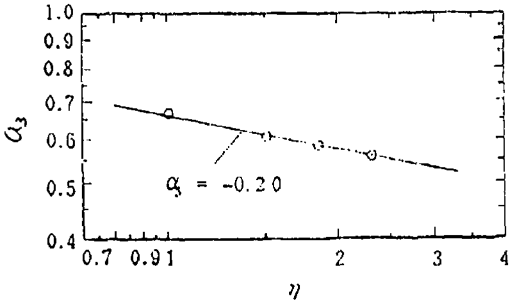

Fig.6 Dependence of a_3 on η.

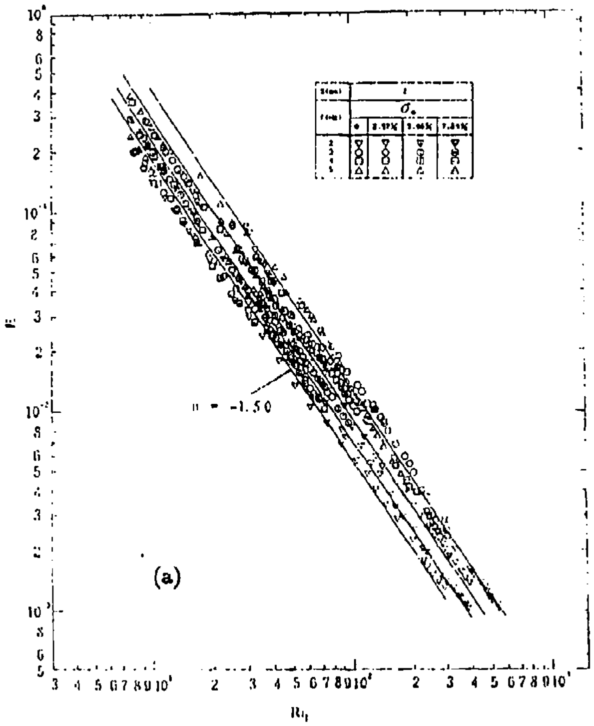

Fig. 7

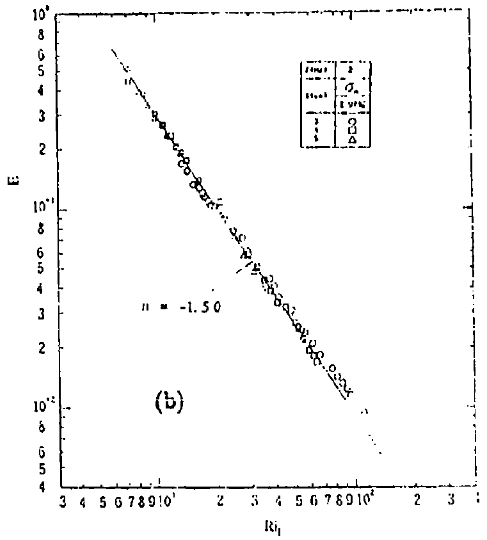

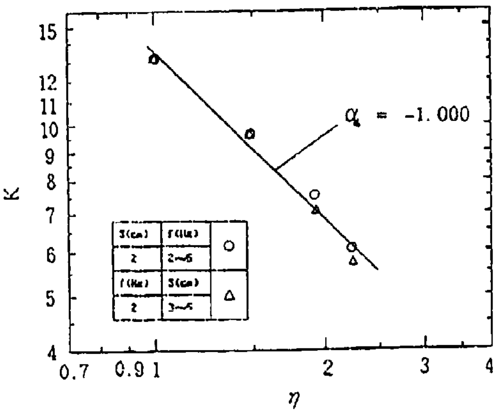

Fig.8 Relation between K and η.

Fig.7 Entrainment rate E plotted logarithmically as a function of local Richardson number Ri_l.

(a) S=2cm, at different grid oscillation frequencies;

(b) f=2Hz, $\sigma_0 = 2.97\%$, S=3–5cm.

Transition to stable state and mixing of initially unstable continuously stratified fluid.

Ya.D.Afanasyev

Institute of Oceanology, Russian Academy of Sciences, Krasikova 23, Moscow 117851, Russia. Fax: Russia + (095) 1245983

1.Introduction

The gravitational instability occurs in a system consisting of heavier fluid lying on top of less dense fluid. Any sinusoidal perturbation of the interface with not too small wave length (otherwise it is smoothed by diffusion) will grow under the action of a buoyancy force. An array of convective elements (mushroom-like structures) develops in the fluid forming the mixing layer. The convective motions will continue until an ultimately stable stratification is established. The process of transition from unstable to stable stratifications is determined by the initial density distribution. When a system consists of two layers of equal depths and with different densities, the depth (h) of the mixing layer grows with time as $h \propto t^2$ (Andrews, Spalding, 1990; Linden,Redondo, 1991). When the density anomaly is initially concentrated in a thin fluid layer at the surface, a different asymptotic behaviour is observed: $h \propto t$ (Dikarev, Zatsepin, 1983; Voropayev, Afanasyev, van Heijst, 1993). For the case of a continuously stratified fluid, when the density decreases linearly with depth initially, a more complex transition process is observed (Voropayev, Afanasyev, van Heijst, 1993). The laboratory experiments show that the flow evolution is characterized by a number of distinct stages: different modes of instability emerge subsequently through the entire fluid column, leading to the overturning motions in thin horizontal layers, which finally break up into thermal - like convective structures. For many applications it is important to determine the mixing efficiency of the particular transition process. For the numerical models of oceanic flows the estimates of vertical mixing are required. Various natural circumstances can create different initially unstable stratification. In a case of surface cooling, a thin surface layer becomes heavier and, hence, unstable. The unstable density distributions can be generated also by breaking internal waves in a continuously stratified ocean. The mixing efficiency (η) was measured by Linden, Redondo (1991) in the laboratory experiments with two-layer fluid. It was suggested that the value $\eta = 0.35$ (that corresponds to an uncomplete mixing) rather than $\eta = 0.5$ (complete mixing) can be recommended for the numerical models. The aim of the present paper is to consider the mixing efficiency of the flows with different initial density distributions: thin layer on the surface; two layers of equal depths; linear stratification. The results of conductivity measurements in the recent experiments by Voropayev, Afanasyev, van Heijst (1993) are used to obtain the estimates of mixing efficiency.

2. Experiments

Experimental arrangement

Since the experimental set-up was described in Voropayev, Afanasyev, van Heijst (1993), only a brief description is presented here. The experiments were conducted in a narrow transparent tank of dimensions 93 * 55 * 2 cm, which could be rotated about its long horizontal axis. The stable density stratification (step-like or linear) was created by variation in the salt concentration in the vertical direction and was measured by a conductivity probe. The probe was fixed on a vertical traversing mechanism. In the experiments with a thin layer the initial height of the layer of denser fluid was $h_0 = 1cm$. The density excess ($\Delta\rho$) was varied in the range $\Delta\rho = (0.2 - 16)10^{-3}gcm^{-3}$. Two experiments with layers of equal height ($1/2H$ where $H = 55cm$ is the height of the tank) and density difference $\Delta\rho = 8\ 10^{-4}; 1.2\ 10^{-3}gcm^{-3}$ was also conducted. The third series of experiments was carried out with a fluid layer with an aproximately constant undisturbed density gradient $d\rho/dz = -\gamma = const$, with the z- axis directed upward. Very weak initial density gradient was applied, $\gamma = (10^{-5} - 10^{-4})gcm^{-4}$. An inverse and hence, unstable density stratification was obtained by turning the tank upside down. The conductivity probe was used than to measure the final density distribution which established after the transition process. The density profiles were taken when the motions in the tank decayed.

Observations

During the overturning of the tank, the fluid undergoes an irrotational displacement with respect to the tank. As a result, the interface between layers, or the isopycnals in the case of a linear stratification tilt at an angle $\varphi = tan^{-1}2\pi \approx 81^0$ (Simpson, Linden, 1984). This process determines the unstable density distribution after the overturning. In the experiments with a thin layer, the heavy layer is localized near the upper part of the back wall of the tank at depth 4 - 5 cm after the overturning. Small convective (thermal-like) elements with a typical mushroom shape form along the layer as a result of gravitational instability.The convective elements grow with time, their number decreases because of subsequent pairing of interacting elements. The potential energy of the system decreases as a result of downward movement of heavier convective elements. The elements effectively mix the fluid because of viscous entrainment of adjacent fluid. In a case of linear stratification, the resulting density distribution in the tank after overturning will be the following. At the midplane, the density profile is inversed compared to the profile before the overturning of the tank. At the front and back walls of the tank the density distribution is represented by the profiles with the same unstable density gradient as at the midplane, but shifted up and down, respectively, over a distance $\Delta z = (l/2) tan\varphi = \pi l, l = 2cm$ being the width of the tank. Such a density distribution determines the subsequent development of instability process. The fluid at the front wall of the tank turns out to be lighter than the fluid at the back wall, so that the linearly stratified fluid begins to move upward and downward along the front and back walls of the tank. As a result, the fluid separates into two vertical layers with different density and, hence, pressure at any horizontal level. The vertical interface between two layers becomes unstable and the layers begin to intrude into one another forming horizontal layers of different density. Thus, this system turns out to consist of alternating horizontal layers of relatively denser and lighter fluid. Each pair of layers subsequently begins to overturn. This leads to the formation of small-scale layers which then break up into numerous convective elements. The development of convective flow structures leads to an effective turbulent mixing of fluid.

3. Mixing efficiency

The potential energy of the stratified fluid layer with a density distribution $\rho(z)$ can be defined as

$$P = g \int_0^H (\rho(z) - \rho_0) z dz \qquad (1)$$

where ρ_0- is the density of fresh water. After the overturning of the tank when a heavier fluid is at the top, a system contains the initial potential energy P_i given by (1) where $\rho(z)$ is the density profile immidiately after the overturning. If no mixing occurs during the subsequent transition process, the density profile would simply be overturned again back to the stable profile that was before the overturning of the tank. In a two-layer case, the two layers would simply exchange places without any change in their densities as would be the case with immiscible fluids. The potential energy (P_0) of the system before the overturning (or after the transition process when there is no mixing) is

$$P = g \int_0^H (\rho(H - z) - \rho_0) z dz \qquad (2)$$

Thus, the maximum amount of potential energy that can be released in the transition process is $P_{max} = P_i - P_0$. For three cases of interest, the energies P_i and P_0 are given by the following formulas:

(i) Thin layer

$$\rho(z) = \rho_0 \ for \ 0 \leq z \leq H - h_0$$

$$\rho(z) = \rho_1 \ for \ H - h_0 \leq z \leq H$$

$$P_i = g\rho_1 h_0 (H - \frac{h_0}{2}) \approx g\rho_1 h_0 H \ (h_0 << H)$$

$$P_0 = g\rho_1 \frac{h_0^2}{2} \approx 0$$

$$P_{max} \approx P_i$$

(ii) Two layers with equal depths

$$\rho(z) = \rho_0 \ for \ 0 \leq z \leq H/2$$

$$\rho(z) = \rho_1 \ for \ H/2 \leq z \leq H$$

$$P_i = g\rho_1 \frac{3H^2}{8}$$

$$P_0 = g\rho_1 \frac{H^2}{8}$$

$$P_{max} = \frac{2P_i}{3}$$

(iii) Linear stratification

$$\rho(z) = \rho_0(1 + \gamma z)$$

$$P_i = g\rho_0\gamma\frac{H^3}{3}$$

$$P_0 = g\rho_1\gamma\frac{H^3}{6}$$

$$P_{max} = \frac{P_i}{2}$$

Thus, almost all initial potential energy can be released in a thin-layer case. Another extreme is a trivial case of a completely mixed (homogeneous) fluid when zero energy can be released. The cases (ii) and (iii) are between the extremes. Following Linden, Redondo (1991), define the mixing efficiency η as a part of P_{max}, that is used to mix the fluid

$$\eta = \frac{P_f - P_0}{P_{max}} = \frac{P_f - P_0}{P_i - P_0}$$

where the final potential energy P_f is calculated from (1) where $\rho(z)$ is the measured final density profile. Another part of energy $(1 - \eta)P_{max}$ is dissipated by viscosity during the transition process. Values of the mixing efficiency η versus the Atwood number A for the experiments with different initial stratifications are shown in Table 1.

Table 1

η	0.22	0.34	0.41	0.35	0.39	0.31	0.33	0.41	0.28
$A * 10^3$	0.2	0.8	2.0	4.0	0.4	0.6	0.6	1.2	2.0
	(i)				(ii)		(iii)		

The Atwood number is defined as

$$A = \frac{\rho_1 - \rho_0}{\rho_1 + \rho_0}$$

for step-like stratification and as

$$A = \frac{\gamma H}{2}$$

for the linear stratification. Though all the experiments were carried out with small values of A, the high values of η were obtained. The mean value of η is $\eta \approx 0.35$ that is consistent with the results obtained by Linden, Redondo (1991).

Acknowledgments

The author is greatly indebted to Dr S.I.Voropayev and Prof. G.J.F.van Heijst who made possible his participation in experiments on convection at the Fluid Dynamics Laboratory in Eindhoven. It is a pleasure to thank Prof. E.J.Hopfinger for the invitation to attend the ISSF in Grenoble.

References

1 M.J.Andrews, D.B.Spalding, A simple experiment to investigate two-dimensional mixing by Rayleigh - Taylor instability. Phys.Fluids A2, 922 (1990)

2 S.N.Dikarev, A.G.Zatsepin, Evolution of convection in a two-layer unstably-stratified fluid. Okeanologia 23, 950 (1983)

3 P.F.Linden,J.M.Redondo, Molecular mixing in Rayleigh-Taylor instability. Part 1: Global mixing. Phys.Fluids A3, 1269 (1991)

4 S.I.Voropayev, Y.D.Afanasyev,G.J.F.van Heijst, Experiments on the evolution of gravitational instability of an overturned, initially stably stratified fluid. Phys.Fluids A5, 2461 (1993)

Laboratory Measurements of Vortex Evolution in a Stratified Shear Flow

Donald P. Delisi
Northwest Research Associates, Inc.
PO Box 3027, Bellevue, WA 98009-3027

ABSTRACT

Laboratory measurements of the evolution of a two-dimensional vortex pair in a stratified shear flow are reported. The measurements were obtained in a rectangular-shaped tilting tank, where salt was used for density variations, and a vertical shear was generated by tilting the tank through a small angle. Measurements were obtained in Richardson number flows varying from 0.6 to infinity (no shear). A vortex pair was generated in the tank after the flows were established, and the evolution of the vortex pair was observed. A solitary vortex was observed to evolve when the Richardson number was of order five or less.

BACKGROUND

The vertical distance a vortex pair migrates is a function of the ambient stratification. As the background stratification increases, the vertical migration distance decreases (Sarpkaya, 1983). In these cases, there is no asymmetry in the flow, and the vortices decay symmetrically, each vortex in the pair decaying at the same rate.

Robins and Delisi (1990) reported on numerical studies which examined the evolution of a vortex pair in a stratified, shear flow. Those studies showed that when the shear is small enough, the vortices decayed symmetrically, as in the nonsheared case. When the shear is large, however, the vortices decayed asymmetrically, with the vortex whose rotation was opposite to the rotation of the mean shear decaying while the other vortex survived. The study showed that a solitary vortex evolved from the vortex pair when the Richardson number was of order one or less.

Initial laboratory observations by Delisi et al (1991) showed the evolution of a vortex pair in a flow with Richardson number equal to one. In this flow, the vortex pair evolved into a solitary vortex. Supporting numerical calculations were consistent with the observations.

In this paper, additional laboratory observations are presented. Measurements include rise height with time, vortex separation, and estimates of vortex circulation with time.

THE EXPERIMENTAL FACILITY

The experiment was performed in a rectangular-shaped tilting tank similar to one used by Thorpe (1968). The tank is 488 cm long, 61 cm high, and 15 cm wide. A linear density profile is used in the tank, resulting in a linear velocity profile. Figures 1 and 2 show typical density and velocity profiles, respectively. In both figures, the symbols indicate the measurements, and the dashed line is a linear, least-squares fit to the data.

Three cases are presented here: (a) a nonstratified, nonsheared case, (b) a stratified, nonsheared case, and (c) a stratified, sheared case. In all three cases, nominally identical initial vortices were used. These vortices were generated by moving two wings, initially at rest, down the tank in opposite directions. The starting vortices generated by the wings formed the vortex pair. To minimize the effect of the wings on the background flow, the wings are placed just below the centerline of the tank, where the flow velocities are low.

To perform an experiment with stratification and shear, we filled the tank with water, tilted the tank to create the vertical shear, moved the wings down the tank, and observed the resulting vortex pair. The observations continued until surges from the end walls modified the flow in the test section. In the stratified sheared flows, experiments were performed with Richardson numbers ranging from 0.6 to over 6.

RESULTS

The nonstratified, nonsheared vortices migrated with a nearly constant speed and a nearly constant separation between the vortices. The migration speed was 4.9 cm/sec, and the separation was 13.6 cm. This gives an initial vortex circulation of $\Gamma_o = 2 \pi b_o V_o = 419$ cm^2/sec, where b_o = the initial separation, and V_o = the initial migration speed. The vortex Reynolds number, Γ_o / ν, is 41,900. The vortex Froude number, defined as $V_o / N b_o$, where N is the Brunt-Vaisala (B-V) frequency, is 1.0. This low Froude number was used because we needed to have a B-V frequency large enough to limit the migration distance of the vortices, due to the finite depth of the tank.

Results for a stratified, nonsheared case are shown in Figure 3. Here, we plot H vs T, where $H = h / b_o$, and $T = V_o t / b_o$, where h is dimensional height and t is dimensional time. Because we generate each vortex separately, we have plotted both the left and right vortices separately. Data from Sarpkaya (1983) for Froude number 1.0 is plotted as the solid symbols. The data from the present study is consistent with Sarpkaya's data. The dashed line is H = T.

In the run shown in Figure 3, $N = 0.323$ sec^{-1}. In Figure 3, one-third of a B-V period corresponds to $T = 2.1$, and is consistent with the maximum, observed migration of the vortex pair. In this run, the average, initial vortex separation was 15.0 cm, which is ten percent larger than in the nonstratified case. We believe this larger separation is due to the vortices pulling heavier water up in the center and lighter water down on the sides at the top, thus generating a horizontal pressure gradient which pulls the vortices apart.

Figure 4 shows a series of four streak photographs for the stratified, sheared case with Richardson number = 2.32. Only part of the tank is shown in the photographs. We nondimensionalize time as in Delisi et al (1991) by t / T_o, where $T_o = b_o / V_o$. Here, $T_o = 2.79$ sec. In the top left photo, $T_o = 0.49$, and the vortices are symmetric. In the next photo, at the top right, $T_o = 1.16$. At this time, the vortices have migrated vertically but are still nearly symmetric. The bottom left photo is at $T_o = 1.84$. In this photo, the left vortex is noticably weaker than the right vortex. In the final photo at the bottom right, at $T_o = 2.51$, the left vortex is essentially destroyed, leaving only the right vortex remaining.

Circulation estimates for all three runs are shown in Figure 5. These measurements were obtained from the streak photographs over a circle of 5 cm radius, centered on the vortex core. For all three runs, the open symbols denote the left vortex, and the closed symbols denote the right vortex. The nonstratified, nonsheared case is shown by the circles. The closed square on the y-axis shows the calculated, initial vortex circulation for this case. The circulations decay with time, presumably due to turbulent diffusion. The nonstratified, nonsheared measurements end when the vortices migrate into ground effect with the top of the tank.

The diamonds in Figure 5 show the measurements for the stratified, nonsheared case. These measurements continue on further in time than those for the nonstratified case since the stratification inhibits the vertical migration of these vortices. The initial decay of the stratified, nonsheared vortices follows the decay of the nonstratified vortices.

The stratified, sheared measurements are shown by the triangles. In this case, the rate of decay of the right vortex is similar to the decay of both the nonstratified, nonsheared vortices and the decay of the stratified, nonsheared vortices. The left vortex, however, decays much faster, starting at t / T_o around 1.6. This behavior is similar to that shown in Robins and Delisi (1990), who showed in numerical calculations that the maximum vorticity for the opposite sign vortex in a vortex pair in a low Richardson number flow decayed like the vorticity in a higher Richardson number flow for a while, and then rapidly decayed. This rapid decay was observed in the last two photographs in Figure 4.

SUMMARY

Results from laboratory experiments of the evolution of a vortex pair in stratified and sheared environments have been presented. In the nonstratified, nonsheared flows and the stratified, nonsheared flows, the results are consistent with the results of previous investigations. In the stratified, sheared flows, the observations clearly show the evolution from a vortex pair to a solitary vortex when the Richardson number of the background flow is 2.3. Additional experiments show that this behavior occurs when the Richardson number is around five or less.

REFERENCES

DELISI, D. P., ROBINS, R. E. and LUCAS, R. D. 1991 Initial laboratory observations of the evolution of a vortex pair in a stratified shear flow. *Phys. Fluids A* 3 (11), 2489-2491

ROBINS, R. E. and DELISI, D. P. 1990 Numerical study of vertical shear and stratification effects on the evolution of a vortex pair. *AIAA Journal* 28, 661-669.

SARPKAYA, T. 1983 Trailing vortices in homogeneous and density-stratified media. *J. Fluid Mech.* 136, 85-109.

THORPE, S. A. 1968 A method of producing a shear flow in a stratified fluid. *J. Fluid Mech.* 32, 693-704.

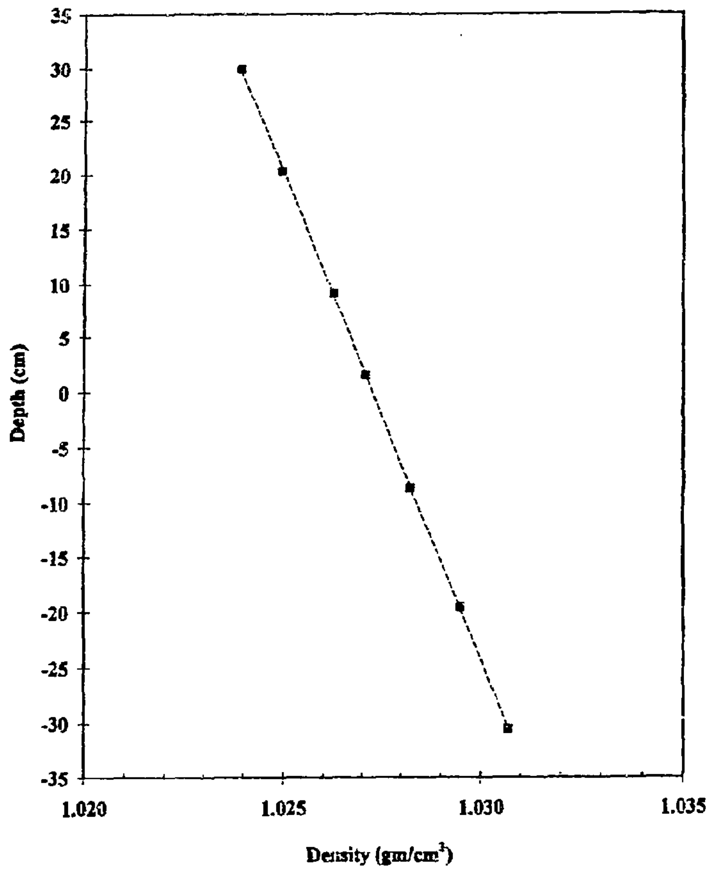

Figure 1. Density profile for the stratified, sheared run. The dashed line is a linear, least-squares fit through the data. The Brunt-Vaisala frequency is 0.32 sec^{-1}.

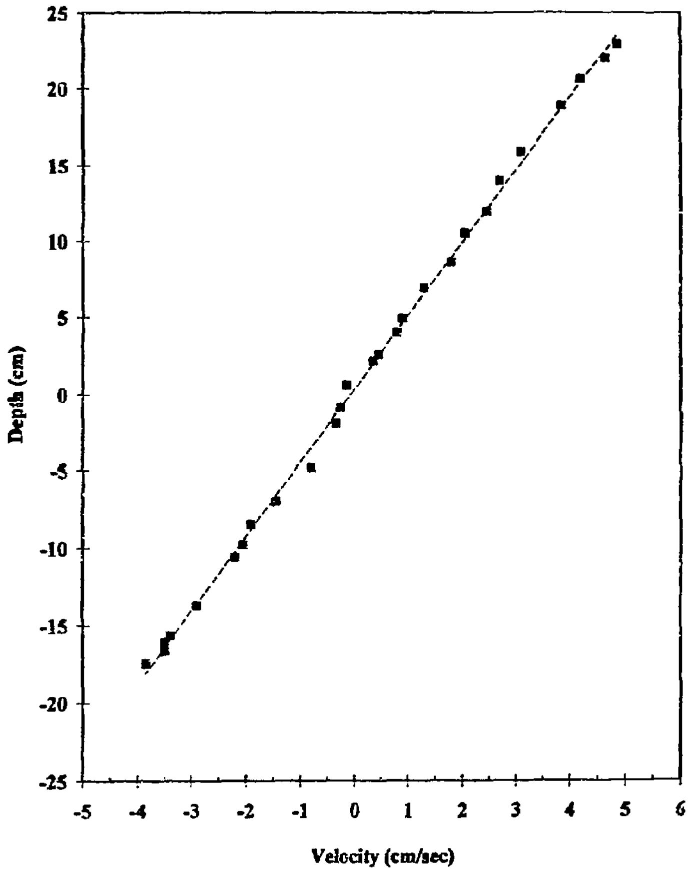

Figure 2. Velocity profile for the stratified, sheared run. The dashed line is a linear, least-squares fit through the data. The shear is 0.21 sec^{-1}.

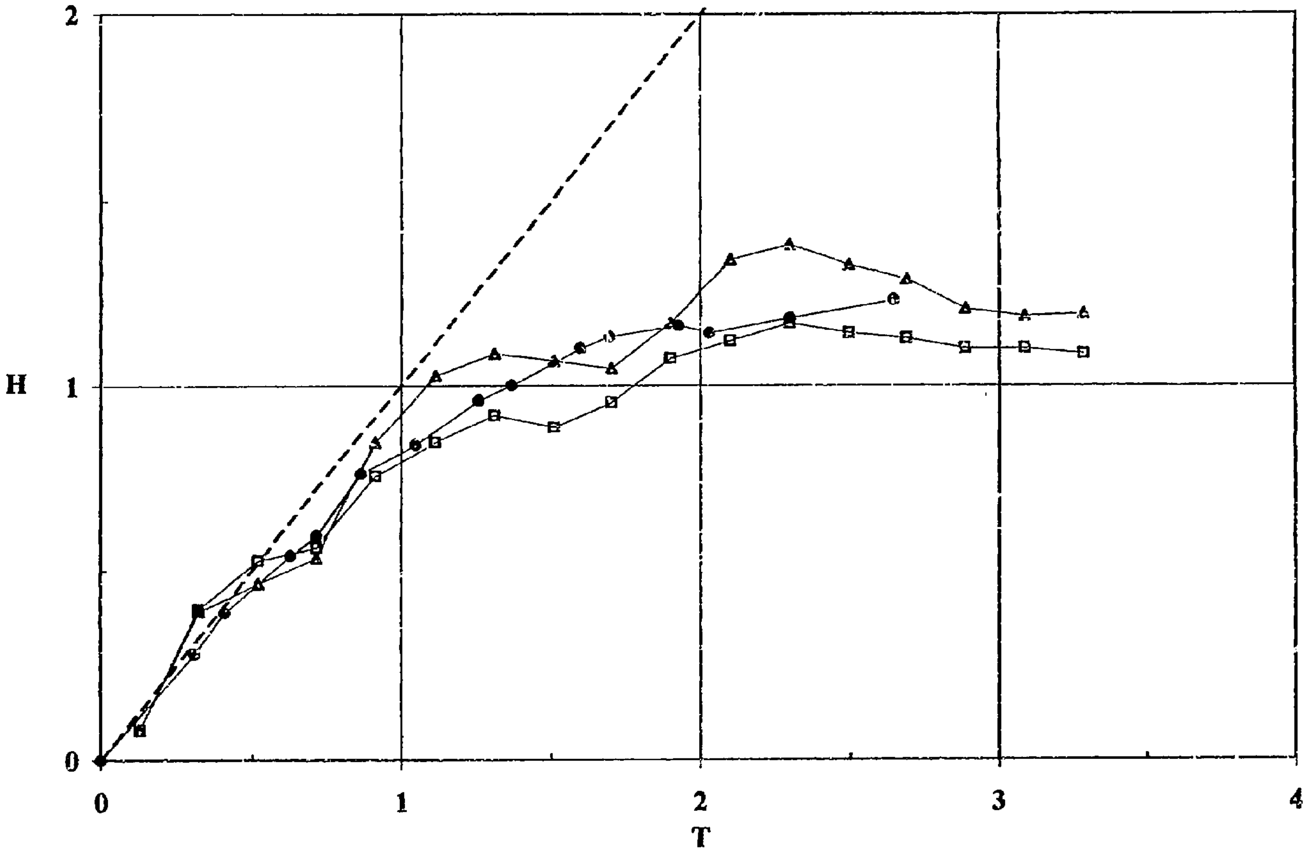

Figure 3. H vs T for the stratified, sheared case with Froude number = 1. The left vortex is shown by the open triangles; the right vortex by the open squares. Data from Sarpkaya (1983) for Froude number = 1 is shown by the closed circles. The dashed line is H = T.

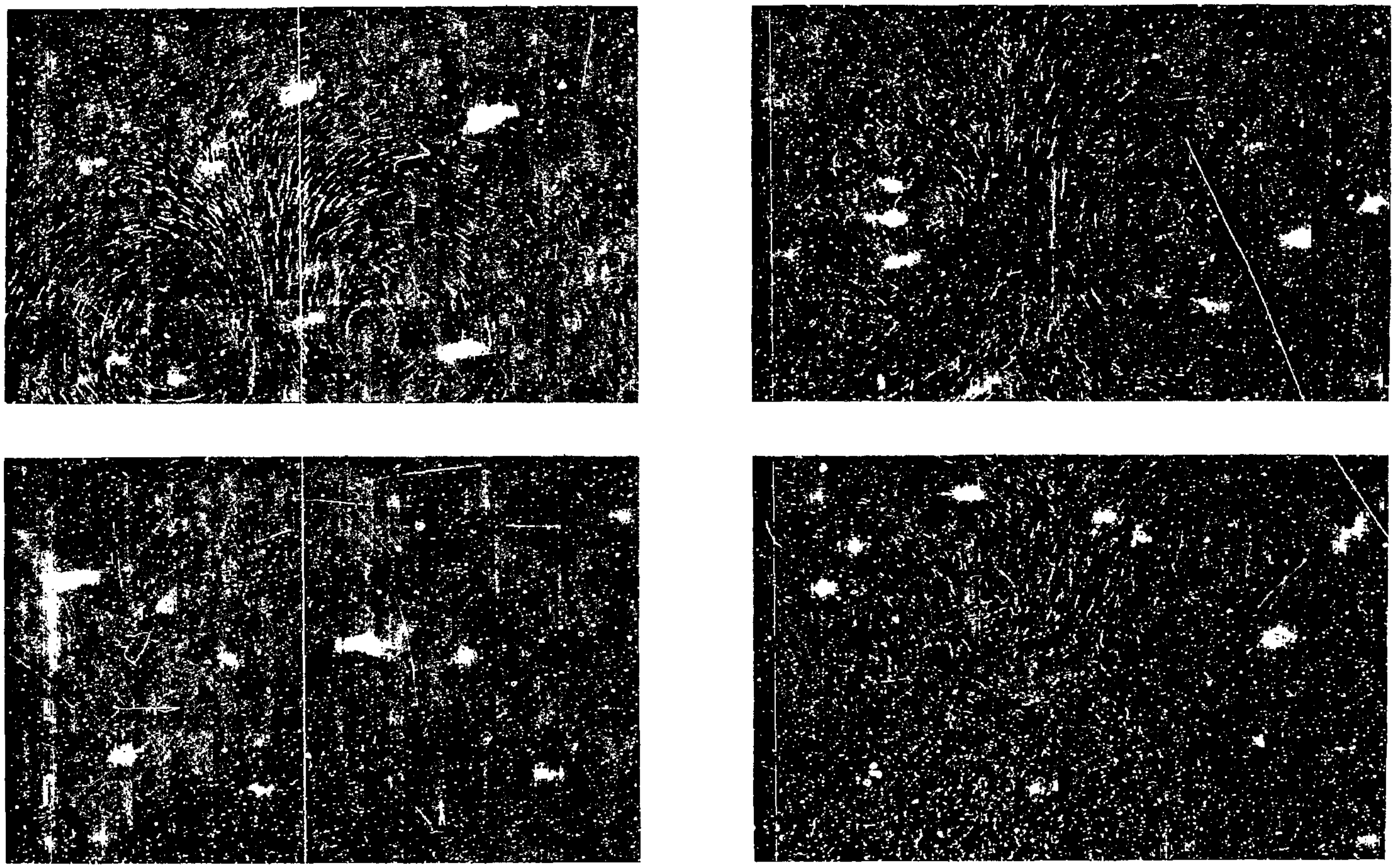

Figure 4. A series of four streak photographs for the stratified, sheared case. Values of t/T_c are (a) 0.49 (top left), (b) 1.16 (top right), (c) 1.84 (bottom left), and (d) 2.51 (bottom right).

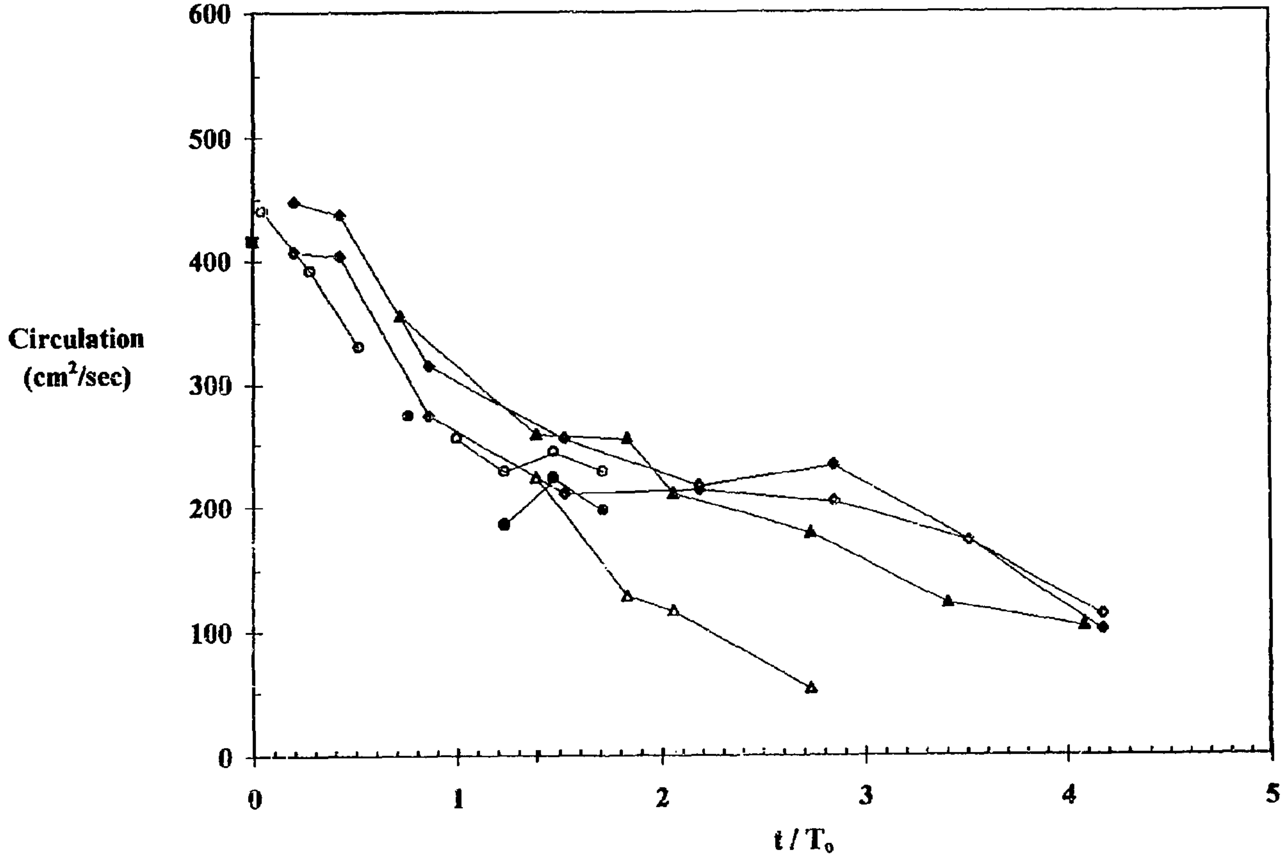

Figure 5. Circulation vs t/To for all three cases. The left vortices are denoted by the open symbols, and the right vortices are shown by the closed symbols. Circles show the nonstratified, nonsheared run; diamonds show the stratified, nonsheared run; and triangles show the stratified, sheared run. The closed square on the y-axis shows the initial vortex circulation from the nonstratified, nonsheared case.

The motion of coherent structures

Y.G. Morel
C.M.O./I.M.G., Grenoble, France
and
X.J. Carton
C.M.O./S.H.O.M., Brest, France

April 1994

Abstract

In this study, the motion of a three-layer baroclinic vortex, representing mediterranean water eddies, is investigated. Among all the mechanims that can induce a motion, we focus on the action of bottom topography. In particular, we are looking for steadily translating structures over a constant bottom slope. Depending on hydrological data, "strongly isolated eddies" move with the deep waters at their right or at their left.

Experiments in a rotating tank are also presented that confirm the fact that the lens propagate along isobathes in both directions.

1 Introduction

Many recent campaigns at sea near the strait of Gibraltar have revealed the presence of very strong long-lived baroclinic vortices of mediterranean water (Armi et al, 89; Arhan et al; Prater, 92; Le Squere 94).

This paper aims at describing several processes that can have a significant effect on the displacement of these "meddies" according to us: beta and beta-topographic effects and a mean current in the upper layer. Since this is a mechanism that has never been proposed as far as the motion of meddies is concerned, we will focus on the effect of a bottom topography. Indeed, when an intermediate vortex is propagating, there must be a motion in the lower layer. Thus, it can interact with a bottom topography. In Morel (94), we have used a three-layer Shallow Water model to study the effect of a constant bottom slope. When the eddy is strong (high Rossby number and variation of depth comparable to second layer depth at rest), the equations for the second layer are non linear and can not be solved. However, we have shown how an hypothesis of strong isolation (i.e. nul axisymetric part beyond a certain distance from the center of the meddy in each layer) constraints the displacement speed to be entirely determined by the surrounding hydrological data. But we were not able to prove that the problem had a solution. In this paper we will study the problem in the context of quasi-geostrophic theory for which the equations are simpler.

We will first review previous studies that have been done to explain the observed trajectories of mediterranean lenses. Then we will discuss the quasi-geostrophic equations for a three layer-ocean and show how a mean upper layer current can generate a displacement of a vortex (section 2). In section 3, we will focus on the effect of a bottom slope and look for steadily translating structures with "no potential vorticity anomaly" in the upper or lower layer. Experiments in a rotating tank (the Coriolis tank in Grenoble) are presented and discussed in section 4. Some preliminary numerical results are examined in the conclusion.

2 The three-layer Quasi-Geostrophic model

Observations and previous studies

McWilliams and Flierl (79) have shown that isolated vortices can resist dipersion providing they are strong enough. As mediterranean water vortices are strong (see Prater, 92 for a review), they can live for a long time. In particular, Armi et al (89) have followed a meddy (Meddy 1, Sharon) which moved southward almost continuously during two years! Many mechanisms have been proposed to explain this trajectory.

First, it is well known that the planetary beta effect initially induces a southward motion on islolated axisymetric anticyclones. However, numerical studies have shown that this motion is too weak and other mechanisms must be considered to explain the observed trajectories (Beckmann & Kase, 89).

Hogg and Stommel (89) showed that the meddy could have been advected southward by the mean upper layer current. Their mechanism rely on the presence of a strong enough vortex in the upper layer to trap the mediterranean lens. However, they have neglected the effect of the mean deviation of the interface due to the mean current. We shall show that, in the context of a three layer Quasi-Geostrophic model, this effect can in fact modify the beta coefficient in the layer of the meddy. This induces a propagation in the direction of the mean current without the need of potential vorticity in the upper layer.

Colin de Verdiere (92) has proposed an interesting mechanism based on lateral mixing. However, some numerical experiments are needed to quantify the importance of this process.

Equations of the model

We assume that meddies are well represented by a three layer quasi-geostrophic ocean. This hypothesis is certainly verified for the upper and lower layers but is questionnable in the meddy itself. However, we expect it has not a very important consequence on the displacement of the lens. We make the beta plane approximation and consider a North-South constant bottom slope, so that both beta and topographic beta act along the same direction. We consider a state of reference with a constant mean velocity field in the upper layer U_1 along the x axis and no motion in the layer of the meddy and below. The equations for the streamfuction in each layer are:

$$\begin{aligned}
&\partial_t \; PV_i \; + \; J(\psi_i - U_i y, PV_i + \beta_i y) \; = \; 0 \\
&\text{with} \\
&J(a,b) \; = \; \partial_x a \partial_y b - \partial_y a \partial_x b \\
&PV_1 \; = \; \nabla^2 \psi_1 + f_1(\psi_2 - \psi_1) \\
&PV_2 \; = \; \nabla^2 \psi_2 + f_2(\psi_1 - \psi_2) + f_3(\psi_3 - \psi_2) \\
&PV_3 \; = \; \nabla^2 \psi_3 + f_4(\psi_2 - \psi_3)
\end{aligned}$$

In these dimensional equations, $f_1 = f^2/g_1 H_1$, $f_2 = f^2/g_1 H_2$, $f_3 = f^2/g_2 H_2$, $f_4 = f^2/g_2 H_3$, with $g_1 = (\rho_2 - \rho_1)/\rho_3 g$, $g_2 = (\rho_3 - \rho_2)/\rho_3 g$ and $\beta_1 = \beta + f_1 U_1$, $\beta_2 = \beta - f_2 U_1$, $\beta_3 = \beta + fs/H_3$.

Many studies were done on the role of the planetary beta effect and underline the influence of the horizontal and vertical structure of the vortex on the propagation speed. We will not discuss this effect here. For details, the reader is refered to Flierl et al (80), McWilliams & Flierl (79), Flierl (84) and Beckmann & Kase (89).

In the previous formulation, we have thrown into relief the influence of a mean upper layer current. Indeed, in the layer of the meddy (layer 2), the beta effect is modified by the slope of the interface due to the upper layer mean velocity field. For instance if $U_1 > \beta/f_2$ we expect the propagation of the lens under the effect of beta and mean velocity to be eastward even if the meddy is not trapped by an upper layer vortex. This can of course be generalized to any direction of the mean velocity field. If U_1 is strong enough, the meddy will move in the direction of the upper layer speed. The critical value when U_1 becomes as important as beta is about $U_1^{crit} \simeq 4 cm.s^{-1}$ for data chosen from Armi et al (89): $\beta = 2.\ 10^{-11}\ m^{-1}.s^{-1}$, $f = 7.3\ 10^{-5}\ s^{-1}$, $H_2 = 1000\ m$, $g_1 = 10^{-2}\ m.s^{-2}$. Thus we expect that a mean velocity field will have a serious consequence on the displacement of a meddy. We are presently undertaking numerical experiments to quantify this effect.

We would like to point out that this mechanism also provides the possibility of time variations in the "equivalent" beta in the layer of the lens and can thus explain some irregularities in the observed trajectories (though these irregularities have been succesfully explained as instability events during the life of meddies by Beckmann & Kase, 89).

3 Isolated modons

As they have very long lifetimes, coherent structures such as meddies, have sometimes been modelled as modons, that is to say vortices steadily propagating under the influence of the planetary beta. In this section we are looking for strong intermediate structure steadily translating under the effect of a bottom slope ($\beta_1 = \beta_2 = 0$, $\beta 3 = \frac{fs}{H_3}$. There are many reasons for that. First, there are good corellations between the trajectory of meddy Sharon and isobathes (see Morel 94). Also, the beta topographic effect is known to be equivalent to the planetary beta for barotropic flows. When stratification is taken into account, this no longer holds and the differences are certainly interesting. Last but not least, the principle of the calculations are the same if one wants to consider modons on a beta plane with an effect of a mean velocity field in the upper layer. It can be shown that the speed of displacement $\vec{C}$ can only be along the x axis. Replacing the t derivatives by $-C\partial_x$ and using a frame translating with the structure, the previous equations become (see Flierl et al, 80):

$$J(\psi_i - U_i y + Cy, PV_i + \beta_i y) = 0$$

This simply states that there is a functional relationship between the total potential vorticity and the streaklines (lines of constant $\psi_i - U_i y + Cy$):

$$PV_i + \beta_i y = F_i(\psi_i - U_i y + Cy)$$

If we assume that the eddy is isolated (ψ_i and PV_i are nul at infinity), the functions F_i can be evaluated on every streakline that extends to infinity: $F_i(Z) = \frac{\beta_i}{C-U_i} Z$.

For closed streaklines, the function F_i can have a different form and can be multivalued. To simplify the problem, we will only consider a multivalued function for the second layer. This can be understood as an hypothesis of no "potential vorticity anomaly" in the upper and lower layers: particules in these layers have the same potential vorticity as they will have if they were at rest. Also, it permits the motion in these layers to be weak enough, so that there are no closed streaklines and no particles carried along. We only consider strong potential vorticity anomaly and particles transport in the layer of the meddy. Finally, to make analytical progress we will only consider linear functions $F_2(Z) = S\ Z\ +\ Q$ and a matching boundary between closed and extending to infinity streaklines that is a circle of radius a, as in the previous studies on modons (see Flierl et al, 80). Thus the problem we will have to solve is the following:

$$PV_1 = 0$$
$$PV_3 = \frac{\beta_3}{C}\psi_3$$
$$PV_2 = S\ (\psi_2 + Cy) + Q \text{ for } r \leq a.$$
$$PV_2 = 0 \text{ for } r \geq a.$$

As for modons under the effect of planetary beta, we can find steadily translating structures for various values of C (negative and positive). The first two equations are the same we studied in Morel (94). When studying the propagation of "almost steady vortices" (generating a weak Rossby waves field), some authors have considered the case of strongly isolated vortices, i.e. for which the axisymetric part of the velocity field is null beyond a certain radius R (see Swaters & Flierl, 91; Sutyrin & Flierl and Sutyrin, 94). We have shown that in that case, the displacement speed is determined so that ψ_1 and ψ_3 are proportional. We obtained:

$$C = \frac{\beta_3}{f_1 - f_4}$$

So that C is positive or negative, depending on the surrounding hydrological data (f_1 and f_4) and the slope of the bottom.

It is however not possible to have strongly isolated axisymetric part with the "simple" model just described. We do not want to enter into all the details but let us just point out that this is due to a lack of degrees of freedom. We found a way to add more degrees of freedom in the model (as many as wanted!) and that still permits analytical calculations. The principle is very simple in fact and consist of using many regions separated by closed circular streaklines inside of which we can choose other values for S and Q. This adds two degrees of freedom for each new region. It can be shown that for our problem (to have strongly isolated solutions) we must add at least two more regions. On each boundary we will have to solve a set of non-linear equations that is overdetermined.

We would like to point out that this new method is very close to Contour Dynamics models (see Sutyrin & Flierl) because there is a jump of potential vorticity on each boundary. Also the modons with riders (superimposed axisymetric part) that were found by Flierl et al (80) were proved to be unstable (Swenson, 86). We believe that this new method can yield the possibility of finding steadily translating modons with stable riders: it adds a lot of degrees of freedom and thus permits considerable modifications in the rider part.

4 Rotating tank experiments

To test the previous formula giving the propagation speed, we made experiments on the Coriolis rotating tank in Grenoble. This tank is 13 m. diameter and permits the use of low rotation rates.

We injected an intermediate density water in a two-layer stratified fluid above a slopping bottom (see fig. 1). Several experiments were realised in the following ranges of parameters: density difference between upper and lower layers $\sigma \simeq 0.3 - 1.1\%$, upper layer thickness $H_1 \simeq 10 - 25cm$, lower layer thickness $H_3 \simeq 15 - 45cm$, bottom slopes $s \simeq 3 - 10\%$. The rotation period for the tank was 100 s. Twenty to fifty liters of intermediate density water were injected within 10 minutes. The radius of the lens we obtained depended on the stratification but roughly ranged between 40 and 80 cm, giving a maximum thickness of about 5 cm for the lens.

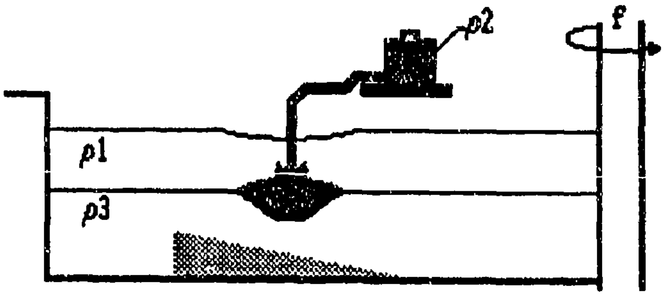

fig.1: Sketch of the experiment. An intermediate density water is injected vertically in a two-layer stratified background.

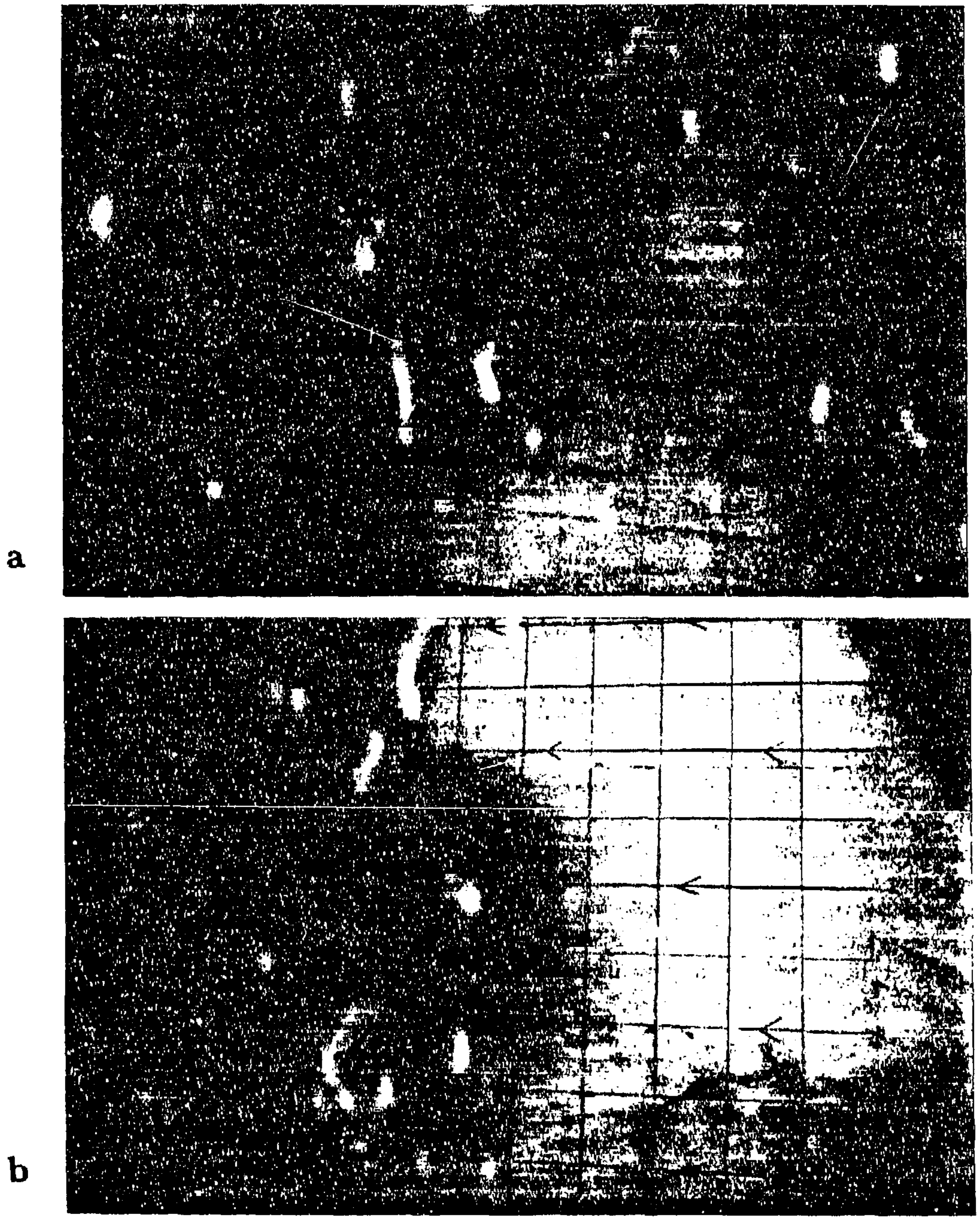

fig.2: Two meddies propagating in different directions. The arrows indicate the shallow waters, the small circles indicate the initial position. Notice also the velocity field in each layer: anticyclonic in the upper layer (green line), strong anticyclone in the intermediate layer (red line), cyclonic in the lower layer (blue).

a/ slope s=8%, $H_1 = 15\ cm$, $H_3 = 27\ cm$, $\rho_1 = 0\%$, $\rho_2 = 0.5\%$, $\rho_3 = 0.8\%$.

b/ slope s=3%, $H_1 = 15\ cm$, $H_3 = 27\ cm$, $\rho_1 = 0\%$, $\rho_2 = 0.4\%$, $\rho_3 = 0.5\%$.

As in Bormans (92), the injection of intermediate fluid was vertical, so that the fluid sinked, adjusted (see McWilliams, 88 for an explanation of the adjustment mechanism) and a stable anticyclonic lens was created. We used dye to follow its displacement. There was also an anticyclonic (cyclonic) motion in the upper (lower) layer (see fig.2 a-b). Usually the lens began to move during the injection. The propagation speeds we get were always well below the predicted one but we have found lenses propagating with deep waters on their right as well as on their left. The order of magnitude of the propagation speed was about half a radius of the lens ($\simeq 30cm.$) within 6 rotation of the tank ($600s.$). As in Bormans (92), weakly unstable events (filaments shedding) sometimes occured for thick lenses.

We would like to point out that in comparison with oceanic meddies, our lenses had a much lower lifetime (non-dimensionalised by the rotation period). Indeed, we observed that after about 10 rotations of the tank the Rossby number decreased by a factor 3 and after 50 rotations, the flow in the lens was hardly visible.

5 Conclusion

In this paper we described an analytical theory we developped to evaluate the effect of a bottom slope on the propagation of meddies. This model can be generalized to study the effect of an upper layer mean velocity field. In particular it can perhaps yield new results as far as modons with riders are considered.

Experiments in the Coriolis rotating tank were realized to test for this model. In these experiments, the displacement of the meddies were positive or negative roughly in agreement with the theory. However, the order of magnitude of the propagation speed was always well below the predicted one.

We began numerical experiments with a three layer Quasi-Geostrophic model to test the non-stationary evolution of meddies. When initiating an axisymetric vortex with no or small potential vorticity anomaly in the upper and lower layers, we also get a displacement in both direction in agreement with the theoretical formula for the displacement speed. But again, this speed is well below the predicted one in intensity. We believe we can have a stronger effect of the bottom topography if there is a stronger initial flow in the lower layer. According to Dewar & Gailliard (94), several observations show that there might be important deep flow below oceanic eddies. We have undertaken a study on the propagation of an intermediate vortex with potential vorticity anomaly in the lower layer.

Aknowledgments

The authors are very grateful to Drs G. van Heijst, G. Sutyrin and J. McWilliams for their relevant comments and help. In particular, G. van Heijst invited Y. Morel in Eindhoven to do preliminary experiments. Discussion with G. Chabert d'Hieres was proved to be valuable. All this work was supported by the French Navy's Oceanographic Center (C.M.O.).

References

Arhan M., Colin de Verdière A. and Mémery L.: The Eastern boundary of the subtropical North-Atlantic. Submitted.

Armi L., Hebert D., Oakey N., Price J.F., Richardson P.L., Rossby H.T. and Ruddick B., 1989: Two years in the life of a mediterranean salt lens. J. Phys. Oceanography, Vol. 19, p. 354-370.

Beckmann A. and Käse R., 1989: Numerical simulation of the movement of a mediterranean water lens. Geoph. Research Letters, Vol. 16, No 1, p. 65-68.

Bormans M., 1992: An experimental study on the formation and survival of subsurface eddies. J. Geoph. Research, Vol. 97, No C12, p. 20,155-20,167.

Colin de Verdière A., 1992: On the southward motion of mediterranean salt lenses. J. Phys. Oceanography, Vol. 22, p. 413-420.

Dewar W.K. and Gailliard C., 1994: The Dynamics of Barotropically dominated Rings. J. Phys. Oceanography, Vol. 24, p. 5-29.

Flierl G.R., Larichev V.D., McWilliams J.C. and Reznik G.M., 1980: The Dynamics of Baroclinic and Barotropic Solitary Eddies. Dyn. Atm. Oceans, Vol. 5, p. 1-41.

Flierl G., 1984: Rossby wave radiation from a strongly nonlinear warm eddy. J. Phys. Oceanography, Vol. 14, p. 47-58.

Hogg N. and Stommel H., 1989: How currents in the upper thermocline could advect meddies deeper down. Deep-Sea Research, Vol. 37, No 4, p. 613-623.

Le Squere B., 1994: Campagne Semaphore, Phase 3. Rapport interne, CMO, SHOM.

McWilliams J. and Flierl G., 1979: On the evolution of isolated, nonlinear vortices. J. Phys. Oceanography, Vol. 9, p. 1155-1182.

McWilliams J., 1988: Vortex generation through balanced adjustment. J. Phys. Oceanography, Vol. 18, p. 1178-1192.

Morel Y., 1994: The influence of topography on the motion of coherent structures. Release of the Colloquium on the Modelling of Oceanic Vortices, Amsterdam 1993.

Prater M. D., 1992: Observations and Hypothesized Generation of a Meddy in the Gulf of Cadiz. PHD thesis, Seattle, Washington 98105-6698.

Richardson P., Walsh D., Armi L., Schröder M. and Price J.F. , 1989: Tracking three Meddies with SOFAR floats. J. Phys. Oceanography, Vol. 19, p. 371-383.

Sutyrin G. and Flierl G.: Intense vortex motion on the beta-plane due to development of the beta-gyres. Submitted.

Sutyrin G., 1994: Nonlinear Rossby Waves and Vortices. Release of the Colloquium on the Modelling of Oceanic Vortices, Amsterdam 1993.

Swaters G. and Flierl G., 1991: Dynamic of ventilated coherent cold eddies on a sloping bottom. J. Fluid Mech., Vol. 223, p. 565-587.

Swenson M., 1986: Instability of equivalent-barotropic Riders. J. Phys. Oceanography, Vol. 17, p. 492-506.

MULTIFRACTAL ANALYSIS OF COHERENT STRUCTURES IN TROPICAL STRATIFIED TROPOSPHERE.

Y. Chigirinskaya[1], D. Schertzer, S. Lovejoy[2],
(L.M.D., Univ. P. et M. Curie, 4 Pl. Jussieu, 75252 Paris Cedex 05, France)
A. Lazarev
(Space Research Institute, Profsoyuznaya ul., 84/32, Moscow-810, Russia)
A. Ordanovich
(Mathematical and Mechanical Dept., Moscow University, Lenin Hills,
Moscow-234, Russia)

Abstract:

New experimental data on the structure of the turbulent stratified boundary layers have indicated that very often despite strong mixing, there are strongly ordered structures . A visual confirmation of the occurrence of such structures in atmospheric boundary layer is given by the ordered "cloud streets" structures observed in photographs of the earth's cloud cover. Their stratification is rather extreme since the horizontal extension of these structures reach easily hundreds of kilometers, whereas their heights do not exceed 3 km.

As these structures encompass a wide range of scales and intensities, we choose thus a universal multifractal approach, since in this case the mean as well as the extreme events are ruled by few exponents which we empiricaly determine with the help of data collected by aircraft and radiosondes during three Typhoon expeditions over South China Sea.

In conclusion, we discuss the rather low critical order of divergence of moments and corresponding low dressing dimension ruling the self organized criticality of extreme wind shears, temperature gradients and generation of related structures, in particular typhoons, and their stratification .

1. Data sets and experimental procedure:

We analyzed data profiles on wind fluctuation characteristics of convection in the tropical temperature-stratified boundary layer.

Horizontal wind speed profiles have been measured using the aircraft-laboratory IL-18D "Cyclone" during three Soviet-Vietnamese flying expeditions over the South China Sea in 1988, 1989 (Karmazin and Mikhailova, 1991) and 1990. Measurements were usually performed on levels increasing from 50 meters up to 5 km heights, along 20-40 km distances, every 0.125 s (i.e. the frequency was $\omega_0 = 8$ Hz and corresponding spatial distance $\Delta x \approx 12$ m for a speed of ≈ 100 m/s) in the horizontal for each level across the largest clouds bands. For our preliminary study we selected one profile per year corresponding to different meteorological situations (Chigirinskaya at al, 1994) For each profile we studied 10 samples each of length 2^{10} at a fixed level.

Vertical wind speed profiles have been measured using radiosondes during two expeditions of a research ship to a tropical part of the Pacific Ocean (Lazarev at al, 1994). All atmospheric variables were measured along the balloon rise paths, which for simplicity of interpretation, were considered vertical. The vertical resolution of the balloon sensors was about 20-25 m (data were transmitted every 5 sec of balloon flight). The time difference between the beginning and the end of balloon flight was neglected. The data were first interpolated into regularly spaced intervals with vertical resolution of 25 m, and then averaged over 50 m layers from near the surface to approximately 30-35 km. The total data base contains 287 individual profiles (167 for 1989, and 120 for 1990).

2. Universal multifractals and multifractal phase transition:

In the case of a stochastic multifractal field, - for example the turbulent energy flux density (ε) - observed at different scale ratios λ (=Λ/l, where Λ is the outer scale and l is the scale of observation), the

---

[1] (On leave from Mathematical and Mechanical Dept., Moscow University, Lenin Hills, 117234 Moscow, Russia).

[2] On leave from the physics dept., McGill University.

statistics of the field can be described in the framework of the codimension multifractal formalism (Schertzer and Lovejoy 1987, 1989, 1992, Schertzer et al. 1991, Mandelbrot 1991) either in terms of probability distributions or statistical moments, involving respectively the codimension function ($c(\gamma)$) of the order of singularities (γ) and scaling function ($K(q)$) of the moments order q:

$$\Pr\left(\varepsilon_\lambda \geq \lambda^{\gamma}\right) \approx \lambda^{-c(\gamma)}, \qquad \left\langle \varepsilon_\lambda^{q} \right\rangle \approx \lambda^{K(q)} \tag{1}$$

$c(\gamma)$ and $K(q)$ are dual for the (involutive) Legendre transform (Parisi and Frisch, 1985):

$$c(\gamma) = \max_{q}(q\gamma - K(q)); \quad K(q) = \max_{\gamma}(q\gamma - c(\gamma)) \tag{2}$$

The only constraints that must be respected by the two functions $c(\gamma)$ and $K(q)$ are that they should be both convex, and $c(\gamma)$ should be an increasing function.

Due to the existence of stable and attractive multifractal processes under rather general circumstances, mixing of different multifractal processes may lead to universal processes which depend on very few aspects of the initial processes. Indeed -up to a critical order discussed below- these universal multifractal processes have codimension and moments scaling functions ruled by only three common exponents. The three basic universal exponent are:

-The Hurst exponent H measuring the degree of non conservation of the mean field,

$$\langle \varepsilon_\lambda \rangle \approx \lambda^{-H} \tag{3}$$

-The mean singularity C_1, i.e. those contributing to the mean field, measures the fractality/sparseness of the mean field, it corresponds at the same time to the codimension of the mean field. Therefore (by Legendre transform) it corresponds to the following fixed point:

$$c(C_1-H) = C_1 \tag{4}$$

- The Lévy index α determine the extent of multifractality, it is indeed the Levy index α of the generator of the process and is proportional to curvature radius of the codimension function around the mean singularities:

$$R_c(C_1-H) = 2^{3/2}\, C_1 \alpha \tag{5}$$

The energy spectrum E(k) of wind velocity fluctuations (Fig. 1, 2) were first computed in order to estimate the exponent H. The ubiquity of scaling with $\beta_h \approx 5/3$ (close to the Kolmogorov-Obukhov value 5/3) in the horizontal and $\beta_v \approx 11/5$ (excellent agreement with Bolgiano-Obukhov value 11/5) in the vertical corresponds to the unique anisotropic but scaling regime of atmospheric dynamics as conjectured in the "unified multifractal model of atmospheric dynamics". There is no evidence for either isotropic three dimensional nor for isotropic two dimensional turbulence, the atmosphere appears to be anisotropic but scaling throughout. It should perhaps be recalled that such anisotropic scaling implies that the atmosphere is progressively more and more stratified at larger and larger scales (see Lazarev at al, 1994 for developed discassion).

Universal multifractal exponents C_1 and α can be estimated with the help of the double trace moment technique (DTM; Lavallée 1991, Lavallée et al. 1992, 1993). Indeed, we may first consider the normalized η powers of the field ε, $\varepsilon^{(\eta)}{}_\lambda$ Obviously, $\varepsilon^{(\eta)}{}_\lambda$ will have a moment scaling function $K(q,\eta)$:

$$\left\langle \left({\varepsilon^{(\eta)}}_{\lambda} \right)^{q} \right\rangle \approx \lambda^{K(q,\eta)}; \quad K(q,\eta) = K(q\eta) - q \cdot K(\eta) \qquad (6)$$

The DTM indeed will be ruled by the scaling exponent K(q,η) (Eq.6) until a critical moment order $q_D(\eta)$ (Fig. 3, 4).

In (Chigirinskaya et al., 1994) we discussed the notion of Self Organized Criticality in the context of stochastic multifractals, as corresponding to a multifractal phase transition and to algebraic or "hyperbolic" fall-off of the probability distribution:

$$\Pr(X \geq x) \approx x^{-q_D}; \quad x \gg 1 \qquad (7)$$

where the critical order of moment q_D corresponds to the following divergence of statistical moments:

$$\langle X^q \rangle = \infty \quad q \geq q_D \qquad (8)$$

The analogy (e.g. Tel, 1988, Schuster H. G. , 1988) between multifractal exponents and thermodynamic variables can be made using the following correspondences (Schertzer and Lovejoy 1991): the singularity order (γ, c(γ)) is the analogue of (energy, entropy), whereas (q, K(q)) is the analogue of (inverse of temperature, thermodynamic potential), the scale ratio is the analogue of the correlation length. And indeed, the first order multifractal transition corresponds to the fact that for a finite q_D and corresponding γ_D, the effective scale ratio will diverge as the correlation length for thermodynamic phase transition. Indeed, the scale of observation becomes irrelevant since the D-integration becomes unable to smooth singularities $\gamma \geq \gamma_D$, i.e. the small scale activity is dominant. Only the scale of homogeneity of the phenomena remains relevant and its corresponding ratio diverges for fully developed cascades.

We therefore have a clear framework in order to study the coherent or ordered tropical structures as (stochastic) self organized critical structures. Indeed, we first may define structures by the order of the singularity of their flux (scale by scale and intensity by intensity), i.e. filtering out the rest of the field having flux singularities smaller than a given order of singularity. Self organized critical structures are then those having avalanche-like fluxes, i.e. corresponding to singularities higher than the critical γ_D. We will estimate this critical singularity and the corresponding analogue of critical temperature.

The probability distribution function of wind shear $\Pr(\Delta V \geq \Delta v)$, plotted in Fig. 5 on log-log axes for different thresholds (Δv), exhibit nearly the same type of Self Organized Criticality under the expression of "hyperbolic intermittency", but over a wider range of intensities since our data set is much larger (ours involves $\approx 10^5$ measurements, theirs only $\approx 5 \times 10^3$).

For comparison, the straight lines corresponding to the best fit to the algebraic fall-off (for probability levels $< 10^{-2.5}$) are displayed on Fig.5 leading us to an initial estimate $q_D \approx 5.0 \pm .2$. This is surprisingly close to the previous results (Schertzer and Lovejoy, 1983, 1985), who had found the similar slopes in the range of separations $50\text{m} \leq \Delta z \leq 3200\text{m}$ with[3] $q_D \approx 5.0$, i.e. no preferred scale and convergence of moments only up to ≈ 5th order.

In order to compute the codimension function, we use a single scale implementation of the Probability Multiple Scaling (PDMS Lavallée et al 1991) technique which estimates c(γ) as:

$$c(\gamma) \approx -\mathrm{Log}(\Pr\{ \varepsilon_\lambda > \lambda^{\gamma} \})/\mathrm{Log}(\lambda) \qquad (9)$$

i.e. it ignores a possible slowly varying prefactors of the probability in the definition of c(γ). In Fig. 6 c(γ) calculated from the probability distribution is presented.

---

[3] Other quanities which were also found to display vertical scaling and divergence of moments were the potential temperature and gradient Richardson numbers.

The slope of the asymptote ($\gamma \geq \gamma_D$) of the resulting curves gives us q_D=2.4 ±0.05 (Fig. 7)in close agreement (see table 1) with estimates of wind tunnel experiments. With the estimates of the previous section of α_v and $C_{1,\varepsilon}$, we obtain for the critical singularity of the transition to the self-organized critical behaviour: γ_D=0.7±0.05. The corresponding transition for the velocity field occurs for $q_{D,v}$= $3q_D$≈7±1 and $\gamma_{D,v}$= γ_D/3-H ≈-0.1±0.02. Finally, we may note that the dimension of integration (the "dressing dimension") leading to this phase transition, is the implicit solution of:

$$K(q_D)=D(q_D-1) \qquad (10)$$

using the estimates of α_v and $C_{1,\varepsilon}$, one obtains: D≈0.51±0.1.

We can now compare our results with those obtained earlier in time (Schmitt et al 1993), this is shown in tables 1a, b below.

	Vertical	Horizontal	Time
	(this paper)	(part I)	(Schmitt et al 1993)
α	1.85±.05	1.35±0.07	1.50±0.05
$C_{1,\varepsilon}$	0.59±0.05	0.30±0.05	0.25±0.05
H	0.60±0.1*	0.33±0.03	0.33±0.03
$q_{D,\varepsilon}{}^{+}$	1.7±0.1	2.3±0.3	2.5±0.3
$\gamma_{D,\varepsilon}{}^{**}$	1.28±0.05	0.70±0.05	0.70±0.05
$\gamma_{d,s,\varepsilon}(D_s=0)$ #	0.94±.05	0.72±.05	0.68±.05
$\gamma_{d,s,\varepsilon}(D_s=0.5)$ #	1.26±.05	0.87±.05	0.88±.05
$\gamma_{d,s,\varepsilon}(D_s=1)$ #	1.56±.05	1.16±.05	1.08±.05
D†	.91±.1	.51±.1	.46±.1

Table 1a: Comparison of universal multifractal indices (including the dressing dimension D) for *kinetic energy flux* in the atmosphere in the vertical, horizontal and time. The underlined values of the maximum observable (dressed) singularity corresponds roughly to the sizes of the data bases used for the estimates.

+The divergence of moments exponents q_D are obtained from the wind field: $q_{D,\varepsilon}$=$q_{D,v}$/3.

* This value is the average of 0.6 (spectrum), 0.7 (probability distributions), 0.5 (c(γ)), and is equal to the theory value 3/5.

The $\gamma_{d,s,\varepsilon}$ (D_s) corresponds to the maximum observable dressed singularity (see Schertzer and Lovejoy, 1992) for respective sampling dimension D_s=0, .5,1 (D_s= Log(N_s)/Log(λ)).

**This value is obtained by K'($q_{D,\varepsilon}$).

† The dressing dimension D is obtained as solution of the implicit equation K($q_{D,\varepsilon}$)= D($q_{D,\varepsilon}$-1)

	Vertical	Horizontal	Time
	(this paper)	(part I)	(Schmitt et al 1993)
α	1.85±.05	1.35±0.07	1.50±0.05
$C_{1,v}{}^{*}$	0.078±0.01	0.068±0.01	0.05±0.01
H	0.60±0.1	0.33±0.03	0.33±0.03
$q_{D,v}{}^{**}$	5±0.2	7.0±1	7.5±1
$\gamma_{D,v}$	+0.07±.03	-0.10±.02	-0.10±.03
$\gamma_{d,s,v}(D_s=0)$	-0.15±.05	0.00±.05	-0.04±.05
$\gamma_{d,s,v}(D_s=0.5)$	-0.04±.05	0.07±.05	0.03±.05
$\gamma_{d,s,v}(D_s=1)$	0.00±0.05	0.15±.05	0.10±.05
D_v†	.33±.1	.22±.1	.20±.1

Table 1b: Comparison of universal multifractal indices for *velocity* in the atmosphere in the vertical, horizontal and time.

*Calculated from $C_{1,v}=C_{1,\varepsilon}\,3^{-\alpha}$.

** $q_{D,v}=3\,q_{D,\varepsilon}$

† The dressing dimension D_v is obtained as solution of the implicit equation: $K_v(q_{D,v})= D_v(q_{D,v}-1)$.

In the table we have shown the values of $\gamma_{d,s}$ corresponding to a single sample ($D_s=0$) and increasing sample size (calculated from $c_d(\gamma_{d,s})=D+D_s$, D is the dimension of the observing space = 1 in all these cases). Note that for single samples, the divergence cannot be detected in the vertical ($\gamma_{d,s}<\gamma_D$) and it is marginally detectable in the horizontal and in time ($\gamma_{d,s}\approx\gamma_D$). Another interesting point is that the critical order of singularity for the divergence of moments of the wind field ($\gamma_{D,v}$) is consistently close to the value 0., i.e. the corresponding velocity is rather scale invariant.

3. Conclusion:

The combination of aircraft analyses with the radiosonde results performed on data collected in the same area and period, gave us the unique opportunity to test the unified multifractal model of atmospheric dynamics with data with essentially the same meteorological and climatological characteristics. Using a single generator of anisotropy, our model unifies the small and large scale horizontal and vertical structures by a single anisotropic scaling regime rather than two separate isotropic 2D and 3D regimes.

For intensities near the mean, we reconfirm that the mono-fractal exponent H (characterizing the deviation of the velocities from the conserved energy and buoyancy fluxes) are close to the theoretical values obtained by dimensional arguments: $H_h = 1/3$, $H_v= 3/5$. Empirically, we find that the other monofractal exponent C_1 (characterizing the sparseness of the mean) is transformed from the horizontal to the vertical using the anisotropy implied by the different H values: $C_{1,h} = H_v\,C_{1,v}\,/H_h$. The original unified scaling model is therefore adequate for singularities, not too far from the mean (i.e. for not too extreme events), and this in tropics as well as in the mid latitudes.

However, using the Double Trace Moment technique, we obtained convincing results showing that the multifractal index α was not the same for vertical and horizontal (and also probably different from that in time) and as a consequence we obtain somewhat different behaviours for the extreme fluctuations (associated with Self Organized Critical structures) along the vertical when compared to the horizontal. In order to account for this effect, we must go beyond the original scalar framework in order to take into account a more complex balance between the fundamental shears and buoyancy forces

Anyway, the underlying dynamical multifractal processes undergoes a first order phase transition, which explains the appearance of self-organized critical structures in a stochastic manner contrary to the usual deterministic models of self-organized criticality. We therefore propose to identify (scale by scale) the different types of structures by the order of singularities of their associated fluxes. In particular the critical singularity at which the phase transition occurs defines the self-organized critical structures whose dynamics - contrary to the weaker structures - are dominated by the small scale interactions. The apparent constancy of γ_D values suggests that they are new universal exponents. In addition, the fact that the $\gamma_{D,v}$ values for the horizontal, vertical and time are (to within experimental precision) the same (see table 1.) may be significant. This opens an original way of understanding not only the generation of cyclones and other tropical structures, but more generally of coherent structures.

4. Acknowledgments:

We acknowledge L. Mikhailova for having help to handle the data. We are particularly indebted for many stimulating discussions with F. Schmitt.

Part of this research was supported by contract EEC # FI3PCT930077

5. References:

Y. Chiriginskaia, D. Schertzer, S. Lovejoy, A. Lazarev, A. Ordanovich, : Unified Multifractal atmospheric dynamics tested in the tropics: part I, horizontal scaling and self organized criticality, **Nonlinear Processes in Geophysics**, (in press).

Karmazin and Mikhailova, 1991: Experimental studies of heat and momentum transport by roll vortices in the boudary layer of tropical atmosphere. **Meteorology and Hydrology**, 7, 40-49.

Lavallée, D., S. Lovejoy, D. Schertzer, F. Schmitt, 1992: On the determination of universal multifractal parameters in turbulence. **Topological aspects of the dynamics of fluids and plasmas**, Eds. K. Moffat, M. Tabor, G. Zaslavsky, p.463-478, Kluwer.

Lavallée, D., S. Lovejoy, D. Schertzer, P. Ladoy, 1993: Nonlinear variability and Landscape topography: analysis and simulation. **Fractals in Geography**, Eds. L. De Cola, N. Lam, 158-192, PTR, Prentice Hall.

Lazarev, A., Y. Chiriginskaia, D. Schertzer, S. Lovejoy: Unified Multifractal atmospheric dynamics tested in the tropics: part II, vertical scaling and Generalised Scale Invariance, **Nonlinear Processes in Geophysics**, (in press).

Lovejoy, S., D. Schertzer, Generalised scale invariance and fractal models of rain, **Wat. Resour. Res., 21**, 1985, p.1233-1250.

Lovejoy, S., D. Schertzer, Multifractals, universality classes and satellite and radar measurements of clouds and rain fields, **J. Geophy. Res., 95**, 1990, p.2021-2034.

Lovejoy, S. , D. Scherzer, Multifractal analysis techniques and the rain and cloud fields from 10^{-3} to 10^{6} m, **Non-linear variability in geophysics**, D. Schertzer and S. Lovejoy éd., Kluwer, Dordrecht-Boston, 1991, p.111-144.

Lovejoy, S., D. Schertzer, P. Silas, Y. Tessier, D. Lavallée, 1993: The unified scaling model of the atmospheric dynamics and systematic analysis of scale invariance in cloud radiances. **Annales Geophysicae, 11**, 119-127.

Mandelbrot, B., 1991: **Turbulence and Stochastic processes**, Eds. J.C.R. Hunt, O.M. Phillips and D. Williams, The Royal Society, p. 79-88.

Parisi, G. and U. Frisch, 1985: A multifractal model of intermittency, **Turbulence and predictability in geophysical fluid dynamics and climate dynamics**, M. Ghil, R. Benzi and G. Parisi eds., North Holland, p. 84-88.

Schertzer D., S. Lovejoy, 1985: The dimension and intermittency of atmospheric dynamics, **Turbulent Shear flow 4**, 7-33, B. Launder ed., Springer.

Schertzer, D. , S. Lovejoy, 1987: Physical modeling and analysis of rain and clouds by anisotropic scaling multiplicative processes, **J. Geophys. Res, 92**, p. 9693-9714.

Schertzer, D., S. Lovejoy, 1989: Nonlinear variability in geophysics: multifractal analysis and simulation, **Fractals : physical origin and properties**, L. Pietronero ed., Plenum, New-York, p.49-79.

Schertzer, D., S. Lovejoy, D. Lavallée, F. Schmitt, 1991: Universal hard multifractal turbulence, theory and observations. Nonlinear Dynamics of Structures, R. Z. Sagdeev et al, eds., World Scientific R. Z. Sagdeev, U.Frisch, F. Hussain, S.S. Moiseev, N.S. Erokhin eds., World Scientific, 213-235.

Schertzer, D. , S. Lovejoy, 1992: Hard and soft multifractal processes, **Physica A., 185**, p.187-194.

Schertzer, D., S. Lovejoy, D. Lavallée, 1993: Generic multifractal phase transitions and self-organized criticality. **Cellular Automata: Prospects in astrophysical applications**, Eds. J.M. Perdang, A. Lejeune, World Scientific, p 216-227.

Schertzer, D., S. Lovejoy, 1993: Multifractal Generation of Self-Organized Criticality, in **Fractals 93** (in press).

F. Schmitt, D. Lavallée, D. Schertzer and S. Lovejoy, 1992: Empirical determination of universal multifractal exponents in turbulent velocity fields, **Phys. Rev. Lett. 68**, 305.

Schmitt, F. D. Schertzer, S. Lovejoy, Y. Brunet, 1994: Estimation of universal multifractal indices for atmospheric turbulent velocity fields. **Fractals**, in press.

Schmitt, F., D. Schertzer, G. Brethenoux, S. Lovejoy, 1994: Transition de phase multifractale du premier ordre en turbulence atmosphérique, (submitted to **Compte Rend. Acad. des Sciences**).

Tel, T., 1988: **Z. Naturforsch, 43A**, 1154.

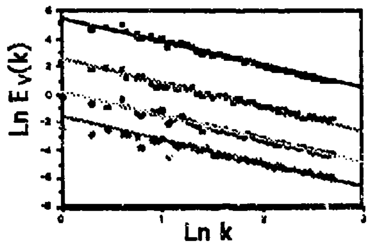

Fig. 1 The spectrum of horizontal wind velocity fluctuations, averaged over the 3 data sets taken raughly at one year interval (each contains 10 samples) and also 3 individual spectra obtained by averaging over the 10 samples. The absolute slope are close to Kolmogorov-Obukhov value 5/3 : β_v = 1.68 ±0.05 over the frequencies range $\omega_0/20$–$\omega_0/20480$ (ω_0= 8 Hz).

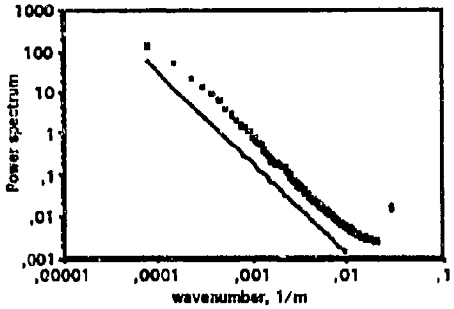

Fig. 2. The mean spectrum of 287 radiosondes at 50m resolution, over a total depth of 13.3km. The straight line is for reference with slope -2.2 .

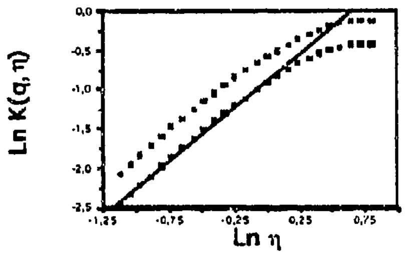

Fig. 3. A plot of Log(K(q,η)) vs. Log(η) for q=1.5 and q=2 (bottom to top). The α_ε is then estimated as the slope of Log(K(q,η)) vs. Log(η), C_1 from the intercept with the vertical axis. We display the straight line with corresponding equation y=-0.91+1.35x .

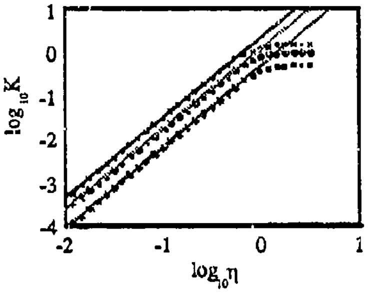

Fig. 4. Results of the DTM analysis with q=2.5, 2, 1.5 , top to bottom, respectively.

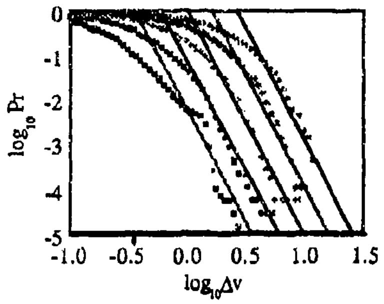

Fig. 5 Probability distributions for layers of thickness varying from 50m to 800m (left to right) with straight lines with H_v=0.7, q_D=5 for comparison.

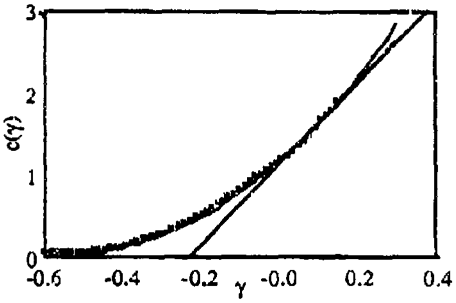

Fig. 6. c(γ) calculated from the probability distribution for 50m thick layers (points) compared to the theoretical bare and dressed c(γ) calculated with the parameters C_1=0.08, α=1.85, H_v=0.5, q_D=5.

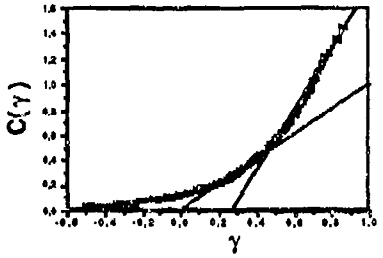

Fig. 7. Codimension function c(γ) estimated by single scale PDMS on the whole data set (30 samples) at maximum resolution ($\Lambda=2^{10}$). One may note the tangency to the first bisectrice at the point (C_1, C_1); C_1=0.3±0.05 and the linear asymptote ($\gamma \geq \gamma_D$) with the slope q_D= 2.4 ±0.05.

STABILITY CRITERION OF A STRATIFIED TWO-LAYER SHEAR FLOW WITH HYPERBOLIC-TANGENT VELOCITY PROFILE

Shuzo NISHIDA [1] and Shizuo YOSHIDA [2]

[1] Department of Civil Engineering, Hachinohe Institute of Technology, Hachinohe 031, Japan
[2] Department of Engineering Science, Hokkaido University, Sapporo 060, Japan

ABSTRACT

We investigate the stability criteria of a two-layer shear flow on the basis of linear stability theory considering viscosity. The numerical calculation was made for $10 \leqq Re \leqq 2000$. The inclusion of viscosity effects enables the neutral curves derived by Holmboe and Hazel to be closed in the (α , Ri) plane; as a result there exists a critical Richardson number Ric, above which the flow is stable for all wavenumbers. The critical Richardson number is nearly constant for $20 < Re < 1000$, and the stability criterion can be represented as approximately $Ric = 1.4$. The parameter $\theta = (Ri \; / \; Re \;)^{1/3}$, which corresponds to the Keulegan number, is found to be approximately proportional to $Re^{-1/3}$. The results agree qualitatively with those of Ippen & Harleman's experiment for lower layer flow on slopes, and experimental results for upper layer flow in an open channel also support the present numerical results. Applying the αRe expansion method of the asymptotic analysis, we obtained the results that Ric is approximately proportional to Re for small Re; the stability criterion is represented by $\theta = const.$

1. INTRODUCTION

Many theoretical studies on the stability of inviscid and continuously stratified shear flows have been performed, presenting much new knowledge about such flows. One of the most important results is the sufficient condition for stability which states that the gradient Richardson number Ri' must be greater than 1/4 everywhere throughout the flow (Miles (11)). Moreover, it has been shown that the stability criterion can be generally described as $Ri_0' = 1/4$, where Ri_0' is the Richardson number defined as Ri' at the center of the transition layer (Drazin & Howard (3)).

Stability of an inviscid two-layer flow with a density gap and tangential stress at the interface was studied theoretically by Holmboe (8) , and numerically by Hazel (7) . However, though their results showed that the flow is always unstable for some wavenumbers, they did not provide a definition of the critical Richardson number, as shown in Figs.1, 2. This suggests a need to study stability analysis account for viscosity.

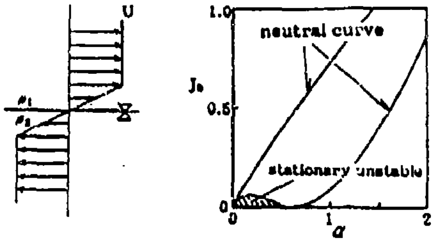

Fig.1 Flow model and resulting neutral curve by Holmboe

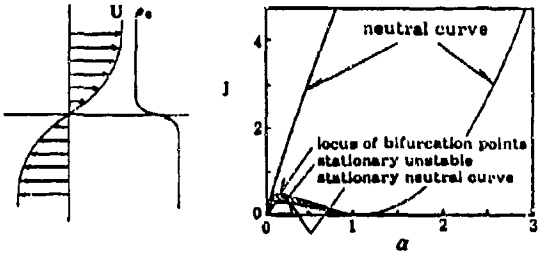

Fig.2 Flow model and resulting neutral curve by Hazel

Hayakawa & Unny (6) studied the stability of two-layer shear flow, accounting for viscosity. As the stability parameter, however, they adopted not the Richardson number but other parameters also including the wave number. As a result, the critical Reynolds number or the critical Richardson number did not appear explicitly ; they concluded from this no critical value existed. Their results, however, can not explain experimental results which show that interfacial waves are always generated once the velocity difference between upper and lower layers has passed a critical value (*e.g.* experiments of Browand & Winant (3) and Yoshida (16)).

In this paper we numerically investigate the stability criterion of two-layer shear flow on the basis of the linear stability theory considering viscosity, and represent the stability criterion as the function of *Ri* and *Re*.

2. EIGENVALUE EQUATION

We consider a two-dimensional incompressible parallel flow with a velocity profile

$$U^* = V\, tanh(y^* / h) \tag{1}$$

which is a statically stable two-layer system with densities of fluids ρ_1 and ρ_2 ($\rho_1 < \rho_2$) in the upper and lower layer, respectively. Supposing a two-layer flow such as a fresh-saline water system, we ignore the surface tension at the interface and the difference in kinematic viscosities. If we take the dimensionless stream function of disturbance as $\phi\,(y) exp\{i\,\alpha\,(x - Ct)\}$, the well-known Orr-Sommerfeld equation for each layer is deduced with a linearization procedure:

$$\begin{aligned}(U - C)(\phi_1'' - \alpha^2\phi_1) - U''\phi_1 &= \frac{1}{i\alpha R_e}(\phi_1^{iv} - 2\alpha^2\phi_1'' + \alpha^4\phi_1)\\(U - C)(\phi_2'' - \alpha^2\phi_2) - U''\phi_2 &= \frac{1}{i\alpha R_e}(\phi_2^{iv} - 2\alpha^2\phi_2'' + \alpha^4\phi_2)\end{aligned} \tag{2}$$

where U is the dimensionless velocity profile given by $U = tanh(y)$, C ($= Cr + iCi$) the dimensionless complex phase velocity, α the dimensionless wavenumber, R_e the Reynolds number defined by $R_e = hV/\nu$, and primes denote differentiation with respect to the dimensionless height y.

From the continuities of velocity and stress at the interface, boundary conditions can be obtained as

$$\begin{aligned}
&\phi_1 = \phi_1' = 0 \quad (y = +\infty)\\
&\phi_2 = \phi_2' = 0 \quad (y = -\infty)\\
&\phi_1 = \phi_2,\\
&\phi_1' - \frac{U'}{(U-C)}\phi_1 = \phi_2' - \frac{U'}{(U-C)}\phi_2,\\
&\gamma\phi_1'' - \gamma\left\{\frac{U''}{(U-C)} - \alpha^2\right\}\phi_1 = \phi_2'' - \left\{\frac{U''}{(U-C)} - \alpha^2\right\}\phi_2,\\
&i\gamma\phi_1''' + \gamma\alpha\{R_e(U-C) - 3i\alpha\}\phi_1' - \gamma\alpha R_e U'\phi_1\\
&\quad = i\phi_2''' + \alpha\{R_e(U-C) - 3i\alpha\}\phi_2' - \alpha R_e U'\phi_2 - \frac{\alpha R_e R_i}{(U-C)}\phi_2 \quad (y = 0)
\end{aligned} \tag{3}$$

where $\gamma = \rho_1 / \rho_2$ is the density ratio, $R_i = (1-\gamma)gh/V^2$ the Richardson number, and g the gravitational acceleration. Since Eqs.(3) show that effects of changes of γ on the stability can be disregarded except the term containing g in our flow field, we let γ be the constant value 0.99 (Boussinesq approximation). Thus we obtain the eigenvalue equation from the boundary conditions as follows:

$$|\Delta(\alpha, C, R_e, R_i)| = 0 \tag{4}$$

Particular solutions of the Orr–Sommerfeld equation are solved with a numerical integration following the Runge–Kutta–Gill procedure. In carrying out the calculation, we took the asymptotic solution at $y = \pm 3$ (or ± 5 when C is large) as the initial value. Furthermore, to overcome the parasitic growth problem (Drazin & Reid (4)), we made rearrangements of viscid and inviscid solutions at every 5 or 10 steps using the filtering method descrived by Betchov and Criminale (1) so that independent particular solutions at the interface can be obtained.

In the case of a inviscid flow, the stability is governed by the Rayleigh equations

$$\begin{aligned}
&\phi_1'' - \left\{\frac{U''}{(U-C)} + \alpha^2\right\}\phi_1 = 0\\
&\phi_2'' - \left\{\frac{U''}{(U-C)} + \alpha^2\right\}\phi_2 = 0
\end{aligned} \tag{5}$$

and boundary conditions are written as

$$\begin{aligned}
&\phi_1 = 0 \quad (y = +\infty),\\
&\phi_2 = 0 \quad (y = -\infty),\\
&\phi_1 = \phi_2,\\
&\gamma(U-C)\phi_1' - \gamma U'\phi_1 = (U-C)\phi_2' - U'\phi_2 - \frac{R_i}{(U-C)}\phi_2 \qquad (y = 0)
\end{aligned} \tag{6}$$

From these conditions, we can get an eigenvalue equation similar to Eq.(4).

$$|\Delta(\alpha, C, R_i)| = 0 \qquad (7)$$

Solutions of the Rayleigh equation were obtained theoretically by the method of Frobenius (written in Nishida & Yoshida (14)), and eigenvalues were found numerically using the solutions.

3. NUMERICAL RESULTS

(1) *Neutral curve*

Figure 3 shows the neutral curves obtained in the (α , Ri) plane for several Re values. The enclosed area of the curve represents the unstable region and the area outside represents the stable region. The inviscid flow is unstable in the region bounded by the α -axis and line $Ri = 2\alpha$ denoted $Re = \infty$. Although Hazel shows that there exist two neutral points in the case where the ratio of the density scale to the velocity scale is 1/5 for the inviscid gradually stratified flow, in our results for the two-layer flow there is only one neutral point. The appearance of the neutral curve at high α obtained by Hazel is due to the existence of a density transition layer, *i.e.* continuity of density profile (Nishida & Yoshida (14)). However, considering viscosity, another neutral point also appears on the high α side for our calculation, and so the neutral curves become closed in the (α , Ri) plane as shown in the figure. As the unstable region is reduced with decreasing Re, we can say that the viscosity generally has a stabilizing effect. Moreover Fig.3 suggests that the stability criterion for our flow system can be almost expressed by Ri alone in the broad range of Re, because the unstable region does not expand much into the high Ri side, whereas it expands considerably into the high α side as Re increases.

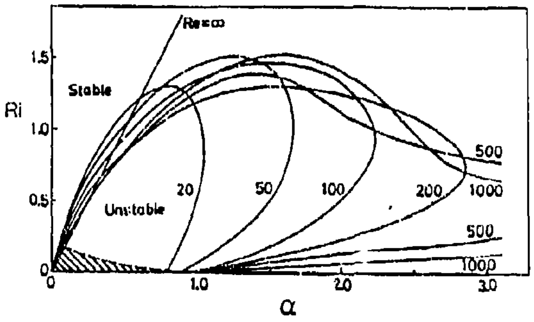

Fig.3 Neutral curves in the (α , Ri) plane

Figure 4 shows neutral curves described in the (Re, α) plane. The area bounded by each curve is an unstable region and the exterior is a stable one. The curve with $Ri = 0.0$ corresponds to that of a homogeneous flow, and this result agrees with the results of Gotoh (5) . As seen in Fig.4,

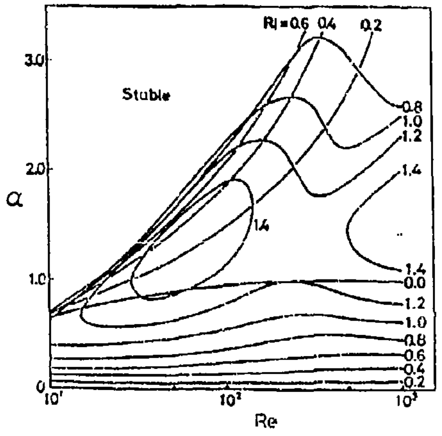

Fig.4 Neutral curves in the (Re, α) plane

the unstable region expands considerably into the high α side in the case of high Re. It is very interesting that the range of unstable α can expand more than in the homogeneous system in spite of the fact that our model must be gravitationally stable. The growth rate, however, is not so large as that of the homogeneous flow.

(2) *Stability criterion curve*

Figure 5 shows a neutral stability curve drawn in the (α , Ri) plane for the case of Re = 100. As mentioned above, the neutral stability curve is closed in the (α , Ri) plane; thus there exists a critical Richardson number Ri_c, above which the flow is stable for all wavenumbers. Meanwhile, in the inviscid case the flow is always unstable for some wavenumbers; thus the critical Richardson number doesn't exist any longer. This is essentially different from results in continuously stratified shear flows where the density scale is nearly equal to or greater than the velocity scale. In such cases the stability criteria can be almost completery described with $Ri_0' = 1/4$; this also applies to inviscid flows.

Figure 6 shows a neutral stability curve drawn in the (Re, α) plane for Ri = 1.2. In this case we can get a critical Reynolds number Re_c instead of a critical Richardson number. In either case we can express the stability criterion by the relation between Ri and Re.

Figure 7 shows the stability criterion obtained in the manner described above. As seen from the figure, Ri_c decreases as Re increases in the range 50 to 200, and has a tendency to increase in the other ranges. However, the rate of its increase and decrease is small in the broad range of $20 < Re < 1000$; thus considering the cases of usual experiments, where Re is on the order of 10^1 to 10^3, we can conclude that the stability criterion of two-layer shear flow is hardly dependent on the Reynolds number and that it can be represented only by the Richardson number as approximately $Ri_c = 1.4$. It is very interesting that in spite of the theoretical necessity for Ri_c owing to considerations of the viscosity, Ri_c for moderate Reynolds number is hardly affected by the viscosity. However, it is notable that Ri_c has a tendency to be dependent on Re for the lower Re and the higher Re.

Nishida & Yoshida (13) observed the hyperbolic-tangent type flow of the fresh water layer in an open channel of rectangular section in exchange flow with a salt water layer. An LDV and a tracer were used; the

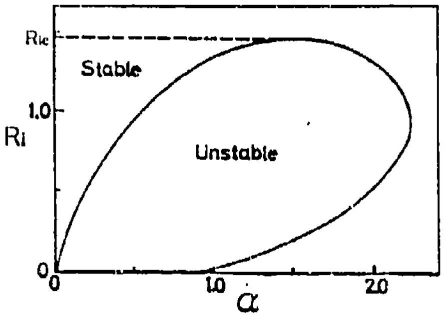

Fig.5 Neutral curve for Re=100

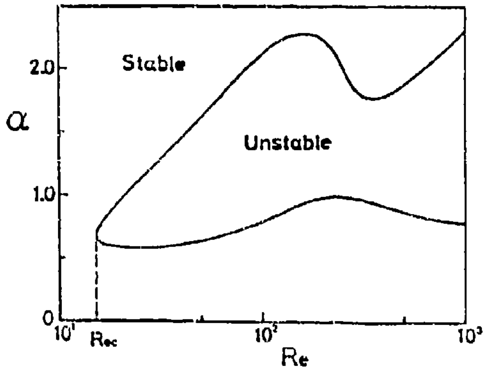

Fig.6 Neutral curve for Ri=1.2

obtained profiles fit the tanh profile well. The experimental results for the stability criterion were in good agreement with the numerical results in the experimental range of $20 < Re < 200$.

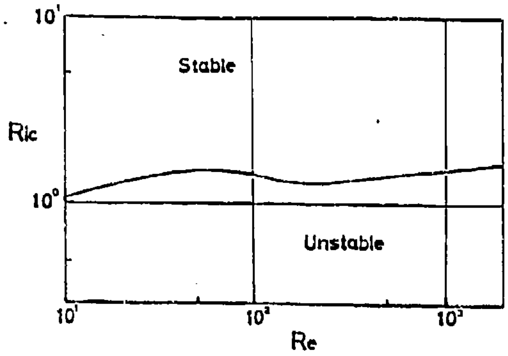

Fig.7 Stability criterion curve

(3) *Stability criterion and Keulegan number*

Figure 8 shows the stability criterion represented by $\theta = (Ri \,/\, Re)^{1/3}$, which corresponds to the Keulegan number $\bar{\theta}$ non-dimensionized by $\bar{V}$. The $\bar{\theta}$ is usually non-dimensionized by the mean velocity and has been thought a dominant parameter of stability criteria of two-layer flows. Hereafter quantities marked with a bar represent overall ones such as a depth or a mean velocity, and quantities without a bar represent those at specific points pertaining to the information near the interface such as a thickness of the transition layer or velocity gap.

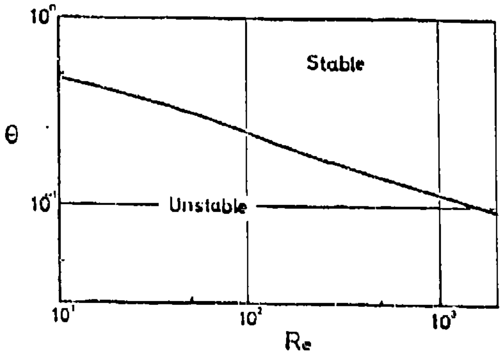

Fig.8 Stability criterion curve

The stability criterion has very little dependence on Re once it is above the broad range mentioned above; we get a relation approximately as follows;

$$\theta \propto Re^{-1/3} \tag{8}$$

This means that the viscosity does not contribute to the stability criterion as pointed out by Keulegan (10), and supports qualitatively the results of Ippen & Harleman (9) as follows;

$$\bar{\theta} = \bar{R}e^{-1/3} \quad \text{(Ippen \& Harleman)} \tag{9}$$

$$\bar{\theta} = 0.127 \quad \text{(Keulegan)} \tag{10}$$

At $Re < 20$ and $1000 < Re$, however, the contribution of Re to the stability criterion has a tendency to increase, and if there appears a region where the gradient of the stability criterion curve in the (Re, Ri) plane is unity, we will obtain a relation $\theta =$ constant as mentioned below.

4. STABILITY CRITERION FOR SMALL $\alpha\, Re$

Applying the $\alpha\, Re$ expansion method of the asymptotic analysis by Tatsumi & Gotoh (15) to our two-layer model, we obtain the following equation for eigenvalues as a first approximation:

$$2C\,(\beta_1+\beta_2)\,[\,\alpha^2+(\beta_1+\beta_2)\,\alpha+\beta_1{}^2+\beta_2{}^2-\beta_1\beta_2\,]$$
$$+\,iR_eR_i\,(\beta_1+\beta_2+2\,\alpha)=0 \qquad (11)$$

with

$$\beta_1{}^2=\alpha^2-iR_e(C-1) \qquad Real(\beta_1)>0$$
$$\beta_2{}^2=\alpha^2-iR_e(C+1) \qquad Real(\beta_2)>0$$

This equation agrees with that derived by Hayakawa & Unny (6) . Setting $C_i=0$, we can get the asymptotic neutral curves and the critical Richardson number for small R_e as shown in Figs.9, 10. The phase velocity C_r and the critical Richardson number R_{ic} are approximately represented by

$$C_r{}^2=0.350(\,R_i\,/\,\alpha\,) \qquad (12)$$

$$R_{ic}=0.277R_e \qquad (13)$$

Although C_r was slightly dependent on R_e for at moderate values (Nishida & Yoshida (12)), at low R_e, C_r is independent on R_e and is approximately proportional to $(\,R_i\,/\,\alpha\,)^{1/2}$. The critical Richardson number is approximately proportional to R_e. This means that the stability criterion at low R_e is represented by

$$\theta=0.652 \qquad (14)$$

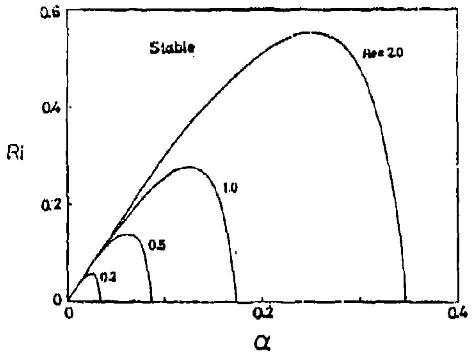

Fig.9 Neutral curves for small R_e

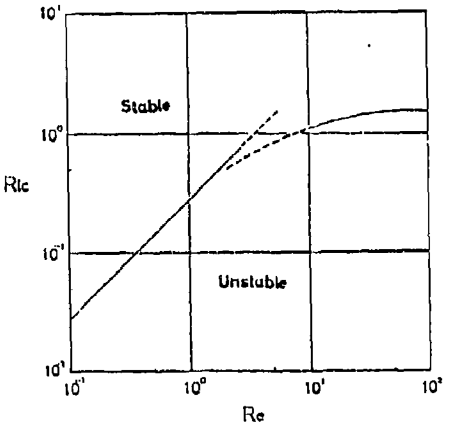

Fig.10 Stability criterion curve for small R_e

5. Conclusions

The stability criterion of the two-layer shear flow has been investigated. The results obtained from the present study are summarized as follows;

(1) The critical Richardson number R_{ic} hardly changes over a broad range of the Reynolds number R_e, and the stability criterion can be represented as approximately $R_{ic}=1.4$.

(2) At higher R_e, R_{ic} tends to increase as R_e increases.

(3) The asymptotic solutions for small R_e show that R_{ic} is approximately proportional to R_e and stability criterion is represented by the Keulegan number $\theta = 0.652$.

REFERENCES

(1) Betchov, R., Criminale, Jr.W.O., "*Stability of Parallel Flows*", Academic Press, New York, 1967, 330p.

(2) Browand, F.K., Winant, C.D., "Laboratory observation of shear-layer instability in a stratified fluid", Boundary Layer Met., vol.5, 1973, pp.67–77.

(3) Drazin, P.G., Howard, L.N., "*Advances in Applied Mechanics*", vol.9, Academic Press, New York, 1966, pp.1–89.

(4) Drazin, P.G., Reid, W.H., "*Hydrodynamic Stability*", Cambridge University Press, 1981, 527p.

(5) Gotoh, K., "Hydromagnetic instability of a free shear layer at small magnetic Reynolds number", J. Fluid Mech., vol.49, 1971, pp.21–31.

(6) Hayakawa, N., Unny, T.E., "Viscous stability of parallel streams of superposed fluids", Phys. Fluids, vol.17, 1974, pp.879–882.

(7) Hazel, P., "Numerical studies of the stability of inviscid stratified shear flows", J. Fluid Mech., vol.51, 1972, pp.39–61.

(8) Holmboe, J., "On the behavior of symmetric waves in stratified shear layers", Geophys. Publ., vol.24, 1962, pp.67–113.

(9) Ippen, A.T., Harleman, D.R.F., "Steady-state characteristics of subsurface flow", Gravity Wave Symposium, Nat. Bureau Stands., Circulation 521, 1951, pp.79–93.

(10) Keulegan, G.H., "Interfacial instability and mixing in stratified flow", J. Research, Nat. Bureau Stands., vol.43, 1949, pp.487–500.

(11) Miles, J.W., "On the stability of heterogeneous shear flows", J. fluid Mech., vol.10, 1961, pp.496–508.

(12) Nishida, S., Yoshida, S., "Theoretical analysis of shear instability for two-layer flow", Proc. 29th Japanese Conf. Coastal Eng., 1982, pp.550–554.(in Japanese)

(13) Nishida, S., Yoshida, S., "Experimental study on the stability of a two-layer shear flow", Proc. 28th Japanese Conf. Hydraulics, 1984, pp.338–343.(in Japanese)

(14) Nishida, S., Yoshida, S., "Influence of the density and velocity profiles on calculated instability characteristics in an inviscid two-layer shear flow", J. Hydoscience and Hydraulic Eng., vol.7, 1990, pp.61–68.

(15) Tatsumi, T, Gotoh, K., "The stability of free boundary layers between two-uniform streams", J. Fluid Mech., vol.7, 1960, pp.433–441.

(16) Yoshida, S., "Mixing mechanism of density current system at river mouse", Proc. 2nd Int. Symposium on Stratified Flows, Tronheim, 1980, pp.1062–1073.

Stability of vortices with nonstationary elliptical streamlines in stratified fluid

E. Gledzer and V. Ponomarev
Institute of Atmospheric Physics, 109017, Pyzhevsky 3, Moscow, Russia

Abstract

The problem of a stability of oscillating stratified flow with elliptical streamlines is considered. The parameters of unstable modes are found in dependence of external frequency and stratification of fluid. It is shown that nonstationary strain rate can excite an instability for any stratification of fluid.

1 Introduction

Concentrated vorticity regions often appear in high Reynolds number flows. The theoretical and some experimental investigations show a possibility of the 3-D instability of flows with elliptical streamlines connected with a resonance between the inertial vortex waves and the locally imposed strain field [1-6]. It has been proposed that this instability constitute a relevant mechanism in turbulence that is capable of giving rise to excitations on all scales. The elliptical vorticity regions in external strain flow may be nonstationary [7], and, in general, a vortex may be subjected to straining fields with unsteady strain rates.

We formulate the problem of stability for oscillating vorticity region, the simplest case of that is the flow in a flexible elliptical cylinder with periodically changing main axes. The fluid is assumed to be inviscid and incompressible. The linear stability problem is reduced to a system of equations with quasi-periodical coefficients. For small ellipticity it is possible to reduce the governing equations to a Floquet problem. This allows to define the changing of stability conditions and parameters of unstable modes in dependence of external frequency.

2 Statement of the problem

The equations of motion for inviscid, incompressible fluid are written as

$$\frac{\partial \mathbf{u}}{\partial t} + \mathbf{u}\nabla\mathbf{u} = -\frac{1}{\rho}\nabla p + \beta \mathbf{g} T,$$
$$\frac{\partial T}{\partial t} + \mathbf{u}\nabla T = 0, \qquad (1)$$
$$div\mathbf{u} = 0.$$

For the flow in an elliptical cylinder with a border

$$f(x,y,t) = \frac{x^2}{a^2} + \frac{y^2}{b^2} - 1 = 0, \qquad (2)$$

the boundary condition $\mathbf{un}|_f = 0$ take the form

$$\frac{\partial f}{\partial t} + \mathbf{u}\nabla f = 0 \qquad (3)$$

where $\mathbf{n}$ is the normal to the surface (2).

2.1 Basic state

We assume that the cross-section area of a cylinder is not changed in time ($ab = const$). Then the solution of (1) – (3) has the form

$$\mathrm{U} = \{-\Omega\frac{b^2}{a^2+b^2}y + \mu x, \Omega\frac{a^2}{a^2+b^2}x - \mu y, 0\},$$

$$T = \gamma z \tag{4}$$

where $\mu = \frac{d\ln a}{dt}$. It describes a flow with the constant vorticity Ω in time dependent strain flow.

We shall consider here the flow of a stably stratified fluid ($\gamma > 0$).

2.2 The stability equations

We introduce new variables for velocity $\mathbf{u}$, temperature T and pressure p disturbances and for independent variables x, y, z, t as follows

$$u' = \frac{u}{\Omega a}, v' = \frac{v}{\Omega b}, w' = \frac{w}{\Omega c}, p' = \frac{2p}{\Omega^2 c^2}, \theta = \frac{(\beta g\gamma)^{1/2}T}{\Omega c},$$

$$x' = \frac{x}{a}, y' = \frac{y}{b}, z' = \frac{z}{c}, \frac{dt'}{dt} = \Omega\frac{ab}{a^2+b^2}, \tag{5}$$

where $c = (ab)^{1/2}$.

The linear equations for disturbances take the form (the primes are omitted henceforth)

$$(1+\epsilon)(Du + 2\mu u - v) = -\frac{\partial p}{\partial x},$$

$$(1-\epsilon)(Dv - 2\mu v + u) = -\frac{\partial p}{\partial y},$$

$$(1-\epsilon^2)^{1/2}Dw - N\theta = -\frac{\partial p}{\partial z},$$

$$(1-\epsilon^2)^{1/2}D\theta + Nw = 0,$$

$$div\mathbf{u} = 0, \tag{6}$$

where $D = \frac{\partial}{\partial t} + x\frac{\partial}{\partial y} - y\frac{\partial}{\partial x}$, $\epsilon = \frac{a^2-b^2}{a^2+b^2}$ and $N = 2(\beta g\gamma)^{1/2}/\Omega$ is nondimentional Brunt-Vaiaisala frequency.

We suggest that the eccentricity has the form

$$\epsilon = \epsilon_0\cos(\omega_0 t) \tag{7}$$

For unbounded flow the system (6) may be transformed by the substitution

$$\mathbf{u} = \hat{\mathbf{u}}(t)\exp(i\mathbf{k}(t)\mathbf{r}), \tag{8}$$

with a vector $\mathbf{k} = (h\cos t, h\sin t, \kappa)$ to the set of ordinarily equations [3,4]

$$\frac{d\hat{u}}{dt} = \frac{k_x G}{1+\epsilon} - 2\mu\hat{u} + \hat{v},$$

$$\frac{d\hat{v}}{dt} = \frac{k_y G}{1-\epsilon} + 2\mu\hat{v} - \hat{u},$$

$$\frac{d\theta}{dt}=\frac{N}{(1-\epsilon^2)^{1/2}\kappa}(k_x\hat{u}+k_y\hat{v}), \tag{9}$$

$$G=\frac{2(k_y\hat{u}-k_x\hat{v})+2\mu(k_x\hat{u}-k_y\hat{v})-\theta\frac{N\kappa}{(1-\epsilon^2)^{1/2}}}{\frac{k_x^2}{1+\epsilon}+\frac{k_y^2}{1-\epsilon}+\frac{\kappa^2}{(1-\epsilon^2)^{1/2}}}$$

It contains the coefficients with two periods 2π and $2\pi/\omega_0$.

For small values of eccentricity parameter ϵ_0 we have $\mu=\frac{1}{2}\frac{d\epsilon}{dt}$ and taking into account only the terms of the order 1 on ϵ and making the transformation to the cylindrical coordinate system (r,φ,z), we receive the equations

$$\begin{gathered}
Du_r-2u_\varphi+D\epsilon u_r\cos 2\varphi-u_\varphi\sin 2\varphi=-\frac{\partial p}{\partial r},\\
Du_\varphi+2u_r-D\epsilon(u_r\sin 2\varphi+u_\varphi\cos 2\varphi)=-\frac{\partial p}{r\partial\varphi},\\
Dw-N\theta=-\frac{\partial p}{\partial z},\\
D\theta+Nw=0.
\end{gathered} \tag{10}$$

The system (10) is considered in the region

$$x^2+y^2<1$$

with the boundary condition

$$u_r(1,z,\varphi)=0$$

We shall seek a solution of equations (10) in the form

$$\mathbf{u}=\sum C_\alpha\mathbf{u}_\alpha,\ \theta=\sum C_\alpha\theta_\alpha. \tag{11}$$

where $\mathbf{u}_\alpha$ is the solution of the eigenvalue problem for unperturbed equations (10) .

The function set

$$\begin{gathered}
(u_r+iu_\varphi)_\alpha=(2+q)J_{n+1}(hr)\cos(kz)\exp(in\varphi),\\
(u_r-iu_\varphi)_\alpha=(2-q)J_{n-1}(hr)\cos(kz)\exp(in\varphi),\\
w_\alpha=q\frac{h^2}{k}J_n(hr)\sin(kz)\exp(in\varphi)\\
\theta_\alpha=iN\frac{h^2}{k}J_n(hr)\sin(kz)\exp(in\varphi)
\end{gathered} \tag{12}$$

describes the inertial waves in a stably stratified fluid rotating as a whole and has the imagine characteristic values $i\omega_\alpha$. The "vector" subscript $\alpha=\{j,n,k\}$ defines the wave numbers on the variables r,φ,z, correspondingly. The index j numbers the roots of the equation

$$qh\frac{J_n(h)}{dh}+2nJ_n(h)=0, \tag{13}$$

following from the boundary condition $u_r|_{r=1}=0$.

The frequency ω_α is connected with disturbances parameters by the relations

$$\omega_\alpha=q_\alpha-n,\ q^2=\frac{N^2+4\sigma^2}{1+\sigma^2},\ \sigma=\frac{k}{h}$$

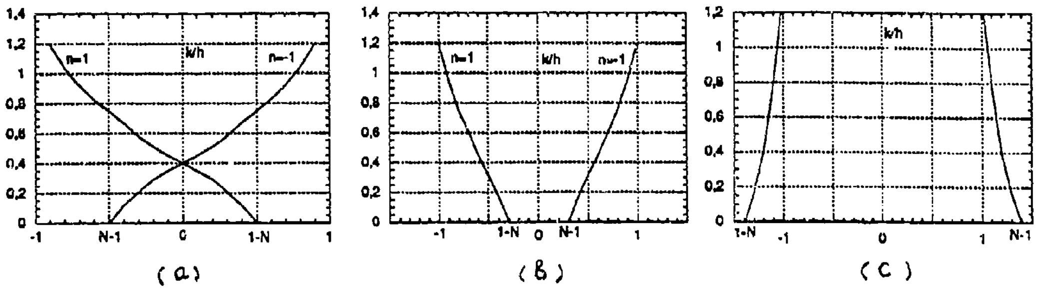

Figure 1: The general dependence k/h on ω_o for $n, n' = \pm 1$ and a) $N < 1$, b) $1 < N < 2$, c) $2 < N$.

The general picture of spectra for azimuthal wave numbers $n = 1$ and $n' = -1$ is shown in Fig. 1. We can mark out three cases. The first case take place for $N < 1$ (Fig.1(a)). There is a coincidence of frequencies for some wave number ratio σ and this leads to instability of stationary vortex [6,9,10]. A coincidence is absent for $N > 1$ and instability may be caused by a resonance with external frequency.

The C_α satisfy to equations

$$(\frac{d}{dt} - i\omega_\alpha)C_\alpha + \epsilon_0 \sum V_{\alpha\alpha'}(\frac{d}{dt} + in)\cos(\omega_0 t)C_{\alpha'} = 0 \tag{14}$$

This system has a Floquet type.

The general structure of the expression for the interaction coefficients $V_{\alpha\alpha'}$ shows that they are nonzero only for azimuthal wave numbers $n' = n \pm 2$ and their values are small if $h_\alpha \neq h_{\alpha'}$ [6]. Therefore we consider here only the interaction between the modes having the same value of $h_\alpha = h_{\alpha'} = h$. It is does not vanish in the limit $h \to \infty$ and can describe the stability of an unbounded flow or the small scale instability of the vortex in the neighborhood of its core. The asymptotic value of this coefficient is

$$V = \frac{(2+q)}{8} \frac{1}{2 + N^2\sigma^{-2}} \tag{15}$$

3 Conditions of the instability

At the first order of perturbation theory on parameter ϵ_0, we can take into account only the interaction between two modes [6] and the system (13) is reduced to the sets of two coupled equations

$$\begin{aligned}(\frac{d}{dt} - i\omega_\alpha)C_\alpha + \epsilon_0 V(\frac{d}{dt} + i)\cos(\omega_0 t)C_{\alpha'} = 0,\\ (\frac{d}{dt} + i\omega_\alpha)C_{\alpha'} + \epsilon_0 V(\frac{d}{dt} - i)\cos(\omega_0 t)C_\alpha = 0\end{aligned} \tag{16}$$

In the case $\omega_0 = 0$ the solution of equations (16) defines the instability in a stationary vortex, considered in refs. [1-6].

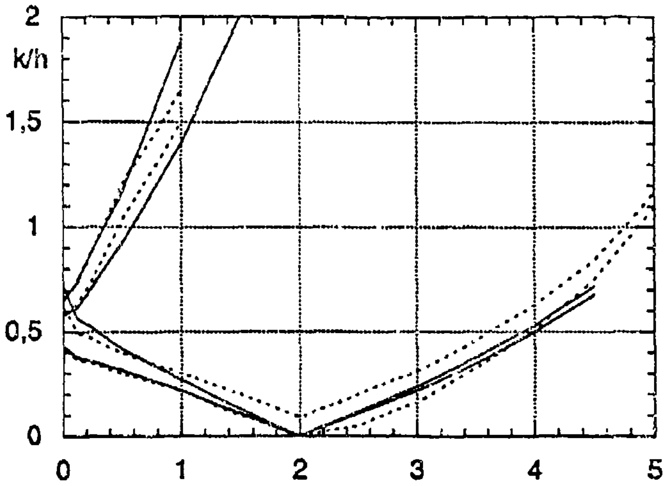

Figure 2: The comparison of instability borders for unbounded flow solution (9) (solid lines) and for approximate solution of (17) (dashed lines). Upper branch for $\epsilon = 0.5$, low branch for $\epsilon = 0.2$.

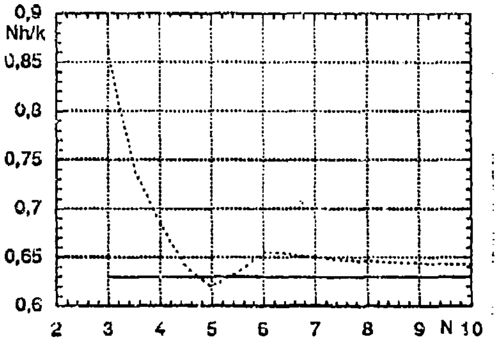

Figure 3: The border of instability in dependence of N ($\epsilon = 0.1$) (dashed line). Solid line corresponds to asymptotic value $\sigma = N/2\epsilon_0^{1/2}$

The leading instability in flows with elliptical streamlines is defined by the interaction between the modes having the same wave numbers [6].

For $\epsilon_0 \ll 1$ we obtain the instability described by expression for growth rate δ

$$\delta^2 = \frac{\epsilon_0^2 V^2}{4}(1 - \omega_\alpha \pm \omega_0)^2 - (\omega_\alpha \pm \frac{\omega_0}{2})^2 \qquad (17)$$

They define the resonance conditions for the inertial modes with the frequency ω_α and the strain flow frequency ω_0.

The results of analyses show that the resonance conditions for small value ϵ are possible only for $\omega_\alpha = \pm\omega_0/2$. The regions of instability following from (17) are presented in Fig. 2 for $N = 0$ (solid lines show the borders calculated according to (9)). These results show that effective interaction between the modes take place only for $q_\alpha > 0$.

Let us consider the stability of strongly stratified fluid $N > 2$. In this case the effective interaction is possible only for large values of σplace for $\sigma > N/2\epsilon_0^{1/2}$, ($\omega_0 = 2$). This result corresponds to numerical data, following from equations (9) (see Fig. 3).

References

[1] Gledzer E. B., Dolzhansky F. V., Obukhov A. M. & Ponomarev V. M. 1975 An experimental and theoretical study of the stability of motion of a liquid in an elliptical cylinder. Izv.Acad. Sci. USSR, Atmos. Oceanic Phys. 11, 617-622.

[2] Pierrehumbert R. T. 1986 Universal short-wave instability of two-dimensional eddies in an inviscid fluid. Phys. Rev. Lett. 57, 2157.

[3] Bayly B. J. 1986 Three-dimensional instability of elliptical flow. Phys. Rev. Lett. 57, 2160.

[4] Malkus W. V. R. 1989 An experimental study of global instabilities due to the tidal (elliptical) distortion of a rotating elastic cylinder. Geophys. Astrophys. Fluid Dyn. 30, 123.

[5] Waleffe F. 1990 On the three-dimensional instability of strained vorticies. Phys. Fluids A 2, 76.

[6] Gledzer E. B. & Ponomarev V. M. 1992 Instability of bounded flows with elliptical streamlines. J. Fluid Mech. 240, 1-30.

[7] Kida S. 1981 Motion of an elliptic vortex in a uniform shear flow. J. Phys. Soc. Jpn. 50, 3517.

[8] Craik A. D. D. & Criminale W. O. 1986 Evolution of wave-like disturbances in shear flows: a class of exact solutions of Navier-Stokes equations. Proc. R. Soc. Lond. A 406, 13.

[9] Gledzer E. B. 1991 Wave generation in elliptical rotation of an inhomogeneous fluid. Sov.Phys.Doklady. 36, 282.

[10] Miyazaki T., Fukumoto Y. 1992 Three-dimensional instability of strained vorticies in a stably stratified fluid. Phys.Fluids A 11, 2515.

Numerical study of a thermally stratified flow and its interaction with a conducting wall

C. Péniguel
EDF/LNH, 6 quai Watier BP 49 F-78401 Chatou

SUMMARY

In PWR's, stratified flows may appear. This situation sometimes arises when the flow is non-isothermal. For piping systems, due to gravity effects, hot water fills the top portion of the pipe section while the cold and therefore heavier water settles down at the bottom. This particular loading could partly explain mechanical damages (like cracks) encountered in some piping systems.

Several mock-ups and numerical studies have been performed during the past years. This paper presents numerical calculations performed on the geometry of the FLUO experiment studied at CEA. The goal of this work is a better understanding of the stratification phenomena and the wall effects on temperature phenomena. Indeed previous studies indicated that wall effects or azimuthal fluxes through a conducting wall may have to be accounted for.

The numerical study reported in this paper relies on the CFD code ESTET 3.1 developped at EDF in the past years, coupled with a module (Syrthes 1.0) solving the thermal phenomena inside the conducting wall. A second aspect looked at is related to the temperature fluctuations which may lead to thermal stripping. Comparisons between experimental data and numerical simulation are presented.

1. INTRODUCTION

Several mock-ups have been used in previous studies [1],[2],[3],[4],[5], to gain some understanding of parameters likely to influence the stratification phenomena. Theses mock-ups, sometimes full scale, did point out that wall effects may in some cases play a part in the phenomena. For exemple when a thermal stratification is being created, wall inertia is taking place. Even when a stable state has been reached, the conductive wall still influences the phenomena, through azimuthal conduction. Indeed transfer through the wall may be greater than across the sharp fluid interface, where gravity effects reduces the exhange going on between hot and cold layers. Therefore simulating the global phenomena requires thermal equations to be solved, both inside fluid and solid regions.

A fairly general purpose development has been proposed [6] to handle the problem. It is based on the CFD code ESTET 3.1 coupled with a module (Syrthes 1.0) solving the conduction equation inside the solid wall. The originality of the approach is that ESTET 3.1 uses finite volumes-finites differences technique on a structured grid while the module Syrthes 1.0 discretizes the thermal equations on an unstructured grid (triangles in 2D, and tetrahedra in 3D), and uses a finite element technique. This development hase been used on the present case, indeed one goal of this work is to help validating the numerical tool. Confronting experimental and numerical approaches on a wider range of applications help increasing the confidence we place in the ability of the numerical tool to predict real situations, for which experimental approaches turn out to be both difficult and expensive.

Another aspect looked at is related to the temperature fluctuations which may lead to thermal stripping phenomena. Experimental results show that the amplitude of the fluctuations tends to decrease when approaching the wall.

2 PRESENTATION OF THE EXPERIMENTAL FACILITY.

A sketch of the experimental facility is presented on figure (1). Made of perspex it allows good visualisations (Laser techniques can also be used to investigate velocity fields). One side wall is made of conducting metal. The experimental facility has been built at CEA and all measurements have been performed by Tenchine and Baroill [7] at CEA.

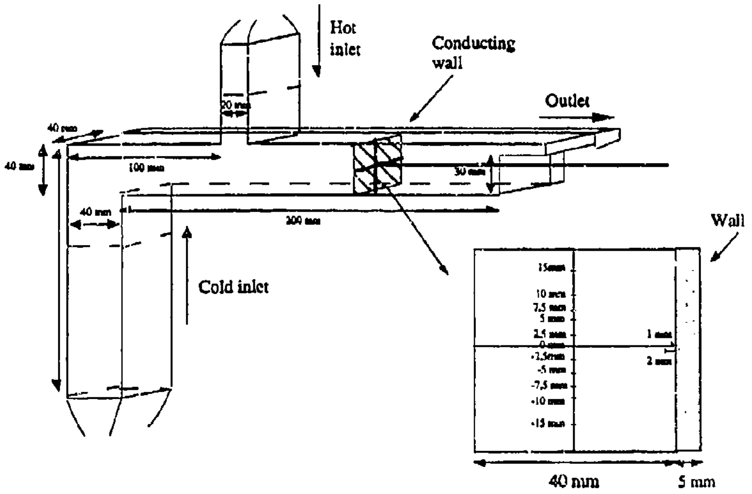

Figure 1 : Geometry of the mock-up FLUO

This small size mock-up (see dimensions in mm), is composed of two legs connected together with a T junction. A cold flow is injected upwards through the vertical pipe and forms an horizontal flow after the elbow. A hot flow is injected downwards through the upper vertical pipe. Flow rates and temperatures of cold and hot legs are monitored to stay as stable as possible. Regarding measurements, thermocouples have been used for temperature. Two rakes of thermocouples forming a cross (see sketch 1) allow to access temperature profiles. For each experiment, four locations along the x direction have been studied in detail :20 mm, 60 mm, 100mm and 160 mm after the T junction. Measurements in the near wall vicinity are quite challenging.

3 COMPUTATIONAL APPROACH

ESTET is a general purpose code solving the averaged Navier-Stokes equations. Thus, the basic equations, (mass, momentum and energy conservation) read :

$$\frac{\partial \rho}{\partial t} + \frac{\partial \rho U_i}{\partial x_i} = 0 \tag{1}$$

$$\frac{\partial U_i}{\partial t} + U_j \frac{\partial U_i}{\partial x_j} = \frac{1}{\rho} \frac{\partial}{\partial x_j} \left(\mu_m \left(\frac{\partial U_i}{\partial x_j} + \frac{\partial U_j}{\partial x_i} \right) - \rho\, \overline{u_i u_j} \right) - \frac{1}{\rho} \frac{\partial p^*}{\partial x_i} - \frac{\rho - \rho_o}{\rho} g_i \tag{2}$$

$$\frac{\partial T}{\partial t} + U_i \frac{\partial T}{\partial x_i} = \frac{1}{\rho C_p} \frac{\partial}{\partial x_i} \left(K_m - \rho C_p\, \overline{u_i T} \right) \tag{3}$$

In these equations, U_i are the components of the mean velocity, u_i the velocity fluctuation, p^* is the pressure difference from an hydrostatic equilibrium involving a reference density ρ_o, T is the mean temperature, μ_m and K_m are the molecular viscosity and conductivity. The eddy viscosity concept has been used to close the sytem. It means that Reynolds stress tensor and turbulent heat flux are assumed to be colinear to mean strain tensor and mean temperature gradient. Spectral equilibrium as well as constant energy transfer (of value ϵ) along the inertial subrange is assumed, leading to the following expressions.

$$-\rho\, \overline{u_i u_j} = \mu_t \left(\frac{\partial U_i}{\partial x_j} + \frac{\partial U_j}{\partial x_i} \right) - \frac{2}{3} \left(\rho k \delta_{ij} + \mu_t \frac{\partial U_l}{\partial x_l} \right) \tag{4}$$

$$-\rho C_p\, \overline{u_i T} = K_t \frac{\partial T}{\partial x_i} \tag{5}$$

with

$$\mu_t = \rho C_\mu \frac{k^2}{\varepsilon} \quad \text{and} \quad K_t = \frac{\rho C_\mu}{\sigma_T} \frac{k^2}{\varepsilon} \tag{6}$$

The determination of k and ε the turbulent kinetic energy and its dissipation rate respectively, is done by the following transport equations (see Launder [8]).

$$\begin{cases} \dfrac{\partial k}{\partial t} + \vec{U}\ grad\ k = \dfrac{1}{\rho}\, div\Big((\mu + \dfrac{\mu_t}{\sigma_k}) grad\ k\Big) + P + G - \varepsilon & (7) \\ \dfrac{\partial \varepsilon}{\partial t} + \vec{U}\ grad\ \varepsilon = \dfrac{1}{\rho}\, div\Big((\mu + \dfrac{\mu_t}{\sigma_\varepsilon}) grad\ \varepsilon\Big) + C_{\varepsilon_1} \dfrac{\varepsilon}{k}(P + (1 - C_{\varepsilon_3})G) - C_{\varepsilon_2} \dfrac{\varepsilon^2}{k} & (8) \end{cases}$$

where :

$$P = \Big(\frac{\mu_t}{\rho}(\frac{\partial U_i}{\partial x_j} + \frac{\partial U_j}{\partial x_i}) - \frac{2}{3}(k + \frac{\mu_t}{\rho}\frac{\partial U_l}{\partial x_l}\delta_{ij})\Big)\frac{\partial u_i}{\partial x_j} \quad \text{and} \quad G = \frac{K_t}{\rho}\beta g_i \frac{\partial T}{\partial x_i} \tag{9}$$

The choice of the constant $C_{\varepsilon 3}$ is still under discussion. For the present calculation, we follow Viollet [9].

$$\begin{cases} C_{\varepsilon 3} = 1 & \text{if G} \leq 0 \text{ stable stratified flow} \\ C_{\varepsilon 3} = 0 & \text{if G} \geq 0 \text{ unstable stratified flow} \end{cases} \tag{10}$$

This term, relating buoyancy effects and turbulence, is of importance in stratified flows, since it ensures the stability of such stratified flows by inhibiting the turbulent mixing at the interface.

An equation for the temperature fluctuations variance has been used. It relies on a simplified modelling for the dissipation term (see Rodi [10]), assuming a constant ratio R between dynamical and thermal turbulent time scales.

$$\frac{\partial \theta^2}{\partial t} + u_i \frac{\partial \theta^2}{\partial x_i} = \frac{\partial}{\partial x_i}\left(\left(K_n + \frac{C_\mu}{\sigma_\theta}\frac{k^2}{\varepsilon}\right)\frac{\partial \theta^2}{\partial x_i}\right) + 2\frac{C_\mu}{\sigma_T}\frac{k^2}{\varepsilon}\left(\frac{\partial T}{\partial x_i}\right)^2 - \frac{1}{R}\frac{\varepsilon}{k}\theta^2 \tag{11}$$

Usual boundary conditions apply. At the wall, a wall function approach is used.

In order to solve these equations, ESTET uses orthogonal grids. Fairly complex 3D geometries can be approximated since slanted boundary cells are allowed.

Numerically the code uses a finite differences-finite volumes method based upon a fractional step technique. Advection is solved by a three dimensional characteristic method. Diffusion is handled through a spatial splitting technique, and mass conservation is ensured by solving the resulting Poisson equation with a conjugate residual method. More details about the code ESTET can be found in reference [11].

The module Syrthes 1.0 is solving the conduction equation within solids with efficient finite element techniques on non structured grids. The equation to be solved is :

$$\begin{cases} \rho C_p \dfrac{\partial T}{\partial t} = div\ (k_s\ grad\ T) + \Phi_v \\ \text{with } \lim\limits_{t \to 0} T(x,y,z,t) = \Theta_o(x,y,z) \qquad \forall\ (x,y,z) \in \Omega \\ \text{and boundary conditions on } \Gamma = \Gamma_d \cup \Gamma_q \\ T(x,y,z,t) = \theta(x,y,z,t) \qquad \forall\ (x,y,z) \in \Gamma_d \\ -k_s \dfrac{\partial T}{\partial n} = q(x,y,z,t) \qquad \forall\ (x,y,z) \in \Gamma_q \end{cases} \tag{12}$$

In equation (12) ρ, C_p, and k_s respectively density, specific heat, and conductivity of the solid, are allowed to vary in space and time. Θ_o is the initial distribution, Φ_v a heat source, and θ (Dirichlet) and q (Neumann) are the boundary conditions. These conditions may also vary with time and space.

For optimisation reasons, elements available are limited to 6 nodes triangles in 2D, and 10 nodes tetrahedra in 3D. The discretization used is of iso-P2 type, which means that variables vary linearly between two nodes of the element. Within each time step an iterative procedure described in [6], ensures the transfer of information through the interface between the solid and fluid regions.

4 GRIDS USED

As stated earlier, the fluid region is descretized with a rectangular mesh generated here with the pre-processor CEZANNE. In order to reduce slightly the number of nodes only half of the domain has been simulated. A previous calculation has shown that lateral walls are not influencing the middle plane, therefore a symmetry condition has been used. The mesh (see figure 2) chosen is (69 x 10 x 29). Tests on a coarser mesh and finer meshes indicate that the solution is almost mesh independent, when taking finer meshes than the one chosen here.

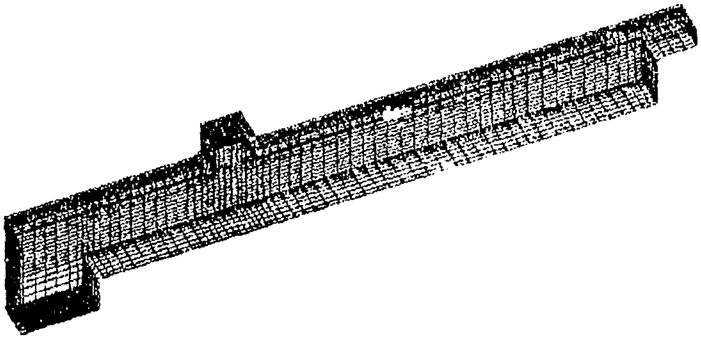

Figure 2 : Grid used in the fluid region

The mesh of the adjacent solid wall has been generated using the mesh generator SIMAIL. The mesh (see figure 3) is composed of 12180 tetrahedra and 18997 nodes. It is interesting to note that a refinement in the region where the steepest gradients are likely to occur has been chosen. This is possible since the module Syrthes 1.0 allows nodes not to be coincident at the interface between solid and fluid regions.

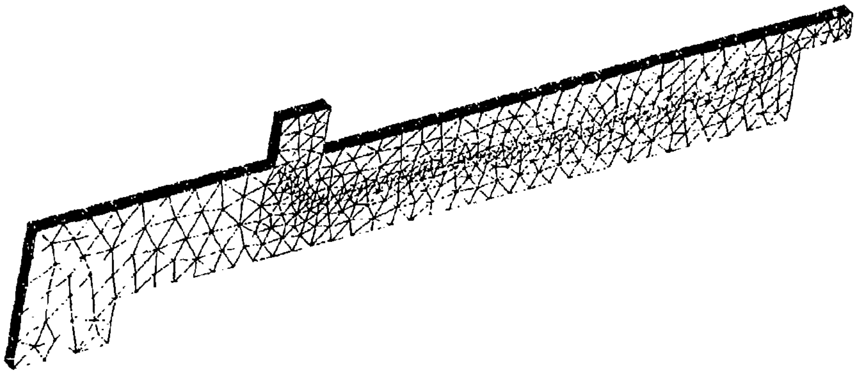

Figure 3 : Mesh used in the solid region

5 RESULTS OF THE SIMULATION

Four cases have been simulated numerically. The following table is presenting the operating conditions corresponding to these cases.

	Case 1	Case 2	Case 3	Case 4
V_{cold}	0.026	0.026	0.026	0.052
T_{cold}	20	20	15	15
V_{hot}	0.026	0.026	0.026	0.052
T_{hot}	40	30	55	55

Table 1 : Test matrix (velocity in m/s and temperature in degree C)

Initially the simulation starts with a field set at a uniformally cold temperature, then at time $t = 0$, a hot flow is injected through the upper vertical pipe. Due to gravity effect a co-courant stratification forms downstream. It is interesting to underline the fact that ESTET is able to predict (like in the experiment) that not counter-flow forms in this particular geometry, although the Froude number is small enough to allow the creation of such a counter-flow in different geometrics as has been demonstrated in [5]. After some time, a converged state is reached. Figure 4 presents respectively the velocity field and the temperature field and the temperature fluctuation variance on the middle plane for case 4. The hot jet is influencing the incoming cold flow, however for the present case it can be seen that the mixing between the two layers stays quite small. This is partly due to the fact that at the interface the stably stratified flow tend to inhibit the turbulent diffusion between the two layers. At the junction, there is simultaneously high temperature gradients and turbulence. Therefore production of temperature fluctuations exists. Then due to the stable stratification effect, a decrease in the level of temperature variance is predicted. The same type of figures could be presented for all cases.

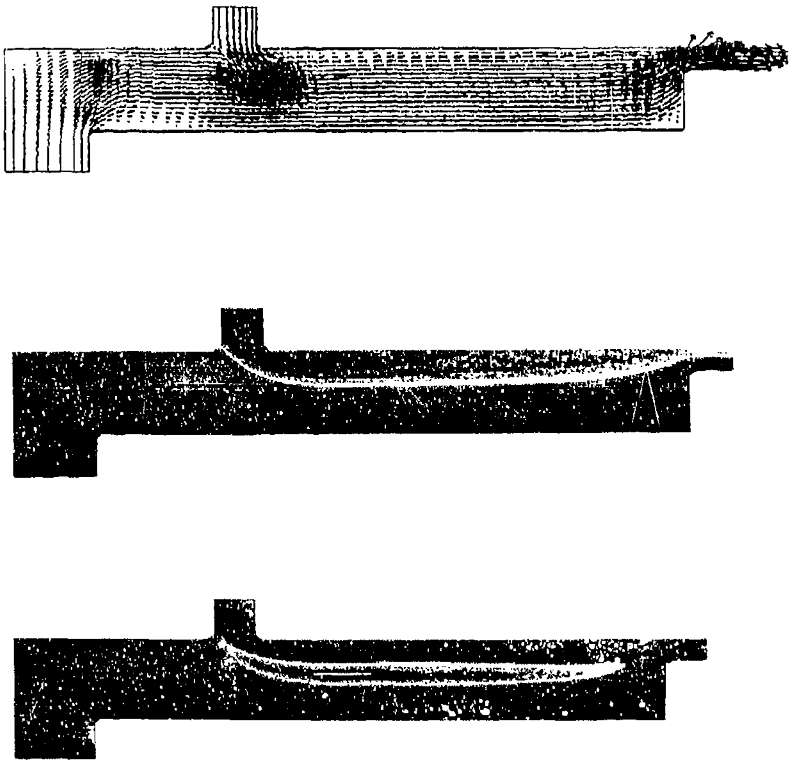

Figure 4 : Velocity and temperature, and rms temperature fluctuations fields on the middle plane

As stated in the introduction, the simulation presented here includes the calculation of the thermal field within the solid wall. At the beginning, wall thermal inertia is leading to observe temperature differences between the two sides of the solid wall. However after some time the following isothermals are obtained within the wall.

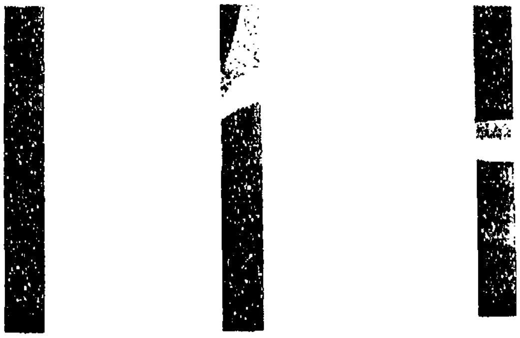

Figure 5 : Solid temperature in section 100mm,10s, 20s and 100s after injection

The same phenomena is illustrated by figure 6, where it is clear that conduction through the wall takes place and leads to heat the cold fluid layer in contact with the solid wall.

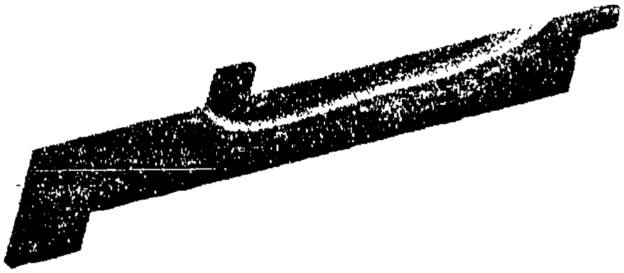

Figure 6 : Solid temperature

Some more quantitative comparisons have been done between experimental data and numerical results. Pictures 7 to 10 present non dimensional comparisons of temperature profiles and temperature fluctuations profiles at sections 20mm, 60mm, 100mm and 160mm.

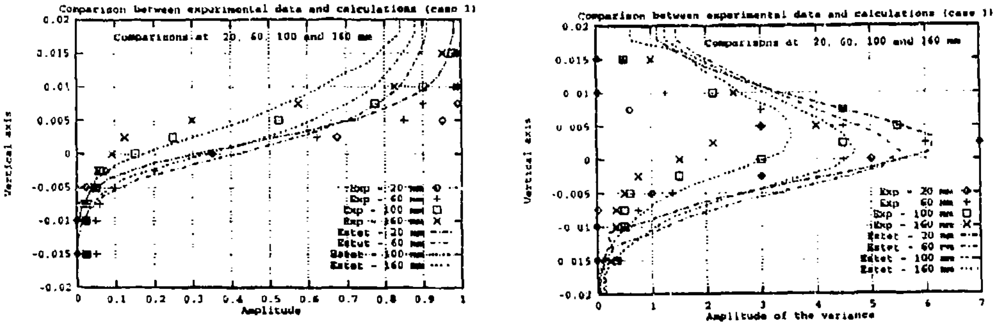

Figure 7 : Temperature and rms fluctuations profiles for case 1

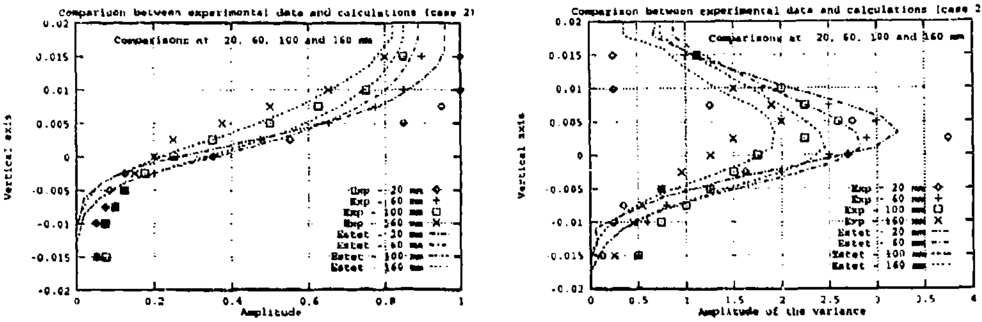

Figure 8 : Temperature and rms fluctuations profiles for case 2

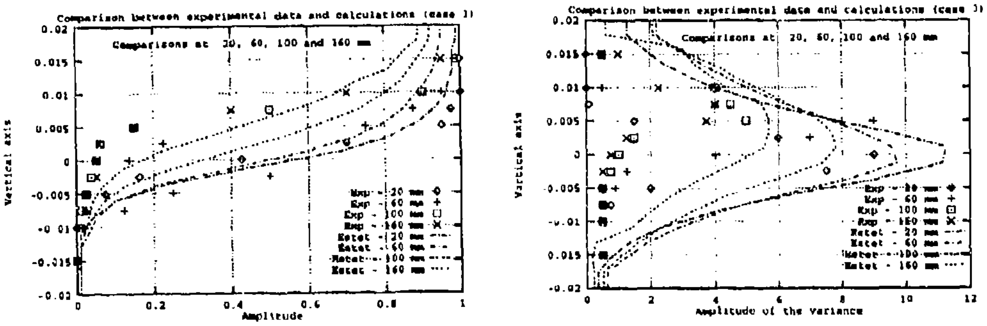

Figure 9 : Temperature and rms fluctuations profiles for case 3

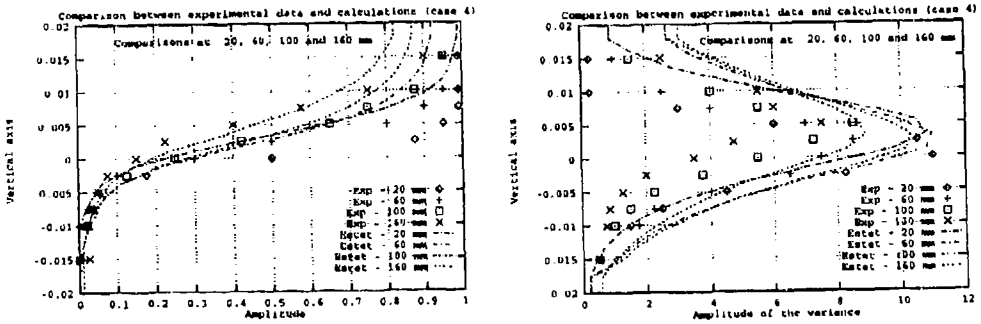

Figure 10 : Temperature and rms fluctuations profiles for case 4

Regarding the temperature fluctuation attenuation, the calculation is reproducing a decrease in the level of the temperature variance when approching the wall. Indeed, in the simple model used in this study (see equation 12), the production term is getting smaller due to reduction of turbulent viscosity when approaching the wall. Moreover the dissipation term is proportionnal to the ratio of ϵ and k which increases quite a lot in the vicinity of the wall. The combination of the two trends leads to predict a strong reduction of the temperature variance when approaching the wall.

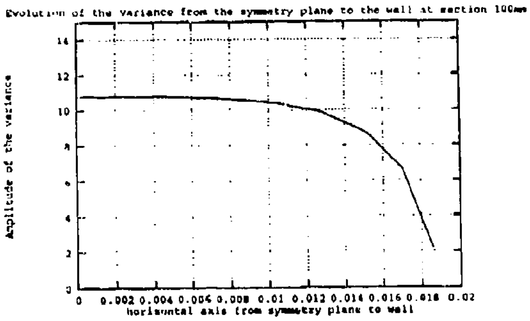

Figure 11 : Attenuation of the temperature fluctuations when approaching the wall

Figure (11) presents a temperature variance profile (case 4), for a given section (here 100mm), to show the attenuation near when approaching the wall. Interpretation should however be carefully done, indeed the attenuation being frequency dependent, it seems most unlikely that a simple $k-\varepsilon$ based model can reproduce faithfully the phenomena happening in that region.

A large eddy simulation, which whould take into account the different eddy size and the attenuation through the conductive layer would seem much more adequate. Moreover, it would lead to the prediction of a time dependant evolution of the temperature (which is really what mechanical engineer are looking for), taking into account the instantaneous inertia of the wall. Such a simulation is planed in the future.

6 CONCLUSION

A numerical simulation has been performed with ESTET on the geometry of experimental mock-up FLUO studied at CEA. Comparisons between experiments and calculations agree reasonnably well on the mean temperature, but an accurate simulation of near wall temperature fluctuations will require more work to be done.

REFERENCES

[1] L. BRUNEL
"T142. Bilan et synthèse des essais ADAGIO"
Note DER/SCC/LECC/90006

[2] G. CABARET, P. LALLINEC, J. LAURENT
"Etude des fluctuations thermiques le long de la ligne d expansion "
Maquette DUPLEX. Note DMT/91/498

[3] M. PICUT, D. TENCHINE
"Etude des fluctuations de température dans la
maquette RISTOURNE (T142)"
Note STR/LES/91-05

[4] PENIGUEL C., STEPHAN J.M.
"Thermalhydraulic study of a stratified flow in a piping elbow"
NURETH-5. Sept 1992 Salt lake city

[5] PENIGUEL C., HECKER M
"Thermalhydraulic study of a stratified flow in a piping elbow
(Model SUPER NIMBUS) NURETH-6. Sept 1993 Grenoble

[6] PENIGUEL C., RUPP I.
"A numerical method for thermally coupled fluid and solid problems "
8th Int Conf on Numerical Methods in Thermal Problems
Swansea 1993

[7] TENCHINE D., BARROIL J
"Fluctuations de température en écoulement stratifié
Atténuation des fluctuations de température "
Notes STR/LES/92-105 and STR/LES-93-113

[8] LAUNDER B.E., SPALDING D.B
"The numerical computation of turbulent flows"
Comput. Meth Applied Mech. Engineering 3 (1974)

[9] VIOLLET P.L
"The modelling of turbulent recirculating flows
for the purpose of reactor thermal-hydraulic analysis".
Nuclear Engineering Des. 99 365-377 (1987)

[10] RODI W.
"Turbulence Models and their Application in Hydraulics".
IAHR, Delft, The Netherlands (1980)

[11] MATTEI J.D., SIMONIN O
"Logiciel ESTET- Manuel théorique de la version 3.1".
Rapport EDF-93

Fourth International Symposium
on
STRATIFIED FLOWS

Mathematical modeling of wind-induced turbulent flows in a stratified water body.

O.F.Vasiliev, V.I.Kvon, D.V.Kvon
Institute for Water and Environmental Problems (IWEP)
Siberian Division of the Russian Academy of Sciences,
630090, Novosibirsk, Morskoy Prosp. 2, Russia.

Synopsis

The paper deals with a vertical 2-D model of wind-driven flow in a water body. The hydrodynamic equations are written in the conservative form in the Boussinesq approximation on the assumption of vertical hydrostatic pressure distribution. The transport equations include advective terms. The two-equation turbulence closure model based on the equations for turbulent energy and its dissipation is used. Some results of the numerical simulations of the wind-induced currents and their effect on mixing have been presented.

1. Introduction

Mixing in stratified water bodies can be conditioned by a variety of natural factors including wind action and horizontal shear flow induced by that, waves (surface and internal ones), unstability etc. An intensity of a turbulent mixing is varied considerably in stratified water bodies, such as lakes and reservoirs. Therefore to describe the mixing processes in stratified flows with the use of numerical modeling it is essential to apply such turbulence models which allowa wide range of phenomena and conditions. On this account the two-equation turbulence closure model founded on the two equations for the turbulent energy and its dissipation is used.

A vertical two-dimensional (2-D) model of laterally averaged stratified flow in an oblong water body was proposed in the paper[1]. The model was subsequently applied to the simulation of unsteady stratified flows in a channel [2] and in an estuary [3,4].

2. Formulation of a vertical plane problem

The plane turbulent stratified flow in a water body is considered with use of 2-D vertical model [1]. The equations of momentum, continuity and heat (mass) transport are as follows:

$$\frac{\partial u_1}{\partial t} + \frac{\partial u_1 u_1}{\partial x_1} + \frac{\partial u_2 u_1}{\partial x_2} = - g \frac{\partial}{\partial x_1} \left[z + \frac{1}{\rho_0} \int_{x_2}^{z} \rho dx \right] +$$

$$+ \frac{\partial}{\partial x_1} \left[K_H \frac{\partial u_1}{\partial x_1} \right] + \frac{\partial}{\partial x_2} \left[K_V \frac{\partial u_1}{\partial x_2} \right] \qquad \ldots\ldots\ldots\ldots\ldots \quad (1)$$

$$\frac{\partial u_1}{\partial x_1} + \frac{\partial u_2}{\partial x_2} = 0, \qquad \ldots\ldots\ldots\ldots\ldots\ldots\ldots\ldots\ldots\ldots\ldots (2)$$

$$\frac{\partial T}{\partial t} + \frac{\partial u_1 T}{\partial x_1} + \frac{\partial u_2 T}{\partial x_2} = \frac{\partial}{\partial x_1} K_{TH} \frac{\partial T}{\partial x_1} + \frac{\partial}{\partial x_2} \left[K_{TV} \frac{\partial T}{\partial x_2} \right], \ \ldots \quad (3)$$

the equation of state

$$\rho = \rho_0 [1-6.8 \times 10^{-6} (T-4)^2] \ \ldots\ldots\ldots\ldots\ldots\ldots\ldots\ldots\ldots (4)$$

Here t is the time, (x_1, x_2) are axis of coordinate, (u_1, u_2) - are velocity components, T is the temperature of water, ρ и ρ_0 are the density of water and its reference value, respectively; z is the deviation of a water surface from its undisturbed position, g is the acceleration of gravity, K_H and K_V are the coefficients of exchange in the horizontal and vertical directions.

The coefficients of the vertical turbulent exchange coefficients are defined by means of the equations of turbulence energy and its dissipation rate

$$\frac{\partial e}{\partial t} + \frac{\partial u_1 e}{\partial x_1} + \frac{\partial u_2 e}{\partial x_2} = \frac{\partial}{\partial x_1} K_{He} \frac{\partial e}{\partial x_1} + \frac{\partial}{\partial x_2} K_{ve} \frac{\partial e}{\partial x_2} +$$

$$+ P + G - \varepsilon \ \ldots\ldots\ldots\ldots\ldots\ldots\ldots \quad (5)$$

$$\frac{\partial \varepsilon}{\partial t} + \frac{\partial u_1 \varepsilon}{\partial x_1} + \frac{\partial u_2 \varepsilon}{\partial x_2} = \frac{\partial}{\partial x_1} K_{H\varepsilon} \frac{\partial \varepsilon}{\partial x_1} + \frac{\partial}{\partial x_2} K_{V\varepsilon} \frac{\partial \varepsilon}{\partial x_2} +$$

$$+ \frac{\varepsilon}{e} (c_1 (P + G) + c_2 \varepsilon) \ \ldots\ldots\ldots \quad (6)$$

where e is the turbulent energy, ε is its dissipation rate,

$$P = K \left[\frac{\partial u_1}{\partial x_2} \right]^2,$$

$$G = -1.36\times10^{-5} g K_{VT}(T-4)\frac{\partial T}{\partial x_2},$$

$$K = \alpha\frac{e^2}{\varepsilon}, \quad K_v = \nu + K, \quad K_{vT} = \lambda + \alpha_T K_T,$$

$$K_{ve} = \nu + \alpha_e K, \quad K_{v\varepsilon} = \nu + \alpha_\varepsilon K,$$

$$\alpha = 0.09, \quad \alpha_e = 1, \quad \alpha_\varepsilon = 0.77, \quad c_1 = 1.44,$$

$$c_2 = 2.0\,[1.0 - 0.3\exp(-Re_\tau^2)], \quad \alpha_T = 0.8,$$

$$Re_\tau = e^2/(\nu\varepsilon).$$

Here K is an eddy viscosity, ν is the molecular viscosity.

For the system (1)-(6) the following boundary conditions are imposed. On the water surface at $x_2 = z(x_1,t)$:

$$\frac{\partial z}{\partial t} + u_1\frac{\partial z}{\partial x_1} = u_2, \qquad K_v\frac{\partial u_1}{\partial x_2} = \frac{\tau_w}{\rho_0} \quad \ldots\ldots\ldots\ldots\ldots\ldots \quad (7)$$

$$\frac{\partial T}{\partial x_2} = 0 \quad \ldots\ldots\ldots\ldots\ldots\ldots\ldots\ldots\ldots\ldots\ldots\ldots \quad (8)$$

$$K_{ve}\frac{\partial e}{\partial x_2} = k_e\left|\frac{\tau_w}{\rho_0}\right|^{3/2}, \qquad \varepsilon = c_\varepsilon\frac{e^{3/2}}{y^0} \quad \ldots\ldots\ldots\ldots\ldots \quad (9)$$

On the horizontal bottom at $z = z_0$:

$$u_2 = 0, \qquad K_v\frac{\partial u_1}{\partial x_2} = k_b|u_1|u_1 \quad \ldots\ldots\ldots\ldots\ldots\ldots\ldots \quad (10)$$

$$\frac{\partial T}{\partial x_2} = 0 \quad \ldots\ldots\ldots\ldots\ldots\ldots\ldots\ldots\ldots\ldots\ldots\ldots\ldots \quad (11)$$

$$\frac{\partial e}{\partial x_2} = 0, \qquad \varepsilon = c_\varepsilon\frac{e^{3/2}}{y_0} \quad \ldots\ldots\ldots\ldots\ldots\ldots\ldots\ldots \quad (12)$$

Here τ_w is a wind friction stress; y^0 and y_0 - the roughnesses of water surface and bottom, respectively.

Considering below the cases when a channel is bounded with vertical walls the boundary conditions are taken as the following:

$$u_1 = 0, \qquad \frac{\partial T}{\partial x_1} = 0, \quad \ldots\ldots\ldots\ldots\ldots\ldots\ldots\ldots\ldots\ldots \quad (13)$$

The above problem is solved numerically using a semi-implicit finite-difference scheme, which is formulated for the spatially staggered Arakawa C-grid [5]. The calculation algorithm is developed with the use of the fractional step method, in combination with the double sweep method.

3. Numerical simulations

The model was used to simulate a some turbulent shear flows which are similar to those induced by wind in a water body. It is assumed that $K_H = K_{HT} = 0$. Some of the calculations were performed for comparing with the laboratory experimental data.

The first comparison was done with the experimental results by W.D.Baines and D.J.Knapp [6] for wind-driven currents in a laboratory flume. The results of simulations and measurement data are presented in Fig.1 for the currents at the middle part of the flume. The computation was made with the following data: $Re_w = u_* h/\nu = 1900$ and 2870, a water depth in the flume $h = 0.3$m, the length $l=3.0$m. Here $u_*=(\tau_w/\rho_0)^{1/2}$ is a dynamic velocity. The computed [illegible]ty profiles given in the Fig.1 are practically the same f[illegible] experiments.

The second comparison was car[illegible] out for the shear stratified flow in the annular flume under a rotating lid at the conditions of the H.Kato and O.M.Phillips experiments [7]. It is worth to remind that the experiments were conducted with a constant shear stress at the lid upon the the surface of water in the flume. At the initial moment of rest the salt water layer has a linear density distribution over the depth.

To simulate the case the computation was carried out with a value of the density gradient $\partial\rho/\partial x_2 = 1.92\times10^{-3}$ g/cm^3/cm, the lid stress $\tau_w=0.995$ gynes/cm^2, the depth $h=0.3$m. For numerical simulation it is assumed that a concentration of salt in water is proportional to the salt water density and that the coefficient of the turbulent diffusivity of salt in water is equal to the turbulent thermal diffusivity. The computational results are given in Fig. 2.

The qualitative comparison of the computational results with the experimental data shows that the theory describes satisfactory the process of motion generation observed in the experiment. Initially the turbulent shear flow is generated in the upper layer of linearly-stratified fluid. Then it penetrates into the underlying quiescent fluid. Similar to the experimental data, the computation ones reveals a significant variation of the density at the lower part of mixing layer and the fluid re[illegible]ed under it. The evolution of mixing layer depth computed is quantitatively in a rather good agreement with the experiment.

Next the computations were performed to simulate the wind-induced currents in a plane oblong water body of rectangular form. At first the computations were carried out for the homogeneous fluid (ρ = const). The currents in a deep water body length of 1000 m and depth of 100m are compared with that in a similar water body of a smaller size (20m and 2m, respectively). In both cases the wind velocity is the same: 10 m/s. The wind shear stress is determined according the relationship:

$$\tau_w/\rho_0 = 3.25\times10^{-6}\ w^2$$ (w is the wind velocity in m/s).

Fig. 3 presents the computed velocity field (a,c) and the eddy viscosity distribution (b,d) for the terminal, steady-state situation. At the depth of 100m the turbulent mixed layer penetrates only into the upper part of the water volume. In the case when the depth equals 2m the turbulent mixing occupies all volume.

Then an unsteady flow in a deep stratified water body was considered. The fluid is assumed to be initially at rest with linear stratification (the surface temperature of 20^oC and the bottom one of 10^oC). The water currents are induced by the same wind speed of 10 m/s.

The results of computation are presented in Fig. 4 with the use of the following non-dimensional parameters:
$K^o=[100/(u_*h)]K_v$ - the normalized dimensionless eddy viscosity and $t^o= (u_*/h)t$ ($u_*^2= \tau_w/\rho_0$) - the dimensionless time. It is seen that the recirculation area coincides with the turbulent mixing area. Both are located in upper part of water volume.

REFERENCES

1. Vasiliev, O.F., Kvon, V.I., Chernyshova, R.T. (1973). Mathematical modelling of the thermal pollution of a water body. Proc. of the 15 Congress of IAHR, vol.2, Istanbul.

2. Vasiliev O.F., Chernishova R.T. (1975). Numerical simulation of the lock exchange flow in a channel // Proc. of the 16 Congress of IAHR, vol.3. San Paulo,

3. Vasiliev, O.F., Dumnov, S.V. (1983). A two-dimensional Mathematical Model for salt Water Intrusion // Proc. of the XX Congress of IAHR. Moscow, vol.2, p.p. 10-19.

4. Vasiliev O.F., Dumnov S.V. (1987). Numerical modelling of flow in a river estuary // Hydraulic modelling, Proc.of the XXII Congress of IAHR. Lausann.

5. Backhaus, J.O. (1983). A semi-implicit scheme for the shallow water equations for application to shelf sea modelling. Continental Shelf Research, vol.2, no.4.pp.243-254

6. Baines, W.D., and Knapp, D.J. (1965). Wind driven water currents. J. Hydr. Div., ASCE, 91(2), pp.205-221.

7. Kato, H., and Phillips, O., M. (1969). On the penetration of a turbulent layer into stratified fluid. J. Fluid Mech., vol. 37, part 4, pp.643-655.

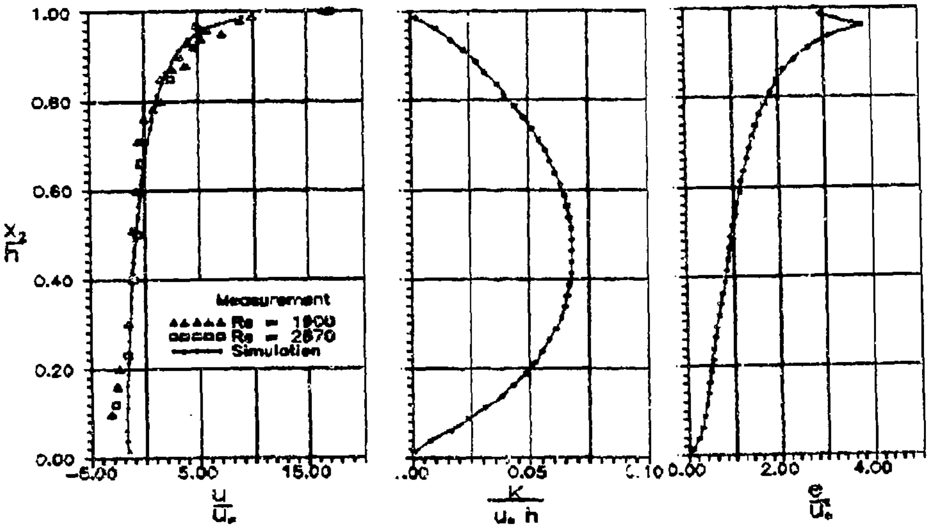

Fig.1. Distributions of velocity, eddy viscosity, turbulent energy computed under conditions of experiments by W.D. Baines & D.J.Knapp [6].

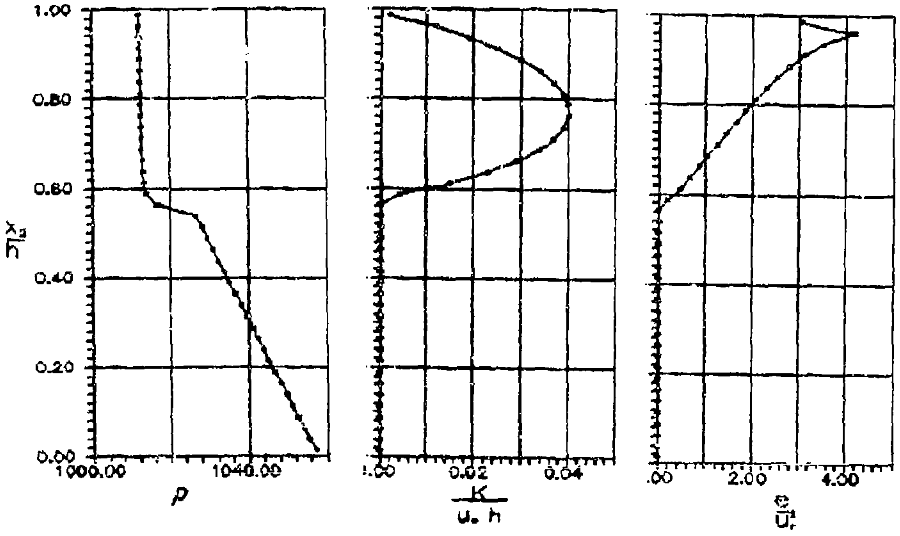

Fig.2. Distributions of water density, eddy viscosity, turbulent energy computed under conditions of experiments by H.Kato & O.M.Phillips [7].

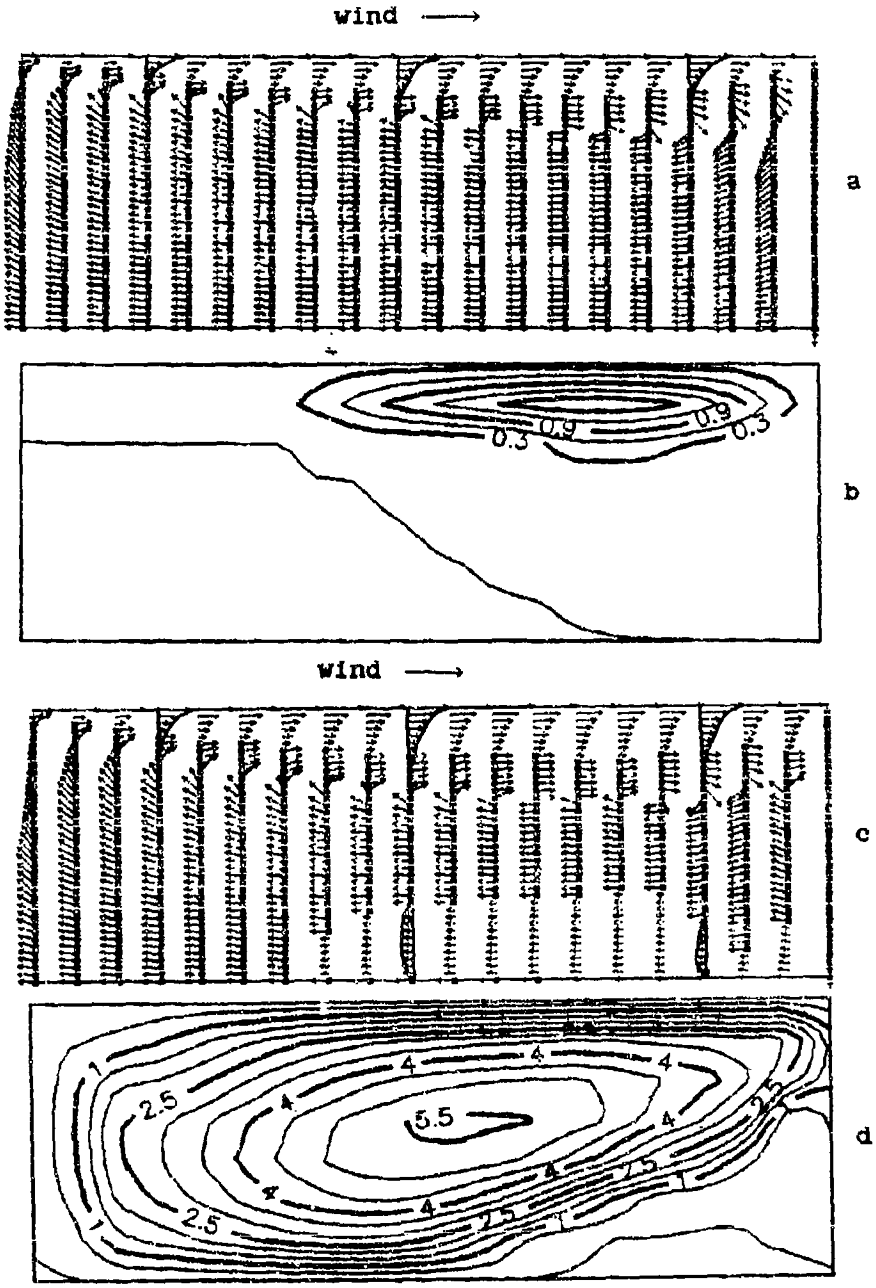

Fig.3. Velocity field and eddy viscosity distribution in the cross-sections of water body: depth 100 m (a,b) and depth 2 m (c d). Vectors ■⟶ with a square are negligibly small and specified only its directions.

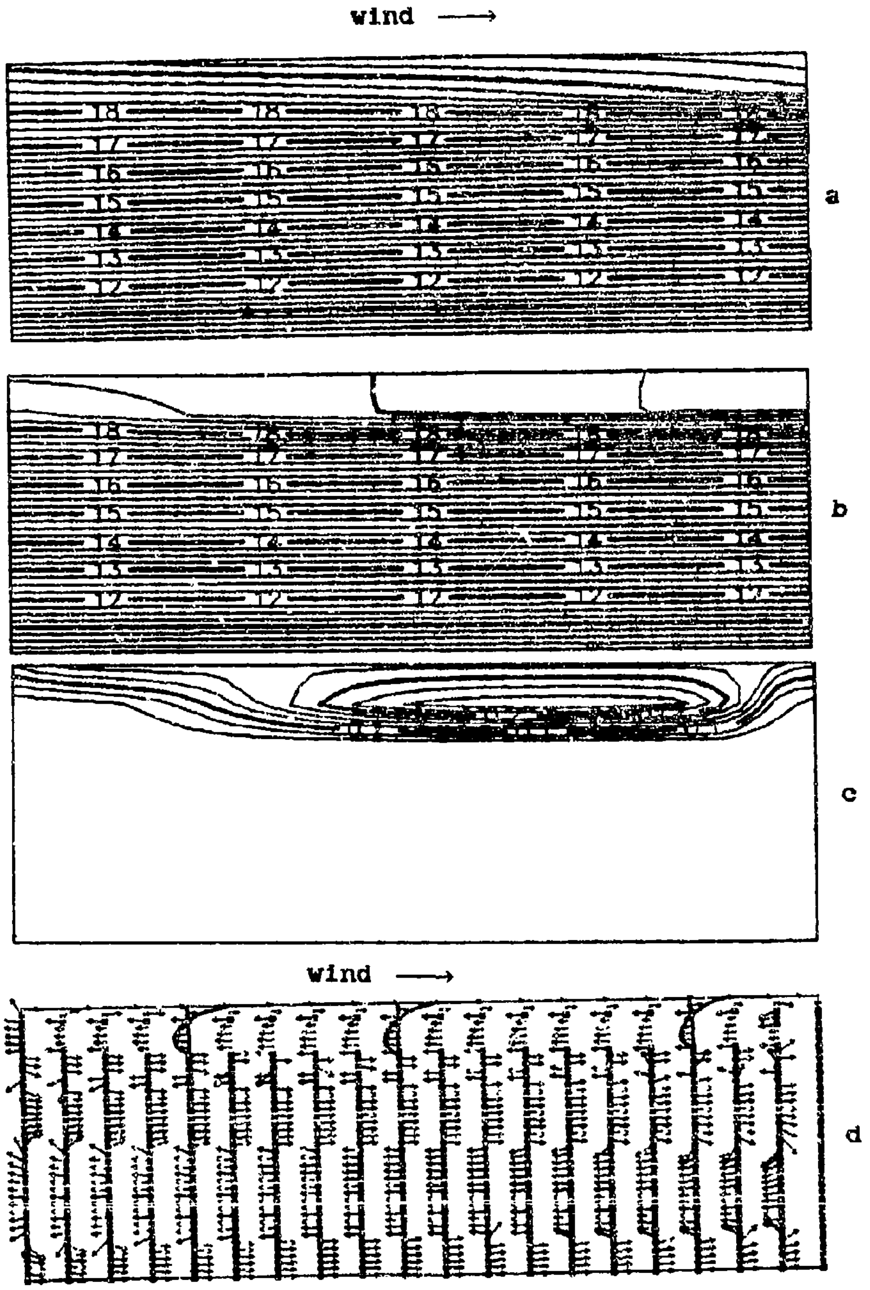

Fig.4. Isotherms (a, $t^{\circ}=1$; b, $t^{\circ}=5$), distributions of eddy viscosity (c, $t^{\circ}=5$) and velocity field (d, $t^{\circ}=5$).

Layer Formation in Stratified Circular Couette Flow

B. M. Boubnov*, E. B. Gledzer* and E. J. Hopfinger†

Abstract

The stability of circular Couette flow with axial density stratification, characterized by the buoyancy frequency N, is considered for different values of the non-dimensional width gap ϵ between the cylinders. It is shown that onset of instability and the structure of the resulting flow regimes, namely non-axisymmetric vortices, Taylor vortices and the related layer formation strongly depend on N in addition to Reynolds number and ϵ.

1 Introduction

One of the classical hydrodynamic stability problems of major importance is the flow of fluid confined to the annulus between concentric, rotating cylinders. Since the pioneering works by Couette (1890) and Taylor (1923) a very large number of experimental and theoretical studies have considered different aspects of instability and transitions of this flow configuration (see for instance Di Prima & Swinney, 1981; Andereck et al., 1986; Chossat & Iooss, 1994). Various modifications of this problem have also received considerable attention and these include the influence of axial flow (Gravas & Martin, 1978; Lueptov et al., 1992), unsteadyness of the rotation rate (Cooper et al., 1985) and the effect of radial temperature or density variations with and without an axial gravitational field (Snyder & Karlson, 1964; Yao & Rogers, 1989; Kubotani et al., 1989; Ali & Weidman, 1990).

In the simplest case of Couette-Taylor flow, with only the inner cylinder rotating, a variety of different regimes are observed: Taylor vortices, wavy vortices, modulated wavy vortices, turbulent Taylor vortices. When additional effects are included (Coriolis force, velocity shear, radial density stratification etc.) significant changes in stability occur and the flow states reveal a reach variety of phenomena (e.g. Andereck et al., 1985, found more than fifteen principal flow regimes between independently rotating cylinders in homogeneous fluid). Surprisingly, the case of the interaction of centrifugal and buoyancy forces - Couette flow with axial density stratification has not received any attention.

The aim of this work is to study experimentally and with the help of linear stability theory, the instabilities and transition regimes in Couette flow with axial, linear density statification for the case when only the inner cylinder rotates. It is shown that density stratification has a strong effect on the onset of instability and the resulting vortex structures giving rise to layer formation. It is noteworthy to

---

*Institute of Atmospheric Physics, 109017, Moscow, Russia
†LEGI/IMG, CNRS-UJF-INPG, B.P. 53 X, 38041 Grenoble Cedex, France

mention that descrete layers are formed and the results are thought to be relevant for equatorial zonal jet formation.

The instability and flow states of the small gap problem have been treated in some detail in Boubnov et al., (1994). Here, we will put more attention on the influence of the gap between the cylinders on the flow instability and layer formation.

The main non-dimensional parameters of the problem are the usual Reynolds number $Re = \Omega a(b-a)/\nu$ (see e.g. Andereck et al.,1985), the non-dimensional gap width $\epsilon = \frac{b-a}{a}$ (a and b are the radii of inner and outer cylinders respectively, Ω - rotation rate of the inner cylinder, and the viscosity ν is taken constant because of its weak dependence on density). The stratification is expressed by the Brünt-Väisälä frequency $N = \left(-\frac{g}{\rho}\frac{\partial \rho}{\partial z}\right)^{1/2}$, ($\rho$ is the density and g the gravitational acceleration), and this introduces an additional non-dimensional parameter which is the Froude number $Fr = \Omega/N$.

2 Experimental apparatus and procedure

The experimental installation for circular Couette flow in stratified fluid is similar to those which are used for studying Couette-Taylor flow in homogeneous fluid. It consists of long coaxial transparent plexiglass cylinders with the outer cylinder, the bottom and upper surface being at rest and the inner cylinder rotating with constant angular velocity Ω. The outer cylinder has an inner radius of $b = 51mm$, while three different inner cylinders with outer radii a=20, 30 and 40 mm were used, giving respectively non-dimensional gap widths ϵ=1.55, 0.7 and 0.275. The last case of $\epsilon = 0.275$ permits to interpret the results within the small gap approximation theory and is still suitable for the study of the vortex and layer structures. The length of the cylinders L was taken large enough: $L = 573mm$, giving $\Gamma = L/(b-a) = 52, 27$ and 18 for $\epsilon = 0.275, 0.7$ and 1.55 respectively. In most experiments the upper surface of the cylinder was rigid, and only in experiments with large density gradient, when $N > 1.5 rad/s$, the upper boundary was free, because, in order to reach a large value of N it was necessary to fill the space between cylinders to a height less than L. In our experiments, stable density stratification protects against propagation of disturbances from the top and bottom surfaces to the fluid interior and there is practically no influence of end boundary conditions on the flow regimes (which is not the case in non-stratified fluid, where end boundary conditions can be very important in the onset of instability).

The inner cylinder rotation for a given Ω was maintained constant within 1% and the value of Ω could be changed continiously from 0.1 to $3.7 rad/s$. Constant cylinder rotation was reached in less than $2s$ and when $\Omega < \Omega_{cr}$ a stable, steady state flow was established in a time of about 1 minute. The time for onset of instability of the zonal axisymmetric flow depends how close the rotation rate is to critical conditions.

Generally, experiments were made by starting with the fluid rest and by setting the rotation of the inner cylinder at the desired value. Changing the rotation rate of this cylinder from one value to another was used only near onset of instability of the azimutal flow and also in special experiments devoted to studying the variations of the formed layer structures and transitions between different regimes.

The linear stratification was accomplished by using a salt solution and the standard "double-box" filling method. The time of filling was of the order of two hours. Normally, density measurements were made at four heights, but in some controlled experiments these measurements were closer spaced. The linearity of the density profile was also verified with the help of shadowgraph, in which the outer surface of the inner cylinder appears as a line inclined at some angle to the vertical, proportional to the density gradient. The deviations of the density profiles from linearity in the main part of the fluid column ($0.1 < z/L < 0.9$, where z is the vertical coordinate) were less than 5%. The value of N was changes in the limits $0.35 < N < 1.78 rad/s$. After an experiment with one rotation rate Ω was finished and the formed layer structure was allowed to diffuse, the linearity of the main stratification was checked and a new experiment could be started.

In order to reduce optical distortions due to the curvature of the cylinder the apparatus was placed in a large square box filled with water (also, there is water in the inner cylinder). For the flow visualizations two different and complementary techniques were used: the shadograph technique, sensitive to the second derivative of density which allows us to see the horizontally everaged density structures, and particle streak line methods to visualize the vortex motion. Aluminium powder and kalliroscope particles were used in this case. The aluminium particle are almost isotropic and move together with the fluid and show the motions in the vortices, while plane kalliroskope flaques outline the total structure of the flow.

3 Narrow gap (ϵ=0.275)

3.1 Experimental results

First we will summarize the observations of flow patterns in the narrow gap experiments ϵ=0.275 (Boubnov et al.,1994). The regime diagram in Ω - N space is shown in Fig.1.

To produce this diagram we used the following procedure. For each value of N, the rotation rate Ω was increased by small increments until the critical value of $\Omega_c(N)$ for onset of instability was reached. For $\Omega < \Omega_c(N)$ the flow has only an azimuthal component of velocity (circular Couette flow) with no changes in the density field along the vertical axis (regime A, Fig.1). This steady flow is established in about 1 minute or 5 rotation periods after beginning of rotation of the inner sylinder. For $\Omega \geq \Omega_c(N)$ on the other hand, the shadowgraph images indicate vertical variations in density with the appearance of well identifiable layers of nearly equal height (Fig.2). By this means it was thus possible to determine Ω_c as a function of N. In the neutral case of $N = 0$ the critical value of Ω has been determined from the onset of motion of particles suspended in the fluid. For the present experimental conditions $\Omega_c(0) \approx 0.2$, giving a Reynolds number $Re_c(0) = \Omega_c a(b-a)/\nu \approx 90$, in agreement with the expected value (Di Prima & Swinney,1981). For $N = 0$ the instability of Couette flow is linked with axisymmetric Taylor vortices of vertical size equal to the width of the gap.

For stratified Couette flow when N is large enough ($N > 0.4$) and Ω just above $\Omega_c(N)$, the first unstable structures are of height approximately equal to one half of the gap width ($n_l = \frac{h}{b-a} \approx \frac{1}{2}$, region S in Fig.1, n_l is the non-dimensional layer height or layer height factor). The bound of transition between regimes A and S, i.e. the neutral stability curve is the curve a in Fig.1.

With increasing Ω, the usual Taylor vorticies are also appearing. Steady Taylor vortices with vertical wave length factor $n = \frac{\pi}{k(b-a)} = 1$ (k is the vertical wave number) giving $n_l = 1$ are observed for values of Ω and N lieing in the region T, Fig.1. Between regions S and T there exists a transition region ST in which both regimes with $n_l \approx 1/2$ and $n_l = 1$ are observed. When we move to larger Ω (for the

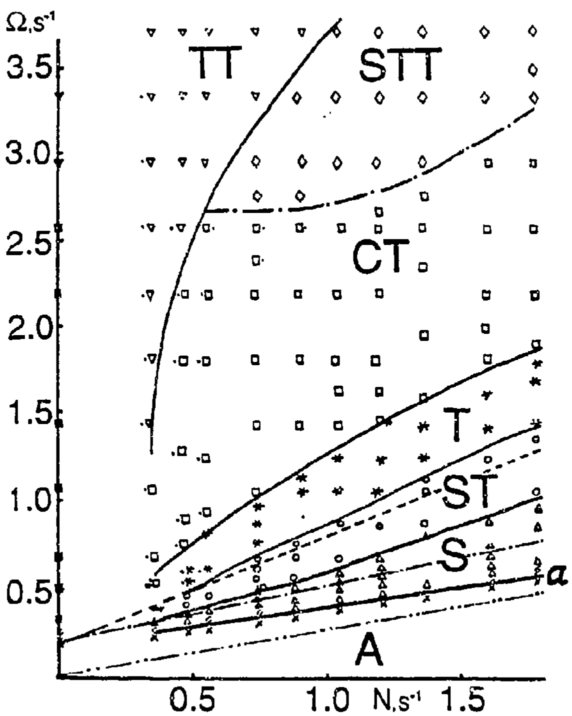

Figure 1: Main instability regimes for stratified circular Couette flow: Experiments with $\epsilon = 0.275$. Theory: — · · — · · —, inviscid instability bound for $n = 1/2$; — · — · — and — — —, viscous instability bounds for $n = 1/2$ and $n = 1/1$ respectively. The solid lines are included to show more clearly the experimentally observed transitions between the regimes.

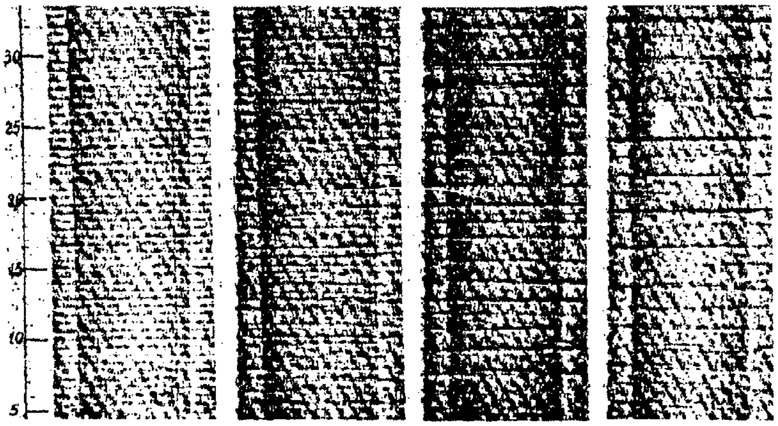

(a) $\Omega = 0.6\,\mathrm{s}^{-1}$ (b) $\Omega = 0.9\mathrm{s}^{-1}$ (c) $\Omega = 1.2\mathrm{s}^{-1}$ (d) $\Omega = 2.4\mathrm{s}^{-1}$

Figure 2: Shadowgraph visualizations of the change in layer height for different angular velocities Ω of the inner cylinder for $\varepsilon = 0.275, N = 1.2\mathrm{s}^{-1}$. (a), $h \approx (b-a)/2$; (c), $h \approx (b-a)$; (d), $h \approx 2(b-a)$; (b), transition from $h \approx (b-a)/2$ to $h \approx (b-a)$.

same N) the Taylor vortices become more and more unsteady and neighbouring vortices begin to interact with each other. As a result, instead of wave regimes observed in homogeneous fluid for large Ω (see Andereck et al., 1986), layers of $h \approx 2(b-a)$ arise with two compact Taylor vortices inside and a weak mode [illegible] superimposed. This is the region CT in Fig. 1 (regime $n \approx 2$). From Fig. 1 we can see that onset of instability and the boundaries between the main regimes are characterized by a Froude number Ω/N rather than by Reynolds number.

By further increasing Ω more complicated interactions go on between the vortices may be observed (region STT in Fig. 1). For small N and for the large Ω the regime of transition to strong turbulent mixing also exists (regime TT) where it is very difficult to identify more or less regular layers. It should also be remarked that for all regular regimes the formed layer structure is conserved during a long time after stopping the rotation of the cylinder: for example in regime T layers remained visible up to half an hour. The rotation period [illegible]. Shadowgraph images of the different layers corresponding to regimes S, ST, T and CT are shown in Fig. 2 for $N = 1.2s^{-1}$, $\epsilon = 0.273$.

Very surprising is that the onset of instability is connected with vortices and corresponding density layer structure of height approximately equal to half of the gap width, $h \approx \frac{b-a}{2}$ (Fig. 2a). Moreover, the vortices in this regime are not axisymmetric and have an elliptical form in the plane perpendicular to the axis of the cylinders. This means, that a vortex tube is close to the inner, rotating cylinder on opposite sides of it and close to the nonrotating outer cylinder at points 90° away. The neighbouring vortex tube is rotated by 90°. This pair of vertex tubes with the same wave length factor $n \approx 1/2$ produces the layer structure $n_l \approx 1/2$. The layer height h close to the instability bound depends not only on the gap width but also on stratification N and the angular velocity Ω. This experimental dependence can be represented as (for $\Omega/N < 0.5$)

$$n_l = \frac{h}{b-a} = C_1 \frac{\Omega}{N}, \quad C_1 \approx 1.38 \tag{1}$$

3.2 Theoretical results

The circular Couette flow is given by

$$u_\varphi^0 = Ar + \frac{B}{r},\ u_r^0 = 0,\ w^0 = 0,$$

where

$$A = -\Omega\frac{a^2}{b^2 - a^2} = -\Omega\frac{1}{\mu^2},\ B = -Ab^2 = \Omega a^2 \frac{\mu^2}{\mu^2 - 1},\ \mu = \frac{a}{b} \tag{2}$$

and (u_r, u_φ, w) are the velocity components in the cylindrical coordinates system (r, φ, z). The density stratification is $\rho_0(z) = \rho_0 - \alpha z$ with $\alpha = const$ and, hence, $N \approx const$.

When neglecting the diffusion term in the mass conservation equation (large Prandtl or Schmidt number), the linearized equations for axisymmetric $(\partial/\partial\varphi = 0)$ disturbances, periodic in the axial direction are (Boubnov et al., 1994)

$$(u_r, u_\varphi, w)(r, z, t) = (u_r, u_\varphi, w)(r)e^{i(\omega t + kz)} \tag{3}$$

$$\left[(\nu\hat{D} - i\omega)\hat{D} + i\frac{N^2}{\omega}(\hat{D} + k^2)\right](\nu\hat{D} - i\omega)u_\varphi = 4k^2 A\left(A + \frac{B}{r^2}\right)u_\varphi \tag{4}$$

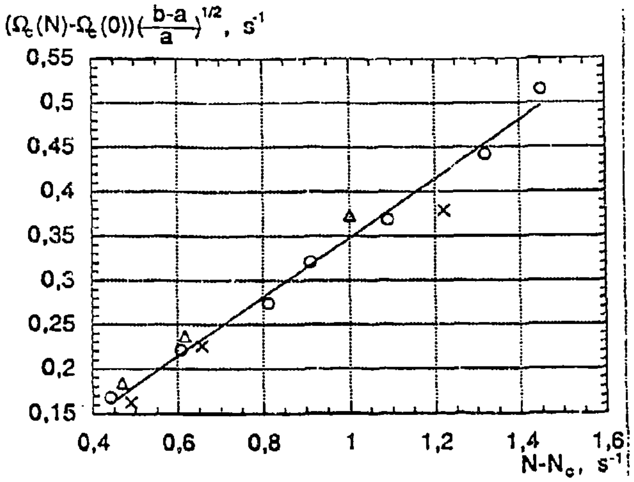

Figure 3: Critical curve for onset of instability for different gap widths ($\epsilon : \circ - 0.275; \times - 0.7; \Delta - 1.55$). N_c is the value of N above which the linear dependence of $\Omega_c(N)$ on N is a good first approximation. The solid line is traced only to show the near linearity of the experimental points.

with boundary conditions

$$u_\varphi|_{r=a,b} = 0,\ (\nu\hat{D} - i\omega)u_\varphi|_{r=a,b} = 0,\ \frac{\partial}{\partial r}(\nu\hat{D} - i\omega)u_\varphi|_{r=a,b} = 0 \qquad (5)$$

For inviscid ($\nu = 0$) and small gap ($\epsilon = \frac{b}{a} - 1 \rightarrow 0$), expressions (4),(5) reduce to

$$\frac{d^2}{d\xi^2}G = -\left(\frac{\pi}{n}\right)^2 \frac{\Omega^2}{N^2 - \omega^2}\frac{\xi}{4\epsilon^4}G,\ G = (kr)^{-1}u_\varphi,\ G|_{\xi=0,2\epsilon} = 0,\ \xi = \frac{b^2 - r^2}{a^2}, \qquad (6)$$

where the wave number is defined by $k = \pi\frac{1}{a\epsilon n}$ and n is the wave length factor. Hence, $\frac{1}{n}$ corresponds to the number of vortices on the height equal one gap width.

The solution of equation (6) is $G = \xi^{\frac{1}{2}} J_{1/3}(\eta_i \left(\frac{\xi}{2\epsilon}\right)^{3/2})$, where η_i are the roots of the Bessel function equation $J_{\frac{1}{3}}(\eta_i) = 0$ and $\eta_i = \frac{2\pi}{3n}\left(\frac{2\Omega^2}{\epsilon(N^2-\omega^2)}\right)^{\frac{1}{2}}$. This gives the following conditions for inviscid instability ($\mathrm{Im}(\omega) \neq 0$):

$$\frac{\Omega}{N} \geq \sqrt{\frac{\epsilon}{2}\frac{3\eta_i n}{2\pi}} \qquad (7)$$

For one vortex across the gap we have $\eta_1 \approx 2.9$. The bounds corresponding to the right hand side of (7) for $n = \frac{1}{2}$ is shown in Fig.1 by a dashed double-dotted line. So, above this line the axisymmetric inviscid disturbances with $n \leq \frac{1}{2}$ are unstable.

For the viscous case the results obtaind from (4),(5) for instability of monotonic type $\omega = i\Omega s, s \leq 0$ give the bounds shown on Fig.1 by a dotted (for $n = \frac{1}{1}$) and dashed-dotted (for $n = \frac{1}{2}$) lines. In the neutral case $N = 0$ the disturbances with $n = \frac{1}{1}$ are unstable if $\Omega > 0.18$ that corresponds to the usual estimates (for $\frac{a}{b} = 0.8, \Omega \approx 0.2$ (see Andereck et al.(1986))).

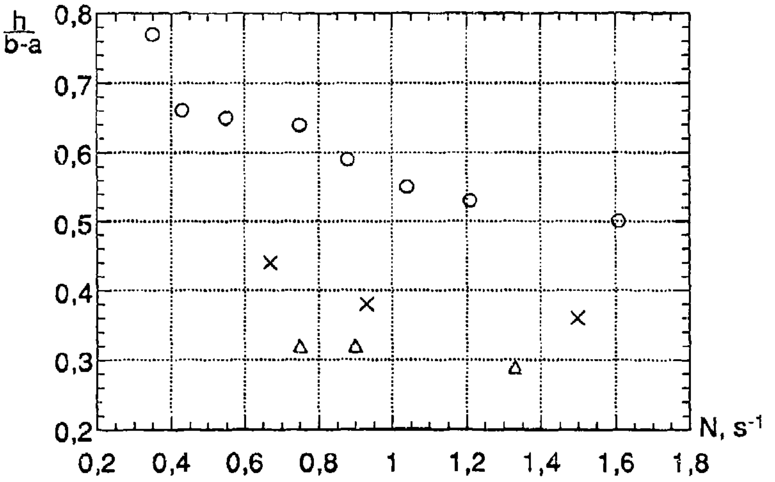

Figure 4: Non-dimensional minimum layer height as a function of N for ϵ = 0.275(○), 0.7(×), 1.55(△).

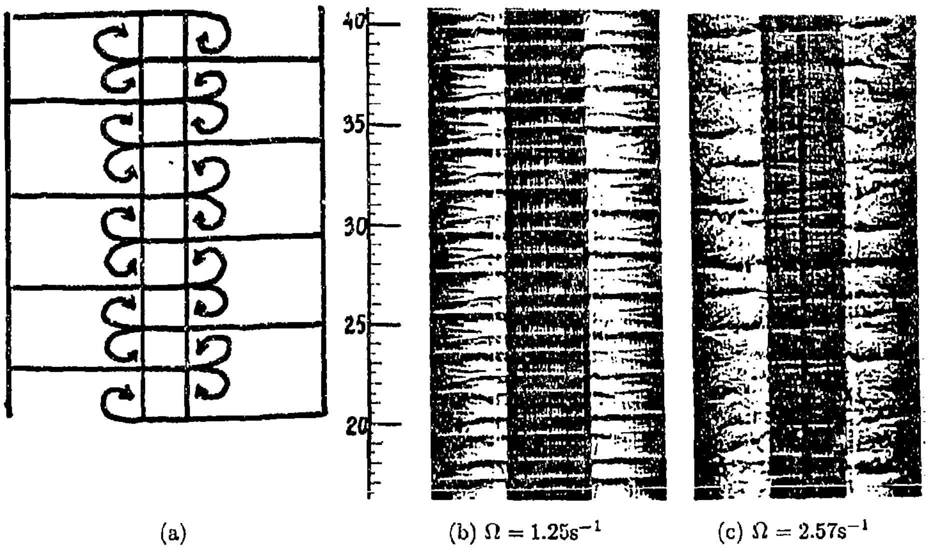

(a)

(b) $\Omega = 1.25s^{-1}$

(c) $\Omega = 2.57s^{-1}$

Figure 5: Sketch of vortex motions (a) and corresponding shadograph pictures (b) for the case of $\epsilon = 1.55$. Case (c) is a nearly turbulent state.

4 Wide gaps

In our experimental study we used also two large gaps $\epsilon = 0.7$ and 1.55 which do not satisfy the small gap approximation. Nevertheless, as in the small gap experiments, the critical value of Ω for onset of instability is also a nearly linear function of N. The experimental points collapse reasonably well onto one curve when plotted in a way shown in Fig.4 where N_c is the value of N above which the linear dependence of $\Omega_c(N)$ on N is a good first approximation.

The main reason for using wide gaps was to give some answer to the question whether or not the minimum layer height depends on the gap width. The minimum layer heights normalized by the gap width $b - a$ are presented in Fig.4. There is a definite dependence on the gap width with h_{min} being about $(b-a)/2$ for $\epsilon = 0.275$ and decreasing to about $(b-a)/3$ for $\epsilon = 1.55$. It is not clear at this stage whether h_{min} depends on ϵ or $(b - a)$ keeping for instance ϵ the same (dependence on Reynolds number).

The vortex structures and resulting layers in the wide gap $\epsilon = 1.55$ are asymmetric (Fig.5b) and have the appearance of a double helix as is shown in Fig.5a. A pair of vortices originates at the inner cylinder and propagate toward the outer boundary, mixing fluid in between them. On the opposite side a density interface forms in the central plane of the vortex pair. The vortex pairs on diametrally opposite sides are shifted vertically by one vortex size or layer height. How these join is not clear; a spiral local structure is one possibility. The whole pattern rotates with a constant velocity less than Ω. For the large angular velocities the flow regimes in the large gap case are similar to the Taylor vortices regimes ($n = 1$) in the small gap system. Taylor vortices of size equal to the gap width are present (or interacting Taylor vortices). The main difference here, compared with the small gap, is stronger turbulent motions and hence more intensive mixing in the layers.

References

[1] M. Couette, Ann. Chim. Phys. **21** (1890) 433.

[2] G. I. Taylor, Philos.Trans.R.Soc.London Ser.A **233** (1923) 289.

[3] R. C. Di Prima & H. L. Swinney, *Hydrodynamic Instability and the Transition to Turbulence* (ed. H. L.Swinney & J. P.Collub, Springer-Verlag,New York, 1981) **45** 139.

[4] C. D. Andereck, S. S. Liu & H. L. Swinney, J.Fluid Mech.**164** (1986) 155.

[5] H. A. Snyder & S. K. Karlsson, Phys.Fluids **7** (1964) 1696.

[6] N. Gravas & B. W. Martin, J.Fluid Mech. **86** (1978) 385.

[7] E. R. Cooper, D. F. Jankowski, G. P. Neitzel & T. H. Squire, J.Fluid Mech **161** (1985) 97.

[8] L. S. Yao & B. B. Rogers, J.Fluid Mech. **201** (1989) 279.

[9] H. Kubotani, S. M. Miyama, M. Sekiya & Y. Kojima, Progr.Theor.Phys. **82** (1989) 523.

[10] M. Ali & P. D.Weidman, J.Fluid Mech. **220** (1990) 53.

[11] R. M. Lueptov, A. Docter & K. Min, Phys.Fluids A **4** (1992) 2446.

[12] P. Chossat & G. Iooss, Appl. Math. Sc. **102**,Springer Verlag (1994)

[13] B.M. Boubnov, E.B. Gledzer & E.J. Hopfinger. Subm. to J.Fluid Mech.,1994.

Stratified Taylor-Couette flow: numerical simulation

P.ORLANDI

Università di Roma "La Sapienza" Dipartimento di Meccanica e Aeronautica, Italy

ABSTRACT

The combined effect of stratification and rotation is very important in several geophysical applications. For a better understanding of the vortical structures Boubnov *et al.* (1993) designed a Taylor-Couette experiment with stable stratification, where the rotation of the inner cylinder Ω and the frequency N related to the mean vertical density gradient S_T, play opposite effects. By increasing Ω Taylor-Couette instabilities form as recirculating cells, on the other hand by increasing N the formation of these cells is shifted to higher Ω. As in the flow without stratification, the instabilities depend on the width of the gap. The purpose of the present study is to perform numerical experiments for the same conditions as in the real experiments. The numerical validation of the experimental outcome permits a better understanding of the instabilities. Since the experiments showed no azimuthal waves, numerical simulations of the axisymmetric case are thought to be a good first approximation of the real flow.

1. INTRODUCTION

In many geophysical applications the combined effect of density stratifications and rotation give rise to different types of vortical structures. For example in the equatorial regions the stratification of the sea seems to be the cause of the observed recirculating cells along the vertical direction extending in the nord-south direction. In an attempt to understand the causes for these different cells Boubnov *et al.* (1993) set-up a Taylor-Couette laboratory experiment with stable stratification. This simplified experiment could explain some of the features of the geophysical flows but also it is a very interesting case *per se*. A large number of Taylor-Couette experiments have been performed in a concentric annulus without stratification, among them one by Gorman and Swinney (1982) devoted to study the wavy vortex regime, which occurs at Reynolds numbers above the critical Re_c at which the flow goes from the Couette regime to the Taylor-Couette regime.

Numerical simulations were also performed to reproduce these transitions. Marcus (1984) reproduced the experimental results in the different regimes and Vastano and Moser (1991) extended the study to the evaluation of the Lyapunov exponents in this closed system. Pseudospectral methods were used in these simulations and it is well known that these methods are very onerous. In the present paper, we used a finite difference scheme, second order accurate in time and space. The method has been tested by reproducing the critical Reynolds number for the onset of the Taylor vortices regime and the results were in good agreement with the experimental results, pseudospectral simulations and linear stability theory.

In the presence of stratification the aim was to reproduce the Ω, N diagram obtained in the Boubnov *et al.* experiments. In the small gap case $\delta = (b-a)/a = 0.275$ the numerical simulation confirmed the experimental and the linear stability theory outcome, namely the linear dependence of Ω_c on N. As in the experiment it was also found that the size of the Taylor cell increases with Ω. That is at low Ω the vertical size of a single roll is $L_c = h/(b-a) \approx 0.5$, it becomes $L_c \approx 1$ for larger Ω and finally $L_c \approx 2.0$. This behavior was found when the numerical simulations were performed by setting the rotation of the inner cylinder at the desired speed at $t = 0$. The time evolution of the maximum of v_r shows that for $L_c = 0.5$ it reaches a steady value. On the other hand for $L_c = 1$, the velocity oscillates with a single frequency at low Ω and with a large band of frequencies at high Ω. For $L_c = 2$ the frequency spectrum has a large band. All these results were obtained by axisymmetric simulations, and this might be a very strong limitation. By changing the way by which the inner cylinder is put into rotation the scenario was different. At low N stationary cells with size $L_c = 0.5$ and non-stationary with size $L_c = 1$ were obtained but no cells with size $L_c = 2$ are observed. At high N on the contrary only stationary cells with $L_c = 0.5$ were obtained. The aim of the simulation was to complement the experimental observations and to explain the experimental inaccuracies in the distinction between the different regimes. In fact by flow visualisations Boubnov *et al.*(1993) produced schematic plot of streamfunction, that could be erroneous mainly because of the unsteadiness of the flow.

2. PHYSICAL MODEL

The Navier-Stokes equations in primitive variables were solved together with the equation for the perturbed density. By assuming as reference velocity the rotation velocity of the inner cylinder Ωa, as reference length the width gap $b-a$, and by introducing the quantity $\sigma = (T - T_0)/S_T(b-a)$, with $T_0 = S_T z$ the reference temperature, the dimensionless equations are:

$$\begin{aligned}
\frac{Dq_\theta}{Dt} &= -\frac{1}{r}\frac{\partial p}{\partial \theta} + \frac{1}{\mathrm{Re}}\left[\frac{1}{r^2}\left(\frac{\partial}{\partial r}r^3\frac{\partial}{\partial r}\frac{q_\theta}{r}\right) + \frac{1}{r^2}\frac{\partial^2 q_\theta}{\partial \theta^2} + \frac{\partial^2 q_\theta}{\partial z^2} + \frac{2}{r^3}\frac{\partial q_r}{\partial \theta}\right], \\
\frac{Dq_r}{Dt} &= -r\frac{\partial p}{\partial r} + \frac{1}{\mathrm{Re}}\left[r\frac{\partial}{\partial r}\left(\frac{1}{r}\frac{\partial q_r}{\partial r}\right) + \frac{1}{r^2}\frac{\partial^2 q_r}{\partial \theta^2} + \frac{\partial^2 q_r}{\partial z^2} - \frac{2}{r}\frac{\partial q_\theta}{\partial \theta}\right], \\
\frac{Dq_z}{Dt} &= -\frac{\partial p}{\partial z} + \frac{1}{\mathrm{Re}}\left[\frac{1}{r}\frac{\partial}{\partial r}\left(r\frac{\partial q_z}{\partial r}\right) + \frac{1}{r^2}\frac{\partial^2 q_z}{\partial \theta^2} + \frac{\partial^2 q_z}{\partial z^2}\right] + Ri\sigma, \\
\frac{D\sigma}{Dt} &= +q_z\frac{S_T}{|S_T|} + \frac{1}{\mathrm{Re}Pr}\left[\frac{1}{r}\frac{\partial}{\partial r}\left(r\frac{\partial \sigma}{\partial r}\right) + \frac{1}{r^2}\frac{\partial^2 \sigma}{\partial \theta^2} + \frac{\partial^2 \sigma}{\partial z^2}\right],
\end{aligned} \tag{1}$$

with

$$\begin{aligned}
\frac{Dq_\theta}{Dt} &\equiv \frac{\partial q_\theta}{\partial t} + \frac{1}{r^2}\frac{\partial r q_\theta q_r}{\partial r} + \frac{1}{r}\frac{\partial q_\theta^2}{\partial \theta} + \frac{\partial q_\theta q_z}{\partial z}, \\
\frac{Dq_r}{Dt} &\equiv \frac{\partial q_r}{\partial t} + \frac{\partial}{\partial r}\left(\frac{q_r^2}{r}\right) + \frac{\partial}{\partial \theta}\left(\frac{q_\theta q_r}{r}\right) + \frac{\partial q_r q_z}{\partial z} - q_\theta^2, \\
\frac{Dq_z}{Dt} &\equiv \frac{\partial q_z}{\partial t} + \frac{1}{r}\frac{\partial q_r q_z}{\partial r} + \frac{1}{r}\frac{\partial q_\theta q_z}{\partial \theta} + \frac{\partial q_z^2}{\partial z}, \\
\frac{D\sigma}{Dt} &\equiv \frac{\partial \sigma}{\partial t} + \frac{1}{r}\frac{\partial q_r \sigma}{\partial r} + \frac{1}{r}\frac{\partial q_\theta \sigma}{\partial \theta} + \frac{\partial q_z \sigma}{\partial z},
\end{aligned} \tag{2}$$

Where the Reynolds number is $Re = \Omega(b-a)a/\nu$, the Richadson number is $Ri = (N/\Omega)^2[(b-a)/a]^2$ with $N^2 = gS_T\beta$ and $Pr = \nu/k$. The quantity S_T is the constant temperature gradient, which when positive accounts for a stable stratification. The continuity equation with the quantities q_i is

$$\frac{\partial q_r}{\partial r} + \frac{\partial q_\theta}{\partial \theta} + r\frac{\partial q_z}{\partial z} = 0 \tag{3}$$

The system of equations was integrated by a numerical scheme based on a fractional step method. The accuracy was tested for several flows in cylindrical coordinates (Verzicco & Orlandi 1993). In the present case since there are two horizontal walls we used a non-uniform grid in the radial direction to capture the vorticity gradients near the walls. Periodicity was assumed in the vertical direction and its size was changed depending on Ω. At low Ω the vertical extension was $L_z = L/(b-a) = 2$ to reproduce the formation of two and one cells. At higher Ω the size was $L_z = 4$ to capture one cell with $L_c = 2$.

As initial condition we used the Couette profile $q_\theta = \frac{1}{1-\eta^2}(\frac{1}{r} - \eta^2 r)$. Superimposed to this we introduced a random velocity distribution of q_z with amplitude $q_M = .0125$ at the interior and reduced to one fourth in a layer near the walls. The incompressibility of the perturbed velocity allows the calculation of q_r. The initial perturbed density had a random distribution similar to that of q_z. As initial parameters we assigned the values of the experiments a, b, Ω, ν and N, from these quantities Re and Ri were evaluated. The major part of the simulations were performed by a grid 129 × 129. When the vertical extension was $L_z = 4$ the mesh size remained unchanged and 257 points were used.

3. RESULTS

In the available literature experimental and numerical results concerning the critical Reynolds number have been reported for $\eta = a/b = 0.875$, different from $\eta = a/b = 0.784$ used in the Boubnov's experiment. We therefore evaluated Re_c for $\eta = a/b = 0.875$ to check the quality of the numerical method. The pseudospectral simulations give $Re_c = 118.4$ which is in very good agreement with $Re_c = 118.2$ obtained from the linear stability theory with $\alpha = 3.13$. We performed the simulations with random initial disturbances described above and with $L_z = 2\pi/\alpha$, using a grid 48 × 48 in r and z. We found $Re_c = 118.8$ corresponding to $\Omega = 0.52$. This critical value was obtained by calculating $\partial log|v_r|_{max}/\partial t$, at different values of Ω, after the transient. Whatever the value of q_M the short transient consisted in a rapid decay of the disturbances which afterwards either grow or decay, depending on whether Ω is above or below the critical value. The choice of an initial random perturbation makes the present simulations closer to what occurs in an experiment. On the other hand the eigenfunctions of the linear stability theory were generally used in the previous numerical simulations by Marcus (1984) and Vastano & Moser (1991). This different choice of the initial perturbation could be the reason for the small difference between the present $Re_c = 118.8$ and $Re_c = 118.4$ in the pseudospectral simulations. We think the reason can not be attributed to the accuracy of the numerical method since we performed grid refined calculations. The dependence of the critical Re_c on the vertical size L_z was checked by evaluating the critical Ω_c for $L_z = 3$ giving $\Omega_c = 0.55$. The results did not change by introducing a clean disturbance $q_z = q_M \sin(2\pi r)\sin(2\pi z/\alpha)$ with the radial distribution still different from that of the eigenfunctions of the linear stability theory.

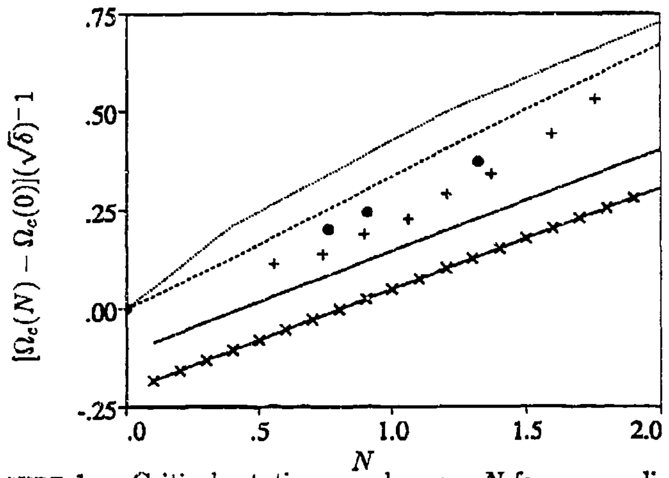

FIGURE 1 . Critical rotation speed versus N for ——, linear stability theory $\delta = 0.275$; —— ×——, linear stability theory $\delta = 1.55$; present results for $\delta = 0.275$, ---- and $\delta = 1.55$ ······· ; Boubnov *et al.* exp., + , $\delta = 0.275$, • , $\delta = 1.55$.

Boubnov *et al.* (1993) evaluated for three values of the non-dimensional gap width how Ω_c changes with stratification and they observed that the critical value increased linearly with N. They performed also linear stability calculation, in the narrow gap case in the limit of $\delta \to 0$ and found the following relationship

$$\Omega_c(N) - \Omega_c(0) = \frac{3b_1}{2^{1.5}\pi} L_c \sqrt{\delta} N \qquad (4)$$

The numerical simulations were performed for non-dimensional gap values of $\delta = 0.275$ and $\delta = 1.55$ and respectively, in the non-stratified case, the critical Ω_c were $\Omega_c = 0.208$ and $\Omega_c = 0.111$ in perfect agreement with the experiments. In Fig.1 we reported the experimental and the numerical values of $[\Omega_c(N) - \Omega_c(0)](\sqrt{\delta})^{-}1$. The dependence of Ω_c on N given by the inviscid linear theory, Eq. (4), is shown for comparison. On plotting the results of the inviscid theory the values of $\Omega_c(0)$ for the small and wide gap have been subtracted. The experimental results collapse reasonably well whereas the numerical results do not collapse on a single curve. The simulations were done with a 128 x 128 and a coarse grid but the difference still persisted. At the critical speed the size of the Taylor cell was $L_c \simeq 0.5$.

It is of interest to investigate whether the size of the cell changes with rotation rate or Reynolds number. In the experiment Boubnov *et al.* found a strong dependency on Ω. We know that from flow visualisations, especially when some unsteadiness is present, it is difficult to have a clear picture of the streamfunction. Moreover, as in all the flows in closed systems the number of cells could depend on how the inner cylinder reaches the desired speed. For example it is possible to reach the desired rotation in a very short transient starting from rest, or the desired rotation can be obtained by different stages where at each one the simulations are performed for a sufficiently long time, usually larger than 30 rotation periods. We performed, therefore two sets of simulations at $N = 0.4$ and $N = 1.8$ where the final rotation $\Omega = 3.0$ was reached in different ways.

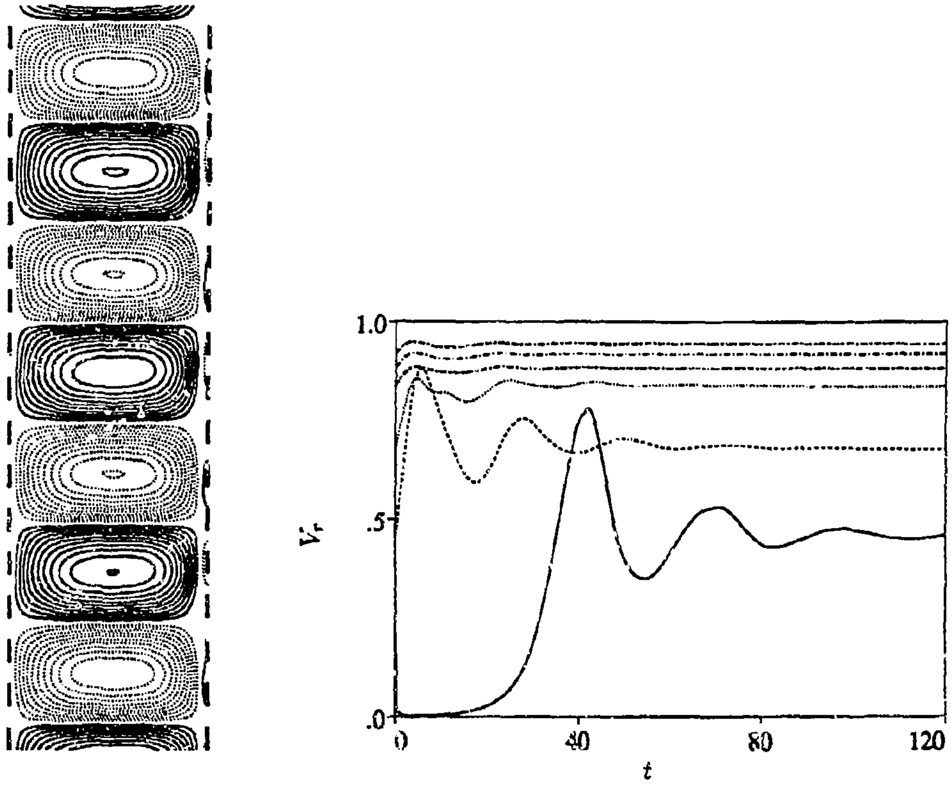

FIGURE 2. Taylor Couette calculations with 128 × 257 non-uniform grid ,; $\delta = 0.275$, $N = 1.8$. The rotation is increased from 0 by successive steps to $\Omega = 3.0$.

Fig.2 shows (solid line) for $N = 1.8$ that the maximum of the velocity component V_r initially decreases and then increases rapidly and trough an oscillation reaches a steady state. At this point the rotation of the inner cylinder is increased, oscillations are again observable with a smaller amplitude (dashed line) and these are dumped to reach a new state with a greater velocity. At each stage this behavior is repeated and finally a condition is reached with steady cells of size $L_c = 0.5$. On the contrary when at $t = 0$ the inner cylinder is suddenly put into rotation at $\Omega = 3.0$, Fig.3 shows that no steady state is reached and the maximum of V_r oscillates with a large band of frequencies. This condition is reminiscent of a turbulent state and it should occur in a three-dimensional simulation at higher rotation speed. We are expecting that an axisymmetric simulation more difficulty should produce velocities with a spectrum with a a large band of frequencies than in the three dimensional case. These simulations show that the solution is very sensitive to the way by which the final state is reached. In the case of Fig.3 the exact size of the cell is difficult to establish because the vortical structures change in time. We could speculate

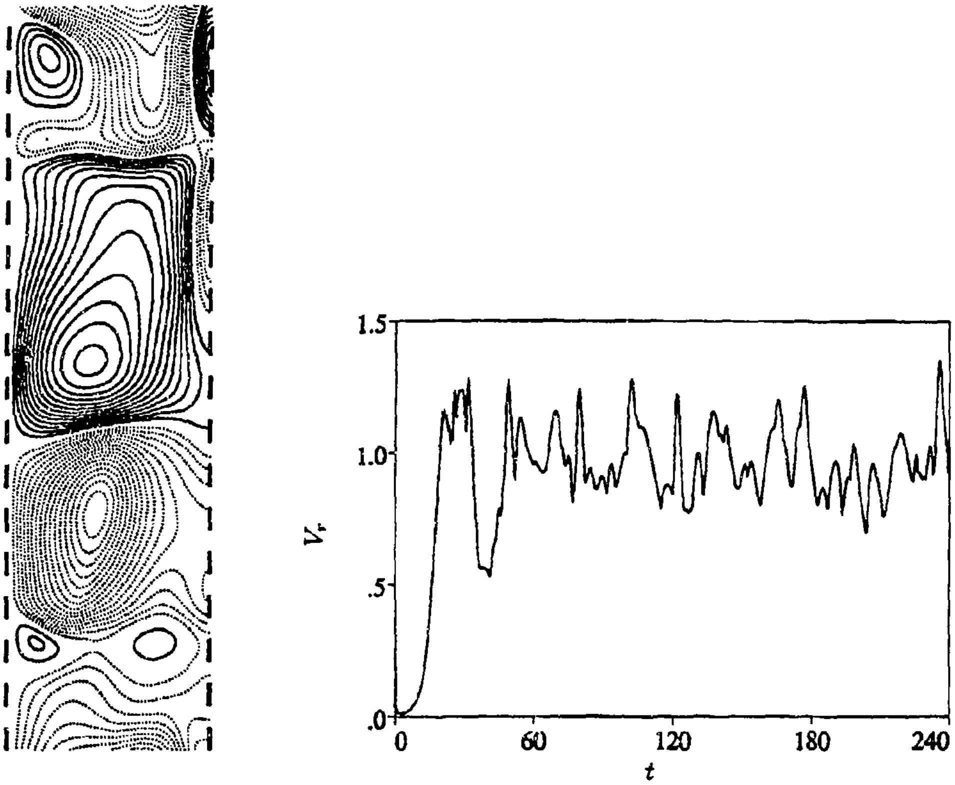

FIGURE 3. Taylor Couette calculations with 128 × 257 non-uniform grid ,; $\delta = 0.275$, $N = 1.8$. The rotation is suddenly increased from 0 to $\Omega = 3.0$.

that $1 < L_c < 2$. The experiments on the other end seem not to show this dependency on initial conditions.

For $N = 0.4$, even when the high rotation is reached through several stages an unsteady flow is produced. The results for $N = 0.4$ have been furthermore analysed to see by which mechanism the passage from $L_c = 0.5$ to $L_c = 1.0$ takes place, a very difficult task in the laboratory. At $\Omega = 1.8$, the contour plots of azimuthal vorticity shown in Fig.4 indicate that there are cells with $L_c = 0.5$ with thin layers of opposite sign vorticity near the inner and outer walls. These wall layers, for effect of the still large perturbations at this Reynolds number loose the symmetry and at their turn break the symmetry of the large vortical structures at the centre. The symmetry breaking give rise to a sort of merging between the wall and the vorticity structures at the centre. The larger cell is then again unsteady, it persists at higher rotation and at $\Omega = 3.0$ a new merging is initiated which will give rise at a cell of size $L_c = 2$.

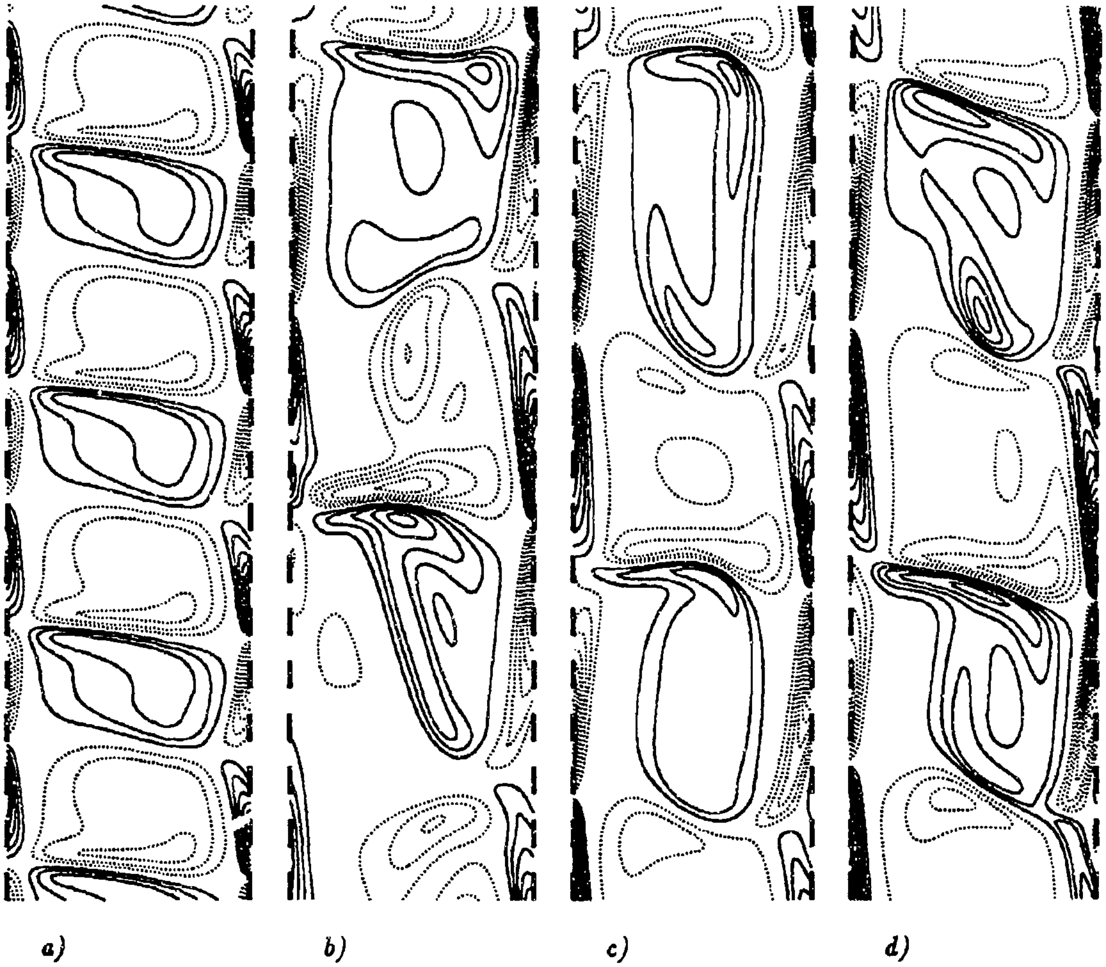

FIGURE 4. Taylor Couette by 128 × 128 ,; $\delta = 0.275$, vorticity field at $t = 120$ with $N = 0.4$ at a) $\Omega = 2.1$, b) $\Omega = 2.4$, c) $\Omega = 2.7$, d) $\Omega = 3.0$,

4. CONCLUSIONS

In the present paper we performed numerical simulation of the stratified Taylor-Couette flow experimentally investigated by Boubnov *et al.*(1993). The numerical method was tested by evaluating the critical rotation number in the absence of stratification for $\eta = 0.875$ previously studied experimentally and numerically. The calculations were then extended to find the critical rotation number in the presence of axial stratification. In this case Boubnov *et al.* (1993) performed the linear stability analysis by finding a linear relationship between Ω_c and the stability parameter N, in the limit of δ tending to zero. The present results lie on a straight line with the slope intermediate between the theoretical and the experimental one. The independence of the results on the grid size was checked as well as on the time step.

In the experiment the size of the Taylor vortices were analysed by looking at flow visualisations. Flow visualisations can be misleading when some sort of unsteadiness. The size of the vortices could also depend on the way the rotation speed is reached. Thus we decided to perform simulations reaching a high rotation speed trough a series of stages and also by assigning the desired rotation at $t = 0$. Completely different answers were obtained depending on the stratification. For high N and a step by step increase in rotation the size of the Taylor cell remained unchanged and is equal to $L_c = 0.5$. In the case of small N ($N = 0.4$) on the other hand a step by step increase in rotation gave $0.5 < L_c$ and in the case of a sudden increase we found, as in the experiment, that the size of the cell reached the value $L_c = 2$. By looking at the vorticity field we speculated that the formation of cells with a large size is due to merging of the inner vorticity with the thin layers near the walls.

ACKNOWLEDGMENTS

The authors wish to thank Prof. Emil Hopfinger who suggested the study of this flow and for the useful comments on a draft of this manuscript. The fruitful discussions with Dr. Roberto Verzicco are also acknowledged. The research was supported by a grant from "Ministero dell' Università e della Ricerca Scientifica".

REFERENCES

1. Boubnov, B., Hopfinger, E.J. & Gledzer, E. "Instability and transition in circular Couette flow with axial stratification "Draft presented in a seminar at the University of Roma. May 1993 see also the present preprints.
2. Verzicco, R. & Orlandi, P. " A finite-difference scheme for three-dimensional incompressible flows in cylindrical coordinates " Submitted to Journal of Comp. Physics 1993.
3. Gorman,M. & Swinney, H.L. " Spatial and temporal characteristics of modulated waves in the circular Couette system " J.Fluid Mech. **117**, 123-142, 1982.
4. Marcus,P.S. " Simulation of Taylor-Couette flow. Part.1 Numerical methods and comparison with experiment" J.Fluid Mech. **146**, 45-64, 1984.
5. Vastano J.A, Moser R.D. " Short-time Lyapunov exponent analysis and the transition to chaos in Taylor-Couette flow" J.Fluid Mech. **223**, 83-118, 1991.

opinion on this. Should I change the equations by introducing the mean vertical density variation? In this case the numerical simulations should be closer to the experiment where the stratification was obtained by density rather than by temperature.

About correction you corrected Fig.1 putting the linear stability teory line below the experiments. . was copying this figure from one of your trasparency where the experimental results of Oc(n)-Oc(0)*eps**(-1/2) lyed below the teoretical results. If I am plotting Oc(n)*eps**(-1/2) instead Oc(n)-Oc(0)*eps**(-1/2) the experimental results do not coalesce on a single curve. I am litle confused and I need an answer from you or from Boubnov or Glezer. Could you thank Boubnov too for the further correction.

I am sending through my department only the conference fee I will pay the banquet and the accomodation deposit in Grenoble, if it is possible.

REgards Paolo

Fourth International Symposium on Stratified Flows

Streamwise Vortices near a Density Interface

Nobuhiro BABA

Department of Marine System Engineering
University of Osaka Prefecture
Sakai, Osaka 593, Japan

Abstract

The interaction of streamwise vortices with a density interface is investigated by the experiments and the computations of the stratified cavity flow. The flow pattern of the primary circulation is quite different from that of homogeneous fluid. The results show that the deepening of a mixed layer into a region of constant density gradient proceeds with three dimensional deformation of the interface and that the pairs of counter-rotating streamwise vortices appear in the strong shear layer near the interface. The comparison between the three-dimensional and two-dimensional computations indicates that this streamwise vortical structure contribute the mixing across the interface.

1. Introduction

Numerous experiments on the mixing in stratified fluids have been made to obtain a universal form of the entrainment law. At present, however, there is no consensus but a wide variety of entrainment laws and the mechanisms have been proposed. Indeed different investigators in the experiments using similar apparatuses and ranges for the Richardson number have reported different entrainment rates. The knowledge of the subject is summarized by a recent review by Fernando (1991).

The turbulent shear flows near an interface have some common features. It is well known that when the wind blows over the sea streaks may appear on the surface. They are caused by Langmuir circulation which is a parallel system of counter-rotating streamwise vortices beneath a free surface. The streakiness has been also found in wall turbulence, which is attributed to the presence of streamwise vortices in the inner layer. Although understanding of the mechanism of their formation has not been satisfactory, there is enough evidence to support their existence. Since a density interface has the same effect on the flow as a wall and a free surface by suppressing the motion to penetrate it, it is expected that in the turbulent shear flow near the density interface exists such a flow structure of streamwise vortices, which possibly contributes to the mixing across the interface.

The aim of the present study is to examine this possibility in both experiments and computations on the stratified flow in a cavity. The recirculating flow in a cavity has been one of the targets for validating the computational methods. Among a lot of studies of the cavity flow Freitas et al. (1985) have showed in their experiment and computation that the streamwise vortices appear on the bottom wall and that their presence may modify the flow structure. The stratified cavity flow can be considered as one of the simplest models for the mixing by the surface shear flow induced by wind in the closed region. In this study we will examine the deepening process of the mixed layer into a region of constant density gradient in a lid driven cavity and discuss the effect of three-dimensional flow structure on the mixing.

2. Method

2.1 Experiment

The experiments were carried out using a rectangular Perspex tank with a length L of 20 cm, a depth D of 20 cm and a lateral span B of 40 cm on the top of which a belt-drive system was mounted as shown in figure 1. A speed-variable 6W motor equipped with a reduction gear and a timing-belt and pulley set drove the 1 mm thick synthetic-resin belt at selected speeds U from 2.0 cm/s to 4.0 cm/s.

The tank was filled with a salt solution such that the density increased linearly with depth. The initial density profile was measured by traversing a conductivity probe and the buoyancy frequency was calculated from

$$N^2 = -\frac{g}{\rho_0}\frac{d\rho(x_3)}{dx_3} \qquad (1)$$

where $\rho(x_3)$ is the density at a given vertical coordinate x_3, ρ_0 is the reference density $\rho(0)$, g is the acceleration due to gravity. The value of N was varied over 0.2–0.7/s. The narrow gap between the lower surface of the moving belt and the top of the tank was sealed with a styrene-foam plate to prevent the salt solution from leaking out.

The experiments were started by turning on the motor. The belt achieved its selected speed immediately at time t=0, and the depth and characteristics of the mixed layer were monitored at discrete times thereafter. Since in running the density interface was usually distorted by the fluid motion, the depth of the mixed layer was defined as a spanwise-averaged depth of the lowest level to which the mixed layer penetrated, and it was determined visually from a shadowgraph as shown in figure 6. The density profiles were also measured by stopping the belt temporarily to insert a conductivity probe and transverse it vertically at various times during an experiment.

The fluid motions were visualized by suspending aluminium particles in the salt water and then slit lighting the tank from the side. Photographs were taken with a 35mm camera with exposure time of 4 to 6s to obtain well defined pathlines in the flow field.

2.2 Computation

The Navier–Stokes equations for a heterogeneous fluid with the force of gravity included can be written as

$$\rho\left(\frac{\partial u}{\partial t} + \nabla\cdot(uu)\right) = -\nabla p'' - \rho'' Fr^{-2}k + Re^{-1}\nabla^2 u \qquad (2)$$

where **k** is the unit vector along the x_3 axis. **u** is the flow velocity, ρ is the density, p is the pressure, and ρ'' and p'' mean the deviations of ρ and p from a state of hydrostatic equilibrium. All the variables are made dimensionless with respect to the reference density ρ_0, the speed U of the upper wall and the depth D of the cavity, and Re is the Reynolds number UL/ν (ν :the kinematic viscosity) and Fr is the Froude number $U/\sqrt{gD}$. If the fluid is assumes to be incompressible and diffusive, we have the continuity equation

$$\nabla\cdot u = 0 \qquad (3)$$

and the transport equation for the variation of the density

$$\frac{\partial \rho'}{\partial t} + \nabla \cdot (\rho' u) = Rs^{-1}\nabla^2 \rho' \qquad (4)$$

where $\rho'=\rho-1$ and $Rs=UL/\kappa$ (κ:the diffusivity of salt). The explicit use of the deviation and the variation of the density is essential to the accurate computation of such a flow affected by these small quantities.

The solution procedure used here is the finite volume method similar to the MAC method by Harlow and Welch (1965). The discretization using the volume fluxes across the faces of the cell, the pressure and the density at the centre of the cell as primitive variables attains the second-order of accuracy in space while the time advancement is made by the first-order accurate Euler explicit method. The simultaneous iterative procedure proposed by Chorin (1968) is applied to satisfy the continuity equation. In this procedure instead of solving the Poisson equation the pressure is determined from the divergence of the velocity vector as the steady solution of the equation

$$\frac{\partial \rho'}{\partial \hat{t}} = -\frac{\partial(\nabla \cdot u)}{\partial t} \qquad (5)$$

where $\hat{t}$ is an artificial variable for the iteration.

No-slip boundary conditions on velocity is imposed at the walls while no boundary condition on pressure is necessary in the simultaneous iterative procedure. In evaluating the diffusion terms for u and ρ' in the equations (2) and (4) the gradients of these quantities in the direction normal to the boundary are assumed to be constant.

The computations were performed in the same way as the experiments. The upper wall was started impulsively at a constant speed over a linearly stratified fluid in the cavity with the same geometry. The computations presented below used the rectangular grid systems with uniform spacing of 1/20 and 1/40, and according to the linear stability restriction, the time increments were set to be 1/100 and 1/400, respectively. The initial density difference between the values at the top and at the bottom $\Delta\rho/\rho_0$ was 0.00082 and the Froude number Fr was 0.0143, which corresponded to the experiment at N=0.2/s, U=2.0cm/s.

It is difficult to solve the nonlinear flow with very weak diffusivity because of limited resolution. Since the present computational method does not include any artificial dissipation, the fluid motions of all the scales included should be resolved explicitly over the finite grid points to obtain reasonable solutions. For this reason the Reynolds number and the salt diffusivity in the computational conditions did not corresponds to those in the experiments : Re=3000, Rs=3000 or 6000 for the computation while Re=3500-4000, Rs=10^6 for the experiment.

First the two-dimensional computation was carried out using the finer grid system to study the formation of the density interface in the experiment and the deepening of the mixed layer. Assuming that the density gradient increases to a maximum at the density interface, the depth of the mixed layer was determined from the horizontally averaged field. Next the three-dimensional computations were conducted to examine the effects of the three-dimensional motions on the mixing process. The periodic conditions were assumed in the spanwise direction in some cases. In such cases a random three-dimensional perturbation of the velocity fields with the magnitude of 3% of U was given to the initial field to cause the flow to be three-dimensional.

3. Results

When the upper wall started to move the adjacent fluid dragged by the wall collided with the downstream vertical wall and penetrated to some finite depth almost immediately. After this initial stage a primary circulation formed in the top downstream corner which then grew gradually into the region of constant density gradient. Figure 2 shows a typical photograph of the primary circulation in the centre plane. This pattern of the primary circulation bounded by a stratified fluid beneath as it were a wall is quite different from that in homogeneous fluid. In the upper layer upstream of the primary circulation some smaller secondary eddies can be seen as well, but the fluid motion in the lower layer is not clear in this photograph because it is much slower. Figure 3 shows a series of density profiles taken at intervals of half a day which indicates that the total mass has been conserved during the experiment. The density interface with a considerable density step has been formed by mixing the upper layer to be uniform. This process and the density profiles shown on figure 3 are similar to those given by Linden (1975) in the experiment on the mixing with no mean shear.

Figure 4 shows the time evolution of the primary circulation and the density field produced by the two-dimensional computation. The flow pattern of the primary circulation and the secondary eddies with the opposite rotation shows qualitative agreement with the flow visualization experiment. The main feature to notice on the contour maps of density is that the primary circulation raise heavy fluid out of the interface as it penetrates into the region of the constant density gradient. However, the density gradient of the lower layer decreases in time and as a result the density step at the interface is much smaller than expected from the measured density profile as shown in figure 3. This rapid diffusion of density is due to the extremely low value of Rs.

The depth of the mixed layer as a function of time is plotted on figure 5(a) for comparison between the two-dimensional computation and the experiment at the same N and U. The line is the best fit to the experimental data. The computed data are the depth of the finite grid points at which the density gradient is maximum, and therefore they are represented by discrete values. Further there are some points indicating the bottom of the cavity in the process of the deepening because the density step in the interface is not large enough to recognize it. Neglecting these points, the result of the two-dimensional computation shows a much reduced rate of the deepening of the mixed layer compared with the experimental data.

Figure 6 shows the shadowgraphs of the density interface taken from the downstream side. The interface is of a wave shape in the spanwise direction, sharper near the crests and flatter in troughs, the wave length of which increases as the interface descends. Figure 7 gives the flow structure in the x_2-x_3 plane across the primary circulation, which displays the presence of some pairs of counter-rotating vortices in the upper layer near the interface distorted by them. These streamwise vortices move around, varying in size and keeping their life for a while. Since they raise the interface by a few cm and seem to break it at the crests as shown in figure 6, they are considered to contribute to the mixing across the interface.

To study this vortical structure near the interface and to examine how much it contributes to the mixing, the three-dimensional computations was carried out. Figure 5(b) shows the increase in depth of the mixed layer produced by the computation with the periodic boundary condition being imposed in the spanwise direction. The same line fitted to the experimental data as figure 5(a) is plotted for a reference. This shows that the rate of the deepening in the three-dimensional computation is much higher than that in the two-dimensional computation and closer to the experimental data. The flow structure in the x_2-x_3 plane is shown in figure 8. There are many pairs of counter-rotating streamwise vortices of various scales on the density interface, among which the large-scale vortices seem to correlate with the strong distortion of the interface. These results imply that the three-dimensional structure of streamwise vortices near the interface increases the rate of the mixing across the interface.

4. Concluding remarks

The deepening of a mixed layer in a stratified cavity flow have been examined by the experiments and the computations. The results show that the streamwise vortices exist in the mixed layer near the density interface and that they contribute to the mixing across the interface.

This work was supported by a Grant-in-Aid for Scientific Research and through grants from the Society of Scientific Research Promotion of Naval Architecture. I would like to thank K.Takamatsu, S.Hirano, N.Kimura, Y.Ikeda and K.Maruno for their help in running the experiments and the computations.

References

Chorin, A. J. 1968. Numerical solution of the Navier-Stokes equations. Math. Comput. 22, 745-762

Fernando, H. J. S. 1991. Turbulent mixing in stratified fluids. Annu. Rev. Fluid Mech. 23, 455-493.

Freitas, C. J., Street, R. L., Findikakis, A. N. and Koseff, J. R. 1985. Numerical simulation of three-dimensional flow in a cavity. Inter. J. Numer. Methods Fluids 5, 561-575.

Harlow, F. H. and Welch, J. E. 1965. Numerical calculation of time-dependent viscous incompressible flow with free surface. Phys. Fluids. 8, 2182-2189.

Linden, P. F. 1975. The deepening of a mixed layer in a stratified fluid. J. Fluid Mech. 71, 385-405.

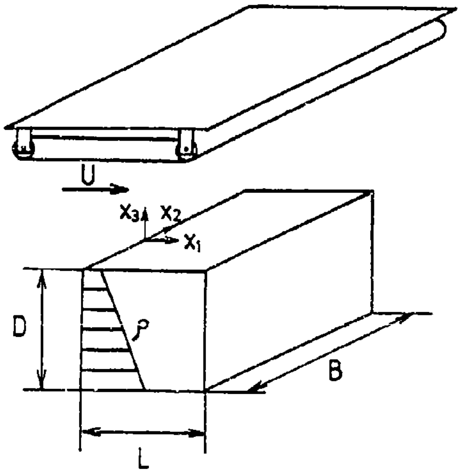

Figure 1. Schematic diagram of lid-driven cavity.

Figure 2. Visualization of primary circulation at the centre plane at N=0.20/s, U=2.6cm/s, t=32min, using aluminium particles in salt water with the exposure time of 6s.

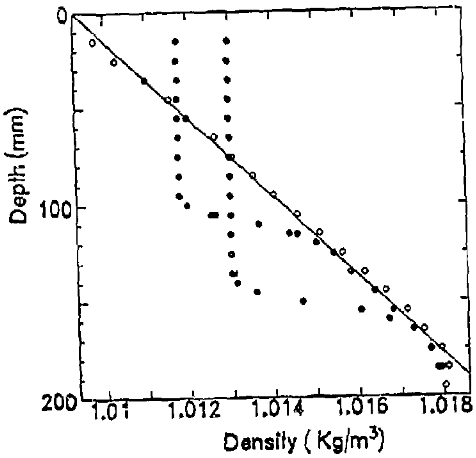

Figure 3. Density profiles showing the penetration of a mixed layer into the region of a constant density gradient at N=0.71/s, U=2.0 cm/s, ○ :t=0; ● :t=12 hour; ◎ :t=24hour.

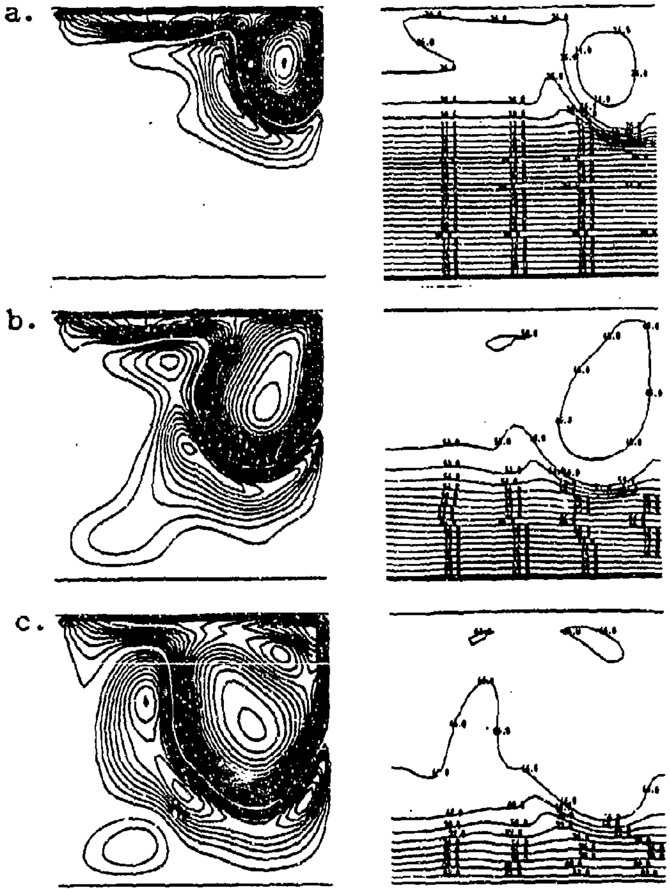

Figure 4. Streamlines (left) and density contours (right) in the 2D computation at N=0.2/s, U=2cm/s (Rs=6000, finer grids) (a) t=1000s, (b)t=5000s, (c) t=10000s.

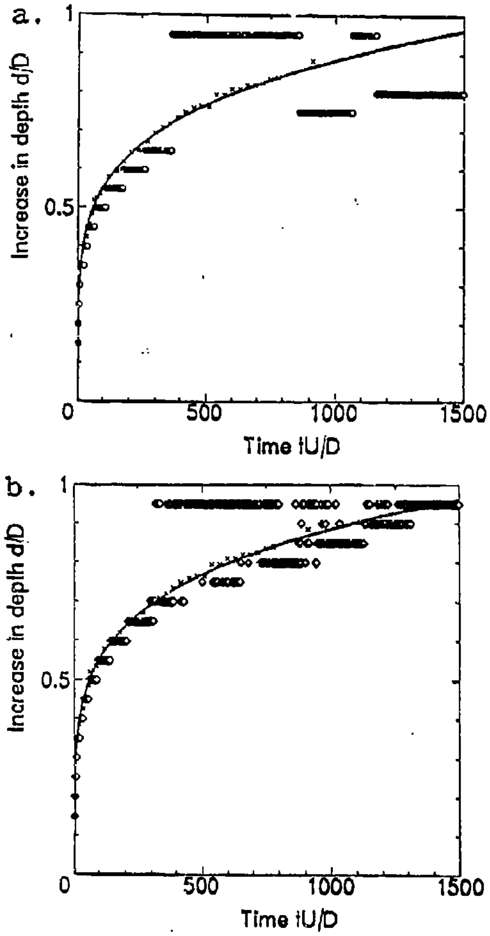

Figure 5. The increase in depth of a mixed layer. × :experiment at N=0.21/s, U=2.0cm/s. (a) ○ :2D computation at N=0.2/s, U=2cm/s (Rs=3000, coarser grids), (b) ◇ :3D computation at N=0.2/s, U=2cm/s (Rs=3000, coarser grids, periodic, B=D).

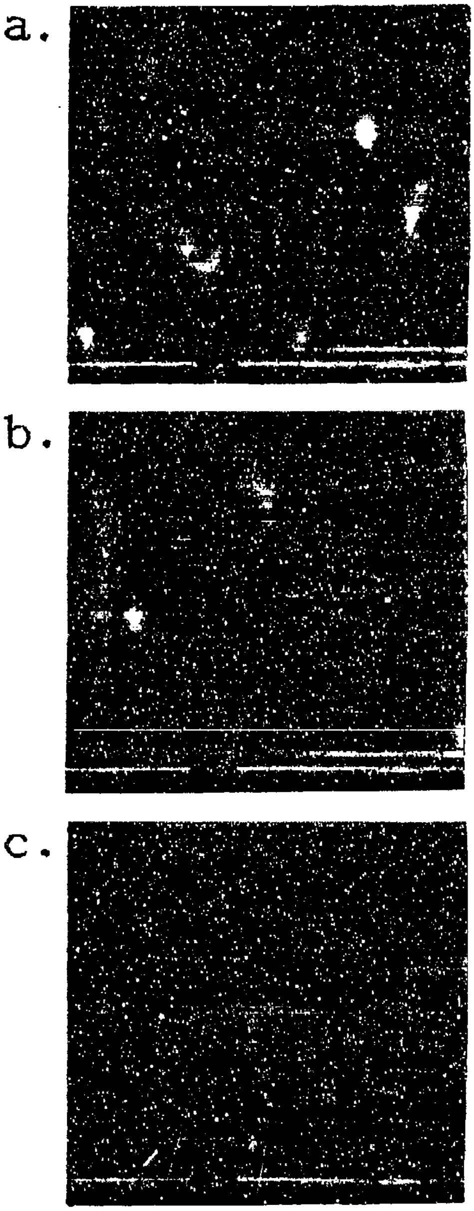

Figure 6. Shadowgraphs of a density interface taken from the downstream side, showing the spanwise distortion at N=0.41/s, U=2.0cm/s at (a) t=30 min, (b) t=90 min, (c) t=330 min.

Figure 7. Visualization of streamwise vortices near a density interface in the x_2-x_3 plane 4 cm upstream of the downstream wall at N=0.20/s, U=2.6cm/s, t=47min, using aluminium particles in salt water with the exposure time of 4s.

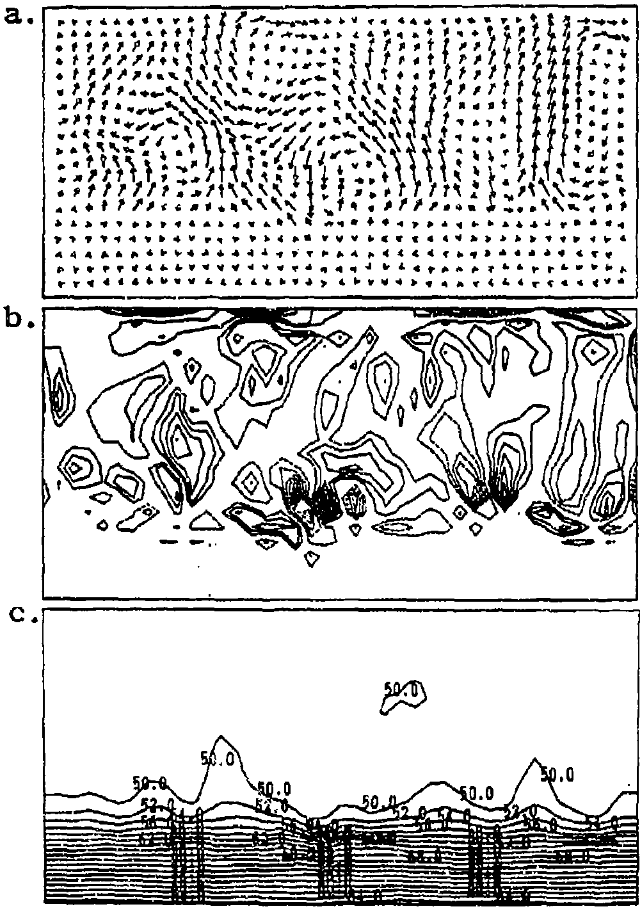

Figure 8. Streamwise vortices near a density interface in the 3D computation at N=0.2/s, U=2cm/s (Rs=6000, coarser grids, with side walls, B=2D), (b) streamwise vorticity contours, (c) density contours in the x_2-x_3 planes 4cm upstream of the downstream wall at t=8000s.

Characteristics of turbulence by a breaking gravity wave below its critical level

Andreas Dörnbrack and Thomas Gerz
DLR, Institute of Atmospheric Physics, 82230 Oberpfaffenhofen, Germany

Introduction

The generation of turbulence by overturning internal gravity waves is an important factor in the microscale dynamics of the atmosphere and ocean. For instance, the overturning of internal gravity waves and the resulting turbulence are thought to be the primary cause for clear-air turbulence (Pao and Goldburg, 1969) and the occurence of thin turbulent layers in free atmosphere (Sato and Woodman, 1982; Nastrom and Eaton, 1993; Sidi, 1993).

One of the fundamental mechanisms leading to the breaking of gravity waves and to the production of turbulence is the interaction of an internal gravity wave with a critical level. In a shear flow, a critical level is the height where the phase speed of a wave equals the mean flow speed (Booker and Bretherton, 1967). As a propagating wave approaches its critical level, the wave propagation is strongly suppressed: the wave amplitude decays exponentially in the region above the critical level (the trapping effect of the critical layer). At the critical level, all momentum of the wave is transferred into the mean motion. Depending on the excitation energy of the initial wave field and on shear and stratification of the basic flow, turbulence can be generated.

The gravity wave critical layer interaction is difficult to study observationally in the free atmosphere because of the broad spectrum of scales which prevent the observation of isolated events. In the stably stratified boundary layer, the gravity wave critical level interaction can only be investigated by support of simple models. Nappo (1991) presented a climatological study of turbulent events over simple and complex terrain in the nighttime boundary layer. He supposed that the major portion of the frequently observed sporadic outbreaks of turbulence are caused by wave-turbulence interaction near critical levels. Nappo and Chimonas (1992) used a linear wave model to support this hypothesis and to study the wave exchange between the ground surface and the critical level. In the laboratory, the interaction can be observed under controlled conditions by defining wavelength and amplitude of the disturbances and by skilful set-up of the mean flow (Thorpe, 1981; Koop and McGee (1986); Delesi and Dunkerton, 1989). Hitherto, mainly two-dimensional numerical simulations of the interaction have been made (Winters and D'Asaro, 1989; Mobbs and Rabbitt, 1992; Dunkerton and Robins, 1992). First results of three-dimensional simulations by Andreassen (1993) and Dörnbrack and Schumann (1994) confirm the finding of stability calculations by Winters and Riley (1992) and Lin et al. (1993) that a three-dimensional treatment of the problem is necessary.

In this paper, the nonlinear interaction of a vertically propagating internal gravity wave with the critical layer and the subsequent generation of turbulence are investigated by means of three-dimensional numerical simulations. We consider a constant shear flow with zero mean over a wavy surface in a stably stratified fluid with constant Brunt-Väisälä frequency. The length x, width y, and height z of the domain are $(1.56, 1.56, 1)\,H$, respectively. The surface is sinusoidal in x direction with one

greno94 paper a5 april 15th, 1994

wavelength and amplitude $\delta = 0.03H$. At the beginning (time $t = 0$), the fluid is at rest (see, e.g., Fig. 1). For $t > 0$, the mean flow is towards the left in the lower half and towards the right in the upper half of the domain, such that the fluid is at rest at $z = 0.5H$. The sinusoidal corrugation excites gravity waves with zero phase speed. Hence, the critical layer is situated at $z = 0.5H$. The bulk Richardson number Ri of the mean flow just after initialization is one.

Based on the successful comparison of a two-dimensional version of the model with the laboratory observations by Thorpe (1981) – presented in Dörnbrack and Schumann (1994), we discuss here results of three-dimensional simulations for two different models of viscosity. For a smooth breaking, we use a direct numerical simulation (DNS) with constant viscosity. The flow structure remains essentially two-dimensional. The mixing takes place as a process of repeated rolling-up of density surfaces. The flow shows permanently overturning waves which generate vertical motions in a quasi periodic manner without real turbulence. In the large-eddy simulation (LES), the initial field is randomely disturbed and a turbulent viscosity is used. The turbulent viscosity is assumed to be proportional to the fluctuation of the local shear and is a function of the Richardson number. The breakdown of the convectively unstable regions occurs immediately after the appearance of instability and three-dimensional small-scale turbulence is generated. The mixing produced by the LES is much more efficient than the two-dimensional counterpart in the DNS.

The governing equations and the numerical model, including initial and boundary conditions, are described in detail in Dörnbrack and Schumann (1994). Here, we restrict ourselves to the discussion of the simulation results.

Results and Discussion

Fig. 1 and Fig. 2 depict the flow evolution by means of contour plots of the temperature field for DNS and for LES, respectively. The amplitude of the excited waves increases with height (up to nearly 3δ) but falls to zero just below the critical level. No wavy motion is found above this level which acts as an absorber whereby momentum is transfered to the mean flow causing an advection in the positive x-direction. This process gradually transports colder fluid over warmer fluid, leading to regions of reduced temperature gradients (characterized by thickening of the marked areas). The local Richardson number drops and the regions, which are mostly found above the trough, become convectively unstable. Between these sites of instability the gradient is enhanced (characterized by thin marked areas). The resulting structure is also reported from observations of Kelvin-Helmholtz instability.

The first overturning occurs at about $t = 14t_{ref}$, where $t_{ref} = H/\Delta U$ (ΔU is the velocity difference between top and bottom). Only for times larger than $18t_{ref}$, the wave structure evolves significantly different in DNS and LES. The uniform viscosity case shows a smoothly breaking regime, which consists of the repeated rolling-up of contour lines, whereas the turbulent viscosity case leads to a fully turbulent mixed layer below the critical level.

In the DNS, we see no indication of the onset of secondary, smaller-scale instabilities, neither in the statically unstable cores, nor in the braids, where a shear-driven insta-

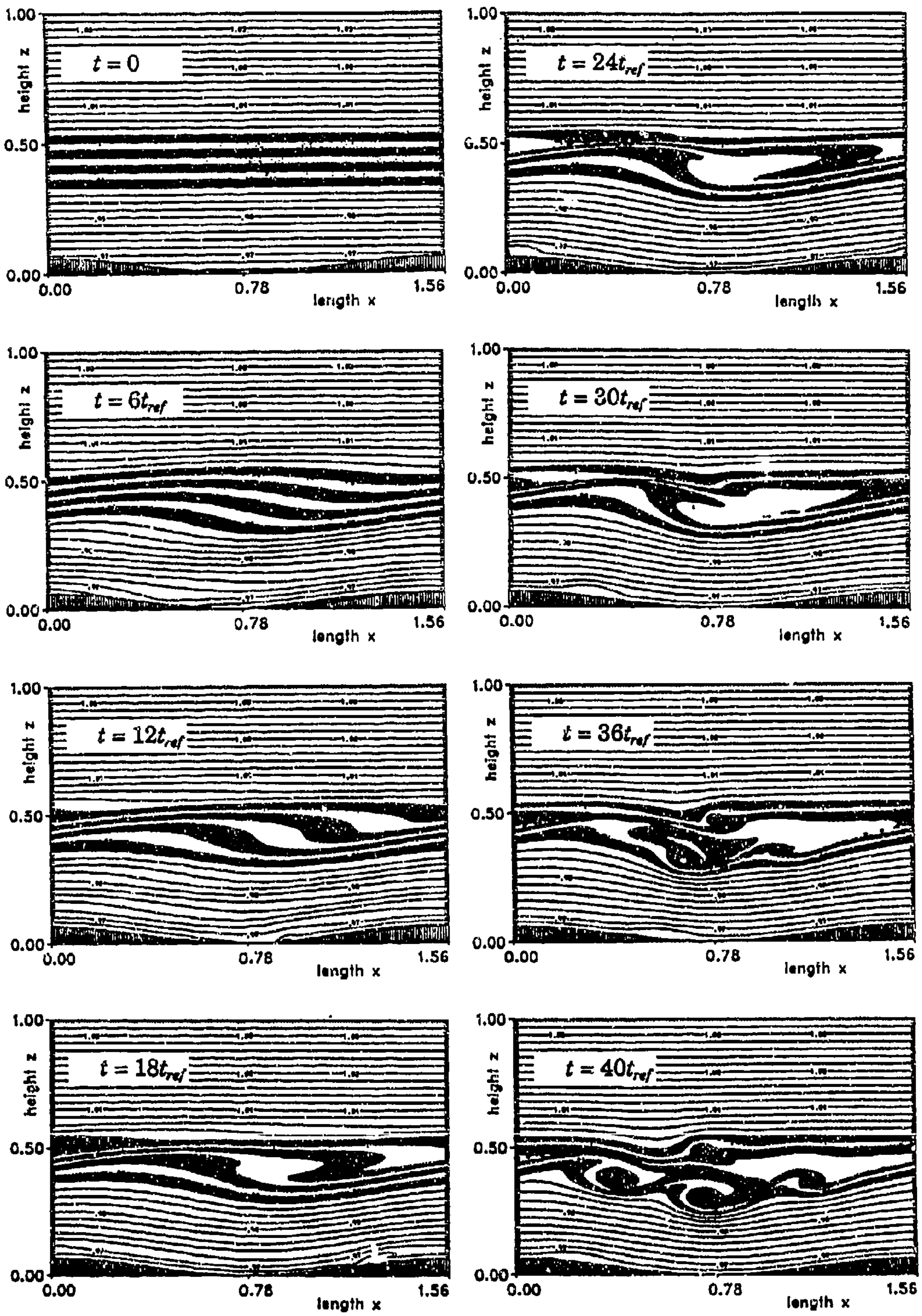

Figure 1. Temporal evolution of the flow structure at high viscosity (DNS). Shown are contour lines of the temperature $\vartheta' + \Theta(z)$.

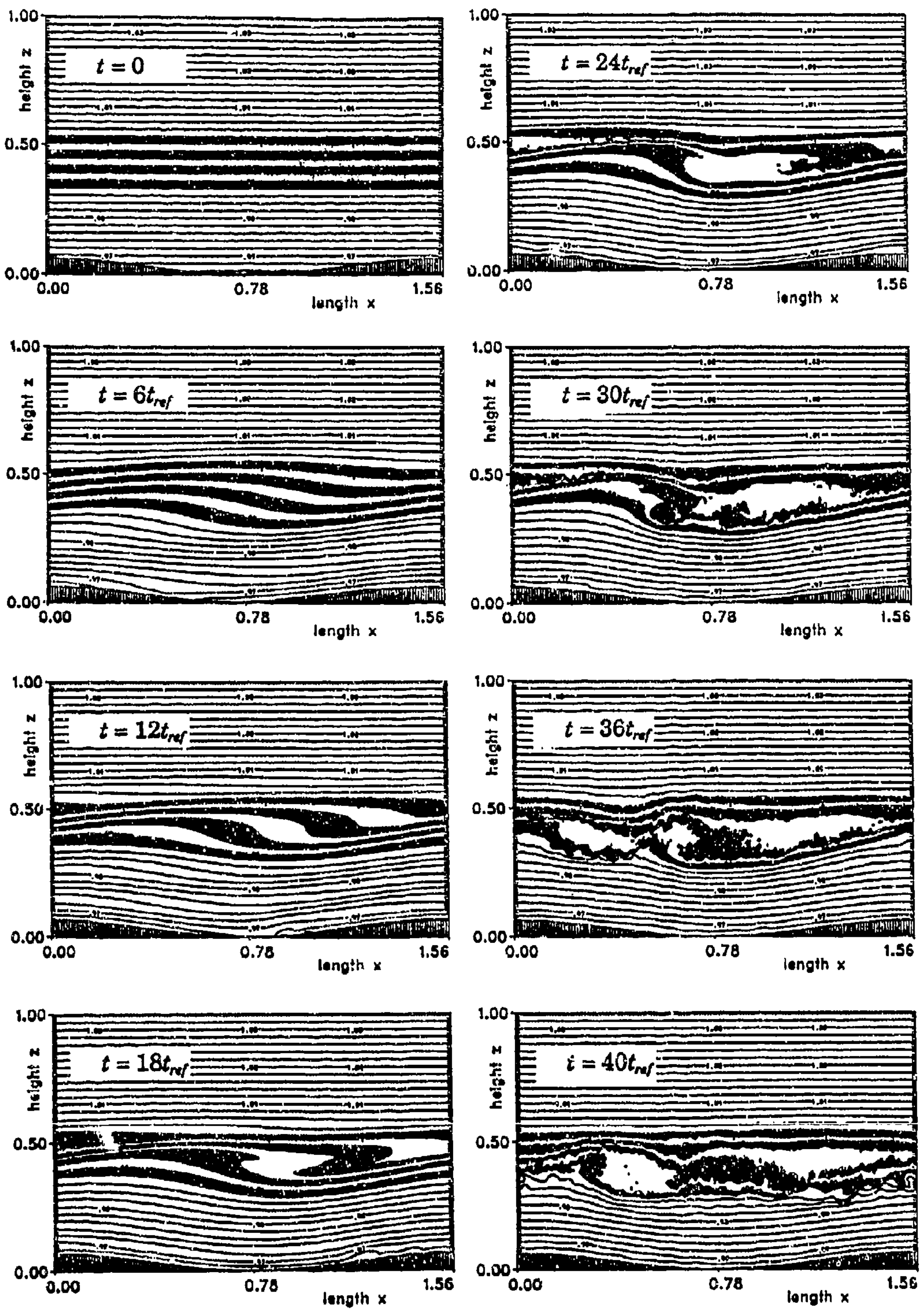

Figure 2. Temporal evolution of the flow structure at low viscosity (LES). Shown are contour lines of the temperature $\vartheta' + \Theta(z)$.

bility could be possible. In fact, at $t = 36t_{ref}$, we do observe small-scale disturbances in the braids over the crest. However, these disturbances are damped due to viscosity and no further growth can be observed. In the DNS, the main characteristic is the continuous generation of overturning waves induced by shear and primary waves. After the overturn of the first wave between $t = 30$ and $36t_{ref}$, we find a second unstable region which itself creates a smaller wave with growing amplitude.

In contrast to the DNS, we see in the LES that, when $t < 18t_{ref}$, the overturning wave breaks immediately causing a strong turbulent mixing in the unstable regions. As in the DNS, we observe a tendency to build up a secondary wave structure at the same time and position. But this structure is destroyed quickly by the mixing. At the end of simulation we find large areas of reduced density gradients but only small portions of the fluid are convectively unstably stratified.

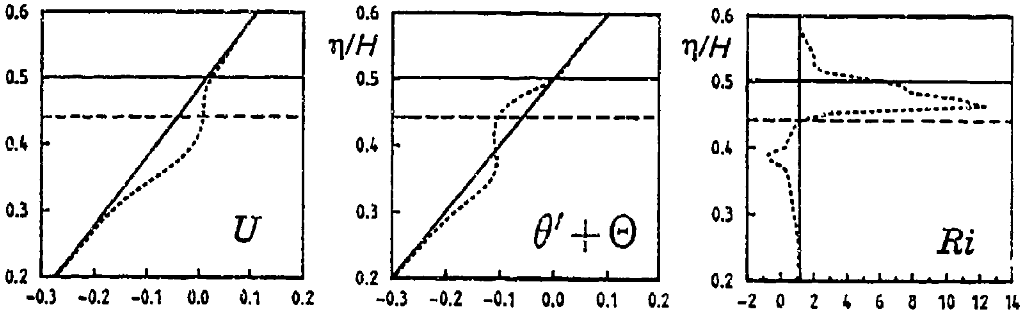

Figure 3. **Typical vertical profiles of mean quantities.** Horizontally averaged profiles of the mean velocity U, the temperature ϑ and the Richardson number Ri at beginning of the simulations (solid line) and during the breaking (dashed line). Velocity and temperature are normalized by the corresponding reference values.

Fig 3. shows the horizontally averaged profiles of the mean velocity, the temperature and Richardson number at the beginning of the simulations and during the breaking at $t = 40t_{ref}$ for the DNS. Below the critical level the mean velocity increases in time. While the increase up to about $t = 20t_{ref}$ is similar in the DNS and the LES, the final speed up at $t = 40t_{ref}$ is $0.011\Delta U$ in the DNS and just $0.007\Delta U$ in the LES. The layer directly influenced by the momentum transfer between the wave and the mean flow has a thickness of about H/4. Just below the critical level the Richardson number is much larger compared to the initial value due to the decreasing shear and the increasing stratification at this altitude. Below this stably stratified layer, the shear is large and the Richardson number drops below the critical value and becomes even negative indicating a layer with small or negative temperature gradients.

Which instability – convective or Kelvin-Helmholtz type – is responsible for the breaking event? Assuming that $Ri < 0.25$ is a necessary condition for the onset of the breaking process, we realize with Fig. 4 that regions with $Ri < 0.25$ are also regions of weak lateral vorticity (hence, weak shear). Therefore, also the local temperature gradient must drop in order to bring Ri below 0.25. This suggests that the breaking process is mainly caused by the wave-induced convective instability and not by a mainly shear-driven Kelvin-Helmholtz instability.

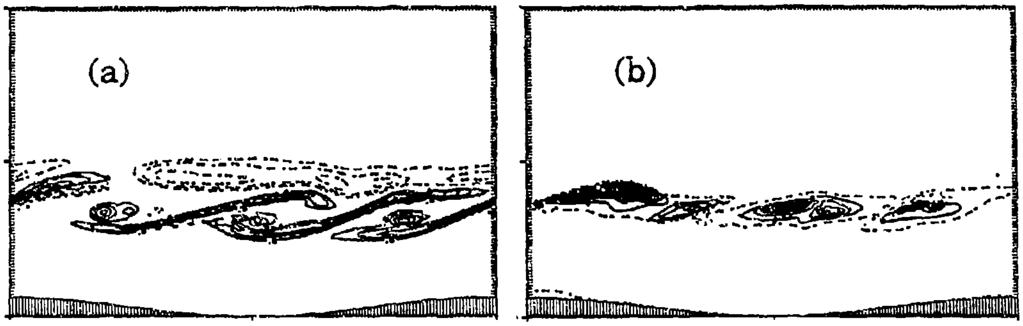

Figure 4. **Vertical cross-section** of the vorticity ω_y (a) and the Richardson number Ri (b) at $t = 60t_{wi}$ (DNS). In (b), the dashed line is Ri=0.25, the solid lines denote negative values. Same scale as in Fig. 1.

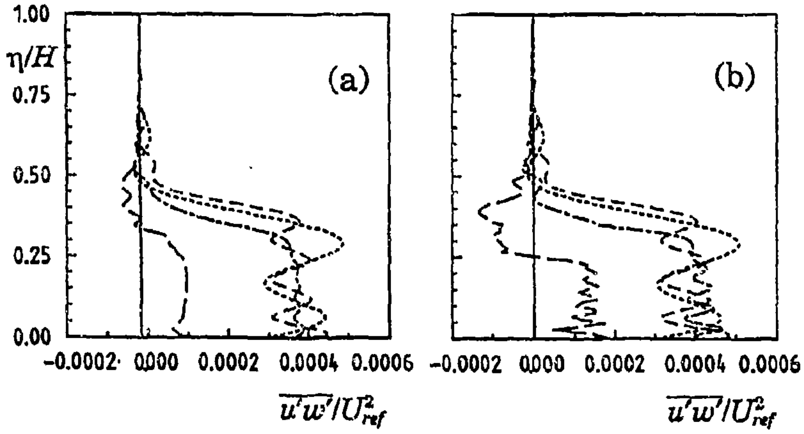

Figure 5. **Profiles of the momentum flux** $\overline{u'w'}$. (a) DNS and (b) LES. The times are: $t = 0t_{wi}$: ________; $t = 6t_{wi}$: _ _ _ _; $t = 12t_{wi}$: __ __ __; $t = 24t_{wi}$: __ . __ ; $t = 40t_{wi}$: ___ ___.

One of the most important features of the absorption of a wave at the critical level is the acceleration of the mean flow. This acceleration requires a vertical gradient of the shear stress, because $\partial u/\partial t = -\partial \overline{u'w'}/\partial z$. Idealized waves with infinite extent have an uniform momentum flux and the gradient is zero, i.e. on average the fluid is never forced. In our simulations, the profiles of $\overline{u'w'}$ manifest a strong vertical structure (Fig. 5). Initially, the vertical flux of horizontal momentum is constant (zero for the disturbed, slightly negative for the uniform viscosity case). At $t = 6t_{wi}$, the $\overline{u'w'}$-profile exhibits vertically a wavelike structure. Its amplitude increases with altitude but strongly decreases to the initial value just below the critical level. Between $\eta \cong 0.3H$ and $\eta \cong 0.5H$ the gradient is negative and large and causes the strong acceleration of the mean flow. Due to the wavelike structure of the profiles, other layers exist below this region with an accelerated or decelerated motion. At $t > 12t_{ref}$, the number of waves is increased and at $t > 24t_{ref}$, the shear stress is nearly uniform below the critical level. After the breaking event, the shear stress is heavily reduced and becomes negative in the formerly forced region. The reduction is much stronger in the LES than in the DNS. This means, the turbulent mixing (which now actually includes the third dimension) in the LES is much more efficient than the more or less two-dimensional regime of the DNS.

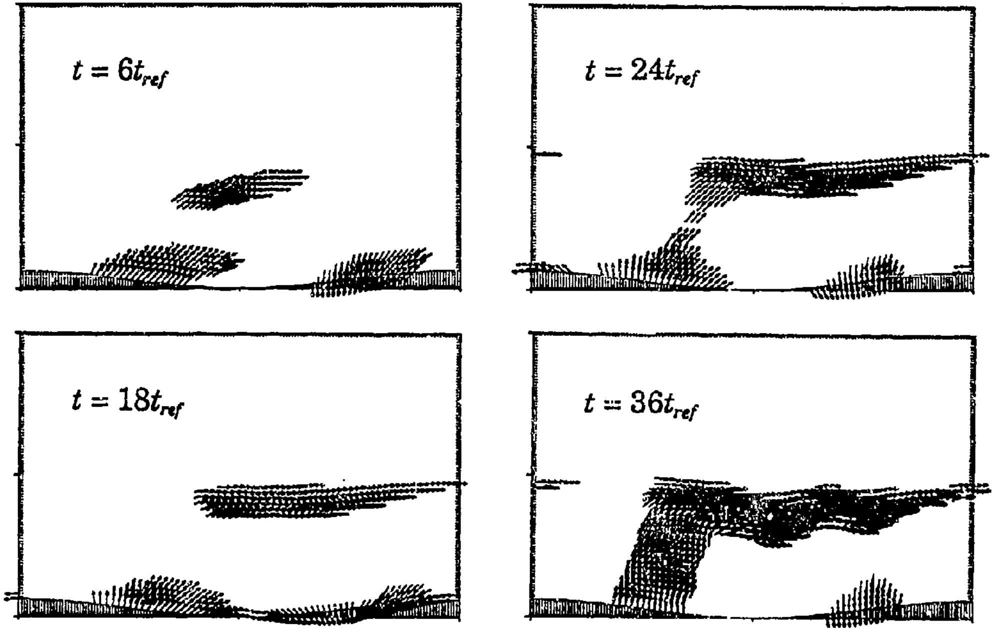

Figure 6. **Vertical cross-section** of the (u,w)-vectors at different times (DNS). The mean profile U(z) is subtracted from the local velocity field. Plotted are vectors of a magnitude from 0.05 to 0.2 U_{ref}. Same scale as in Fig. 1.

Fig. 6 shows the vector plots of the pertubation velocity field in a xz-plane at four different moments for the DNS. The direction of the vector arrows above the surface is upwards in the positive x-direction. Therefore, the vertically propagating wave carries small packets of positive momentum towards the critical level ($t = 6t_{ref}$). At the critical level the momentum is transferred to the mean flow causing its acceleration. The interaction between the fixed surface wave and the critical level (U=0) can be denoted as a kind of resonance. The critical level experiences a long lasting excitation due to the continious momentum deposition at just the position where the wave encounters the critical level ($t = 24t_{ref}$ and $t = 36t_{ref}$). At other levels the mean flow U(z) of the fluid prevents such an excitation.

We conclude that the differences in the flow evolutions due to different simulation techniques, namely DNS and LES, correspond to physical breaking events observable in a rather viscous fluid (as DNS) and in a fluid with small effective viscosity (as LES).

Acknowledgements

This work has been supported by the Deutsche Forschungsgemeinschaft.

References

Andreassen, Ø., 1993: *Numerical problems in gravity wave simulation* in: Coupling Processes in the Lower and Middle Atmosphere, E. V. Thrane et al. (eds.), Kluwer Amsterdam, pp. 219-231.

Booker, J. R., Bretherton, F. P., 1967: *The critical layer for internal gravity waves in a shear flow.* J. Fluid Mech. 27, 513-539.

Delesi, D. P., Dunkerton, T. J., 1989: *Laboratory observations of gravity wave critical-layer flows.* Pure Appl. Geophys. **130**, 445-461.

Dörnbrack, A., Schumann, U., 1994: *Numerical simulation of breaking gravity waves below a critical layer.* Proc. First ERCOFTAC Workshop on direct and large-eddy simulation, (P. Voke, ed.), Kluwer Academic Publishers, Dordrecht, Holland, in press.

Dunkerton, T. J., Robins, R. E., 1992: *Radiating and nonradiating modes of secondary instability in a gravity-wave critical layer.* J. Atmos. Sci. **49**, 2546-2559.

Koop, C. G., McGee, B., 1986: *Measurements of internal gravity waves in a continiously stratified shear flow.* J. Fluid Mech. **172**, 453-480.

Lin, C.-L., Ferzinger, J. H., Koseff, J. R., Monismith, S. G., 1993: *Simulation and stability of two-dimensional internal gravity waves in a stratified shear flow.* Dyn. Atmos. Oceans **19**, 325-366.

Nappo, C. J., 1991: *Sporadic breakdown of stability in the planetaray boundary layer over simple and complex terrain.* Boundary-Layer Meteor. **54**, 69-87.

Nappo, C. J., Chimonas, G., 1992: *Wave exchange between the ground surface and a boundary-layer critical level.* J. Atmos. Sci. **49**, 1075-1091.

Nastrom, G. D., Eaton, F. D., 1993: *The coupling of gravity waves and turbulence at White Sands, New Mexico, from VHF radar observations.* J. Appl. Meteor. **32**, 81-87.

Mobbs, S. D., Rabbitt, M. J., 1992: *A model for the turbulent breakdown of internal gravity waves.* in: Adv. in Turbulence **3**, Berlin, pp. 335-342.

Pao, Y., Goldburg, A. (Eds.), 1969: *Clear air turbulence and its detection.* Plenum Press, New York.

Sato, K., Woodman, R. F., 1982: *Fine altitude resolution radar observations of stratospheric layers by the Arecibo 430 MHz radar.* J. Atmos. Sci. **39**, 2546-2552.

Sidi, C., 1993: *Waves-turbulence coupling.* in: Coupling Processes in the Lower and Middle Atmosphere, E. V. Thrane et al. (eds.), Kluwer Amsterdam, pp. 291-304.

Thorpe, S. A., 1981: *An experimental study of critical layers.* J. Fluid Mech. 103, 321-344.

Winters, K. B., D'Asaro, E. A., 1989: *Two-dimensional instability of finite amplitude internal gravity wave packets near a critical level.* J. Geophys. Res. **94**, 12209-12719.

Winters, K. B., Riley, J. J., 1992: *Instability of internal waves near a critical level.* Dyn. Atmos. Oceans **16**, 249-278.

SIMULATED AND EXPERIMENTAL TWO-LAYER FLOWS PAST ISOLATED TWO-DIMENSIONAL OBSTACLES

Patrick F. Cummins
David R. Topham
Hugh D. Pite

Institute of Ocean Sciences
P.O. Box 6000
Sidney, British Columbia
Canada, V8L-4B2

ABSTRACT

Numerical simulations of unsteady, two–layer flows past an isolated two–dimensional obstacle are compared with laboratory measurements. Two numerical models are considered: a streamfunction–vorticity formulation valid for a Boussinesq fluid, and the SOLA–VOF coding for the primitive equations. A detailed model–data comparison of the interface position and drag force over a wide Froude number range is discussed. Inviscid runs with the streamfunction–vorticity model accurately simulate the upstream propagating disturbances and reproduce the interface displacement in the vicinity of the obstacle. Model drag forces from a Bernoulli calculation agree with experimental forces over part of the Froude number range considered. However, at higher Froude numbers the obstacle drag is underestimated by the model due to neglect of viscous effects. Simulations with SOLA–VOF are generally less accurate than with the vorticity–streamfunction model.

Mixing efficiency of decaying grid turbulence in a stratified fluid

Chris R. Rehmann and Jeffrey R. Koseff
Environmental Fluid Mechanics Laboratory
Department of Civil Engineering, Stanford University
Stanford, California 94305-4020, U.S.A.

ABSTRACT

We have studied the effects of the Richardson and Schmidt numbers on the mixing efficiency of decaying grid turbulence in a stratified fluid. A scaling analysis was used to predict how the efficiency should vary with the grid Richardson number Ri_0, and towed grid experiments were performed to verify some of the predictions. Experiments with salt and heat show that the Schmidt number has little effect on the efficiency over the range of Ri_0 considered, a result that can be explained by comparing mixing and decay time scales.

I. INTRODUCTION

One of the fundamental problems in the study of mixing in stratified fluids is to determine the mixing efficiency, or the fraction of the work done on the fluid that appears as a change in potential energy. Different forms of the efficiency are used, but we adopt a flux Richardson number based on the mean potential energy change ΔPE during a turbulent event and the total work W done on the fluid to create the event:

$$R_f = \frac{\Delta PE}{W} \tag{1.1}$$

Since dimensional analysis and simple physical arguments suggest that the efficiency can vary with the stability of the flow and possibly the stratifying agent, we review some of the previous studies of these effects and extend them with scaling and experiments.

Several studies have focused on the effects of stratification on the efficiency of turbulence generated by a grid towed horizontally through a linearly-stratified fluid. For weak stratifications, entrainment arguments (Linden 1979) and a gradient-transport analogy (Britter 1985) both yield

$$R_f \propto Ri_0 \tag{1.2}$$

where the grid Richardson number $Ri_0 = (NM/U)^2$, N is the initial buoyancy frequency, M is the grid mesh, and U is the grid speed. For stronger stratifications, Britter (1985) used results from a Lagrangian dispersion analysis and experiments to predict that

$$R_f \propto Ri_0^{1/2} \tag{1.3}$$

Data for $0.01 < Ri_0 < 0.8$ (Britter 1985, Rottman & Britter 1986) fit this relationship reasonably well, but the exponent of a power law fit to data for $3 \times 10^{-3} < Ri_0 < 8 \times 10^{-3}$ (Barrett and Van Atta 1991) falls between 0.5 and 1. The behavior for stronger stratifications is even less certain: Linden (1979, 1980) believes that since buoyancy forces will suppress the turbulence, the efficiency should decrease to zero, while Rottman & Britter (1986) propose R_f should approach a constant.

Since all of the previous grid towing experiments used salt to establish the stratification, less is known about the effect of the molecular diffusivity D of the stratifying agent. Oscillating grid experiments with a two-layer system (Turner 1968) showed that the entrainment rate for turbulence in heated water exceeds that for turbulence in salt water, but an argument based on the range of scales contributing to mixing suggests that Sc should have no effect when $Sc > 1$ (Ivey and Imberger 1991). In fact, mixing efficiencies based on rates of change of potential energy and work input are independent of the Schmidt number for all but the strongest stratifications (Ivey *et al.* 1994).

To unify previous predictions and explore the effects of strong stratification on mixing efficiency, we developed a scaling analysis that predicts four regimes of R_f-Ri_0 behavior, and to study effects of the Schmidt number, we compared time scales of mixing and decay. We performed towed grid experiments in heat-stratified and salt-stratified water to check the analyses.

II. THEORY

A. Scaling: relationship between R_f and Ri_0

To derive relationships between R_f and Ri_0, we relate the mean potential energy change to the vertical mass flux $\overline{\rho' u'_3}$ through the equation for the mean density and obtain an expression for R_f in terms of a vertical overturn scale and a decay time for the turbulence. We then examine four regimes of turbulence behavior to estimate the overturn scale and decay time.

1. General expression and scaling for the flux Richardson number

Computing the flux Richardson number from (1.1) requires estimates for the potential energy change and the work done by the grid. The change in mean potential energy,

$$\Delta PE = g\int_V x_3 \Delta\rho \, dV \tag{2.1}$$

where $\Delta\rho$ is the change in mean density, x_3 is the vertical coordinate, and V is the volume of the fluid, can be computed by multiplying both sides of the mean density equation by gx_3 and integrating over both the fluid volume and the duration of the mixing event. For turbulence generated by a grid towed in a rectangular tank with length L, width B, and depth H, we neglect mean flow and variations in horizontal directions and obtain

$$\Delta PE = gLB\int_0^\infty \left[\int_0^H \overline{\rho' u'_3}\, dx_3 + D(\rho(0,t) - \rho(H,t)) + H D \left.\frac{\partial \rho}{\partial x_3}\right|_{x_3 = H} \right] dt \tag{2.2}$$

The terms represent potential energy changes due to turbulence, diffusion of the density profile, and losses from the surface, respectively. If losses are negligible and the Peclet number UM/D is large, then

$$\Delta PE \approx gLB\int_0^\infty \int_0^H \overline{\rho' u'_3}\, dx_3 \, dt \tag{2.3}$$

Rottman and Britter (1986) used a similar expression to compute R_f from flux measurements.

We approximate the integrals in (2.3) by simply multiplying an estimate for the vertical mass flux by the depth and a time for decay of the turbulence T_D. The mass flux can be replaced with a restatement of the definition of the vertical flux correlation coefficient

$$\overline{\rho' u'_3} = R_{\rho w} \tilde{\rho} \tilde{u}_3 \tag{2.4}$$

where the tildes denote RMS values. If the horizontal length scale scales with the grid mesh and horizontal components of the turbulent velocity scale with the grid speed, continuity yields

$$\tilde{u}_3 \sim U \frac{h}{M} \tag{2.5}$$

where h is a vertical overturning scale. For all but very strong stratifications the RMS density fluctuation should scale as the product of the mean density gradient and the vertical overturn scale

$$\tilde{\rho} \sim h\left(-\frac{d\rho}{dx_3}\right) = h\frac{\rho_0}{g}N^2 \tag{2.6}$$

where ρ_0 is the mid-depth density. Then, since the work done by the grid can be found by multiplying the drag force F_D by the length of the tow L_t

$$W = F_D L_t = \frac{1}{2} C_D \rho_0 U^2 BHL_t \tag{2.7}$$

(where C_D is the grid's drag coefficient), we use (2.3) through (2.7) in (1.1) and ignore constants to obtain

$$R_f \propto R_{\rho w}\left(\frac{h}{M}\right)^2 NT_D Ri_0 \tag{2.8}$$

To relate the mixing efficiency to the grid Richardson number with (2.8), we must estimate the decay time T_D and the vertical overturn scale h. In the next section, we classify the behavior of the turbulence based on the stratification strength--or grid Richardson number, estimate the decay time and vertical overturn scale to compute the mixing efficiency from (2.8), and determine the values of Ri_0 for which the behavior should change.

2. Regimes

a. Regime I: Weak stratification

If there is no stratification, there is nothing to mix, and the efficiency must be zero. If the stratification is weak, the turbulence should be nearly isotropic and relatively unaffected by buoyancy. Thus, we assume that the vertical and horizontal scales of the eddies are equal ($h \sim M$), that the decay time scales as the eddy turnover time ($T_D \sim M/U$), and that the correlation coefficient is constant. Substituting these estimates in (2.8) yields

$$R_f \propto Ri_0 \tag{2.9}$$

which agrees with (1.2).

b. Regime II: Significant stratification

For cases with stronger stratification, we assume the turbulence is still nearly isotropic but account for buoyancy effects on the decay. Previous stratified turbulence experiments (for example, Barrett and Van Atta 1991) have shown that the decay time T_D is approximately π/N. Since buoyancy may also affect the correlation coefficient, we retain it and obtain

$$R_f \propto R_{pw} Ri_0^{1/2} \qquad (2.10)$$

If the correlation coefficient is independent of stratification, then Britter's result (1.3) is recovered.

We can determine when this regime begins by finding the value of Ut/M in an unstratified turbulence experiment (Comte-Bellot and Corrsin 1966) for which the same amount of decay (which we take to be the value of the streamwise turbulence intensity) has occurred as in the stratified turbulence experiments at $t = \pi/N$. This process suggests the transition between regimes I and II should occur when $Ri_0 = 4 \times 10^{-3}$.

c. Regime III: Strong stratification

When the stratification is so strong that vertical overturns are inhibited, the largest overturn scale h is the Ozmidov scale $L_O = (\varepsilon/N^3)^{1/2}$. Assuming an inertial estimate for dissipation $\varepsilon \sim U^3/M$ still holds--at least near the grid--and keeping the decay time estimate $T_D \sim N^{-1}$, we find

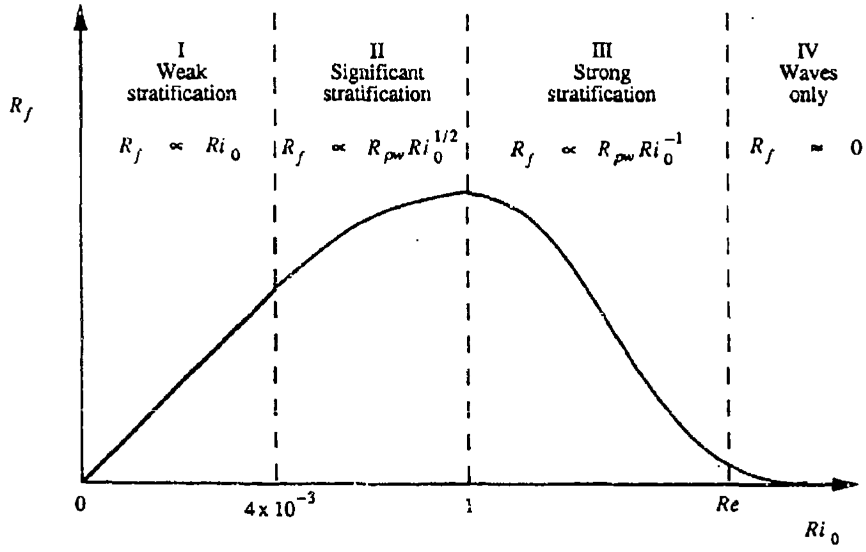

Figure 1. Schematic of the variation of the mixing efficiency with grid Richardson number and transitions between the regimes as predicted by the scaling analysis. The regime III behavior and high-Ri_0 boundary are based on an inertial estimate for dissipation. The scaling does not predict the magnitude of the efficiency.

$$R_f \propto R_{\rho w} Ri_0^{-1} \qquad (2.11)$$

If the dissipation does not depend on the grid mesh (that is, $\varepsilon \sim U^2 N$) then the exponent changes from -1 to -1/2. In either case, the scaling supports Linden's (1979, 1980) idea that the efficiency reaches a peak and decreases. Without detailed measurements in strongly stratified flows, we can say only that the peak should occur when $Ri_0 = O(1)$.

d. Regime IV: Waves only

When the stratification is so strong that the grid generates only waves, no mixing occurs, and the efficiency is zero. This regime should begin when no scales are turbulent, or when the Ozmidov and Kolmogorov scales are equal (see, for example, Gibson 1980)--that is, $Ri_0 = O(Re)$.

B. Time scale analysis

Although the scaling analysis in section II.A predicts the effect of stratification on the mixing efficiency, it does not give information on the effect of the Schmidt number. To investigate Schmidt number effects, we compare time scales of mixing and decay to determine whether mixing can occur before the turbulence decays. If the ratio J of the mixing time to the decay time is small, mixing occurs before the turbulence decays, and if J is large, the turbulence decays before mixing can occur. We consider only the $Sc > 1$ case here, although we have also analyzed the $Sc < 1$ case.

We model the mixing as a combination of two processes: stirring the scalar from the large scales to the small and diffusing the scalar across the small scales. For $Sc > 1$, the stirring also consists of two steps: stirring from the large scale L_ϵ to the Kolmogorov scale via the energy cascade and stirring from the Kolmogorov scale to the Batchelor scale L_B via small-scale straining. Estimates of the two stirring times from Broadwell and Breidenthal (1982) and Batchelor (1959), respectively, give a total stirring time

$$T_S = c_1 \frac{L_e}{\tilde{u}}(1 - Re^{-1/2}) + c_2 \frac{L_e}{\tilde{u}} Re^{-1/2} \log Sc \qquad (2.12)$$

where $Re = \tilde{u} L_\epsilon / \nu$ and the c_i's are constants. Combining (2.12) with the standard diffusion estimate $T_{MD} \sim L_B{}^2/D$ gives the total mixing time. For moderate stratifications ($Ri = (NL_\epsilon/\tilde{u})^2 < 1$), the ratio of the mixing time to the decay time ($T_D \sim N^{-1}$) is

$$J = \frac{T_S + T_{MD}}{T_D} = Ri^{1/2}\left[A_1 + Re^{-1/2}(A_2 + A_3 \log Sc)\right] \qquad (2.13)$$

where the A_i's are constants that can be found from data of previous experiments.

In this form, (2.13) cannot predict the mixing efficiency, but it does show how the Schmidt number--as well as the Reynolds and Richardson numbers--might affect the mixing. Since J depends on the logarithm of Sc, differences in mixing of heat-stratified water and salt-stratified water should be small for moderate stratifications. For stronger stratifications, when the largest overturning scale is the Ozmidov scale, a similar analysis shows that Schmidt number effects may become important when $\varepsilon/\nu N^2$ is small; results from numerical simulations (Ivey *et al.* 1994) support this prediction.

III. EXPERIMENTS

A. Procedures and equipment

To perform the experiments, a 4-m long, 0.8-m wide tank is filled to a depth of 0.35 m and stratified with linear distributions of either salt or heat. Initial density profiles are measured with a Precision Measurements Engineering model 125 temperature-conductivity probe. A wooden biplane grid with rectangular bars, 5-cm mesh, and 36% solidity is towed through the water at speeds between 4 and 20 cm/s to create turbulence, and the drag force on the grid is measured with a Western Load Cell force transducer and integrated over the tow length to obtain the work done on the water. After about five minutes, when the motions in the tank have decayed, the grid is towed again. After a set of four or eight tows, the fluid is allowed to settle for an additional twenty minutes before density profiles are measured at several locations along the centerline of the tank. The flux Richardson number is taken as the slope of the least-squares line fit to the potential energy change after *n* tows

$$(\Delta PE)_n = gB \int_0^L \int_{-H}^0 x_3(\rho_n - \rho_0)\,dx_3\,dx_1 \qquad (3.1)$$

(where ρ_n is the density profile after *n* tows) plotted against the total work done on the fluid.

The major uncertainty is due to heat losses. Losses are reduced by insulating the tank sides and bottom with 7.5-cm thick Styrofoam and heating and insulating the Plexiglas enclosure above the water surface. With these precautions, the ratio of the mass change in a profile to its initial value is less than 10^{-3}. Since we use (3.1) to calculate the potential energy change, any heat loss tends to decrease ΔPE. Estimates based on (2.2) suggest that this error can be from 1 to 20%.

B. Results

The results of our experiments resemble those from other experiments in several ways (figure 2). Most of the work done by the grid (more than 96%) is dissipated, and if the scaling analysis is correct and the efficiency decreases for higher Ri_0, then an efficiency of about 4% should be the maximum. Also, density profiles evolve as in other experiments: Turbulence causes a flux along the gradient, and near the top and bottom of the profiles, where the fluxes must vanish (at least approximately), mixed layers form. Additional tows cause the mixed layers to entrain fluid and erode the gradient zone.

Although the trends of the data from different experiments agree, the values can differ by as much as a factor of three. Reasons for this discrepancy include differences in grid geometry, drag coefficient estimates, and methods for computing the flux Richardson number. However, since the profile evolution depends on the boundary conditions, the most likely explanation is that the efficiency depends on the depth, or the length scale ratio H/M, which probably sets the mixed layer size. In fact, simply plotting the data against $Ri_H = (NH/U)^2$ collapses data from the different experiments to within 20% over most of the range. To suppress effects of H/M, we have used the same depth for every run shown in figure 2.

The data give some support to the scaling analysis. Power laws fit to our salt water data, heated water data, and data from Britter (1985) and Rottman & Britter (1986) for $5 \times 10^{-3} < Ri_0 < 1$ give exponents between 0.5 and 0.6. As long as the vertical flux correlation coefficient depends only weakly on the grid Richardson number, these results agree with the regime II scaling (equation 2.10). The high-Ri_0 boundary of regime II may be correct since the data for $Ri_0 > 1$ suggest that the efficiency has reached a peak; however, more data are needed to investigate both the high and low Ri_0 behavior more thoroughly.

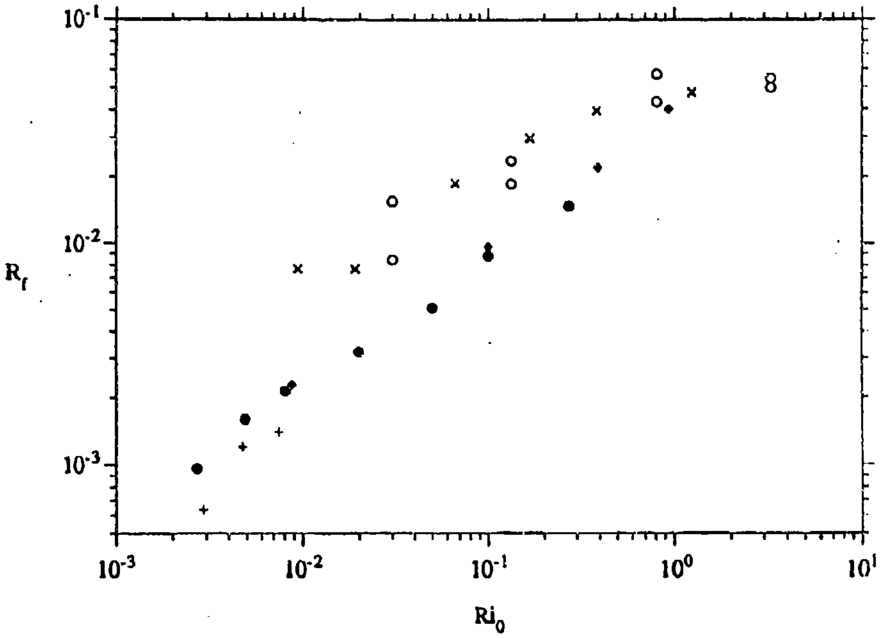

Figure 2. Effects of stratification and Schmidt number on the mixing efficiency.
♦ Present data--salt water, • Present data--heated water, o Britter (1985),
× Rottman & Britter (1986), + Barrett & Van Atta (1991).

For the range of grid Richardson numbers we have used, the effect of the Schmidt number is negligible--within the accuracy of our experiments. The efficiencies for heated water are up to 10% lower than those for salt water, but as we mentioned in section III.A, heat losses can reduce the potential energy change and R_f by up to 20%. Thus, the measurements agree with the suggestion of the time scale analysis that Schmidt number effects are small when $Sc > 1$.

IV. SUMMARY AND FUTURE WORK

We have examined effects of stratification and diffusivity of the stratifying agent on the mixing efficiency of decaying grid turbulence. We related the efficiency to the grid Richardson number by computing the potential energy change from the mean density equation and estimating the decay time and vertical overturn scale. Data from towed grid experiments suggest that the predictions for cases with significant stratifications (regime II) are approximately correct. The experiments also confirm the idea from a time scale analysis that effects of the Schmidt number are small when $Sc > 1$.

Future work includes investigating the behavior at higher and lower Ri_0, determining the dependence of the vertical flux correlation coefficient on Ri_0, and developing analytical work--including the time scale analysis and a linear theory--to predict the efficiency for the regimes not accessible with experiments. Once the simple case of grid turbulence is understood, the efficiency of phenomena more relevant to ocean mixing, such as breaking internal waves, can be studied.

V. ACKNOWLEDGMENTS

The work was supported by the U.S. Department of Energy. C.R.R. received support from an Office of Naval Research graduate fellowship.

VI. REFERENCES

Barrett, T.K. and Van Atta, C.W. 1991 Experiments on the inhibition of mixing in stably stratified decaying turbulence using laser Doppler anemometry and laser-induced fluorescence. *Phys. Fluids A*, 3(5), 1321-1332.

Britter, R.E. 1985 Diffusion and decay in stably-stratified turbulent flows. In *Turbulence and Diffusion in Stable Environments*, ed. J.C.R. Hunt, Clarendon, Oxford, 3-13.

Broadwell, J.E. and Breidenthal, R.E. 1982 A simple model of mixing and chemical reaction in a turbulent shear layer. *J. Fluid Mech.*, **125**, 397-410.

Comte-Bellot, G. and Corrsin, S. 1966 The use of a contraction to improve the isotropy of grid-generated turbulence. *J. Fluid Mech.*, **25**, 657-682.

Gibson, C.H. 1980 Fossil temperature, salinity, and vorticity turbulence in the ocean. In *Marine Turbulence*, ed. J.C.J. Nihoul, Elsevier, Amsterdam, 221-257.

Ivey, G.N. and Imberger, J. 1991 On the nature of turbulence in a stratified fluid. Part I: the energetics of mixing. *J. Phys. Ocean.*, **21**, 650-658.

Ivey, G.N., Koseff, J.R., and Imberger, J. 1994 Mixing in a stably stratified shear flow. submitted to *J. Phys. Ocean.*

Linden, P.F. 1979 Mixing in stratified fluids. *Geophys. Astrophys. Fluid Dyn.*, **13**, 2-23.

Linden, P.F. 1980 Mixing across a density interface produced by grid turbulence. *J. Fluid Mech.*, **100**, 691-703.

Rottman, J.W. and Britter, R.E. 1986 The mixing efficiency and decay of grid-generated turbulence in stably-stratified fluids. *9th Australasian Fluid Mech. Conf.*

Turner, J.S. 1968 The influence of molecular diffusivity on turbulent entrainment across a density interface. *J. Fluid Mech.*, **33**, 639-656.

STRATIFIED FLOWS IN URBAN SCALE ATMOSPHERE

SANDRINE ANQUETIN, CLAUDE GUILBAUD, JEAN-PIERRE CHOLLET
L.E.G.I., UJF-INPG-CNRS, GRENOBLE, FRANCE

Abstract. Urban air pollution problems may be analysed with a pronostic model, which is able to describe the evolution of the urban boundary layer, coupled with a dispersion model for chemically reacting pollutants, which takes into account all significant reactions. A code is developed on the basis of ARPS (University of Oklahoma), a 3D, nonhydrostatic model where fully compressible equations are solved with time-splitting procedure. The set of time dependent equations is dicretized in a general coordinate system, allowing a fine description of the terrain. Subgrid phenomena are parametrized with a subgrid-scale mixing coefficient for momentum and scalars from a Smagorinsky-Lilly closure scheme.

Test cases are carried out in order to analyse phenomenology and provide validation for constitutive elements of the model as regard dynamics evolution. Isolated hills are classicaly used to test the representation of a complex terrain as well as the production of large eddy recirculations and the production of orography induced wave. Various cases of stratification are considered and compared against known solutions.

Then, an idealized valley is simulated to highlight geographical effects on the local winds.

1. INTRODUCTION. The specific attention to the urban air quality is due to increasing photochemistry events especially in cities located in deep valleys. Among the various pollution sources, road traffic is usually the predominant one, associated with disadvantageous topographical and climatological characteristics of the city. The dynamics of the atmosphere above such sites is mainly governed by local thermal conditions with weak synoptic influence, and wind direction determined by the valley configuration. Pollution problems are mostly associated to low wind conditions, with significant stratification including often an inversion layer. Pollutants emitted into this inversion layer can build to high concentrations because of the trapping between the valley slopes, and can be harmful for people, animals, and plant life.

Because of the large structural, temporal, and spatial variability of the urban lower atmosphere, it appears that measurements will not suffice to assess and to predict the flow structure, the dispersion processes, and the air quality or pollutant contents, and their impact. The improvement of the knowledge of the combined physics and photo-chemistry of the urban atmosphere calls for the development of a new generation of numerical simulation codes taking into account natural complex terrain, modelized heterogeneous urban canopy, parametrized eddy mixing at subgrid scales and urban characteristic chemistry. The development of sub-meso scale models (i.e. scales up to 20 km, where the atmospheric flow is strongly influenced by the orography and the ground characterization) will allow to study the interactions of the city fabrics and urban sources of heat and pollutants, with the surrounding orography. This is a special importance for the cities located in valleys where the urban radiative budget interacts with the along-valley and katabatic cross-valley winds.

Such code is under development within a national collaborating project, on the basis of ARPS (Advanced Regional Prediction System, University of Oklahoma), a 3D, non hydrostatic model where fully compressible equations are solved with time splitting procedure. Although our code (ARPS-SM) is devoted to the simulation of the atmospherical dynamics within complex orography, a first step is dedicated to its validation on more simplified flows with well marked effects of buoyancy and where the geographical effects govern the local dynamic.

The flow over an isolated hill is the simpliest and the most studied atmospherical test case in which the buoyancy forces play a major role. The aim of this study is to analyse the gravity waves due to the displacement of air parcels above hill within a stably stratified atmosphere. These so-called mountain lee-waves have been observed in mountaineous regions all over the world and predicted by numerous codes (for example [4] and [11]). For various cases of stratification (characterized by the atmospherical Froude number) the predicted response of the atmosphere can be compared to both analytical solutions or previous numerical results, in order to validate the ARPS-SM code.

Beside this validation aspect, first results of simulation within a stylized valley hightlight the geographical effect on the development of local winds, and the trapping effect due to a specific atmospherical situation characterized by an inversion layer. This last configuration tends to represent the Isère valley located on the North-East part of Grenoble. As all deep valleys, the dynamics of the atmsophere is strongly influenced by the diurnal and complex evolution of the stratification.

2. THE SET OF EQUATIONS. At the sub-meso scales, the dynamic fields keep up with a mean anelastic continuity equation ($\partial(\rho U_i)/\partial x_i = 0.$). The density fluctuations act with a very small time constant to bring back the flow to a non divergent state. Therefore, the least accurate set of equations is the Boussinesq system, which will be a poor approximation unless the vertical scale is less than the density scale height. The Boussinesq system was probably the most used for atmospheric applications. But now with the new numerical developments and the new scales of interest, it is thus necessary to go further than the classical Boussinesq hypothesis to take into account of a more complete thermodynamic in order to simulate flows at sub-meso scales where the local density variations can be of the order of magnitude of the variations of the mean gradient.

The type of numerical solver is then dependent on the type of the physical restrained hypothesis. As we mentionned above the effect of acoustic waves is not relevant at our studied scales. Historically, nonhydrostatic model using anelastic equations [7] where sound waves are filtered out, were first put into practical use. In the late 1970s, along with the advancement of computer science and techniques of numerical computation, nonhydrostatic models using compressible equations where sound waves were not filtered out were developed and put into practical use. Tanguay et al. [12] treated the terms related to sound waves semiimplicitly in both the horizontal and vertical direction, whereas Klemp et al. [5] used a so-called "time splitting" technique in which the sound waves are explicitly time integrated. The interest of this last approach is the explicit formulation of the pressure which avoids the inversion of a complex matrix at each time step. Moreover, this technique is easier to be implemented on the parallel or vector computers.

2.1. The governing equations. The 3D non hydrostatic governing equations of ARPS-SM include the prognostic equations for momentum, pressure, potential temperature and the equation of state.

A base state (P_n, Θ_n, ρ_n) is defined to be horizontally homogeneous, hydrostatic and time invariant.

$$\begin{aligned} P(x,y,z,t) &= \Delta P(x,y,z,t) + P_n(z) \\ \Theta(x,y,z,t) &= \Delta\Theta(x,y,z,t) + \Theta_n(z) \end{aligned} \tag{1}$$

with $\partial P_n/\partial z = -\rho_n g$ and $P_n = \rho_n R \Theta_n \left(\frac{P_n}{P_o}\right)^{R/Cp}$. In this paper, U_i stands for the 3 components of the velocity, Θ is the potential temperature, P is the total pressure whereas ΔP is the perturbation pressure, ρ stands for the fluid density, c is the sound velocity, ν is the kinematic viscosity, R and Cp are the universal gas constant and the specific heat at constant pressure. f_i represents the Coriolis contribution terms within the momentum equations, whereas B_i stands for the buoyancy force. The source/sink term S_θ represents the contribution from radiation and any other heating/cooling process.

The $\langle\Phi\rangle$ variable denotes the large scale field of the variable Φ after the filtering operation using Δ as the characteristic length of the filter ($\Delta = (\Delta_x \Delta_y \Delta_z)^{1/3}$). The subgrid-scale field is noted ϕ. The variable Φ is thus substituted by $\Phi = \langle\Phi\rangle + \phi$ and the equations are written as :

$$\frac{\partial \langle U_i\rangle}{\partial t} + \langle U_j\rangle \frac{\partial \langle U_i\rangle}{\partial x_j} = -\frac{1}{\langle\rho\rangle}\frac{\partial \langle P\rangle}{\partial x_i} + \langle B_i\rangle + \langle f_i\rangle + \frac{\partial}{\partial x_k}\left(\nu\left(\frac{\partial \langle U_i\rangle}{\partial x_k} + \frac{\partial \langle U_k\rangle}{\partial x_i}\right) - \langle u_i u_k\rangle\right) \tag{2}$$

$$\frac{\partial \langle \Delta P\rangle}{\partial t} + \langle U_j\rangle \frac{\partial \langle P\rangle}{\partial x_j} = \langle\rho\rangle c^2 \left(\frac{1}{\langle\Theta\rangle}\frac{\partial \langle\Theta\rangle}{\partial t} - \frac{\partial \langle U_i\rangle}{\partial x_i}\right) \tag{3}$$

$$\frac{\partial \langle\Theta\rangle}{\partial t} + \langle U_j\rangle \frac{\partial \langle\Theta\rangle}{\partial x_j} = \frac{\partial}{\partial x_j}\left(-\langle u_j\theta\rangle\right) + \langle S_\theta\rangle \tag{4}$$

$$\langle P\rangle = \langle\rho\rangle R \left\langle \Theta \left(\frac{P}{P_o}\right)^{R/Cp} \right\rangle \tag{5}$$

Since the pressure is directly responsible for the mass balance in the system through the pressure gradient forces in the momentum equations (2), it should be accurately predicted. For this reason, the pressure is chosen over density as the prognostic variable and diagnose density from temperature and pressure (eq. 5). The pressure equation (3) is obtained by taking the material derivative of the equation of state and replacing the time derivative of density by velocity divergence using the mass continuity equation.

The determination of the subgrid scale turbulent fluxes (momentum $\langle u_iu_j\rangle$ and heat $\langle u_i\theta\rangle$) is based on the eddy viscosity concept calculated with the classical Smagorinsky/Lilly expression [9].

$$\langle u_iu_j\rangle = \frac{2}{3}k_{sg}\delta_{ij} - \nu_t\left(\frac{\partial\langle U_i\rangle}{\partial x_j}+\frac{\partial\langle U_j\rangle}{\partial x_i}\right), \text{ and } \langle u_i\theta\rangle = -K_t\frac{\partial\langle\Theta\rangle}{\partial x_i}$$

where :

* the subgrid-scale kinetic energy is defined with :

$$k_{sg} = 2\,(0.43\Delta)^2\left(\frac{\partial\langle U_i\rangle}{\partial x_j}+\frac{\partial\langle U_j\rangle}{\partial x_i}\right)^2$$

* the subgrid-scale eddy viscosity is parametrized as :

$$\nu_t = (0.21\Delta)^2\left\{\max\left(\left|\frac{\partial\langle U_i\rangle}{\partial x_j}+\frac{\partial\langle U_j\rangle}{\partial x_i}\right|^2 - N^2/Prt, 0.\right)\right\}$$

* the subgrid-scale eddy diffusivity is given by : $K_t = \nu_t/Prt$.

N and Prt stand for the Brunt Väisälä frequency and the turbulent Prandtl number respectively.

2.2. The numerical method. The governing equations are written in a curvilinear coordinate system (ξ,η,ζ) that is orthogonal in the horizontal plane. The spatial discretization uses a second-order quadratically conservative spatial differences on the Arakawa C-grid [1]. The time integration is totally explicit in time and is made by means of the so-called "time splitting" technique [5]. The equations are, therefore, split into sound-wave and gravity-wave components with sound wave components being time-integrated with a small time step, and remaining terms being evaluated with a large time step. The temporal discretization is carried out by the second-order leapfrog scheme with Asselin time filter [2] at each iteration on the big time step.

2.2.1. Boundary conditions. The ground is the only boundary associated with the mountain wave problem. We require the normal velocity to vanish at the surface.

The radiation boundary condition, which requires that all energy transport be directed out of the domain, is approximated at the upper boundary through the

Rayleigh damping. In the absorbing layer ($z_b < z < z_t$), only the perturbations of a variable from its upstream value are damped. The damping terms, which are added to the right-hand side of equations (2 and 4), are :

$$R_\Phi = \tau(z)(\Phi - \overline{\Phi}) \text{ with } \tau(z) = \alpha\left(1 - \cos\left[\pi\frac{z - z_b}{z_t - z_b}\right]\right)^{1/2}$$

The finite difference formulation requires lateral boundary conditions in which the inflow/outflow must be correctly parametrized. The lateral boundary conditions are similar to the wave permeable boundary conditions proposed by Orlanski [8]. The formulation of the phase velocity is based on the work published by Thompson [13].

2.2.2. Initial conditions. At the initial time, t=0., all the prognostic variables are initialized to the those defining the base state atmosphere.

3. DEVELOPMENT OF MOUNTAIN LEE WAVES. This part concerns the analysis of the different thresholds of mountain lee wave appearance over a 2D hill obtained with 3D simulations. The obstacle is defined by :

$$h(x) = \frac{h}{1 + (x/L)^2}$$

where h is the mountain height and L is the mountain half width at half-height. The atmospheric flow U at the inlet is uniform with height, and we consider the Brunt-Väisälä frequency N constant in the vertical section. At the scales of interest ($U = 5\ m/s, L = 2\ km$), the Rossby number ($R_o = U/fL$) is much greater than unity, therefore the Coriolis force within eq(2) is neglected.

The 2D test case is probably the most studied but not as clearly resolved. When we want to evaluate the atmospheric model performances, it is natural to choose a configuration for which linear and non linear analytical solutions have been obtained. We can thus validate our arbitrary decisions such as the numerical method, the initialization, the boundary conditions ...

The nondimensional height or Froude Number $F = Nh/U$ acts only as an amplitude factor in the linear theory [10] developed for not elevated relief ($Nh/U << 1$), whereas the nondimensional width NL/U gives the structure of the flow. For small value of this number, no energy is transferred in the vertical, the vertical perturbation is thus absorbed. For value around unity, non hydrostatic effects are well marked, the energy is propagated downhill and vertically. For higher value of NL/U, the energy is propagated straight up. We chose to validate the code on this last configuration described by an analytical expression. In fig. 1, the iso-Θ obtained from the analytical solution (a) and from the simulation (b) are compared. The height h is chosen in order to be within the scope of the hydrostatic hypothesis (i.e. $F << 1$, $F = 0.5$). The wave structure (wavelength and phase) is correctly predicted with a slight underestimation of the wave amplitude. The magnitude of the vertical velocity is higher in the simulation, which tends to amplify the velocity close to the ground. The results obtained by Stein [11] with the hydrostatic model PERIDOT show the same tendency.

The Long model [6] takes into account the non linear effects, and can thus predict the destabilization of the vertical potential temperature profile due to higher obstacle. The non linearities are directly responsible of the iso-Θ bending which can produce the destabilization of the initially stable vertical profile. The Froude number $F = Nh/U$ gives, in this case, the structure of the flow. This theory is valid for 2D flow, and uniform U and N profiles. The critical Froude number is determined as the wave breaking threshold, and found equal to 0.85 for a 2D bell mountain. This threshold has to be compared to the unity value predicted with the linear theory. Thus, the non linearities tend to break the wave for lower obstacle than the linear theory. For $F > F_{crit}$, the flow is subjected to important modifications. In fig. 2, we present the calculated longitudinal component of the wind and the iso-Θ for $F = 1.4$. We observe a strong increase of the wind close to the ground and, the creation and then the downhill propagation of a "hydraulic jump" predicted by the Long's theory. These modifications could be responsible of the storms (after [3]) such as the one in Boulder in 1972, with intense winds near the ground, and developed turbulence in altitude close to the wave breaking regions. For even higher hill (Fig. 3, results of the simulation for $F = 2.0$), the flux deceleration is more and more marked. The flux is then stopped onto the obstacle, the lower level air layers do not have enough kinetic energy to overcome the buoyancy force which tend to prevent them to get over the obstacle. This type of atmospherical situation can further intense photochemical episode by the pollution trapping upwind of the hill. The threshold of the air block can not be predicted by the Long's theory. Our results have been, then, compared with Stein [11] and show the same behavior.

4. VALLEY GENERATED LOCAL WINDS. Valleys create their own climates by containing and channeling airflow within their physical boundaries and by having different radiation budgets on their valleys slopes. It is important to study and understand valley microclimates, mainly in relation to air pollution and land use planning considerations. Very little previous work has been done in modeling strong inversion conditions within small valleys. For a first study, we have thus considered an idealized valley described in fig. 4. The initial conditions are that a zero wind flow atmosphere with a stable stratification ($N = 10^{-2}s^{-1}$) above the inversion layer initially located at $z = 1800m$. The west side of the valley is warmed up due to the solar radiation ($Q = 350W/m^2$), whereas the opposite slope is still subjected to the nocturnal radiative cooling ($Q = -300W/m^2$). These radiative fluxes are remained constant during the simulation. This simple configuration tends to reproduce the sunrise in the North-East valley of Grenoble. A more realistic study should take into account time-dependent radiative fluxes. Fig. 5 highlights some characteristics of local winds within a valley after two hours of simulated time. The differential solar heating of the valley slopes generate purely thermal effects such as the slopes winds (anabatic wind along the west side; and katabatic wind on the opposite side), and the along valley wind (also called drainage wind) due to the valley ground slope. The order of magnitude of these local winds is in good agreement with observations, i.e. 1 to 8 m/s.

5. **CONCLUSION.** Geographical effects have been validated on both theoritical analysis and experimental observations. Air pollution problem is essentially associated to the local climatology, and therefore to the terrain generated winds for cities located within complex terrain. The present results highlight the appropriateness of ARPS-SM to simulate air flow at urban scale. The future developments will deal with a better description of the nature of the ground (parametrization of the city), and the coupling with a simple dispersion model for chemically reacting pollutants which will take into account all significant reactions occuring in the considered area.

ACKNOWLEDGEMENTS. The simulations have been performed on the CRAYII of the Commissariat à l'Energie Atomique of Grenoble and on the C98 of the Institut du Développement et Des Ressources en Informatique Scientifique of the C.N.R.S. thanks to their attributed CPU time.

REFERENCES

[1] A. Arakawa and V.R. Lamb, 1977, Computational design of the basic dynamical processes of the UCLA general circulation model, *Methods in computational Physics*, **17**, Academic Press, 174-265.

[2] R.A. Asselin, 1972, Frequency filter for time integration, *Monthly Weather Review*, **100**, 487-490.

[3] T.L. Clark and W.R. Peltier, 1977, On the evolution and stability of finite amplitude mountain waves, *J. Atmos. Sci.*, **34**, 1715-1730.

[4] D.R. Durran, 1981, The effect of moisture on mountain lee waves, *Ph.D. Thesis*, MIT and NCAR.

[5] J.B. Klemp and R. Wilhelmson, 1978, The simulation of three-dimensional convective storm dynamics, *J. Atmos. Sci.*, **35**, 1070-1096.

[6] R.R. Long, 1954, Some aspects of the flow of stratified fluids. II experiments with a two fluids system, *Tellus*, **6**, 97-115.

[7] Y. Ogura and N.A. Phillips 1962, Scale analysis of deep and shallow convection in the atmosphere, *J. Atmos. Sci.*, **19**, 173-179.

[8] I. Orlanski, 1976, A simple boundary condition for unbounded hyperbolic flows, *J. Comp. Phys.*, **21**, 251-269.

[9] J. Smagorinsky, 1963, General circulation experiments with the primitive equations, *Monthly Weather Review*, **91**, 99-164.

[10] R.B. Smith, 1979, The influence of the Earth's rotation on mountain wave drag, *J. Atmos. Sci.*, **36**, 177-180.

[11] J. Stein, 1992, Contribution à l'étude des régimes hydrostatiques d'écoulements orographiques, *Ph.D. Thesis*, Université Paul Sabatier de Toulouse.

[12] M. Tanguay, A. Robert and R. Laprise, 1990, A semi-implicit semi-Lagrangian fully compressible regional forecast model, *Monthly Weather Review*, **118**, 1970-1980.

[13] K.W. Thompson, 1987, Time-dependent boundary conditions for hyperbolic systems, *J. of Comp. Physics*, 68, 1-24.

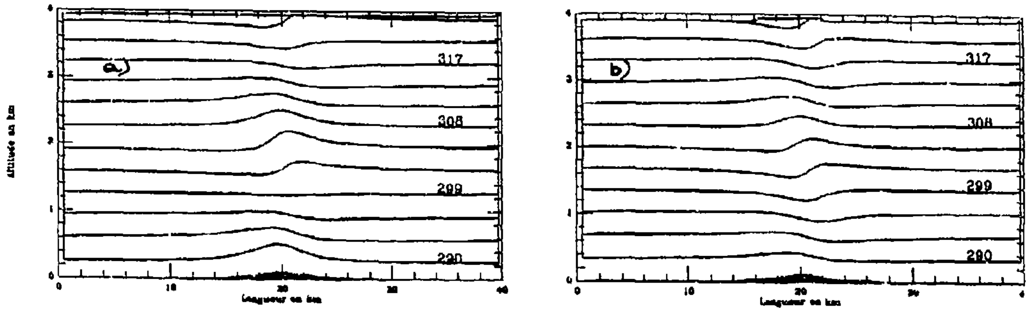

FIG. 1. *Iso-*$\Theta, F = 0.5, NL/U = 10.$, *a) analytical solution, b) simulation.*

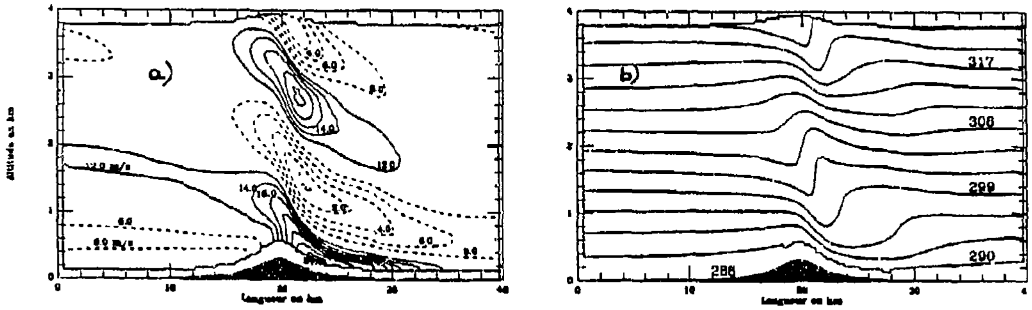

FIG. 2. *Breaking wave case,*$F = 1.4, NL/U = 10.$, *a) longitudinal velocity, b) iso-*Θ.

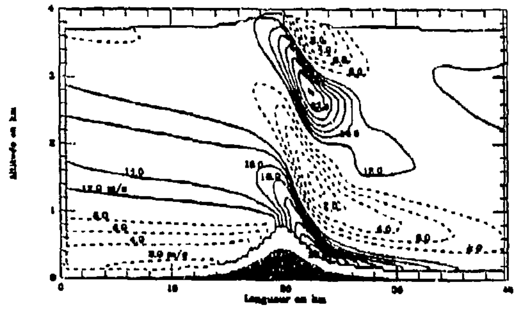

FIG. 3. *Blocked wave case,* $F = 2., NL/U = 10.$, *Longitudinal velocity.*

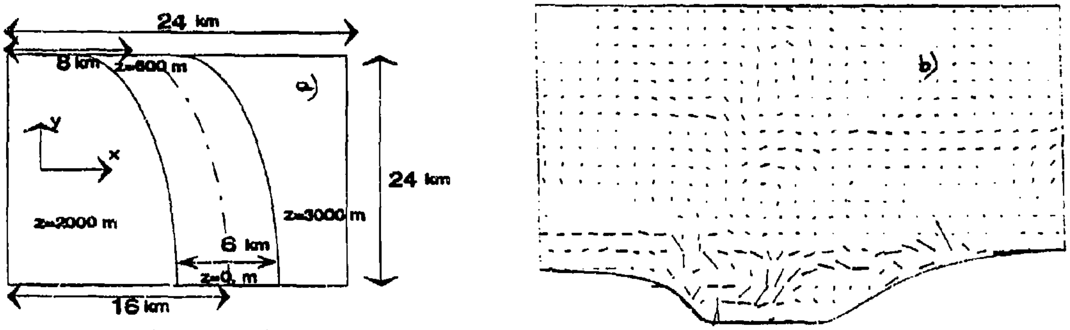

FIG. 4. *a) Configuration of the valley, b) Wind field within the valley*

The horizontal and vertical structure of the vorticity field in freely-decaying, stratified grid-turbulence

A.M. Fincham, T. Maxworthy & G.R. Spedding

Department of Aerospace Engineering, University of Southern California,
Los Angeles, CA. 90089-1191

Full field DPIV measurements of strongly stratified grid turbulence have been carried out for long times (up to Nt~1000). Quasi-2D vortices were formed that were separated vertically by strong horizontal vortex sheets. Dissipation scales were resolved and an attempt has been made to determine the relative dissipation fractions in the horizontal and vertical planes. A simple vortex model, involving a dense packing of *discus* shaped structures connected by vortex lines that alternate between horizontal and vertical orientation, is shown to be consistent with the observed velocity and vorticity fields as well as the ratio of the measured vorticity and length scales in orthogonal planes.

Introduction

In the low Froude number regime, one hypothesis for the approach to the final state of stratified turbulence characterizes it as a field of quasi 2D vortices the members of which grow in time by pairing, see Maxworthy, Caperan and Spedding [1987], Yap & Van-Atta [1993]. Many experiments, see the review of Hopfinger [1987], have characterized the initial collapse and the statistical properties at early times. Numerical simulations by Metais & Herring [1989], Lelong & Riley [1991] have more carefully examined the vertical structure, and the distribution of energy between wave and vortical modes. Experiments by Liu, Maxworthy & Spedding [1987], and Browand, Guyomar & Yoon [1987] have provided information on the vertical spacing of these vortical structures. Such structures are thought to model those found in a stratified ocean, where they would be interacting with mixing events covering a wide range of scales in both space and time. The present experiments provide data for comparison with numerical simulations and oceanic observations as well as for addressing the, as yet unanswered question concerning the importance of the vertical coupling between horizontal layers.

Experiments

The experiments were performed in a 2.4 m square tank that was linearly stratified to a depth of 15 cm with salt water. A rake of vertical flat-plates, of width W=3.8 cm and mesh spacing M=15 cm, was towed the full length of the tank. The vertical plates minimized internal wave generation and were chosen over rods as they provide a well defined separation point, independent of the towing speed. Stepper motors drove both the rake and a profiling conductivity probe used to measure the density gradient before and after each run. The good repeatability attained by this automated set up allowed the velocity fields in the horizontal and vertical planes to be measured in separate realizations of the same experiment. A high resolution Digital Particle Image Velocimetry (DPIV) system was developed. This system was carefully optimized to maximize the measurable range of scales and velocities by using a combination of simulated and experimental flows. Under optimum conditions the measured mean rms error on velocity is less than 2% (Fincham & Spedding [1994]). Fig.1 shows the experimental facility and the orientation of the measurement planes described below.

The measurements in the horizontal plane were made by densely seeding the central isopycnal with polystyrene beads of diameter~800 micron and density $1.0473<\rho<1.0477$ and lighting uniformly from above. This technique requires no light slice (or refractive index matching) and measurements of horizontal velocity were obtained on an isopycnal surface. Two CCD cameras were synchronized in time to simultaneously resolve both the small dissipation scales and the larger flow features.

Vertical plane measurements were made in a 20 cm x 15 cm rectangle located in the center of one end of the tank parallel to the rake. The fluid was seeded with micro-encapsulated Rhodamine particles of diameter ~50 μ. An oscillating mirror was phase locked to a single CCD camera and used to scan a thin vertical sheet of monochromatic laser light across the test area. This arrangement allowed effective pulsing of the light sheet without the complications associated with mechanical shuttering mechanisms.

Pairs of images were acquired direct to PC memory at 64 logarithmically spaced time steps over the typical 30 minute duration of each experiment. Over 6000 images were processed using a 2D spatial cross correlation to track groups of particles between image pairs. Each resulting velocity field was visually verified for "possible" wrong vectors before being fit with a 2D smoothing spline (Spedding & Rignot [1993]) and spectrally "flip-filtered" to remove grid scale fluctuations caused by pixel locking bias errors (Fincham & Spedding 1994). Horizontal and vertical data planes were adjusted to a common origin in time based on the location of the rake, statistical quantities could then be computed utilizing data from both planes. Due to the discrete sampling, it was often necessary to fit quantities from one plane with a continuous function of time so as to obtain values at times corresponding to measurements in the orthogonal plane.

Experiments were performed for towing speeds of 0.5, 1, 2, 4 and 8 cm/s and density gradients with buoyancy frequencies, N, of 1 and 2 rad/s. The initial Reynolds number (Re_M) range, based on the mesh spacing M, and Froude number (Fr) range, based on the bar width W, were $700 < Re_M < 12,000$ and $0.1 < Fr < 2$.

Results & Discussion

For a constant value of N, a noticeable change in horizontal and vertical structure was observed as the towing speed was increased. This was associated with the individual wakes of the rake bars undergoing a transition to turbulence. Even after long times these differences were still evident in the kinetic energy decay rates. A general description of the flow at low and high Reynolds number will be followed by a more detailed analysis of the viscous energy dissipation. Vortex interactions are then investigated with the help of a simple 3D vortex model.

General structure

At low Re_M [$O(10^3)$] a regular von Karman type of vortex shedding was observed in the horizontal plane. The structures formed in this way immediately grouped together in a complex sea of opposite-signed vortices, Fig.2(a),(b). There was an apparent transfer of energy to larger scales as vortices grew by pairing and diffusion until limited by the size of the tank, Fig.2(c). The shed vortices immediately became unstable in the vertical plane as can be seen from the inflections in the velocity profile in Fig.3(a); they quickly sheared apart producing multiple layers of eddies Fig.3(b). These layers were characterized by strong horizontal vorticity which has the sheet like appearance shown in Fig.3(c). Vertical interactions appeared to play a major role in the development of the flow and specific instances of merging of like signed vortex sheets were observed at all Reynolds numbers. At low speeds the vertical rake bars produced little vertical velocity, but the fluctuating rms velocities w and u decayed at the same rate, Fig.4(a). Horizontal length scales were computed from the integral of the longitudinal two-point velocity correlation function. This integral scale L_p was found to agree with a mean vortex diameter, D, computed from a vortex counting algorithm, Fig.5. A vertical length scale was obtained from averaged vertical power spectra of the horizontal component of vorticity. Vertical, transverse two-point velocity correlations indicated an approximately similar scale, which corresponded to some mean spacing of like signed bands of vorticity and is henceforth equated to the vortex thickness, T_v. Due to the small sampling area of the vertical light sheet the determination of this vertical scale was noisy and biased toward thicker bands (larger scales contain more energy in the spectra) but in general, it seems to agree quite well with that obtained from a manual counting method.

At higher Re_M [$O(10^4)$]the flow was initially fully turbulent immediately behind the rake bars. Coherent horizontal vortex structures emerged from the collapsing wakes as the vertical velocity component was suppressed by buoyancy forces. Quasi-2D vortex pairings were accelerated due to the shorter eddy turnover times and D initially grew more quickly than in the low Re runs, Fig.5. In the vertical plane the layers were well developed by the time of the first measurement, vertical overturning was evident and continued until the local minimum gradient Richardson number was greater than 1, Fig.6. Initially w decayed more quickly than u but after Nt~30 they both decayed at approximately the same rate, Fig.4(b). Shearing between layers was large and the horizontal rms vorticity ω_x was a factor of three times stronger than the vertical rms vorticity of the larger horizontal structures themselves ω_z.

Energy Decay

The rate of decay of kinetic energy per unit volume, $\dot{E}$, can be determined from a power law fit of the $E(t)$ data from both the horizontal and vertical planes. Decay rates varied from $t^{-1.4}$ to t^{-1} as Re_M was increased from 10^3 to 10^4. Energy was lost primarily to viscous dissipation and a small increase in the mean potential energy due to a buoyancy flux caused by small scale vertical mixing. Whitehead (1993), measured mixing efficiencies for a stratified tank stirred by a single cylindrical rod, and extrapolating from his data, it is estimated that less than 5% of the kinetic energy input by the rake is used for mixing. This is also consistent with our own conductivity measurements. Furthermore any such mixing will occur in the very early stages of the experiment right behind the grid, before our data acquisition process has started. Other losses due to friction on the side walls and floor of the tank, cannot be avoided but are believed to be small.

Viscous dissipation due to in-plane velocity gradients can be computed from the strain rate tensor, s_{ij}, where dissipation due to gradients in a plane normal to the unit vector, $\hat{k}$, is given by:

[1] $$\varepsilon_k = -2\nu\overline{s_{ij}s_{ij}} \qquad i,j \neq k \qquad \text{where} \quad s_{ij} = \tfrac{1}{2}\left(\frac{\partial u_i}{\partial x_j}+\frac{\partial u_j}{\partial x_i}\right).$$

For *isotropic homogeneous* turbulence, pure straining can be related to simple shear by,

$$\overline{\left(\frac{\partial u}{\partial x}\right)^2} = \tfrac{1}{2}\overline{\left(\frac{\partial v}{\partial x}\right)^2} = \tfrac{1}{2}\overline{\left(\frac{\partial w}{\partial x}\right)^2} \qquad \text{[Batchelor (1953) pg. 110],}$$

and from continuity,

$$\overline{\left(\frac{\partial u}{\partial x}\right)^2} = -2\overline{\frac{\partial u}{\partial y}\frac{\partial v}{\partial x}} \qquad \text{[Lamb (1932) pg. 580],}$$

hence, the total dissipation ε_{tot} can be expressed in terms of $\overline{\left(\frac{\partial u}{\partial x}\right)^2}$, and the in-plane velocity gradients will account for approximately $\frac{7}{15}$ th's of the total energy dissipation.

The peaks in the dissipation spectra were fully resolved in both horizontal and vertical planes so that all dissipation scales are accounted for. In-plane dissipations ε_x and ε_z were computed from [1] for different Reynolds numbers. At low Re_M the gradients in the horizontal plane account for slightly over 20% of the total energy decay ($\dot{E}$); this fraction is quickly reduced to less than 5% with increasing Re_M. Due to isotropy in the horizontal plane $\varepsilon_x = \varepsilon_y$ and the total viscous dissipation ε_{tot} can be expressed as:

$$\varepsilon_{tot} = \varepsilon_z + 2\varepsilon_x - 2\left[\overline{\left(\frac{\partial u}{\partial x}\right)^2} + \overline{\left(\frac{\partial v}{\partial y}\right)^2} + \overline{\left(\frac{\partial w}{\partial z}\right)^2}\right]$$

At higher Re_M vertical shearing increases, $\overline{\left(\frac{\partial u}{\partial z}\right)^2}$ accounts for over 90% of ε_{tot}, and

$$\varepsilon_{tot} \approx 2\varepsilon_x \approx 2\overline{\left(\frac{\partial u}{\partial z}\right)^2} \approx \dot{E} \qquad \text{(see Fig.7.)}$$

The relatively slow decay of these stratified flows at high Reynolds numbers, relative to the isotropic homogeneous case $E \sim t^{-1.5}$, is directly related to a break-down of the isotropic dissipation mechanism. Strong anisotropy in the strain field results as the rapid growth of horizontal scales separates horizontal and vertical velocity gradients in wave-number space.

In these types of flow it appears that the energy is contained in oblate-spheroidal or *discus* shaped structures, but is being dissipated in thin horizontal shear layers at their borders. The smoothness of the vorticity fields, shown in Figs. 2 & 3, indicates a continuum of structures that densely fill the volume. This suggests a vortex packing in which vortex lines can connect a number of structures, as they meander through the fluid and eventually form closed vortex loops. Vertical vorticity is bent horizontally in the high shear regions, these dissipative vortex sheets can then connect with neighboring structures on either side, Fig.8. This tendency, for vortex lines to connect to adjacent structures, helps explain why we do not observe the strong, isolated vortices often found in numerical simulations of 2D turbulence, see for example McWilliams [1984].

A consequence of this model is that on average the total vertical-flux of vorticity through a central, horizontal area within a structure, should be equivalent to the total horizontal-flux of vorticity through a circular strip around its upper or lower half, see Fig.9.

Hence, on average:

$$[2] \qquad \overline{\omega_z}\,\pi\left(\frac{D}{2}\right)^2 \approx \overline{\omega_x}\,\pi D\frac{T_v}{2} \qquad \text{or} \qquad \frac{\overline{\omega_z}}{\overline{\omega_x}} \approx 2\frac{T_v}{D}$$

Where D and T_v are the mean diameter and thickness of the structures, respectively. This appears to be a reasonable approximation that is independent of time, see Fig.10.

Conclusions

The hypothesized two-dimensionality of collapsed stratified flows has been re-examined in the light of the observation that strong, vertical shearing exists between horizontal layers, and the requirement that vortex lines form closed loops. This suggests a complex 3D network of structures in which layers of eddies cannot evolve independently of one another. The velocity fields generated by the simulations of Metais & Herring [1989], see their fig.22(b), in which the flow is initially dominated by the vortical component, have some qualitative similarities to our measurements and a more detailed comparison involving 3D eddy structures themselves should be made. No attempt has been made here to decouple wave and vortex modes. Since we believe that meso-scale eddies in the ocean and stratosphere exhibit similar interactions to those observed here, our measurements can be used to identify the locations and dynamics of these sources of strong, local dissipation.

Acknowledgments

We gratefully acknowledge support from the ONR Fluid Mechanics Program under contract no. NOOO14-J-92-1062.

References

Browand, F. K., Guyomar, D. & Yoon, S. C.;1987: The behavior of a turbulent front in a stratified fluid. *J. Geophys. Res.*, **92**, 5427-5433.

Fincham, A. M.; Spedding, G. R.; 1994: Low cost high resolution DPIV for turbulent flows. *Exp. Fluids*, (manuscript in preparation).

Hopfinger, E. J.; 1987: Turbulence in stratified fluids: a review. *J. Geophys. Res.*, **92**, 5287-5303.

Lelong, M. P., Riley, J. J.; 1991: Internal wave-vortical interactions in strongly stratified flows. *J. Fluid Mech.*, **232**, 1-19.

Liu, Y. N., Maxworthy, T. & Spedding, G. R.; 1987: Collapse of a turbulent front in a stratified fluid. *J. Geophys. Res.*, **92**, 5427-5433.

Maxworthy, T., Caperan, P. and Spedding, G.R., 1987, The kinematics of quasi-2D, freely decaying turbulence in a stratified fluid. Third International Symp. on Strat. Flows, Pasadena, CA.

McWilliams, J.; 1984: The emergence of isolated coherent vortices in turbulent flow. *J. Fluid Mech.*, **146**, 21-43

Metais, O.; Herring, J. R.; 1989: Numerical simulations of freely evolving turbulence in stably stratified fluids. *J. Fluid Mech.*, **202**, 117-148

Spedding, G. R.; Rignot, E. J. M.; 1993: Performance analysis and application of grid interpolation techniques for fluid flows. *Exp. Fluids*, **15**, 417-430

Whithead, J. A.; 1993: Stirring a stratified fluid- energetics and layer generation. (submitted to *J. Fluid Mech.*)

Yap, C. T., Van Atta, C. W.; 1993: Experimental studies of the development of Quasi-2-dimensional turbulence in a stable stratified fluid. *Dyn. Atmos. Oceans*, **19**, 289-323

Figures

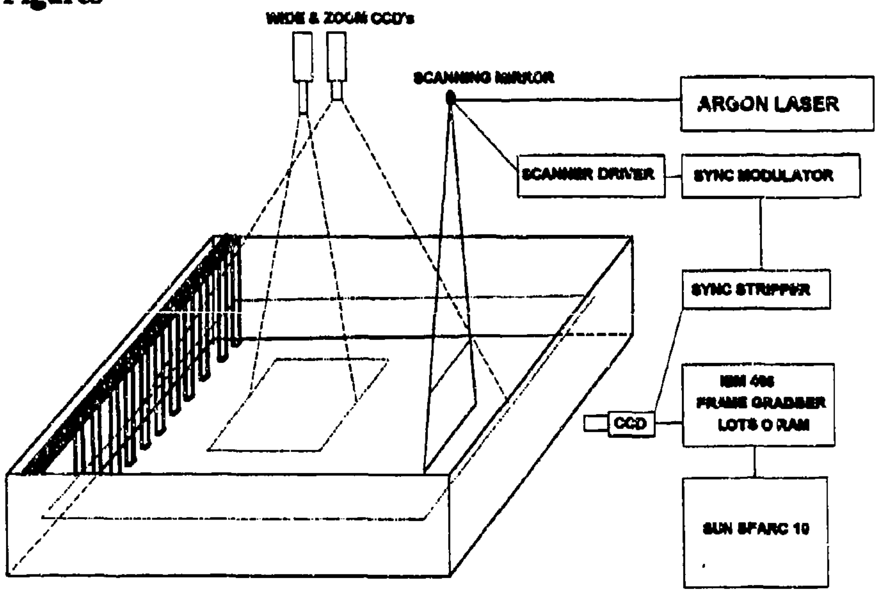

Fig. 1 Experimental configuration

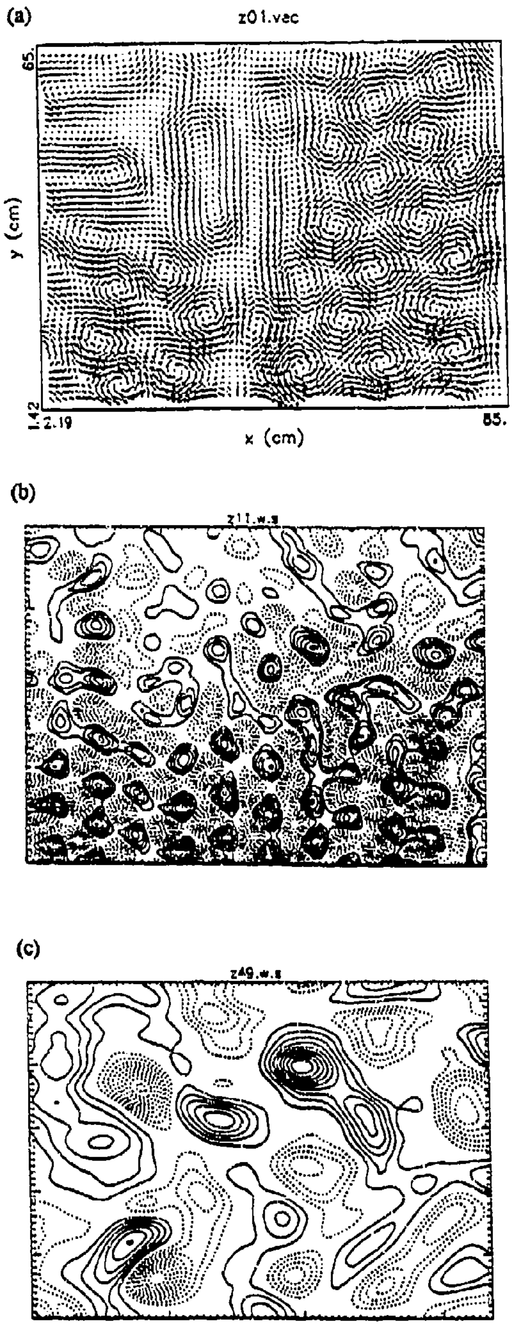

Fig. 2: Horizontal plane, Re_M=760, N=2.3 rad/s (a) Velocity from close-up camera, t=93 s. (b) ω_z from wide-angle camera t=190 s. Area is 170x140 cm. (c) ω_z from wide-angle t=1260 s.

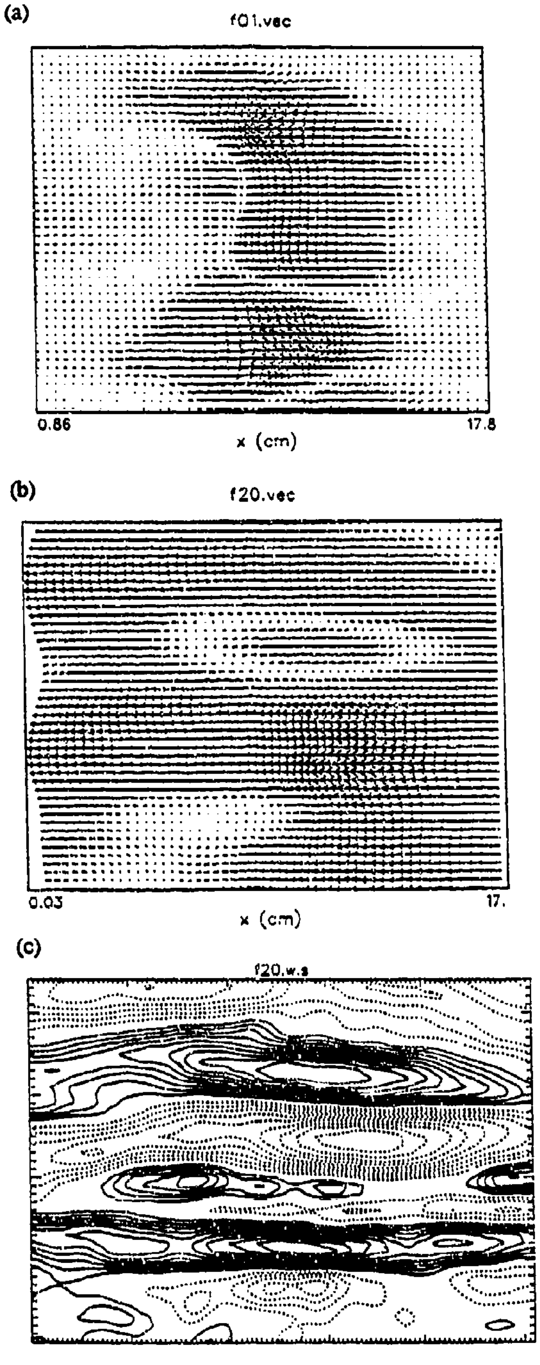

Fig. 3: Vertical slice Re_M=760, N=2.3 rad/s (a) Initial instability, t=4 s. (b) Formation of layers, t=86 s. (c) ω_z for t=86 s.

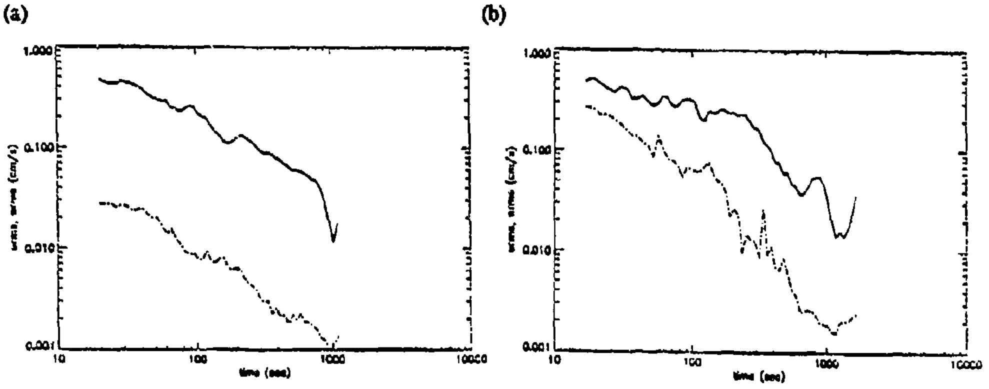

Fig. 4 Decay of u & w fluctuating velocities. (a) Re=1520, N=2.3 decay rates are similar and the ratio w/u ~ const. (b) Re=6000, N=1.05 after an initial collapse they decay at similar rates.

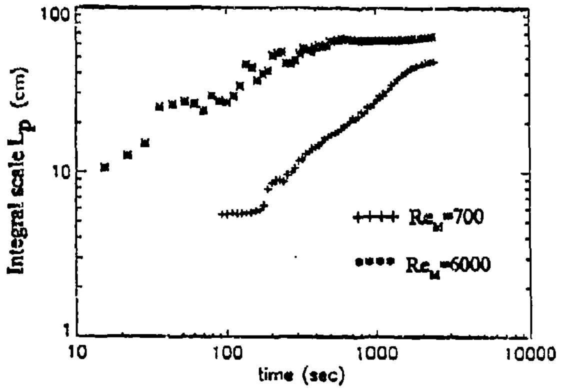

Fig. 5 Growth of integral scale L_p for differnt Re_M. The average vortex diameter D is very close to L_p.

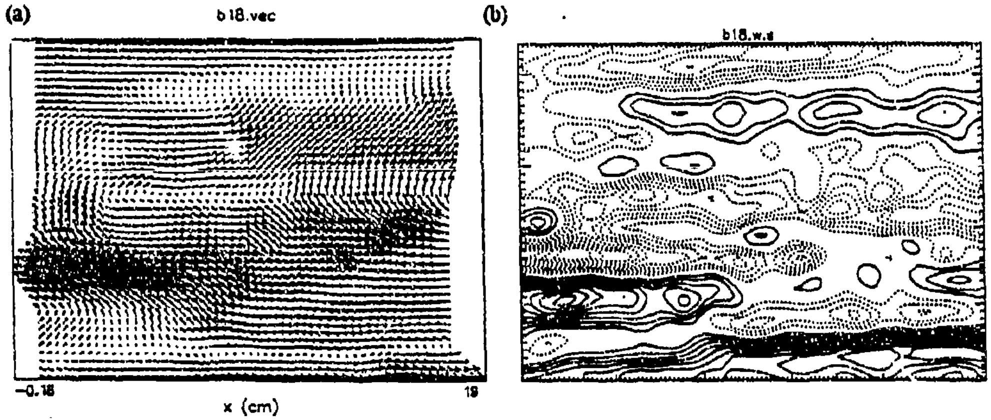

Fig. 6 At higher Re_M vertical overturning appear to be present for long times, even after the local minimum value of the Richardson number defined using the largest shear in the field, is greater than 1. Here Re_M=12,000, N=2.3, Ri_{min}~4 and t=85 s. (a) velocity (b) vorticity.

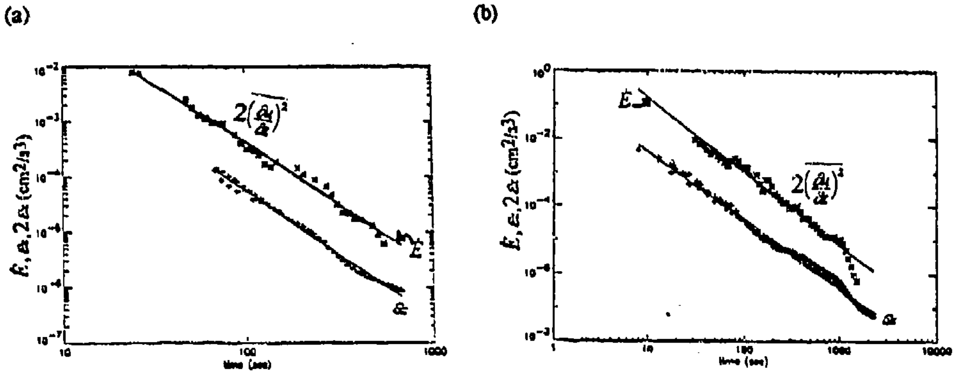

Fig. 7 Total energy decay rate $\dot{E}$, horizontal-plane dissipation ε_h and $2\overline{\left(\frac{\partial u}{\partial z}\right)^2}$ vs time for (a) $Re_M=1500$, $N=1.05$ rad/s. (b) $Re_M=6000$, $N=2.3$ rad/s. The total energy decay $\dot{E}$ can be accuratly described by $2\overline{\left(\frac{\partial u}{\partial z}\right)^2}$

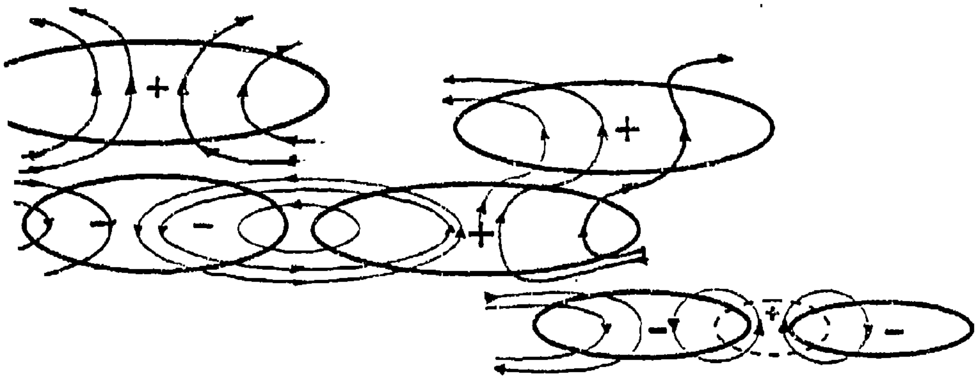

Fig. 8 Schematic of possible vortex line connections between adjacent structures.

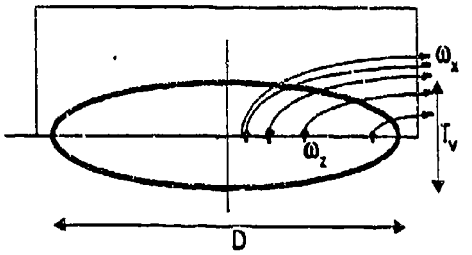

Fig. 9 Vertical section through a structure indicating the areas used for the vorticity flux calculation in eqn (2).

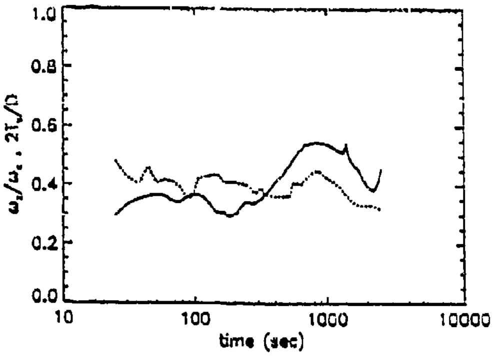

Fig. 10 Ratios of vorticity and length scales for an average structure, corresponding to eqn. (2) & Fig. 9.

Fourth International Symposium on Stratified Flows, Grenoble, June 1994

STABILITY OF A LATERALLY CONFINED ROUND PLUME

by

Wai-tak Lee and Joseph Hun-wei Lee
Department of Civil and Structural Engineering
The University of Hong Kong, Hong Kong

ABSTRACT: We study experimentally the mixing of a vertical round buoyant jet discharging inside a concentric enclosure of diameter D_r and height H_r before release into a large stagnant ambient fluid. The flow characteristics are found to depend on a confinement index $\beta = H_r/(D_r - D)$, where D is the jet diameter: i) for $\beta \gg 1$, a highly confined jet with negligible dilution inside the enclosure; ii) for $\beta \rightarrow 0$, a free buoyant jet; and iii) for $1.5 < \beta \leq 2.8$, an unstable vertical jet resulting in a swirling wall-attached plume. The swirling frequency of the unstable plume and the effect of the confinement on plume mixing are discussed.

1. INTRODUCTION

Wastewater is often discharged into shallow coastal waters as a series of adequately-spaced turbulent buoyant jets from a submerged multiport diffuser. By virtue of the jet momentum and buoyancy, rapid mixing of the effluent with the ambient sea water can be achieved. In some designs, the outfall pipeline is laid in a dredged trench, and the sewage jet discharges inside a protective riser tube before release at the sea bed level into the surrounding sea (Fig.1a). For example, in Hong Kong the typical depth of the dredged trench is 3 m, with a jet diameter of 0.1 – 0.15 m. The diameter of the concentric enclosing riser tube, however, is typically only 2 – 4 times the jet diameter. Whereas the mixing of a free round buoyant jet in still water has been extensively studied, and reliable initial dilution predictions can be made (e.g. Fischer *et al.* 1979; Muellenhoff *et al.* 1985), the effect of such a lateral confinement on the mechanics of a buoyant jet has hitherto not been studied.

We study experimentally the mixing characteristics of a round buoyant jet (nozzle diameter D) that issues vertically inside a concentric enclosure (diameter D_r) of height H_r (Fig.1b). The discharge jet velocity, density and tracer concentration are W_j, ρ_j and C_j respectively. At the end of the lateral confinement the mixed fluid enters a large, otherwise stagnant, receiving water body with ambient density ρ_a and tracer concentration C_a. The scalar field of the confined plume is measured. The observed behaviour of the buoyant plume, in particular the occurrence of a swirling plume for a certain range of confinement, is presented herein. The effect of the confinement on the initial dilution is also discussed.

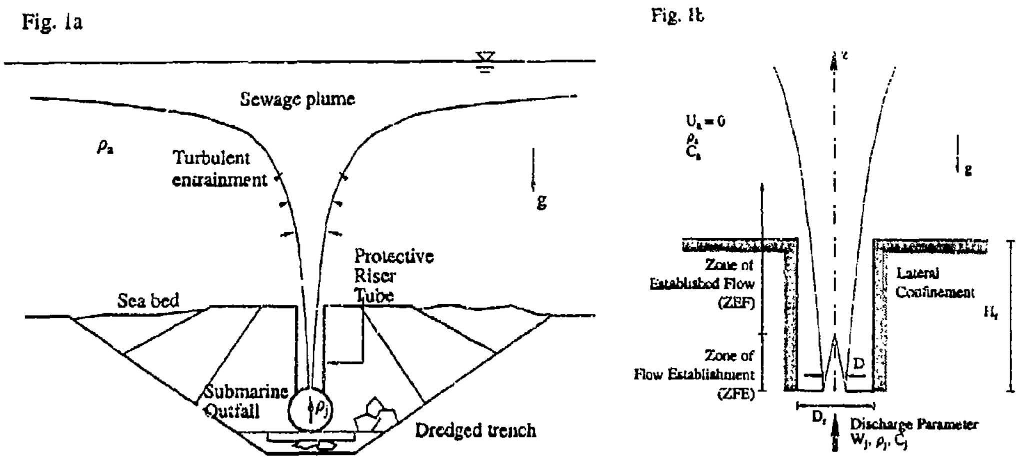

Figure 1: a) A round plume discharges inside a riser tube of a submarine sewage outfall; b) Schematic diagram of a vertical buoyant jet in lateral confinement.

2. EXPERIMENTS

Dimensional analysis shows that a characteristic scalar concentration C at an elevation z above the source is governed by:

$$\frac{C_j}{C} = f(Fr = \frac{W_j}{\sqrt{\frac{\rho_a - \rho_j}{\rho_a} g D}}, \frac{z}{Fr\, D}, \frac{H_r}{D}, \frac{D_r}{D}) \qquad (1)$$

where Fr is the jet densimetric Froude number. Further, our results suggest that the last two parameters can be combined to form a *confinement index* β defined as $H_r/(D_r - D)$.

A comprehensive series of experiments have been performed with a vertical laterally confined heated jet with diameter $D = 8 - 12\,mm$, $Fr = 3 - 15$, $D_r/D = 2.6 - 18$, and $H_r/D = 15 - 30$. The combination of these parameters covered a wide range of confinement geometry. Tests in otherwise stagnant ambient were carried out both in i) a 1 m × 1 m by 0.5 m deep water tank with constant depth and a cold inflow supply for jet entrainment, and ii) a 10 m × 6 m by 0.8 m deep shallow water basin. In each experiment, the radial temperature distribution at different elevations above the riser was measured to an accuracy of 0.1 °C by an array of calibrated Fenwal UUA35J1 thermistor probes (response time 0.5 s). The mixing pattern and ambient water intrusion into the riser tube were visualized by shadowgraph and laser-induced fluorescence (LIF) techniques. In cases when a swirling plume is observed (see later discussion), the swirling frequency was also determined from the temperature time history at 4 equi-distant radial positions around the circumference of the riser exit, $z = H_r$. The wall pressure at the inside base of the riser tube was also measured. A total of 159 experiments, which include some tests with a uniform crossflow, have been performed. Details of the experimental set up and run parameters can be found in Lee (1993).

3. RESULTS AND DISCUSSION

3.1 Observations of the Laterally Confined Plume

Both the flow visualization and the scalar field measurement show that the behaviour of the buoyant jet varies considerably under different confining situations. The flow characteristics can be categorized using the confinement index β.

Highly confined buoyant jet

When the confinement index is large ($H_r/D \gg 1$ *or* $D_r/D \to 1$), say $\beta \geq 10$, the buoyant jet is highly confined. Fig. 2 (a) and (b) show two highly confined jets, one at high Froude number (> 10) and the other at low Fr (< 10). The jet mixes with the water inside the riser as it rises by virtue of its initial momentum and buoyancy. The jet increases its width and quickly hits the riser wall. Eventually, the mixed effluent fills up the whole riser, with virtually no dilution; the nearly undiluted effluent discharges into the ambient fluid from the riser exit, which acts as a bigger nozzle.

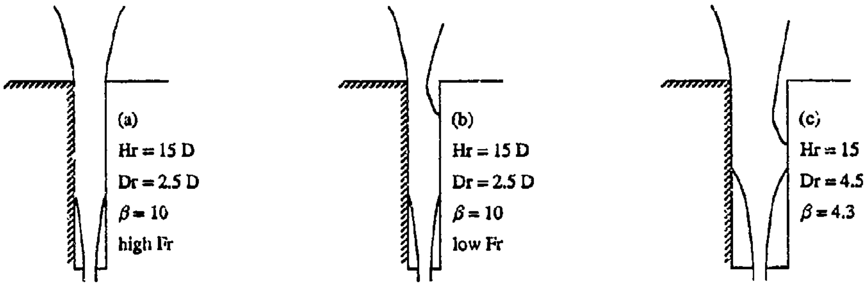

Jet fills up the riser completely

At low Froude number, intrusion occurs sporadically.

Extent of intrusion increases as β decreases.

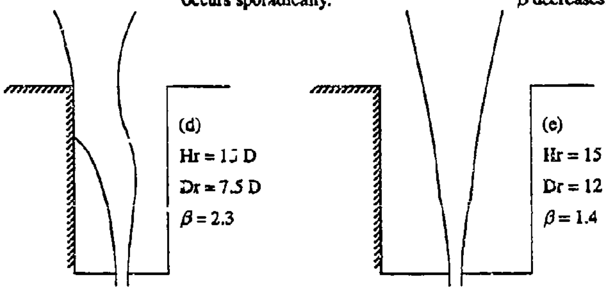

At sufficient small β, the plume attachs to the wall and swirls within the riser.

Confinement has no effect on the buoyant jet.

Figure 2: Flow pattern of a laterally confined buoyant jet at different confinement geometries, (a) highly confined jet at high Fr; (b) highly confined jet at low Fr; (c) moderately confined jet; (d) unstable confined jet; and (e) weakly confined jet.

If we define a riser Froude number Fr^* (based on the average velocity at the riser exit and the riser diameter), then for $Fr^* \gg 1$, no ambient water intrudes into the riser since the inertia force of the jet outweighs the buoyant force (Wilkinson 1988). As the discharge decreases, and $Fr^* \approx 1$, sporadic but minor incipient intrusion occurs. As the jet discharge decreases further, the ambient fluid penetrates deeper into the riser and a counter flow is established. If we assume that there is no dilution within the confinement, $Fr = Fr^*(D_r/D)^{2.5}$; for example, if $D_r/D = 2.5$, Fr should be at least 10 to avoid intrusion into the riser. As the diameter ratio increases, higher jet Froude number is required to prevent intrusion.

Moderately confined buoyant jet

As β decreases (D_r/D increases or H_r/D decreases) the flow pattern is similar to that of the highly confined jet, except that the extent of intrusion is greater (Fig.2c); dilution of the effluent starts within the riser. At given Fr, the amount of dilution achieved within the riser will be greater for smaller β. When D_r is large compared to the jet width of the corresponding unconfined buoyant jet at the level of riser exit, significant intrusion occurs and the ambient water descends even to the near bottom of the riser before it is entrained into the buoyant jet. This downward current together with the ascending buoyant jet produces a vigorous shear layer which enhances entrainment and mixing.

Unstable confined buoyant jet

For $1.5 < \beta \leq 2.8$, an interesting circumferential instability is observed. The buoyant jet is always deflected to the riser wall instead of remaining at the axis of symmetry. Once instability occurs, the plume remains attached to the riser wall and swirls around within the riser at a distinct frequency (Fig.2d). Fig.3 shows LIF images (digitized and post-processed to enhance quality) of the centre plane of the swirling plume as well as the moderately and highly confined plumes. The intrusion of the outside ambient fluid into the riser and the deflection of the swirling plume can be clearly observed.

This phenomenon is illustrated in Fig.4 for four experiments with $\beta = 3.6, 2.1$ & 1.7, and 1.5 (corresponding to the moderately confined, unstable, and weakly confined situations). For each experiment, the time-history of the temperature recordings at four sampling points located around the circumference of, and slightly above the riser exit, $z = H_r$, is shown along with the power spectrum. The signal peaks and troughs represent respectively stages of passage of the swirling buoyant heated plume and intruding cold ambient water.

For $\beta = 3.6$, Fig.4 shows that the ambient water intrudes into the riser randomly. However, when the vertical plume is unstable, as illustrated by $\beta = 2.1$, it is clear the wall-attached plume rotates within the riser at a distinct frequency. The signals at the four stations indicate a definite sequence of peaks; in this case the direction is anti-clockwise – i.e. W,S,E, and N; whenever a peak is observed at a particular point, a trough is also observed at the diametrically opposite station. When β decreases further to 1.7, instability is still observed, although the fluctuations within each peak increase. There is no apparent preferred direction of rotation; both clockwise and anti-clockwise rotation have been observed even for experiments with the same β.

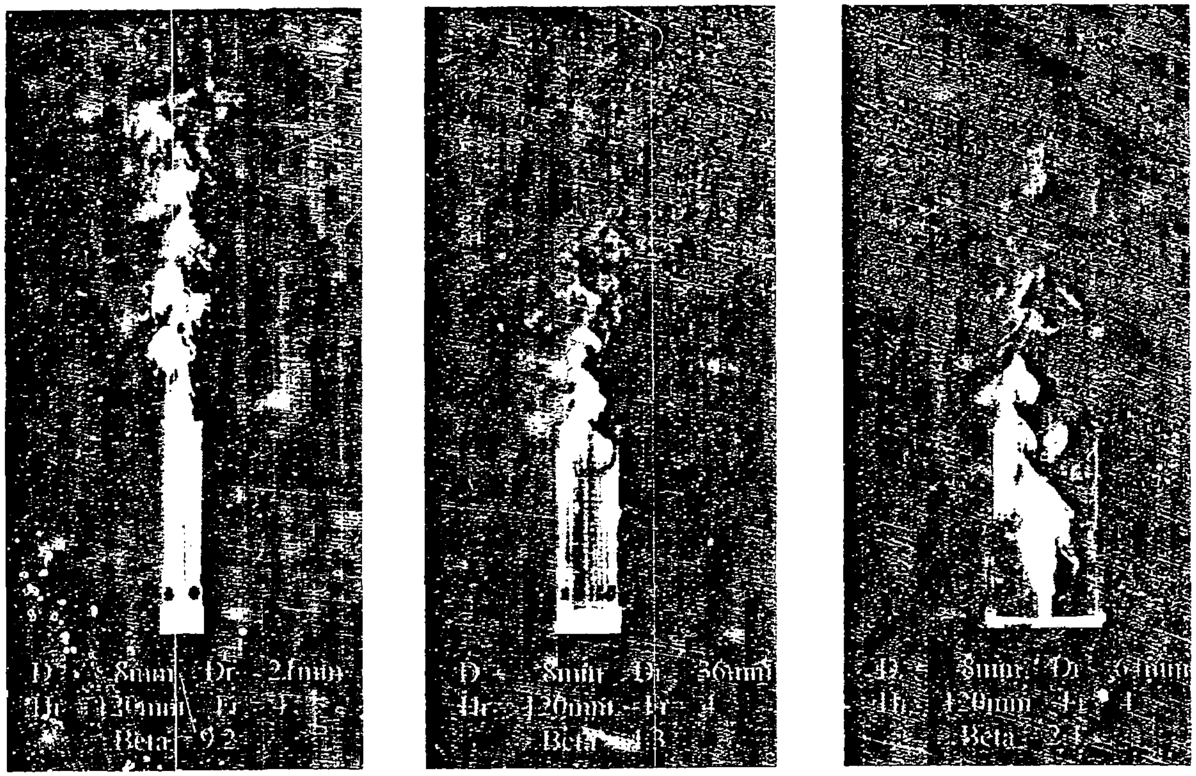

Figure 3: Mixing pattern in centre plane of confined buoyant jet with $\beta = 9.2, 4.3$ and 2.1

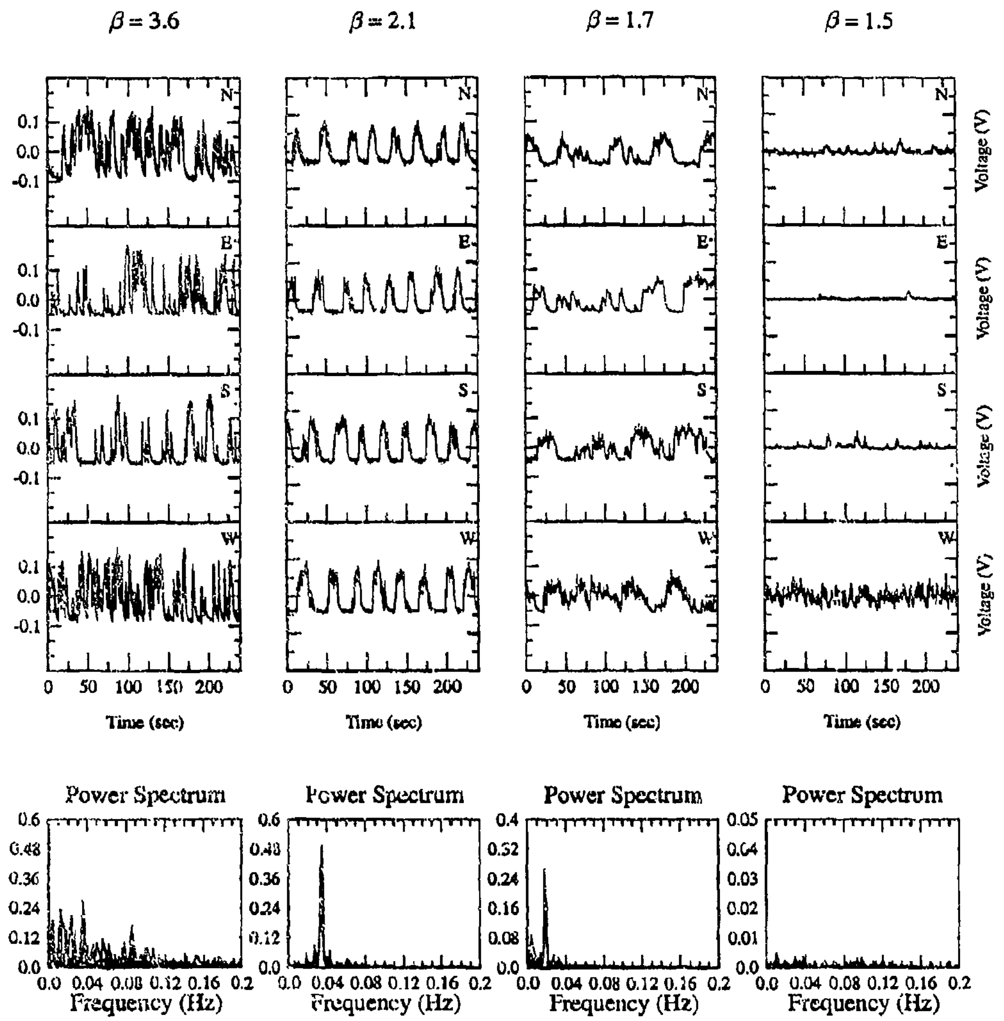

Figure 4: Temperature time history at 4 locations (N, E, S, W) at circumference of riser exit, $z = H_r$, for $\beta =$ a) 3.6, b) 2.1, c) 1.7 and d) 1.5 (0.1V ≈ 4 °C)

Although a theoretical explanation of this instability has yet to be offered, the results have been checked carefully by experiments; the instability is not due to the scale of the experimental setup, error in vertical jet alignment, or any initial swirl of the jet discharge.

Weakly confined buoyant jet

When $\beta < 1.5$, the riser wall is too far away to exert any influence and the confinement has little effect on the buoyant jet. The jet deflects no more and is stable again (Fig.2e). Near the riser exit, ambient condition prevails most of the time (Fig.4d).

3.2 Swirling frequency of the unstable buoyant jet

For $1.5 < \beta \leq 2.8$, a distinct peak is observed in the power spectrum indicating a distinct swirling frequency f. The magnitude of the peak varies from case to case, depending on the temperature difference and the location of sampling. For the swirling plume within the riser, if we adopt the riser diameter D_r and $\sqrt{g'D_r}$ as the length and velocity scales respectively, it can be shown that the Strouhal number, $St = fD_r/W_j$, depends on $\sqrt{D_r/D}/Fr$. Fig.5 shows that the dimensionless swirling frequency is linearly proportional to Fr^{-1} for different confinement ratios. It is interesting to note that this result suggests that such an instability or swirling plume will be absent for a pure momentum jet, $Fr \rightarrow \infty$. This is also supported by limited observations in our experiments.

4. CONCLUDING REMARKS

The behaviour of a laterally confined vertical buoyant jet has been studied experimentally. The results can be well-interpreted with the use of a confinement index β. When $1.5 < \beta \leq 2.8$, an instability which results in a swirling plume is observed. The swirling frequency can be correlated with the jet discharge and confinement geometry parameters. In Fig.6 we show the dimensionless concentration as a function of elevation. Compared with the free buoyant jet (Chen & Rodi 1980), the mixing of such a confined jet is severely impaired for large β. However, the dilution of the swirling plume is actually greater (lower concentration) than that of a corresponding free buoyant jet, $\beta \rightarrow 0$. Limited experiments with a crossflow have also been performed. Numerical calculations with a free shear layer model have also resulted in a qualitative understanding of the effect of confinement on the pressure and flow field (Lee 1993).

ACKNOWLEDGEMENT: This work was supported by a research grant from the Croucher Foundation.

References

[1] Chen, C.J. and Rodi, W. 1980 Turbulent buoyant jets -- a review of experimental data, HMT Vol.4, Pergamon.

[2] Fischer, H.B. et al. 1979 Mixing in inland and coastal waters. Academic Press, New York.

[3] Lee, W.T. 1993 Mixing of a vertical round buoyant jet in lateral confinement. Ph.D. Thesis, The University of Hong Kong, Hong Kong.

[4] Muellenhoff, W.P. et al. 1985 Initial mixing characteristics of municipal ocean discharges. Report EPA-600/3-85-073, U.S. Envir. Protection Agency, Newport, Oreg.

[5] Wilkinson,D.L. 1988 Avoidance of seawater intrusion into ports of ocean outfalls. J. of Hydraulic Engineering, ASCE, **114(2)**, 218–228.

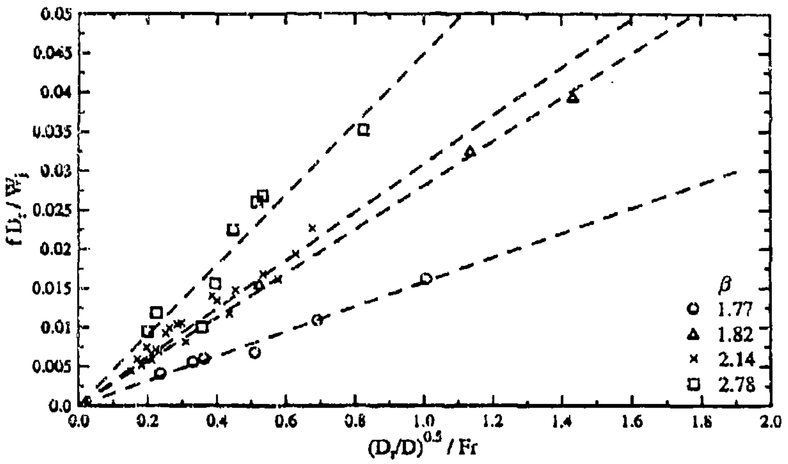

Figure 5: Normalized swirling frequency of the unstable confined buoyant jet.

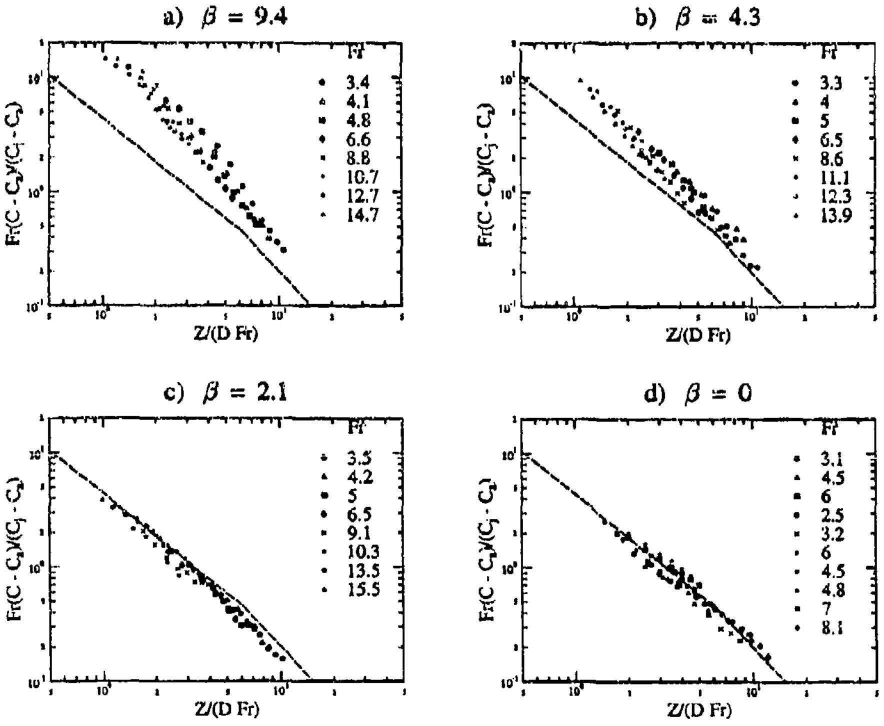
a) β = 9.4

b) β = 4.3

c) β = 2.1

d) β = 0

Figure 6: Dimensionless centreline concentration of confined buoyant jet for β = a) 9.4, b) 4.3, c) 2.1 and d) 0 (- - - : free buoyant jet)

Buoyant Surface Discharges into Unsteady Ambient Flows

Jonathan D. Nash and Gerhard H. Jirka
DeFrees Hydraulics Laboratory, Cornell University, Ithaca, New York

Abstract

The dynamics of buoyant surface discharges into unsteady ambient crossflows have been studied in a schematic experiment, simulating the specific case of tidally reversing flows. The time evolution of the discharge is shown to be uniquely related to the jet-to-unsteady-crossflow scale measures: a length scale $L_u = (M_0/|du_a/dt|)^{1/3}$ and time scale $T_u = (M_0/|du_a/dt|^4)^{1/6}$ which relate the discharge momentum flux M_0 to the acceleration du_a/dt of the ambient flow. The experiments show that jet parameters, such as the buoyancy build-up around reversal and the unsteady trajectory deflection, can be represented in a reasonably self-similar fashion if these scales are used for normalization.

Introduction

Many buoyant discharges occur in the coastal environment, where the ambient flow is time-varying. Time-evolving turbulent jets or plumes result from the interaction between these discharges and the accelerating or decelerating ambient current. Examples include such geophysical flows as rivers entering tidal estuaries and man-made effluxes from municipal or industrial sources, such as cooling water discharges. Many other flows which are not tidally reversing, such as wind driven currents, may also exhibit significant time variance, making the characterization of jet behavior in unsteady flows important.

Earlier studies have considered the mixing of buoyant surface jets under two limiting conditions. First, discharges into a stagnant ambient (e.g. Hayashi and Shuto [4]) have shown an initial strongly entraining jet region followed by the buoyant damping and collapse leading to an unsteady buoyant *pool* with horizontally spreading density fronts. Second, discharges into a uniform steady crossflow (e.g. Abdelwahed and Chu [1]) exhibit time-invariant behavior with gradual deflection of the surface plume and final advection by the crossflow. Appropriate length scales for these processes and predictive models (usually in form of jet integral equations) have been developed and shown to be reasonably accurate measures of the mixing processes under these limiting conditions (see Jirka et al. [5], Chu and Jirka [3], Jones and Jirka [6]).

In contrast, little is known about the behavior of buoyant discharges in highly unsteady ambient environments, which include velocity reversals. A few studies (e.g. Brocard [2], Padmanabhan [8]) performed site-specific model investigations of coastal cooling-water discharges, which qualitatively show the unsteady jet deflection that decreases as the tidal velocity diminishes, the build-up of a buoyant pool near slack conditions, front formation, and the re-entrainment of mixed effluent into the jet in the accelerating phase after reversal. However, no quantitative measures have been developed which characterize these processes arising from the dynamic interaction of the discharge parameters with the degree of ambient unsteadiness. In particular, specific length and time scale measures have *not* been identified so far that appropriately describe this unsteady interaction.

The development of such quantitative measures and elucidation of these unsteady dynamics is the objective of this study. In particular, a schematic model has been used to simulate a generic thermal discharge into a time-varying, turbulent ambient flow. The model conditions replicate a typical cooling water discharge into a deep, tidally reversing current, but scaling arguments allow

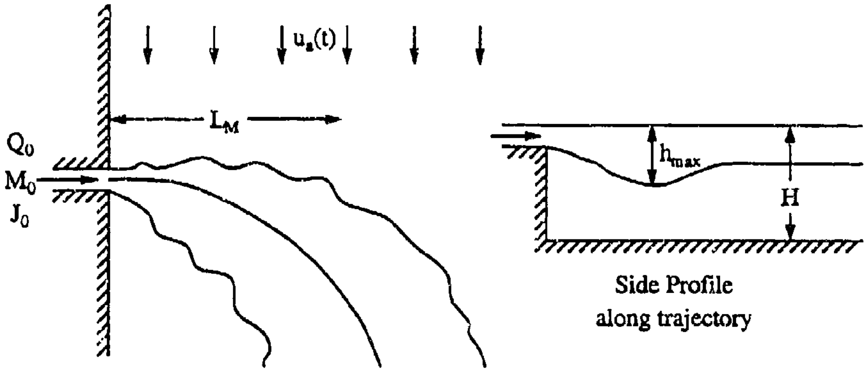

Figure 1: Plan and cross-sectional views of a buoyant discharge at some velocity $u_a(t)$.

the present results to be extended to many other time-varying flows. This report systematically investigates the effects of linear changes in velocity on near field mixing of a thermal discharge in order to determine 1) when unsteadiness can be considered negligible and steady-state models accurately applied; and 2) how these effects can be characterized universally using length and time scale arguments.

Length and Time Scales: Steady and Unsteady Conditions

Steady ambient conditions: The structure of a buoyant surface discharge and its interaction with a steady receiving environment is described primarily by the discharge buoyancy (J_0) and momentum (M_0) fluxes, and the receiving water body's depth (H) and velocity u_a (see figure 1). Length and time scales can be formed from these four parameters using dimensional analysis. First, the transition where the initial jet momentum becomes dominated by buoyant spreading is described by the jet-to-plume scales:

$$L_M = \frac{M_0^{3/4}}{J_0^{1/2}} \qquad T_M = \frac{M_0}{J_0}$$

which represent the transition distance (L_M) and development time (T_M), the *internal clock* of a buoyant discharge.

In addition, the jet-to-plume length scale L_M provides a measure of the maximum depth of the jet h_{max}, and is used to determine whether bottom interaction will produce a shallow, two-dimensional jet, where full depth mixing blocks the ambient flow, deflecting the mean current around the discharge, or a *deep* discharge situation having negligible bottom interaction. Only deep discharges, given by the condition $L_M/H \leq 1$ (Jirka et al. [5]), are considered here.

A measure of the deflection of the jet is the jet-to-crossflow length scale,

$$L_m = \frac{M_0^{1/2}}{u_a}$$

which relates the discharge momentum to the crossflow velocity, u_a. Using steady-state analysis, the properties of near field mixing and trajectory can be shown to depend primarily on the non-dimensional parameter, L_M/L_m.

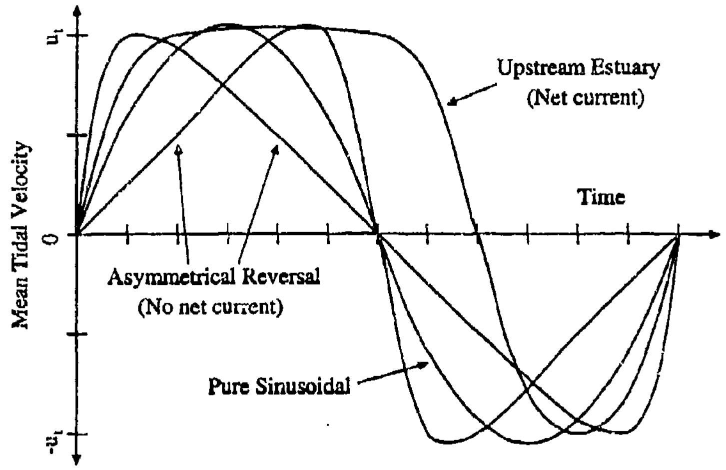

Figure 2: The tidal velocity variation (scaled by the maximum velocity u_t) may have significantly different rates of reversal at slack tide.

Unsteady ambient conditions: Figure 2 shows the large variation in ambient tidal velocity profiles $u_a(t)$, that arises from the local coastal morphology. This variation gives rise to different rates of acceleration $du_a(t)/dt$, a parameter found to be critical in characterizing unsteady flows.

The variation of the jet-to-crossflow length scale L_m over a sinusoidal tidal half-cycle is displayed in Figure 3. (The physical dimensions given in the figure correspond to the present laboratory simulation which represent dynamically scaled ambient conditions.) Near slack tide, $u_a(t) \sim 0$, L_m becomes unbounded and thus is an unsatisfactory measure of the buoyant jet behavior under these weak and transient ambient velocity conditions.

A preferred measure for describing the unsteady trajectory and the build-up of the buoyant pool in this transient low-velocity phase is given by a relationship between discharge momentum flux M_0 and the ambient acceleration $du_a(t)/dt$, which, in contrast to L_m, remains finite as $u_a(t) \rightarrow 0$. On dimensional grounds, this leads to the *jet-to-unsteady-crossflow length and time scales* (reversal scales):

$$L_u = \left(\frac{M_0}{\left| \frac{du_a(t)}{dt} \right|} \right)^{1/3} \qquad T_u = \left(\frac{M_0}{\left| \frac{du_a(t)}{dt} \right|^4} \right)^{1/6}$$

Although other scales can be formed from the interaction between the discharge buoyancy flux J_0 and ambient acceleration, $du_a(t)/dt$, those scales are not considered dominant, following Jirka et al. [5] who showed that buoyant surface jet deflection in crossflow is primarily influenced by the discharge momentum, not the buoyancy.

Physically, the reversal length scale is representative of the distance at which the effects of acceleration become appreciable. Figure 3 shows the interplay between the two length scales L_m and L_u for a typical coastal discharge. During most of the tidal cycle, $L_u \gg L_m$, so that the ambient acceleration is negligible compared to the instantaneous velocity. However, as slack tide is approached, $L_u \ll L_m$, and the reversal length scale becomes the dominant influence.

The amount of the pooling resulting from buoyant accumulation of discharge can be related to the time during which the ambient can be considered quiescent (slack tide). If the ambient velocity is approximated as having a linear variation with time ($u_a(t) = \left[\frac{du}{dt}\right]_0 t$) then the duration

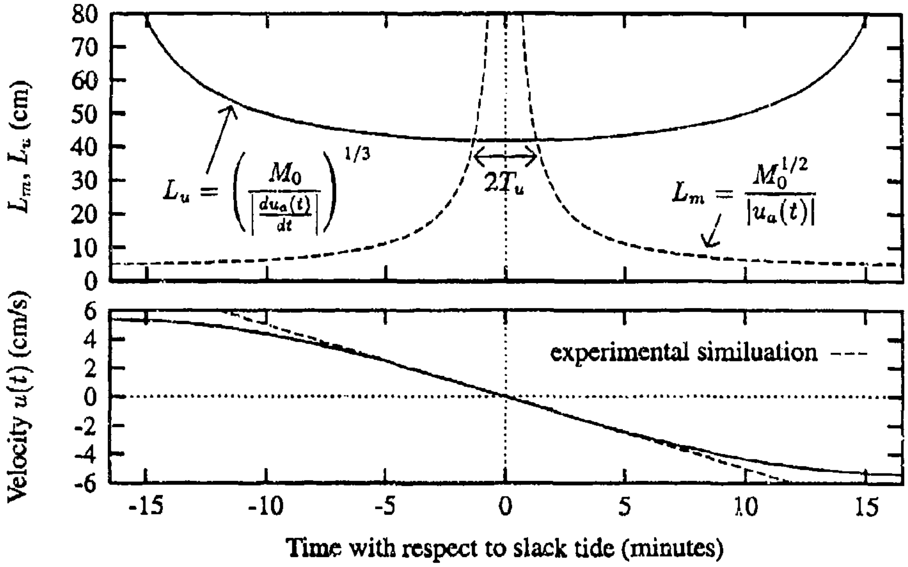

Figure 3: Variation of the length scales L_m and L_u during a sinusoidal change in the ambient velocity $u_a(t)$. In the interval $-T_u < t < T_u$, the length scale L_m becomes very large, indicating that the crossflow velocity has negligible effect on the plume. L_u remains constant and finite during this interval, and becomes the dominant scale. Dimensions relate to experimental simulation.

of slack tide, as defined by the intersection of L_u and L_m in figure 3, is given by $t = \pm T_u$. The time scale T_u can thus be interpreted as the duration of slack tide. For most flows, this time scale is much greater than the intrinsic discharge time scale T_M, indicating that there is a relatively long time period during which the instantaneous velocity is unimportant, when the plume may fully evolve through the influence of the unsteadiness alone ($\sim L_u$).

Thus, for unsteady flows, the nondimensional parameter of L_M/L_u is proposed to replace L_M/L_m to uniquely characterize the geometry and mixing of the flow during reversal. In addition, this ratio also describes the duration of slack tide, as $L_M/L_u = \sqrt{T_M/T_u}$ and thus reflects the temporal as well as the spatial behavior of the discharge. This proposal is investigated in the experimental simulation.

Experimental Simulations

A 1:125 scale model, based on densimetric Froude number similarity, was chosen to investigate the near field behavior of a typical prototype thermal surface discharge ($M_0 = 10\text{m}^4/\text{s}^2$, $u_0 = 1\text{m/s}$, $T_0 = 20°\text{C}$, $L_M = 13.6\,\text{cm}$) and ambient ($H = 12.5\,\text{m}$, $T_a = 14°\text{C}$) under fully turbulent conditions (model discharge Reynolds number $Re \sim 3000$).

A continuous time series of surface temperature mappings was obtained in a 6 m × 8 m × 20 cm deep reversing flow basin using Planar Laser Induced Fluorescence (PLIF). Although the model tidal excursion is $\lambda_m \sim 70$ m, this basin is large enough to contain the entire plume evolution while the effects of unsteadiness are significant ($-T_u < t < T_u$), which is the important consideration in this experiment. The mappings were stored on Super-VHS video, and digitized at times of interest.

The application of PLIF to such large scales with density stratification requires special image processing (Nash et al. [7]), as turbulent density gradients cause substantial reflection

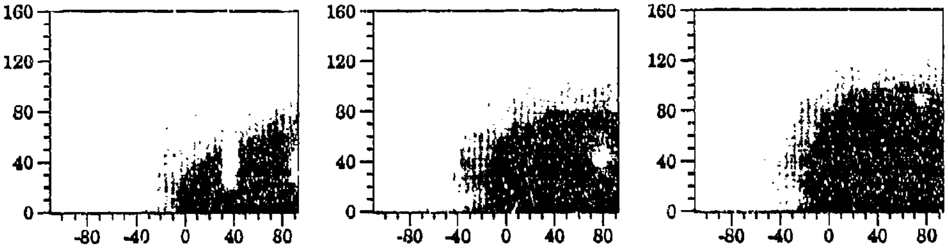

t/Tu=-2.69 (before reversal) t/Tu=-1.34 (before reversal) t/Tu=-0.68 (before reversal)

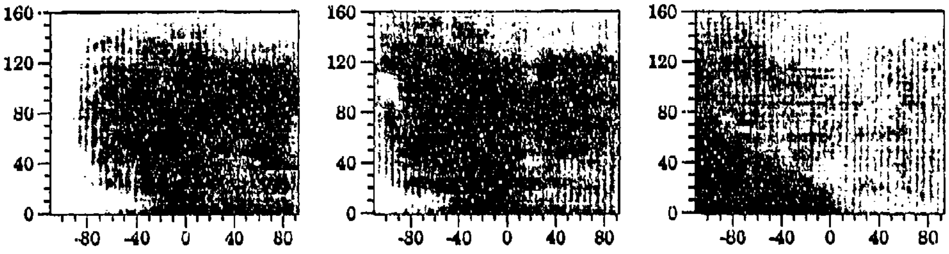

t/Tu=0.68 (after reversal) t/Tu=1.34 (after reversal) t/Tu=2.69 (after reversal)

Figure 4: Time series of instantaneous surface temperature mappings (plan view) shows the evolution of the plume (L_u = 31.8 cm, T_u = 46.9 s) during ambient flow reversal. Distances in cm. The most significant effects of the unsteadiness occur over the interval ($-2 < t/T_u < 2$), and at distances approximately $\ell > L_u/2 \sim 15$ cm from the outfall site. At $t/T_u = \pm 2.69$ the plume shows only slight asymmetry.

and refraction of the illuminating laser sheet. By calculating the spatial gradient of the image, this attenuation due to turbulent density gradient fluctuations can be found, and through calibration of the image with six temperature probes, an algorithm can be applied to produce accurate representations of the flow for both flow visualization and quantitative temperature measurements.

Four linearly transient velocity variations with constant $du_a(t)/dt$, ranging from very rapid $(du_a/dt)_m = 0.02$ cm/s^2 to very mild $(du_a/dt)_m = 0.005$ cm/s^2, and varying between velocity plateaus of $u_t = \pm 6$ cm/s were chosen to represent typical environmental flows. This linear representation is a good approximation in the time frame of reversal (see figure 3). For comparison, figure 3 shows an acceleration around reversal of $(du_a/dt)_m = 0.0085$ cm/s^2.

A typical time series of near-surface temperature distributions, as indicated by the grey scales of the video images obtained from the PLIF method, is shown in Figure 4 for a case of a surface jet in rapidly reversing flow ($L_u/L_M = 2.4$). The mappings reveal the asymmetrical behavior of the jet before and after reversal, and maximum induced temperature rise occurring slightly after slack tide. The effects of unsteadiness become negligible outside the duration of slack tide ($t \ll -T_u$ and $t \gg T_u$), and mappings having the same instantaneous velocity become symmetric before and after reversal.

The detailed analysis of all the unsteady simulations conducted shows that the time evolution of plume trajectory and mixing has, indeed, a substantial dependence on the rate of ambient acceleration, du_a/dt, given in relative terms by the scales L_u and T_u. The experiments reveal, as hypothesized, that the temperature buildup, or pool formation around slack tide is more severe in less rapid reversals, as there is a longer duration for buoyant accumulation. In contrast,

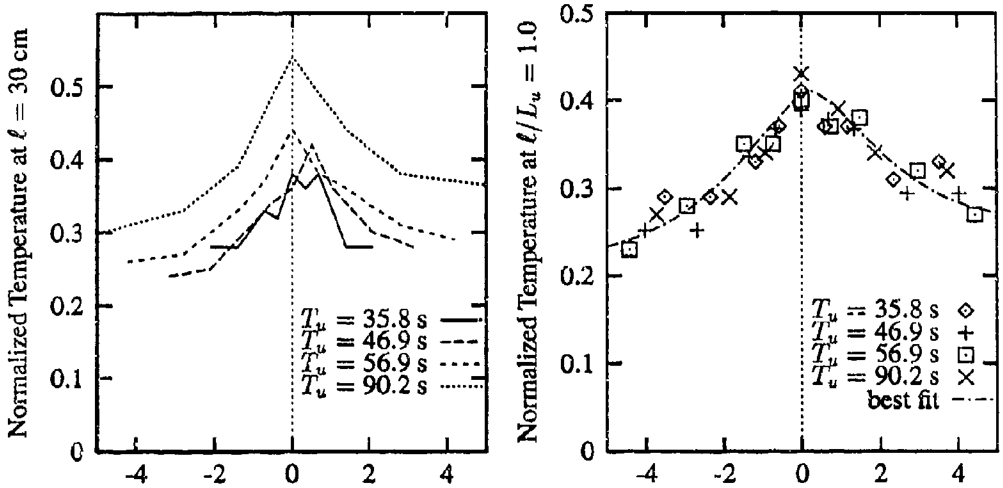

a) Time relative to slack tide (minutes) b) Normalized time (t/T_u) relative to slack tide

Figure 5: Time variation of centerline temperature excess at given distances along the trajectory. Self-similar behavior is achieved after normalization by the unsteady scales L_u and T_u.

discharges into quickly reversing current have little time for near field accumulation, but have highly asymmetrical trajectories before and after slack tide.

A buoyant surface discharge can be described by its centerline trajectory and buoyancy (temperature) decay along that trajectory. Some unique, approximately self-similar, properties of the unsteady jet behavior can be extracted from the complete data series if the appropriate scale measures, L_u and T_u, are employed. This is demonstrated in the following for two unsteady plume measures: the maximum centerline temperature rise at a given distance along the trajectory, and the centerline trajectory.

Figure 5a shows the induced temperature rise (normalized by the discharge temperature excess) at given distance along the trajectory as a function of time within the simulated tidal variation. The plot reveals that the less rapid reversal produces the greatest temperature rise 30 cm from the outfall site. On the other hand, if the temperature measurements are made at distance $\ell = L_u$, specific for each time series, along the centerline and if time is also nondimensionalized by T_u relative to slack tide, then these temporal and spatial effects produce a single unique curve (see figure 5b), supporting the significance of the scales L_u and T_u. The peak in this plot represents the buoyant buildup resulting from the rapidity of the reversal, indicating that the effects of the unsteadiness are significant for $|t| < 2T_u$ ($L_m > L_u/2$).

Figure 6 displays the unsteady trajectories at a given instantaneous velocity, $u_a = \pm 0.45$ cm/s (before and after reversal). A large variation with the ambient acceleration $\sim L_u$ is evident. Because the mappings represent a specific time t and instantaneous velocity $u_a(t)$, large scale time averaging has not been performed, and the effect of individual eddies can be observed in the trajectories. The effect of using the appropriate scaling is demonstrated in figure 7 which shows the corresponding non-dimensional trajectories, scaled by L_u and displayed at a consistent time $t = \pm T_u/2$ before and after the reversal. Despite some lingering scatter the different trajectories exhibit reasonably unique behavior.

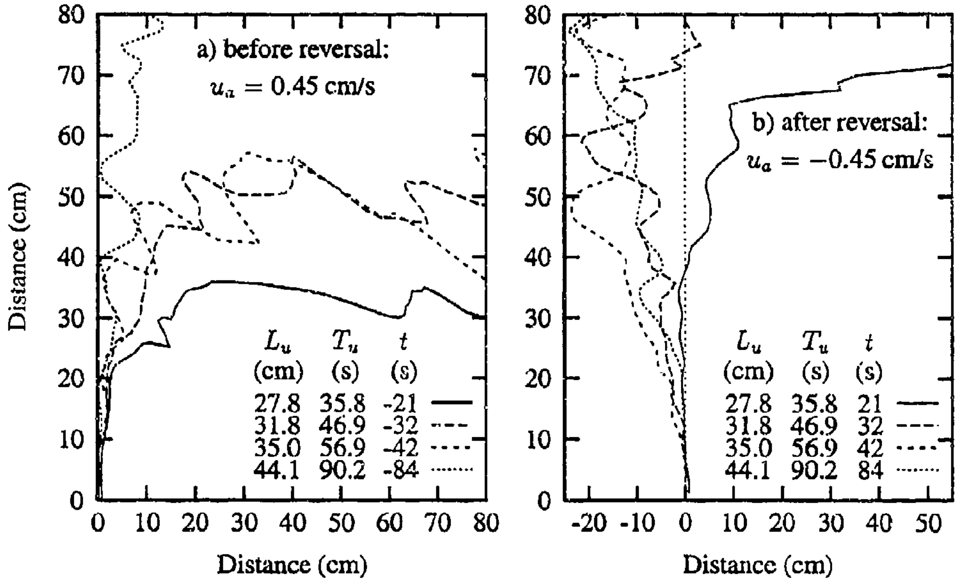

Figure 6: Plume trajectories in dimensional units at an instantaneous velocity of 0.45 cm/s. Various ambient accelerations L_u are shown a) before and b) after reversal.

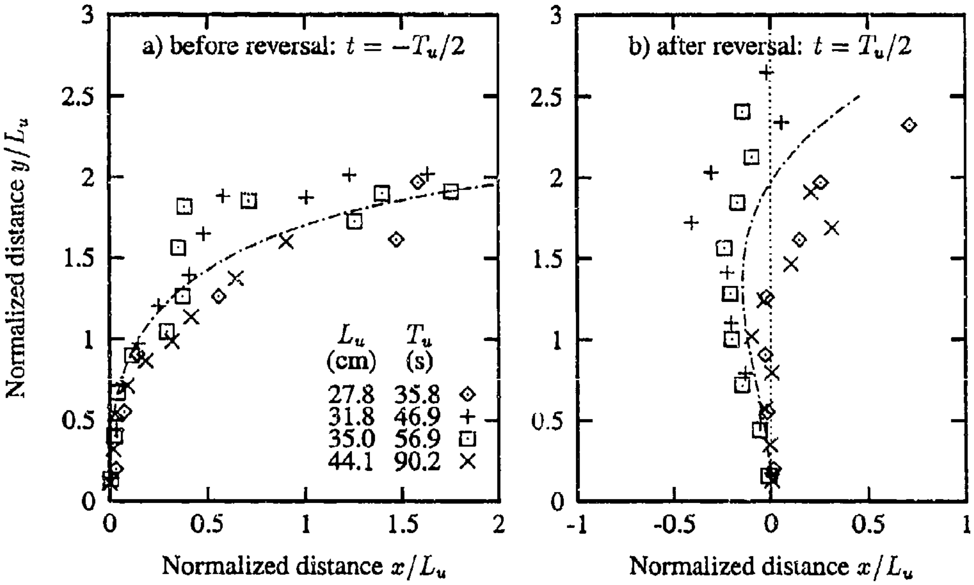

Figure 7: Normalized plume trajectories a) before and b) after reversal. Self-similar behavior results by scaling with the parameters L_u and T_u.

Conclusions

The present experimental investigation demonstrates that buoyant surface discharges in unsteady ambient flows exhibit self-similar geometry and mixing. However, correct time and length scales must be used to elicit these properties. The unsteady reversal conditions, in particular, are governed by a relation between the discharge momentum flux and the ambient flow acceleration, giving rise to the jet-to-unsteady-crossflow scales, L_u and T_u.

From the data, it is proposed that the ratio of the steady to unsteady crossflow scales L_m/L_u will describe the importance of the unsteadiness in a deep, time-varying ambient. Specifically, the unsteadiness is expected to be dominant when $L_m/L_u > 1/2$. Using this criteria, slack tide can be defined by the interval $-2T_u < t < 2T_u$: a duration where mixing is governed primarily by the unsteadiness of the flow, and steady-state analysis is not applicable. Furthermore, it is expected that the ratio L_M/L_u will characterize the discharge during these transient conditions, in analogy to the steady-state ratio L_M/L_m. A full characterization of the similarity relations governing buoyant discharges is the topic of ongoing research, including the discharge into an unsteady shallow ambient, where the persistence of strong recirculation zones plays a large role in the time evolution of a jet.

We gratefully acknowledge research support from the State of Maryland (Power Plant Research Program) and the U.S. Environmental Protection Agency.

References

[1] M.S.T. Abdelwahed and V.H. Chu. Surface jets in plumes and crossflows. Technical Report 81-1 (FML), McGill University, Montreal, Canada, 1968.

[2] D.N. Brocard. Surface buoyant jets in steady and reversing crossflows. *J. of Hydraulic Engineering* 111(5), 1985.

[3] V. Chu and G.H. Jirka. Surface buoyant jets and plumes. In N.P. Cheremisinoff, editor, *Encyclopedia of Fluid Mechanics*. Gulf Publishing Company, Houston, Texas, 1986.

[4] T. Hayashi and N. Shuto. Diffusion of warm water jets discharged horizontally at water surface. In *Proceedings of the Twelfth Congress of the International Association for Hydraulic Research*, Fort Collins, Colorado, 1967.

[5] G.H. Jirka, E.E. Adams, and K.D. Stolzenbach. Properties of surface buoyant jets. *J. of Hydraulics Div., ASCE*, 106 (HY11), 1981.

[6] G.R. Jones and G.H. Jirka. CORMIX3: An expert system for the analysis and prediction of buoyant surface discharges. Technical report, Cornell University, Ithaca, New York, 1991.

[7] J.D. Nash, G.H. Jirka, and D. Chen. Large scale planar laser induced fluorescence in density stratified flows. submitted to *Experiments in Fluids*, 1994.

[8] M. Padmanabhan. Evaluation of tidal effects on thermal plumes using a physical model. In E.A. Adams and G.E. Hecker, editors, *International Conference on Physical Modeling of Transport and Diffusion*, Cambridge, Mass., 1990.

4. Int. Symposium on STRATIFIED FLOW
Grenoble, June 29 - July 2, 1994

INVESTIGATION OF A BUBBLE PLUME IN A CROSS FLOW

Andreas Müller, Christoph Hugi
Institute of Hydromechanics and Water Resources Management
Swiss Federal Institute of Technology
CH-8093 Zurich, Switzerland

ABSTRACT

Experiments were conducted in a laboratory tank to determine the effect of a crossflow on the evolution of a bubble plume. Cross flow was simulated by towing the bubble source in a quiescent fluid. This allowed the flow field to be scanned with a stationary light sheet and a LDA. Flow visualization shows how the liquid flow passes through the bubble stream. The buoyancy force generates shear layers which develop into a system of counterrotating vortices in the wake. LDA-measurements allow a quantification of the location and the vertical velocity in the plume as a function of buoyancy flux and cross flow velocity.

INTRODUCTION

Several lakes in Switzerland are aerated by bubble plumes for maintaining an adequate concentration of oxygen. These lakes are eutrophic due to an excessive growth of algae in summer. The oxidation of this organic material depletes the oxygen in the lower layer. In winter, when these lakes are not stratified, compressed air is released at the bottom to create a plume that intensifies the natural convection. Oxygen of the air is then mainly dissolved at the free surface and transported to greater depth by the return flow. In summer, when the lakes are stratified, the oxygenation is performed by a discharge of small bubbles of oxygen at the bottom which are dissolved in the hypolimnion. These bubble plumes are exposed to lateral currents.

There are specific differences between a thermal plume and a bubble plume, which become especially important when the plume is exposed to a cross flow. The density difference which drives the thermal plume is a property of the fluid, and this buoyancy is dispersed by mixing with the entrained fluid only. The water flow in a bubble plume is driven by the drag of the bubbles, a force which can be described in an integral model as a mean buoyancy determined by the void fraction. Due to the slip velocity of the bubbles this buoyancy is transported at a different velocity than the fluid and can leave the fluid parcel which was accelerated at one time.

In a horizontal cross flow the horizontal component of the fluid velocity, c, is , to a first order, not affected by the vertical acceleration due to the bubbles. When the bubbles are released locally and rise in a body of water with a cross flow they form an inclined bubble plume as shown in Fig. 1. The horizontally moving fluid which enters the bubble region (zone I) is accelerated and displaced vertically. After leaving the bubble region the fluid retains its vertical and horizontal motion due to its momentum (zone II). An inclined bubble plume in a cross flow shows a behavior between the limiting cases of a stationary bubble plume (c=0) and a bubble line thermal (c>>w) where a volume of air per unit length is released at time t=0.

EXPERIMENTS

The experiments were conducted in a 5.8m x 3m and 3m deep laboratory tank with glass walls on the longer walls and additional observation windows on the shorter sides. Three types of bubble sources were used for the release of compressed air at the bottom of the tank: (1) a point source, consisting of a tube of 1 mm diameter, (2) a porous ceramic plate of 50 mm diameter, and (3) a porous plate of 150 mm diameter. The point source produced bubbles with equivalent diameters of 5 to 15 mm. The porous plates had a bubble size spectrum between 0.2 and 3 mm, which depended on the gas discharge per unit area. The flow rates, Q, were chosen 1, 3 and 10 normal cm^3/s.

The crossflow was simulated by towing the source along the bottom of the tank at the crossflow velocity, c (Fig. 2). The steady flow to be modeled was produced in the frame of reference moving with the source. This method has the advantage, that a stationary instrument or visualization setup can be utilized to scan the flow field. The data is recorded in time sequence and can be transformed into a steady spatial distribution. A steady light sheet in the tank normal to the tow-velocity was used to visualize the spatial distribution of the flow field. Neutrally buoyant particles of 100μm diameter were used as tracers. These particles were exposed for times of 3-5 s. The velocity was measured on the axis of symmetry of the bubble plume and in its wake with a two-component Laser-Doppler-Anemometer (LDA).

The inclined plume of the point source is shown in Fig. 3 in a double exposure, which was used for the determination of the slip velocity, w_b and the carriage velocity, c. The bubbles at the upstream edge of zone I rise in fluid with vertical velocity, w=0, with their slip velocity w_b. The narrow spectrum of bubble size leads to a uniform slip velocity with the consequence that the bubbles move together upward along the line $z=x\ w_b/c$. The plume of the sources (2) and (3) showed a different behavior. The wider distributions of bubble sizes and of slip velocities lead to a seperation of the faster rising larger bubbles from the smaller bubbles. From the variation of inclination of the different bubble paths in Fig.1 and the cross flow velocity, c=20 mm/s, it can be estimated, that the larger bubbles have a rise velocity of 330 mm/s and that the smaller bubbles move with 65 mm/s. The rise velocity is the sum of the fluid velocity and the slip velocity.

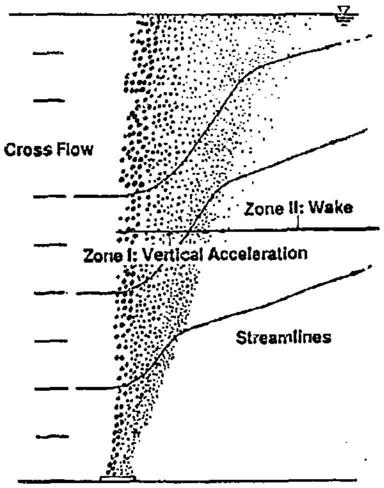

Fig. 1: Sketch of the streamlines of an inclined bubble plume in a cross flow. Q=1 cm^3/s, c=20 mm/s, extended source (3)

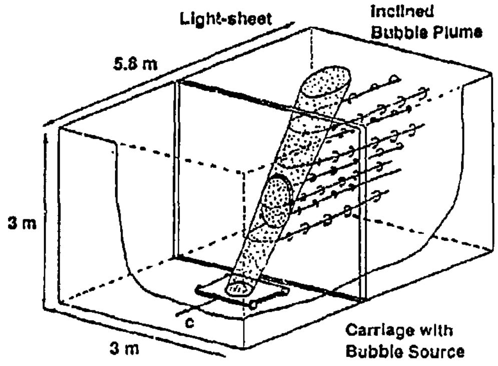

Fig. 2: Experimental setup for the simulation of an inclined bubble plume in a cross flow by towing the bubble source with the crossflow velocity c.

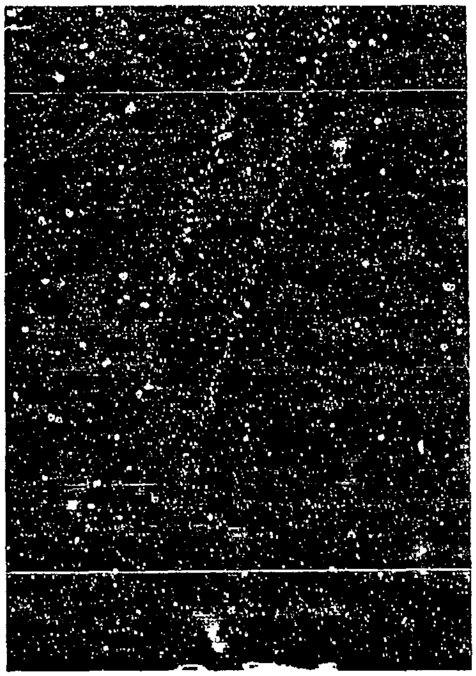

Fig. 3: Double exposure of the bubble plume of the point source (1), showing the rise of the bubbles along the line $z=xw_b/c$.

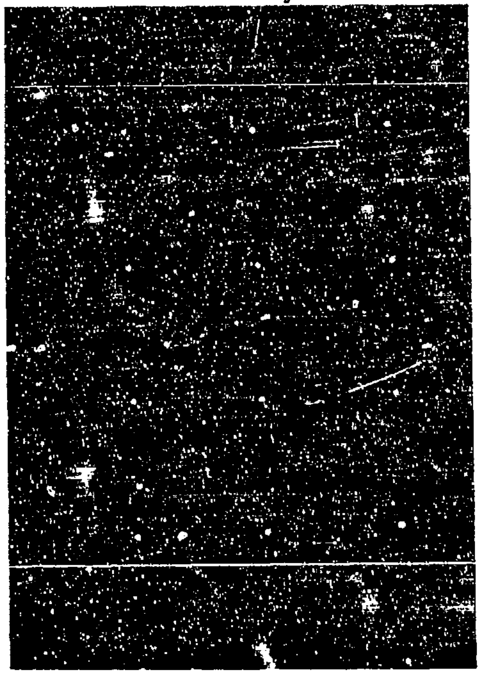

Fig. 4: Visualization of a cross section of the wake (zone II) showing the discrete vortices on both sides of a meandering inertial flow.

RESULTS

The *visualization* shows that the shear layers produced by the buoyancy force roll up into two rows of discrete vortices on both sides of a meandering wake (Fig. 4). The streamline pattern as sketched in Fig. 5 shows the topology of the flow with its vortices, the corresponding stagnation points, and the entrainment from the compensating downward flow in the tank. Fig. 7 shows the positions $y(x_i)$, $z(x_i)$ of the vortex cores in different cross planes $x=x_i$, and the positions of the cores in a side view.

This set of vortices develops out of the "uniform" shear layer produced by the inclined bubble plume. It seems to find its stable form when the vortices in the two rows are staggered and the distance of the vortices to its nearest neighbors is (within ±15%) the same across the wake as in the same row. The vortices move then vertically upward as sketched in Fig. 5 based on the Biot-Savart-law. At the upstream edge of the bubble plume the vorticity lines are connected.

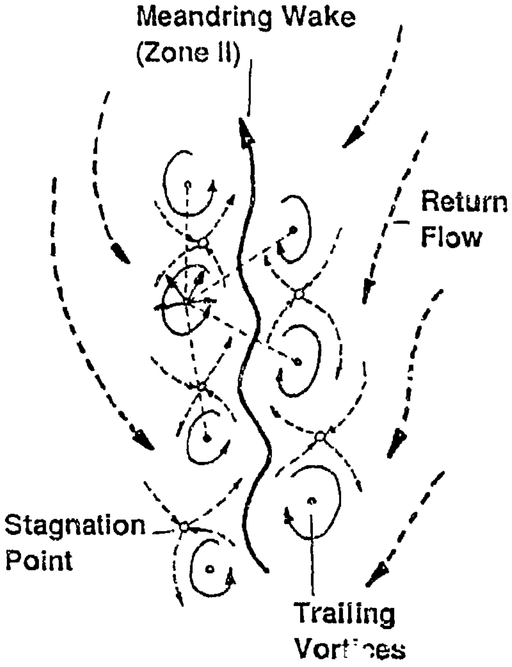

Fig. 5: Sketch of the streamline pattern, corresponding to Fig. 4, showing the vortices, the return flow and the stagnation points. The displacement due to the Biot-Savart-law of one vortex is indicated by arrows.

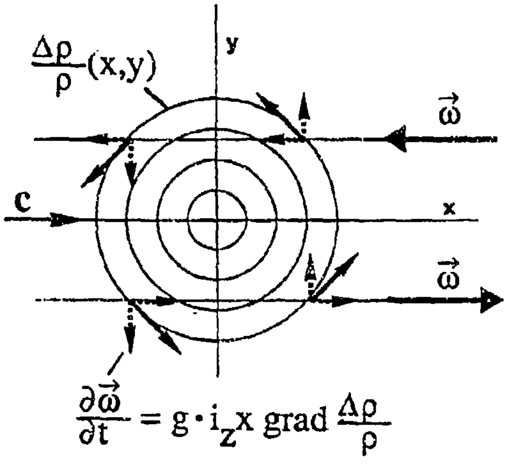

Fig. 6: Sketch illustrating the accumulation of vorticity in cross flow direction during the traverse of a fluid parcel through the bubble region.

It follows from an analysis of the vorticity generated by the density gradients of the inclined bubble plume that the vorticity component in the cross flow direction finally dominates the flow in the wake. In every horizontal plane $z=z_i$, the density distribution in the inclined bubble plume has roughly a bell shaped form with a maximum at the center and a decrease to zero in all directions as sketched in Fig. 6. A fluid particle, which traverses the region of the bubbles due to the crossflow, integrates the rate of change of vorticity along its path. The vorticity component normal to the crossflow direction is first increasing and decreasing afterwards to zero again. The vorticity component in crossflow direction integrates on one side to a positive value, on the opposite side to negative value. This statement holds as long as the density distribution is independent of z, and the horizontal acceleration of the fluid due to its vertical displacement is neglected. In reality, a fluid particle will move slower near the upstrem edge of the bubbles region and acquire a small vorticity component normal to the cross flow.

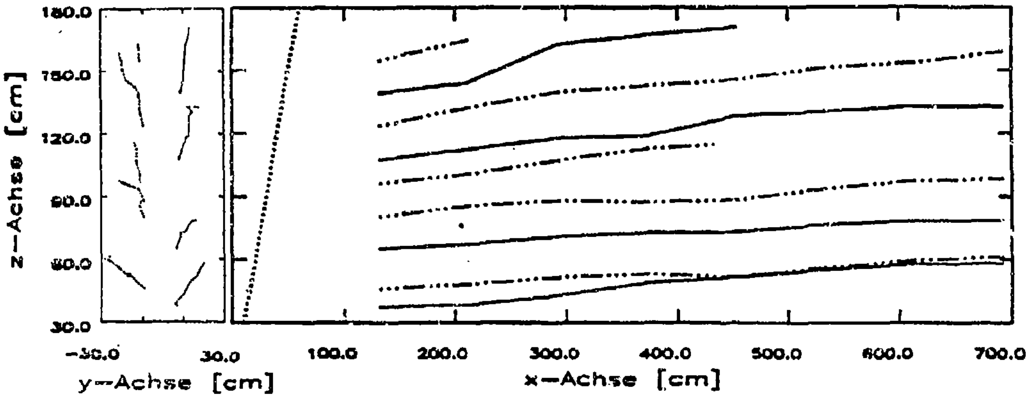

Fig. 7: Position of the vortices in the wake. Left: (y,z) plane, right: (x,z)-plane), $\overline{Q}=10$ cm^3/s, c=80 mm/s, point source (1).

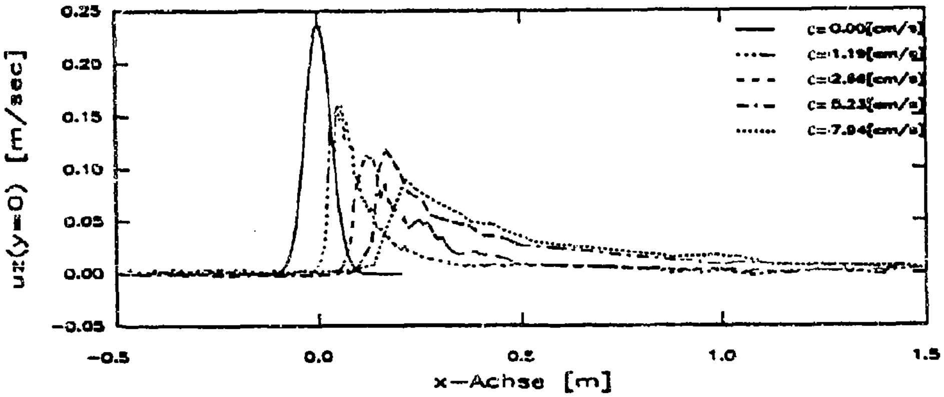

Fig. 8: Spatial velocity distribution w(x) on the axis of the inclined bubble plume of the point source (1) for Q = 10 cm^3/s, z=0.53 m, and increasing tow-velocity c.

LDA-measurements on the axis of the inclined bubble plume of the spatial velocity distribution w(x), averaged over 12 individual runs, are shown in Fig. 8 for z=0.53m and for increasing tow-velocity, c. When the tow-velocity, c, is zero, w(x) is identical with the radial velocity profile of a stationary plume. With increasing c, the limit of a bubble thermal from a line source is approached. The maximum of w(x) gets shifted in the flow direction due to the increased inclination of the plume. The maximum also decreases due to the reduced air concentration. Fluid acceleration within the bubbles (zone I) and the wake (zone II) can clearly be distinguished (Fig. 1).

The LDA data, w(x), gives information on the maximum velocity w_{max} and on its location x_{max} as well as on the decrease of the velocity in the wake. The spatial distribution depends on the buoyancy flux, B=gQ, on the tow-velocity, c, and on the height z. In the following, results for the point source with its narrow size spectrum (Fig. 3) and a water depth, h=2 m are given. Fig. 9 shows different locations (x_{max},z) for two cross flow velocities. The points of maximum velocity are, as expected, located closly behind the bubbles which follow the line $z=xw_b/c$. This behavior is different from the behavior of a thermal plume in a cross flow, which follows a line $z \sim x^{3/4}$ for a weak cross flow (c<<w), and $z \sim x^{2/3}$ for a strong cross flow (c>>w) (Fischer et al., 1979).

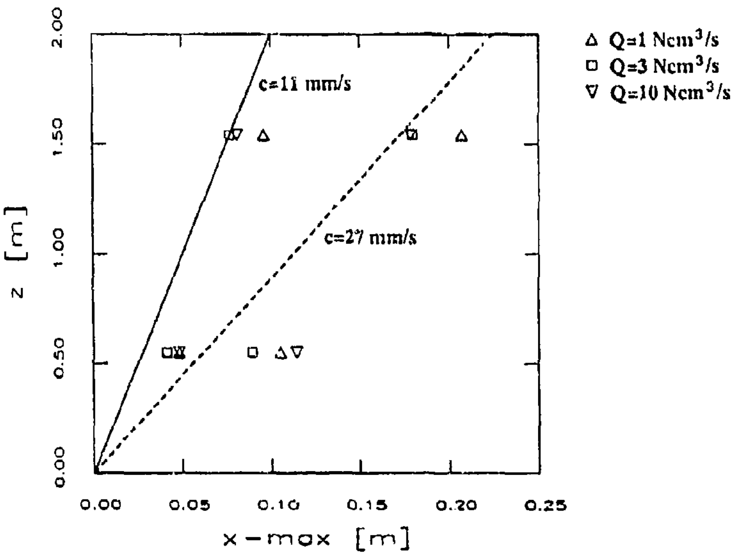

Fig. 9: Position of the maximum of w(x) relative to the line, $z=xw_b/c$ of the bubbles.

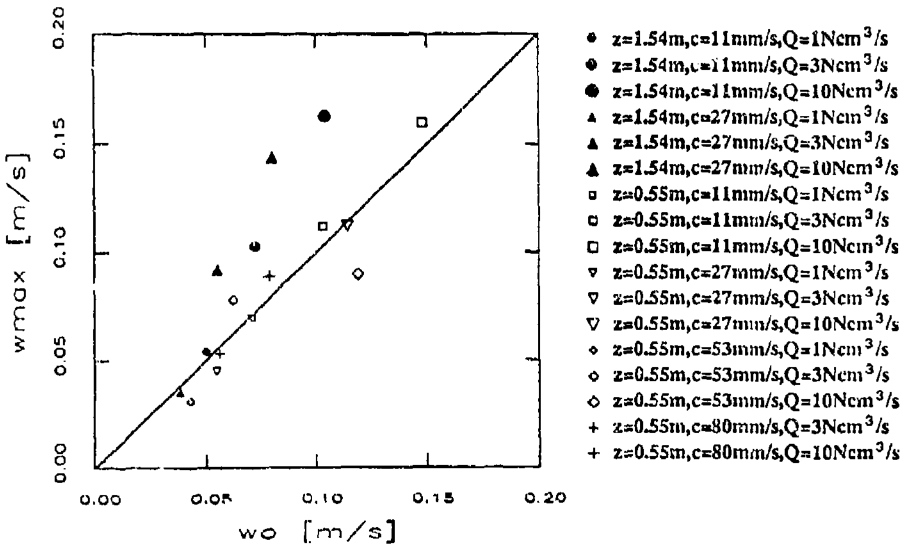

Fig. 10: Scaling of the measured maximum of w(x) with $w_0=(Bw_b/z_0c)^{1\,3}$

Based on the idea that a bubble plume in a cross flow with c>>w can be regarded as line thermal the following scaling of the vertical velocity can be postulated. From the buoyancy, A, per unit length of the thermal and the time, t, a velocity scale, $(A/t)^{1/3}$ can be formed (Escudier and Maxworthy, 1973). A is related to the buoyancy flux, B, of the inclined plume by Adx=Bdt, where dx/dt=c, is the cross flow velocity. It follows that A=B/c. The time, t, is given by z/w_b. It results a velocity scale, w_0 of

$$w_0= (Bw_b/zc)^{1/3}) = (B/x_0)^{1/3}$$

for w_{max} at the hight z. In Fig. 10 w_{max} is compared with w_0. The proposed scaling represents the variations of w_{max} for z=0.53m quite well. At z=1.53m the scaling is successful for the smaller gas discharge only. Obviously this scaling fails in the limit c=0.

In Fig. 11 the decrease of the velocity in the wake is represented in a (log w/w_0,log $x-x_0$) plot for c=28 mm/s and z_0=1.5 m, and $x_0=z_0c/w_b$. It shows a decay with $(x-x_0)^{-1/2}$, which is equivalent to $w^2 \sim (x-x_0)^{-1}$.

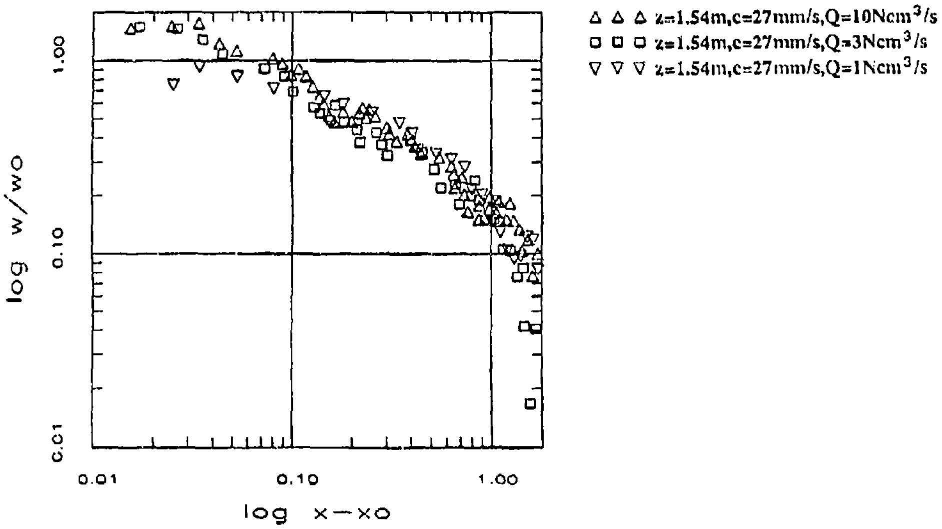

Fig. 11: Plot of (log w/w_0, log $x-x_0$), showing the decrease of $w(x)$ in the wake.

CONCLUSIONS

The bubble stream released locally at the bottom of a body of water with a cross flow forms an inclined bubble plume along the line $z=xw_b/c$. As the cross flow passes through the bubble stream, a system of staggered counterrotating vortices is generated with vorticity in cross flow direction. This system is different from the vortex structures observed in shear- and mixing-layers. Maximum flow velocities are observed at the downstream edge of the bubbles.

REFERENCES

Escudier, M.P., Maxworthy, T., (1973), "On the motion of turbulent thermals", JFM, Vol. 61, pp. 541-552

Fischer, H.B., et al., (1979), "Mixing in Inland and Coastal Waters", Academic Press

Mueller, A., Grass, E., Wuest, A., Gyr, A., (1987), "Modelling of bubble plumes" in *Hydraulic Modelling*, Cunge, J.A., Ackers, P. (ed.), Lausanne: Proc. XXII IAHR-Congress (1987) pp. 348 - 353

Wüest, A., Brooks, N.H., Imboden, D.M., (1992), "Bubble plume modelling for lake restoration", J. of Water Resources Research, Vol. 28, pp. 3235-3250

Destratification of Reservoir with Bubble Plume

Takashi Asaeda [*] Hirokazu Ikeda [†] Jörg Imberger [‡] and Vu Thanh Ca [§]

Abstract

The process of the destratification of a reservoir using bubble plume was investigated experimentally and numerically. It was found that an improved double-plume model simulated this process well. With strong bubbling and weak stratification, lower layer water, lifted by the gas released from the bottom could reach the free surface but with low bubbling rate and strong stratification, only a dome was formed on the interface without the lower layer water reaching the free surface.

In both cases the lower layer water is mixed with the upper layer water, spreads out, plunges to the neutral buoyancy level, and produces a stratified intermediate layer between the upper and the lower layers. Both upper and lower layers are eroded by the evolution of the intermediate layer, bounded from these layers by fronts. In the former case, the upper front ascends fast with a small density jump, whereas the lower front descends slowly preserving a large density jump. In the latter case, both the upper and the lower fronts behave in a reverse manner.

1 Introduction

Observational data suggest that stratification in natural water bodies often resembles a step stratification (Imberger & Patterson, 1989). The simplest structure with a step stratification is the two-layered system. In this case, with the application of bubble plume to the water body, a unique intrusion is formed between the layers, which is the same pattern as occurs in uni-phase gravity plumes (Germeles, 1975, Kumagai, 1984). Unlike the uni-phase plume, however, the continuous supply of buoyancy due to bubbles leads to higher mixing in the upper layer. This easily establishes a large column of the lower layer water throughout the upper layer for sufficient gas flow rate (Baines & Leitch, 1992).

The purpose of this study is to illuminate the structure of bubble plume in the two-layered stratification and the destratification process.

2 Experimental Procedures and Flow Pattern of Bubble Plume

Two tanks with 1mx1m section, 80cm deep (T-series) and 2mx2m section, 1.8m deep (BT-series) were used alternatively depending on the experimental purposes. A bubble

---

[*] Department of Civil and Environmental Engineering, Saitama University, Japan

[†] Department of Civil Engineering, Utsunomya University, Japan

[‡] Center for Water Research, The University of Western Australia, Australia

[§] Department of Civil and Environmental Engineering, Saitama University, Japan

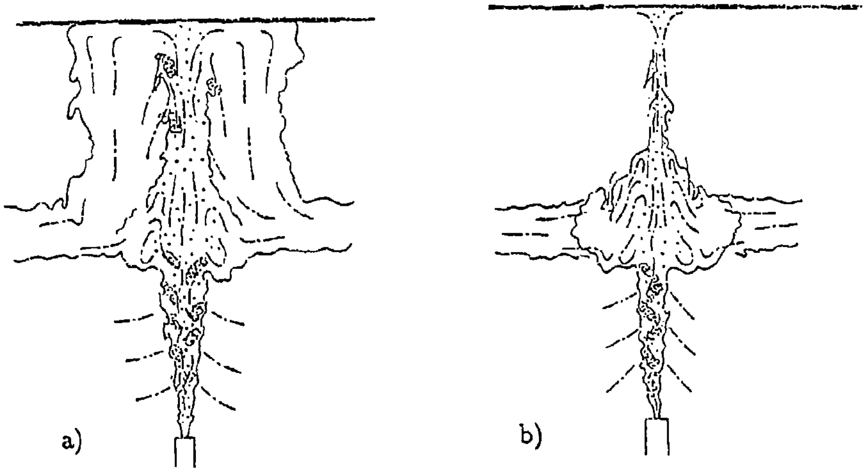

Figure 1: Schematic diagram of typical flow patterns. (a) Strong bubbling and weak stratification; (b) Weak bubbling and strong stratification. Solid spirals show strong eddies, and dash-dotted arrows, fluid motion.

maker was installed at the center of the bottom of the tanks. It was connected to a compressor with a tube, in the middle of which was attached a relief to adjust the gas flow rate to the bubble maker. A gas flow meter was inserted between the relief and the compressor. A two-layered step stratification was made in the tank using salt water. The bubble maker consisted of a tube with a circular ceramic top, through which gas was decomposed into fine bubbles (Asaeda and Imberger, 1993).

Density profiles were measured using a movable conductivity probe for both series. The probe moved vertically at 1cm/sec, measuring conductivity at every 1.82mm for the T-series, and 4.6mm for the BT series. In addition, density profiles in a vertical section were measured at every 10cm in the section, including the plume axis.

The instantaneous flow structure was visualized by the shadow graph method, with light source at the density interface height. The accumulated diffusion of the plume water was visualized by dye injected 5cm above the bubble maker. The visualized structure was photographed and then analyzed.

Results of experiments revealed that, the bubbles induced an upward plume in the lower layer, which broke through the interface forming a column of lower-layer water there. Because of its high density, the water fell down to an interface, where it spread out radially. The intrusion reduced its advancement rate when it experienced the side-wall effects. Then, the sectional density is uniformized gradually, becoming an intermediate layer. After that, the following water intruded at the neutral level in the intermediate layer thickened the layer both upwards and downwards.

According to the relation between the bubbling rate and the stratification intensity, two different regimes were observed.

When the bubbling rate was high and the stratification was relatively weak (Figure 1a), the plume broke through the interface with large momentum and reached the free surface without losing the lower-layer water. After impinging on the free surface violently, the water spread out horizontally before suddenly plunged down into the water body together with a large amount of the ambient surface water. This formed an annular downdraft around the inner upward plume. In this regime, the density of the downdraft is closer to that of the upper layer water than to that of the lower-layer. Therefore, the intermediate layer was separated from the lower layer by a strong density jump (lower front), and from the upper layer by a weak density jump (upper front). This flow pattern is called "type 1".

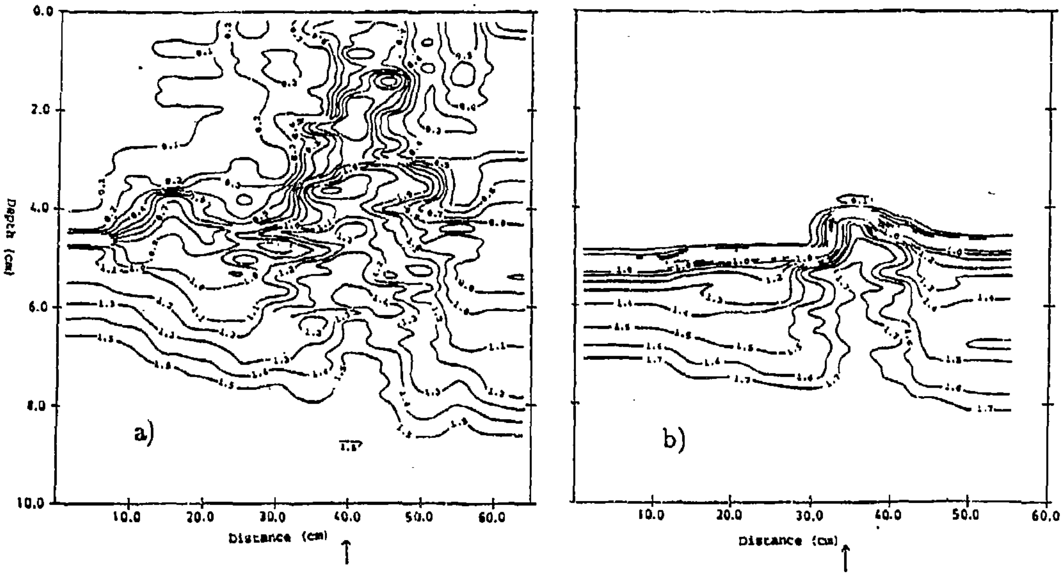

Figure 2: Isopicnals of a vertical section: (a) type 1, (b) type 2.

With low bubbling rate and relatively strong stratification, the upward momentum associated with bubbling built up a dome of the lower-layer water on the interface (Figure 1b). After reaching the top of the dome, the water fell along the side slope down to the interface. Since a small amount of upper layer water was entrained into the dome, the density of the intermediate layer was closer to that of the lower layer than that of the upper layer. Therefore, the layer was separated from the upper layer with a large density jump (upper front), whereas, from the lower layer with a small density jump (lower front). This flow pattern will be called "type 2".

Isopicnals of the vertical sections indicated in Figures 2 are also reveal clearly the two flow patterns.

With the formation of the intermediate layer, the original two-layered system is deformed into three-layered one, then the original upper and lower layers are gradually eroded by the intermediate layer.

In type 1, the intermediate layer expands more upwards than downwards. In type 2, on the other hand, the intermediate layer erodes the lower layer more rapidly than the upper layer. The lower front descends gradually through the water underneath carried up above it by the plume (Baines, 1974), i.e.,

$$\frac{dz_l}{dt} = -\frac{Q_w(z_l)}{A} \tag{1}$$

where, z_l is the lower front height, $Q_w(z)$ is the volume flux of water at z, A is the sectional area of the container, and t is time.

At the height of the lower front, the volume flux of gas is given by $Q_0 g H_A/(H_T - z_l)$, where $H_T = H + H_A$; H and Q_0 are the water depth and gas flow rate at the bubble source, respectively; H_A is the atmospheric pressure head; g is the gravitational acceleration. The descend rate of the lower front has been determined as

$$\frac{dx_l}{d\tau} = -0.45\left(\frac{1}{x_l(1 - H_R x_l)}\right)^{1/3} x_l^2 \tag{2}$$

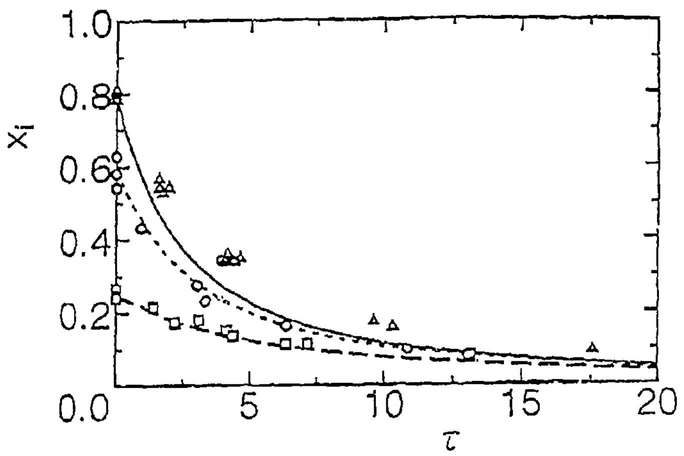

Figure 3: The height of the lower front; calculated results of (3) in comparison with the experiments. Calculated results ($H_R = 0.118$): — — — —, $x_0 = 0.25$; - - - - - - - - -, $x_0 = 0.6$; ————, $x_0 = 0.8$. Experimental results: squares, BT-4,5,9 ($x_0 = 0.2 \sim 0.3$); circles, BT-1,2,10 ($x_0 = 0.55 \sim 0.65$); triangles, BT-3,6,7,11 ($x_0 = 0.75 \sim 0.85$).

where $x_l = z_l/H$ is the nondimensional height, $\tau = (4\pi\alpha^2 H M_H^{1/3} u_B t)/A$ is the nondimensional time, u_B is the bubble slip velocity, $H_R = H/H_T$, and α and M_H are later defined in (6).

The above relation is shown in Figure 3. Associated with the reduction of z_l, $Q_w(z_l)$ decreases and the descending rate of the lower front is decclerated.

The upper front advances at the rate of the entrainment of the upper layer water through the front. Its height z_u is, therefore,

$$\frac{dz_u}{dt} = \frac{Q_e}{A} \tag{3}$$

where Q_e is the entrainment rate of the upper layer water.

Unlike the flux through the lower front, however, the flux through the upper front is much affected by the gravity force which the plume receives in the intermediate layer. Figure 4 shows Q_e as a function of z_u. It can be found that the entrainment rate decreases significantly even with the small rise of the upper front.

At first, the plume directly attacks the front without losing momentum, causing a high entrainment rate. However, as the intermediate layer thickening, the plume loses its upward momentum in the layer, before attacking the upper front. Eventually, less amount of the upper layer water is entrained.

A following relationship was obtained

$$\frac{D}{H_T - z_0} = 80F_r^2 \text{ for } F_r^2 \leq 0.053 \tag{4}$$

$$\frac{D}{H_T - z_0} = 1 \text{ for } F_r^2 > 0.053 \tag{5}$$

where $F_r^2 = \{Q_0 g H_A/[z_0(H_T - z_0)]\}^{2/3}/[g'_{al}(H_T - z_0)]$, g'_{al} is the initial reduced gravity difference between the lower layer water and the upper layer water, D is the height of the column of the lower layer water in the upper layer, and z_0 denotes the initial height of the interface. The boundary between type 1 and 2 is $F_r^2 = 0.053$.

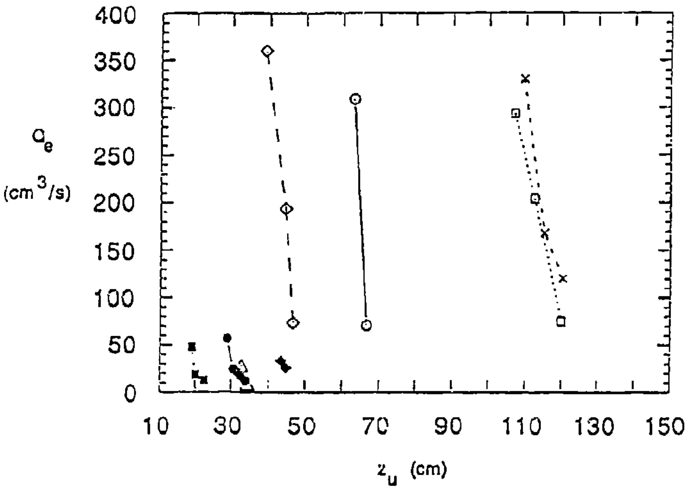

Figure 4: The entrainment through the upper front as a function of the front height. —— with open circles: BT-1, ····· with open squares: BT-3, — — — — with open diamonds: BT-4, - - - - - - - with X: BT-7, - - - - - - - - with open triangles: T-2, —·— —·— with closed circles: T-3, —·—·— with closed squares: T-4, and —··—··—··— with closed diamonds: T-5.

3 Analysis of the evolution of the intermediate layer

As was described, with the evolution of the intermediate layer, it becomes difficult to relate the flow pattern to the initial conditions and bubbling rate. Therefore, a numerical model is introduced to analyze the flow pattern at any stage and the destratification process.

Similarly with the linearly stratified case (Asaeda & Imberger, 1993), the double-plume integral model was used to simulate the density distribution in the ambient.

Using nondimensionalizing variables

$$z = Hx, r_1 = 2\alpha HR_1, r_2 = 2\alpha HR_2, v_1 = u_B M_H^{1/3} V_1, v_2 = u_B M_H^{1/3} V_2,$$

$$g_1 = \frac{{u_B}^2 M_H^{2/3} G_1}{H}, g_2 = \frac{{u_B}^2 M_H^{2/3} G_2}{H}, \alpha_\beta = \beta, \alpha_\gamma = \gamma,$$

$$G_{1l} = G_1 - \frac{1}{(1 - H_R x)(V_1 + M_H^{-1/3})(\lambda R_1)^2}, M_H = (Q_0 g H_A)/(4\pi\alpha^2 H_T^2 {u_B}^3), \tag{6}$$

where v denotes the vertical velocity; r the plume radius, subscripts 1 and 2 denote the inner and the outer plume variables; and $g_1' = g(\rho_a - \rho_1)/\rho_r$, $g_2' = g(\rho_2 - \rho_a)/\rho_r$ and ρ_a is the density of the ambient water, ρ_r is a reference density. The liquid density of the inner plume is given by $g_{1l}' = g_1' - gA_B$, with A_B is the total fraction occupied by gas. Here, it is assumed that pressures are constant across the section, the velocity and density are assumed to have a top-hat profile, and the diffusion effect is neglected. α_β, α_γ, and α are the entrainment coefficients for the outer to inner plumes, the inner to outer plumes, and the ambient to the outer plume respectively. λ is the ratio of radii of the bubble core and the inner plume. The notations are given in Figure 5

Equations of the conservations of mass, momentum and buoyancy are derived as

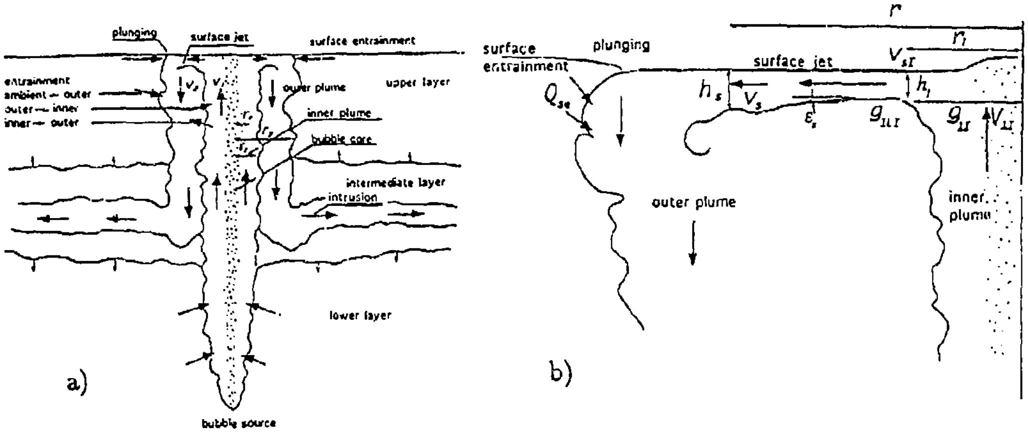

Figure 5: The diagram of the double-plume model, (a) general structure, (b) near the plunging zone.

$$
\begin{aligned}
\frac{d(R_1^2V_1)}{dx} &= \beta R_1(V_1 - V_2) - \gamma R_1 V_2 && (7)\\
\frac{d(R_1^2V_1^2)}{dx} &= R_1^2 G_1 + \beta R_1 V_2 (V_1 - V_2) + \gamma R_1 V_1 V_2 && (8)\\
\frac{d(R_1^2V_1G_1)}{dx} &= R_1^2 V_1 \frac{dG_a}{dx} - \beta R_1 G_2 (V_1 - V_2) + \gamma R_1 V_2 G_{1I} \\
&+ \frac{d}{dx}\frac{V_1}{(1 - xH_R)(V_1 + M^{-1/3})} && (9)
\end{aligned}
$$

for the inner plume

$$
\begin{aligned}
\frac{d(S^2V_2^2)}{dx} &= -\beta R_1(V_1 - V_2) - \gamma R_1 V_2 - R_2 V_2 && (10)\\
\frac{d(S^2V_2^2)}{dx} &= -S^2 G_2 - \beta R_1 V_2 (V_1 - V_2) - \gamma R_1 V_1 V_2 && (11)\\
\frac{d(S^2V_2G_2)}{dx} &= -S^2 V_2 \frac{dG_a}{dx} - \beta R_1 G_2 (V_1 - V_2) + \gamma R_1 V_2 G_{1I} && (12)
\end{aligned}
$$

for the outer plume

The ambient density evolution is calculated by introducing the assumption that the equivalent amount of water to the intrusion spreads immediately over the container section.

The inner plume equations (7) through (9) are integrated up with suitable starting conditions. Since the plume starts in the homogeneous lower layer, the condition of the single plume (McDougall, 1978, and Asaeda & Imberger, 1993) was used. For the first integration up the inner plume , the presence of the outer plume was ignored.

When the plume does not reach the free surface, the inner plume stops rising in the upper layer, which is the beginning of the outer downdraft.

Nondimensionalization leads to the starting conditions of the outer plume given by

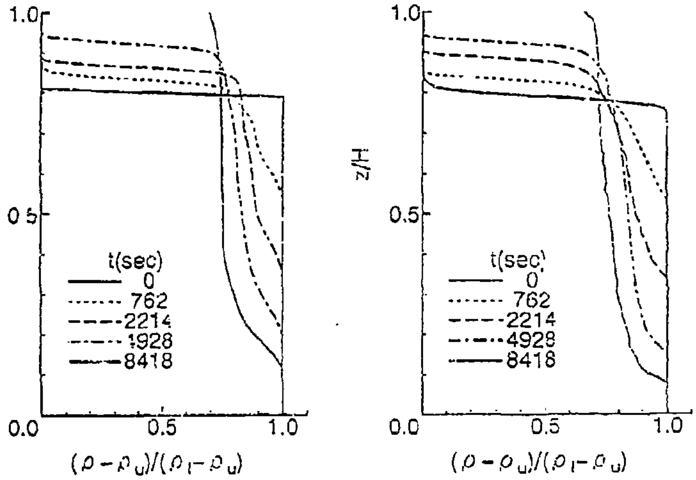

a)

b)

Figure 6: Examples of the simulated evolution of the ambient stratification in comparison with corresponding experiments. (a) BT-3 (simulation), (b) BT-3 (experiment).

$$G_2 = G_{1l} \tag{13}$$

$$V_2 = -\frac{V_1 R_1^2}{S^2} \tag{14}$$

$$R_2 = \sqrt{R_1^2 + S^2} \tag{15}$$

The outer plume equations are integrated down to the neutral buoyancy level. During this downward integration, the values used for R_1, V_1, and G_1 at each level are those derived by the previous integration up the inner plume. An intrusion forms at the neutral buoyancy level. This process was repeated until it converged; the criterion for the convergence was less than 1% difference in the buoyancy of the inner plume from the previous value.

The entrainment coefficient α was taken as the value of a pure plume, 0.083, and β was given by 0.5. γ equals unity, since it corresponds to the falling outer draft.

For the case that the inner plume reaches the free surface, the water flows out radially along the free surface, then suddenly plunges into the water body. Assuming the homogeneous density for the surface outflow, the nondimensional initial quantities of the outflow are related to the inner plume values by

$$G_{sI} = G_{1I} \tag{16}$$

$$V_{sI} = \alpha\frac{R_I}{H_I}V_{1I} \tag{17}$$

$$\frac{1}{2}[(1-K_L)-(\frac{\alpha R_I}{H_I})^2]V_{1I}^2 - \frac{1}{2}G_{1I}H_I = \frac{1-H_I}{R_I^2(1-H_R x_I)(V_{1I}+M_H^{-1/3})} \tag{18}$$

where subscripts I and s denote the values at the impingement region and of the surface jet respectively; in nondimensional form R_I is the radius of the point where the horizontal jet starts, H_I is the initial thickness of the horizontal jet, V_{1I}, G_{1I}, and G_{1lI} are the velocity and the reduced gravity of the inner plume and the reduced gravity of the water at $1-H_I$, V_{sI} and G_{sI} are the velocity and the reduced gravity at the beginning of the horizontal jet, and K_L is the energy loss coefficient (=0.2), x_I is the nondimensional height of the lower boundary of the impingement zone(= $1-H_I$). x_I, G_{sI}, and V_{sI} are obtained by solving (16) to (18) simultaneously using the quantities of the inner plume.

In the ambient, the mass and the momentum conservations of the bubble plume are given by

$$\frac{\partial G_a(x)}{\partial \tau} = -\frac{(R_1^2 V_1 + S^2 V_2)}{A}\frac{\partial G_a(x)}{\partial x} \tag{19}$$

Therefore, the density at z is

$$G_a(x, \tau + \Delta\tau) = G_a(x + \frac{(R_1(x)^2 V_1(x) + S^2(x) V_2(x))\Delta\tau}{A}, \tau) \tag{20}$$

Intrusion velocity was assumed to be infinite. Therefore, the new layer, $G_a(z_{int})$ in density, and $-(S(z_{int})^2 V_2(z_{int}))/A$ in thickness, was inserted at the neutral buoyancy level.

Figure 7 depicts the evolution of the ambient stratification simulated using the double-plume model (Figure 7 a) and measured in the experiment (BT-3) (Figure 7 b). It is clear that the double-plume model can simulate the phenomena with satisfactory accuracy.

References

Asaeda, T. & Imberger, J. 1993 Structure of bubble plumes in linearly stratified environments. J. Fluid Mech., 249, 35-57.

Baines, W.D. 1974 Entrainment by a plume or jet at the density interface, J. Fluid Mech. 68, 309-320.

Baines, W.D. & Leitch, A.M. 1992 Destruction of stratification by a bubble plume, J. Hydr. Engrg., ASCE, 118, 559-577.

Fannelop, T.K., Hirschberg, S. & Kuffer, J. 1991 Surface current and recirculating cells generated by bubble curtains and jets. J. Fluid Mech., 229, 629-657.

Fischer, H.B., List, E.G., Koh, R.C.Y., Imberger, J. & Brooks,N.H. 1979 Mixing in Inland and Coastal Waters, Academic Press, New York.

Germeles, A.E. 1975 Forced plumes and mixing of liquids in tanks. J. Fluid Mech., 71, 601-623.

Imberger, J. & Patterson, J.C. 1989 Physical Limnology, Adv. Appl. Mech., 27, 303-475.

Kumagai, M. 1984 Turbulent buoyant convection from a source in a confined two-layered region. J. Fluid. Mech., 147, 105-131.

McDougall, T.J. 1978 Bubble plumes in stratified environments. J. Fluid Mech., 85, 655-672.

Milgram, J.H. 1983 Mean flow in round bubble plumes. J. Fluid Mech., 345-376.

Milgram, J.H & Van Houten, R.J. 1982 Plumes from sub-sea well blowouts, Proc. 3rd Intl. Conf., BOSS, Vol.1, 659-684.

Plume Interaction Above An Outfall Diffuser

M. J. Davidson[1] and I. R. Wood[2]

[1]Department of Civil and Structural Engineering
Hong Kong University of Science and Technology, Clear Water Bay, Kowloon

[2]Department of Civil Engineering
University of Canterbury, Christchurch, New Zealand

Abstract

Waste water is generally disposed of, in the ocean, via an outfall. The outfall pipeline, resting on or beneath the ocean floor, transports the waste water offshore to the disposal site. At this site the effluent is discharged through a diffuser. Diffusers take on a variety of forms, ranging from a simple pipe with a number of holes placed alternately on either side, to a complex system of risers and radial diffusers typical of large scale tunnelled outfalls. The prediction of the initial dilution of the positively buoyant waste water plumes as they rise from the diffuser to the ocean surface is an important step in assessing the performance of any proposed diffuser configuration. In this paper we consider how the interaction of adjacent plumes (due to insufficient port spacing) influences the dilution efficiency of the outfall diffuser. The diffuser configuration studied is that of a pipe with ports placed alternately on either side and the ambient fluid is assumed to be quiescent and well mixed. We present an integral model which uses an under pressure concept to incorporate the effects of plume interaction on the dilution of effluent above such a diffuser. Where the close proximity of neighbouring plumes results in deficiencies in the quantities of fluid available for entrainment, additional currents are induced in the ambient fluid to meet these demands. These induced currents create pressure differentials across the plumes and the resulting forces bring the plumes together. Data from the model agrees satisfactorily with the laboratory data of Liseth [7], although further experimental investigations of these merging phenomena are required.

Introduction

At the beginning of this century waste water outfalls commonly consisted of a pipe discharging untreated effluent onto a beach in a remote location. Remote areas of the past soon became suburbs and with an increasing public awareness of environmental quality these types of discharges have become unacceptable. Unsightly discharges of this nature have gradually been replaced with waste water disposal systems which comprise of a treatment plant, a pipeline and a diffuser. The treated effluent is carried via the pipeline along (or beneath) the ocean floor to an offshore disposal site. At the terminus a diffuser splits the discharge into a number of smaller discharges. These fresh water discharges into a denser salt water environment produce turbulent plumes rising towards the ocean surface. This turbulent mixing greatly enhances the dilution of the effluent and consequently reduces the impact on the local environment.

Traditionally diffusers were designed to provide ample ambient fluid for entrainment into the rising effluent plumes and hence ports were sufficiently spaced to allow plumes to rise to the surface individually. In conjunction with this design philosophy there has been a significant research effort into methods of predicting the behaviour of single buoyant discharges and there are now a number of models available that can predict with reasonable accuracy plume behaviour for a variety of ambient conditions (Lee et al. [6], Wood [12]). However, where there are practical limits on the length of the diffuser section the rising plumes interact before they reach the surface. Indeed a recent investigation by Cheng et al. [3] indicates that where there are persistent currents such interaction may be desirable. In this paper we present a model a single plume as it rises to the surface and interacts with neighbouring plumes. We consider a plume near the centre of a long diffuser and edge effects are therefore neglected. The ports are equally spaced and we assume the ambient fluid is stagnant and unstratified. We believe the concepts developed in this model can be applied to other plume interaction problems such as discharges from radial diffusers typical of large scale tunnel outfall systems (Roberts et al. [11])

The Model

Plumes are typically discharged on alternate sides of the diffuser as shown in figure 1. A representative discharge is initially axisymmetry, but as it grows through turbulent entrainment it begins to interact with neighbouring plumes on the same side of the diffuser. It eventually merges with these plumes to form a two dimensional plume. Identical behaviour on the other side of the diffuser generates a second two dimensional plume and a vertical plane of symmetry exists midway between these two two dimensional plumes at the diffuser centre line. Assuming the two two dimensional plumes are identical there will be no nett mass or momentum fluxes across this plane of symmetry. Thus there is a limit on the local ambient fluid available for entrainment into the inner sides of the two dimensional plumes. Fluid flows up from the areas below where merging began to satisfy the entrainment demands of the plumes (figure 1). These additional induced currents reduce the pressure on the inner side of the plumes creating a pressure difference across each of the plumes. The resulting force brings the two two dimensional plumes together and as they merge they exert positive pressures on each other reducing their horizontal momentums to zero. This region is similar to that of a jet hitting a flat plate and one would expect some down flow associated with the changes in the vertical momentum of the plumes. This down flow will form a small pocket of buoyant fluid resting below the merging plumes. When the merging of the two two dimensional plumes is complete a single two dimensional plume has formed and it rises vertically towards the surface.

In developing a model it is perhaps best to divide the plume into regions of distinct behaviour. We will define *Region 1* as the initial axisymmetric region. *Region 2* where the plumes merge on each side of the diffuser to form two two dimensional plumes and these plumes are drawn together due to additional induced currents in the ambient fluid.

The region where the two two dimensional plumes merge above the outfall diffuser will be designated *Region 3* and finally *Region 4* where the plume rises vertically as a single two dimensional plume.

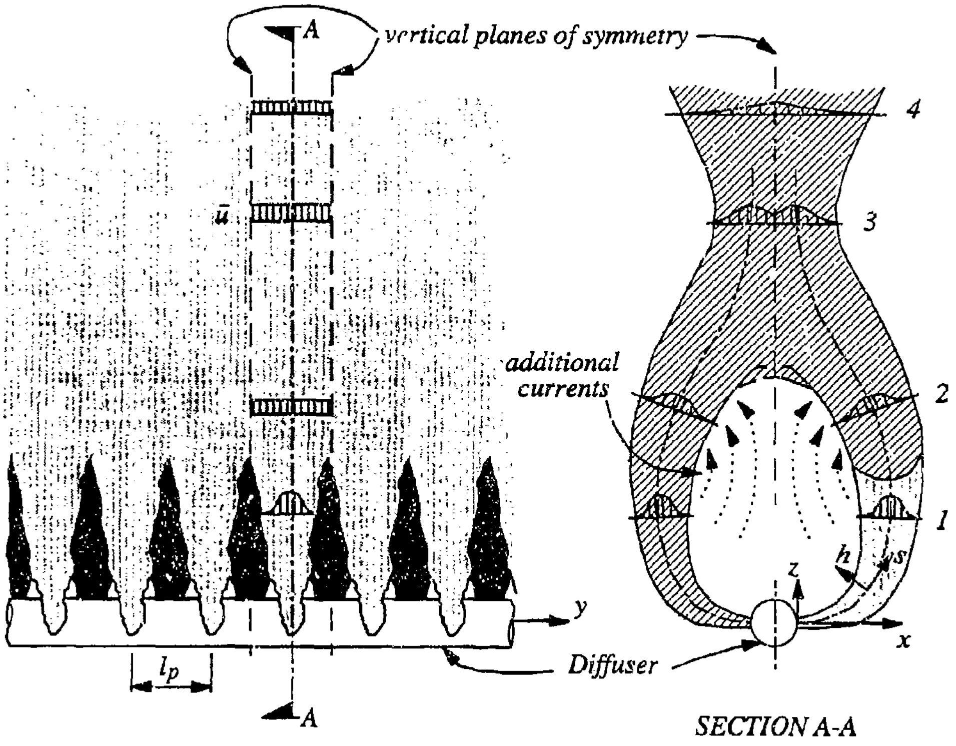

Figure 1: A schematic diagram of the central part of a long diffuser

In addition to the central plane of symmetry discussed above vertical planes of symmetry, through which we can assume no nett fluxes of mass or momentum, also exist midway between plumes on the same side of the diffuser. Thus we can consider the behaviour of a single plume within an open box bounded by the three frictionless planes of symmetry. Within this symmetry frame we can define the behaviour of the plume as it rises towards the surface. We begin by defining general equations which apply in all four regions and then define the modifications necessary to describe the specialised behaviour in *Regions 2* and *3*. Cartesian coordinates (x, y, z) originate from the source and s measures distance along the plume centre line from this origin. The distance h is measured from the plume centreline normal to the $y - s$ plane. These coordinates are shown in figure 1.

The plume volume flux (q) and momentum flux (M) can be written as:

$$q = I_q U b \ell_p, \text{ and } M = I_m U^2 b \ell_p; \tag{1}$$

in which

$$I_q = \int_{-3b}^{3b}\int_{-\frac{\ell_p}{2}}^{\frac{\ell_p}{2}} \frac{\overline{u}}{U}\frac{dy}{b}\frac{dh}{\ell_p}, \tag{2}$$

$$I_m = \int_{-3b}^{3b}\int_{-\frac{\ell_p}{2}}^{\frac{\ell_p}{2}} \left[\frac{\overline{u}}{U}\right]^2 \frac{dy}{b}\frac{dh}{\ell_p}, \tag{3}$$

ℓ_p is the distance between the port centre lines on the same side of the diffuser,
$\overline{u}$ is the time averaged velocity,
U is the plume centreline value of $\overline{u}$, and
b is a representative plume radius defined as the distance from the centre line to a point where $\overline{u} = exp(-1)U$,

Assuming that the results of Miller et al. [8] and Bradbury [2] for two dimensional jets can be applied to this problem we neglect the turbulent flux term in the definition of I_m.

The plume buoyancy (B) and flux of density deficit ($q_{\Delta 0}$) can be written as:

$$B = I_\Delta \Delta b \ell_p, \text{ and } q_{\Delta 0} = I_{q\Delta} U \Delta b \ell_p; \tag{4}$$

in which

$$I_\Delta = \int_{-3b}^{3b}\int_{-\frac{\ell_p}{2}}^{\frac{\ell_p}{2}} \frac{\overline{\Delta_\ell}}{\Delta}\frac{dy}{b}\frac{dh}{\ell_p}, \tag{5}$$

$$I_{q\Delta} = 1.19\int_{-3b}^{3b}\int_{-\frac{\ell_p}{2}}^{\frac{\ell_p}{2}} \frac{\overline{\Delta_\ell}}{\Delta}\frac{\overline{u}}{U}\frac{dy}{b}\frac{dh}{\ell_p}, \tag{6}$$

$\overline{\Delta_\ell}$ is time average density difference ($\frac{\Delta \rho_\ell}{\rho}$) multiplied by the gravitational acceleration (g), and
Δ is the plume centre line value of $\overline{\Delta_\ell}$.

The constant 1.19 in the definition of $I_{q\Delta}$ replaces a turbulent flux term (Papanicolaou [9]).

These equations have been developed for a finite control volume extending from $-\ell_p$ to ℓ_p in the y direction and from $-3b$ to $3b$ in the h direction. A finite control volume extending across essentially the whole plume $(-3b, 3b)$ was chosen because we are interested in quantifying the external forces acting on the plume. This subtlety has a negligible effect on the values of the shape functions $I_q, I_m, I_{q\Delta}$ and I_Δ when compared to those developed for a control volume extending from $-\infty$ to ∞ in the h direction.

The values of the shape functions depend on the shape of the velocity and density distributions and these shapes change as the plumes interact and merge with one another. For a line of identical discharges we define the velocity and density distributions as:

$$\frac{\overline{u}}{U} = \frac{exp - \left[\frac{h}{b}\right]^2 \left(\sum_{-\infty}^{\infty} exp - \left[\frac{y+n\ell_p}{b}\right]^2\right)}{\sum_{-\infty}^{\infty} exp - \left[\frac{n\ell_p}{b}\right]^2}, \text{ and} \tag{7}$$

$$\frac{\overline{\Delta_\ell}}{\Delta} = \frac{exp - \left[\frac{h}{b}\right]^2 \left(\sum_{-\infty}^{\infty} exp - \left[\frac{y+n\ell_p}{b}\right]^2\right)}{\sum_{-\infty}^{\infty} exp - \left[\frac{n\ell_p}{b}\right]^2}. \tag{8}$$

Simplified definitions of the shape function were developed for the merging of the two dimensional plumes in *Region 3*. Taking the definition of I_m as an example; in the three dimensional limit ($\frac{b}{\ell_p} < 0.3$) it has the form:

$$I_m = \frac{\pi}{2}\frac{b}{\ell_p}. \tag{9}$$

and in the two dimensional limit ($\frac{b}{\ell_p} > 0.8$) it becomes a constant:

$$I_m = \sqrt{\frac{\pi}{2}}. \tag{10}$$

The variations of this and the other functions between these limiting forms are shown in Davidson et al. [4].

If we define β as the clockwise angle between a tangent to the plume centre line and the horizontal plane; we can then write the horizontal momentum (M_H) as:

$$M_H = M cos\beta \tag{11}$$

and the vertical momentum (M_V) as:

$$M_V = M sin\beta. \tag{12}$$

The momentum equations are then written in the following form:

$$\frac{dM_H}{ds} = \mathcal{F}_x, \text{ and } \frac{dM_V}{ds} = B + \mathcal{F}_y. \tag{13}$$

Where $\mathcal{F}_x$ and $\mathcal{F}_y$ represent the effect of external forces acting on the control volume and their definitions are dependent upon the Region we are modelling. In *Regions 1* and *4* the plumes are unaffected by the behaviour of neighbouring plumes and hence $\mathcal{F}_x = \mathcal{F}_y = 0$. In *Region 2* the additional induced currents in the irrotational ambient fluid near the inner side of plume reduce the pressure. The pressure difference between the inner and outer sides of the plume can be defined using the Bernoulli equation and this difference generates an external force acting on the control volume leading to following definitions of $\mathcal{F}_x$ and $\mathcal{F}_y$:

$$\mathcal{F}_x = \frac{U_u^2}{2}\ell_p sin\beta, \text{ and } \mathcal{F}_y = \frac{U_u^2}{2}\ell_p cos\beta. \tag{14}$$

In which U_u is the average velocity of the additional induced currents. These currents are defined as the ambient fluid passing by the control volume as opposed to the entrained fluid which passes into it. The additional induced velocity is further defined by:

$$U_u = \frac{Q_u}{A_u}, \tag{15}$$

where A_u is the area between the inner side of the plume and the vertical plane of symmetry passing through the diffuser centreline. We define the volume flux of fluid passing by the control volume (Q_u) by considering the conservation of volume flux in the area confined by the plume and the planes of symmetry. This dictates that the decrease in the volume flux of fluid passing by the control volume must equal an be opposite to the flux of fluid into the control volume due to entrainment on the inner side of the plume. This will be approximately one half of the total flux into the control volume (dQ_e). We can therefore write:

$$\frac{dQ_u}{ds} = -\frac{1}{2}\frac{dQ_e}{ds} = -\frac{1}{2}\frac{d}{ds}(I_q U b \ell_p). \tag{16}$$

In *Region 3* the plumes merge and exert a positive pressure on each other reducing their respective horizontal momentums to zero. The horizontal force required to achieve this can be determined by considering a control volume which extends from the point where merging begins to the point where the plumes are rising vertically. This force will be applied over some length scale which we arbitrarily assume to equal $4b$. Using a *cosine* function to apply the force smoothly we get following form for $\mathcal{F}_x$:

$$\mathcal{F}_x = \frac{I_m U^2 b \ell_p}{4b}\left[1 - cos\left(\frac{2\pi(s - s_m)}{4b}\right)\right], \tag{17}$$

in which s_m is value of s at the point where the two two dimensional plumes being to merge. A vertical force associated with the small pool of fluid resting below the merging plumes will also be exerted on the control volume. However, for the moment we assume that the effect of this force is small and hence $\mathcal{F}_y = 0$.

The geometric relationships can be defined generally as:

$$\frac{dx}{ds} = \frac{M_H}{M}, \text{ and } \frac{dy}{ds} = \frac{M_V}{M}. \tag{18}$$

The spread equation is:

$$\frac{db}{ds} = k\mathcal{G} \tag{19}$$

where the constant $k = 0.11$ (Papanicolaou [9]) and the function $\mathcal{G} = 1$ in *Regions 1,3* and *4*. In *Region 2* the spread of the plume will be reduced by the induced currents on the inner side of the plume. This reduction will be similar to that for a jet in a coflowing current and following Patel [10] we can define $\mathcal{G}$ as:

$$\mathcal{G} = \frac{2U - U_u}{2U} \tag{20}$$

The equations described above can be organised into a system of ordinary-differential equations and solved with a Runge-Kutta routine. Initial conditions are determined at the end of the zone of flow establishment and are based on the results of Ayoub [1]. At the beginning of *Region 3* however, an additional equation is introduced and an initial value of the volume flux passing by the control volume Q_{ui} is required. As there is no information available for estimating this value it has been determined through trial and error. The value of Q_{ui} must be just sufficient to meet the entrainment demands prior to the merging of the two two dimensional plumes. Indications from the model are that this value is sensitive to port spacing, less sensitive to the port Froude number and least sensitive to the diffuser diameter. Predictions of dilution data from this model are compared with the experimental data of Liseth in figure 2.

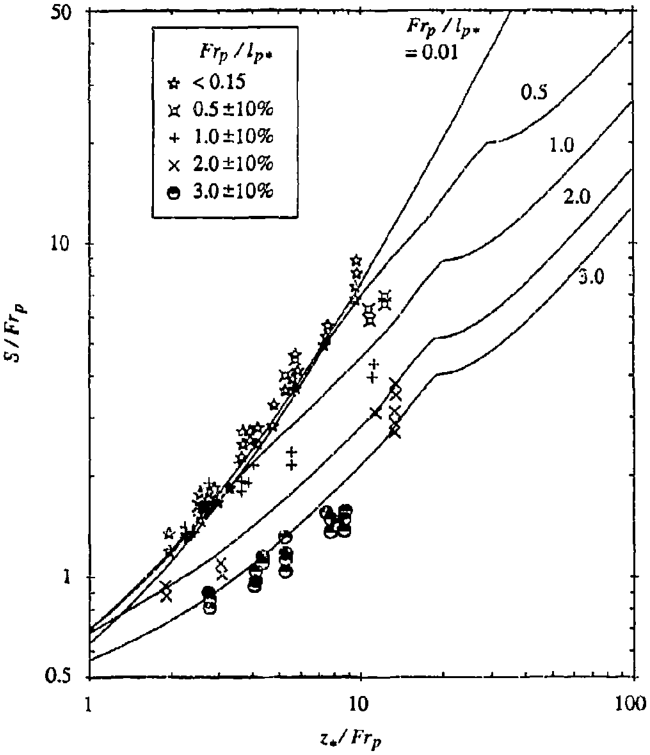

Figure 2: Minimum dilution ($S = \frac{\Delta_p}{\Delta_m}$) versus depth. In which Δ_p is the value of Δ at the port and Δ_m is the minimum value of Δ in a cross section. The subscript $*$ indicates division by the port diameter (d_p). The port Froude number (Fr_p) is defined by the port exit velocity (U_p), Δ_p and d_p.

Conclusions

Considering the significant variations in the data the model predicts the dilutions reasonably well and somewhat better than previous attempts to model this problem (Davidson [5], Wood [13]). The principle reason is the inclusion of the effects of the induced currents on the vertical momentum of the plume. Previously this has been assumed to be insignificant. Results from the model indicate the induced currents on the inner side of the plume reach magnutudes as high as 50 percent of the centre line mean velocity and have a significant effect on the vertical and horizontal momentum of the plume. The model also indicates that plume interaction alters the shape, spread, dilution and trajectories of a plume. A detailed experimental investigation is now required to further assess and modify the assumptions made during the development of this model.

References

[1] Ayoub, G. M. 1973 Test results on buoyant jets injected horizontally in a cross flowing stream, *Water Air and Soil Pollution* **2**, 409-426.

[2] Bradbury, L. J. S. 1965 The structure of a self preserving turbulent plane jet, *J. Fluid Mech.* **23**(1), 31-64.

[3] Cheng, C. W., Davidson, M. J. and Wood, I. R. 1992 Merging buoyant discharges in an ambient current, *Journal of Hydraulic Research* **30**(3), 361-372.

[4] Davidson, M. J. 1989 The behaviour of single and multiple horizontally discharged buoyant flows in a non-turbulent coflowing ambient flow, Report No. 89-3, Department of Civil Engineering, University of Canterbury, New Zealand.

[5] Davidson, M. J., Papps, D. A. and Wood, I. R. 1993 The behaviour of merging buoyant jets, in *Recent advances in the fluid mechanics of turbulent jets and plumes*, Davies, P. A. and Neves, J (ed.), Kluwer Acadamic.

[6] Lee, J. H. W. and Cheung, V. W. L. 1990 Generalised lagrangian model for buoyant jets and plumes, *J. Envir. Eng.*, ASCE, **116**(61), 1085-1106.

[7] Liseth, P. 1970 Mixing of merging buoyant jets from a manifold in a stagnant receiving water of uniform density, Report No. HEL 23-1, Hydraulic Engineering Laboratory, Unversity of California, Berkely, California, USA.

[8] Miller, D. S. and Cummings, E. W. 1957 Static pressure distribution in the free turbulent jet, *J. Fluid Mech.* **3**, 1-16.

[9] Papanicolaou, P. N. 1984 Mass and momentum transport in a turbulent buoyant vertical axisymmetric jet, PhD Thesis, W. M. Keck Laboratory of Hydraulics and Water Resources, California Institute of Technology, Pasadena, California, USA

[10] Patel, R. P. 1971 Turbulent jets and wall jets in a uniform streaming flow, *Aeronautical Quarterly*, XXII, Nov., 311-326.

[11] Roberts, P. J. W. and Snyder, W. H. 1993 Hydraulic Model Study for the Boston Outfall.II: Environmental Performance, *J. Hyd. Eng*, ASCE, **119**(9), 988-1003.

[12] Wood, I. R. 1993 Asymptotic solutions and behaviour of outfall plumes, *J. Hyd. Eng.*, ASCE, **119**)(5), 555-580.

[13] Wood, I. R., Bell, R. G. and Wilkinson, D. L. 1993 *Ocean Disposal of Wastewater*, World Scientific.

Particle Clouds In Density Stratified Environments

David Luketina and David Wilkinson
Department of Civil Engineering
University of New South Wales
Sydney 2052 Australia

A particle cloud descending in a stably stratified fluid entrains or captures ambient fluid. The cloud reaches a maximum depth when its downward motion is arrested by its loss of buoyancy due to the entrained fluid and to the particles separating from the particle cloud. The captured fluid then rebounds to its level of neutral buoyancy. It is shown via laboratory experiments and a numerical model that the maximum penetration and final depths of the captured fluid depend upon the non-dimensional buoyancy of the particles and the non-dimensional settling velocity of the individual particles where the non-dimensionalising variables are the fluid density and stratification.

Introduction

Each year vast quantities of particulate matter are dumped into the ocean. In 1990 over 20 Gigatonnes of dredge spoil was disposed of in this way with some individual releases from bottom dump barges exceeding 15,000 tonnes. Additionally some 40 Megatonnes of sewage sludge and industrial wastes were also dumped into the ocean, usually on the continental margins. The dispersion of material disposed of in this manner is of environmental concern and this paper aims to clarify certain aspects of the settling processes in stratified water bodies.

The behaviour of clouds of dense particles sinking in homogeneous fluids has been examined experimentally by Nakatsuji, Tamai and Murota (1990) and by Rahimipour and Wilkinson (1992). These studies indicated that following their release, an initially packed group of dense particles would accelerate downwards with shear forces at the boundaries of the group producing turbulent motions which cause the particles to disperse into a particle cloud. The effective density of the cloud was reduced by this process and the particles acted more like a distributed buoyancy. The velocity of the cloud reached a maximum and its form approached the mushroom shape of a miscible thermal. The characteristic internal circulation of a self-preserving thermal was strongly evident. a necessary requirement for the development of this phase was that the fall velocity of individual particles within the cloud should be much less than the velocity of the cloud itself. Figure 1 shows a photograph of a particle cloud in the self-preserving thermal phase. The strong vortical structure characteristic of thermals is clearly visible and it can be seen that most of the particles are contained within the vortex ring comprising the thermal. When sinking in homogeneous fluid, the negative buoyancy (submerged weight) of the cloud remains constant as in a simple miscible thermal and its increasing volume due to entrained ambient fluid causes its velocity to decrease. This can also be demonstrated by means of simple scaling arguments.

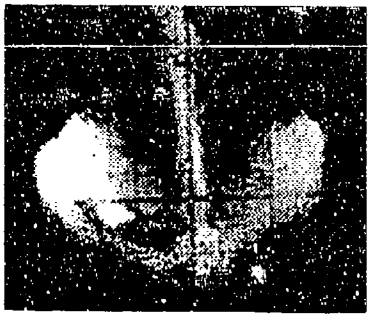

Figure 1 Photograph of a particle cloud in the self-preserving thermal phase. The cloud was illuminated by a light sheet traversing its central axis.

Ultimately the velocity of the cloud decreases to a point where its speed is comparable with the settling velocity of individual particles. The internal circulation becomes suppressed by the presence of the particles which then continue to settle as a particle swarm with all particles sinking downwards. This phase has been studied by Buhler and Papantoniou (1991) who argued that the cloud enters a third self-preserving phase. The velocity of the swarm front was found to approach a constant value which they found to be about 1.4 times the fall velocity of individual particles. In this final phase the particles continued to spread but at a very much slower rate than is the case during the thermal like phase. Buhler and Papantoniou (1991) suggested that the spread of particle swarms is due to the outward flow induced by the wake behind each particle and by shear induced entrainment at the lateral fringes of the swarm.

Rahimipour and Wilkinson (1992) showed that the transitional behaviour between the thermal phase and the swarm phase could be characterised by a parameter expressing the ratio of the settling velocity of individual particles (w_s) to a local characteristic velocity of the plume expressed by $(B/\rho R^2)^{1/2}$ where B is the submerged weight of the particles in the cloud, ρ is the density of the ambient fluid and R is the local cloud radius. This ratio was termed the cloud number N_c so that

$$N_c = w_s R \left(\frac{\rho}{B}\right)^{1/2} \qquad (1)$$

Scaling Relationships

Consider a mass of particles M with individual particles having density ρ_p and settling velocity w_s in a fluid of density ρ. The submerged weight or effective buoyancy of the particle mass (henceforth referred to as simply "the buoyancy") is given by

$$B = \frac{\rho_p - \rho}{\rho} g M \qquad (2)$$

where g is gravitational acceleration.

If a group of particles is released from rest, and there are sufficient numbers of them so that the group accelerates to a velocity which is substantially greater than the settling velocity of individual particles, then they behave as if they were a distributed buoyancy and the resulting particle cloud has a structure which is thermal-like. The velocity of the particle group during the phase of initial acceleration scales as

$$w = \left(\frac{Bz}{M}\right)^{1/2} \qquad (3)$$

where B/M is a measure of the group's acceleration.

Once in the self-preserving thermal phase, the characteristics of a particle cloud in ambient fluid of uniform density are determined by its buoyancy, its distance z from some virtual origin and the fluid density. On dimensional grounds its size (expressed in terms of its overall radius R) is given by

$$R = c_1 z \qquad (4)$$

and its velocity w by

$$w = c_2 \left(\frac{B}{\rho}\right)^{1/2} z^{-1} \qquad (5)$$

where c_1 and c_2 are constants with values of 0.34 and 1.5 respectively where z is taken as positive downwards. Equating velocities in the initial acceleration phase and the thermal phase gives the extent of the acceleration phase z_a as

$$z_a = \left(\frac{M}{\rho}\right)^{1/3} \tag{6}$$

It will be noted from Eq. (5) that the velocity of the cloud in the thermal phase decreases as it sinks so that ultimately it will approach the settling velocity of particles within the cloud. At this stage, velocities of circulation within the cloud induced by entrainment of ambient fluid into the cloud are insufficient to advect the particles with them. The buoyancy can no longer be regarded as distributed and the thermal-like structure decays. The extent z_t of the thermal-like phase in a homogeneous fluid is obtained by comparing the thermal velocity with that of the particles to give

$$z_t = \left(\frac{B}{\rho}\right)^{1/2} w_s^{-1} \tag{7}$$

Bühler and Papantoniou (1991) argued that during the final phase in which the cloud evolves into a 'swarm' of sinking particles, the flow remains nearly self-preserving and entrainment is primarily through the frontal face of the swarm. The velocity of the swarm is close to the settling velocity of individual particles and momentum and continuity arguments led to the cloud radius increasing as $z^{1/3}$ or z^1 depending on whether the entrainment velocity scales as the velocity of fluid passing through the swarm or the much larger fall velocity of the particles themselves. The former relationship would seem the more probable in that during this phase the particles occupy only a small fraction of the fluid region affected by their presence. Bühler and Papantoniou pointed out (with admirable honesty) that their experimental data was unable to resolve between the two power laws because of uncertainties regarding the location of the virtual origin.

Ambient Stratification

The pressure of stratification in the ambient fluid has a profound influence on the behaviour of the particle clouds. Fluid entrained into the cloud becomes buoyant as it is advected in the cloud below its level of capture. Thus the buoyancy of the cloud decreases as the cloud sinks. The structure of the cloud remains thermal-like as long as the cloud velocity is sufficiently greater than the settling velocity of the particles. The particles are then maintained in the circulation and act as a distributed buoyancy. Ultimately, however, the downward motion of the cloud is arrested by its loss of buoyancy and at this point the particles move as a swarm from the interstitial fluid which rebounds to a higher level because of its buoyancy. Figure 2 shows the motion of the cloud in a linearly stratified fluid.

The penetration (z_p) of a miscible thermal into a stratified environment scales as

$$z_p = \left(\frac{B}{\rho N^2}\right)^{1/4} \tag{8}$$

where N is the buoyancy frequency defined by

$$N = \left(\frac{g}{\rho}\frac{d\rho}{dz}\right)^{1/2} \tag{9}$$

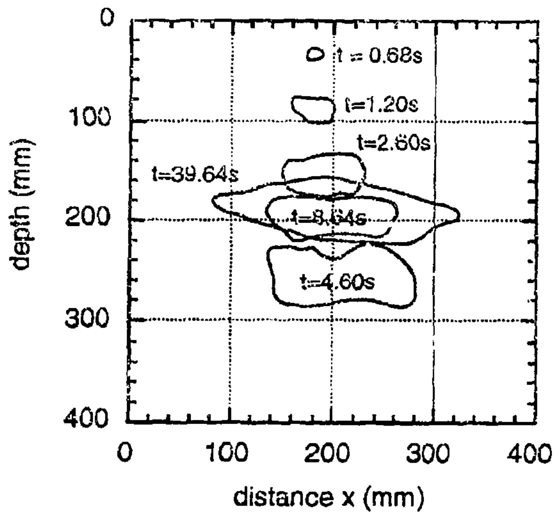

Figure 2 Digitised picture of the fluid captured by a particle cloud due to 2 g of 0.153 mm diameter glass beads released at the surface. The linear stratification was 10.3 kg/m^4. The rebound of the interstitial fluid occurs at a time t of 4.6 seconds after the particles were released.

The velocity of the thermal is no longer given by the simple formulation of Eq.5 and because the motion is oscillatory may be multivalued for any specified depth z. Dimensional analysis of the relevant variables yields a relationship of the form

$$\frac{w}{(BN^2/\rho)^{1/4}} = f_1\left[z(\rho N^2/B)^{1/4}\right] \qquad (10)$$

where f_1 denotes a functional relationship.

The particles separate from the thermal when its velocity is comparable with the settling velocity of individual particles and the distance to this transition z_t is therefore

$$z_t = \left(\frac{B}{\rho N^2}\right)^{1/4} f_2\left[\frac{w_s}{(BN^2/\rho)^{1/4}}\right] \qquad (11)$$

Thus separation can occur at any stage depending on the settling velocity of the particles. However, if the particle settling velocity is small compared with typical velocities of the thermal [characterised by $(BN^2/\rho)^{1/4}$] then they will not leave the thermal until it has nearly reached its maximum depth. In such cases, the maximum depth of penetration and the final equilibrium depth would be relatively insensitive to w_s. The term $w_s/(BN^2/\rho)^{1/4}$ is a cloud number for particle clouds in a stratified fluid and will be termed N_{cs}.

Mathematical Modelling

To proceed further analytically it is necessary to involve the conservation laws governing the phenomenon. The conservation laws for mass, buoyancy and momentum are:

$$\frac{dR}{dt} = 2E|w| \qquad (12)$$

$$\left(V - \frac{M}{\rho\, rd}\right)\frac{d\rho_t}{dt} + (\rho_t - \rho)4E\pi R^2|w| = 0 \qquad (13)$$

$$\left[M - (1+\psi)\left(\frac{M}{rd} + V\rho_t\right)\right]\frac{dw}{dt} + (1+\psi)\rho_t 4E\pi R^2|w| = gM\left(i - \frac{1}{rd}\right) + F_D\frac{w}{|w|} + (\rho - \rho_t)Vg \quad (14)$$

where:

	V	is the volume of the particle cloud
	F_D	is the drag force acting on the particle cloud
	E	is the entrainment coefficient
	rd	is the relative density of the particles
	ρ_t	is the density of fluid within the particle cloud
	ψ	is the virtual mass coefficient

and:

$$\rho = z\frac{d\rho}{dz} + \rho_{surface} \quad (15)$$

$$V = \frac{4}{3}\pi R^3 \quad (16)$$

$$F_D = C_D\pi R^2\rho\frac{w^2}{2} \quad (17)$$

where C_D is the drag coefficient. Equations (12), (13) and (14) are derived on the basis that the fluid is incompressible and that the Boussinesq approximation may be used. Also, it is assumed that there are negligible losses of momentum and buoyancy to the wake of the particle cloud (Escudier and Maxworthy, 1973).

Numerical Modelling

The conservation equations were converted to a difference form and solved numerically. The numerical model showed that form drag played a relatively small role in the particle cloud behaviour. For simplicity, the entrainment coefficient E was kept fixed at a value of 0.31 while the thermal was descending. For later times E was set to zero as the laboratory experiments indicated that circulation in a particle cloud is rapidly weakened during this stage. The virtual mass coefficient ψ was fixed at a value of 0.5 (see Escudier and Maxworthy, 1973). The motion and distribution of particles within a particle cloud are constantly changing with time and, for this reason, are difficult to parameterise. In the modelling it was assumed that the particles are uniformly distributed within the cloud until the fall velocity w_s of the particles exceeds the fall velocity w of particle cloud at which time the particles separate from the cloud. Releasing the particles at earlier times made relatively little difference to the results provided that the mass of the particle cloud was considerably greater than the mass of the particles at the time of the release.

Of the parameters in Equations (12) to (17), the stratification $d\rho/dz$ and the mass M, played the dominant role in determining the particle cloud behaviour. The model was run with particles of 0.1 mm diameter and having a relative density of 2.5 giving a corresponding particle fall velocity of around 7 mm s^{-1}. All model runs were done such that the non-dimensional particle fall velocity N_{cs} was much less than unity. Thus, from (11), the depth z of particle cloud can be normalised by $(B/\rho N^2)^{1/4}$. The time t can be normalised by $1/(2\pi N)$. Figure 3 shows results from the model for a variety of stratifications and particle masses. It is quite clear that the model results collapse very well when normalised despite the stratification and particle masses each spanning over a decade of values.

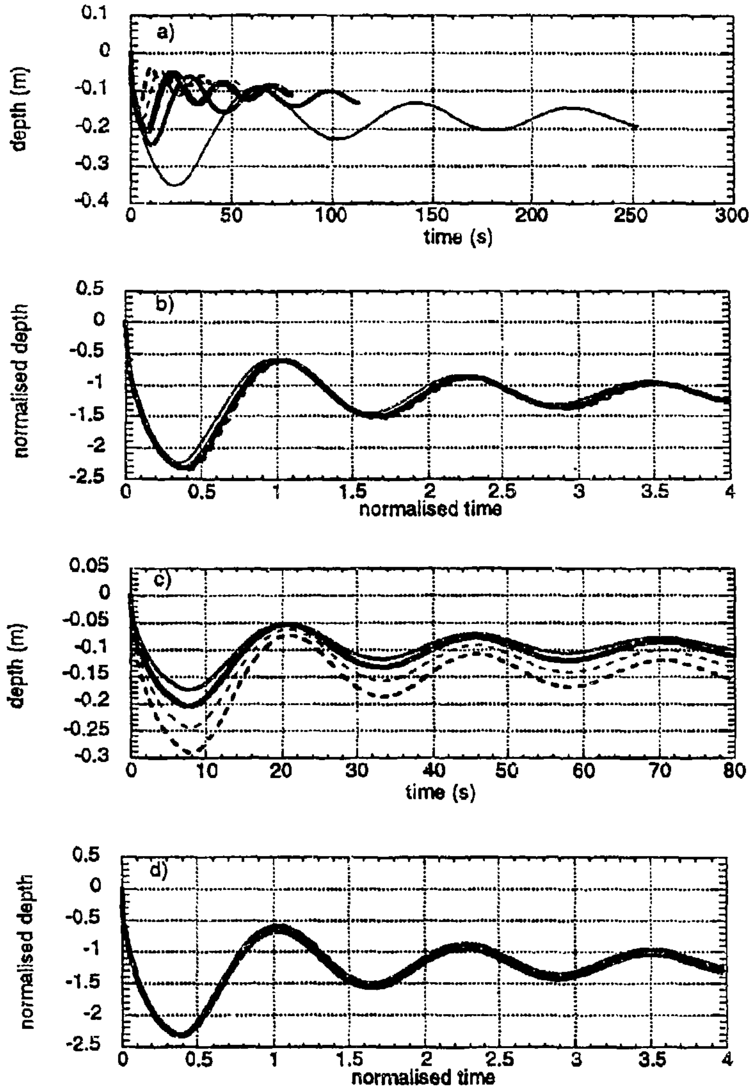

Figure 3 Numerical modelling results for particles of 0.1 mm diameter and having a relative density of 2.5. In a) 1 g of particles were released with stratifications of 1 (thin line), 5 (medium line), 10 (thick line), 20 (thin dashed line) and 40 kg/m^4 (medium dashed line). In c) a stratification of 10 kg/m^4 was used with particle masses of 0.5 (medium line), 1 (thick line), 2 (thin dashed line) and 4 g (medium dashed line). b) and d) show normalised versions of a) and c) respectively where the normalised depth is given by $z/(B/\rho N^2)^{1/4}$ and the normalised time by $Nt/2\pi$. Note that the normalised period of oscillation is not quite 1 unit in duration because of the virtual mass of [illegible] tured fluid.

Experiments

Particle releases were examined in a 1 m × 1 m × 0.8 m deep glass tank. The tank was linearly (salinity) stratified using the two tank method. Particles were released at the surface of the tank using a syringe with the end cut off. This proved to be successful in releasing all of the particles virtually simultaneously without imparting undue momentum to the particles. Particles consisted of either glass beads, sand, brass filings, crushed quartz or plastic beads. This resulted in relative densities ranging from approximately 1.5 to 7.8. Particle sizes varied from 0.15 mm to 2.3 mm. Dye was added to the particles via a small amount of finely crushed potassium permanganate crystals. The dye crystals rapidly dissolved within the fluid captured by the particle cloud. This dyed fluid was then digitised from video images. The digital images were used to calculate the position of the centroid of the particle cloud (fluid) and its size. Figure 2 shows a series of the digitised images for a particle release. It is quite noticeable that the particle cloud (fluid) has a considerable lateral spread following the particle cloud reaching its depth of maximum penetration.

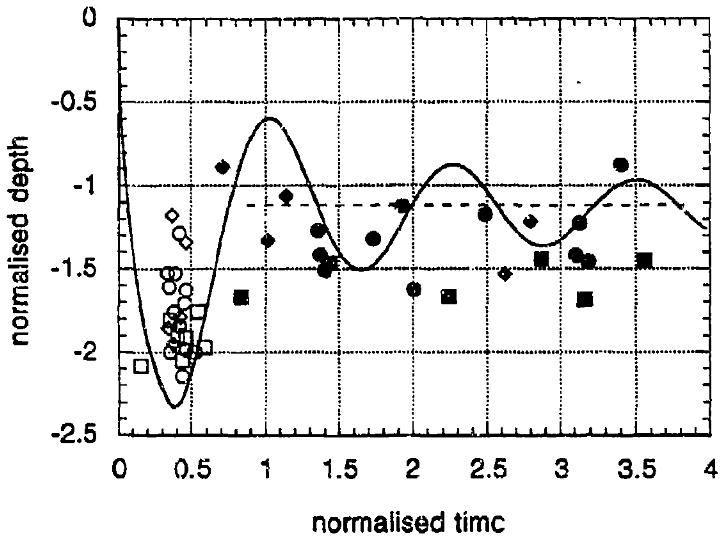

Figure 4 Normalised experimental results for maximum penetration depth (open symbols) and final depth (solid symbols) for fluid captured by particle clouds. The final depths in the laboratory experiments were measured once the oscillations in the depth of the captured fluid had basically ceased. Values of the stratified cloud number N_{cs} between 0.03 and 0.05 are indicated by squares, between 0.07 and 0.09 by circles and greater than 0.10 by diamonds. The line shown is the curve produced by the numerical model for the case where N_{cs} is equal to .03. It should be noted that the oscillations in h for the experiments were dampened more rapidly than those predicted by the model. Therefore, the experimental results for the final depth (ie solid symbols) should only be compared with the average final depth for the model results (dashed line).

The experimental results consistently showed smaller maximum penetration depths than the numerical results (see Figure 4). It is expected that this is due to the cloud number N_{cs} being more significant than in the numerical modelling. Despite some scatter in the experimental data, a general trend of decreasing maximum penetration distance z_p with increasing values of N_{cs} is evident from Figure 4 (as the cloud number N_{cs} increases, the particles drop out of the particle cloud at an earlier stage and reduce the buoyancy B of the cloud). Another possible effect may be greatly increased drag on the particle cloud due to the ambient fluid being stratified (energy is radiated away by internal waves). Both of these effects are currently being investigated in more detail.

The final depths of the fluid entrained by the particle clouds was consistently greater by a small amount than the final value indicated by the modelling. The greater the maximum penetration depth z_p, the greater the final equilibrium depth, suggesting that the maximum equilibrium depth will occur when the greatest maximum penetration depth z_p occurs (ie when the cloud number N_{cs} is small).

Conclusions

The maximum penetration depth and equilibrium depth of fluid captured by a particle cloud in a stratified fluid is a function of $(B/\rho N^2)^{1/4}$ and the cloud number N_{cs}. These depths decrease as $(B/\rho N^2)^{1/4}$ decreases and as N_{cs} increases. The maximum penetration depth will always be less than $2.3(B/\rho N^2)^{1/4}$. Initial results seem to indicate a maximum final depth for fluid captured by particle clouds of $1.7(B/\rho N^2)^{1/4}$.

Stratification may possibly affect the maximum penetration and final depths of a particle cloud by increasing drag on the particle cloud above that occurring in an unstratified fluid.

Acknowledgements

The majority of the laboratory experiments were performed by Mr Peter Horton. Mr Hamid Rahimipour kindly provided the photo that was used in Figure 1.

References

Bühler, J. and Papantoniou, D. A. (1991). "Swarm of coarse particles falling through a fluid." Proceeding of Int. Conf. of Environmental Engrg., Hong Kong, 1991, pp. 135-140.

Escudier, M. P. and Maxworthy, T. (1973). "On the motion of turbulent thermals." J. Fluid Mech., Vol. 61, pp. 225-251.

Nakatsuji, K., Tamai, M. and Murta, A.M. (1990). "Dynamic behaviours of sand cloud in water." Proceedings of Conf. on Physical Modeling of Transport and Dispersion, M.I.T., Boston, 8C.1-8C.6.

Rahimipour, H. and Wilkinson, D. L. (1992). "Dynamic behaviour of particle clouds." Proceedings of 11th Australasian Conf. of Fluid Mechanics, Hobart, Tasmania, pp. 743-746.

Internal waves, vortices and turbulence in a wake past a bluff body in a continuously stratified liquid.

Yuli D. Chashechkin

The Institute for Problems in Mechanics RAS
E-mail:chakin@ipm.msk.su Fax:7/095 9382048

The study of spatial structure of the uniform stratified flow past an obstacle is a traditional problem of fluid dynamics. Lee or associated (attached) internal waves and attached rear vortices determine a structure of "clouds bands" and position of the "windows of transparency" in the down- stream wakes behind mountains. Large internal waves are observed in the ocean with topography. Experimental data collected in an environment, mutual analytical and numerical calculations stimulated a development of a modelling of stratified flows in a compact laboratory tank. Besides wakes past different elements of topography - isolated hills and mountain systems-current in vicinity of perfect 2D and 3D bodies — a cylinder [1], a sphere [2] is studied also. This data is used for testing an analytical and numerical model of internal waves, laminar and vortex wakes.

The traditional model of stratified flow past obstacle includes upstream disturbances (blocked fluid), viscous boundary layer, internal waves ahead and past the body and wake with attached or shedding vortices [3]. Modern optic techniques with high spatial and temporal resolutions resolve additional stable elements of continuously stratified flow i.e. thin density boundary layer and density wake enclosed by the high gradient envelope [4]. The layers of density discontinuity separate the wake, isolated vortices and the internal wave field. The interaction between different elements of flow can be weak or strong in various ranges of parameters.

In this paper main results of studying 2D and 3D wakes in a linearly stratified liquid are given.

Dimensional and dimensionless parameters. Conventional system of fluid mechanics equations, describing the flow of a deep viscous isothermal continuously stratified liquid, includes the state equation for density $\rho = \rho_0(1 + \beta S(z))$ (β — is a salt contraction coefficient, $S = S(z)$ — salinity; axis z is vertical) and equations of momentum, mass and salinity conservation. These equations and appropriate boundary conditions (non–slipping for velocity and non–permeability for salinity on the surface of the body as well as attenuation of all perturbations at infinity) contain such dimensional parameters as density ρ_0 and its gradient $d\rho_0/dz$ (which can be described by reference density and buoyancy scale $\Lambda = (d|\ln\rho|/dz)^{-1}$, period and frequency $T_b = 2\pi/N = 2\pi\sqrt{\Lambda/g}$), velocity u, size of an obstacle d, pressure P, gravity acceleration g, kinematic viscosity ν, salt diffusion coefficient k_s. Conditions of geometric, kinematic and dynamic similarity lead to conservation of the dimensionless parameters such as Reynolds, Froude, Euler, Pecle numbers and density ratio $C = \rho/\Delta\rho(d) = \Lambda/d$. These parameters can be written in other forms if the basic scales will be chosen as the main characteristics of the geometry of the problem and structural elements of the flow.

The buoyancy scale Λ and obstacle size d are external (geometric) parameters of the problem. Intrinsic or dynamic scales depend on the body velocity. They characterize the length of attached internal waves $\lambda_i = 2\pi\lambda = 2\pi U/N$, velocity $\delta_u = \nu/u$ and density $\delta_s = k_s/U$ boundary layers thicknesses. Due to the difference of kinetic coefficients ("discerntion" of medium), effects of viscosity and diffusion can not compensate each other even in the boundary current, induced by diffusion in resting stratified liquids on a sloping plane [5] or in a inclined channel with slowly moving walls [6]. Conventional dimensionless parameters can be written as the ratio of basic scales: Reynolds number $Re = Ud/\nu = d/\delta_u$; Froude number $Fr = U/Nd = \lambda/d$; Pecle number $Pe = Ud/k_s = d/\delta_s$. Density ratio (ratio of geometrical scales) $C = \Lambda/d$ prescribes the value of a density gradient in laboratory tank for a given coefficient of reduction.

The countable number of secondary scales describes the sizes and variability scales of secondary flow elements (shear layers, vortices, sharp interfaces and so on) [7]. Among them can be stressed viscous wave scale $L_\nu = \sqrt[3]{\Lambda\lambda\delta_u} = \sqrt[3]{g\nu}/N$ which characterizes the modal structure of periodical internal wave beam [8] and limited vortex scale $L_u = \sqrt[3]{\nu^2/g} = \sqrt[3]{\delta_u^2\lambda^2/\Lambda}$ [9]. The ratio of thicknesses of velocity $\delta_u = \sqrt{\nu t}$ and density $\delta_s = \sqrt{k_s t}$ boundary layers induced by diffusion does not depend upon time $\delta_u/\delta_s = \sqrt{\nu/k_s} = \sqrt{Sc}$ [5].

For weak stratification the values of basic scales are essentially different $\Lambda \gg d \gg \delta_u \gg \delta_s$; $d >< \lambda$ and form a set of imbedded gauges. The complete set of scales describe distinguished elements — Eigen form of flows. Boundaries on a flow regimes map which divide the regions with different structural elements, characterized by conditions of similarity (or equality) of scales of appropriate origin (condition of scales synchronism). In this case it follows from the definition of scales that the boundary on the flow regimes map plotted in the double logarithmic scales are straight line segments.

From scaling analysis follows that the experimental technique should provide for visualization and independent measurement of different fields simultaneously with high spatial and temporal resolution (the thickness of a density boundary layer in a salt brine is order $\delta_s = k_s/U = O(10^{-4}$ cm).

Techniques. The experiments have been carried out in several transparent tanks ($0.7\times0.25\times0.7\mathrm{m}^3$; $1.5\times0.4\times0.4\mathrm{m}^3$; $2.4\times0.6\times0.6\mathrm{m}^3$; $9\times0.6\times0.6\mathrm{m}^3$; $7\times1.2\times1.2\mathrm{m}^3$) filled from below by linearly stratified salt brine. Profiles of buoyancy and horizontal velocity were measured with density marker (i.e. the trace past vertically arising gas bubble). Different modification of the schlieren technique viz the vertical slit — the Foucault knife, the slit–thread in focus, the horizontal slit — the regular grating producing a colour shadow picture (rainbow method), markers, tracers, dye and electrolytic precipitation (anodic oxidation of tin, of lead or of their alloys under the action of a direct current) were used. Static and dynamic properties of contact sensors are checked during the experiments by methods of vertical oscillations or abrupt displacement [10]. Dynamics parameters of probes is varied due to their strong interaction with the stratified environment.

Main results. The schlieren image of the flow past horizontally moving sphere and density markers visualized the profiles of velocity ahead and past the body, internal waves and non-uniform wake (see Fig. 1). The sharp frontier of the density wake separate internal waves and vortex flow past the body. The onset of instability can be seen in the area of a maximum vertical expansion of the wake ($T_b = 4.1$s, $\Lambda = 4.2$m, $d = 2.0$cm, $C = \Lambda/d = 210$, $U = 1.12$cm/s, $Fr = U/Nd = 0.37$, $Re = Ud/\nu = 224$).

Fig. 1

A special probe and optical techniques were used to measure both the thickness of the thin envelop and the value of sharpened density gradient on it. Past the sphere its thickness was less then 0.8 mm, the original density gradient is two times reinforced. In a laminar wake behind a cylinder the thickness of envelope is 0.06 — 0.5 mm, the density gradient is 15 — 160 times reinforced. The small scale instability which rolled up or distorted the interfaces is observed.

The field of internal waves consists of zero frequency and transient internal waves ahead of a body and regular stationary attached waves past them. The amplitude and phase parameters of apparent waves can be described by the source-sink models. The number and position of point singularities depend upon the body sizes, stratification and velocity of towing. The vertical displacement in case of motion of a source sink systems is

$$\eta = \frac{R^2}{r^*}\frac{\sqrt{a^2+R^2}}{a}\sqrt{\frac{1-\sin^2\varphi\cos^2\theta}{\sin^2\theta}}\sin\left(\frac{Na}{U}\sin\varphi\cos\theta\right)\times$$
$$\times\cos\left(\frac{Nr^*}{U}\sin\varphi\right)+O\left(\frac{1}{r^{*2}}\right),\quad x^*>0 \tag{1}$$

where a is a distance between singularities, $r^*, \theta, \varphi(x^*, y, z)$ is the spherical (Cartesian) coordinates, coupled to the body, R is transverse size.

The shape of crest and trough for point source in the three — dimensional case is given by the equation $x^2+y^2+z^2 = r^2 = 1+y^2/z^2$; $x_i = x_{0i}N/U$, which transforms into semicircle in the centre–plane $x^2+z^2 = 1$.

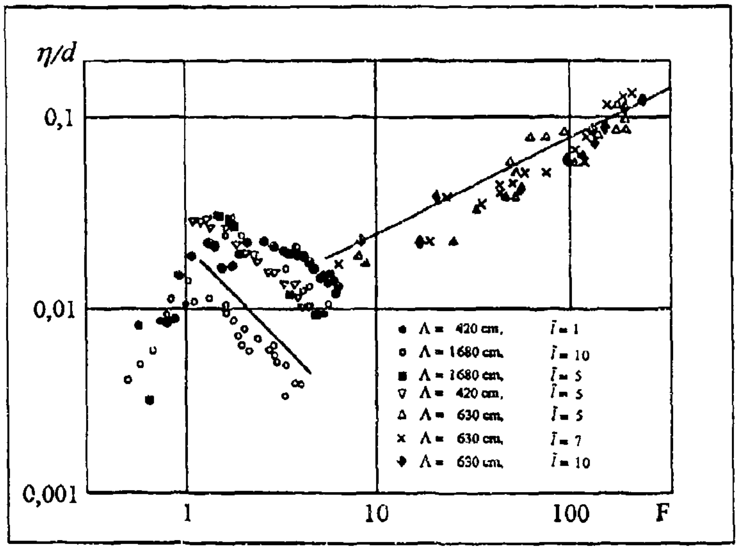

Fig. 2

Calculations of attached internal waves correspond with measurements everywhere except the vicinity of the frontier of the density wakes where the shape of the constant phase surfaces is distorted by a shear flow. The waves do not penetrate inside the density wake. The interaction between internal waves and density wake is strong. The length of domains of compressing and spreading of the wake in the vertical

Fig. 3

Fig. 4

direction corresponds to the local internal waves length. The crests and troughs of internal waves go explicitly through extreme points of the wake vertical size. The local wave length is

$$\lambda = \frac{UT_b \sin\theta}{\sqrt{1 - \sin^2\varphi \cos^2\theta}} = \frac{UT_b}{\sqrt{1 + x^{*2} y^2 / (y^2 + z^2)^2}} \tag{2}$$

The dependence of a maximum vertical displacements in an internal waves fields in the point $h = 12$ above the axis of motion is given in

Fig. 2. For small velocities ($\tilde{l} = l/d$, $F = UN/d \ll 1$) amplitude of wave oscillations is increased with Froude number ($\eta/d \sim \sqrt{F}$) it is decreased in the intermediate range ($1 < F < 6$), $\eta/d \sim 1/F$) and begins to rise again when the wake becomes the main source of internal waves ($\eta/d \sim F^{\frac{1}{8}}$). The shape of constant phase surfaces in the transverse plane is described by the solution for transient waves [11]. The appropriate schlieren image of the turbulent flow past body is shown in Fig. 3 ($\Lambda = 2.8$ m, $T_b = 3.4$ s, $t = 2.8$ s).

Pattern of turbulent flow in the longitudinal center plane is shown in Fig. 4. In this case the vertical slit cuts out a narrow band from the schlieren image of flow which was registrated by the film, moving with constant velocity. The velocity of the body was $u = 0.8$ m/s, $T_b = 4.2$ s, speed of the film was 0.015 m/s, contraction in the longitudinal direction is 53 times. The first group of the short internal waves is produced by the body, the second and the following ones are generated by the turbulent wake. Superfine structure on the periphery of the turbulent wake is caused by elongated interfaces with amplified value of the density gradient.

The sharpening of the initial gradient which takes place in a laminar, vortex (transient) and turbulent regimes of flow effect on the flow structure and its stability. For example in the wide range of parameters, but when the internal Froude number is less then 0.3, the density wake past a horizontally moving sphere in a linearly stratified fluid has a prismatic form. Four distinct enough ribs are formed by the intersections of two horizontal and two vertical high gradient sheets. At the smallest values of the Reynolds and Froude numbers, the density wake is compressed in lateral direction and stretched along the vertical. With increasing of velocity of the body the wake is compressed along vertical direction and stretched in horizontal one. Gradually the trans verse sites of the wake are equalized and its cross section transforms into the square. With further increasing of velocity the wake became narrow in vertical and wide in horizontal directions. The distinguished ribs and sharp corners are maintained during its evolutions. In subsequent regimes the vertical wake size begins to increase due to the vorticity accumulation in the rear part of the body and the corners become more smoothed [9].

In the wakes behind 2D and 3D bodies one observes compact isolated vortex elements of a different form (segments of vertical vortex tubes, vortex billows, 3D circular rear vortices with a sharp boundary, regular vortex axis-symmetrical blobs in the wake ($m_\nu = d/L_\nu > 1$), regular vortices in the turning points of the wake meander ($m_\nu = d/L_\nu < 1$), puffs as well as elongated elements (threads, loops, horse-shoes) and their combinations. The boundaries between the different regimes in the double logarithmic scales are straight line sections ($Re^2 \sim Fr^{-3}$, $L^{*2} \sim \lambda_c^2$, $L^* = U^3/N\nu$; $\lambda_c^2 = d\lambda$ and $Re^2 \sim Fr^{-1}$, $\lambda_c^2 \sim$ or $\lambda_c \sim \delta_u$).

The topological structure of the density wake depends on the angle of the sphere trajectory with the horizon. As the slope increases the upper part of the density wake envelope defects greater than the lower one, they approach one another and eventually merges forming a opened through downstream density "valley". In the wide part of the "valley" a pair of inclined vortex columns can be formed. Simultaneously, the internal waves are restructured. All passive contaminants coming from the sphere surface are collected on the interfaces and on ribs of their intersections.

A more complicated structure has a flow behind 2D body, where together with embedded into the density wake eddies soaring or suspended isolated vortices and vortex systems are observed. Wakes of vortices also create discontinuities in the field of density gradient. In all regimes the density wake is contoured with or contain inside high gradient sheets. An initial continuous density profile undergoes strong distortion and high gradient interfaces are formed near and far from the body [12]. Two types of instability — small– and large–scale ones — and two types of turbulence both structural and active were observed. In the first case the density and its gradient are characterized by random functions but the profiles of velocity are smoothed. In the case of active turbulence all parameters can be described by random functions. All in all, fourteen types of flow past a horizontal cylinder are identified which are separated by straight line sections on the flow regimes map [7].

The experimental data show that the stable geometric properties of the wakes can be described by intrinsic length scales. Due to the difference of kinetic coefficients the scales of variability for different parameters do not coincide. The conditions of the similarity for scales of different origins describe the boundary in the flow regimes maps. High gradient interfaces increase the influence even for weak stratification, stabilize the vortex motion, enlarge the number of vortex forms and lead to strong interaction of different flow elements, including waves, density wake and vortices.

List of references

[1] Boyer D.L., Davies P.A., Fernando H.J.S., Zhang X. Linearly stratified flow past a horizontal circular cylinder. *Phil. Trans. Roy. Soc. Lond.*, 1989, A328, 501–528.

[2] Hopfinger E.J., Flor J.B., Chomaz J.M., Bonneton P. Internal waves generated by a moving sphere and its wake in a stratified fluid. *Exp Fluids*, 1991, v. 11, p. 255–263.

[3] Chashechkin Yu.D. Visualization and Identification of Vortex Structures in Stratified wakes. *Eddy structure Identification in Free Turbulent Shear Flows.* ed. J.P.Bonnet and M.N.Glauser. Kluwer Ac. Publ.,

1993, p.393–403.

[4] Chashechkin Yu.D. Hydrodynamics of a sphere in a stratified fluid. *Izvestiya AS USSR, Fluid Dynamics,* 1989, v. 24, N 1, p. 1–6.

[5] Kistovich A.V., Chashechkin Yu.D. The structure of transient boundary flow along an inclined plane in a continuously stratified medium. *J. Appl. Maths. Mechs.,* 1993, v. 57, N 4, p. 633–639.

[6] Baydulov V.G., Chashechkin Yu.D. Influence of Diffusive Effects on a Boundary Flow in a Continuously Stratified Fluid. *Izvestiya RAS, Atmospheric and Oceanic Physics,* 1993, v. 29, N 5, p. 66–672.

[7] Chashechkin Yu.D., Voeikov I.V. Vortex systems past a cylinder in a continuously stratified Fluid. *Izvestiya RAS, Atmospheric and Oceanic Physics,* 1993, v.29, N 26, p. 821–830.

[8] Makarov S.A., Nekludov V.I.,Chashechkin Yu.D. Spatial Structure of Two–Dimensional Monochromatic Internal Wave Beams in an Exponentially Stratified Liquid. *Izvestiya AS USSR, Atmospheric and Oceanic Physics,* 1990, v.26, N 7, p. 744–754.

[9] Sysoeva E.Ya., Chashechkin Yu.D. Vortex systems in the stratified wake of a sphere. *Izvestiya AS USSR, Fluid Dynamics,* 1991, v. 26, N 4, p. 544–551.

[10] Gvozdev A.V., Nekludov V.I.,Chashechkin Yu.D. Comparative analysis of dynamic characteristics of contact probes. *Izmeritel'naya tekhnika,* 1990, N3, p. 21–23.

[11] Chashechkin Yu.D., Makarov S.A. Transient internal waves. *Docklady AS USSR,* 1984, v.276, N 5, p. 1246–1250.

[12] Voeikov I.V., Chashechkin Yu.D. Formation of discontinuities in the wake of a cylinder in a stratified flow. *Izvestiya RAS, Fluid Dynamics,* 1993, v. 28, N 1, p. 14–18.

The Structure and Long-Time Evolution of Bluff Body Wakes in a Stable Stratification

G.R. Spedding F.K. Browand
A.M. Fincham
Department of Aerospace Engineering,
University of Southern California,
Los Angeles, CA 90089-1191

Abstract

Experiments on late wakes ($Nt > 20$) of towed spheres in a stably stratified fluid reveal some startling similarities and differences when compared with the homogeneous *3D* case. Wake-averaged fluctuating components scale remarkably similarly, but the mean centreline velocity is one order of magnitude higher. The reasons for this may lie in the increased coherence and organisation of the patches of vertical vorticity, which are stable and persist for very long times.

1 Introduction

Wakes of axisymmetric bodies in a stable stratification exhibit certain interesting properties that distinguish them from their non-stratified counterparts. Among the most well known of these is the propensity for the long time wake to evolve to a state that is characterised by the presence of stable patches of vertical vorticity having large horizontal length scales compared with any vertical structure, and for this apparently stable wake structure to persist for very long times. The field was reviewed by Lin & Pao [1], and has been the subject of recent investigations by Lin *et al.* [2], and by Chomaz and colleagues (*e.g.* [3] and references therein). However, with the latter exception, there have been few quantitative measurements of the wake velocity field, particularly at late times. All of the wake structure measurements for axisymmetric bodies in [1] are for self-propelled bodies and, owing to the difficulty of making the measurements, the results in [3] (for towed spheres) were for selected cases only.

In the absence of any influence from exterior boundary conditions, the flow is determined by the values of two dimensionless parameters, the Reynolds number, $Re = 2UR/\nu$ (U is the sphere speed, R its radius, and ν is the kinematic viscosity), and the internal Froude number, $F = U/NR$, where $N = (-g/\rho_0(\partial\rho/\partial z))^{\frac{1}{2}}$ is the Brunt-Väisälä frequency. It is essential, not only to vary these parameters independently, but also that high $[Re, F]$ are considered, bearing in mind the practical applications.

This paper dicusses the evolution of the vortex wake in a single series of experiments at constant $Re \approx 5 \times 10^3$ over a range of Froude number, $F = [1.2, 2, 4, 7.9]$. The data are a subset of independent variations of Re and F over $Re \in [10^3, 10^4]; F \in [1, 10]$.

2 Quantitative Experiments

2.1 Apparatus

Spheres with diameters (D) of 1.9, 2.54 and 3.8 cm were mounted on three thin ($d =$ .025cm) wires, under tension in an inclined plane and suspended between three thicker support cables lying just below the surface and just above the bottom, respectively (Figure 1). The effects of the top and bottom slider assemblies are confined mostly to the boundaries, and $Re_d \approx 50$ so the support wires have little effect on the sphere wake itself. The spheres were towed through a 2.4m^2 plexiglass box with a 1.35m extension to allow for transient and startup effects. Since the water depth, H, is 24cm, confinement effects can be observed, but do not appear to affect the particular results reported here.

2.2 Procedure

The tank was filled with the standard two-tank method to create a linear density gradient. Once full, the tank was seeded with a high spatial density of neutrally-buoyant polystyrene beads, about 1mm in diameter, and sorted by density so that the bead density variation is less than .05% ($\rho_0 = 1.0475 \pm .0005$). The beads thus mark an isopycnal located at the midplane of the body, to within one bead diameter.

In each experiment, the bead distribution in $\{x, y\}$ was first homogenised by towing a vertical rake through the tank. After 40 minutes, allowing most of the residual motions to have decayed, the sphere was towed the length of the tank, beginning at the far end of the extension section. For each tow, a sequence of image pairs was recorded on an overhead CCD camera. The effective 'exposure' time, δt, and interval between successive frame pairs, Δt, were both optimised for the best resolution of the velocity field based on initial experiments. Images were transferred directly into PC RAM, and the entire sequence of events, including the mixing, towing, data transfer and sphere repositioning, was automated, operating under computer control.

Data were taken from early times corresponding to $Nt \simeq 20$, and continued until the wake could no longer be distinguished from the background; this typically occured around $Nt \geq 3000$. Nt could also be related to downstream distance through the correspondence $x = Ut$.

2.3 DPIV

At each time step, two digitised particle images were interrogated and the mean displacement of information in a given subrectangle was estimated from the location of the cross correlation peak. A custom DPIV technique [4]) was used to give velocities with approximately an order of magnitude improvement in accuracy over standard DPIV methods. The two aspects most responsible for this are the decoupling of the interrogation search radius from the correlation box size, and an iterated interpolation/fitting method for accurate fitting of the cross-correlation peak. The velocity vectors were reinterpolated onto the regular interrogation grid to correct for systematic errors from the finite displacement of the particles during the effective exposure time, δt. This was accomplished with a two-dimensional smoothing spline algorithm [5], that also gives analytical expressions for reconstruction of the spatial velocity gradients. The usual errors stemming from finite differencing techniques were thus avoided, and the error in quantities derived from these gradients is much lower than usual, being at most 10% of the mean value.

2.4 Wake energy, enstrophy and dissipation

A wake width, L_W, can be defined by computing an X-averaged $\langle U(y)\rangle_X$ profile, over the streamwise length of the measuring area, $\Delta X = 1.9$m (Figure 2), and L_W can be taken as the crosstream distance where $\langle U(y)\rangle_X > 0.2\langle U_0\rangle$, and $\langle U_0\rangle$ is the mean centreline velocity. L_W thus defines inner and outer wake regions at each timestep. Spatially-averaged quantities within this region will be denoted by $\langle\ \rangle$-brackets. So, defining $q = (u^2 + v^2)^{\frac{1}{2}}$ the local (inner wake) kinetic energy is,

$$E = \frac{1}{2}\langle q^2\rangle. \tag{1}$$

Similarly, given the vertical vorticity,

$$\omega_z = \frac{\partial v}{\partial x} - \frac{\partial u}{\partial y}, \tag{2}$$

then the local mean enstrophy is

$$W = \frac{1}{2}\langle {\omega_z}^2\rangle. \tag{3}$$

The single measurable component of the rate of strain tensor is

$$s_{ij} = \frac{1}{2}\left(\frac{\partial u_i}{\partial x_j} + \frac{\partial u_j}{\partial x_i}\right), i, j = 1, 2, \tag{4}$$

and, denoting ϵ as the kinetic energy dissipation rate due to horizontal gradients in horizontal velocity, then the mean value, S, in the inner wake region is

$$S = \langle\epsilon\rangle = 2\nu\langle\overline{s_{ij}s_{ij}}\rangle. \tag{5}$$

Taking X-averaged statistics at fixed times is equivalent to averaging over a certain downstream portion of the wake in body coordinates. Ideally, the averaging domain, ΔX, should be a small fraction of the total wake length, X. At long times, and for large F, this is so. The general expression for $\Delta X/X$ is

$$\frac{\Delta X}{X} = \frac{\Delta X/R}{\left(\frac{U}{NR}\right)Nt}.$$

3 Results

Figure 3 shows a single example time series of ω_z for $F = 4, Re = 5286$. The wake vortices are coherent and persistent, though not isolated, and like-signed neighbours can be seen merging. At this F, lee waves in the exterior wake and out-of-plane motions in the interior wake have approximately the same amplitude.

Some simple scaling arguments demonstrate why this particular value of F is interesting. In order for the initial wake turbulence to be active over all scales, as would be the case in a non-stratified fluid, both Re and F must exceed some lower limit. One can think of the requirement on F being related to the baroclinic torque exerted by the gravitational field on the vertical overturning motions. The largest vertical size attainable by a turbulent eddy is of the order of the Ozmidov scale,

$$l_0 \approx \left(\frac{\epsilon}{N^3}\right)^{\frac{1}{2}} \approx \left(\frac{u'^3}{lN^3}\right)^{\frac{1}{2}}, \tag{6}$$

where ϵ is the dissipation, u' the fluctuating velocity, and l is a turbulent integral scale. For the turbulence to be initially unaffected by stratification, $l_0 \geq l$, so

$$\left(\frac{l}{l_0}\right) = \left(\frac{u'}{U}\right)^{\frac{3}{2}} \left(\frac{l}{D}\right)^{-\frac{3}{2}} \left(\frac{U}{2NR}\right)^{\frac{3}{2}} \geq 1. \tag{7}$$

Experimental results [6, 7] for turbulent wakes of spheres indicate that initial turbulence intensities are around 0.3, and l/D is about 0.4. This gives the criterion,

$$\left(\frac{U}{NR}\right)^{\frac{3}{2}} \geq 5, \quad F \geq 3, \tag{8}$$

for active turbulence on all scales. Not only is this result consistent with these wake measurements, but it also accords with observations in [8, 3].

3.1 Turbulence quantities scale as *3D* wakes

Similar extrapolation of unstratified, *3D* wake results leads one to predict that the turbulent velocity fluctuations and the integral lengthscales evolve as ([7, 9, 10])

$$\frac{u'}{U} \sim \left(\frac{x}{D}\right)^{-\frac{2}{3}}, \quad \frac{l}{D} \sim \left(\frac{x}{D}\right)^{\frac{1}{3}}.$$

If the horizontal wake width, L_W, scales initially as the *3D* result, then setting $u' = q, x/D = Ut/D, F = U/NR$, predictions can be made for the scaling behaviour of the horizontal wake width, and for the turbulent kinetic energy as

$$\frac{L}{D}\left(\frac{1}{F^{\frac{1}{3}}}\right) \sim (Nt)^{\frac{1}{3}} \tag{9}$$

and

$$\frac{q}{U}(F)^{\frac{2}{3}} \sim (Nt)^{-\frac{2}{3}}. \tag{10}$$

In fully-developed, homogeneous turbulence, only local scales of velocity and length are important and since $\omega_z \sim u/L$,

$$\left(\frac{\sqrt{\langle \omega_z{}^2 \rangle}}{U/D}\right) F \sim (Nt)^{-1}. \tag{11}$$

Finally, $\epsilon \sim u'^3/L$, so

$$\frac{\langle\epsilon\rangle}{U^3/D}(F)^{\frac{7}{3}} \sim (Nt)^{-\frac{7}{3}}. \tag{12}$$

These dependencies on Nt and F are simply the *3D*, unstratified wake scalings couched in stratified wake parameters. One might expect the flow to behave according to these scalings at early times, and then depart from them as stratification effects predominate. This does not appear to be the case, however. Figure 4 shows the normalised wake width as a function of Nt and F, for $Re \simeq 5 \times 10^3$. Figures 5-7 show the decay of q, W and S (3,5) in the same data, together with straight lines given by the exponents in (9-12). Despite the fact that the scaling arguments were derived from *3D* wake flows, they predict the data well in all cases, independent of F. Not only this, but the relationships apparently are followed even into very late times ($Nt > 500$), long after the initial 'collapse' at $Nt \simeq 2$, and long after the dynamics have become quasi-*2D* ($Nt \geq 20$).

3.2 Mean flowfield does *not* scale as isotropic wake

Figure 8 shows the L_W-normalised mean centreline profiles for the data in Fig. 3. The collapse of the data is good, except on the wings of the distribution where $U_0 < 0$. At each Nt the mean $\langle U(y)\rangle_X$ can be fit with a Gaussian of the form

$$\langle U(y)\rangle_X = U_0 e^{-(y/A_1)^2/2},$$

where $A_1 \equiv L_\sigma$, is a characteristic width of the Gaussian function, when $G(y) = \exp(-1/2)$. (Since this is the half width, and $\exp(-1/2) > 0.2$, then $L_\sigma < L_W$, typically $\simeq L_W/4$). Given this similar functional form, one may now search for scaling laws that predict L_σ and U_0 as:

$$\left(\frac{L_\sigma}{D}\right) \simeq B_0\left(\frac{x}{D}\right)^{B_1}, \tag{13}$$

$$\left(\frac{U_0}{U}\right) \simeq C_0\left(\frac{x}{D}\right)^{C_1}. \tag{14}$$

Figure 9 shows the L_σ-normalised wake width as a function of x/D and for the usual values of F. The solid curve is the data of [9]. The spread in the data for different F is approximately the same as in Figure 4, but it is clear that the stratified wakes are narrower than their unstratified counterpart; the highest F result lies closest to the isotropic case. Ignoring this F-dependence, a least-squares fit to all the data (see Table 1 for details) gives:

$$B_0 = 0.20, \quad B_1 = 0.36.$$

B_1 is not significantly different from the value of 1/3 obtained from unstratified wake similarity scaling. The mean centreline velocities are compared with available unstratified results [6, 7, 9] in Figure 10. Although they appear to decay at the same approximate *rate* as the unstratified wakes, the centreline velocities are almost an order of magnitude higher for a given x/D. However, a very approximate single estimate of U_0/U can be extracted from a velocity vector plot in [3] ($Re = 3920, F = 3, z/R = 1.6$), and the data point falls exactly in the range reported here. There is no consistent F-dependence evident over this range of F. The overall least squares fit gives:

$$C_0 = 4.23, \quad C_1 = -0.88.$$

F	B_0	B_1	C_0	C_1
1.2	0.13	0.40	3.16	-0.87
2.0	0.15	0.32	5.13	-0.95
4.0	0.33	0.27	4.58	-0.85
7.9	0.17	0.40	4.05	-0.86
av	0.20	0.36	4.23	-0.88
sd	0.09	0.06	0.84	0.05

Table 1: Constants specifying stratified wake decay rates.

The exponent C_1 is much larger than the nominal $-2/3$ value, but close to the value of -0.85 reported in [6].

4 Summary

Bluff body wakes in a stable stratification are characterised by a very organised and persistent arrangement of patches of vertical vorticity (Figure 3), so that, while the fluctuating velocity components and their statistics show good (and surprising!) agreement with the *3D*, homogeneous wake, the mean centreline wake velocity is an order of magnitude stronger. The increased order in the wake is also consistent with the reduced spreading rate (Figure 9) and with the opposite-signed mean flow on the wake margin (Figure 8). It remains to construct a reasonable model for the evolution and final arrangement of vortex lines that comprise such a wake and correctly predict its dynamics.

Acknowledgements The support provided by ONR Grant no. N00014-92-J-1062, administered by Dr. Pat Purtell, is gratefully acknowledged.

References

[1] JT Lin and YH Pao. Wakes in stratified fluids: a review. *Ann. Rev. Fluid Mech.*, 11:317–338, 1979.

[2] Q Lin, WR Lindberg, DL Boyer, and HJS Fernando. Stratified flow past a sphere. *J. Fluid Mech.*, 240:315–354, 1992.

[3] JM Chomaz, P Bonneton, A Butet, and EJ Hopfinger. Vertical diffusion in the far wake of a sphere moving in a stratified fluid. *Phys. Fluids*, 5:2799–2806, 1993.

[4] AM Fincham and GR Spedding. Low-cost, high-resolution DPIV for turbulent flows. *Exp. Fluids*, 1994. in preparation.

[5] GR Spedding and EJM Rignot. Performance analysis and application of grid interpolation techniques for fluid flows. *Exp. Fluids*, 15:417–430, 1993.

[6] CH Gibson, CC Chen, and SC Lin. Measurements of turbulent velocity and temperature fluctuations in the wake of a sphere. *AIAA J.*, 6:642–649, 1968.

[7] MS Uberoi and P Freymuth. Turbulent energy balance and spectra of the axisymmetric wake. *Phys. Fluids*, 13:2205–2210, 1970.

[8] JM Chomaz, P Bonneton, and EJ Hopfinger. The structure of the near wake of a sphere moving horizontally in a stratified fluid. *J. Fluid Mech.*, 1993. in press.

[9] PM Bevilaqua and PS Lykoudis. Turbulence memory in self-preserving wakes. *J. Fluid Mech.*, 89:589–606, 1978.

[10] H Tennekes and JL Lumley. *A first course in turbulence.* MIT Press, 1972.

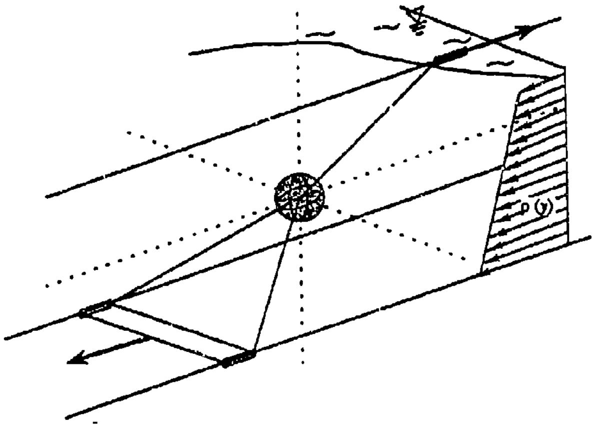

Figure 1. Arrangement of tow wires on the sphere.

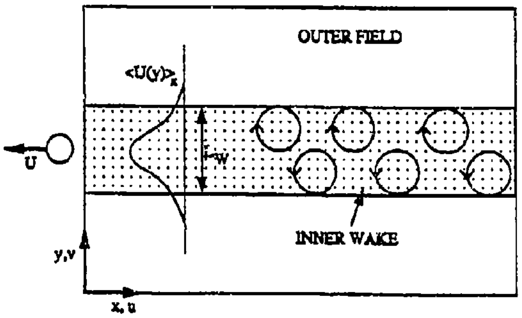

Figure 2. Wake geometry definitions.

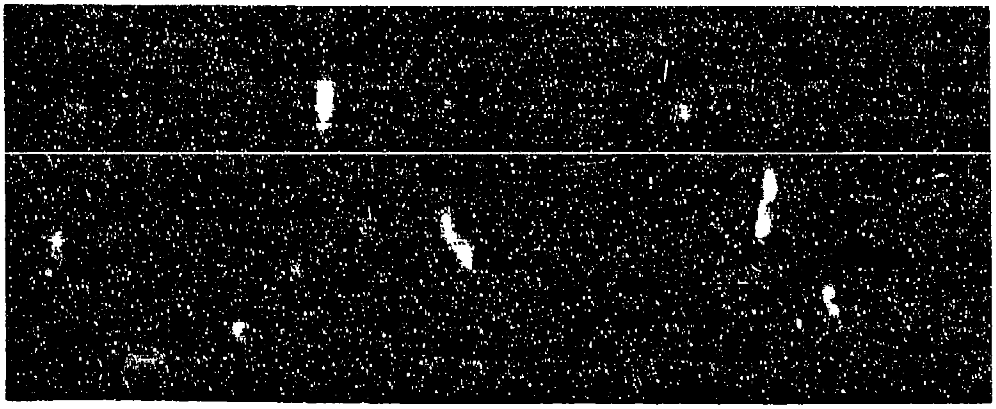

Figure 3. ω_x for 8 timesteps at $Re = 5300$, $F = 4$. $Nt = 40, 84, 138, 203, 283, 379, 497, 640$.

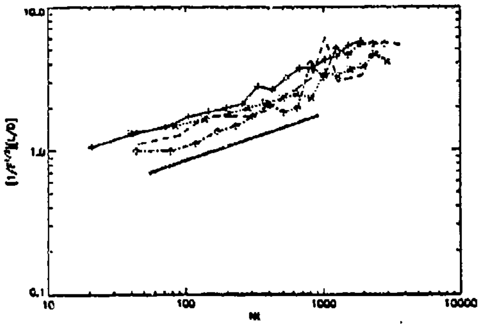

Figure 4. Normalised wake width vs. dimensionless time for $Re \simeq 5 \times 10^3$, and $1.2 \leq F \leq 8$. × — — ×, $F = 1.2$; + · · +, $F = 2.0$; · — —, $F = 4.0$; ◇ — · — ◇, $F = 8.0$.

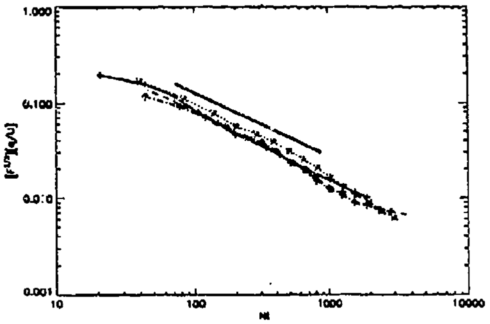

Figure 5. Normalised turbulent velocity decay.

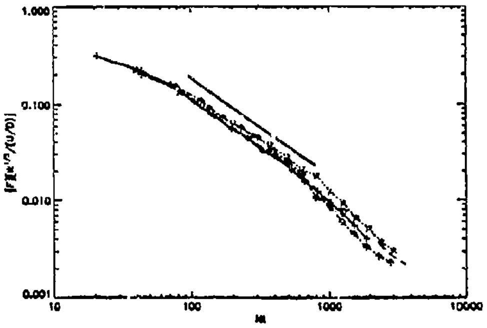

Figure 6. Normalised enstrophy decay.

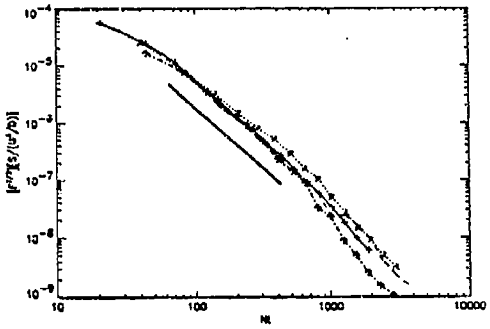

Figure 7. Normalised dissipation rates.

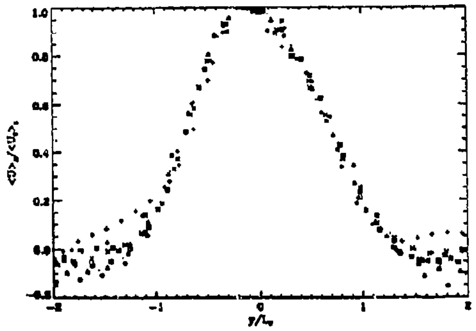

Figure 8. Self-similar scaling of $\langle U(y) \rangle_X$ for 9 values of Nt from $40 - 814$.

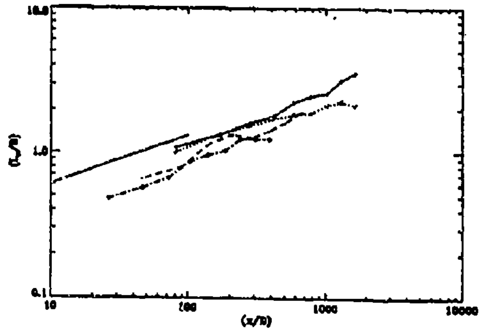

Figure 9. Evolution of L_v vs. x/D for $F = 1.2, 2, 4 \& 8$. Solid line is for $3D$ wake [3].

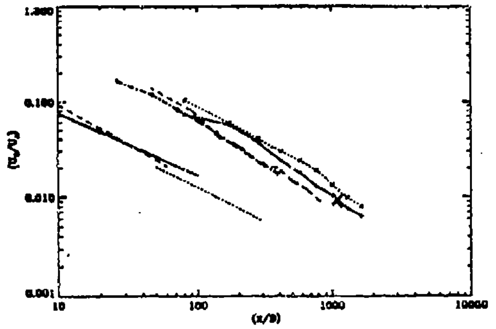

Figure 10. Decay of mean centreline velocity, compared with values from the literature in [5]——,[7]· · ·, [6]— — —. The × point was estimated from Fig. 6 in [3].